THE CATHOLIC UNIVERSITY OF AMERICA

Experimental Study and Modeling of the Mechanical Behavior Of Cross-Anisotropic Sandstone

A DISSERTATION

Submitted to the Faculty of the

Department of Civil Engineering

School of Engineering

Of The Catholic University of America

In Partial Fulfillment of the Requirements

For the Degree

Doctor of Philosophy

By

Niels Trads

Washington, D.C.

2010

Experimental Study and Modeling of the Mechanical Behavior of Cross-Anisotropic Sandstone

Niels Trads, Ph.D.

Director: Poul V. Lade, Ph.D.

In natural soils cross-anisotropic fabric is common due to deposition in a gravitational field. The behavior and properties of sandstone are different from sand due to cementation. The focus of this study is to describe the features connected with cross-anisotropy and cementation. Furthermore, a model capable of predicting the behavior of cross-anisotropic sandstone is developed based on The Single Hardening Model.

First the behavior of cross-anisotropic sandstone is examined in a literature review of cemented geological materials. The behavior is further explored by triaxial and torsion shear tests on artificially cemented sandstone. A review of The Single Hardening Model revealed minor possible improvements, which are addressed by developing an improved plastic potential function and a new softening function.

The triaxial tests showed that cross-anisotropic sandstone has an initial cementation yield surface. Hollow cylinder torsion shear tests confirmed the behavior inside the cementation yield surface to be elastic. The elastic behavior inside the cementation yield surface was found to be stiffer in vertical direction than in horizontal direction. The failure surface at high confining pressures corresponds to the critical state line. At intermediate confining pressures the failure surface is curved and at low confining pressures the failure surface is affected by the initial cementation yield surface similar to overconsolidated soil, increasing the strength further. The cross-anisotropy was

found to decrease as the confining pressure increased and the cementation started to break.

The modeling of the cementation is captured by translation of the stress space. As the cementation breaks down, the stress space moves back towards the origin, corresponding to uncemented sand. The rate of decementation is controlled by the initial cementation yield surface and a second yield surface corresponding to zero tensile strength. The cross-anisotropy is modeled using a microstructural tensor describing the anisotropy in the material. The cross-anisotropic model requires parameters corresponding to vertically cored specimens and horizontally cored specimens. The model then averages the behavior depending on the loading direction. To successfully model the artificial cross-anisotropic sandstone tested here, it was found sufficient to apply the modifications to the failure surface and the yield surface.

This dissertation by Niels Trads fulfills the dissertation requirement for the doctoral degree in Civil Engineering approved by Poul V. Lade, Ph.D., as Director, and by Lu Sun, Ph.D., and George P. Mavroeidis, Ph.D. as Readers.

Poul V. Lade, Ph.D., Director

Lu Sun, Ph.D., Reader

George P. Mavroeidis, Ph.D., Reader

Table of Contents

List of Figures

List of Tables

Acknowledgment

I would like to express thank and gratitude to my advisor Professor Poul V. Lade for advice, help, and encouragement during my studies at The Catholic University of America.

The tuition cost related to the doctoral studies at The Catholic University of America was covered by the Dean of Engineering's Doctoral Scholarship.

This research was funded in part by the American Chemical Society Petroleum Research Fund under grand PRF # 40780-AC9.

1. Introduction

The focus of this study is the behavior and modeling of cross-anisotropic sandstone. The behavior is described based on a literature review and further explored by triaxial and torsion shear tests. The modeling focuses on expanding The Single Hardening Model to capture decementation and cross-anisotropy.

1.1 Cementation and Cross-Anisotropy

Sandstone is differentiated from sand due to cementation binding the grains together. Most grains are composed of quartz or feldspar whereas the origin of the cementation is more varied. However, the most common cementations are calcite, clay, or silica. The cementation prevents the grains from moving until broken down, and as a result the cohesion creates tensile strength in sandstone.

Cross-anisotropic (also named transversely isotropic) material has one axis of symmetry around which the material is isotropic. Due to the deposition in a gravitational field most sedimentary geological materials exhibit some degree of cross-anisotropy. The stress history is known to cause fissures with a preferred orientation thereby creating cross-anisotropic behavior. Furthermore, in large formations differences in porosity and degree of cementation between the individual layers of sandstone, can give rise to macroscopic cross-anisotropic behavior. However, at the level of each layer, the sandstone does not contain the cross-anisotropic features caused by the interlayered nature experienced at a larger scale.

The behavior exhibited by sandstone has many similarities with other porous rocks (e.g. chalk, diatomite, limestone, schist, and shale), weakly cemented sands, and certain types of porous concrete. Results obtained from these materials have to some extent been used as a general guideline for the behavior of cross-anisotropic sandstone.

1.2 Constitutive Modeling and Laboratory Testing

The purpose of a constitutive model is to mathematically express the stress-strain behavior of a material. The model needs to be able to handle the initial conditions of the material, the boundary conditions, and the loading conditions. Once these conditions are known, the model should be able to predict the behavior of the material based on predetermined parameters. A low number of parameters are desirable, to keep the model as simple as possible, while still capturing the behavior accurately. Furthermore, a certain amount of flexibility in the acceptable range of parameters is required to incorporate the large variation in behavior experienced in natural soils.

In laboratory experiments the initial, boundary, and loading conditions are controlled and results are therefore used in development of constitutive relations. During laboratory testing it is assumed that the material distribution, the stresses acting on the specimen, and the strains measured are uniform on the macroscopic level. Any experimental determination of constitutive behavior therefore yields the relationship between the average properties measured in the experiment.

Natural soils experience large variation in initial material conditions due to e.g. composition of the grains, gradation, void ratio, stress history, anisotropy, and

cementation. Some of these features can easily be incorporated in a model while others require additional functions and parameters.

1.3 Aim of Research

1.3.1 Review of The Single Hardening Model

The first goal is an evaluation of The Single Hardening Model based on previously published experimental data on sand. Focus will be on examining the plastic potential function, the hardening parameters, and the softening function.

Predictions of tests on sand performed over a large range of confining pressures show that The Single Hardening Model tends to underestimate the volumetric change at high pressures. Observations during the parameter determination indicate that this arises from the plastic potential function. This will be addressed by modifying the plastic potential function.

In silty sands, the volumetric change differs from that experienced in regular sands. The sand and silt grains form a collapsible structure, resulting in almost identical volumetric change during shearing in triaxial compression irrespective of the confining pressure. The determination of the corresponding yield surface parameters yields ambiguous results. It has been found that changing the procedure for the determination of the hardening parameters solves this problem. The result is different hardening parameters and unambiguous yield surface parameters.

Finally, a new softening function that ensures a smooth transition from hardening over failure to softening has been developed. This allows more precise modeling and opens up to better prediction of shear bands in the vicinity of smooth peak failure.

To fully exercise the enhanced model, predictions of torsion shear tests on sand are performed. These tests contain both triaxial loading and rotation of the principal stresses.

1.3.2 Experiments on Sandstone

The experimental study of the behavior of sandstone consists of two separate studies. First the elastic behavior inside the cementation yield surface is examined by hollow cylinder torsion shear tests. Second, the behavior of cross-anisotropic sandstone is examined by series of triaxial compression tests on vertically and horizontally cored specimens. Furthermore, isotropic compression tests, K_0-tests, and Brazilian tests are performed to supplement the triaxial tests.

Both studies are conducted on artificial sandstone. In the first study three hollow cylinder torsion shear specimens are produced and loaded to determine weather the sandstone behaves elastic or plastic inside the initial cementation yield surface.

For the second study two blocks of artificial cross-anisotropic sandstone are produced and specimens cored vertically and horizontally are tested to determine the effect of cross-anisotropy. Triaxial tests performed over a large range of confining pressures ensure the effect of decementation is captured. Furthermore, the isotropic compression tests and the K_0-loading are used to determine the transition from elastic

behavior inside the cementation yield surface to the plastic behavior associated with decementation. The Brazilian tests are performed to determine the indirect tensile strength.

1.3.3 Modeling of the Behavior of Cross-Anisotropic Sandstone

When modeling the behavior of cross-anisotropic sandstone, the focus will be on two individual features, (1) the effect of cementation and decementation, and (2) the effect of cross-anisotropy. The base for the predictions is the enhanced version of The Single Hardening Model.

The effect of cementation is modeled by translation of the coordinate system along the hydrostatic axis and as the cementation is destroyed the coordinate system slowly moves towards the original location, which corresponds to uncemented sand. The translation is controlled between two yield surfaces, one corresponding to the initial cementation and one corresponding to zero tensile strength.

The cross-anisotropy is modeled using a microstructure tensor describing the inherent anisotropy in the material. The tensor is applied to the yield function and the failure criterion. The advantage of the microstructure tensor approach is that it allows predictions with stress rotation.

2. Previous Studies

2.1 Behavior of Sandstone

The cementation in sandstone acts as bonds between the individual grains, preventing movement of the grains before the cementation is broken (Clough et al. 1981). This results in behavior similar to the behavior of overconsolidated soil, where an initial yield surface exists. According to Leroueil and Vaughan (1990), the initial yield surface is affected by structure in the material. Structure has also been identified in uncemented soil and can be caused by deposition of silica at particle contacts in sands, from cold welding at interparticle contacts under high pressure, from deposition of carbonates, hydroxides, or organic matter from a solution, and from recrystallization of minerals during weathering (Leroueil and Vaughan 1990). In cemented soils, the structure can further arise from interlocking fabric (Clough et al. 1981, Cuccovillo and Coop 1999). Furthermore, the ratio between the strength of the grains and the strength of the cementation, results in different structure (Cuccovillo and Coop 1999). As the effect of cementation and structure are similar and difficult to distinguish in weakly cemented soil (Leroueil and Vaughan 1990), the behavior of weakly cemented soils described in the following sections (2.1.1 - 2.1.7) might arise from either, and no distinction is made.

2.1.1 Failure

During unconfined conditions the cemented soil behaves brittle and the strength is controlled primarily by the void ratio and the degree of cementation. Figure 2.1 shows the conceptual variation of compressive and tensile strength as a function of void ratio and cementation, based on findings by Huang and Airey (1998) and Consoli et al. (2007). An increase in the cementation results in an increase in the strength. Increasing the void ratio decreases the strength. At low void ratios, an increase in the degree of cementation results in a higher increase in strength than at high void ratios. This has been attributed to the particles being closer together at low void ratios causing the cementing agent to be more effective. At higher void ratios the cementing agent fills the voids thus having less of a binding effect on the grains and resulting in a lower increase in strength.

According to Lade and Overton (1989), the effect of cementation on the failure at low confining pressures is an increase in both friction angle and cohesion. This was attributed to cementation as well as an increase in dilation. This is in agreement with later findings by Schnaid et al. (2001), who found the effect of cementation at low confining pressures to increase both friction angle and cohesion.

In the intermediate range of confining pressures, the cementation breaks, and the effect of cementation was interpreted by Lade and Overton (1989) as a parallel shift of the failure surface equal to the cohesion. This corresponds to the findings by Clough et al. (1981) at low confining pressures.

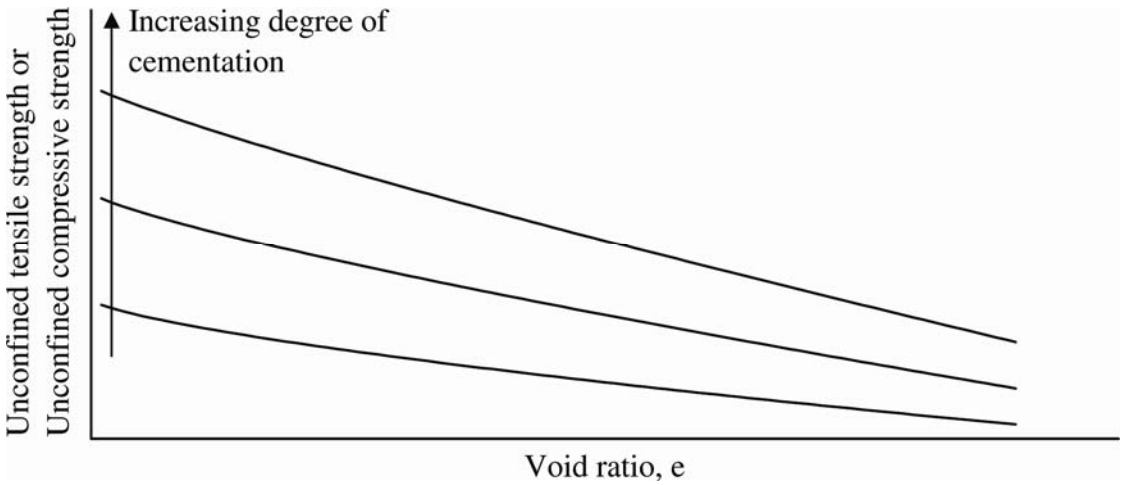

Figure 2.1: Relation between unconfined compressive/tensile strength and void ratio with degree of cementation.

Under high confining pressures, the soil behavior becomes ductile, with a substantial amount of plastic deformation prior to failure. Under these conditions the effect of the cementation is insignificant and only the friction angle is slightly increased by the initial cementation (Coop and Atkinson 1993). Tests by Lade and Overton (1989) indicated the strength at high confining pressures of a material with lower degree of cementation could surpass the strength of the same material but with higher degree of cementation. This was explained by the material with the lower degree of cementation experiencing an increased compression during application of the higher confining pressure, thereby creating additional frictional strength.

After the bonds are broken, the soil does not necessarily return to the behavior of the similar uncemented soil (Clough et al. 1981). This is due to lumps of cemented material acting as larger particles. However, Reddy and Saxena (1993) found the residual strength of an artificially cemented soil to be independent of the initial degree of cementation. This was experienced for triaxial compression tests at both low and high confining pressures.

The effect of the intermediate principal stress on the strength of sandstone and mudstone was examined by Lee et al. (1999, 2002). In both materials the effect of the intermediate principal stress was a reduction of the strength resulting in the octahedral shape of the failure surface to be a smoothly cornered triangle (Figure 2.2). This is in agreement with tests performed by Reddy and Saxena (1993) on artificially cemented sand. This effect of the intermediate principal stress was also noted by Al-Ajmi and Zimmerman (2005) after compiling triaxial strength data of eight different porous rocks.

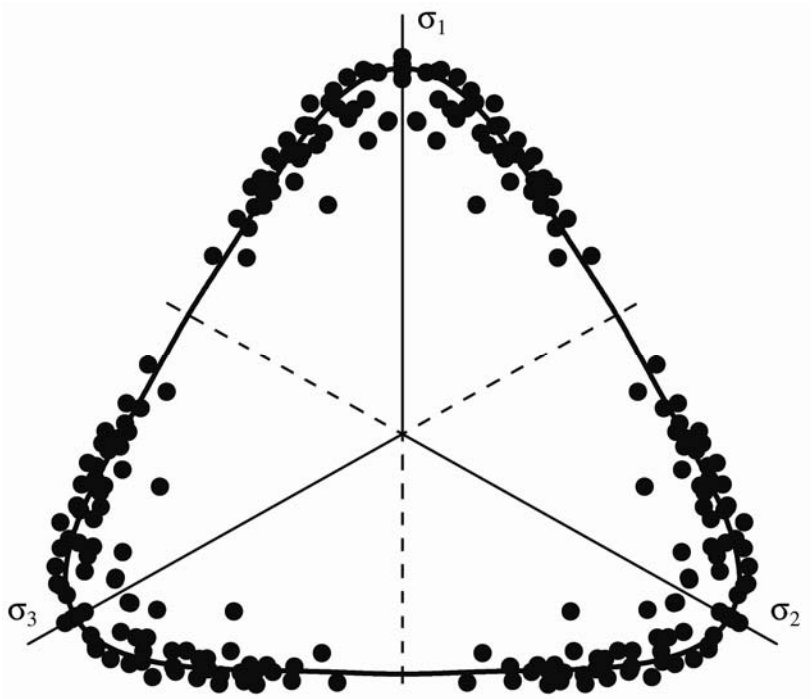

Figure 2.2: Shape of failure surface for Shirahama Sandstone in the octahedral plane. Data from Takahashi and Koide (1989).

2.1.2 Yielding

The presence of cracks and fissures on the micro-scale affects the overall strength of a porous rock. An increase in the overall stress magnitude also causes higher local stresses. If the local stress exceeds the local strength, cracks occur, grow and interact. If the orientation or the magnitude of the principal stresses change, new damage may occur. Apart from the stress magnitude and orientation, the amount of new damage depends on the damage that has previously been induced, Kranz (1983).

The permanent damage results in plastic deformation and can be used to determine the yield surface. Pestman and Van Munster (1996), Wong et al. (1997), and David et al. (1998) measured the acoustic emission to determine the bond breakage in sandstones and cemented sand. They found a significant increase in acoustic emission when the cementation starts breaking. The approximate shape of this damage-surface is shown in Figure 2.3 in the p-q stress space. The mean stress, p is defined in equation (2.1) and the deviator stress q is defined in equation (2.2):

$$p = \frac{\sigma'_1 + 2 \cdot \sigma'_3}{3} \qquad (2.1)$$

$$q = \sigma'_1 - \sigma'_3 \qquad (2.2)$$

in which σ'_1 is the effective major principal stress and σ'_3 is the effective minor principal stress.

The damage-surface determined from the acoustic emission has been linked to the stress-strain relation by Wong et al. (1997). The relation between the mean stress p and the volumetric change ε_{vol} during hydrostatic compression is named the hydrostat. During

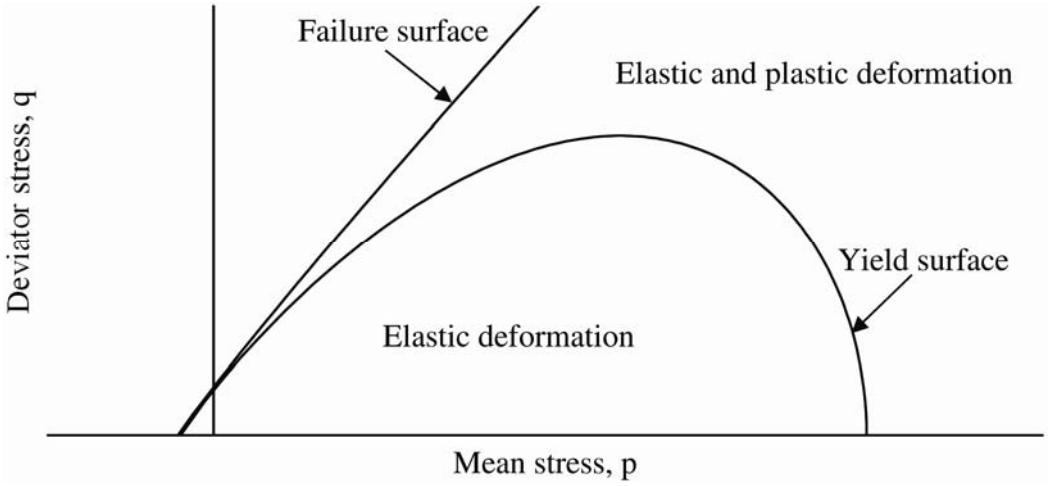

Figure 2.3: Shape of yield surface determined from acoustic emission.

triaxial loading, the relation between the mean stress p and the volumetric change ε_{vol} follows the hydrostat until yielding. This is demonstrated in Figure 2.4 a) where the hydrostat and two triaxial tests are shown. The triaxial test at low confining pressure dilates, and the triaxial test at high confining pressure contracts. The yield point where the triaxial tests deviate from the hydrostat is associated with the increase in acoustic emission.

The method described for determination of the cementation yield surface is used by David et al. (1998) to determine the relation between cement content and the size of the cementation yield surface. They found that by increasing the cement content, the yield surface increased in size, shifting the brittle-to-ductile transition towards higher pressures.

The yield surface separates elastic behavior from elasto-plastic behavior, and the elasticity experienced inside the yield surface is often considered linearly elastic. Therefore, the deviation from a linear stress-strain relation can also be used to determine the yield surface (e.g. Airey 1993, Leroueil and Vaughan 1990). This is shown in Figure 2.4 b) based on a procedure described by Airey (1993) where both axial and radial strains are used.

Post yielding behavior (often referred to as cataclastic flow) is dominated by grain crushing and pore collapse (Wong et al. 1997). According to Pestman and Van Munster (1996), the yield surface expands and provides the state of crushing corresponding to the state of stress to which the material has previously been subjected.

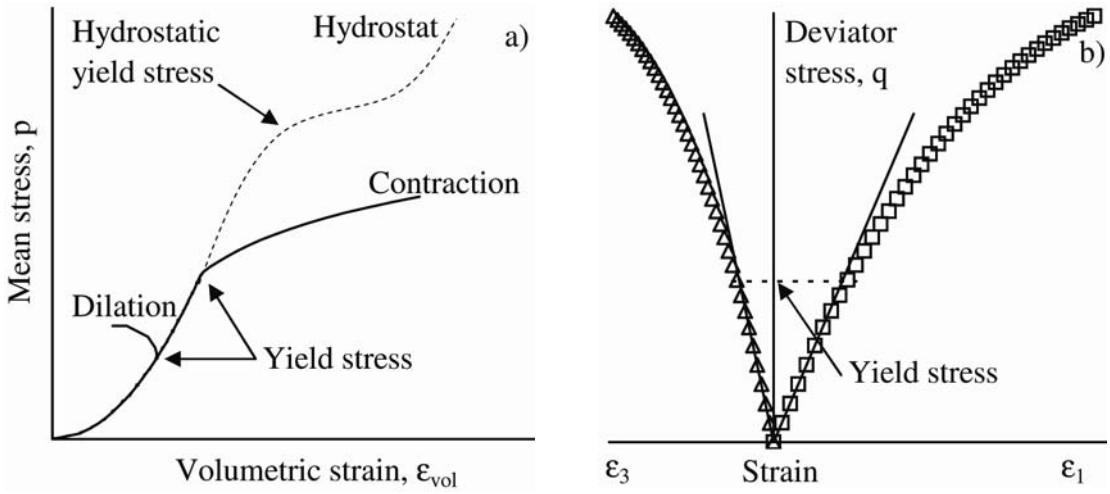

Figure 2.4: Determination of yielding. a) From deviation from hydrostat. After Wong et al. (1997). b) From deviation from linear behavior. After Airey (1993).

2.1.3 Elastic Behavior

The elastic behavior inside the cementation surface varies with the degree of cementation (Clough et al. 1981, Baig et al. 1997, Huang and Airey 1998, Schnaid et al. 2001, Sharma and Fahey 2004). Figure 2.5 summarizes their findings schematically. The relation between the elastic modulus and the stress is shown for increasing degree of cementation. The elastic modulus increases as the stress is increased, and increasing the degree of cementation results in higher elastic modulus as well. Furthermore, the elastic modulus becomes less dependent on the confining pressure with increased cementation. Baig et al. (1997) concluded that the effect of confining pressure was less significant at small strains, rendering the effect of confining pressure negligible for the dynamic properties of cemented soil.

The elastic behavior during cementation bond breakage has been studied under different loading conditions: Huang and Airey (1998) determined the static bulk modulus during isotropic loading, Fernandez and Santamarina (2001) determined the dynamic elastic modulus during isotropic loading, Sharma and Fahey (2003) investigated the degradation of stiffness during triaxial compression, and Yun and Santamarina (2005) examined the dynamic stiffness during K_0-loading. The general evolution of elastic modulus during breakage of the bonds is shown in Figure 2.5. As the bonds start breaking, a decrease in elastic modulus is experienced. As the elastic modulus of the cemented soil reaches that of the uncemented soil, the elastic modulus starts increasing, eventually becoming identical to that for the uncemented soil. If the initial degree of cementation is increased, the stress required to break the cementation increases and the

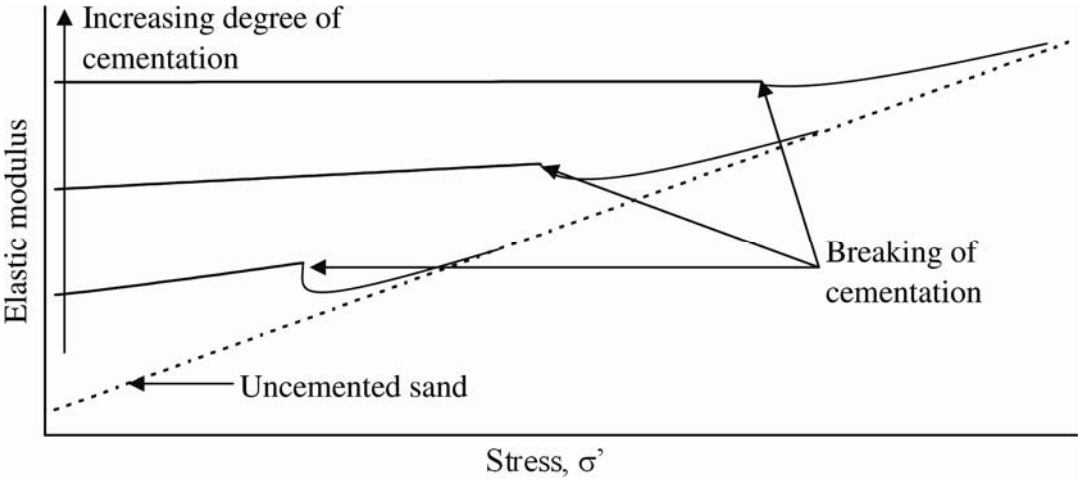

Figure 2.5: Evolution of elastic modulus with increasing cementation and pressure.

subsequent drop in elastic modulus diminishes. The dynamic elastic modulus has been found to not converge towards the elastic modulus of the uncemented soil as easily as the static elastic modulus.

The elastic modulus in tension and compression has been found to be similar. E.g. Talesnick et al. (2000) found the elastic modulus in tension and in compression to be approximately the same in sandstone and cemented sand. Liao et al. (1997) found argillite to be stiffer in tension than in compression. This was attributed to closure of micro-fissures in compression, indicating that stress history causes different elastic moduli in compression and tension. This is demonstrated in Figure 2.6 where the stress-strain relation in compression and tension is shown. In compression, Young's modulus increases as the fissures closes and eventually becomes equal to Young's modulus in tension. In tension the elastic modulus remains constant.

2.1.4 Stress-Strain Behavior during Triaxial Compression

Coop and Atkinson (1993) and Cuccovillo and Coop (1999) identified two types of behavior of cemented soil, based on the degree of cementation. These idealized behaviors are shown in Figure 2.7 and Figure 2.8. Figure 2.7 a) shows the location of the initial cementation yield surface and the critical state line for strongly cemented soil, with indication of three stress paths for triaxial compression. Figure 2.7 b) shows the normalized (with respect to q/p) stress-strain response corresponding to the three stress paths in Figure 2.7 a). Similarly, the yield surface, the critical state line, the failure surface and the stress paths for weakly cemented soil are shown in Figure 2.8 a). The cor-

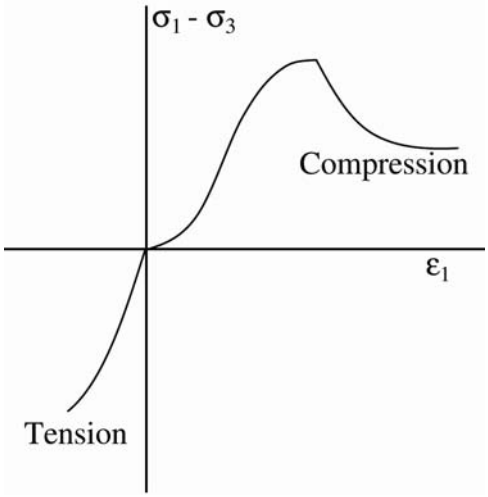

Figure 2.6: Closure of fissures results in initial lower Young's modulus in compression than tension.

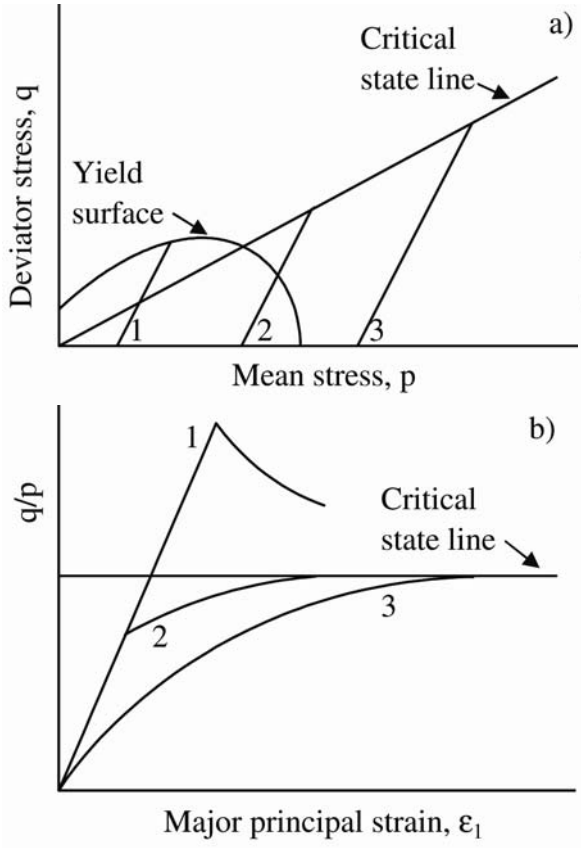

Figure 2.7: Idealized behavior of strongly cemented soil. After Coop and Atkinson (1993).

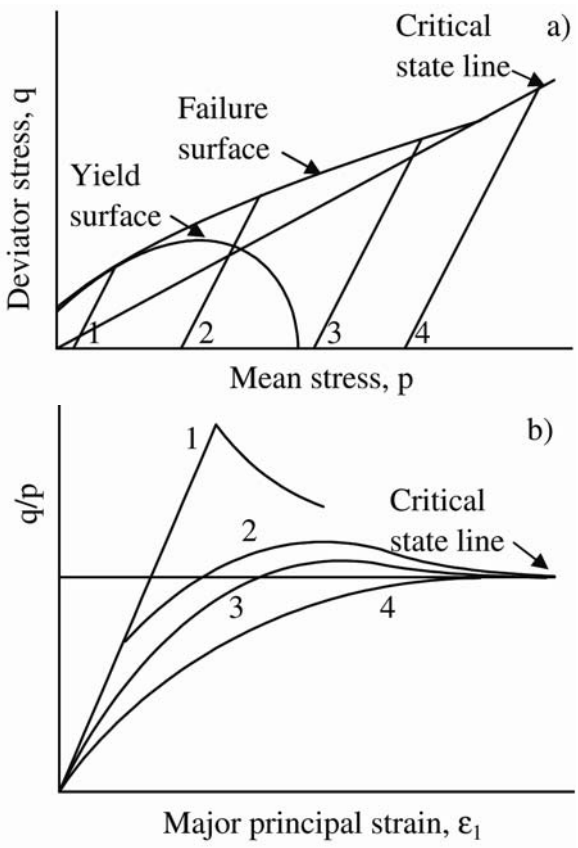

Figure 2.8: Idealized behavior of weakly cemented soil. After Cuccovillo and Coop (1999).

responding normalized stress-strain response is shown in Figure 2.8 b). Note Figure 2.7 a) and Figure 2.8 a) are shown with almost similar size of the cementation yield surface. If shown in the same scales, the cementation yield surface in Figure 2.7 a) would be significantly larger than the yield surface in Figure 2.8 a).

In the strongly cemented soil, the yield surface increases the peak strength at low confining pressures resulting in elastic behavior until failure. As the confining pressure increases, the yield surface is reached before the critical state line, resulting in first elastic, then elasto-plastic behavior. At high confining pressure only elasto-plastic behavior is observed.

In the weakly cemented soil, the stress-strain behavior is similar to the strongly cemented soil at low confining pressures where the behavior is elastic until failure, and at high confining pressures where only elasto-plastic behavior is experienced. In the intermediate range two other types of stress-strain behavior is observed, one starting inside the cementation yield surface and one starting outside. Both experience increased peak strength with subsequent reduction to the critical state line.

Wu et al. (2000) determined the onset of dilatancy inside the cementation yield surface for two different sandstones and found the onset of dilatancy to vary linearly with confining pressure. The best fit line was parallel shifted to intersect the q-axis, resulting in increased contraction (compared to sand) before the onset of dilatancy. This is in agreement with findings by e.g. Lade and Overton (1989) who found delayed onset of dilatancy with increased degree of cementation. Furthermore, the rate of dilatancy experienced was higher in cemented sand than in uncemented sand. As the confining

pressure increases, the rate of dilation decreases and at high confining pressures only contractive behavior is observed.

2.1.5 Stress-Strain Behavior during Isotropic Compression

The influence of cementation on the volumetric behavior during isotropic compression is shown in Figure 2.9. Until yielding, the cemented soil behaves elastic, and the degree of cementation determines the location of the yield point in comparison with the intrinsic compression line. In most cemented soils, yielding takes place beyond the intrinsic compression line. Lagioia and Nova (1995) observed temporarily unstable behavior in a strain-controlled isotropic compression test, corresponding to a reduction in the stress right after yielding. After yielding, the cementation breaks and the soil eventually returns to the behavior of the uncemented soil. Examples of behavior during isotropic compression can be found in e.g. Coop and Atkinson (1993), Leroueil and Vaughan (1990), Cuss et al. (2003).

In some natural soils, the initial behavior is softer due to closure of preexisting cracks and fissures (e.g. Cuss et al. 2003). The development of these cracks is further addressed in section 2.1.7.

2.1.6 Stress-Strain Behavior during K_0-loading

The behavior of sandstone during K_0-loading is similar to the behavior during isotropic compression. The loading starts elastically until yielding, where the cementation starts breaking and the soil eventually returns to the intrinsic compression line of the sand. This

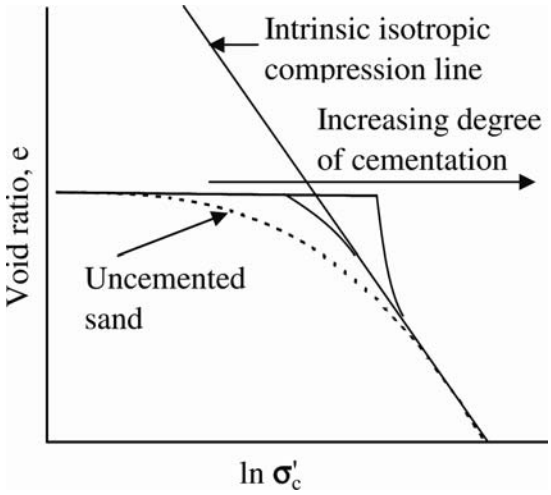

Figure 2.9: Schematic representation of the influence of cementation during isotropic compression. After Cuccovillo and Coop (1999).

is illustrated in Figure 2.10 a). Due to the difference in boundary conditions, compared with the isotropic compression test, the stress path is not predetermined. According to Nova et al. (2003), the transition from elastic to plastic behavior follows the yield surface, if no bond degradation takes place. The degree of cementation influences the transition from elastic to plastic behavior, as illustrated in Figure 2.10 b). Examples of stress paths from K_0-loading can be found in e.g. Coop and Atkinson (1993), and Lagioia and Nova (1995), Leroueil and Vaughan (1990).

2.1.7 Cementation History

According to Rotta et al. (2003) cementation in natural sandstones take place during several different loading-cementation histories, where the three major relations are: (1) At the surface under no confining pressure, (2) at shallow depth after overconsolidation, and (3) progressively with burial. The loading-cementation history affects the results of tests on natural sandstone.

To examine the effect of curing stress on isotropic yielding, Rotta et al. (2003) performed isotropic compression tests on specimens of artificially cemented sandstone. Two specimens with identical void ratio and degree of cementation were tested. Both were loaded to an isotropic pressure of 500 kPa. One was allowed to cure at that pressure while the other was unloaded till 50 kPa and then cured. During further isotropic loading, the specimen cured under high confining pressure would start yielding later than the specimen cured at low confining pressure. After yielding, the specimens behaved similarly, resulting in identical compression lines.

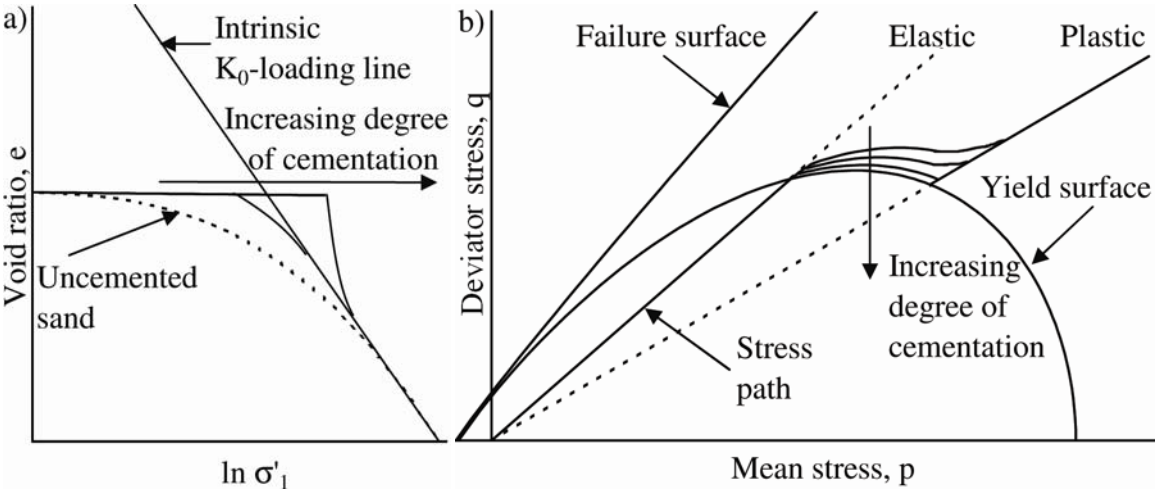

Figure 2.10: a) Schematic representation of the influence of cementation during K_0-loading. After b) Stress paths followed during K_0-loading.

To simulate the damage taking place when retrieving sandstone from in-situ conditions and bringing it to the laboratory, Holt et al. (2000) performed oedometric tests on three different artificial sandstones, all cured under stress. They found that damage occurred during unloading from the simulated in-situ stress. After reloading the sandstones to the curing stress, the bulk modulus and the elastic wave velocities were reduced. In weakly cemented sandstone, enough damage took place to break the bonds between the grains. As a result, the weakly cemented sandstone exhibited a reduction in void ratio during reloading, which was not found in the sandstones with stronger cementation. Fernandez and Santamarina (2001) showed experimentally that sandstone cemented under pressure could have the interparticle bonding damaged by unloading due to local tension on the cementing bonds.

2.1.8 Shear Bands in Sandstone

Shear bands are localized strains often 4-10 grain diameters wide, with further damage restricted to within approximately 2 mm of the shear band (El Bied et al. 2002, Cuss et al. 2003). SEM-photos (Scanning Electron Microscope) performed by El Bied et al. (2002) show that tests performed under low confining pressure has a shear zone characterized by grain cracking with no grain crushing while tests performed under high confining pressure has a shear zone characterized by grain crushing and pulverization. The shear bands at low confining pressures experience an increase in porosity and are therefore often referred to as dilating shear bands. The shear hands at high confining pressures experience a decrease in porosity and are sometimes referred to as contraction shear

bands. According to Sulem and Ouffroukh (2006) both the dilating and contracting shear bands experience a reduction in permeability. However, the reduction in permeability is more pronounced in the contracting shear bands. The shear bands are near failure phenomena and Ord et al (1991) observed that in plane strain tests, the shear band initiates in the hardening regime, resulting in a reduced strength. The angle of the shear band has been found to decrease as the confining pressure increases (Bésuelle et al. 2000, El Bied et al. 2002). The angle of the shear band is here defined as the angle between the major principal stress and the normal to the shear band.

Similar to the shear band is the compaction band observed by e.g. Olsson (1999), Klein et al. (2001), and Baud et al. (2004). Compaction bands are localized deformation with reduction in porosity and are approximately perpendicular to the major principal stress (angle of band equal to zero). They have been observed to form in the stress range around the cap of the cementation yield surface. According to Katsman and Aharonov (2006) compaction bands are likely to nucleate around heterogeneities in the rock properties, such as local variation in porosity or compressive strength.

2.2 Anisotropy in Sandstone

Due to deposition in a gravitational field, many natural soils exhibit some degree of anisotropy. Soil and rock often have one axis of symmetry, making it cross-anisotropic (or transversely isotropic). The coordinate system adopted in this study is shown in Figure 2.11, along with the stresses acting on a small cube of cross-anisotropic material. The z-axis is the direction of symmetry, and the xy-plane corresponds to the bedding planes. The first suffix of the stresses refers to the direction of the normal to the plane on

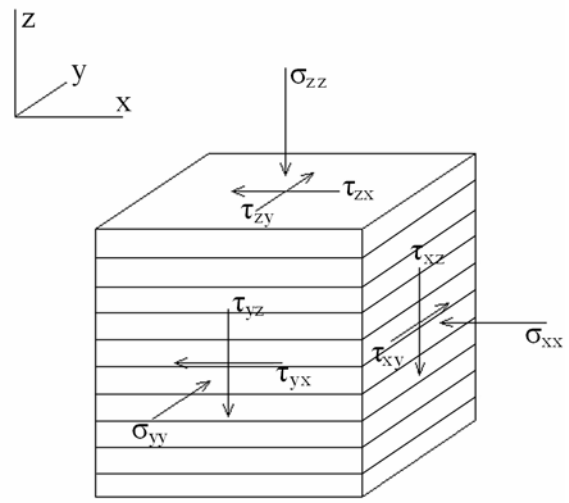

Figure 2.11: Coordinate system adopted and stresses on a small cube.

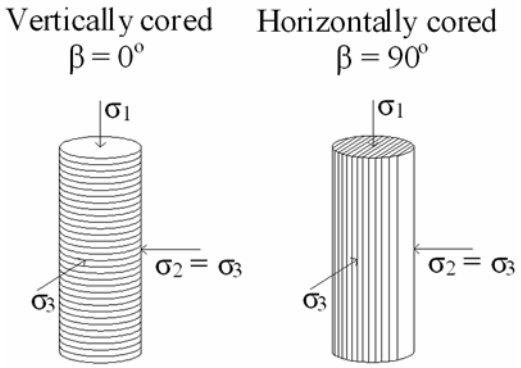

Figure 2.12: Specimens cored with a orientation angle of 0^o and 90^o are referred to as vertically and horizontally cored, respectively.

which the stress act and the second suffix refers to the direction of the stress component itself.

When examining the effect of anisotropy, specimens are often cored in different directions with respect to the bedding planes. The orientation angle, β refers to the angle between the normal to the bedding planes (z-direction in Figure 2.11) and the direction of the major principal stress in triaxial testing. Two specimens cored with orientation angles of $\beta = 0^o$ and $\beta = 90^o$ are referred to as vertically cored specimens and horizontally cored specimens, respectively (Figure 2.12). These two directions are the only orientation angles where only normal stresses are applied to the cube in Figure 2.11. All other orientation angles result in shear stresses on the cube.

Often a distinction is made between inherent and induced anisotropy (e.g. Wong and Arthur 1985). Inherent anisotropy is the result of the deposition process and is an intrinsic property of the material. Induced anisotropy is caused by the strains and varies depending on the magnitude and direction of the stresses applied. The induced anisotropy can both enhance and reduce the inherent anisotropy.

According to Louis et al. (2005) macroscopic inherent anisotropy in sandstone can be caused by several microscopic features: The pores, the cracks, the grains, and the contacts between them, and the respective distribution of each element. However, macroscopic variation in porosity, grain size distribution, and cement content plays a significant role in natural anisotropic sandstone. In other porous rocks, the anisotropy has been attributed to several other mechanisms such as preferred direction of micro-fissures

in argillite (Liao et al. 1997), or preferred orientation of particular minerals in schists (Nasseri et al. 2003).

Tien and Tsao (2000) studied the strength and elastic behavior of interlayered (ABAB) artificial sandstone and found the behavior of the vertically cored specimens to be dominated by the softer/weaker material while the behavior of the horizontally cored specimens was controlled by the stiffer/stronger material. This is equivalent of having two materials working in series for the vertically cored specimens and working in parallel for the horizontally cored specimens. Interlayered material is not of interest in this study as it would be considered (and modeled) as two materials with different properties.

2.2.1 Cross-Anisotropic Failure

When determining the failure of cross-anisotropic rock, a common procedure is to perform series of unconfined compression tests varying the orientation angle, β from 0^o to 90^o, (e.g. Al-Harthi 1998), or performing series of triaxial tests with increasing confining pressure and with varying orientation angles (Donath 1964, Hoek 1964, McLamore and Gray 1967, Attewell and Sandford 1974, Duveau and Shao 1998, Tien and Tsao 2000, Whittles et al. 2002, Tien et al. 2006, Saroglou and Tsiambaos 2008). Also Liao et al. (1997) performed direct tension tests with varying orientation angle, β to determine the failure mode in tension.

Three different types of behavior have been observed depending on the type of anisotropy. These findings are summarized in Figure 2.13, Figure 2.14, and Figure 2.15.

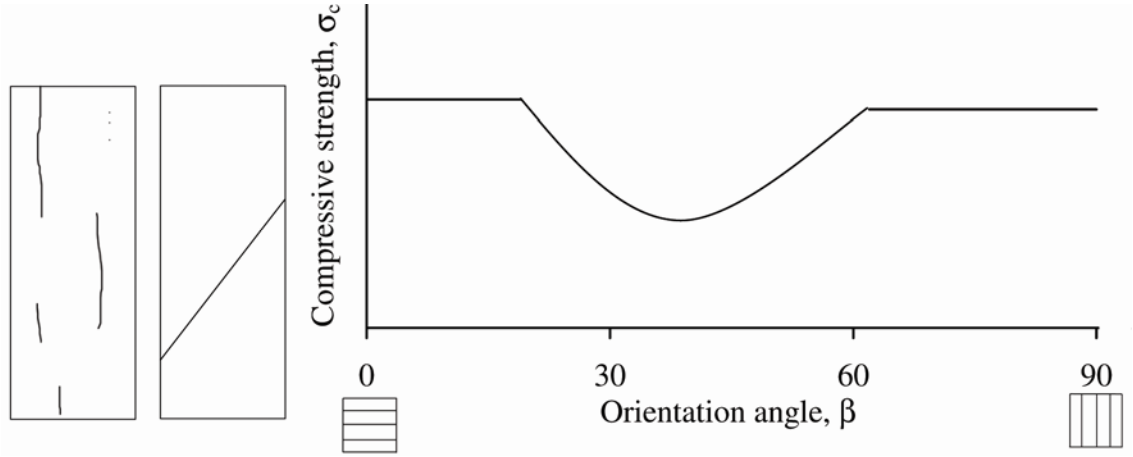

Figure 2.13: Typical strength variation with orientation angle of anisotropic rock failing along a single discontinuity. After Al-Harthi (1998).

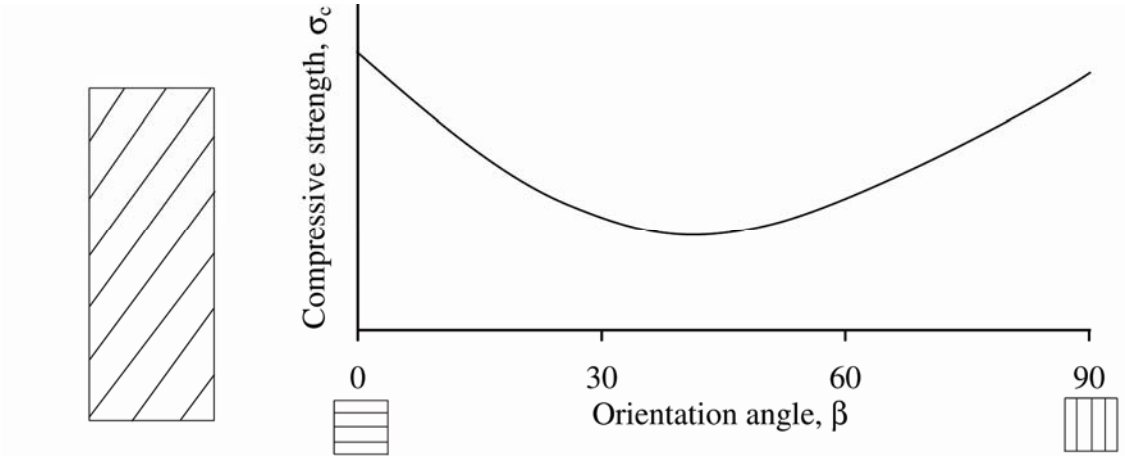

Figure 2.14: Typical strength variation with orientation angle of anisotropic rock failing along one set of discontinuities. After Al-Harthi (1998).

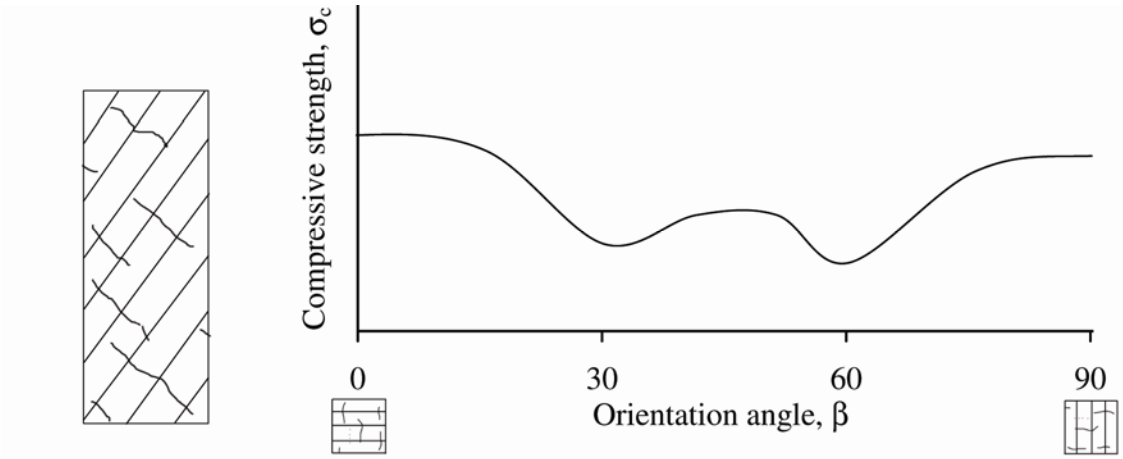

Figure 2.15: Typical strength variation with orientation angle of anisotropic rock failing along two sets of discontinuities. After Al-Harthi (1998).

The first type of behavior (Figure 2.13) is characterized by a large reduction in strength in the midrange of orientation angles. The reduction in strength is due to shearing along the bedding plane. At low and high orientation angles, a strength plateau is observed and the strength is here controlled by the matrix of the soil (McLamore and Gray 1967). In unconfined compression tests the strength plateau is sometimes caused by splitting (Whittles et al. 2002), which is more often found in the horizontally cored specimens.

In the second type of behavior (Figure 2.14) the specimens primarily fail by shearing along a set of discontinuities. The shear strength along the bedding planes control the strength and multiple shear bands, or kinking is observed as failure mechanism (McLamore and Gray 1967). The result is a u-shaped failure curve.

The third type of behavior (Figure 2.15) does not represent cross-anisotropic soil, as two planes of anisotropy perpendicular to each other are observed (e.g. Pomeroy et al. 1970, Al-Harthi 1998). The anisotropy typically comes from foliation and bedding planes in one direction and fissures and cracks in the other direction. Here two u-shaped curves act together and the result is a single curve with two minima combined from the two planes of anisotropy.

The influence of the confining pressure on the failure mode is conceptually shown in Figure 2.16. The reduction in strength experienced at the midrange of orientation angles diminishes as the confining pressure increases. This is observed for all three types of failure (e.g. McLamore and Gray 1967, Whittles et al. 2002, Pomeroy et al. 1970). Furthermore, the anisotropy in the soil matrix gets reduced as the confining pressure in-

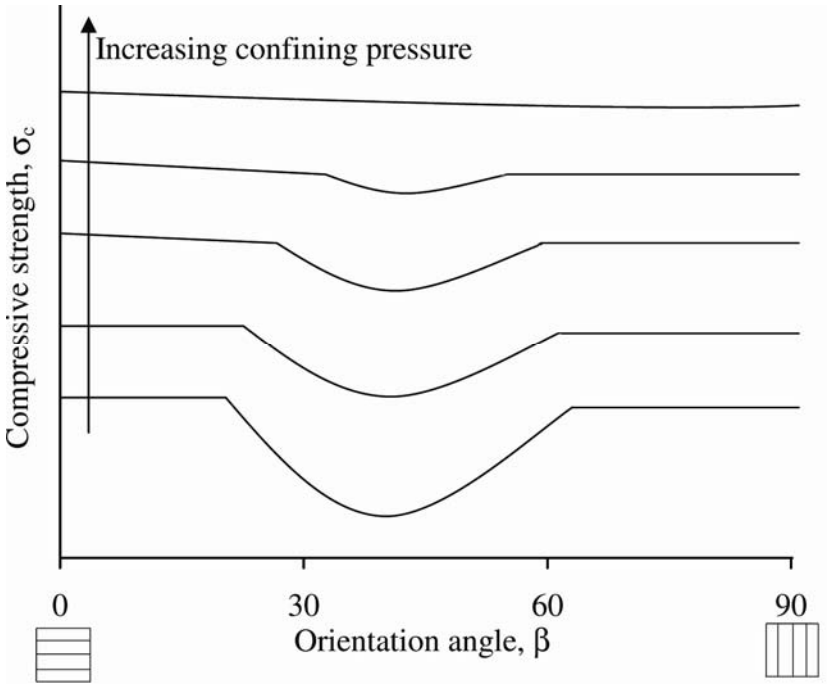

Figure 2.16: Compressive strength of anisotropic rock with increasing confining pressure.

creases.

According to Li and Aubertin (2002), the tensile strength of cross-anisotropic natural rocks, does not follow the same strength variation as the compressive strength, because the tensile strength is controlled by the cohesion in the soil. In direct tension, Liao et al. (1997) found specimens of argillite to be stronger in horizontal direction than in vertical direction. The approximate variation with orientation angel is shown in Figure 2.17, and is in accordance with findings of indirect tensile strength of siltstone determined by Whittles et al. (2002).

To characterize the inherent cross-anisotropy when failure of the soil matrix is experienced, the anisotropy ratio of the strength, R_S defined in equation (2.3) is used:

$$R_S = \frac{S_v}{S_h} \tag{2.3}$$

in which S_v is the compressive strength of vertically cored specimens and S_h is the compressive strength of horizontally cored specimens. Values of R_S close to unity reveal isotropy, while values of R_S larger than unity indicates a material that is stronger in vertical direction, and values of R_S smaller than unity indicates a material that is stronger in horizontal direction.

Figure 2.18 shows the variation of anisotropy ratio with confining pressure for two siltstones determined from tests performed by Whittles et al. (2002). At unconfined compression, the anisotropy ratio is above two indicating higher strength for vertically cored specimens and as the confining pressure increases, the anisotropy ratio decreases. For siltstone I the anisotropy is almost gone at a confining pressure of 8 MPa, whereas for siltstone II anisotropy remains at that pressure. The large drop in anisotropy ratio

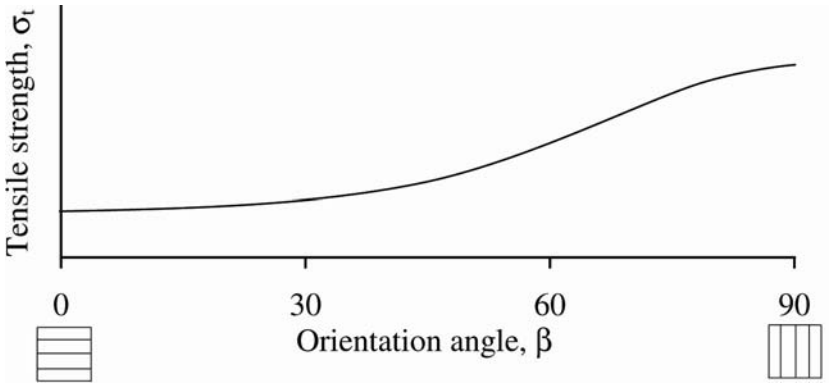

Figure 2.17: Tensile strength variation with orientation angle of anisotropic rock. After Liao et al. (1997).

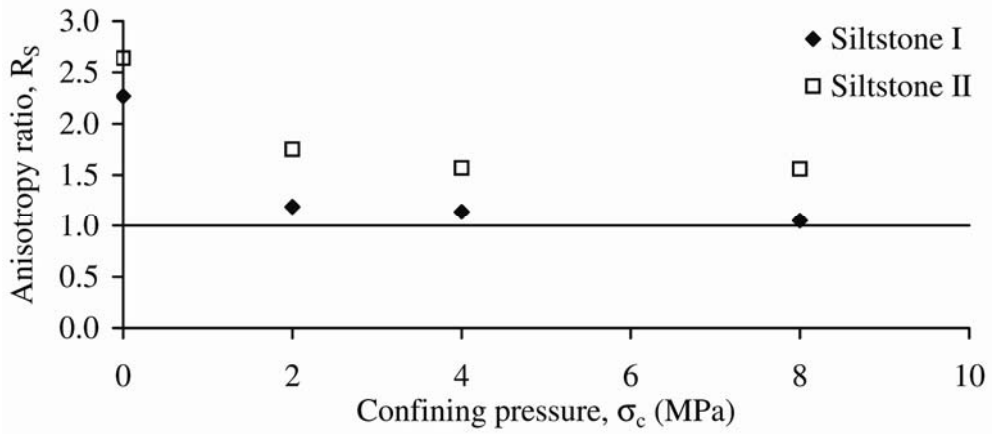

Figure 2.18: Variation of anisotropy ratio with confining pressure of siltstone. Data from Whittles et al. (2002).

from unconfined compression to a confining pressure of 2 MPa was also observed by Duveau and Shao (1998). They further noticed that the horizontally cored specimens were more likely to fail by splitting, resulting in the high anisotropy ratio in unconfined compressive tests to be caused by the failure mode rather than the anisotropy of the soil matrix.

In all the tests examined here, the anisotropy ratio was found to be higher than unity, indicating higher strength in vertically cored specimens than horizontally cored specimens. Furthermore, the anisotropy ratio was found to decrease as the confining pressure increased.

2.2.2 Cross-Anisotropic Elastic Behavior

The relationship between increments of stress and increments of strain for cross-anisotropic elastic material is described in equation (2.4):

$$\begin{Bmatrix} \Delta\varepsilon_{xx} \\ \Delta\varepsilon_{yy} \\ \Delta\varepsilon_{zz} \\ \Delta\gamma_{xy} \\ \Delta\gamma_{yz} \\ \Delta\gamma_{zx} \end{Bmatrix} = \begin{bmatrix} \frac{1}{E_h} & \frac{-\nu_{hh}}{E_h} & \frac{-\nu_{vh}}{E_v} & 0 & 0 & 0 \\ \frac{-\nu_{hh}}{E_h} & \frac{1}{E_h} & \frac{-\nu_{vh}}{E_v} & 0 & 0 & 0 \\ \frac{-\nu_{hv}}{E_h} & \frac{-\nu_{hv}}{E_h} & \frac{1}{E_v} & 0 & 0 & 0 \\ 0 & 0 & 0 & \frac{1}{G_{hh}} & 0 & 0 \\ 0 & 0 & 0 & 0 & \frac{1}{G_{hv}} & 0 \\ 0 & 0 & 0 & 0 & 0 & \frac{1}{G_{hv}} \end{bmatrix} \cdot \begin{Bmatrix} \Delta\sigma'_{xx} \\ \Delta\sigma'_{yy} \\ \Delta\sigma'_{zz} \\ \Delta\tau_{xy} \\ \Delta\tau_{yz} \\ \Delta\tau_{zx} \end{Bmatrix} \qquad (2.4)$$

The direction of the stress increments and the strain increments follow the convention in Figure 2.11, meaning the z-direction is the direction of symmetry, and the xy-plane corresponds to the bedding planes. The suffix on the elastic parameters are adopted from Kirkgard and Lade (1991), where E_v is Young's modulus in vertical direction, E_h is Young's modulus in horizontal direction, ν_{hv} is Poisson's ratio of strain in vertical direction to applied strains in horizontal direction, ν_{vh} is Poisson's ratio of strain in horizontal direction to applied strains in vertical direction, ν_{hh} is Poisson's ratio of strain in horizontal direction to applied strains in orthogonal horizontal direction, G_{hv} is the shear modulus in any vertical plane, and G_{hh} is the shear modulus in any horizontal plane.

The shear modulus in the horizontal plane, G_{hh} can be replaced with

$$G_{hh} = \frac{E_h}{2(1+\nu_{hh})} \tag{2.5}$$

thereby reducing the independent parameters by one. Symmetry of the elastic compliance matrix results in:

$$\frac{\nu_{hv}}{E_h} = \frac{\nu_{vh}}{E_v} \tag{2.6}$$

From equation (2.6) it is evident that only three of the four parameters are required. Therefore only five independent parameters are needed to fully describe cross-anisotropic elastic behavior. Four parameters can be determined from two triaxial compression tests cored in vertical and horizontal directions, with measurement of the normal strains. The last parameter, G_{hv} requires shear stresses applied in a vertical plane of the specimen.

Three common approaches to achieve the G_{hv} are, (1) omit the shear modulus for the vertical plane from the results, (e.g. Lockner and Beeler 2003), (2) perform torsion

shear tests (e.g. Talesnick and Ringel 1999, Talesnick et al. 2000, Gautam and Wong 2006), (3) perform triaxial tests on specimens cored with orientation angles between 0^o and 90^o (e.g. Sargand and Hazen 1987, Liao et al. 1997, Gatelier et al. 2002).

Lockner and Beeler (2003) determined the evolution of elastic anisotropy in Berea sandstone under different loading conditions. Only vertically and horizontally cored specimens were used and G_{hv} was not determined. They found that increased confining pressure reduced the inherent anisotropy, while increased differential stress produced increasing anisotropy. All tests were performed inside the cementation yield surface resulting in the specimens returning to their initial degree of anisotropy upon unloading. Gatelier et al. (2002) also observed a decrease of elastic anisotropy with increasing confining pressure.

Liao et al. (1997) examined the cross-anisotropic elastic response of argillite in tension, and compared the result with the cross-anisotropic elastic response in compression. They found the argillite to be more anisotropic in compression than in tension due to closure of micro-fissures in compression. Similar results were achieved by Talesnick et al. (2000) on Loveland sandstone.

Gautam and Wong (2006) used the anisotropy ratio, R_E defined in equation (2.7) to monitor anisotropy in Young's modulus in different formations of Colorado shale.

$$R_E = \frac{E_v}{E_h} \tag{2.7}$$

in which R_E is the anisotropy ratio for Young's modulus, and E_v and E_h are Young's moduli in vertical and horizontal directions, respectively. Values of R_E close to unity reveals isotropy, while values of R_E smaller than unity means the material is stiffer in

horizontal direction and values of R_E larger than unity means the material is stiffer in vertical direction. Similarly, the anisotropy ratio, R_G for the shear modulus is defined as:

$$R_G = \frac{G_{hh}}{G_{hv}} \tag{2.8}$$

in which G_{hh} and G_{hv} are shear moduli in the horizontal plane and a vertical plane, respectively.

Compiled in Table 2.1 are the values of the anisotropy ratio for Young's moduli (equation (2.7)) and for the shear moduli (equation (2.8)) calculated from the literature reviewed for this study. Most natural deposits are stiffer in horizontal direction than in vertical direction, with the exception of Berea sandstone, Colorado shale, and Siltstone I and II. Furthermore, the presence of micro fissures in one direction seems to create strongly anisotropic behavior. The fissures creating the stone anisotropy would suggest the anisotropic behavior in these materials is a function of the stress history rather than an inherent property. The creation of these directional fissures is described in section 2.2.3.

Table 2.1: Anisotropy ratios determined for Young's modulus and shear modulus. *Compression/Tension. **Indicates the elastic properties at the lowest confining pressure available.

Material	Origin of anisotropy	C/T*	R_E	R_G	Reference
Adamswiller sand-stone, initial state**	preferred orientation of mica minerals	C	0.79	1.16	Gatelier et al. (2002)
Argillite	horizontal micro-fissures	C	0.67	1.70	Liao et al. (1997)
Argillite	horizontal micro-fissures	T	0.87	1.39	Liao et al. (1997)
Artificial sandstone	pouring direction	C	1.04	1.01	Talesnick et al. (2000)
Colorado shale	face to face clay particles	C	1.70-2.19	1.48-1.86	Gautam and Wong (2006)
Indiana limestone	Not known	C	0.87	0.88	Talesnick and Ringel (1999)
Lac duBonnet granite	horizontal micro-fissures	C	0.38	1.10	Talesnick and Ringel (1999)
Loveland sandstone	Not known	C	0.75	0.91	Talesnick et al. (2000)
Marsha chalk	Not known	C	0.73	0.99	Talesnick and Ringel (1999)
Artificial sandstone	pouring direction	T	1.12	N/A	Talesnick et al. (2000)
Artificial sandstone initial state**	interlayered (AAAA)	C	0.94	N/A	Tien and Tsao (2000)
Artificial sandstone initial state**	stratified (ABAB)	C	0.86	N/A	Tien and Tsao (2000)
Bentheim sandstone	pore volume anisotropy and anisotropic grain distribution	C	0.69	N/A	Louis et al. (2005)
Berea sandstone initial state**	Not known	C	1.27	N/A	Lockner and Beeler (2003)
Himalayan schist quartzitic schist	preferred orientation of mica and chlorite minerals	C	1.00	N/A	Nasseri et al. (2003)
Himalayan schist chlorite schist	preferred orientation of mica and chlorite minerals	C	0.81	N/A	Nasseri et al. (2003)
Himalayan schist quartz mica schist	preferred orientation of mica and chlorite minerals	C	0.70	N/A	Nasseri et al. (2003)

Table 2.1: Continued. Anisotropy ratios determined for Young's modulus and shear modulus. *Compression/Tension. **Indicates the elastic properties at the lowest confining pressure available.

Material	Origin of anisotropy	C/T*	R_E	R_G	Reference
Himalayan schist biotite schist	preferred orientation of mica and chlorite minerals	C	0.43	N/A	Nasseri et al. (2003)
Loveland sandstone	Not known	T	0.96	N/A	Talesnick et al. (2000)
Siltstone I	interlayered siltstone/mudstone	C	1.40	N/A	Whittles et al. (2002)
Siltstone II	interlayered siltstone/mudstone	C	1.35	N/A	Whittles et al. (2002)

2.2.3 Yielding and Induced Anisotropy

During yielding, cracks and fissures appear and the cementation breaks. If the cementation breakage has a preferred orientation, e.g. cracks in one direction, then the damage is anisotropic, and the result is induced anisotropy. Ramez (1966) analyzed the direction of fractures in Darley Dale sandstone after failure. In the brittle regime, two kinds of fractures were observed: Tensile fractures parallel to the direction of compression, and fractures that were approximately parallel to the shear band. At high confining pressures Ramez (1966) recognized three types of fractures: Tensile fractures, shear fractures inclined at a small angle to the direction of compression, and fractures that were normal to the compression direction. It was suggested that the fractures normal to the compression direction could originate from the release of elastic strain energy during unloading.

According to Wu et al. (2000) there is a trend towards the induced anisotropy to decrease as the porosity increases. In high porosity rocks like sandstone, the orientation of the inter- and intra-granular cracks are more scattered due to the pores in the material.

The evolution of anisotropy during several different stress paths have been examined by measurement of sound velocities and ultrasonic attenuations (e.g. Crawford et al. 1995, Desai et al. 1995, Benson et al. 2005, Scott and Abousleiman 2005). The sound travels through the matrix of the soil, and as cracks develop, the sound travels a further distance. By measuring the sound velocity in three directions simultaneously, the evolution of directional cracks can be monitored.

During hydrostatic loading, a cross-anisotropic material gradually looses the anisotropy as the cementation breaks down (Desai et al. 1995, Benson et al. 2005). Scott and Abousleiman (2005) found initially isotropic sandstone to maintain the isotropic behavior during isotropic loading.

According to Desai et al. (1995) the anisotropy increases during triaxial loading until the specimen starts dilating, then the induced anisotropy reduces towards zero. This means, the cracks and fissures start propagating in all directions during dilation.

During K_0-loading, Scott and Abousleiman (2005) found the anisotropy of isotropic sandstone to increase rapidly during the initial loading. Then the anisotropy was locked in at a constant level and remained constant.

2.3 Modeling the Behavior of Sandstone

In chapter 3 The Single Hardening Model is reviewed and its capabilities demonstrated for sand. Later, in chapter 8, additions to The Single Hardening Model are proposed to capture the behavior of cross-anisotropic sandstone. Therefore, this part of the review focuses on features relevant for The Single Hardening Model. The features are explained conceptually here, and a detailed description with a formulation applicable for The Single Hardening Model follows in succeeding chapters.

2.3.1 Cementation

Lade (1982) and Kim and Lade (1984) have demonstrated that the failure of concrete and rocks can be captured by translation of the principal stress space along the hydrostatic axis. This captures the effect of cohesion and the tensile strength exhibited by concrete

and rocks. The principal stress space is translated along the hydrostatic axis by the distance ‘a’, as shown in equation (2.9). The parameter ‘a’ is added to the normal stresses, and as the parameter ‘a’ increases, the material is able to withstand larger and larger tensile strength.

$$\bar{\sigma}_{ij} = \sigma_{ij} + \delta_{ij} \cdot a \cdot p_a \qquad (2.9)$$

in which σ_{ij} are the stresses to be translated, δ_{ij} is Kronecker’s delta ($\delta_{ij} = 1$ for $i = j$, $\delta_{ij} = 0$ for $i \neq j$), ‘a’ is a dimensionless parameter, and p_a is atmospheric pressure in the same units as σ_{ij}.

To capture the behavior of concrete in the brittle regime, Lade and Kim (1988)[b] translated the principal stress space as expressed in equation (2.9). This included calculation of elastic and plastic deformation in the translated stress space. This means that the failure surface, yield surface, and plastic potential surface originate through the origin of the translated principal stress space. This is demonstrated in Figure 2.19, where failure surface, yield surface and plastic potential surface are plotted in the translated stress space.

2.3.2 Degradation of Cementation

Yielding of cemented material with and without degradation of the soil structure was described by Nova et al. (2003), using translation of the yield surface. The model only described the plastic deformation, meaning the elastic properties and failure surface were assumed constant during the degradation. The model is conceptually explained here, based on the three yield surfaces in Figure 2.20. For clarity reasons only the parts of the

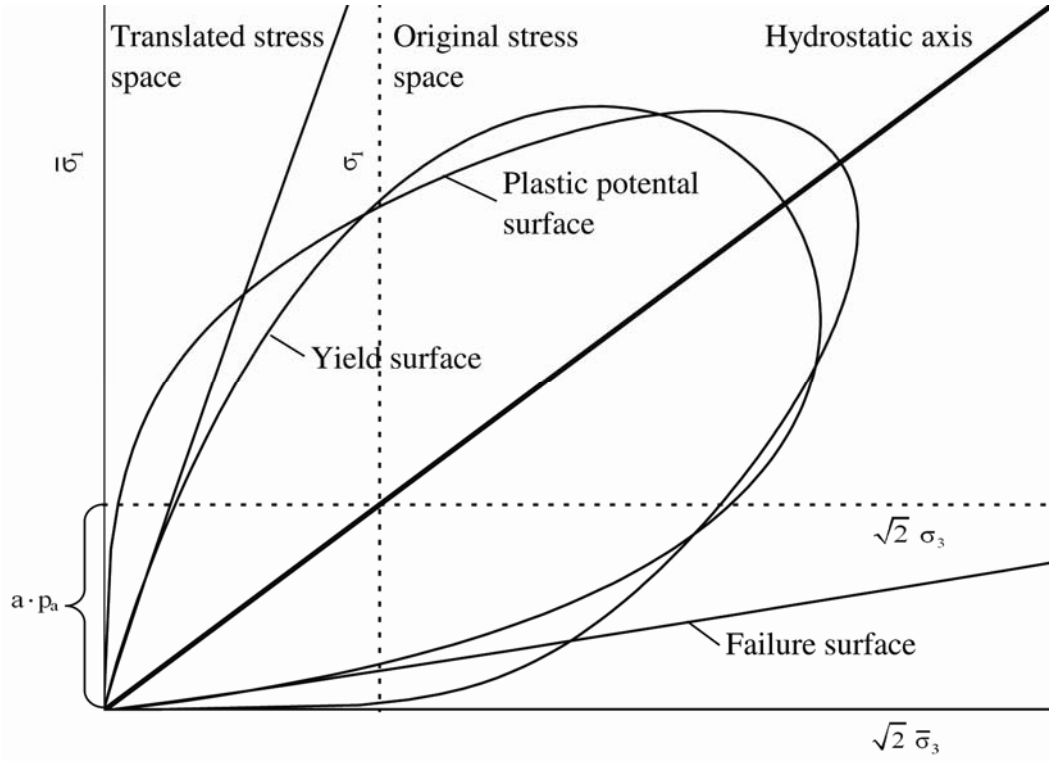

Figure 2.19: Translation of coordinate system to account for cohesion.

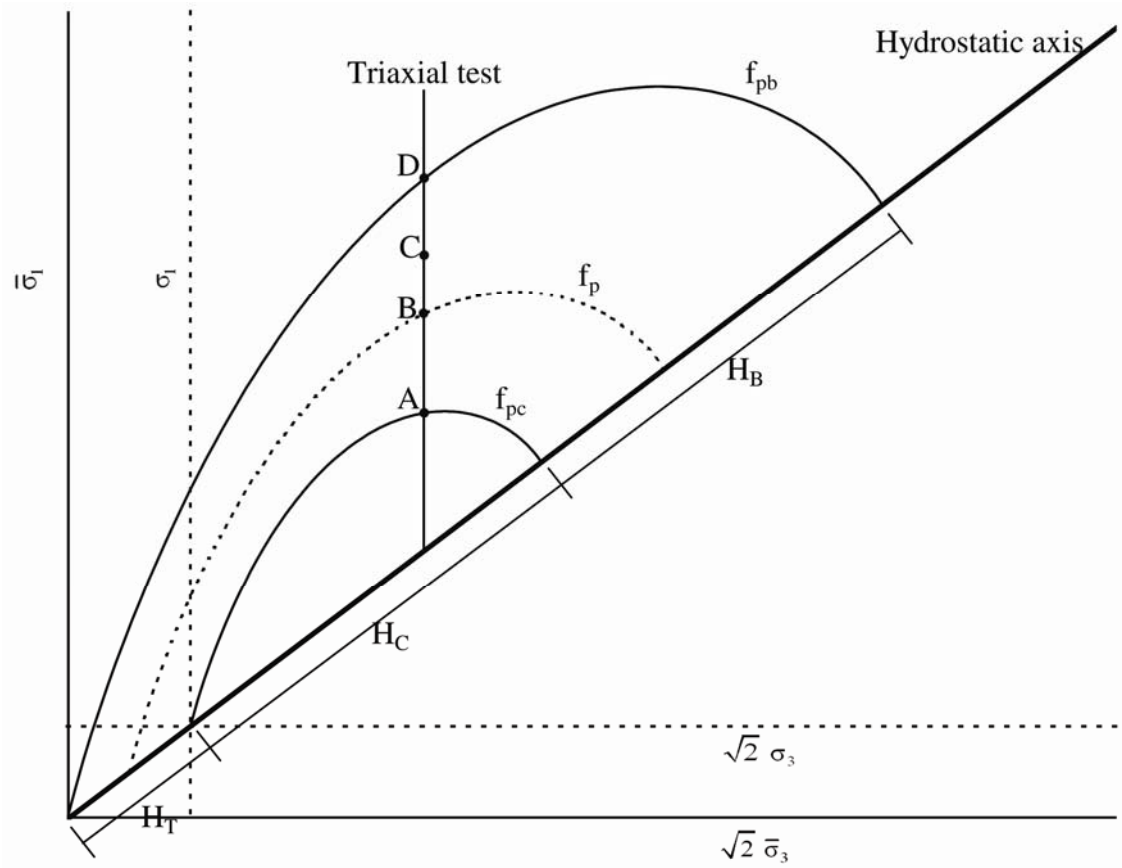

Figure 2.20: The initial yield surfaces due to cementation and breaking of cementation, and the evolution of yield surface during triaxial loading. After Nova et al. (2003).

yield surfaces above the hydrostatic axis are shown. There exists two initial yield surfaces, one caused by cementation f_{pc}, and one describing the state where the cementation is broken, f_{pb}. The cementation surface increases in size like a regular yield surface and defines the elastic area. The broken surfaces decrease in size as the tensile strength is reduced. Inside the cementation surface the material behaves elastic, and between the two surfaces, the cementation breaks down, resulting in zero tensile strength when the two surfaces are equal in size. Outside the broken cementation surface, the soil behaves like the residual soil. The third yield surface, f_p is the yield surface controlling the behavior of the soil. All yield surfaces are assumed to have the same shape.

Three quantities, H_T, H_C, and H_B, are defined in Figure 2.20 and relates to the isotropic stresses. The parameter H_T describes the difference between the original and the translated stress space. The parameter H_C describes the initial location of the cementation surface in the original stress space. The parameter H_B defines the isotropic stress range where the cementation breaks. Nova et al. (2003) used the ratio k defined in equation (2.10) to indicate the rate of degradation.

$$k = \frac{H_T}{H_B} \tag{2.10}$$

in which H_T and H_B, are defined in Figure 2.20.

The evolution of the yield surfaces during the triaxial loading in Figure 2.20 is demonstrated in Figure 2.21. The points A, B, C, and D on the triaxial stress path is shown in Figure 2.21 a), b), c), and d), respectively. The loading until the stresses reach point A is elastic. This is modeled using the translated stress space. After point A, a simultaneously translation and inflation of the yield surface f_p takes place. This is demon-

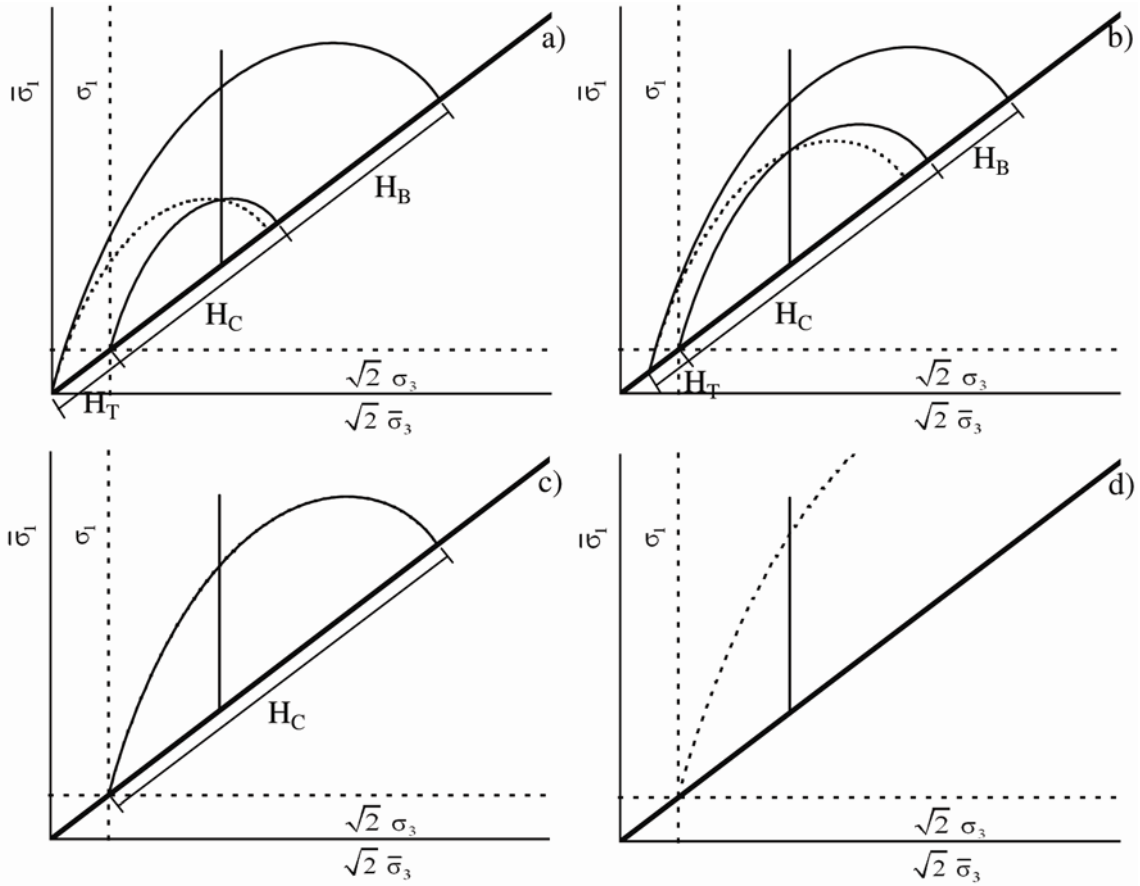

Figure 2.21: Location and size of the yield surfaces in Figure 2.20 during the triaxial stress path shown. a) Point A, b) Point B, c) Point C, d) Point D.

strated in Figure 2.21 b) where the cementation surface has increased. The parameter H_B is decreased by an equal amount, resulting in a decrease of the tensile strength according to equation (2.10) in which k is assumed to be constant. The surface of broken cementation, f_{pb}, and the yield surface controlling the strains, f_p, are both translated to a new origin, defined by the reduction in tensile strength. At point C, no tensile strength is left as the cementation is broken and the three yield surfaces are identical. At point D, only one yield surface remains, f_p and the behavior is modeled as a cohesionless soil.

The model presented by Nova et al. (2003) predicted the behavior of Gravina Calcarenite during isotropic compression, triaxial tests at low and high confining pressure, and oedometric loading. Furthermore, the model was used to predict the degradation due to weathering of cemented silica sand.

2.3.3 Previous Modeling of Cross-Anisotropy

The Single Hardening Model has previously been expanded to incorporate cross-anisotropy in granular materials (Abelev et al. 2007). The model incorporated rotation of the principal stress space to account for cross-anisotropy. After rotation, the model operated isotropically within the rotated stress space. The failure surface was rotated individually from the yield and the plastic potential surfaces. Furthermore, the rotation of the yield surface and plastic potential surface was stress-dependent, meaning the anisotropy decreased as the confining pressure increased. The rotation of the plastic potential surface is demonstrated in Figure 2.22.

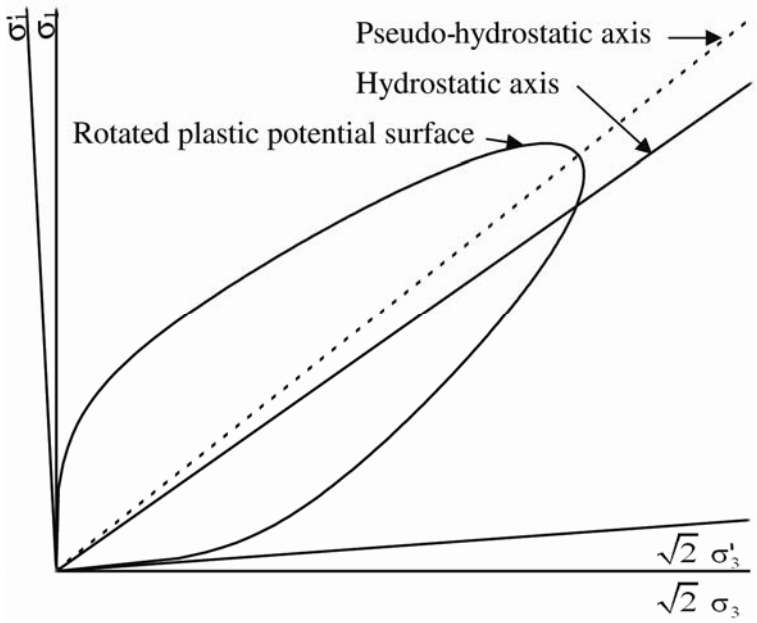

Figure 2.22: Rotation of plastic potential surface to account for cross-anisotropy. After Abelev et al. (2007).

2.3.4 Modeling of Elastic Cross-Anisotropy

Yu and Dakoulas (1993) developed a stress dependent model for the elastic behavior of cross-anisotropic soils. The expressions for the stress dependence of the moduli are derived on the basis of conservation of energy during elastic loading. With that, they follow the idea of Lade and Nelson (1987), who developed an isotropic elastic model based on the same principles. The cross-anisotropic model makes use of five parameters to describe the behavior. However, under isotropic conditions, the cross-anisotropic model reduces down to the isotropic model. The isotropic elastic model is presented in detail in section 3.1.1.

2.3.5 Describing Anisotropy with a Microstructural Tensor

Several authors have incorporated a cross-anisotropic microstructural tensor into the constitutive relations (e.g. Oda and Nakayama 1989, Muhunthan et al. 1996, Pietruszczak and Mroz 2000, 2001, Pietruszczak et al. 2002, Li and Dafalias 2002, 2004, Dafalias et al. 2004, Hicher and Chang 2006, Lade 2007, 2008). The tensor describes the three-dimensional variation of microstructural cross-anisotropic features such as distribution of voids, fissures, grain contacts or cementation. In isotropic soil, the microstructural features are distributed evenly over a sphere. In cross-anisotropic soil, the microstructural features vary depending on the direction. This is demonstrated in Figure 2.23 where the distribution of contact orientations with different degrees of cross-anisotropy is shown.

The fabric tensor is often based on a probability density function of either the solid phase (grain orientation, grain contacts) or the void inside a representative elemental volume. To couple the macroscopic behavior to microstructural features, Muhunthan and Chambau (1997) determined the void fabric tensor by stereological techniques. They concluded that the void fabric added additional information about the cross-anisotropy not obtainable from the grain orientation fabric tensor.

A phenomenological approach, followed by e.g. Pietruszczak and Mroz (2000, 2001), is to describe the combined effect of different cross-anisotropic microstructural features in one tensor derived from the macroscopic behavior. According to Voyiadjis and Kattan (2007), in damage mechanics this approach leads to fabric tensors derived from sound thermodynamic principles.

The fabric tensor approach to cross-anisotropy have been applied to the elastic behavior (e.g. Hicher and Chang 2006), the failure surface (e.g. Pietruszczak and Mroz 2000, 2001, Lade 2007, 2008), and the yield surface/plastic potential function (e.g. Muhunthan et al. 1996, Pietruszczak et al. 2002, Dafalias et al. 2004).

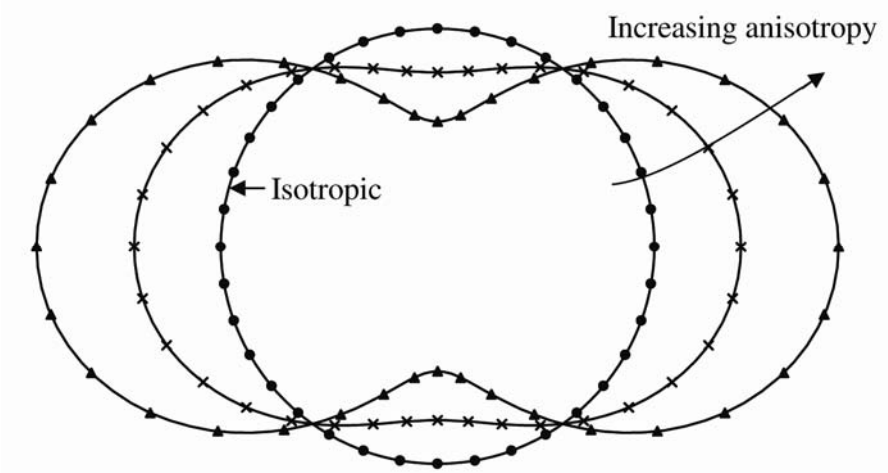

Figure 2.23: Distribution of contact orientations with different degrees of cross-anisotropy. After Hicher and Chang (2006).

3. Review of The Single Hardening Model

3.1 The Single Hardening Model

The Single Hardening Model introduced by Lade and Kim (1988[a], 1988[b]) and Kim and Lade (1988) have predicted the behavior of sand, clay and concrete under a variety of loading conditions. The model is composed of an elastic model, a failure criterion, a plastic potential function, and a yield function with a work hardening/softening relation. For normally consolidated, cohesionless soil eleven parameters are required to fully describe the behavior. All parameters needed to calibrate the model can be found from standard experiments consisting of three triaxial tests and one isotropic compression test.

The total strain increment, $d\varepsilon_{ij}$ is divided into an elastic part, $d\varepsilon_{ij}^{e}$ and a plastic part, $d\varepsilon_{ij}^{p}$. They are calculated separately and then summed as expressed in equation (3.1).

$$d\varepsilon_{ij} = d\varepsilon_{ij}^{e} + d\varepsilon_{ij}^{p} \tag{3.1}$$

All components in the model are expressed in terms of the stress invariants I_1, I_2, I_3 and the second stress deviator invariant, J_2', all of which are defined in equation (3.2), (3.3), (3.4), and (3.5), respectively.

$$I_1 = \sigma'_{xx} + \sigma'_{yy} + \sigma'_{zz} \tag{3.2}$$

$$I_2 = -\left(\sigma'_{xx}\cdot\sigma'_{yy} + \sigma'_{yy}\cdot\sigma'_{zz} + \sigma'_{zz}\cdot\sigma'_{xx}\right) + \tau_{xy}\cdot\tau_{yx} + \tau_{yz}\cdot\tau_{zy} + \tau_{zx}\cdot\tau_{xz} \tag{3.3}$$

$$\begin{aligned} I_3 = {} & \sigma'_{xx}\cdot\sigma'_{yy}\cdot\sigma'_{zz} + \tau_{xy}\cdot\tau_{yz}\cdot\tau_{zx} + \tau_{yx}\cdot\tau_{zy}\cdot\tau_{xz} \\ & - \left(\sigma'_{xx}\cdot\tau_{yz}\cdot\tau_{zy} + \sigma'_{yy}\cdot\tau_{zx}\cdot\tau_{xz} + \sigma'_{zz}\cdot\tau_{xy}\cdot\tau_{yx}\right) \end{aligned} \tag{3.4}$$

$$J_2' = \frac{1}{6}\left[\left(\sigma_{xx}' - \sigma_{yy}'\right)^2 + \left(\sigma_{yy}' - \sigma_{zz}'\right)^2 + \left(\sigma_{zz}' - \sigma_{xx}'\right)^2\right] + \tau_{xy}\cdot\tau_{yx} + \tau_{yz}\cdot\tau_{zy} + \tau_{zx}\cdot\tau_{xz} \tag{3.5}$$

The direction of the normal and shear stresses (σ_{xx}', σ_{yy}', σ_{zz}', τ_{xy}, τ_{yz}, τ_{zx}) are defined in Figure 3.1 where the first suffix refers to the direction of the normal to the plane on which the stress act, and the second suffix refers to the direction of the stress component itself.

In the following sections, the individual components of The Single Hardening Model are described along with the parameter determination process. The determinations of the required parameters are demonstrated for loose Santa Monica Beach Sand (e = 0.810). The test results used for the parameter determination were obtained by Boonyachut (1977) in a study of the behavior of cohesionless soil during large stress reversals. Later, in section 3.3, the parameters determined for the loose Santa Monica Beach Sand will be used to predict the behavior of hollow cylinder torsion shear tests performed by Geiger (1979). The tests were performed on loose Santa Monica Beach Sand ($e \simeq 0.806$) with the purpose of studying large stress reversals and reorientation of the principal stresses. However, as the void ratio is a little lower in the torsion shear tests, the parameters derived from the triaxial tests would predict the behavior of sand with higher void ratio. Furthermore, the triaxial tests were performed with lubricated ends and the torsion shear tests were performed with rough ends. This produces higher apparent stiffness in the torsion shear tests (e.g. Rowe and Barden 1964). To overcome this difference in void ratio and boundary conditions, triaxial loading performed at the beginning of some of the hollow cylinder torsion shear tests were compared with the tri-

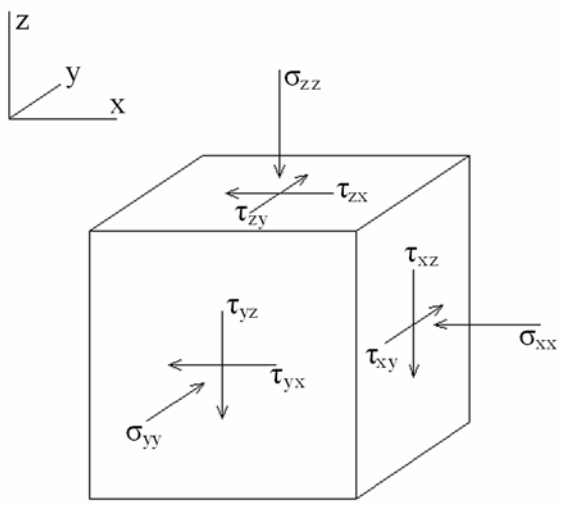

Figure 3.1: Stresses on a small cube.

axial tests. This is done in Figure 3.2, where the stress-strain relations from the tests are compared. The tests performed in the torsion shear apparatus with a confining pressure of 200 kPa are initially stiffer than the tests performed in the triaxial apparatus at 240 kPa. The volume change from the torsion shear tests follows the same patters as the triaxial tests. The difference in stiffness is found to have no significant effect on most parameters determined, except the yield surface parameter α. To be able to predict the torsion shear tests, the parameter α defined in section 3.1.4, is determined using the stress-strain relations from triaxial loading during the torsion shear tests.

Triaxial tests on loose Santa Monica Beach Sand have previously been used for parameter determination for The Single Hardening Model e.g. Lade and Inel (1997) and Lade (2005). Some of the parameters determined here are different from those in the papers due to the reasons discussed above.

3.1.1 Elasticity

The elastic strains are calculated from Hooke's law using a nonlinear variation of Young's modulus developed by Lade and Nelson (1987). Young's modulus is expressed in terms of stress invariants and given by:

$$E = M \cdot p_a \cdot \left[\left(\frac{I_1}{p_a} \right)^2 + R \cdot \frac{J_2'}{p_a^2} \right]^{\lambda} \qquad (3.6)$$

in which M and λ are non-dimensional parameters and p_a is atmospheric pressure in the same units as the stresses used in the calculations of I_1 and J_2' (defined in equation (3.2) and (3.5), respectively). The constant R is defined in equation (3.7):

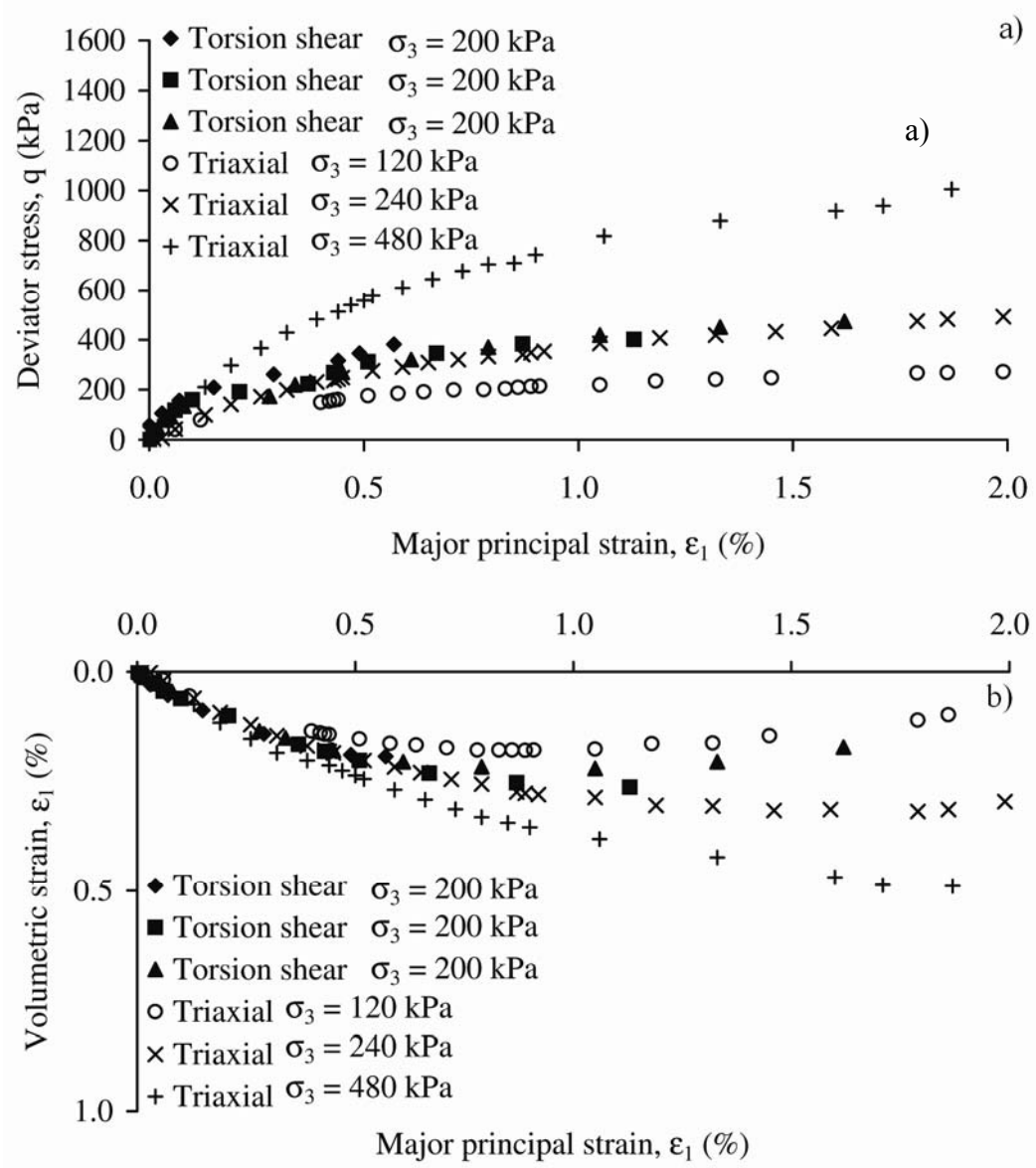

Figure 3.2: Comparison between stress-strain relations on loose Santa Monica Beach Sand performed in torsion shear apparatus and triaxial apparatus. a) Stress-strain relation. b) Vertical strain vs. volumetric strain.

$$R = 6 \cdot \frac{1 + \upsilon}{1 - 2\upsilon} \tag{3.7}$$

in which υ is Poisson's ratio, which is assumed independent of the stress state.

The elastic parameters are determined right after stress reversal during unloading-reloading branches performed during the triaxial tests. The best results for the determination of Poisson's ratio are achieved from the reloading branch. Equation (3.8) shows two different ways of calculating Poisson's ratio: Either from the major and minor principal strains or from the slope of the vertical strain vs. volumetric strain curve.

$$\nu = -\frac{\Delta\varepsilon_3}{\Delta\varepsilon_1} = \frac{1}{2}\left(1 - \frac{\Delta\varepsilon_{vol}}{\Delta\varepsilon_1}\right) \tag{3.8}$$

in which $\Delta\varepsilon_1$ and $\Delta\varepsilon_3$ are the increment in major and minor principal strain, respectively, and $\Delta\varepsilon_{vol}$ is the incremental volumetric strain. For the development of the model used, Lade and Nelson (1987) examined the elastic properties of loose Santa Monica Beach Sand (e = 0.810) and found an average Poisson's ratio of 0.26 with a variation of 0.06. As shown in Figure 3.3, the smaller data set analyzed here supports a value of Poisson's ratio of 0.26.

The parameters M and λ require Young's modulus, E to be determined after stress reversal, where the behavior is assumed elastic. The stress state at reversal is recorded and the stress term inside the parenthesis in equation (3.6) is calculated. By plotting Young's modulus and the stress term on double logarithmic scales, as shown in Figure 3.4, the parameters M and λ can be determined from the best fitted straight line as the value of the normalized Young's modulus at unity and the slope, respectively. The values of M = 600 and λ = 0.27 determined by Lade and Nelson (1987) fits the smaller

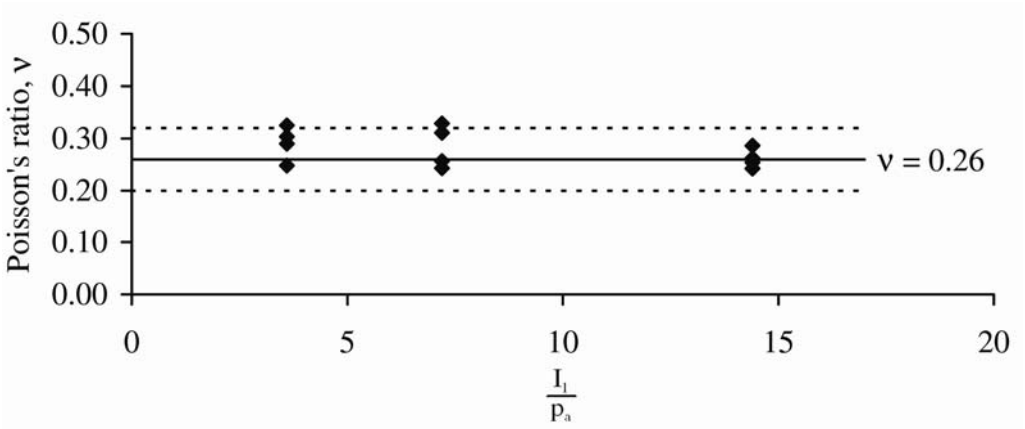

Figure 3.3: Determined values of Poisson's ratio for loose Santa Monica Beach Sand.

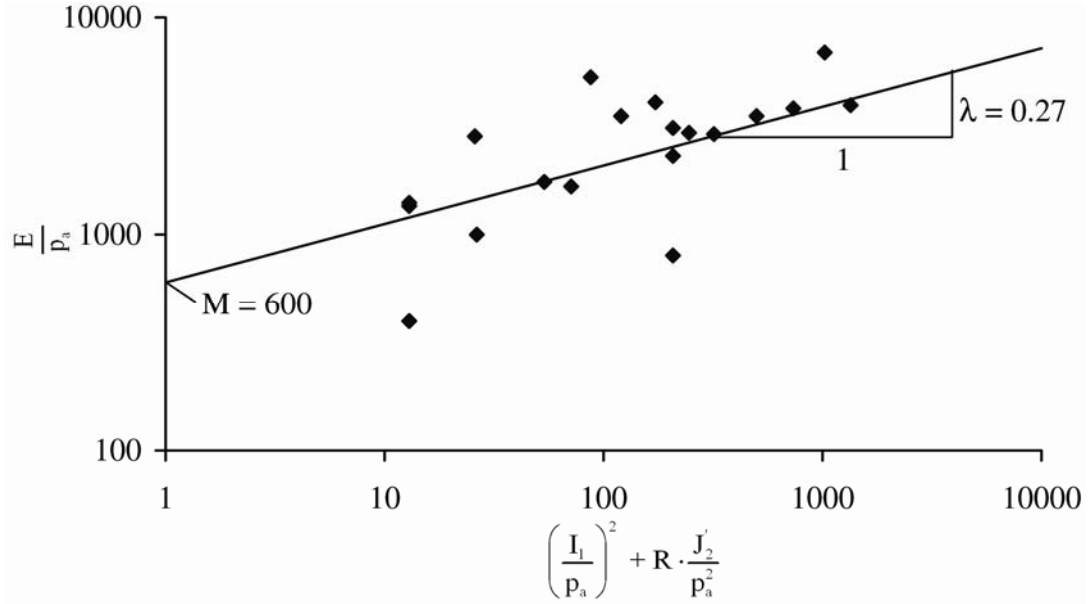

Figure 3.4: Determination of elastic parameters λ and M for loose Santa Monica Beach Sand.

data set analyzed here.

Contours of constant Young's modulus in principal stress space using the elastic parameters for loose Santa Monica Beach Sand are shown in Figure 3.5. The contours are found to be ellipsoidal in the triaxial plane and circular in the octahedral plane. Furthermore, the elastic model is found to be homothetic, meaning the contours do not change shape as they increase in size.

3.1.2 Failure Criterion

The failure criterion used was first presented by Lade (1977) and is expressed in terms of the first and the third stress invariants, I_1 and I_3 respectively:

$$f_n = \left[\frac{I_1^3}{I_3} - 27\right] \cdot \left[\frac{I_1}{p_a}\right]^m = \eta_1 \qquad (3.9)$$

in which η_1 and m are non-dimensional parameters, p_a is atmospheric pressure in the same units as the stresses used in the calculations of I_1 and I_3. The stress invariants, I_1 and I_3 are defined in equation (3.2) and (3.4), respectively.

For the parameter determination, the stresses at failure are recorded and the terms inside the two parentheses in equation (3.9) are plotted on double logarithmic scales as demonstrated in Figure 3.6. The value of the best fitting straight line at unity, defines the parameter η_1 and the slope corresponds to the parameter m. Values of $\eta_1 = 31.2$ and $m = 0.095$ fits the data.

The low value of the exponent m, results in an almost straight failure line, when the failure surface is plotted in the triaxial plane. The plot of the failure surface in the triaxial plane and a plot of two octahedral planes are shown in Figure 3.7.

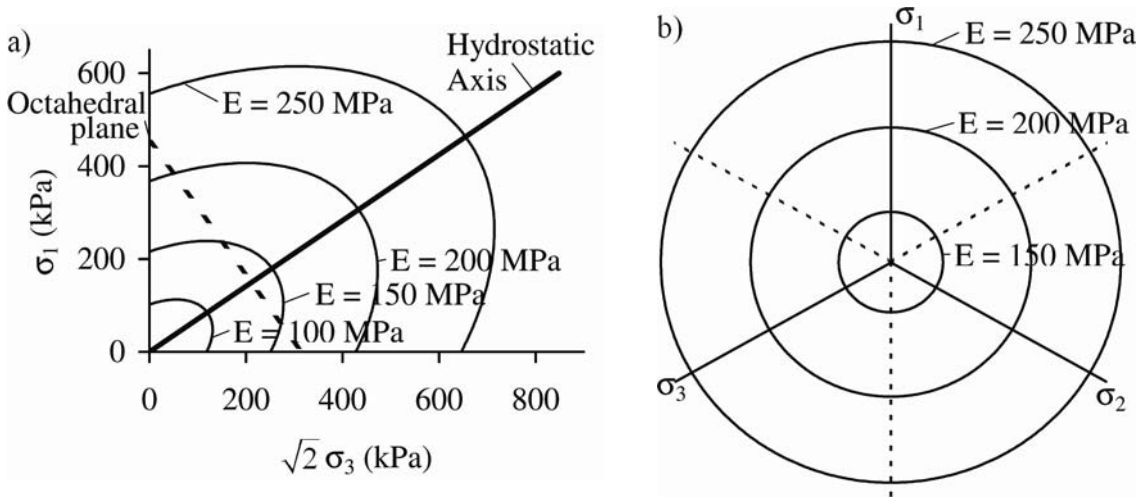

Figure 3.5: Contours of constant elastic modulus in a) triaxial and b) octahedral plane for loose Santa Monica Beach Sand.

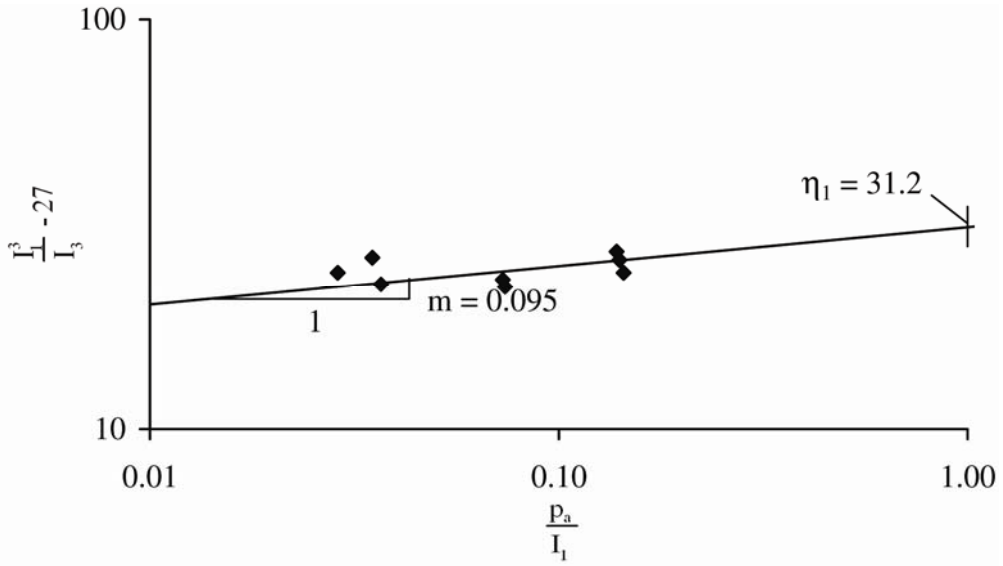

Figure 3.6: Determination of failure parameters m and η_1 for loose Santa Monica Beach Sand.

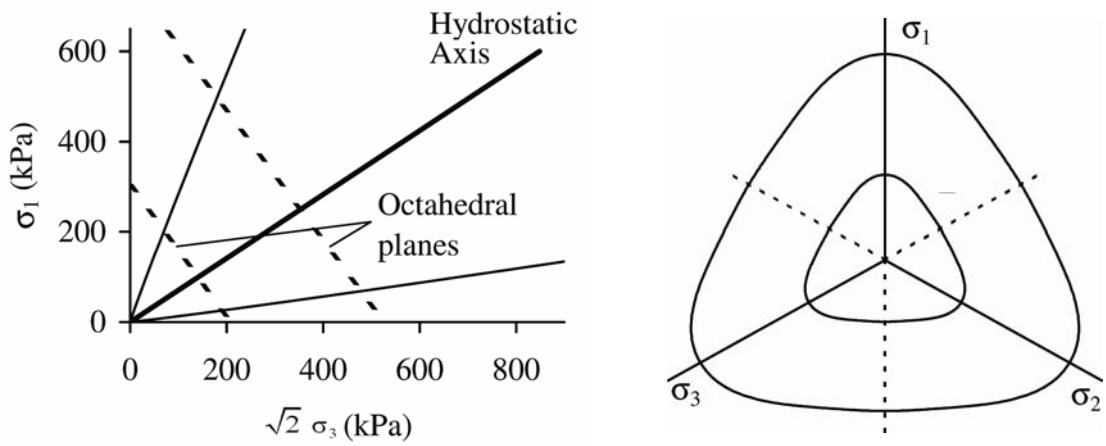

Figure 3.7: Failure surface for loose Santa Monica Beach Sand in a) triaxial and b) octahedral planes.

3.1.3 Flow Rule and Plastic Potential Function

The plastic strain increments, $d\varepsilon_{ij}^{p}$, are calculated from the flow rule in equation (3.10):

$$d\varepsilon_{ij}^{p} = d\lambda_{p} \cdot \frac{\partial g_{p}}{\partial \sigma_{ij}} \tag{3.10}$$

where g_p is a plastic potential function and $d\lambda_p$ is a scalar factor of proportionality. The plastic potential function in The Single Hardening Model was developed by Kim and Lade (1988) and is given by:

$$g_{p} = \left[\psi_{1} \cdot \frac{I_{1}^{3}}{I_{3}} - \frac{I_{1}^{2}}{I_{2}} + \psi_{2} \right] \left[\frac{I_{1}}{p_{a}} \right]^{\mu} \tag{3.11}$$

where Ψ_1, Ψ_2 and μ are dimensionless parameters, I_1, I_2, and I_3 are the first, second, and third stress invariants defined in equation (3.2), (3.3), and (3.4), respectively. The constant p_a is atmospheric pressure in the same units as the stresses used in the calculations of the stress invariants. By differentiating equation (3.11) with respect to the stresses, the derivatives become:

$$\frac{\partial g_p}{\partial \sigma_{ij}} = \left[\frac{I_1}{p_a}\right]^{\mu} \begin{Bmatrix} G - \left(\sigma_{yy}+\sigma_{zz}\right)\frac{I_1^2}{I_2^2} - \psi_1\left(\sigma_{yy}\sigma_{zz}-\tau_{yz}^2\right)\frac{I_1^3}{I_3^2} \\ G - \left(\sigma_{zz}+\sigma_{xx}\right)\frac{I_1^2}{I_2^2} - \psi_1\left(\sigma_{zz}\sigma_{xx}-\tau_{zx}^2\right)\frac{I_1^3}{I_3^2} \\ G - \left(\sigma_{xx}+\sigma_{yy}\right)\frac{I_1^2}{I_2^2} - \psi_1\left(\sigma_{xx}\sigma_{yy}-\tau_{xy}^2\right)\frac{I_1^3}{I_3^2} \\ 2\frac{I_1^2}{I_2^2}\tau_{yz} - 2\psi_1\left(\tau_{xy}\tau_{zx}-\sigma_{xx}\tau_{yz}\right)\frac{I_1^3}{I_3^2} \\ 2\frac{I_1^2}{I_2^2}\tau_{zx} - 2\psi_1\left(\tau_{yz}\tau_{xy}-\sigma_{yy}\tau_{zx}\right)\frac{I_1^3}{I_3^2} \\ 2\frac{I_1^2}{I_2^2}\tau_{xy} - 2\psi_1\left(\tau_{zx}\tau_{yz}-\sigma_{zz}\tau_{xy}\right)\frac{I_1^3}{I_3^2} \end{Bmatrix} \tag{3.12}$$

where

$$G = \psi_1\left(\mu+3\right)\frac{I_1^2}{I_3} - \left(\mu+2\right)\frac{I_1}{I_2} + \frac{\mu}{I_1}\psi_2 \tag{3.13}$$

The scalar factor of proportionality, $d\lambda_p$ introduced in equation (3.10) is related to the plastic work increment, dW_p as shown in equation (3.14):

$$d\lambda_p = \frac{dW_p}{\mu g_p} \tag{3.14}$$

where the increment in plastic work, dW_p is determined from the hardening and softening relations described in equation (3.21) and (3.25) respectively, g_p is the plastic potential function described in equation (3.11), and μ is a parameter in the plastic potential function.

Two of the three parameters used for the plastic potential function need to be determined from triaxial compression tests. However, the parameter Ψ_1 that controls the ratio between the triangular shape of the I_3 term and the circular shape of the I_2 term is

defined as a function of the failure parameter m as:

$$\psi_1 = 0.00155 \cdot m^{-1.27} \tag{3.15}$$

For the determination of the remaining parameters, ψ_2 and μ, the incremental plastic strain ratio, defined in equation (3.16), is calculated by subtracting the incremental elastic strains from the measured strain increments.

$$\nu^p = -\frac{d\varepsilon_3^p}{d\varepsilon_1^p} \tag{3.16}$$

in which ν^p is the incremental plastic strain ratio, $d\varepsilon_3^p$ is the increment in minor principal strain, and $d\varepsilon_1^p$ is the increment in major principal strain. By combining equation (3.12) with equation (3.10) the increment in major and minor plastic strains can be found. By substituting the results under triaxial conditions ($\sigma_2 = \sigma_3$) into equation (3.16), the two parameters, ψ_2 and μ can be isolated as shown in equation (3.17):

$$\xi_y = \frac{1}{\mu}\xi_x - \psi_2 \tag{3.17}$$

where ξ_x and ξ_y are defined in equation (3.18) and equation (3.19), respectively.

$$\xi_x = \frac{1}{1+\nu^p}\left[\frac{I_1^3}{I_2^2}\left(\sigma_1+\sigma_3+2\nu^p\sigma_3\right)+\psi_1\frac{I_1^4}{I_3^2}\left(\sigma_1\sigma_3+\nu^p\sigma_3^2\right)\right]-3\psi_1\frac{I_1^3}{I_3}+2\frac{I_1^2}{I_2} \tag{3.18}$$

$$\xi_y = \psi_1\frac{I_1^3}{I_3}-\frac{I_1^2}{I_2} \tag{3.19}$$

By calculating ξ_x and ξ_y for each increment, and making the ξ_x vs. ξ_y plot shown in Figure 3.8, the parameters ψ_2 and μ can be found. The intersection with the y-axis gives the negative value of ψ_2 and the slope is equal to the inverse of μ. The parameters determined for loose Santa Monica Beach Sand: $\psi_2 = -3.74$ and $\mu = 2.26$.

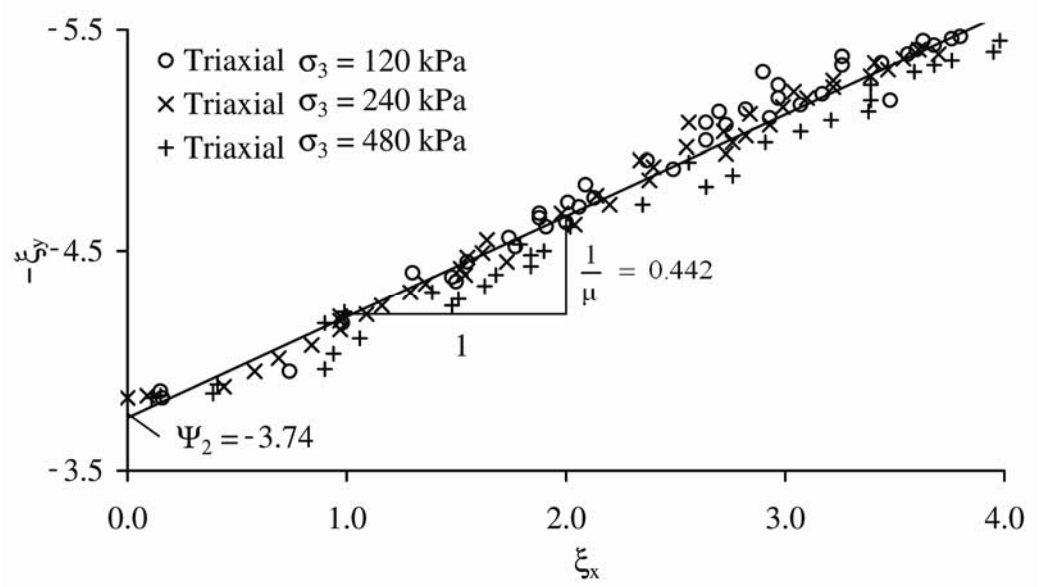

Figure 3.8: Determination of parameters ψ_2 and μ from triaxial compression tests.

In Figure 3.9, the shape of the plastic potential surface defined in equation (3.11) is plotted in the triaxial and octahedral plane, using the parameters determined for loose Santa Monica Beach Sand. As the surfaces of constant elastic modulus (Figure 3.5), the plastic potential surfaces are homothetic. As a consequence, the characteristic line is a straight line in the triaxial plane.

3.1.4 Yield Criterion and Work Hardening/Softening Relation

The yield surface is defined as contours of constant plastic work, and the model uses a single isotropic yield function, defined by Lade and Kim (1988)[a] as:

$$f_p = f'_p(\sigma_{ij}) - f''_p(W_p) = 0 \qquad (3.20)$$

where f'_p describes the yield surface as a function of the stress state and f''_p describes the yield surface as a function of the plastic work. During hardening, the yield surface inflates according to equation (3.21):

$$f''_p = (27\psi_1 + 3)\left(\frac{W_p}{C \cdot p_a}\right)^{\frac{h}{p}} \qquad (3.21)$$

in which C and p are parameters used to model the plastic work during isotropic compression. The parameter ψ_1 is defined in equation (3.15) and the parameter h is related to the shape of the yield surface. The hardening function, described in equation (3.20) is shown in Figure 3.10 along with the softening function that describes the relation between the yield surface and the plastic work after failure.

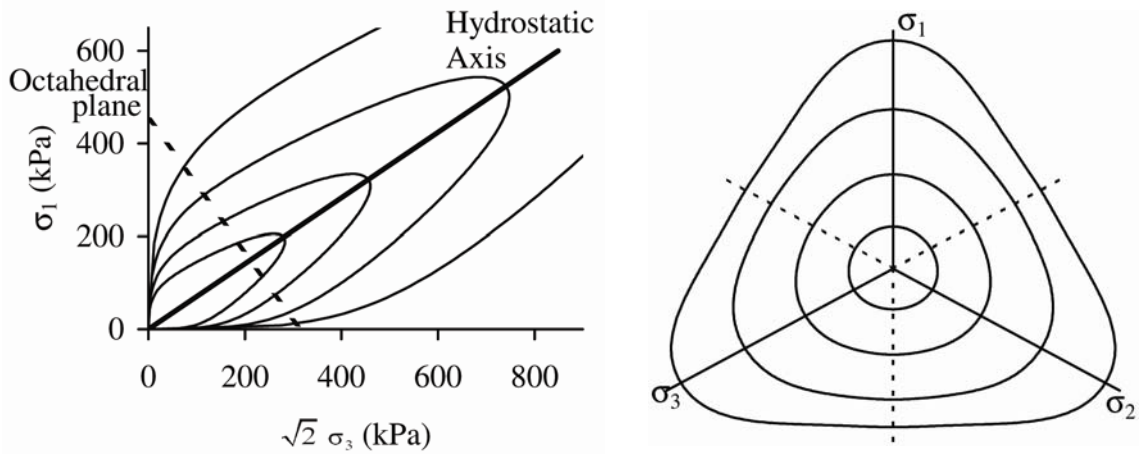

Figure 3.9: Plastic potential surfaces for loose Santa Monica Beach Sand in a) triaxial and b) octahedral plane.

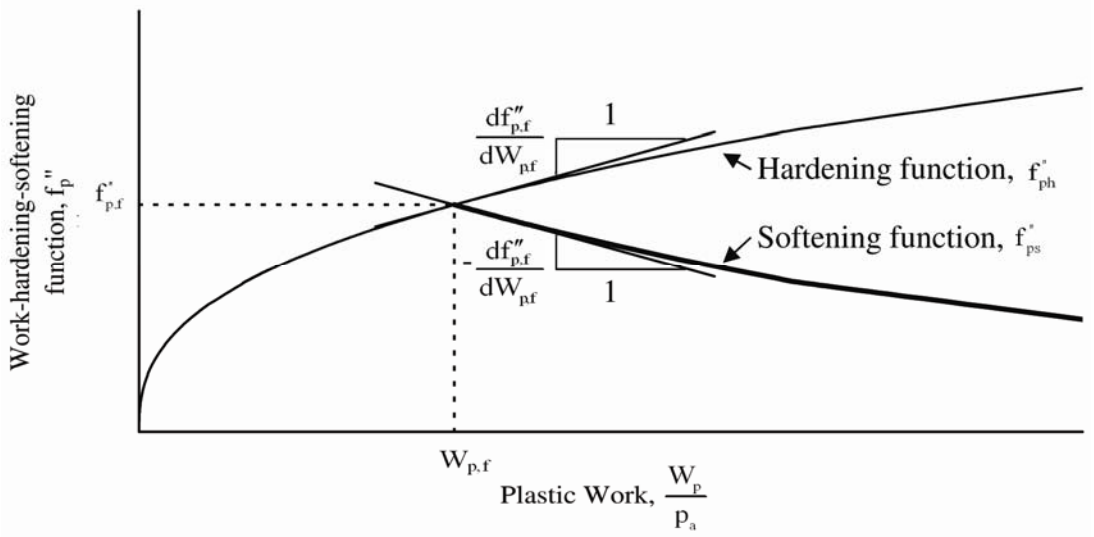

Figure 3.10: The relation between the hardening and softening functions.

The plastic work is calculated as:

$$W_p = \int \left\{ \sigma_{xx} \cdot d\varepsilon^p_{xx} + \sigma_{yy} \cdot d\varepsilon^p_{yy} + \sigma_{zz} \cdot d\varepsilon^p_{zz} + \tau_{xy} \cdot d\gamma^p_{xy} + \tau_{yz} \cdot d\gamma^p_{yz} + \tau_{zx} \cdot d\gamma^p_{zx} \right\} \quad (3.22)$$

in which the direction of the normal stresses (σ_{xx}, σ_{yy}, σ_{zz}) and the shear stresses (τ_{xy}, τ_{yz}, τ_{zx}) are defined in Figure 3.1. The incremental plastic strain in normal directions ($d\varepsilon_{xx}$, $d\varepsilon_{yy}$, $d\varepsilon_{zz}$) and the incremental plastic shear strains ($d\gamma_{xy}$, $d\gamma_{yz}$, $d\gamma_{zx}$) follow the same suffix convention as the stresses. The plastic strains are calculated by subtracting the elastic strains from the measured strains. For isotropic compression, equation (3.22) reduces to:

$$W_p = \int \left\{ \sigma_c \cdot d\varepsilon^p_{vol} \right\} \quad (3.23)$$

where σ_c is the confining pressure during isotropic compression and $d\varepsilon_{vol}$ is the incremental volumetric plastic strain. With the plastic work and the stress state known, the parameters C and p are determined from an isotropic compression test. The plastic work is modeled as:

$$W_p = C \cdot p_a \left(\frac{I_1}{p_a} \right)^p \quad (3.24)$$

Figure 3.11 shows the relation between the normalized first stress invariant and the normalized plastic work in a double logarithmic diagram. The parameter C is determined as the work at unity and the parameter p is the slope of the line.

During softening, the yield surface deflates iostropically and the softening function suggested by Lade and Kim (1988)[a] consists of an exponential decay function that replaces the hardening function at failure:

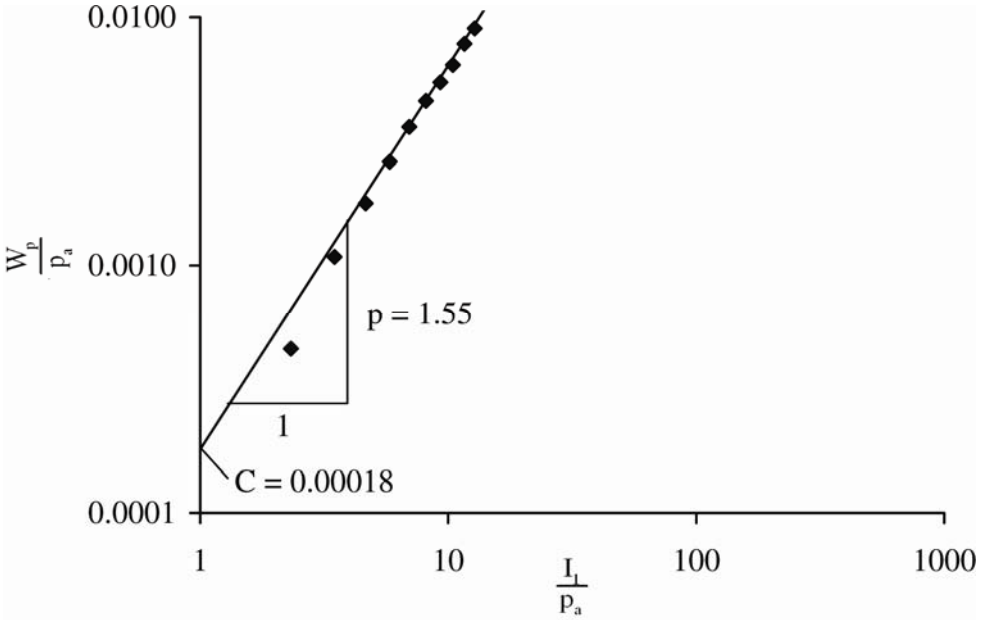

Figure 3.11: Determination of parameters C and p from isotropic compression test.

$$f_p'' = A \cdot e^{-B\frac{Wp}{p_a}} \tag{3.25}$$

in which A and B are positive constants determined on the basis of the hardening curve at failure. The initial slope of the softening curve is equal to the negative slope of the hardening curve at failure, (Figure 3.10) and is controlled by the constants B and A defined in equation (3.26) and (3.27) respectively:

$$B = \frac{df_{p,f}''}{dW_p} \cdot \frac{1}{f_{p,f}'} \tag{3.26}$$

$$A = f_{p,f}' \cdot e^{-B\frac{Wp,f}{p_a}} \tag{3.27}$$

The yield surface is expressed in terms of the stresses:

$$f_p' = \left[\psi_1 \cdot \frac{I_1^3}{I_3} - \frac{I_1^2}{I_2} \right] \left[\frac{I_1}{p_a} \right]^h \cdot e^q \tag{3.28}$$

in which h is a parameter to be determined and q is calculated as:

$$q = \frac{\alpha \cdot S}{1 - (1 - \alpha) \cdot S} \tag{3.29}$$

where α is a parameter to be determined and S is the stress level defined as:

$$S = \frac{f_n}{\eta_l} = \frac{1}{\eta_l} \cdot \left[\frac{I_1^3}{I_3} - 27 \right] \left[\frac{I_1}{P_a} \right]^m \tag{3.30}$$

in which f_n is the expression for the failure surface defined in equation (3.9) and used at any stress state inside the failure surface. The stress level, S varies from zero at the hydrostatic axis to one on the failure surface. The hyperbolic expression between S and q in equation (3.29) results in the value of q varying from zero at the hydrostatic axis to one at failure.

The yield surface being defined as a contour of constant plastic work is used in the determination of the parameter h. Two points, lying on the same yield surface, have the same value of $f_p^{'}$. Point (A) is on the hydrostatic axis and point (B) is at failure. This can be expressed as:

$$\left[\psi_1 \cdot \frac{I_{1A}^3}{I_{3A}} - \frac{I_{1A}^2}{I_{2A}}\right]\left[\frac{I_{1A}}{p_a}\right]^h \cdot e^{q_A} = \left[\psi_1 \cdot \frac{I_{1B}^3}{I_{3B}} - \frac{I_{1B}^2}{I_{2B}}\right]\left[\frac{I_{1B}}{p_a}\right]^h \cdot e^{q_B} \tag{3.31}$$

As the point A is on the hydrostatic axis, q = 0, and point B being at failure, results in q = 1. Furthermore, the relation between the first, second and third stress invariants at hydrostatic stresses results in the following reduction of equation (3.31):

$$[27\psi_1 + 3]\left[\frac{I_{1A}}{p_a}\right]^h = \left[\psi_1 \cdot \frac{I_{1B}^3}{I_{3B}} - \frac{I_{1B}^2}{I_{2B}}\right]\left[\frac{I_{1B}}{p_a}\right]^h \cdot e \tag{3.32}$$

from which h can be calculated as:

$$h = \frac{\ln\left(\psi_1 \cdot \frac{I_{1B}^3}{I_{3B}} - \frac{I_{1B}^2}{I_{2B}}\right) + 1 - \ln\left(27\psi_1 + 3\right)}{\ln\left(\frac{I_{1A}}{I_{1B}}\right)} \tag{3.33}$$

Once the parameter h is known, the variation of q during triaxial compression can be found by substituting equation (3.28) and (3.21) into (3.20) and solving for q. The result is shown in equation (3.34):

$$q = \ln\left(\frac{27\psi_1 + 3}{\psi_1 \frac{I_1^3}{I_3} - \frac{I_1^2}{I_2}} \cdot \frac{\left(\frac{W_p}{C \cdot p_a}\right)^{\frac{h}{p}}}{\left(\frac{I_1}{p_a}\right)^h}\right) \tag{3.34}$$

The variation of the stress level S as a function of q is shown in Figure 3.12. The parameter α is then determined from equation (3.35) using the value of q for S = 0.80.

$$\alpha = \frac{1}{4} \cdot \frac{q_{80}}{1-q_{80}} \tag{3.35}$$

in which q_{80} is the value of q at a stress level S of 0.80.

The line in Figure 3.12 is the relation between S and q defined in equation (3.29) and using the value of α = 0.34 determined for loose Santa Monica Beach Sand. Note that the parameter α is determined from triaxial loading in three torsion shear tests. The reason for this is the difference in stiffness between the triaxial tests and the torsion shear tests. This difference only affects the determination of the yield surface parameter α.

Using the parameters determined for loose Santa Monica Beach Sand, contours of the yield surface in the triaxial and octahedral plane have been plotted in Figure 3.13.

3.1.5 Material with Cohesion

For materials with cohesion an extra parameter, a, is introduced. This parameter is added to the normal stresses, to translate the principal stress space along the hydrostatic axis:

$$\bar{\sigma}_{ij} = \sigma_{ij} + \delta_{ij} \cdot a \cdot p_a \tag{3.36}$$

in which σ_{ij} is the stresses to be translated, δ_{ij} is Kronecker's delta ($\delta_{ij} = 1$ for $i = j$, $\delta_{ij} = 0$ for $i \neq j$), a is a dimensionless parameter, and p_a is atmospheric pressure in the same units as σ_{ij}. The translation should take place before parameter determination, and the predictions, should take place in the translated coordinate system as well. A pre-established yield surface ensures positive plastic work from the beginning of compressive loading (Figure 3.14).

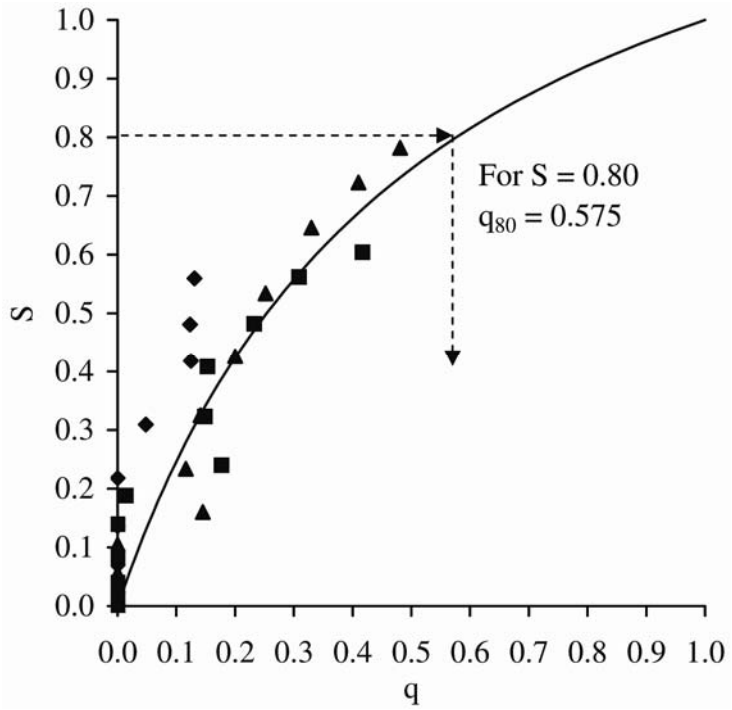

Figure 3.12: Relation between q and stress level S, for determination of the parameter α.

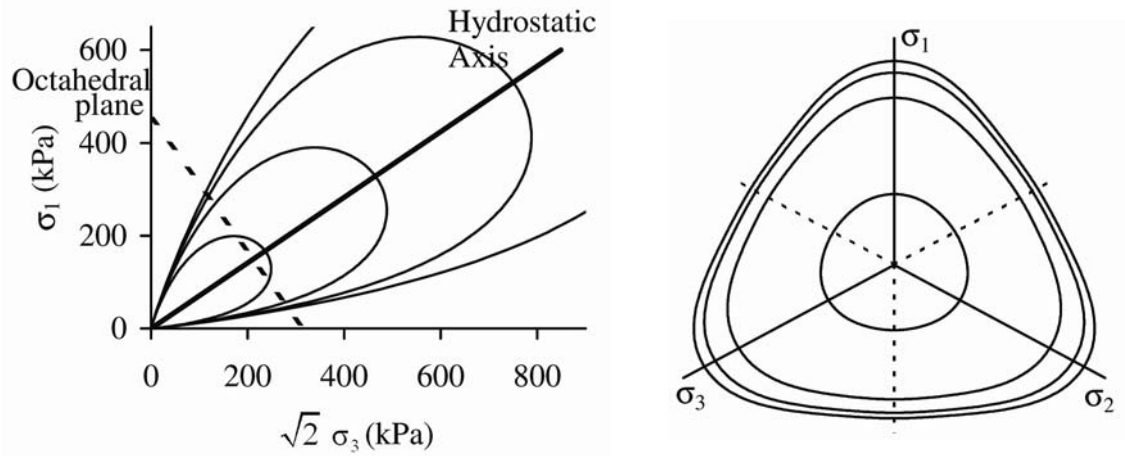

Figure 3.13: Yield surfaces for loose Santa Monica Beach Sand in a) triaxial and b) octahedral plane.

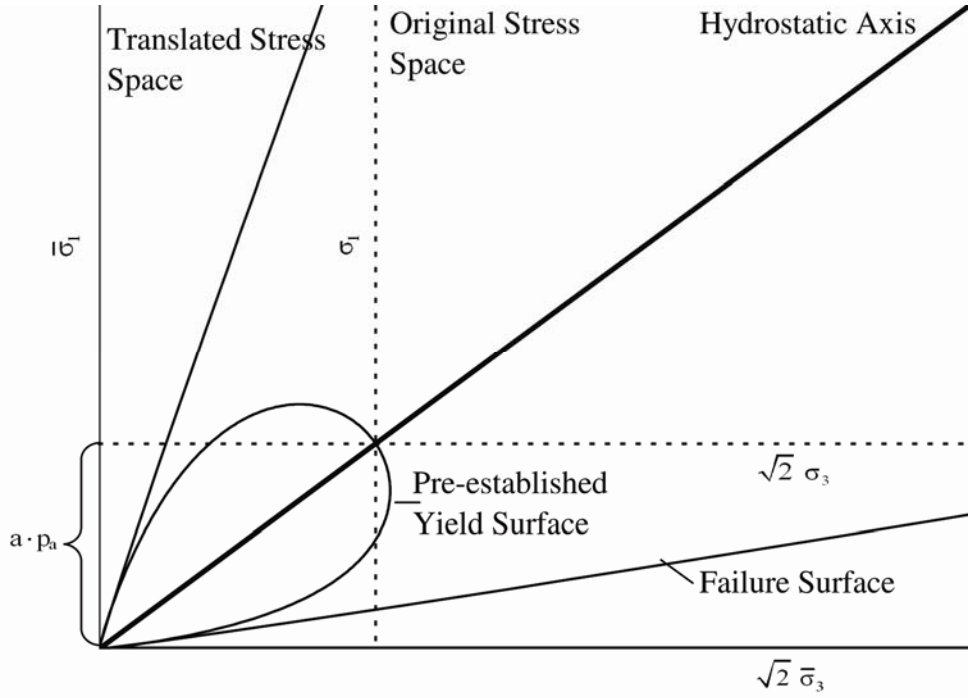

Figure 3.14: Translation of the coordinate system along the hydrostatic axis allows prediction of material with cohesion.

3.1.6 Summary of Parameters Determined

The parameters determined for Santa Monica Beach Sand, are summarized in Table 3.1 and Table 3.2 along with parameters determined for F1-Sand, L1-Sand, L2-Sand, L8-Sand from and Nevada Sand. The test data for the tests on F1-Sand, L1-Sand, L2-Sand, and L8-Sand are acquired from Lade (1992) and repeated in Appendix E. The test data for Nevada Sand are from Yamamuro and Lade (1999).

3.2 Suggested Improvements

3.2.1 Hardening Parameters

The behavior of silty sand in drained triaxial compression differs from regular sand by showing large contractive volumetric strains. Furthermore, very little variation in the volumetric response with confining pressure is experienced (Yamamuro and Lade 1997, Lade and Yamamuro 1997). An example of this behavior is shown in Figure 3.15 where the stress-strain relationship for three triaxial tests on Nevada 50/200 Sand with 20 % fines is shown. The 50/200-designation refers to the particle sizes being between No. 50 and No. 200 sieves. A small amount of dilation is observed at larger strains.

The presence of fines in the soil was identified as the likely cause of this behavior. The silt grains and the sand grains form a structure where some of the silt grains are interlocked between the sand grains. The silt grains separating the sand grains, as shown in Figure 3.16 a), are believed to significantly affect the volumetric behavior of the soil. Figure 3.16 b) shows the effect of loading, where the soil structure collapses as the silt grains fill up the voids in the sand. After the collapse of the structure, the sand behaves

Table 3.1: Elastic, failure, and hardening parameters determined for different sands.

Material	ν	M	λ	m	η_1	C	p
Santa Monica Beach Sand	0.26	600	0.27	0.095	31.2	0.000180	1.55
F1-Sand	0.14	350	0.40	0.23	53	0.000028	1.92
L1-Sand	0.23	300	0.38	0.28	90	0.000045	1.89
L2-Sand	0.23	400	0.37	0.37	140	0.000050	1.69
L8-Sand	0.23	400	0.37	0.19	67	0.000170	1.41
Nevada Sand	0.23	371	0.25	0.071	20.0	0.00018	2.60

Table 3.2: Plastic potential and yield parameters determined for different sands. *The yield parameters h and α were not unique values. This issue is addressed in section 3.2.

Material	ψ_2	μ	h	α
Santa Monica Beach Sand	-3.74	2.26	0.60	0.34
F1-Sand	-3.17	2.23	0.73	0.58
L1-Sand	-3.17	2.31	0.78	0.58
L2-Sand	-3.09	2.29	0.75	1.00
L8-Sand	-3.21	2.04	0.60	0.41
Nevada Sand	-4.07	2.29	N/A*	N/A*

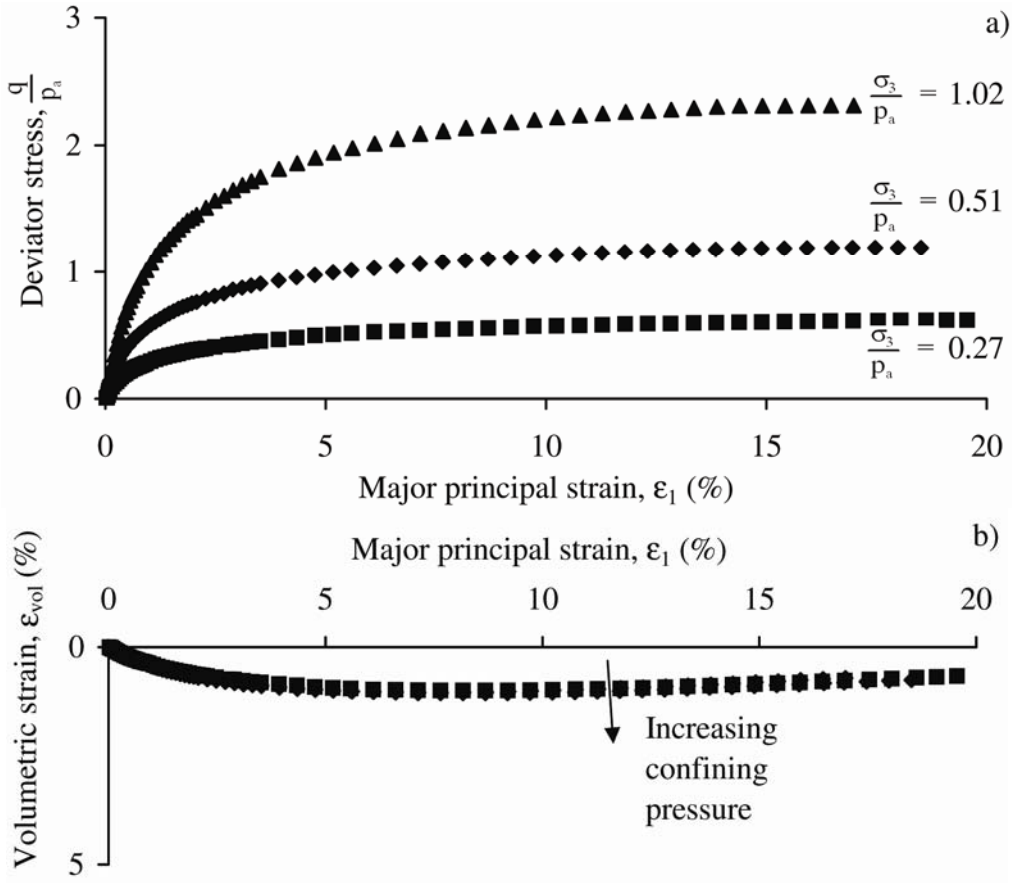

Figure 3.15: Observed behavior of Nevada 50/200 Sand with 20 % fines. a) Stress-stain relation. b) Volume change relation. From Yamamuro and Lade (1999).

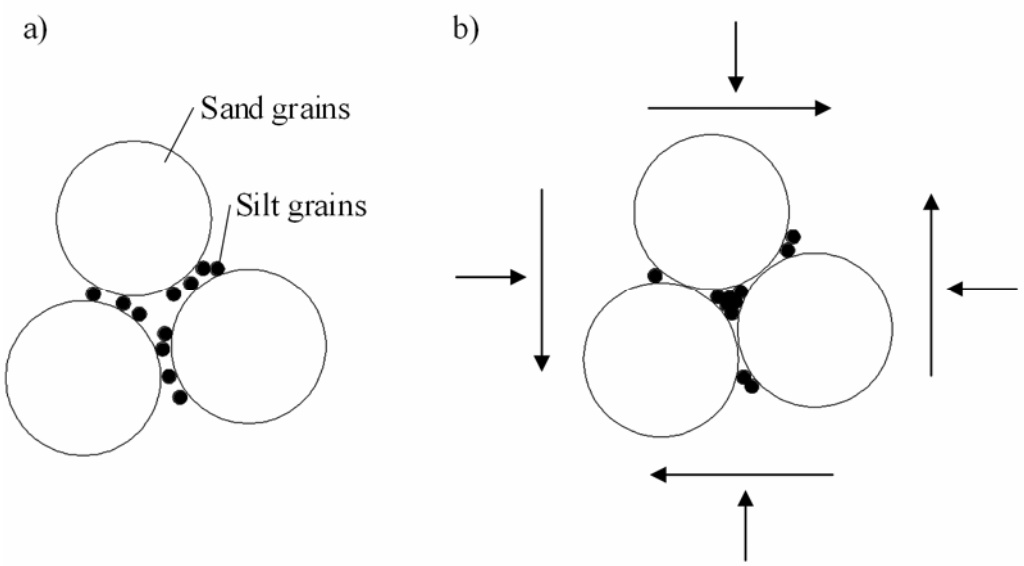

Figure 3.16: Schematic diagram showing silty sand a) deposited in a loose state with sand grains separated by silt grains and b) the silt grains moved into the void spaces by applied stresses, causing large contraction and static liquefaction. After Yamamuro and Lade (1997).

similar to dense sand. A consequence of the densification is the dilation experienced at large strains.

An attempt to model the behavior of silty sand with The Single Hardening Model was done by Yamamuro and Lade (1999), where the three triaxial tests in Figure 3.15 were predicted. This was done by a modification to the yield criterion and the work hardening law. However, the equations used for the parameter determination, later turned out to contain an error, rendering the modified parameter determination impossible.

The decision to modify the yield surface was based on the variation of the yield surface parameters determined for Nevada 50/200 Sand. The parameter h varied from 0.62 in the triaxial test with the lowest confining pressure to 1.06 in the test with the highest confining pressure, with an average of 0.82. Using the average value of h = 0.82 results in the variation between q and S shown in Figure 3.17. There is no unique relation between q and S for the three tests. At low confining pressures, a maximum value of 0.59 for the stress level S is reached when q is equal to one. The q-S relation at the intermediate confining pressure is S-shaped rather than the hyperbolic variation expected. At high confining pressures S reaches unity while q is equal to 0.66.

Because the shape of the yield surface in The Single Hardening Model is defined as a contour of constant plastic work, it is possible to indicate the shape from the triaxial tests. The plastic work during each of the triaxial tests (and the isotropic loading before shearing) is calculated. Based on the work calculated, four contours of constant plastic work are shown in Figure 3.18. The first surface, indicated by the black diamonds is defined by the plastic work produced at the end of isotropic loading in the triaxial test

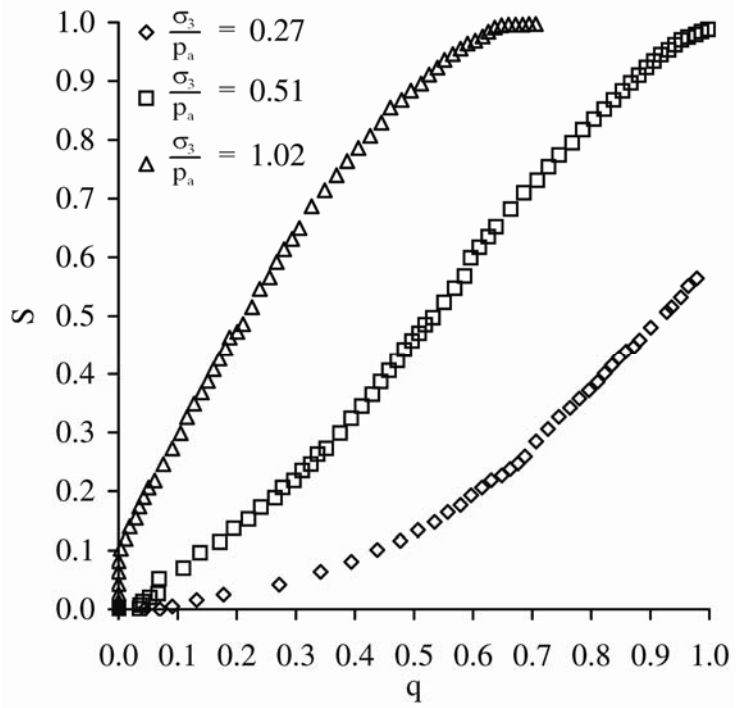

Figure 3.17: Variation between q and S for three triaxial tests on Nevada 50/200 Sand render the determination of yield surface parameter α impossible.

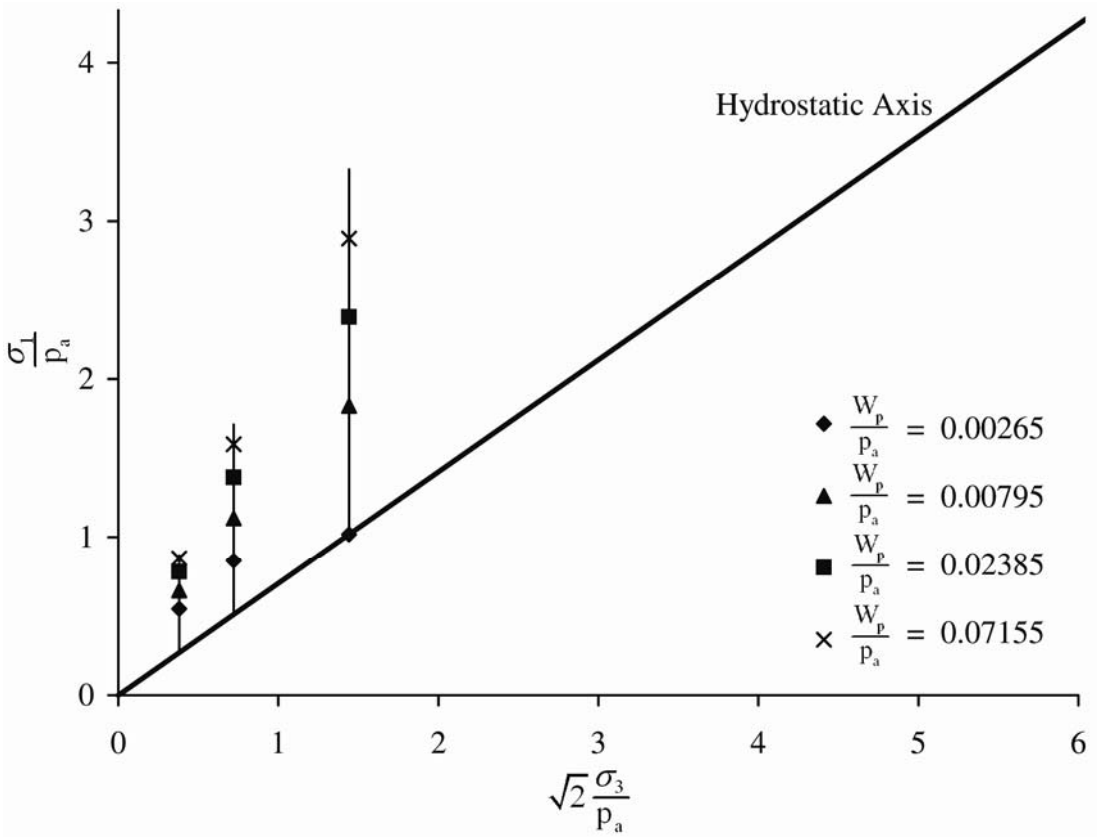

Figure 3.18: Contours of constant plastic work used to determine the shape of the yield surface.

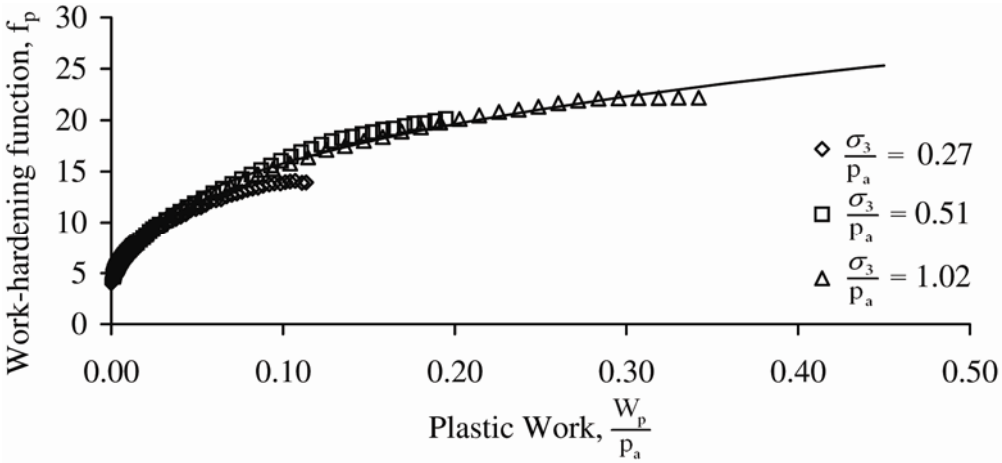

Figure 3.19: Relation between plastic work, W_p and f_p used for determination of parameters C and p.

with the highest confining pressure. The normalized plastic work has a value of 0.00265. The succeeding surfaces all have the plastic work increased by a factor of 3. The contours indicated would suggest a long flat yield surface.

The isotropic compression test used to determine the parameters C and p come from the isotropic loading before shearing of the triaxial test with the highest confining pressure. Comparing the amount of plastic work produced during the isotropic compression test with the plastic work produced at failure gives ratios of 0.024, 0.014, and 0.008 for the tests with the lowest, intermediate, and highest confining pressures, respectively. This means that the isotropic work relation used to determine the parameters C and p, at best represents 2.5 % of the work produced during triaxial loading.

Another way to determine the work-hardening parameters C and p, along with the yield surface parameters h and α, is from the relation between the plastic work, W_p and the value of f_p, using a plot similar to Figure 3.10. The procedure requires a few iterations but can be made relatively simple using a spreadsheet. The values of C and p are estimated, and the parameters h and α are determined as usual (average values are used as the variation is great during the first iterations). The relation between the plastic work, W_p and f_p'' is plotted using equation (3.21). The plastic work during the triaxial tests are determined and the value of f_p' is calculated using the determined values of h and α, and equation (3.28), (3.29), and (3.30). The work-hardening relations from each of the three triaxial tests during hardening should all coincide. The optimum result for Nevada 50/200 Sand is shown in Figure 3.19. The results from the triaxial tests are found to coincide with the isotropic work-hardening relation for values of C^* and p^* equal to

0.0015 and 0.70, respectively. The suffix * is added to indicate the parameters being determined from the triaxial tests.

Using C^* and p^* in the parameter determination of the yield surface parameters, h becomes 0.22 for all three tests. The relation between q and S is plotted in Figure 3.20 and reveals a value of α equal to 0.60.

Using the yield surface parameters ($h = 0.22$ and $\alpha = 0.60$) determined using C^* and p^*, the shape of the yield surface in the triaxial plane in shown in Figure 3.21. The shape is long and flat, as indicated by the constant work contours in Figure 3.18.

The parameters C^* and p^* would suggest a lower rate of work produced than that originally obtained form the isotropic compression of the triaxial test with the highest confining pressure. This can be seen in Figure 3.22 where the plastic work obtained during the isotropic compression is compared with the rate obtained from C^* and p^*. The two lines are found to cross each other at a normalized isotropic stress of 1.02 ($I_1 = 3.06$). The plastic work produced at isotropic stresses lower than 1.02, is found to be higher using C^* and p^*, but since the plastic work only represented between 0.0 and 2.5 % of the total work, the implications by using the parameters C^* and p^* for prediction of the triaxial tests are insignificant. This can be seen in Figure 3.23 where the observed and predicted behavior of Nevada 50/200 Sand is presented. The stress-strain relations and the unusual, similar volumetric response for the three different confining pressures are predicted with good accuracy.

Isotropic compression tests on silty Nevada Sand with a similar gradation curve as Nevada 50/200 Sand but different void ratios indicate high compressibility at low

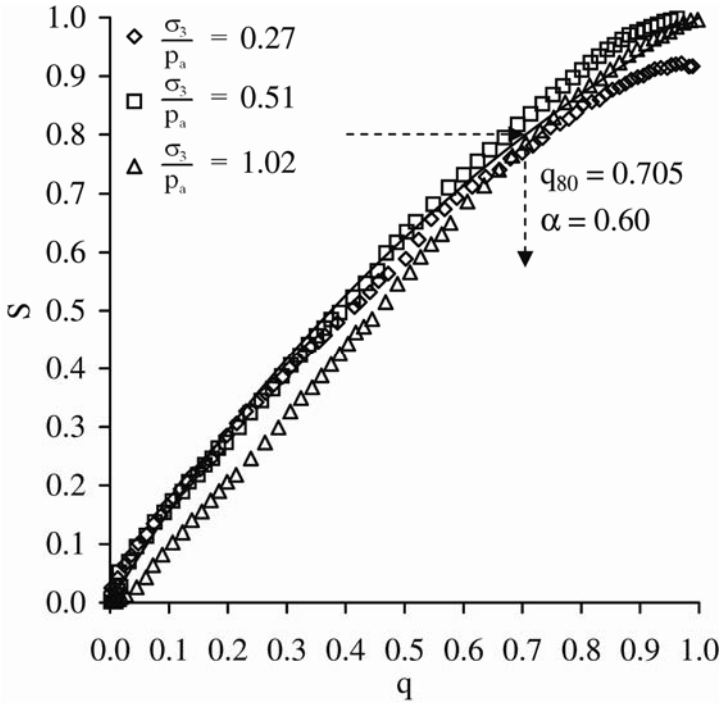

Figure 3.20: Determination of yield surface parameter α for Nevada 50/200 Sand.

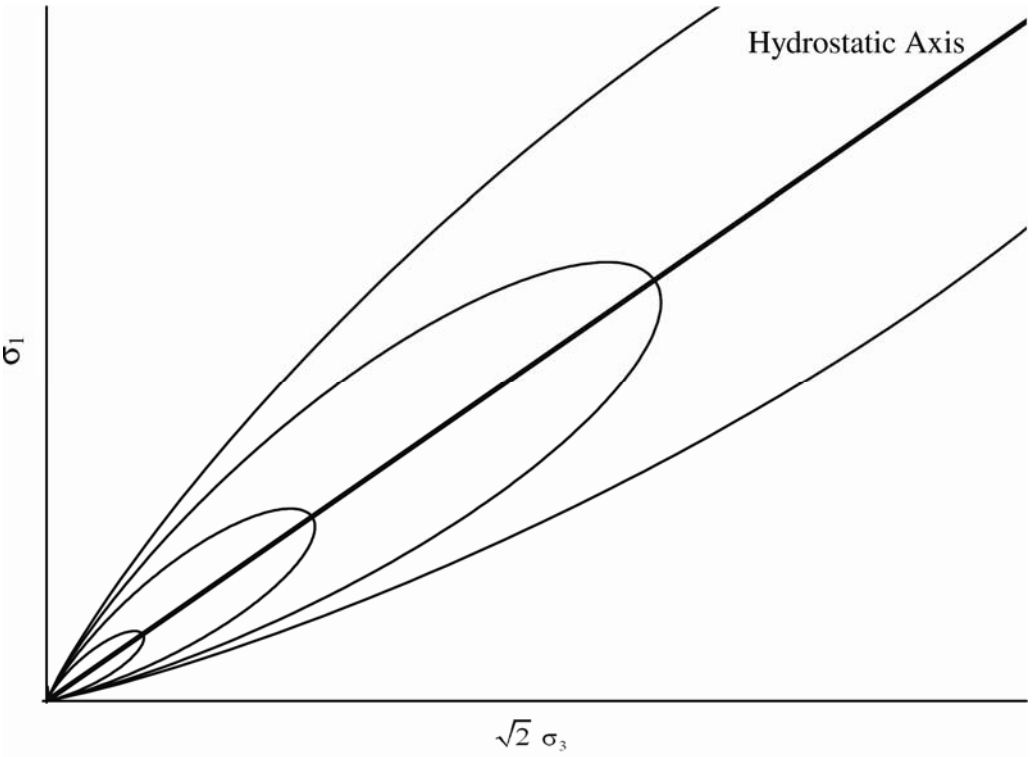

Figure 3.21: The shape of the yield surface for Nevada 50/200 Sand plotted in the triaxial plane.

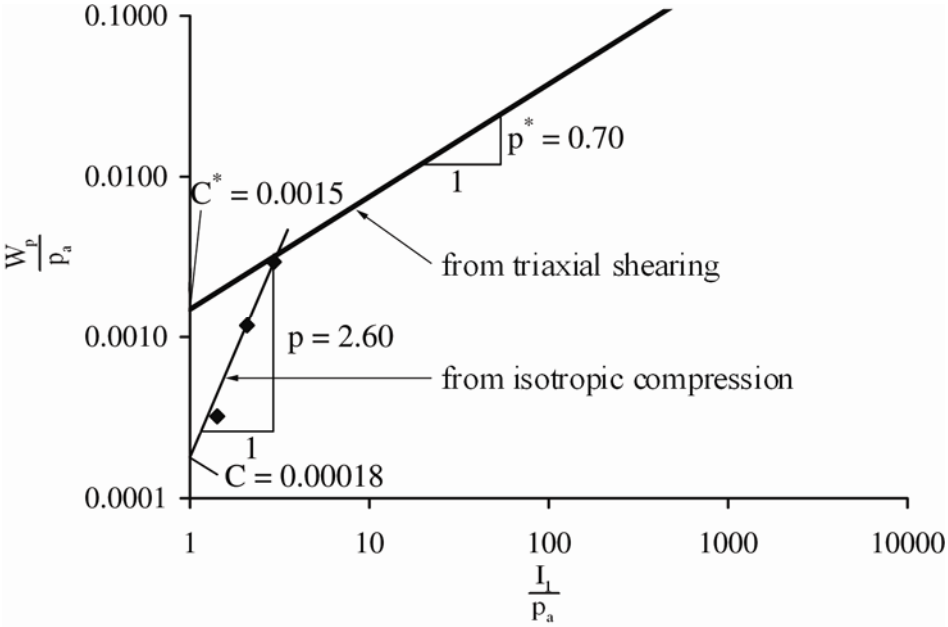

Figure 3.22: Comparison of the two different pair of isotropic hardening parameters determined for Nevada 50/200 Sand. Parameters C and p are determined from the measured isotropic compression test, whereas the parameters C^* and p^* are determined from iteration of the triaxial tests.

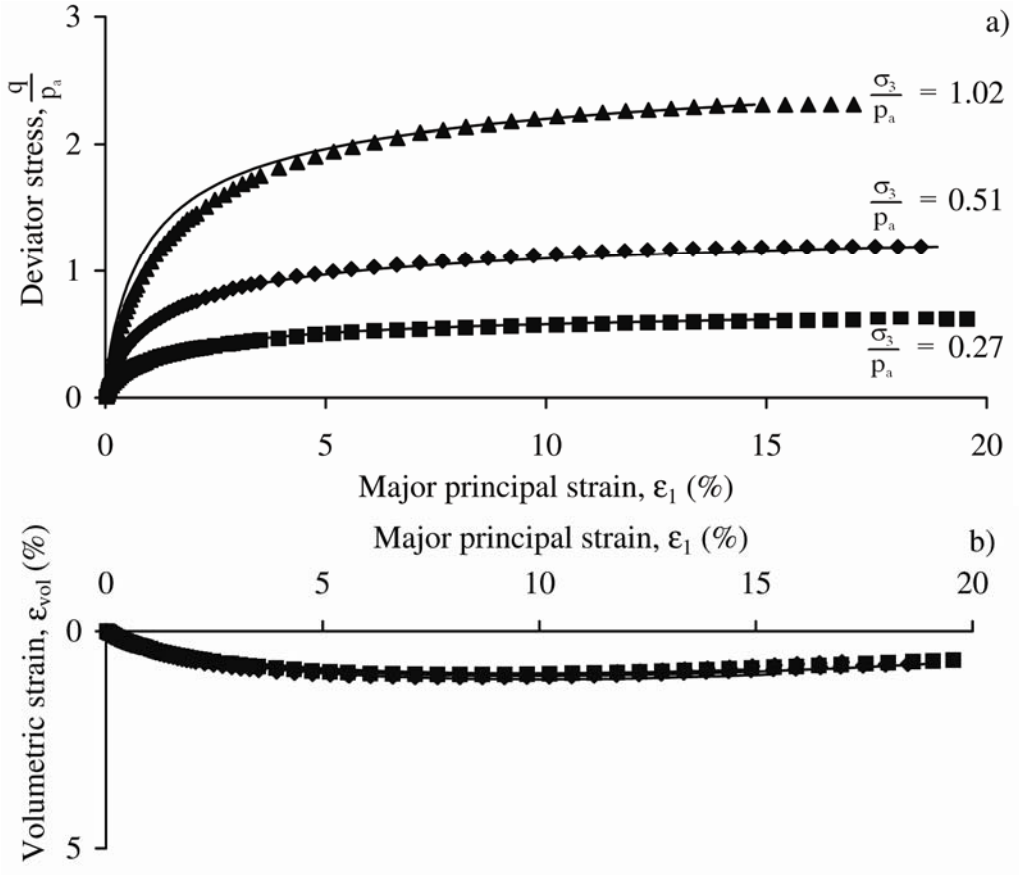

Figure 3.23: Observed and predicted behavior of Nevada 50/200 Sand. a) Stress-stain relation. b) Volume change relation.

confining pressures (Yamamuro and Lade 1997). The high compressibility at low confining pressures was explained by collapse of the sand-silt structure as discussed above. The high compressibility was experienced at normalized isotropic stresses below approximately 1.0-1.5 where the isotropic compression test of Nevada 50/200 Sand took place. This high compressibility would result in a high rate of work produced. As a result, the work produced during isotropic compression at normalized confining pressures above 1.0-1.5 cannot be modeled using the same parameters as below 1.0-1.5. This is demonstrated in Figure 3.24 where the isotropic compression test is back predicted using both C and p, and C^* and p^*. The yield parameters determined using C^* and p^* were used in both cases, as it was assumed the shape of the yield surface did not change. The back prediction of the isotropic loading is done most accurately using C and p. However, at higher confining pressures, the parameters C^* and p^* would produce the most accurate prediction.

A simple sway to overcome the problem of the variation in work hardening parameters is to define an initial hardening yield surface. Inside this hardening surface, the parameters C and p are used, and outside the surface C^* and p^* are used. The shape of the hardening yield surface is defined using the parameters of the ordinary yield surface, and it intersects the hydrostatic axis at a normalized pressure of 1.02. Using this modification, the prediction of the isotropic compression yields the result shown in Figure 3.25. An abrupt bend in the relation between the volumetric strain and the normalized confining pressure reveals the transition between the two sets of parameters.

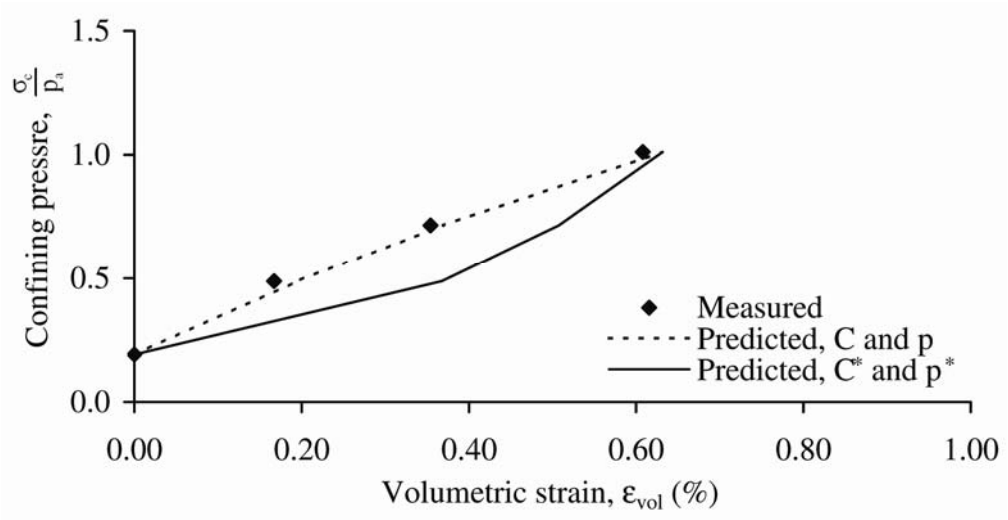

Figure 3.24: Observed and predicted behavior of Nevada 50/200 Sand during isotropic compression.

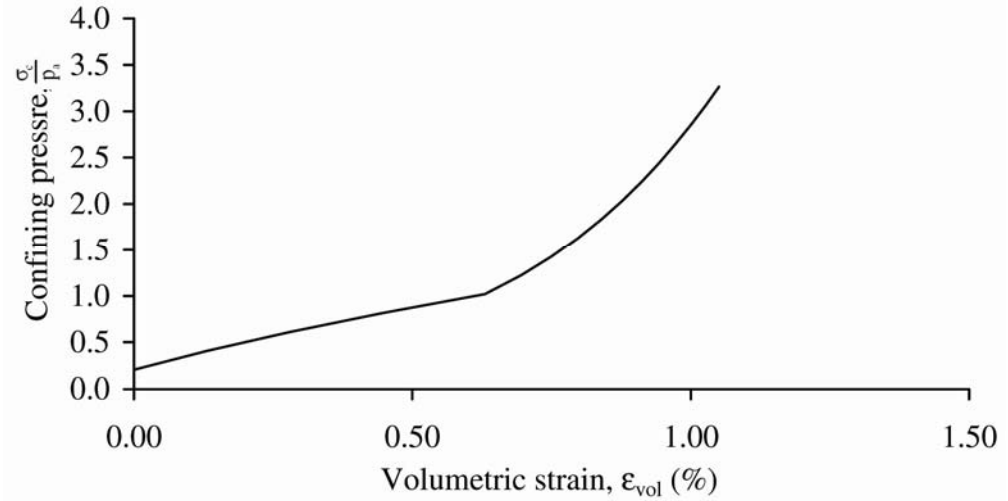

Figure 3.25: Predicted behavior of Nevada 50/200 Sand during isotropic loading, with C and p used inside a hardening yield surface, and C^* and p^* used outside the surface.

A similar bend is experienced when using the model to predict the triaxial tests, and no improvement over just using C^* and p^* is experienced in these tests. To avoid the bend a smooth transition from the high rate of work produced at low pressures to the lower rate at higher pressures is needed. This would make it possible to predict the isotropic compression at low pressures. It would, however, require a work-hardening relation capable of containing the change in compressibility experienced.

The hardening parameters and yield surface parameters for Santa Monica Beach Sand, F1-Sand, L1-Sand, L2-Sand and L8-Sand have all been tested by the procedure described above. Only L1-Sand showed significantly different results, with the new parameters indicated in Table 3.1. The improvement obtained for the prediction of the behavior of L1-Sand by using the new parameters, can be seen in Figure 3.26 and Figure 3.27, where the triaxial tests are predicted using both the originally determined and the newly determined yield and hardening parameters. The predicted stress-strain behavior is improved using the new parameters whereas the volumetric response is somewhat improved at low confining pressures, but still underestimate the contraction at high confining pressures. This is addressed again in more detail in section 3.2.2 where the plastic potential function is reviewed.

The suggested method for obtaining the parameters required to successfully predict the behavior of silty sand, raises some additional questions: (1) when to use the modified method and (2) what to do when predicting isotropic compression tests on silty sand.

Table 3.3: Plastic potential and yield parameter determined.

Material	C	p	h	α
Nevada Sand	0.00150	0.70	0.22	0.60
L1-Sand	0.00014	1.74	0.84	0.58

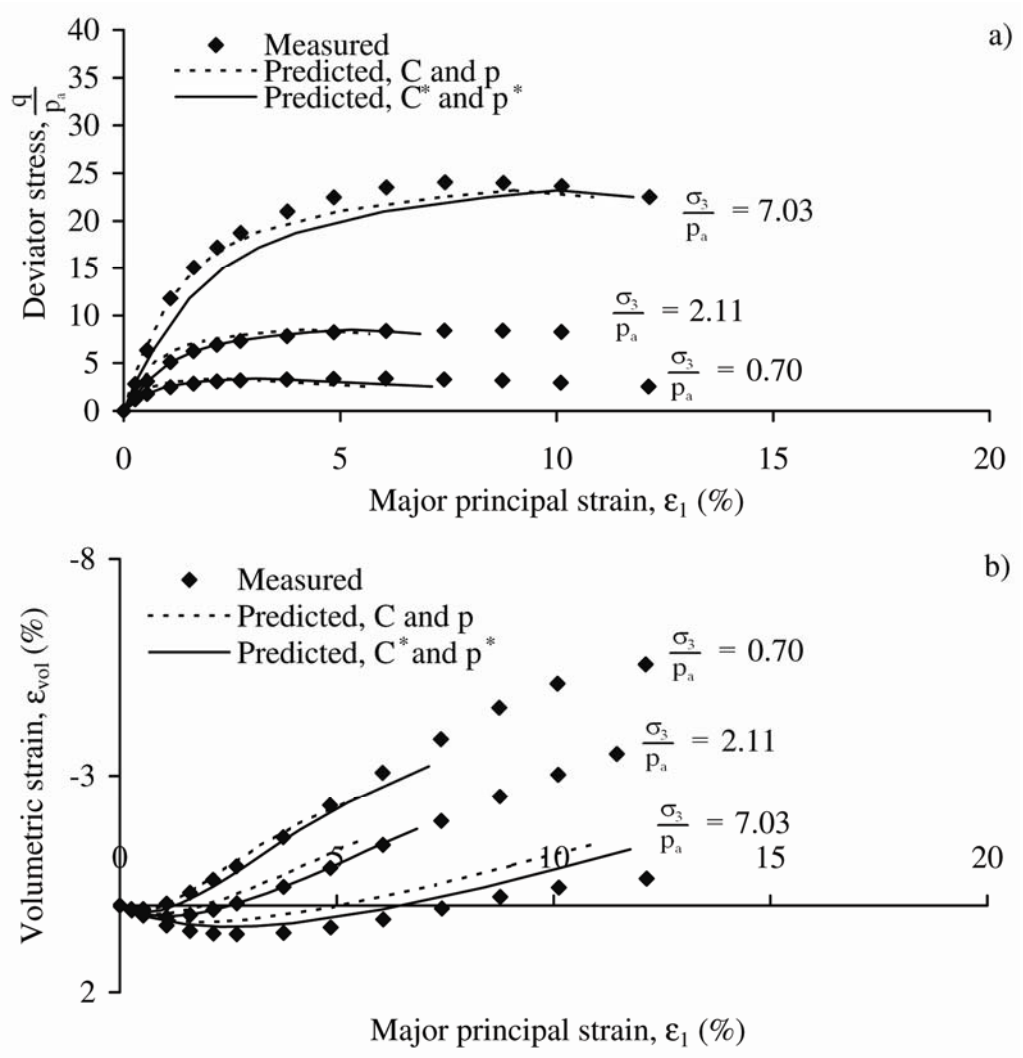

Figure 3.26: Comparison of predicted behavior of L1-Sand at low confining pressures using C and p determined from isotropic compression and from the triaxial tests. a) Stress-strain relation. b) Volume change.

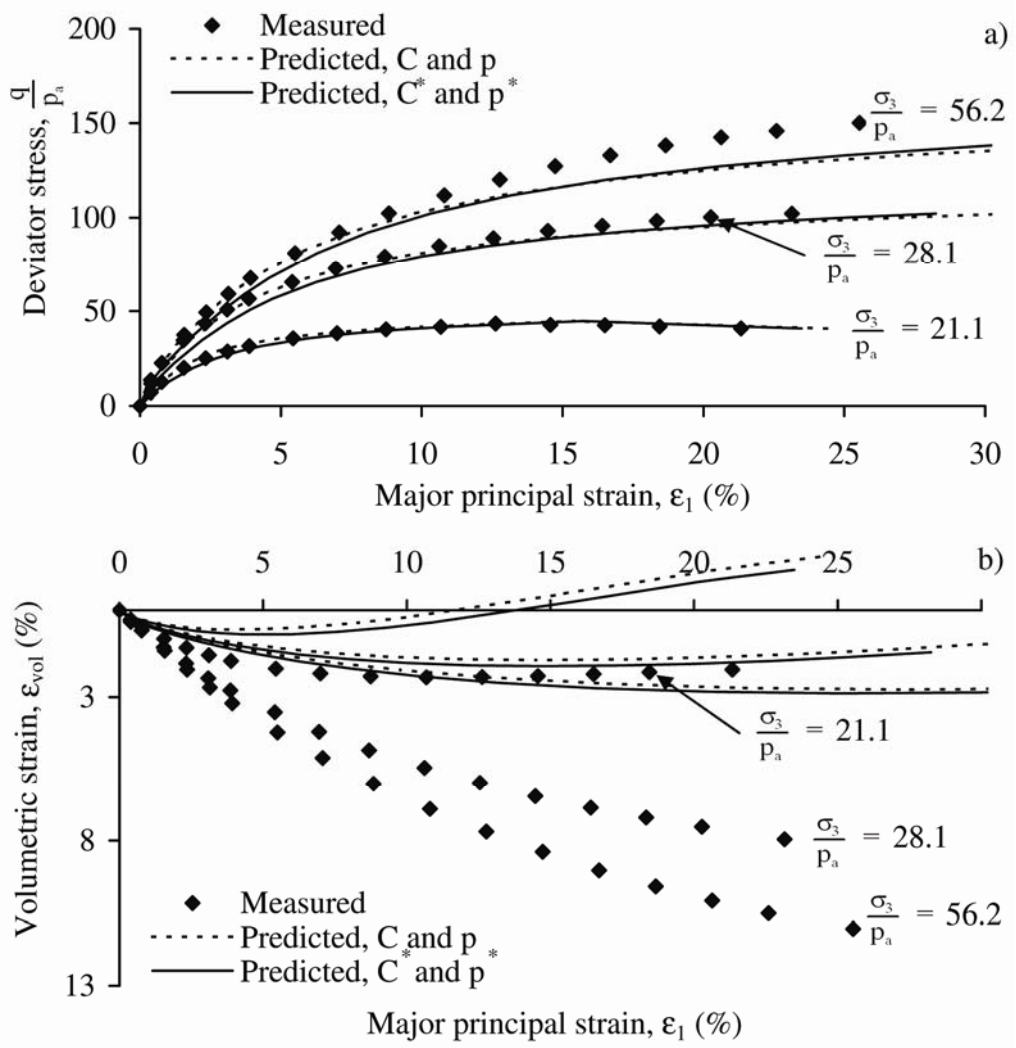

Figure 3.27: Comparison of predicted behavior of L1-Sand at high confining pressures using C and p determined from isotropic compression and from the triaxial tests. a) Stress-strain relation. b) Volume change.

The method should definitely be used if no isotropic compression test is available. If an isotropic test with no substantial amount of work is available, it is recommended to use the triaxial tests for obtaining the parameters C and p. A substantial amount of work means work in the same order of magnitude as the work produced at failure in the triaxial tests. Finally it is recommended to use the method, if the scatter in the parameters h and α makes an unambiguous determination difficult.

The prediction of isotropic compression tests with the transition from high compressibility at low confining pressures, to lower compressibility at higher confining pressures, would require further study of the transition and ultimately a new isotropic work-hardening rule.

3.2.2 Plastic Potential

When predicting the volumetric response from triaxial tests performed over a large range of confining pressures, The Single Hardening Model produce less volumetric contraction than observed at high confining pressures. This can be seen in Figure 3.26 and Figure 3.27 where triaxial tests on L1-Sand are predicted using The Single Hardening Model. The problem was addressed in a report predicting the behavior of F1-Sand, L1-Sand, L2-Sand and L8-Sand with an improved plastic potential function (Lade 1992). The suggested modification is evaluated and compared with other possible modifications.

It was observed that the parameter determination for the plastic potential parameters varied as a function of the confining pressure. This is demonstrated in Figure 3.28 where the determination of ψ_2 and μ is shown for L2-Sand. There are two simple

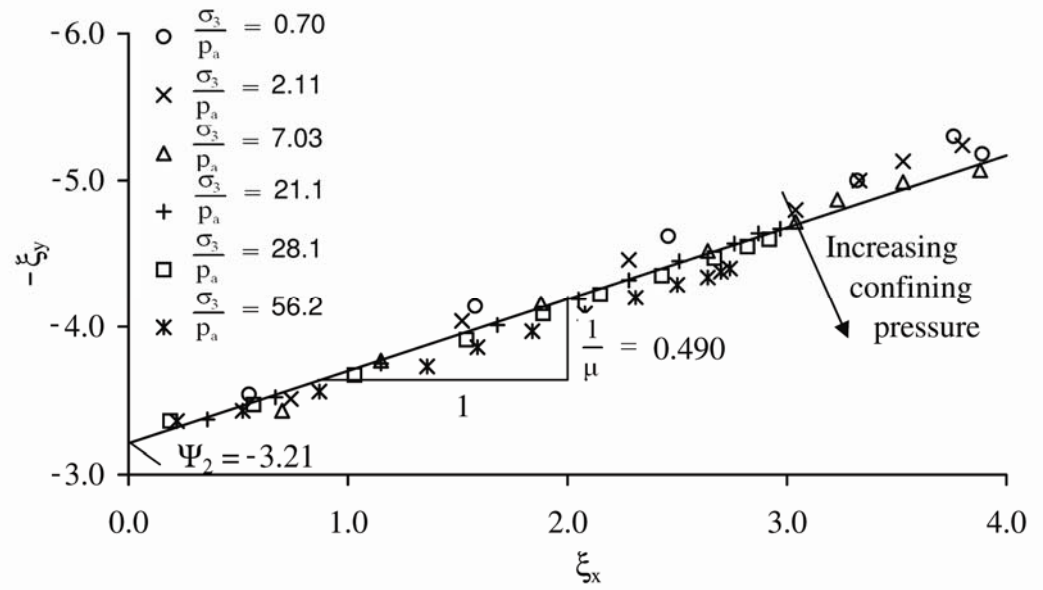

Figure 3.28: Determination of plastic potential parameters ψ_2 and μ for L8-Sand.

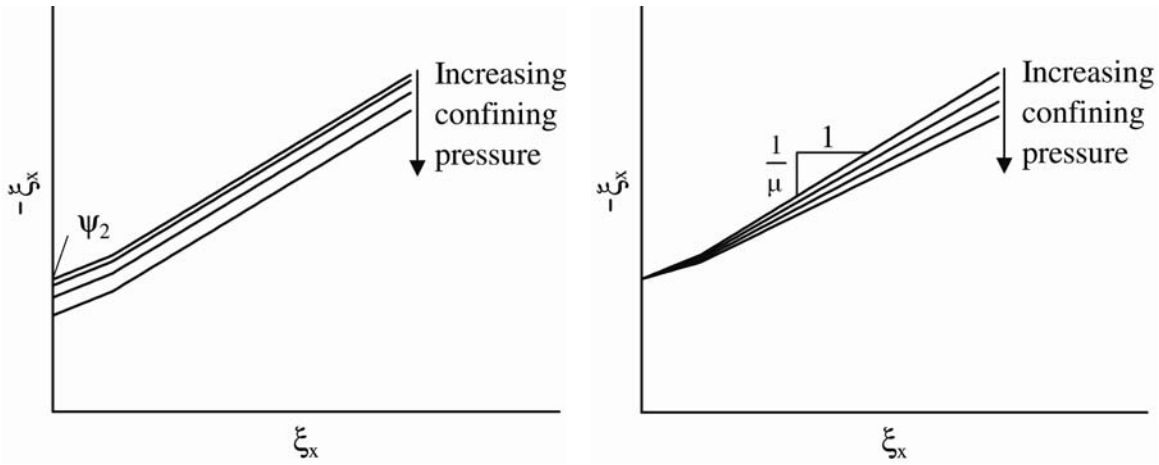

Figure 3.29: a) Parameter determination where the plastic potential parameter ψ_2 varies with confining pressure. b) Parameter determination where the plastic potential parameter μ varies with confining pressure.

variations of the plastic potential parameters that can result in the observed behavior, (1) the parameter ψ_2 increases with confining pressure as shown in Figure 3.29 a) where the line is parallel shifted or (2) the parameter μ increases with confining pressure as shown in Figure 3.29 b) where the line spreads out as a fan with increasing μ. A combination of the two cases is also a possibility.

To examine how the parameters vary with confining pressure, the parameters are determined for each of the triaxial tests individually, and plotted as a function of the confining pressure. This is done for F1-Sand, L1-Sand, L2-Sand and L8-Sand in Figure 3.30 and Figure 3.31 for the parameters ψ_2 and μ, respectively. There is no common variation of the parameter μ as a function of the confining pressure. L8-Sand and L2-Sand show a tendency towards increasing μ while F1-Sand and L1-Sand have high values of μ at low and high confining pressures with a decrease in the mid range. The parameter ψ_2 increases with confining pressure for all the examined sands. Based on Figure 3.30 and Figure 3.31 the variation of ψ_2 with confining pressure seams the most likely solution.

The solution is to let the parameter ψ_2 vary with the first stress invariant. Lade (1992) suggested replacing the parameter ψ_2 with a function varying linearly with the first stress invariant I_1, as shown in equation (3.37):

$$\psi_2 = \psi_{2,0} + b \cdot \frac{I_1}{p_a} \tag{3.37}$$

in which $\psi_{2,0}$ is the limiting value of ψ_2 at a confining pressure of zero, b is a new positive parameter defining the variation with the first stress invariant I_1 and p_a is atmos-

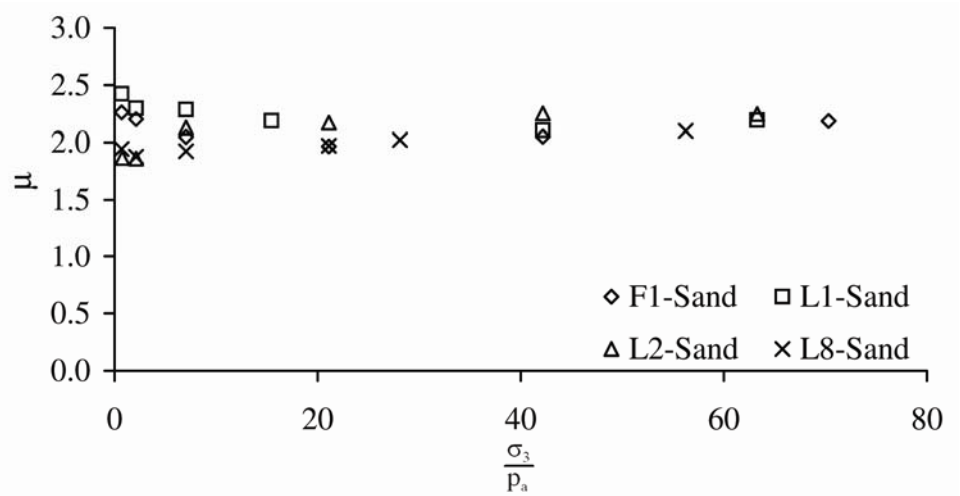

Figure 3.30: Variation of plastic potential parameter μ with confining pressure for F1-Sand, L1-Sand, L2-Sand and L8-Sand.

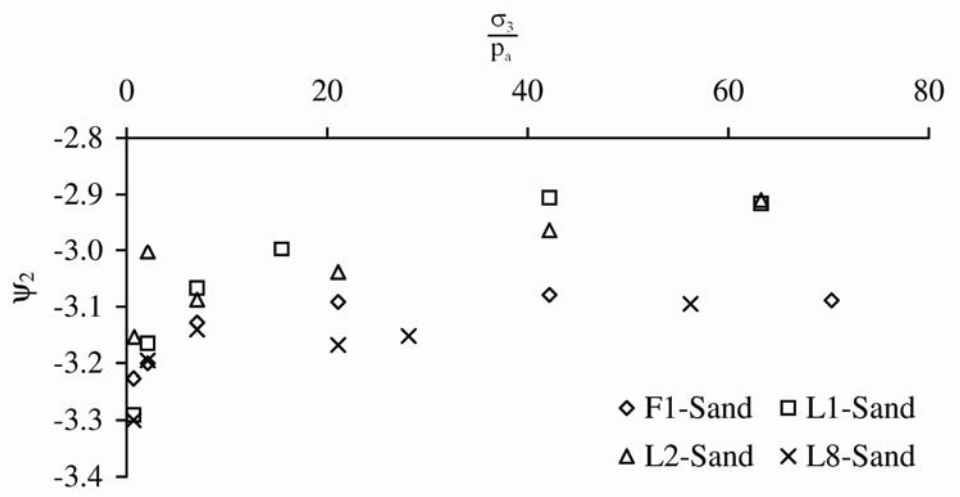

Figure 3.31: Variation of plastic potential parameter ψ_2 with confining pressure for F1-Sand, L1-Sand, L2-Sand and L8-Sand.

pheric pressure in the same units as the stresses used in the calculations of I_1. Due to the condition of reversibility, there is a lower limit to the parameter ψ_2. This limit determined by Kim and Lade (1988) is used to define $\psi_{2,0}$:

$$\psi_{2,0} = -(27 \cdot \psi_1 + 3) \tag{3.38}$$

in which ψ_1 the parameter defined in equation (3.15).

The variation of the parameter ψ_2 with confining pressure in Figure 3.31 shows a tendency towards a non linear relationship. To obtain a better fit, two other variations have been tested: Cubic root and logarithmic function as shown in equation (3.39) and (3.40), respectively.

$$\psi_2 = \psi_{2,0} + b \cdot \left(\frac{I_1}{p_a} \right)^{\frac{1}{3}} \tag{3.39}$$

$$\psi_2 = \psi_{2,0} + b \cdot \ln\left(\frac{I_1}{p_a} + 1 \right) \tag{3.40}$$

in which $\psi_{2,0}$ is the parameter defined in equation (3.38), and b is a positive parameter. I_1 is the first stress invariant defined in equation (3.2) and p_a is atmospheric pressure in the same units as the stresses used in the calculations of I_1. To test which function would potentially be the best fit, a linear regression between ψ_2 and the I_1-term have been performed. The values of the coefficient of determination, R^2 can be seen in Table 3.4. The logarithmic function shows superior fit for F1-Sand and L1-Sand, with the linear variation having the lowest value of R^2. L2-Sand shows the opposite result, with the linear fit being the best. L8-Sand shows low values of the coefficient of determination, independent of the function used. The highest average is the logarithmic function, and

Table 3.4: Coefficient of determination, R^2 for the three possible variations of parameter ψ_2 with first stress invariant I_1.

Material	Linear equation (3.37)	Cubic root equation (3.39)	Logarithmic function equation (3.40)
F1-Sand	0.56	0.83	0.93
L1-Sand	0.68	0.91	0.97
L2-Sand	0.70	0.68	0.64
L8-Sand	0.54	0.53	0.54

this function is therefore compared with the linear function in the evaluation presented here.

Combining the linear variation of ψ_2 in equation (3.37) with the plastic potential function in equation (3.11) results in the new plastic potential function:

$$g_p = \left[\psi_1 \cdot \frac{I_1^3}{I_3} - \frac{I_1^2}{I_2} + \psi_{2,0} + b \cdot \frac{I_1}{p_a} \right] \cdot \left[\frac{I_1}{p_a} \right]^{\mu} \tag{3.41}$$

Using the logarithmic function in equation (3.40), the new plastic potential function becomes:

$$g_p = \left[\psi_1 \cdot \frac{I_1^3}{I_3} - \frac{I_1^2}{I_2} + \psi_{2,0} + b \cdot \ln\left(\frac{I_1}{p_a} + 1 \right) \right] \cdot \left[\frac{I_1}{p_a} \right]^{\mu} \tag{3.42}$$

The condition of reversibility applied to the plastic potential functions in equation (3.41) and (3.42) results in the parameters μ and b having to be positive. The calculations leading to this is demonstrated in Appendix A. The scalar factor of proportionality, $d\lambda_p$ in equation (3.14) gets replaced with:

$$d\lambda_p = \frac{dW_p}{\mu \cdot g_p + b\left(\frac{I_1}{p_a} \right)^{\mu+1}} \tag{3.43}$$

for the linear function and

$$d\lambda_p = \frac{dW_p}{\mu \cdot g_p + \frac{b}{I_1 + p_a}\left(\frac{I_1}{p_a} \right)^{\mu+1}} \tag{3.44}$$

for the logarithmic function. To calculate the strains (using the flow rule in equation (3.10)) the derivative of the plastic potential functions with respect to the stresses needs

to be calculated. This is done in Appendix A, and in both the linear and the logarithmic version, the derivatives can be summarized as in equation (3.12). The definition of G in equation (3.13) changes, and for the linear version it becomes:

$$G = \psi_1 \cdot (\mu+3) \cdot \frac{I_1^2}{I_3} - (\mu+2) \cdot \frac{I_1}{I_2} + \psi_{2,0} \cdot \mu \cdot \frac{1}{I_1} + (\mu+1) \cdot \frac{b}{p_a} \tag{3.45}$$

For the logarithmic version G becomes:

$$G = \psi_1 \cdot (\mu+3) \cdot \frac{I_1^2}{I_3} - (\mu+2) \cdot \frac{I_1}{I_2} + \mu \cdot \left(\psi_{2,0} + b \cdot \ln\left(\frac{I_1}{p_a} + 1 \right) \right) \cdot \frac{1}{I_1} + \frac{b}{I_1 + p_a} \tag{3.46}$$

Following the same procedures as described in section 3.1.3, the parameter determination requires calculation of ξ_x and ξ_y. The calculation of ξ_x remains the same as in equation (3.18) whereas ξ_y becomes:

$$\xi_y = \psi_1 \frac{I_1^3}{I_3} - \frac{I_1^2}{I_2} + \psi_{2,0} \tag{3.47}$$

for both the linear and the logarithmic version. The relation between ξ_x and ξ_y replacing equation (3.17) becomes:

$$\xi_y = \frac{1}{\mu} \cdot \xi_x - b \cdot \frac{I_1}{p_a} \cdot \left(1 + \frac{1}{\mu} \right) \tag{3.48}$$

for the linear version, and

$$\xi_y = \frac{1}{\mu} \cdot \xi_x - b \left[\ln\left(\frac{I_1}{p_a} + 1 \right) + \frac{1}{\mu \cdot (I_1 + p_a)} \right] \tag{3.49}$$

for the logarithmic version. The relation between ξ_x and ξ_y is not linear, but the deviation caused by the second term is negligible. By plotting the relation between ξ_x and ξ_y the

slope yields the inverse of μ. Once μ is known, b can be calculated using equation (3.50) for the linear function and equation (3.51) for the logarithmic function:

$$b = \frac{\frac{1}{\mu}\cdot\xi_x - \xi_y}{\frac{I_1}{p_a}\cdot\left(\frac{1}{\mu}+1\right)} \tag{3.50}$$

$$b = \frac{\frac{1}{\mu}\cdot\xi_x - \xi_y}{\ln\left(\frac{I_1}{p_a}+1\right)+\frac{1}{\mu\cdot\left(I_1+p_a\right)}} \tag{3.51}$$

The determination of the parameter b yields the best results, when determined from the triaxial compression tests with the highest confining pressures.

To compare the models for the plastic potential, the proposed expressions have all been implemented in The Single Hardening model and used for prediction of the behavior of F1-Sand, L1-Sand, L2-Sand, and L8-Sand. The predictions can be found in Appendix C. The linear version proposed by Lade (1992) yields the best results. Both the cubic root and the logarithmic function produce too much contraction at high confining pressures. A comparison of the new plastic potential function with the original function for L8-Sand can be seen in Figure 3.32 and Figure 3.33.

The shapes of the new linear version of the plastic potential function and the original function are compared in the triaxial plane in Figure 3.34. The new plastic potential surfaces are not homothetic. At low confining pressures, the shape of the new plastic potential function is long and flat, and as it inflates, it changes size until it starts to exceed the original version at high confining pressures. The octahedral plane shown in

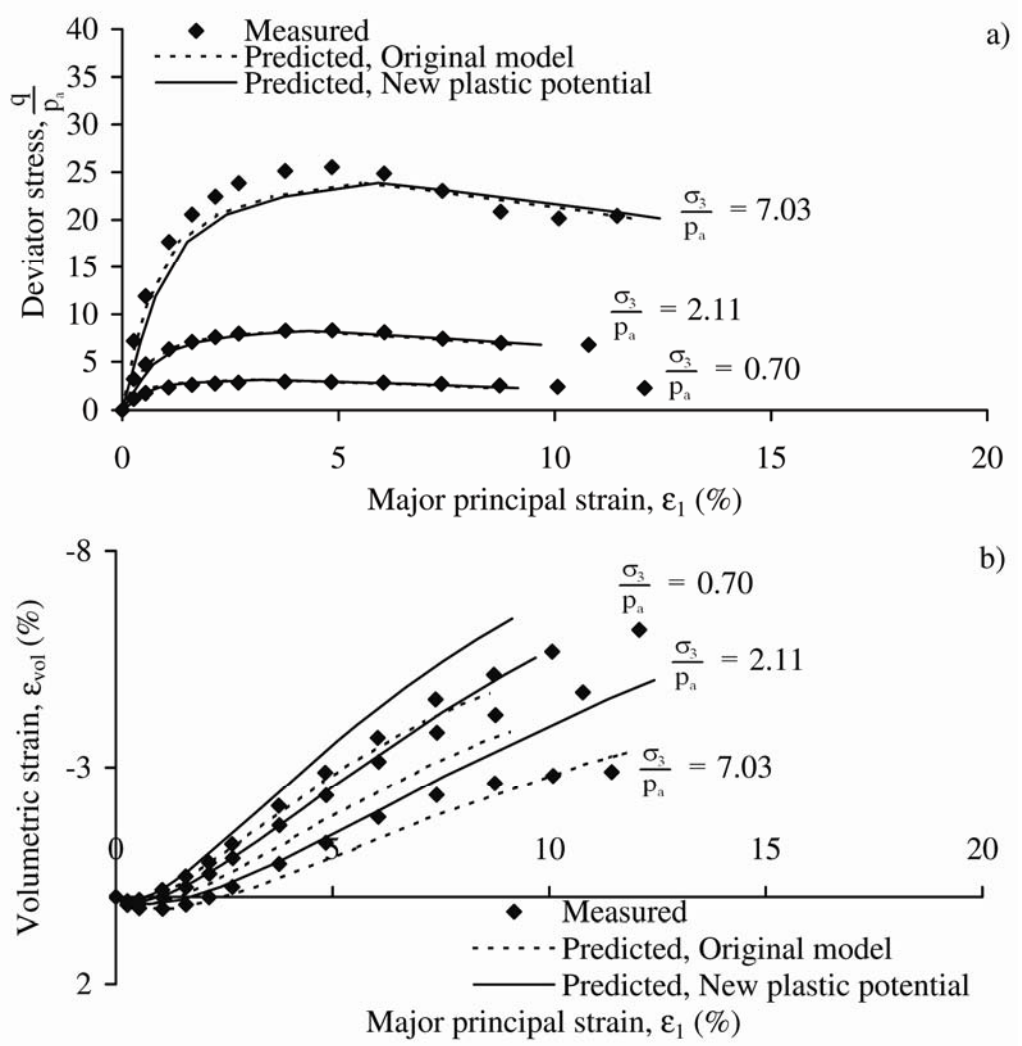

Figure 3.32: Comparison of the new plastic potential function with the original plastic potential function on the prediction of the behavior of L8-Sand at low confining pressures. a) Stress-strain relation. b) Volume change.

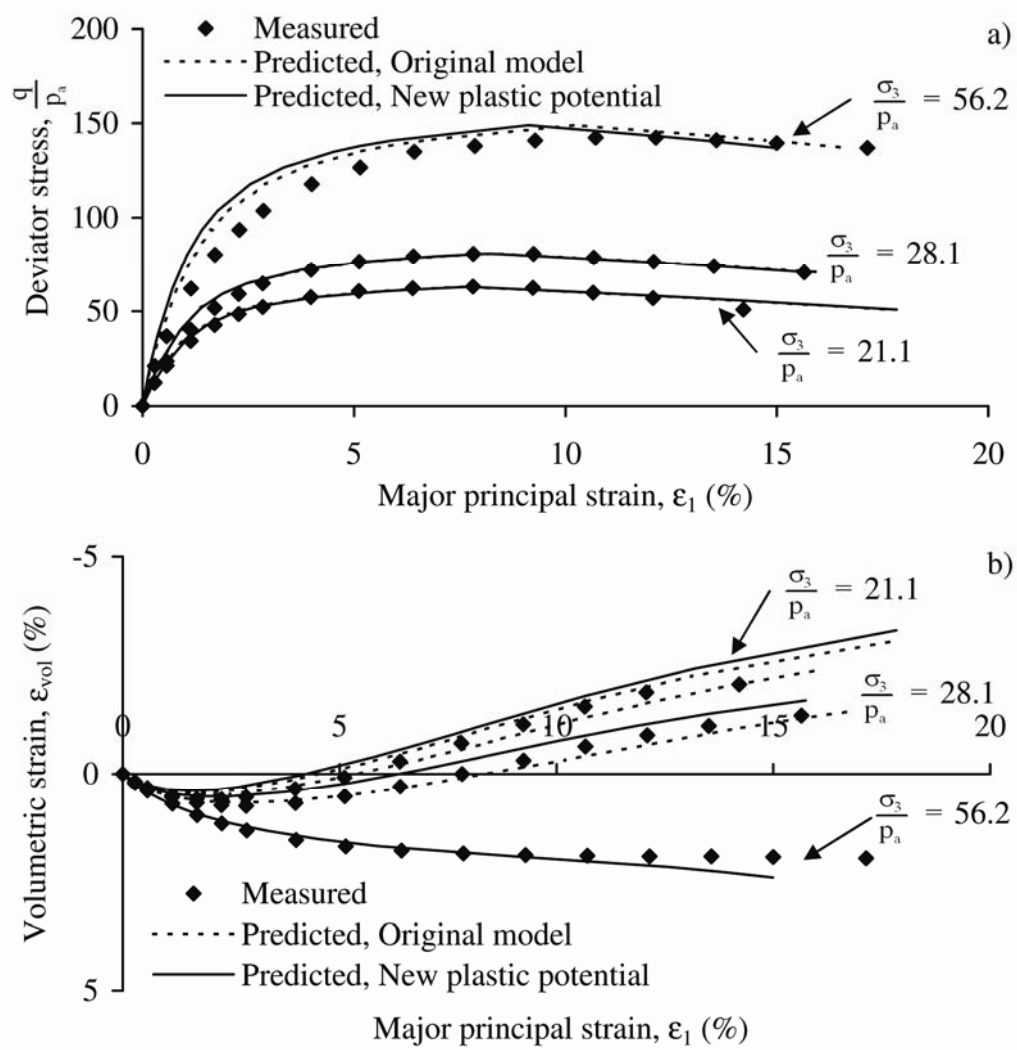

Figure 3.33: Comparison of the new plastic potential function with the original plastic potential function on the prediction of the behavior of L8-Sand at high confining pressures. a) Stress-strain relation. b) Volume change.

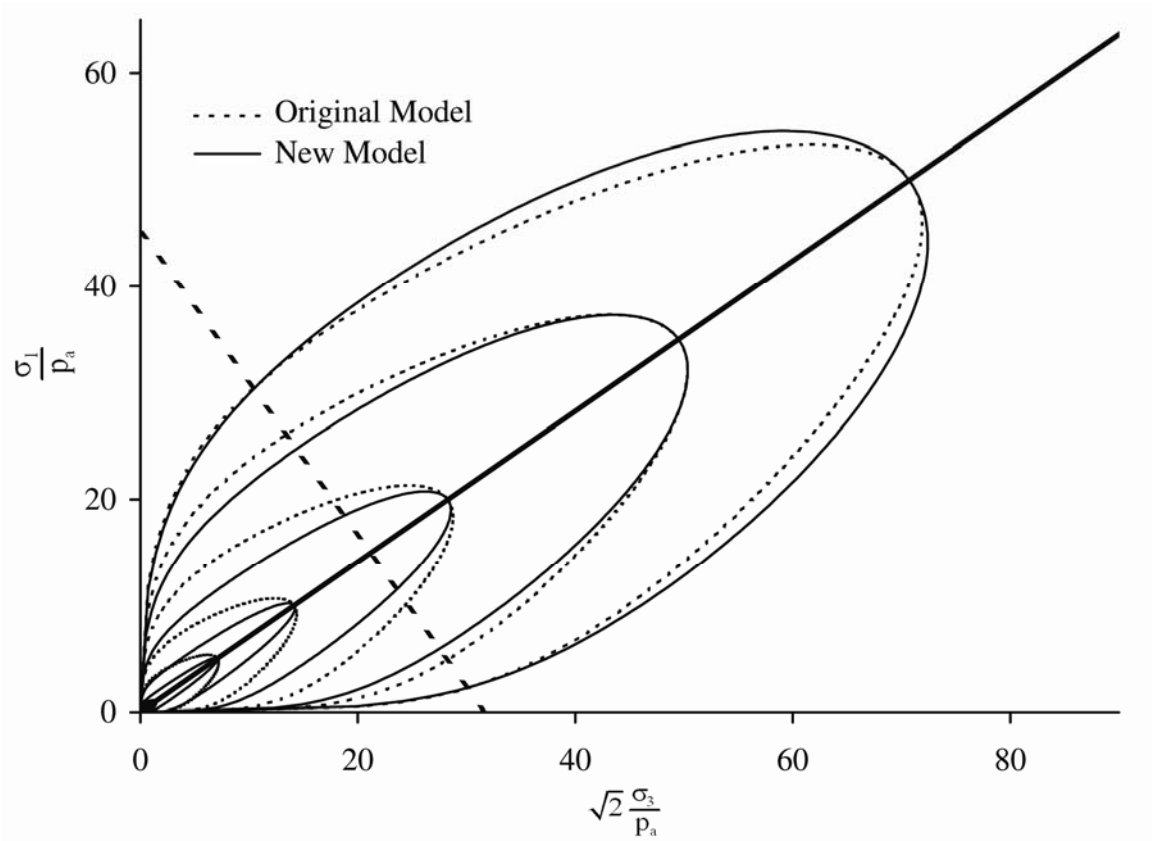

Figure 3.34: The shape of the new plastic potential function compared with the shape of the original function in the triaxial plane.

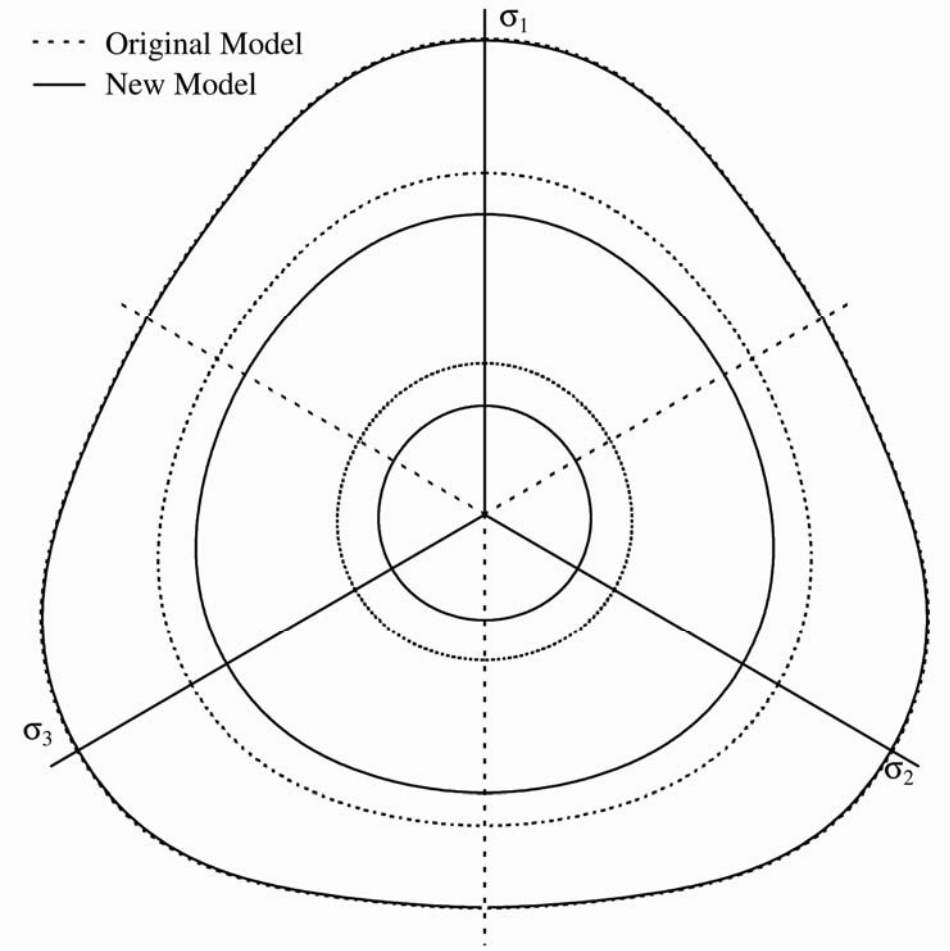

Figure 3.35: The shape of the new plastic potential function compared with the shape of the original function in the octahedral plane.

Figure 3.34 marks the plane in which the octahedral shapes are compared in Figure 3.35. There is no observable change in shape in the octahedral plane, because it is minimal. The change in prediction of cubical triaxial tests due to change in octahedral shape is therefore negligible.

Table 3.5 gives a summary of the new plastic potential parameters determined.

3.2.3 Softening

The softening function suggested by Lade and Kim (1988a) predicts the behavior of soil in softening with good accuracy. However, to be able to predict shear banding, a smoother transition around failure is desired. The prediction of the strain for L2-Sand shown in Figure 3.36 demonstrates the sometimes abrupt transition at failure. To ensure a smooth transition, a softening function controlling the work prior to failure is desirable.

A sketch of the desired softening function is shown in Figure 3.37, along with the hardening function for The Single Hardening Model described in equation (3.21). Three values of the hardening-softening function, f_p'' are of interest: (1) at cut-off, where the softening function takes over from the hardening function, f_p'' is equal to $f_{p,95}''$, (2) at failure, f_p'' is equal to $f_{p,f}''$, and (3) f_p'' is equal to $f_{p,r}''$ when the residual strength is reached. Similarly, three values of plastic work are of interest: (1) at cut-off, W_p is equal to $W_{p,95}$, (2) at failure, W_p is equal to $W_{p,f}$, and (3) the peak value of the softening function $W_{p,peak}$.

There are five boundary conditions to the softening function. At cut-off, where the softening function takes over from the hardening function, the value and slope of the softening function must be equal to the value and slope of the hardening function. These

Table 3.5: Plastic potential parameters determined.

Material	b	μ
Santa Monica Beach Sand	0.005	2.26
F1-Sand	0.0005	2.11
L1-Sand	0.0007	2.23
L2-Sand	0.00085	2.06
L8-Sand	0.0009	1.98
Nevada Sand	0.020	2.21

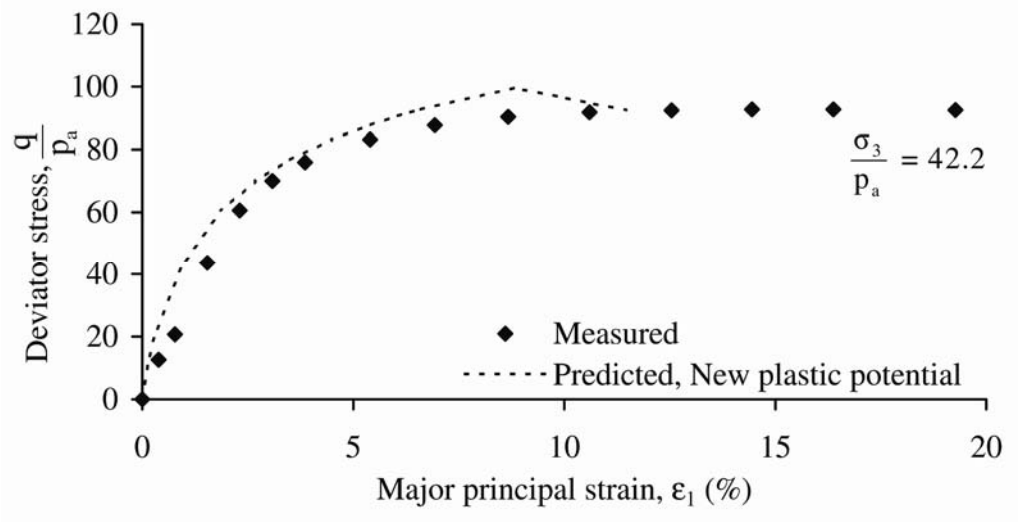

Figure 3.36: Predicted strain for L2-Sand.

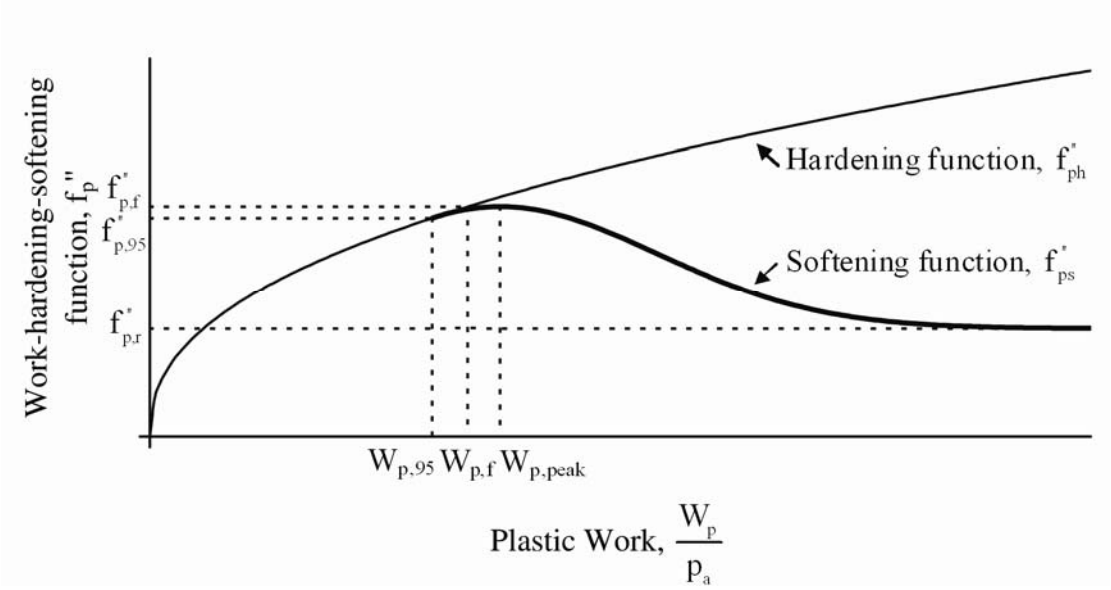

Figure 3.37: Modeling of work-hardening and softening.

conditions are defined in equations (3.52) and (3.53). The peak value of the softening function must be equal to the peak at failure, as defined in equation (3.54). Furthermore, the slope of the softening function at peak is zero, as defined in equation (3.55). Finally, as the work goes towards infinity the softening function goes toward the residual strength (equation (3.56)).

$$f''_{ph}(W_{p,95}) = f''_{ps}(W_{p,95}) \tag{3.52}$$

$$\frac{df''_{ph}(W_{p,95})}{dW_p} = \frac{df''_{ps}(W_{p,95})}{dW_p} \tag{3.53}$$

$$f''_{ps}(W_{p,peak}) = f''_{ph,f} \tag{3.54}$$

$$\frac{df''_{ps}(W_{p,peak})}{dW_p} = 0 \tag{3.55}$$

$$f''_{ps} \rightarrow f''_{p,r} \text{ for } W_p \rightarrow \infty \tag{3.56}$$

The suggested function for softening:

$$f''_{ps} = A_S \cdot W_p^{B_S} \cdot \exp\left[C_S \cdot \left(W_p - W_{p,95} \right)^{D_S} \right] + E_S \tag{3.57}$$

in which A_S, B_S, C_S, D_S, and E_S are constants derived from the boundary conditions in equation (3.52) to (3.56). The constants E_S, B_S, A_S, D_S, and C_S are defined in equation (3.58), (3.59), (3.60), (3.61), and (3.62), respectively. The derivation of the parameters can be seen in Appendix B.

$$E_S = f''_{p,r} \tag{3.58}$$

$$B_S = \frac{\frac{df''_{ph,95}}{dW_p} \cdot W_{p95}}{f''_{ph,95} - E_S} \tag{3.59}$$

$$A_S = \frac{f''_{ph,95} - E_S}{W_{p,95}^{B_S}} \tag{3.60}$$

$$D_S = \frac{B_S \cdot \left(W_{p,95} - W_{p,peak} \right)}{\ln\left[\frac{f''_{ph,f} - E_S}{A_S \cdot W_{p,peak}^{B_S}} \right] \cdot W_{p,peak}} \tag{3.61}$$

$$C_S = \frac{-B_S}{D_S \cdot \left(W_{p,peak} - W_{p,95} \right)^{D_S - 1} \cdot W_{p,peak}} \tag{3.62}$$

The suggested softening function in equation (3.57) does not provide a direct calculation of the work. As a result, the work produced needs to be calculated numerically.

Three parameters need to be defined for the calculation of the constants A_S, B_S, C_S, D_S, and E_S. The first parameter, is the value of the hardening function at cut-off, $f''_{p,95}$. Good results have been achieved using the value described in equation (3.63):

$$f''_{p,95} = 0.95 \cdot f''_{p,f} \tag{3.63}$$

The second parameter is the work at the peak of the softening function, $W_{p,peak}$. The best fits have been found using a value of $W_{p,peak}$ described in equation (3.64):

$$W_{p,peak} = 1.15 \cdot W_{p,f} \tag{3.64}$$

The third parameter is the value of the softening function at the residual strength, $f''_{p,r}$. The characteristic state, described by the rate of volumetric change being equal to zero, is

suggested being used for the residual strength. The three dimensional shape of the characteristic state surface was examined for dense Santa Monica Beach Sand by Abelev (2001). The surface was found to be a straight line in the triaxial plane and having an octahedral shape similar to the failure surface described in equation (3.9). Based on these findings, the residual strength surface described in equation (3.65) is used.

$$\eta_R = \frac{I_1^3}{I_3} - 27 \tag{3.65}$$

in which η_R is a non-dimensional parameter. The stress invariants I_1 and I_3 are defined in equation (3.2) and (3.4), respectively. Once the residual strength is known, η_R can be determined directly from equation (3.65). This is done for the sands examined, and the results are summarized in Table 3.6.

During the derivation of the constants A_S, B_S, C_S, D_S, and E_S, one limitation is imposed on the input parameters. The residual value of the softening function, $f''_{p,r}$ must be lower than the hardening function at cut-off, $f''_{p,95}$:

$$f''_{p,r} < f''_{p,95} \tag{3.66}$$

However, when predicting the behavior of sand at high confining pressures, the residual strength produced from equation (3.65) can be in violation with equation (3.66). When this is the case, the residual value of the softening function, $f''_{p,r}$ is reduced below the value of the hardening function at cut-off, $f''_{p,95}$, according to equation (3.67).

$$f''_{p,r} = f''_{p,95} \cdot 0.99 \tag{3.67}$$

Table 3.6: Parameter values of η_R.

Material	η_R
Loose Santa Monica Beach Sand	22.1
F1-Sand	15.5
L1-Sand	20.8
L2-Sand	19.9
L8-Sand	17.5

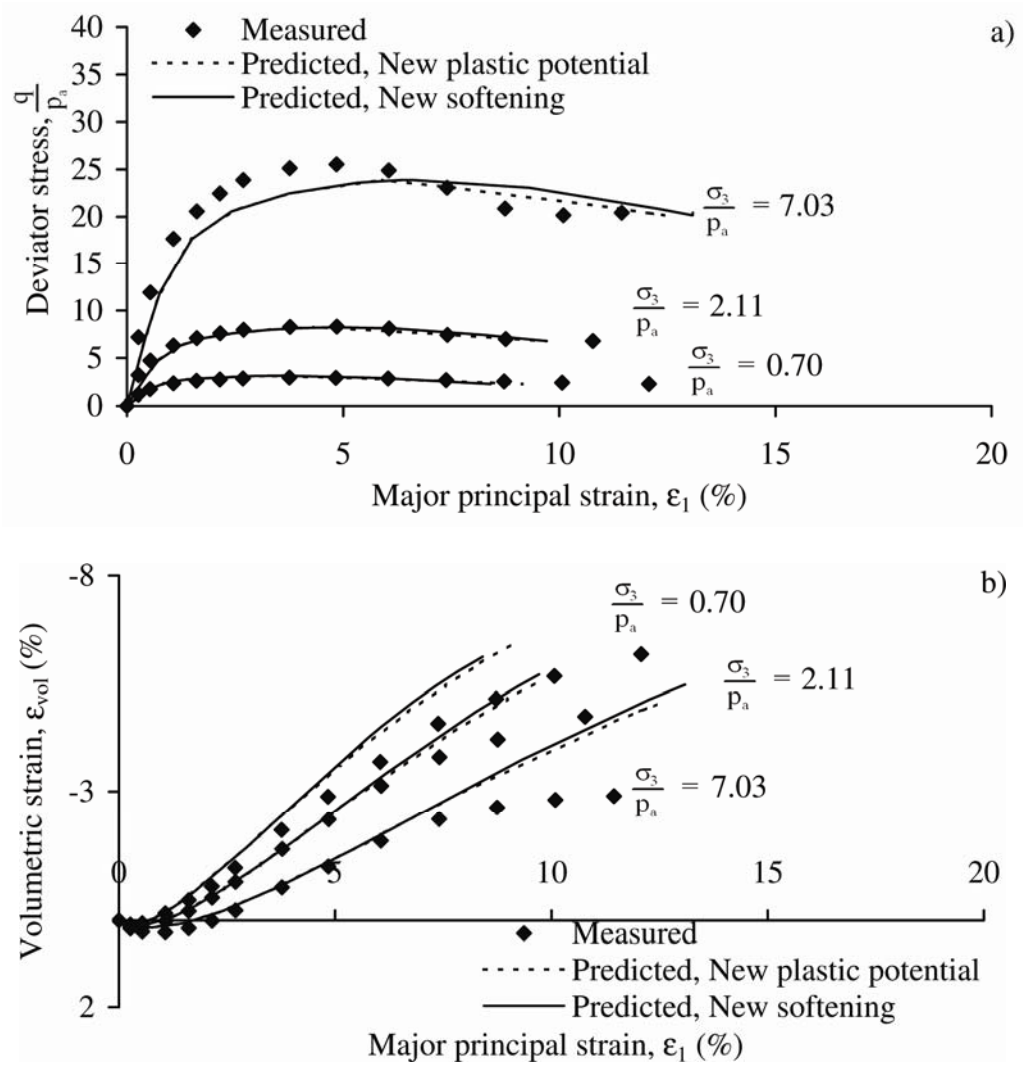

Figure 3.38: Comparison of the new softening function with the original softening function on the prediction of the behavior of L8-Sand at low confining pressures. a) Stress-strain relation. b) Volume change.

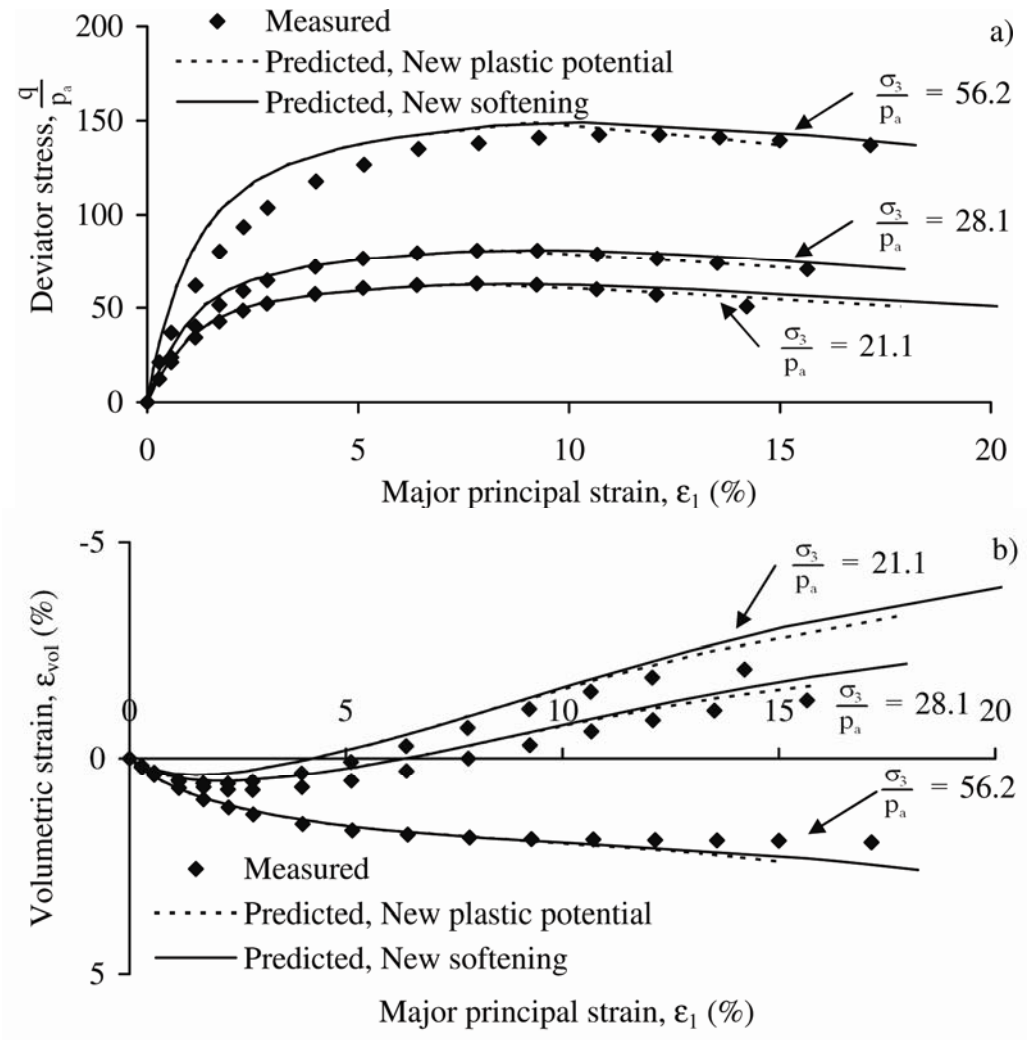

Figure 3.39: Comparison of the new softening function with the original softening function on the prediction of the behavior of L8-Sand at high confining pressures. a) Stress-strain relation. b) Volume change.

The predictions with the new softening function for L8-Sand can be seen in Figure 3.38 and Figure 3.39. Plots of the predicted behavior of the remaining tests (F1-Sand, L1-Sand, and L2-Sand) can be seen in Appendix C. The new softening function does produce a smoother transition from hardening into softening. At high confining pressures, where the characteristic line is close to the failure surface, the major principal strains predicted by the new softening function are larger than the strains produced by the original function.

3.3 Predictions with Improved Single Hardening Model

The behavior of five hollow cylinder torsion shear tests performed on loose Santa Monica Beach Sand have been predicted using the improved Single Hardening Model (test results from Geiger (1979)). The material parameters used for input are derived in the previous sections, and summarized in Table 3.7. All tests were performed with a normalized confining pressure of 2. The tests were performed to study the effect of large stress reversals. As a consequence none of the tests were continued to failure and the new softening function does therefore not come into use.

The first test, L11 starts with triaxial loading after which the vertical stress is kept constant, and the sample is sheared. Finally, the vertical stress is reduced along with a further increase in shear stress. The stress path followed can be seen in Figure 3.40. Two points of interest (A and B) have been marked on the plot. These points are identified in the observed stress-strain relations for easy comparison. As seen in Figure 3.41, there is an overall good agreement between the observed behavior and the predicted behavior in test L11.

Table 3.7: Parameters for loose Santa Monica Beach Sand for the improved Single Hardening Model.

Parameter	Value
ν	0.26
λ	0.27
M	600
a	0
m	0.095
η_1	31.2
η_R	22.1
C	0.00018
p	1.55
h	0.60
α	0.34
b	0.005
μ	2.26

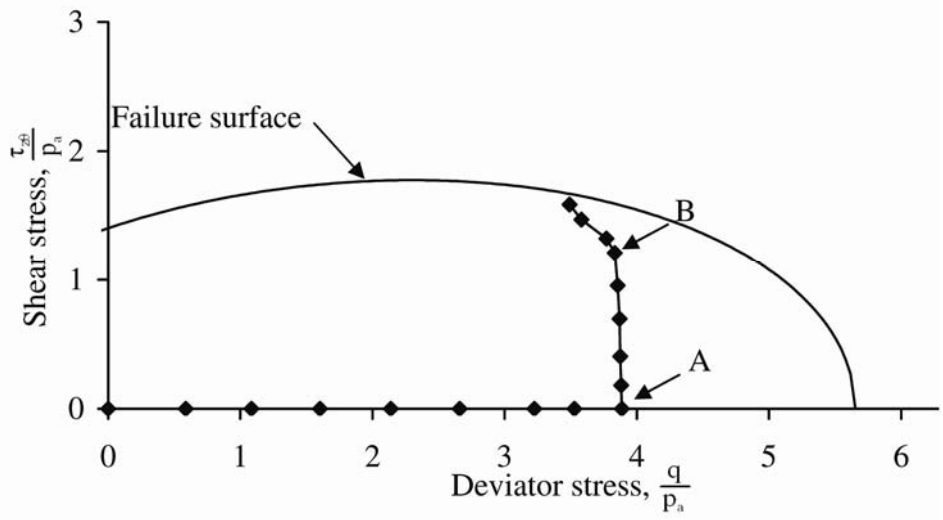

Figure 3.40: Stress path followed for test L11 on loose Santa Monica Beach Sand.

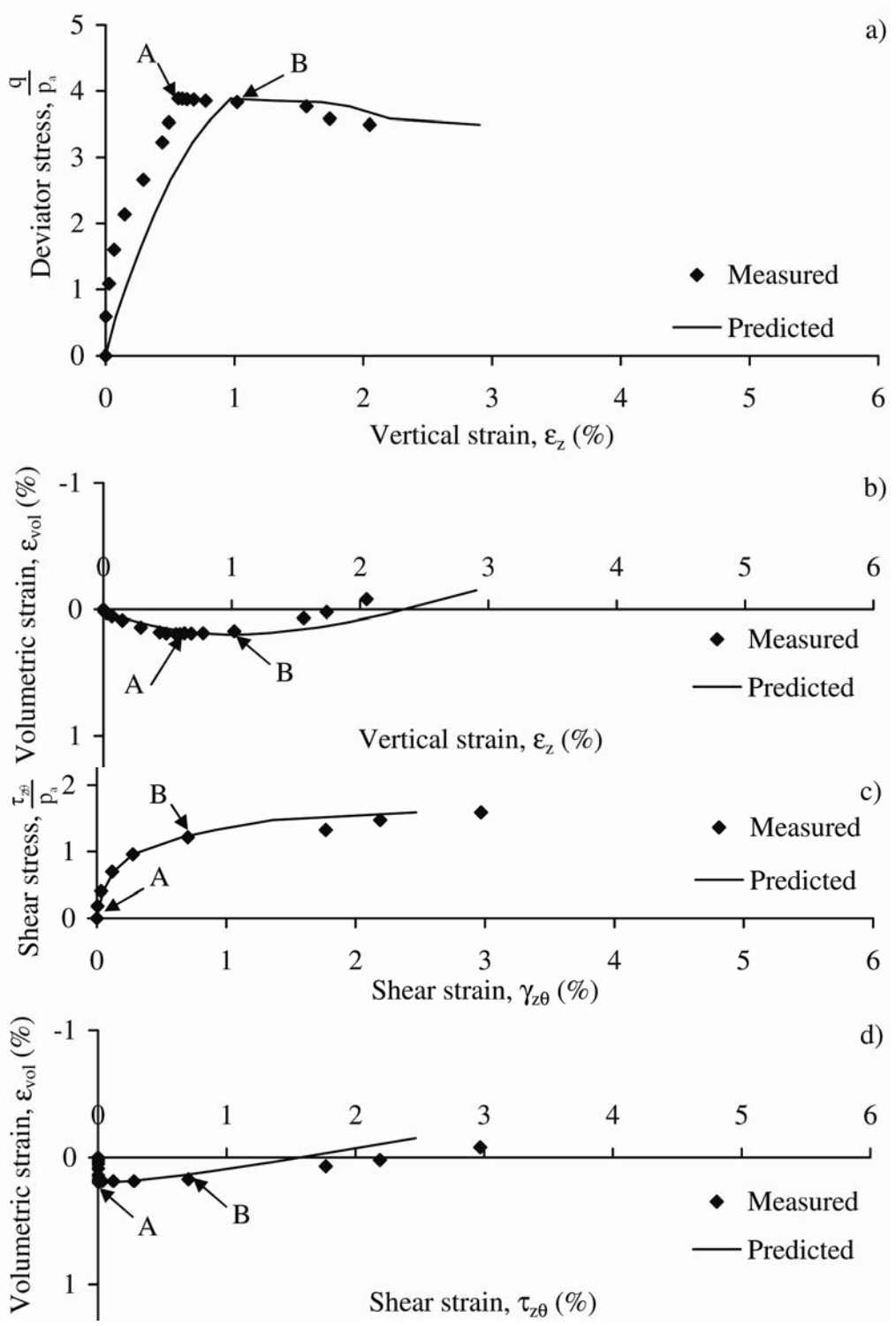

Figure 3.41: Comparison of predicted and observed behavior of loose Santa Monica Beach Sand for test L11. a) Stress-strain relation. b) Vertical strain vs. volumetric strain. c) Shear stress-shear strain. d) Shear strain vs. volumetric strain.

The stress path followed in test L12 is very similar to that in test L11: First the specimen is loaded triaxially, then sheared at a constant vertical stress and finally, the vertical stress is reduced during further increase in shear stress. The stress path followed is shown in Figure 3.42 Again, the predicted behavior shows good agreement with the observed behavior, as would be expected due to the similarity to test L11. Note that after point B, the reduction in vertical stress results in prediction of only elastic strains. Prediction of this behavior is studied further in the next test (L14).

The third test predicted, L14 starts with triaxial compression, as indicated by the stress path shown in Figure 3.44. After the triaxial compression, the vertical stress is reduced and the shear stress is increased. This results in elastic behavior immediately after point A. This can be seen in Figure 3.45 a), where the decrease in vertical stress, results in elastic unloading and in Figure 3.45 c), where the increase in shear stress results in elastic loading. When the stresses start expanding the yield surface again, the observed increases in both shear and vertical strains are captured by the predicted plastic behavior.

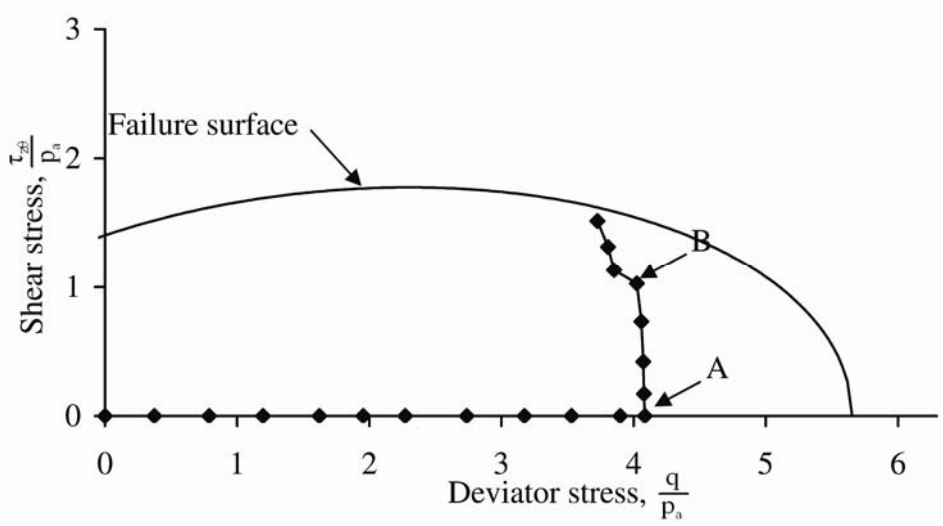

Figure 3.42: Stress path followed for test L12 on loose Santa Monica Beach Sand.

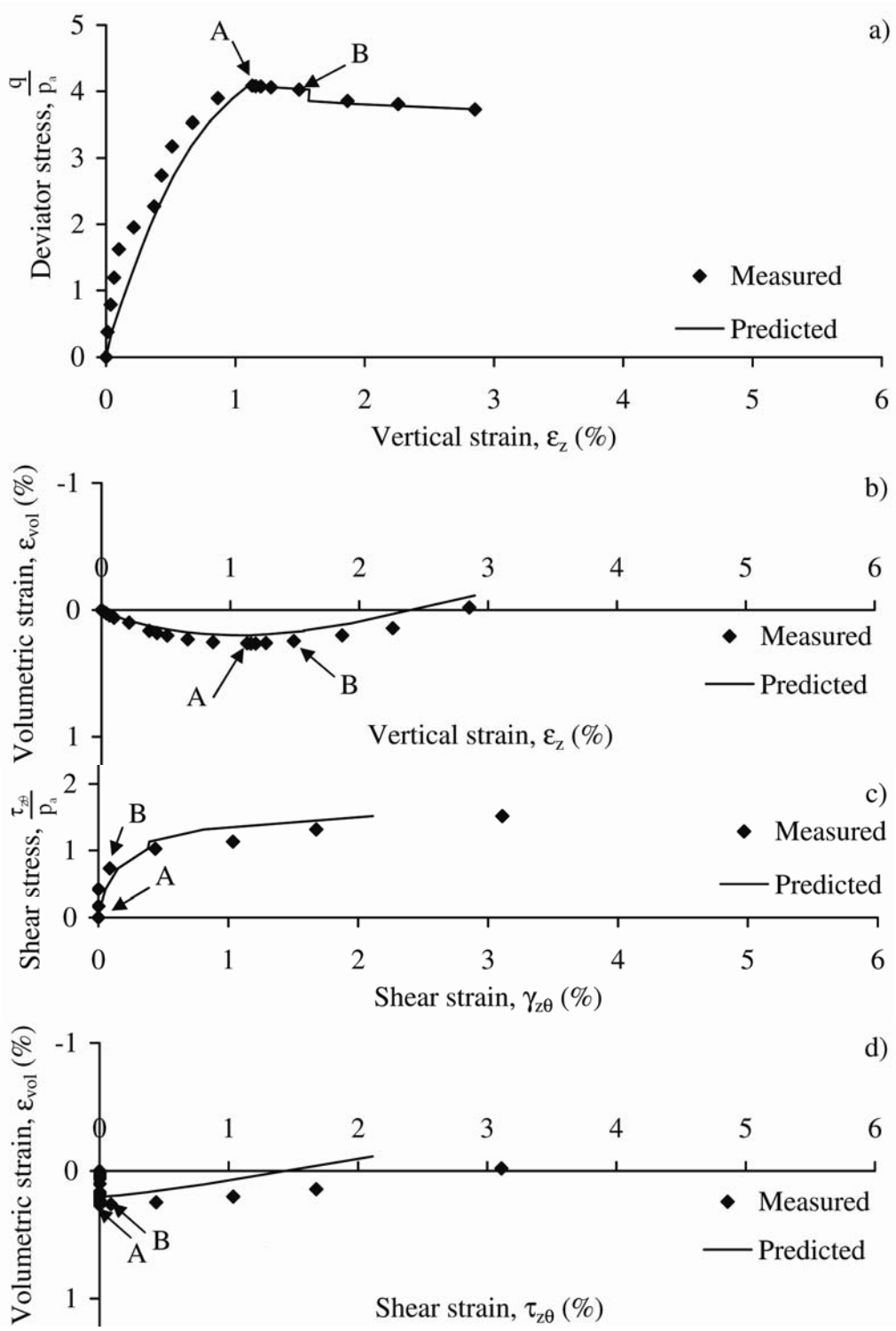

Figure 3.43: Comparison of predicted and observed behavior of loose Santa Monica Beach Sand for test L12. a) Stress-strain relation. b) Vertical strain vs. volumetric strain. c) Shear stress-shear strain. d) Shear strain vs. volumetric strain.

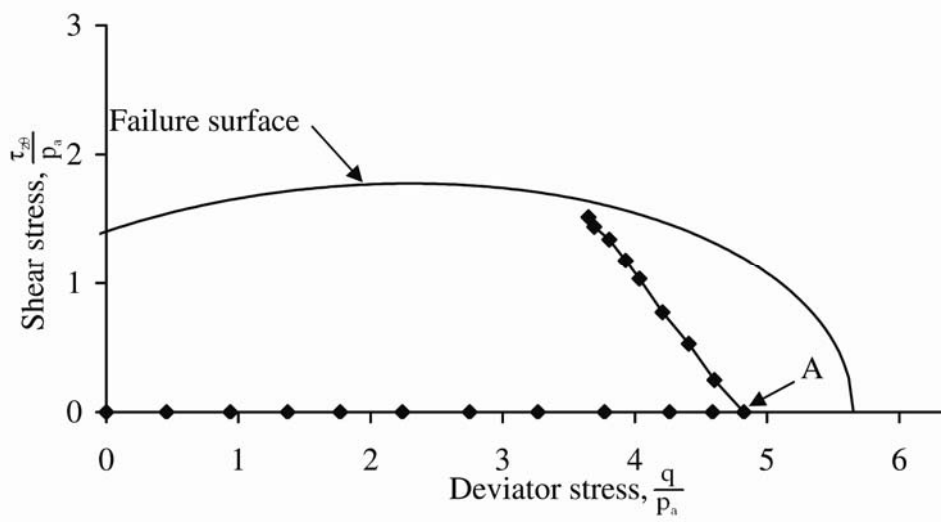

Figure 3.44: Stress path followed for test L14 on loose Santa Monica Beach Sand.

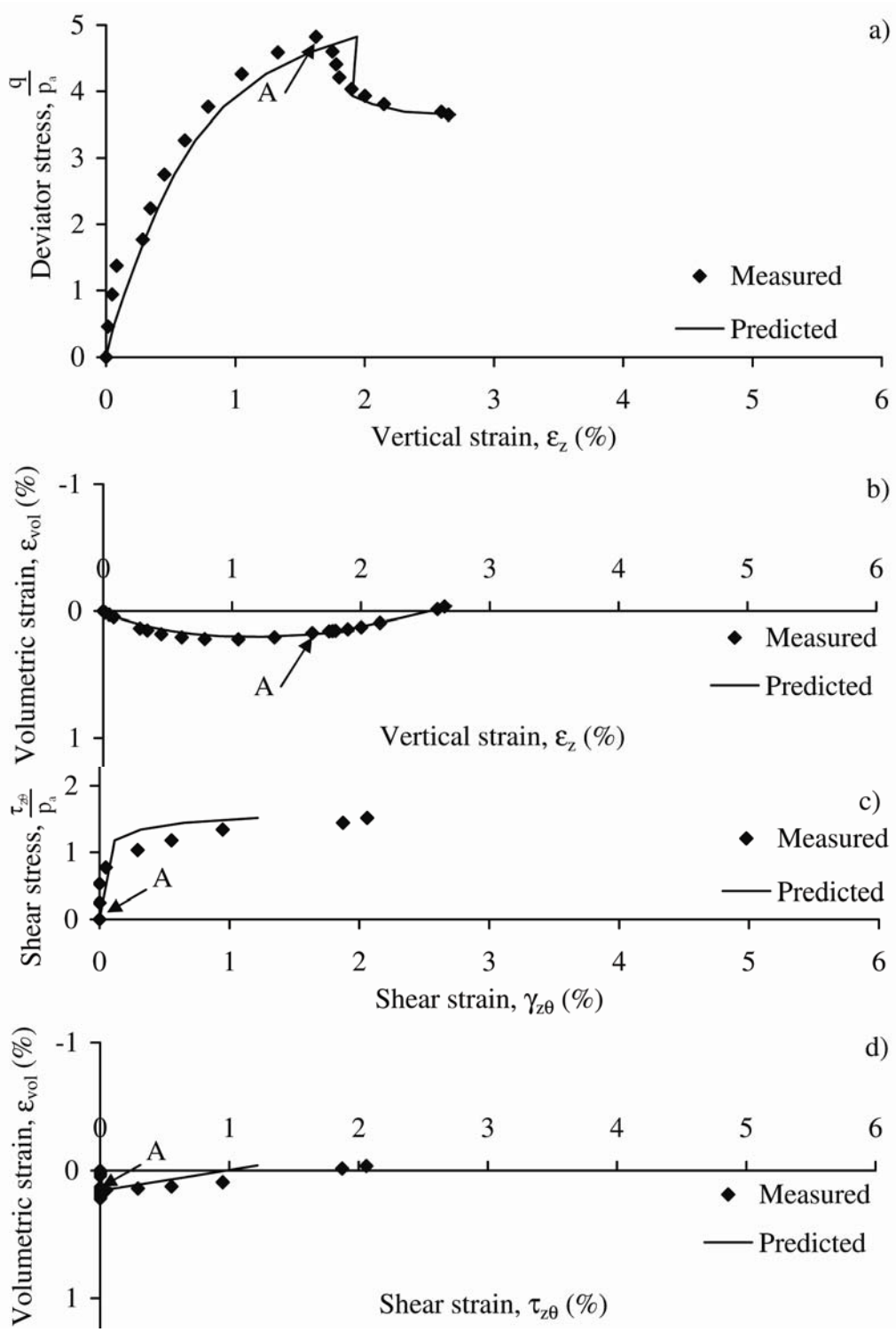

Figure 3.45: Comparison of predicted and observed behavior of loose Santa Monica Beach Sand for test L14. a) Stress-strain relation. b) Vertical strain vs. volumetric strain. c) Shear stress-shear strain. d) Shear strain vs. volumetric strain.

In test L10, the specimen is loaded with both vertical stress and shear stress in a ratio of approximately 2.25, then unloaded in a ratio of approximately 0.75. This is shown in Figure 3.46 where the stress path for test L10 is plotted.

The observed behavior shows a substantial amount of both normal and shear strain right after stress reversal at point A. This is believed to be caused by creep due to the close proximity to failure. Creep is a feature not included in The Single Hardening Model, and the observed behavior can therefore not be modeled accurately after stress reversal. The volumetric strain right after stress reversal shows a little dilation, then a substantial amount of contraction.

There is good agreement between the observed and predicted behavior during loading (Figure 3.47). After stress reversal, when the specimen is unloaded, the predictions indicate a behavior different from the observed. This is believed to be due to time effects in the observed behavior, as previously discussed.

As in test L10, the last test (L15) is loaded with a constant ratio between the vertical stress and the shear stress. This test is performed with a ratio of 0.75 as shown in Figure 3.48. The shear stress in then reduced while the vertical stress is kept constant. The creep observed after stress reversal in test L10 is also present in test L15. However, most of the creep in L15 takes place as shear strains, due to the relative higher shear stresses. The predicted behavior is shown in Figure 3.49. There is good agreement between the observed and predicted behavior during loading. After stress reversal, the observed and predicted behavior differs as discussed in test L10.

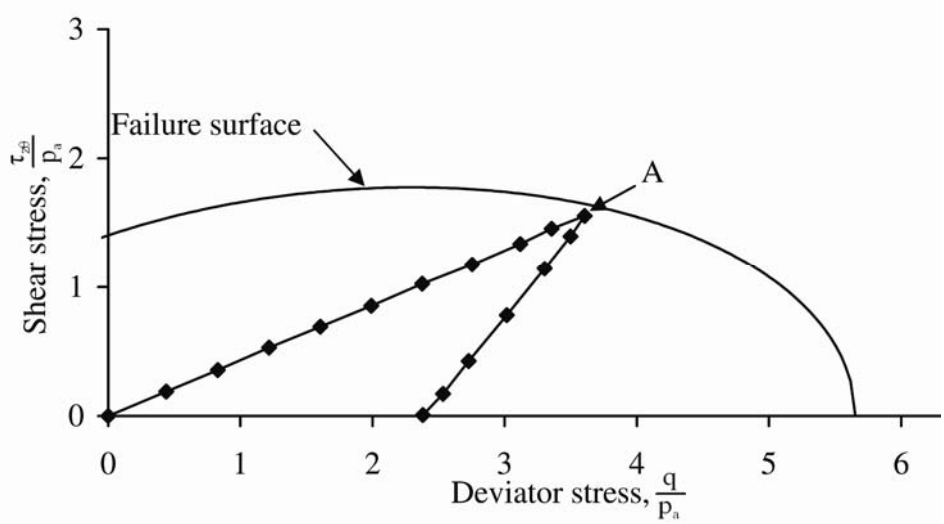

Figure 3.46: Stress path followed for test L10 on loose Santa Monica Beach Sand.

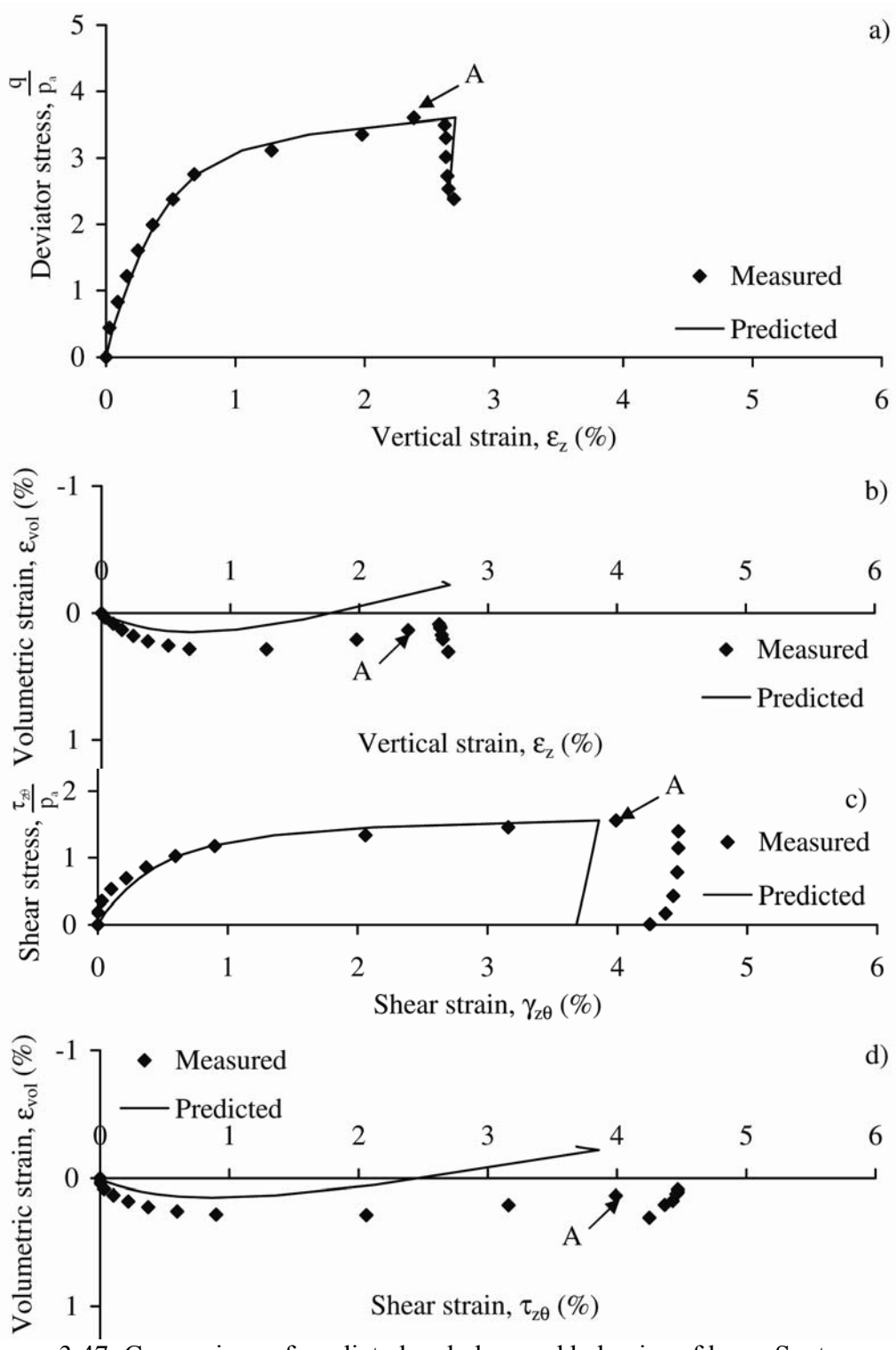

Figure 3.47: Comparison of predicted and observed behavior of loose Santa Monica Beach Sand for test L10. a) Stress-strain relation. b) Vertical strain vs. volumetric strain. c) Shear stress-shear strain. d) Shear strain vs. volumetric strain.

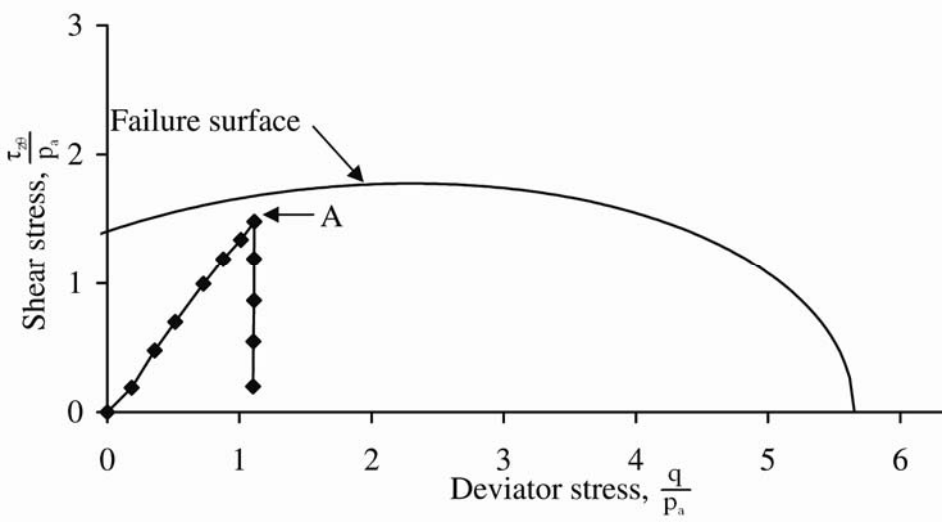

Figure 3.48: Stress path followed for test L15 on loose Santa Monica Beach Sand.

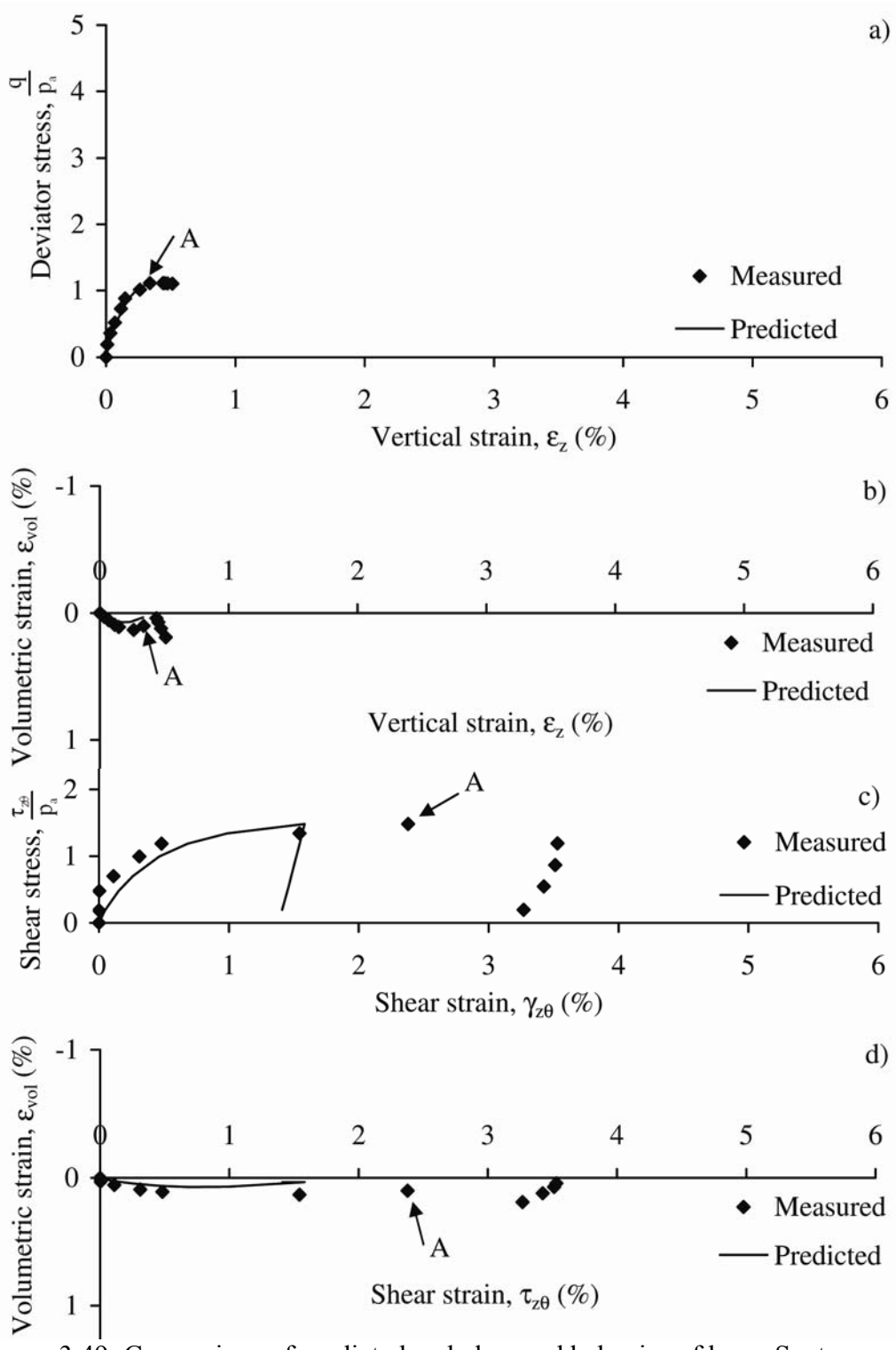

Figure 3.49: Comparison of predicted and observed behavior of loose Santa Monica Beach Sand for test L15. a) Stress-strain relation. b) Vertical strain vs. volumetric strain. c) Shear stress-shear strain. d) Shear strain vs. volumetric strain.

4. Experimental Evidence of Truly Elastic Behavior of Artificial Sandstone within Cementation Yield Surface

4.1 Introduction

When modeling the stress-strain behavior of porous rock, it is important to know whether the material behaves truly elastic. The typical stress-strain behavior in an unconfined compression test on porous rock usually has the three characteristic phases shown in Figure 4.1. The initial, upward curving part of the stress-strain relation has been attributed to the closure of preexisting cracks in the specimen (Bernabé et al. 1994). How pronounced this initial phase is, vary depending on the condition of the material considered. The second part of the curve is usually linear and considered elastic. However, if an unloading reloading cycle is performed at the linear part of the curve, the result is often a higher Young's modulus, indicating plastic strains during the virgin loading. The third part of the curve, where it departs from linear, is plastic.

The triaxial compression tests at low confining pressure can similarly be divided into a linear elastic part and a plastic part as shown in Figure 4.2. The closure of cracks (phase 1 in the unconfined compression test), have often taken place during the hydrostatic loading before the triaxial shearing and is therefore not present. As the confining pressure increases, the linear part of the stress-strain curve decreases and the

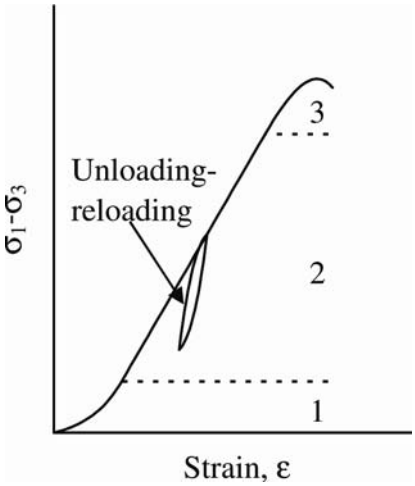

Figure 4.1: Typical stress-strain relation in an unconfined compression test.

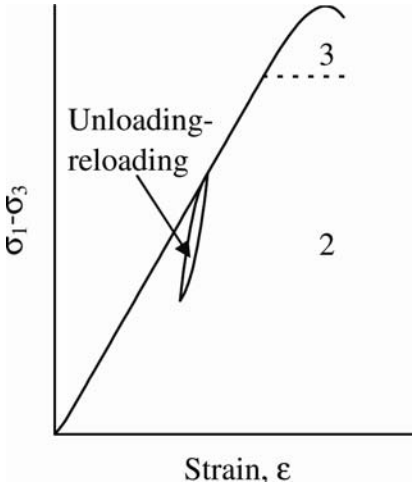

Figure 4.2: Typical stress-strain relation in a triaxial test at low confining pressure.

plastic deformation starts at a lower deviator stress. Examples of stress-strain relations as shown in Figure 4.1 and Figure 4.2 can be found in e.g. Ord et al. (1991) and Bernabé et al. (1994).

The stress space, in which porous rock behaves linearly, can be defined by an initial yield surface. The size and shape of this yield surface vary depending on the material. According to Cuss et al. (2003), the primary factors controlling the size of the yield surface in sandstone, are the porosity and the grain size. The initial yield surface is due to cementation of the grains and the rock is usually considered elastic inside this surface. As the stresses exceed the yield stress, the bonds start to break. The breakage of bonds can be measured by acoustic emission as done by Pestman and Van Munster (1996) and Baud et al. (2004). Both found the shape of the yield surface to be similar to the one depicted in Figure 4.3. The yield surface is shown in the p-q stress space, where p is the mean stress defined in equation (4.1) and q is the deviator stress defined in equation (4.2).

$$p = \frac{\sigma'_1 + 2 \cdot \sigma'_3}{3} \tag{4.1}$$

$$q = \sigma'_1 - \sigma'_3 \tag{4.2}$$

in which σ'_1 is the major effective stress and σ'_3 is the minor effective stress.

The elastic behavior expected inside the initial yield surface can be characterized by two independent criteria: The strains are (1) reversible and (2) uncoupled. The reversibility criterion can be illustrated by the two stress paths in Figure 4.4. If the material is elastic, stress path ABC and stress path ADC would produce equal strains ($\varepsilon_{ABC} = \varepsilon_{ADC}$). Also, the work produced during the entire loop, dW_{ABCDA} would be equal

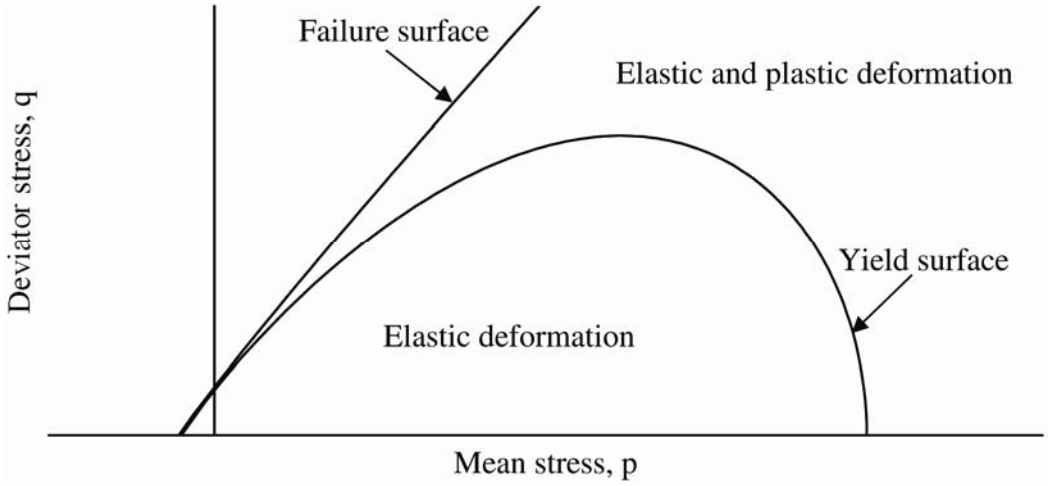

Figure 4.3: The initial yield surface due to cementation separates the elastic deformation from the plastic deformation.

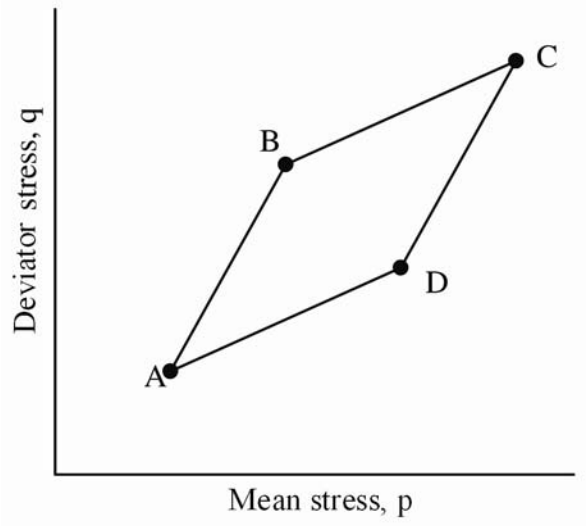

Figure 4.4: Two different stress paths from A to C.

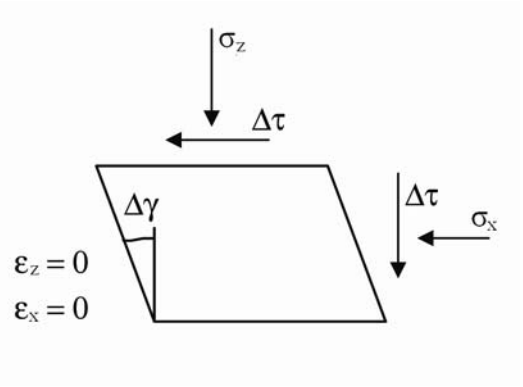

Figure 4.5: Deformation of elastic material.

to zero. The uncoupled behavior is illustrated in Figure 4.5, where an elastic material pre-stressed with normal stresses, σ_z and σ_x is exposed to an increase in shear stress, $\Delta\tau$. The resulting strains are only shear strains. Visa versa, if an elastic material exposed to shear stresses experience an increase in normal stresses, the resulting strains are normal strains.

The uncoupled behavior is also realized by looking at Hook's law in equation (4.3). The nine zeros in the upper right and lower left corner define this behavior.

$$\begin{Bmatrix} \Delta\varepsilon_{xx} \\ \Delta\varepsilon_{yy} \\ \Delta\varepsilon_{zz} \\ \Delta\gamma_{xy} \\ \Delta\gamma_{yz} \\ \Delta\gamma_{zx} \end{Bmatrix} = \begin{bmatrix} \frac{1}{E} & \frac{-\nu}{E} & \frac{-\nu}{E} & 0 & 0 & 0 \\ \frac{-\nu}{E} & \frac{1}{E} & \frac{-\nu}{E} & 0 & 0 & 0 \\ \frac{-\nu}{E} & \frac{-\nu}{E} & \frac{1}{E} & 0 & 0 & 0 \\ 0 & 0 & 0 & \frac{1}{G} & 0 & 0 \\ 0 & 0 & 0 & 0 & \frac{1}{G} & 0 \\ 0 & 0 & 0 & 0 & 0 & \frac{1}{G} \end{bmatrix} \cdot \begin{Bmatrix} \Delta\sigma'_{xx} \\ \Delta\sigma'_{yy} \\ \Delta\sigma'_{zz} \\ \Delta\tau_{xy} \\ \Delta\tau_{yz} \\ \Delta\tau_{zx} \end{Bmatrix} \tag{4.3}$$

E is Young's modulus and ν is Poisson's ratio. G is the shear modulus, which for an isotropic material can be expressed in terms of Young's modulus and Poisson's ratio, as:

$$G = \frac{E}{2\cdot(1+\nu)} \tag{4.4}$$

The direction of the normal and shear stresses (σ'_{xx}, σ'_{yy}, σ'_{zz}, τ_{xy}, τ_{yz}, τ_{zx}) are defined in Figure 4.6, where the first suffix refers to the direction of the normal to the plane on which the stress act, and the second suffix refers to the direction of the stress component itself. The same direction and suffix notion are used for the strains (ε_{xx}, ε_{yy}, ε_{zz}, γ_{xy}, γ_{yz}, γ_{zx}). The engineering shear strains, γ are defined in Figure 4.7 and they relate to

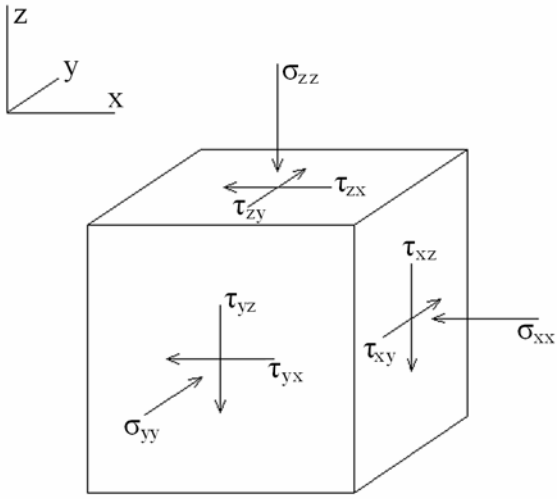

Figure 4.6: Stresses on a small cube.

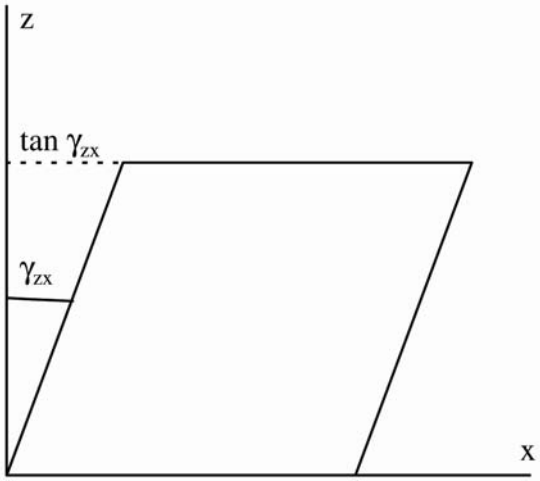

Figure 4.7: Definition of engineering shear strain.

the shear strains, ε, as shown in equation (4.5). Strictly, tan γ and not γ should be used, but the angles are so small that the differences are negligible.

$$\gamma_{xy} = 2 \cdot \varepsilon_{xy}$$
$$\gamma_{yz} = 2 \cdot \varepsilon_{yz} \qquad (4.5)$$
$$\gamma_{zx} = 2 \cdot \varepsilon_{zx}$$

4.2 Previous Studies

4.2.1 Reversibility

According to Jardine (1992) the strains in soils can be divided into three categories. At small strains, the stress-strain behavior is linear elastic, and the strains are fully recoverable. As the strains increase, beyond the small linear elastic region, the stress-strain behavior becomes nonlinear and hysteretic. Further strains will result in irrecoverable plastic strains. Jardine (1992) found the linear region to increase as the stiffness of the soil increased.

After performing small unloading-reloading cycles during triaxial tests on sandstone, Bernabé et al. (1994) found plastic strains to take place inside the cementation surface. The plastic strains increased as the triaxial tests progressed, and they were believed to originate from grain sliding and rotation rather than grain crushing. Similar results were found by Ord et al. (1991) when examining scanning electron micrographs taken around shear bands in plane strain tests on Gosford Sandstone.

4.2.2 Non Coupling Behavior

Talesnick and Ringel (1999) have sheared several porous rocks including Loveland sand-

stone, Indiana limestone, and Marasha chalk in a hollow cylinder torsion shear apparatus. All the tests were performed without confining pressure and without any vertical stress. The results showed the shear strain increased linear with increasing shear stress. Normal strains were practically non-existing. This indicates elastic behavior as the normal strains are independent of the shear stresses. However, they also performed similar tests on Lac duBonnet granite and found non-linear behavior between the shear stress and shear strain. Furthermore, the normal strains (particularly in vertical direction) increased with the shear stress. The authors pointed out that the granite was micro-cracked with the dominant plane of micro-cracking perpendicular to the vertical direction. By increasing the vertical stress and then repeating the shearing the granite not only showed almost linear relations between shear stresses and shear strains, but the normal strains also disappeared. As the cracks were kept closed by the vertical stress, the material behaved elastically, corresponding to the change from phase 1 to phase 2 in Figure 4.1.

4.3 Methodology

During a hollow cylinder torsion shear test the stresses shown in Figure 4.8 are applied to the hollow cylinder specimen: Vertical stress, σ_z, radial stress, σ_r, and shear stress, $\tau_{z\theta}$. The radial stress, σ_r is applied both inside and outside of the specimen. During the tests performed in this study, only vertical stresses and shear stresses were applied to the specimens. As a result the radial and tangential stresses are zero ($\sigma_r = \sigma_\theta = 0$). If no shear stresses are applied during a test, the specimen is exposed to a regular triaxial or unconfined test. The shear stresses, $\tau_{z\theta}$ are not uniform through the specimen, but growing linearly with the distance from the center. The average shear stress found in the

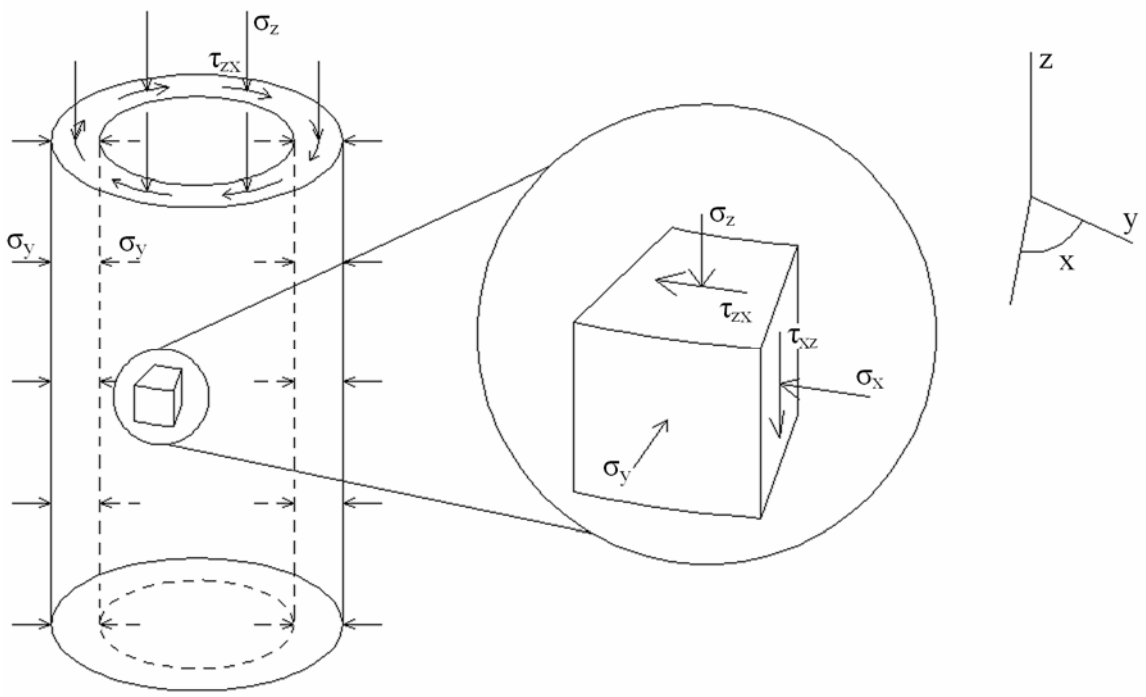

Figure 4.8: Stresses applied to the hollow cylinder specimen during the torsion shear test.

middle of the specimen is used when calculating the shear stresses.

When applying the cylindrical coordinate system and the boundary conditions of the torsion shear test in Figure 4.8 to the elastic matrix in equation (4.3), it reduces to:

$$\begin{Bmatrix} \Delta\varepsilon_z \\ \Delta\varepsilon_x \\ \Delta\varepsilon_y \\ \Delta\gamma_{zx} \end{Bmatrix} = \begin{bmatrix} \frac{1}{E} & 0 \\ \frac{-\nu}{E} & 0 \\ \frac{-\nu}{E} & 0 \\ 0 & \frac{1}{G} \end{bmatrix} \cdot \begin{Bmatrix} \Delta\sigma'_z \\ \Delta\tau_{zx} \end{Bmatrix} \tag{4.6}$$

Two types of loading patterns have been employed to determine whether or not the artificial sandstone behaves elastic: These are referred to as an inside and an outside loop. The stress path followed for an inside loop is demonstrated in Figure 4.9. Assuming the material behaves plastic inside the cementation yield surface, a second yield surface will be formed and expand as the material is loaded. Figure 4.9 a) shows the cementation yield surface with a regular plastic yield surface being pushed out by unconfined loading. Then, in Figure 4.9 b) the vertical stress, σ_z is kept constant and a shear stress, τ_{zx} is applied to the specimen, expanding the potential yield surface further. By reducing the vertical stress, σ_z the stress path turns inside the potential yield surface, and elastic behavior is expected. Finally, the shear stress, τ_{zx} is removed and in Figure 4.9 c) the vertical stress, σ_z is increased again expanding the potential yield surface, preparing the specimen for the next loop.

The outside loop shown in Figure 4.10 starts as did the inside loop with unconfined loading (Figure 4.10 a)) and then shearing with constant vertical stress

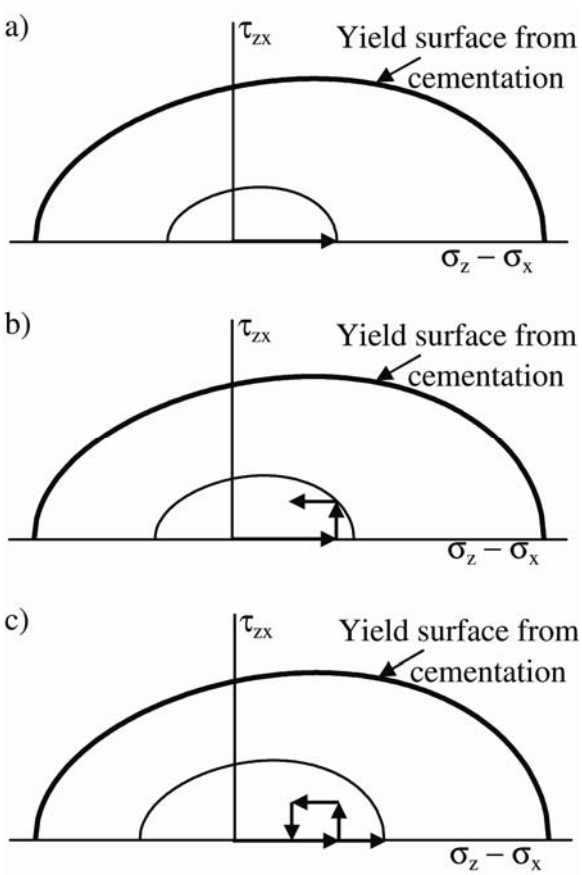

Figure 4.9: Loading pattern for inside loop.

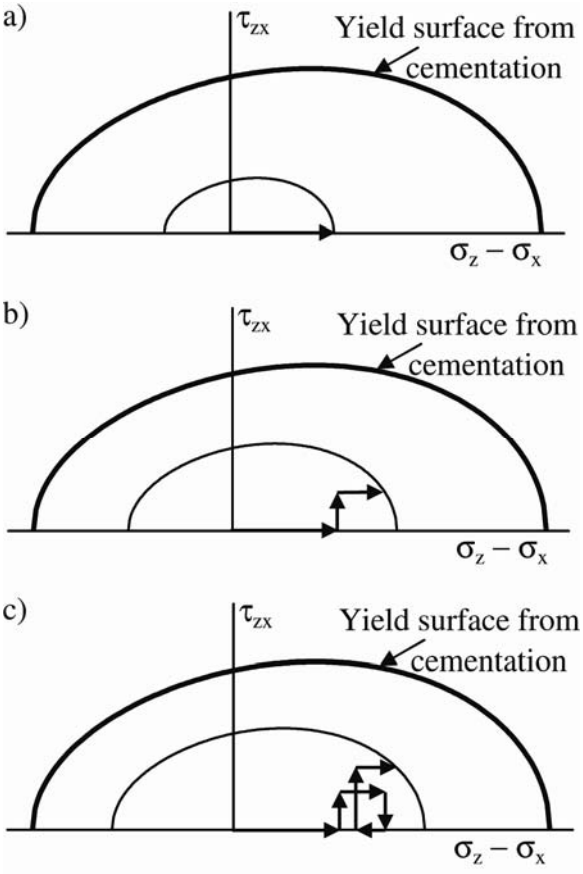

Figure 4.10: Loading pattern for outside loop.

(Figure 4.10 b)). The shear stress, τ_{zx} is then kept constant and the vertical stress, σ_z is increased. This expands the potential yield surface further. The shear stress, τ_{zx} is then decreased to zero and the vertical stress, σ_z is decreased before the next loop starts (Figure 4.10 c)). Because the shear stress for the second loop is reapplied inside the yield surface, elastic behavior is expected.

As the tests are performed without confining pressure the cementation yield surface and the failure surface are practically identical as can be seen in Figure 4.3. The shape of the yield surfaces in Figure 4.9 and Figure 4.10 are therefore assumed similar to the shape of the failure surface.

The response from the two loops defines whether the material behaves elastic or elastic-plastic. If only vertical strains are measured during the vertical loading, and only shear strains are measured when shear stresses are changed, the material behaves uncoupled. To test if the material experience reversible strains, the work produced for each leg of the loop is recorded. If the material exhibits reversible strains, the work produced for a closed loop is zero. If a loop is not closed, comparison of legs pushing the potential yield surface out and legs inside the potential yield surface can determine whether the material exhibits reversible strains.

The elastic constants can be calculated from the stress and strain increments. Young's modulus, E is calculated as:

$$E = \frac{\Delta\sigma'_z}{\Delta\varepsilon_z} \tag{4.7}$$

in which $\Delta\sigma'_z$ is the vertical stress increment and $\Delta\varepsilon_z$ is the vertical strain increment. With the vertical strain increments, $\Delta\varepsilon_z$, and tangential strains increments, $\Delta\varepsilon_x$, known, Poisson's ratio, ν, is calculated from equation (4.8):

$$\nu = \frac{-\Delta\varepsilon_x}{\Delta\varepsilon_z} \tag{4.8}$$

The shear modulus, G can be calculated as:

$$G = \frac{\Delta\tau_{zx}}{\Delta\gamma_{zx}} \tag{4.9}$$

in which $\Delta\tau_{zx}$ is the shear stress increment and $\Delta\gamma_{zx}$ is the shear strain increment. A more sturdy way to calculate Poisson's ratio, ν is from Young's modulus, E and the shear modulus, G (assuming the material is isotropic):

$$\nu = \frac{E}{2 \cdot G} - 1 \tag{4.10}$$

According to Clough et al. (1981) the confining pressure has an effect on the elastic modulus in cemented sand. However, the effect decreases with increasing degree of cementation. As no confining pressure and only low vertical stress and low shear stress were applied to the specimens in this study, the elastic constants are expected to vary very little. To examine the effect of stresses on the elastic constants, two stress dependent formulas for the elastic modulus have been tested. The first is a simple equation, where Young's modulus, E and the shear modulus, G vary with the mean normal stress, p:

$$E = K_E \cdot p_a \cdot \left(\frac{p}{p_a}\right)^{n_E} \tag{4.11}$$

$$G = K_G \cdot p_a \cdot \left(\frac{p}{p_a} \right)^{n_G} \tag{4.12}$$

in which E is Young's modulus, K_E, K_G, n_E, and n_G are constants, p is the mean normal stress defined in equation (4.1), p_a is atmospheric pressure in the same units as E, G, and p. The second stress dependent elastic modulus, was suggested by Lade and Nelson (1987):

$$E = M_E \cdot p_a \cdot \left[\left(\frac{I_1}{p_a} \right)^2 + R \cdot \frac{J_2^{'}}{p_a^2} \right]^{\lambda_E} \tag{4.13}$$

$$G = M_G \cdot p_a \cdot \left[\left(\frac{I_1}{p_a} \right)^2 + R \cdot \frac{J_2^{'}}{p_a^2} \right]^{\lambda_G} \tag{4.14}$$

in which M_E, M_G, λ_E, and λ_G are non-dimensional parameters, R is a constant depending on Poisson's ratio and defined in equation (4.19), p_a is atmospheric pressure in the same units as the stresses used in the calculations of I_1 and $J_2^{'}$. I_1 is the first stress invariant defined in equation (4.15) and $J_2^{'}$ is the second stress deviator invariant defined in equation (4.17).

$$I_1 = \sigma'_{xx} + \sigma'_{yy} + \sigma'_{zz} \tag{4.15}$$

in which σ'_{xx}, σ'_{yy}, and σ'_{zz} are the normal stresses defined in Figure 4.6. Applying the boundary conditions for the torsion shear test to equation (4.15), produces:

$$I_1 = \sigma'_z \tag{4.16}$$

$$J_2' = \frac{1}{6}\left[\left(\sigma'_{xx} - \sigma'_{yy}\right)^2 + \left(\sigma'_{yy} - \sigma'_{zz}\right)^2 + \left(\sigma'_{zz} - \sigma'_{xx}\right)^2\right] + \tau_{xy}\cdot\tau_{yx} + \tau_{yz}\cdot\tau_{zy} + \tau_{zx}\cdot\tau_{xz} \quad (4.17)$$

The normal stresses (σ'_{xx}, σ'_{yy}, σ'_{zz}) and shear stresses (τ_{xy}, τ_{yx}, τ_{yz}, τ_{zy}, τ_{zx}, τ_{xz}) used in equation (4.17) are defined in Figure 4.6. With the boundary conditions in the torsion shear test, equation (4.17) reduces to:

$$J_2' = \frac{1}{3}\sigma'^2_z + \tau^2_{zx} \quad (4.18)$$

$$R = 6\cdot\frac{1+\upsilon}{1-2\upsilon} \quad (4.19)$$

υ is Poisson's ratio which is assumed constant.

To account for cementation, the normal stresses are translated in the principal stress space along the hydrostatic axis:

$$\bar{\sigma}_{ij} = \sigma_{ij} + \delta_{ij}\cdot a\cdot p_a \quad (4.20)$$

in which σ_{ij} is the stresses to be translated, δ_{ij} is Kronecker's delta ($\delta_{ij} = 1$ for $i = j$, $\delta_{ij} = 0$ for $i \neq j$), a is a dimensionless parameter, and p_a is atmospheric pressure in the same units as σ_{ij}. This translation affects the calculation of the mean normal stress p, the first stress invariant I_1, and the second stress deviator invariant J_2'.

4.4 Experimental Procedures

4.4.1 Material Tested

All experiments in this study were conducted on artificially cemented sandstone. The sandstone was produced from a mixture of Virginia Beach Sand and Type III Portland

cement. The basic properties of Virginia Beach Sand are presented in Table 4.1. The sand is mostly made up of quartz with a small amount of feldspar and can be characterized as poorly graded. The sand was washed and sieved to ensure clean sand. Particles larger than 0.425 mm (Sieve no. 40) and smaller than 0.075 mm (Sieve no. 200) were discarded. The grain size distribution curve for the remaining Virginia Beach Sand is shown in Figure 4.11.

4.4.2 Specimen Fabrication

Three hollow cylinder torsion shear specimens were produced with 6 % cement and a water/cement-ratio of 1.5. A void ratio of 0.763 was the target (which is the equivalent of a relative density, D_r = 0.20). The low relative density and low cement content were chosen to reduce the strength of the artificial sandstone. A low strength was desired due to limits on the maximum vertical stress and shear stress available by the torsion shear apparatus.

The mold for the torsion shear tests, shown in Figure 4.12, consisted of outer and inner cylindrical forming jackets with diameters of 22.0 cm and 18.0 cm, respectively. The height of the mold was 40.0 cm. The bottom and top of the mold consisted of the base and cap ring used in the tests. Before the specimens were cast, the mold was covered with paper sheets to prevent the sand/cement/water mixture from sticking to the sides. The sand/cement was mixed together and divided into four containers. After the appropriate amount of water was added to a container and the contents thoroughly mixed, the soil was divided into four equally sized portions. A quarter of a portion was placed in

Table 4.1: Properties of Virginia Beach Sand

Sand	Virginia Beach Sand
Specific gravity, G_s	2.65
Min. void ratio, e_{min}	0.520
Max. void ratio, e_{max}	0.824
D_{10} (mm)	0.213
D_{30} (mm)	0.276
D_{50} (mm)	0.312
D_{60} (mm)	0.332
D_{100} (mm)	0.425
Coefficient of uniformity, C_u	1.56
Coefficient of curvature, C_c	1.08

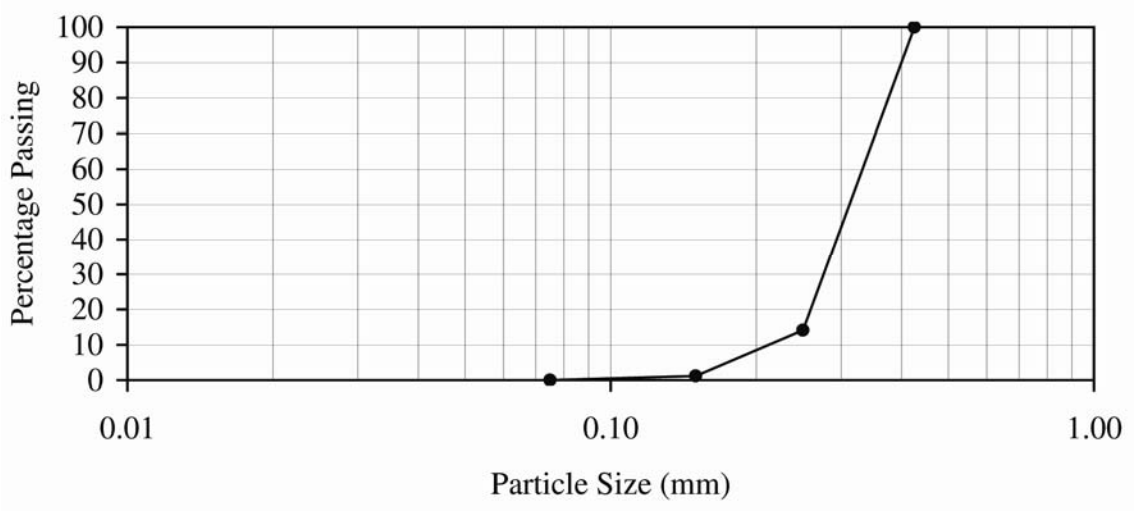

Figure 4.11: Grain size distribution curve for Virginia Beach Sand.

Figure 4.12: Mold for the hollow cylinder torsion shear tests.

the mold and compacted before the next portion was added. Thus, a total of 16 layers were compacted by dropping an aluminum rod with a fall height of approximately 4 cm down to the sand/cement surface. This was done 60 times for each layer. The rod had a diameter of 12.7 mm and a mass of 196 g. The time used to cast a specimen was approximately 80 minutes. This is larger than the initial setting time for Type III Portland cement, which is 45-60 minutes. However, the bottom layers would have received very little impact from the compaction of the top layers resulting in a minimum disturbance after setting. After the final layer was compacted, a little extra sand/cement-mixture was added to smooth the top surface before placing the cap ring on top of the specimen. After the specimens were cast they were covered with a plastic bag and allowed to cure for 5 days before they were removed from the mold, then covered again with plastic and allowed to cure for another 55 days. A total of 90 days went by from the specimens were cast until the tests started.

Three specimens were cast and after the end of curing, the exact height and the mass of the specimens were measured. The void ratios were calculated, and can be seen in Figure 4.13. They are found to be slightly lower than the target of 0.763.

4.4.3 Experimental Setup

Before a test, the specimen was glued to the stainless stell cap and base rings with epoxy. This was done to ensure full fixity between the rings and the specimen. The deformations (vertical, tangential, and shear) were measured by strain gages glued to the outside surface of the specimen. The torsion shear tests were performed with only vertical stress

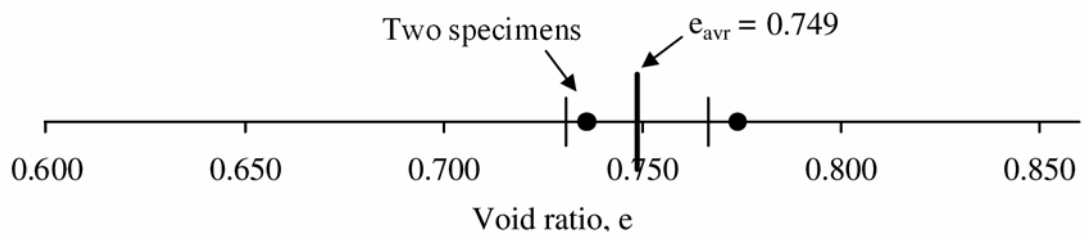

Figure 4.13: Void ratio for torsion shear specimens with indication of average value and standard deviation.

and torque applied to the hollow cylindrical specimens. The forces were provided by a hydraulic system connected to the house line of compressed air and transferred individually to the specimen. A schematic of the loading system can be seen in Figure 4.14. The forces were transferred through a center-shaft and cap plate attached to the cap ring (Figure 4.15). The vertical force was measured by a 7 kN load cell and the shear forces were measured by two 3.5 kN load cells. A detailed description of the torsion shear apparatus is given by Lade (1981).

4.4.4 Experimental Details

All tests were carried out in dry conditions at a temperature of 23^{o}C. The tests were carried out using stress control with stress rates ranging from 15 kPa/min to 95 kPa/min. This was done by loading in steps every 3 minutes. During the third test, a web-camera recorded the abrupt failure of the specimen.

4.4.5 Strain Gages

When using strain gages on concrete (or cemented sand), it is important that the strain gages are at least 5 times longer than the largest grains (Measurement Group 1992). This is to make sure it is the average strain that is measured, not local fluctuations between the individual particles. With a maximum grain size of 0.425 mm and strain gages with a length of 50.8 mm the length of the strain gages were well above the recommended length. Two rosettes, each containing three single wire strain gages were attached on opposite sides of each specimen. The orientation of the strain gages can be seen in

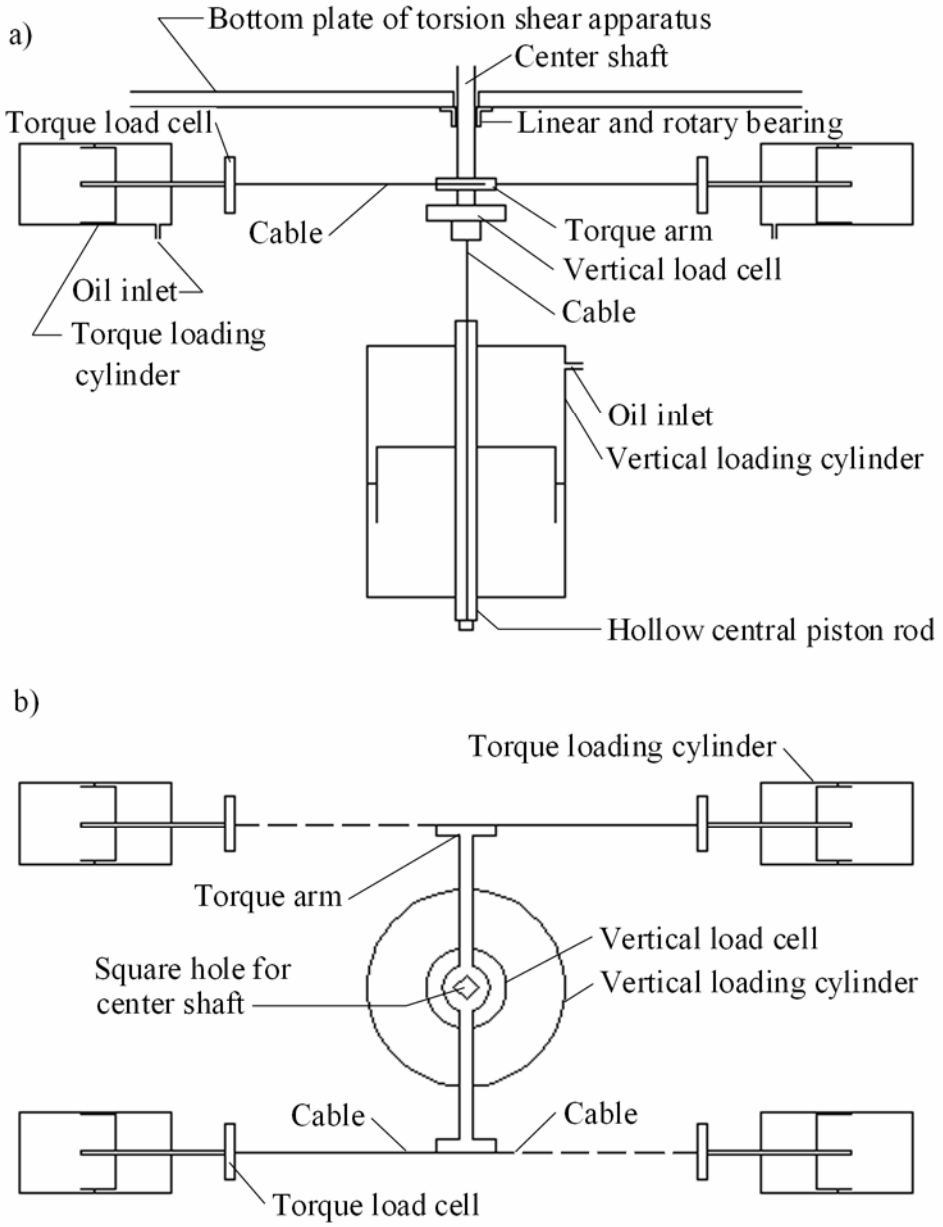

Figure 4.14: Schematic diagram of loading system for torsion shear apparatus. a) Side view. b) Top view. After Lade (1981).

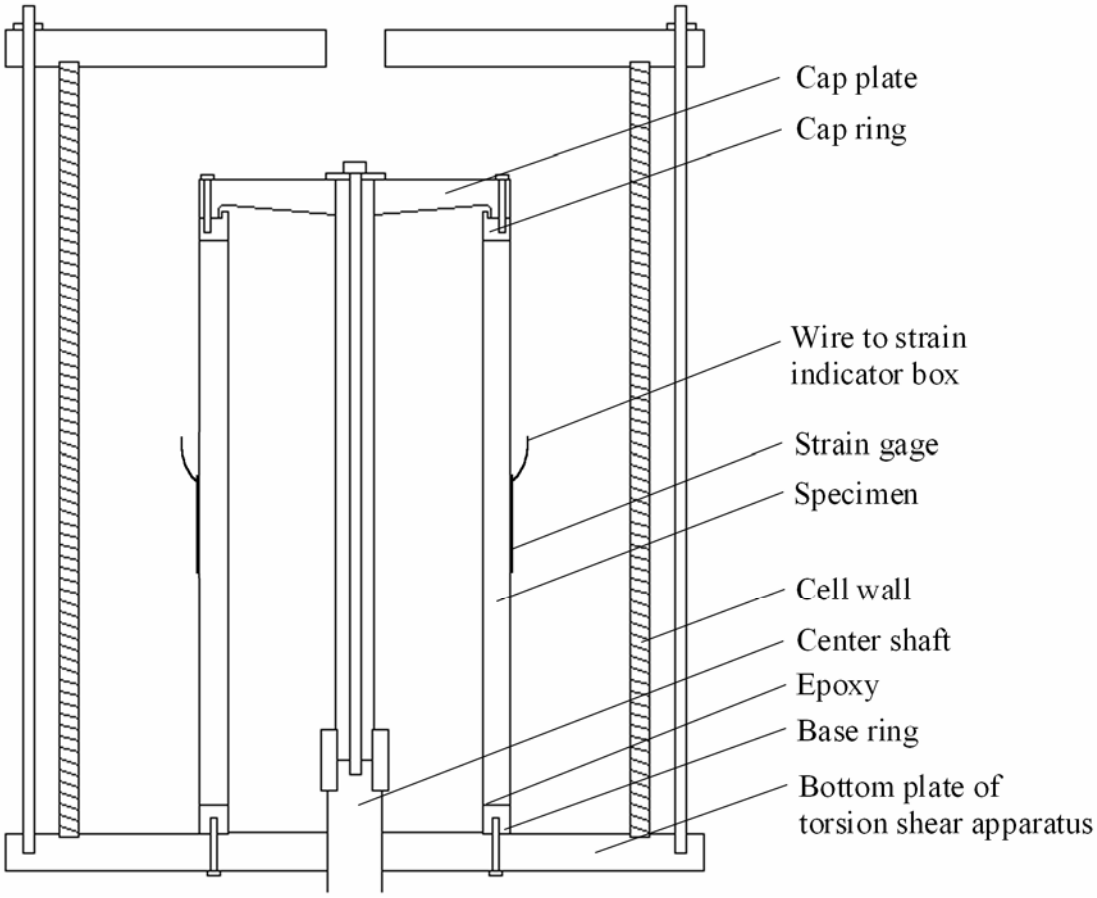

Figure 4.15: Cross section of hollow cylinder specimen and apparatus. After Lade (1981).

Figure 4.16. All the strain gages were individually connected in quarter bridges through a switch box to a strain indicator box. Sandstone is a relatively poor heat conductor, and to avoid correction for temperature changes, the electric charge was applied to each strain gage for only approximately 5 seconds when each reading took place.

The application of strain gages to porous rock involves some additional problems in comparison with metals. By filling the pores with glue, the sandstone stiffens locally and higher elastic moduli are measured. To reduce this effect, the pores were first filled with baking soda. The glue and baking soda reacts to make a stiff porous filler for the pores. The procedure for attaching the strain gages to the specimens required the specimens to be cleaned with acid, then neutralized with a base and finally washed with water. Therefore, after the specimens had dried, the pores were filled with baking soda and a layer of glue was smeared on top of it. The excess material was sanded away with fine sandpaper and the specimen surface was therefore smooth for the strain gages to be glued onto.

The vertical strains, ε_z are measured directly by strain gage E:

$$\varepsilon_z = \varepsilon_E \tag{4.21}$$

The tangential strains, ε_θ are measured directly by strain gage B:

$$\varepsilon_x = \varepsilon_B \tag{4.22}$$

The strains obtained from strain gages A and C, and D and F are used to calculate the shear strains. The strains in direction of strain gage A and strain gage C (Figure 4.17) can be found using Mohr circle in Figure 4.18. The equations describing the strains of strain gage A and strain gage C are:

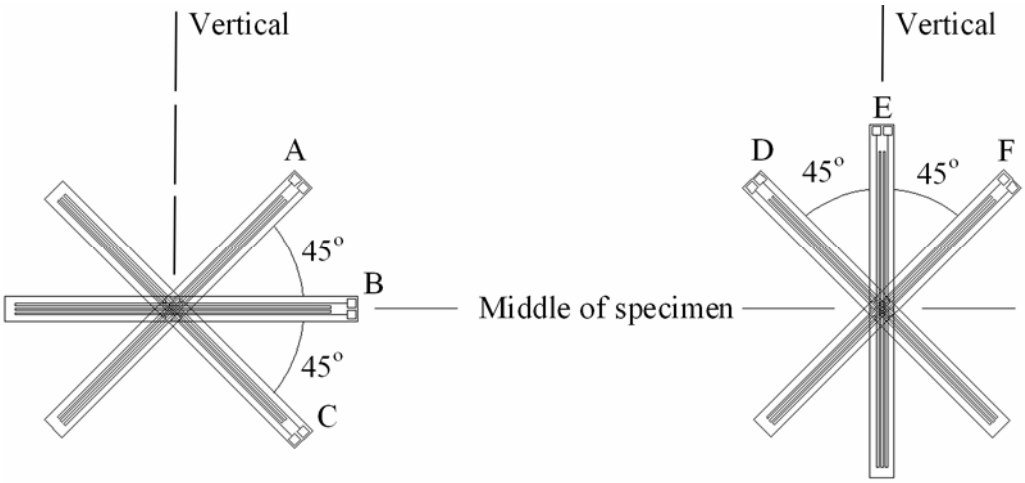

Figure 4.16: Orientation of strain gages glued to opposite sides of hollow cylinder specimens.

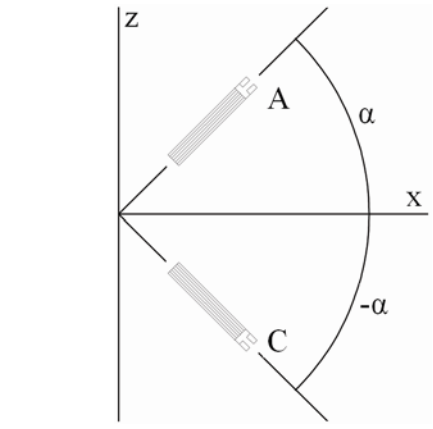

Figure 4.17: Direction of strain gages on specimen used to determine shear strain.

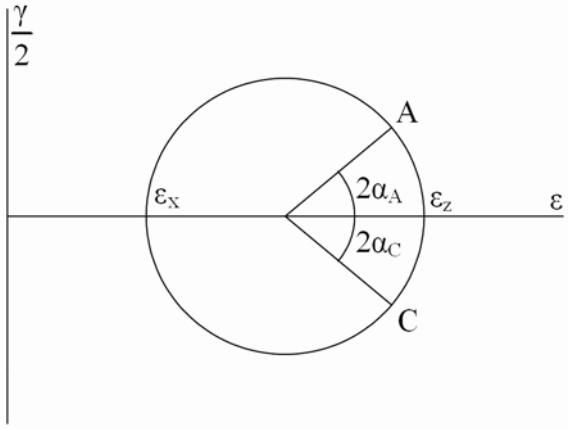

Figure 4.18: Mohr circle for strain used to determine shear strain.

$$\varepsilon_A = \frac{\varepsilon_x + \varepsilon_z}{2} + \frac{\varepsilon_x - \varepsilon_z}{2} \cdot \cos(2\alpha_A) + \frac{\gamma_{xz}}{2} \cdot \sin(2\alpha_A) \quad (4.23)$$

$$\varepsilon_C = \frac{\varepsilon_x + \varepsilon_z}{2} + \frac{\varepsilon_x - \varepsilon_z}{2} \cdot \cos(2\alpha_C) + \frac{\gamma_{xz}}{2} \cdot \sin(2\alpha_C) \quad (4.24)$$

Subtracting equation (4.23) from equation (4.24) and solving for γ_{xz} gives:

$$\gamma_{xz} = \frac{2 \cdot (\varepsilon_C - \varepsilon_A) - (\varepsilon_x - \varepsilon_z)(\cos(2\alpha_C) - \cos(2\alpha_A))}{\sin(2\alpha_C) - \sin(2\alpha_A)} \quad (4.25)$$

As the strain gages are oriented with 45^o angles on each side of horizontal and vertical, α becomes:

$$\alpha_A = -\alpha_C = 45^o \quad (4.26)$$

The shear strains, γ_{xz} can then be found from equation (4.27):

$$\gamma_{xz} = 2\varepsilon_{xz} = \varepsilon_C - \varepsilon_A \quad (4.27)$$

Similarly, the shear strains in the perpendicular direction can be calculated as:

$$\gamma_{zx} = 2\varepsilon_{zx} = \varepsilon_D - \varepsilon_F \quad (4.28)$$

4.4.6 Correction for Transverse Sensitivity

Strain gages measure the strains in one primary direction, but are sensitive to strains in other directions as well. To correct the strains, ε_{ii} for transverse sensitivity, the strains in the same plane and in perpendicular direction, ε_{jj} must be known. The correction for transverse sensitivity can then be calculated from equation (4.29).

$$\varepsilon_{ii\ corrected} = \varepsilon_{ii} - \varepsilon_{jj} \cdot K_t \quad (4.29)$$

where K_t is the transverse sensitivity of the grid (0.3 % for the strain gages used). These corrections were made to all strains discussed above.

4.4.7 Test Program

Unfortunately, only a limited amount of results are available from the first test (TS1) due to incorrect setup of the load cells measuring the shear stress. Two results are available; an unintentional loading to tensile failure during setup of the specimen, and shearing to failure following the stress path shown in Figure 4.19. The tensile failure took place along a horizontal band approximately 2 cm from the top of the specimen. After the top of the specimen was filed down to a smooth horizontal surface, the top ring was again glued on to the specimen and the tests continued.

The stress paths followed in test TS2 and TS3 can be seen in Figure 4.20 and Figure 4.21 respectively. Test TS2 started out with unconfined vertical loading, during which an unloading-reloading cycle was performed. Three loops with increasing magnitude were performed. The first two loops were going inside the potential yield surface, and the third loop was going outside the potential yield surface. Following the third loop, the vertical stress, σ_z was reduced to 385 kPa and the specimen was sheared to failure. In test TS3 three loops of approximately the same magnitude as in test TS2 were performed, but in test TS3, the first two loops were going outside the potential yield surface and the third loop was going inside the potential yield surface. Finally the specimen was sheared to failure at a vertical stress, σ_z of 620 kPa.

When reducing the shear stress, $\tau_{z\theta}$ the hydraulic system did not decrease the force instantaneously. Therefore approximately 8 kPa of shear stress were still applied to the specimen when the vertical stress, σ_z was changed. The 8 kPa would then slowly drop towards zero resulting in both change in vertical stress and shear stress. This in not

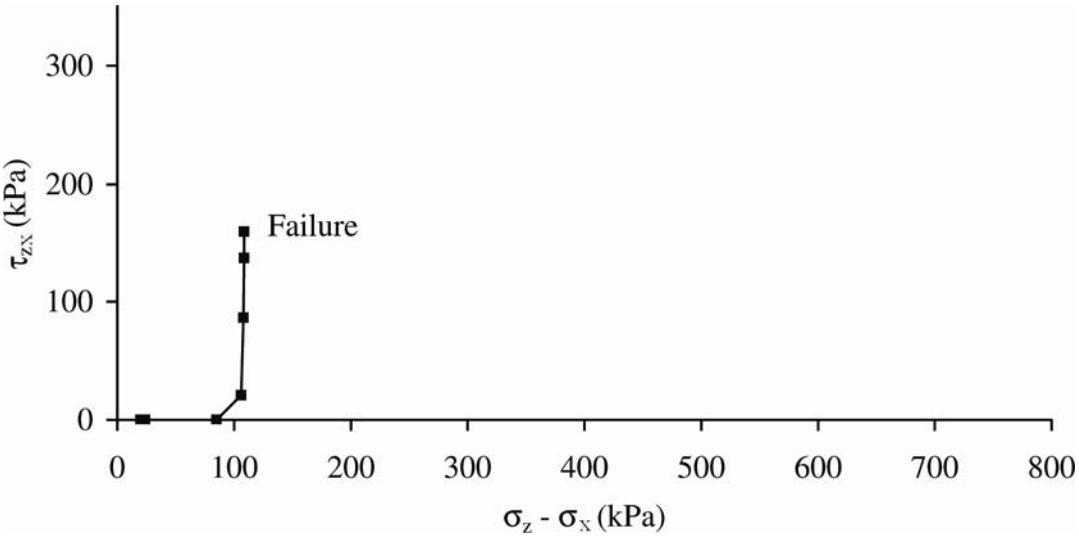

Figure 4.19: Stress path for test TS1.

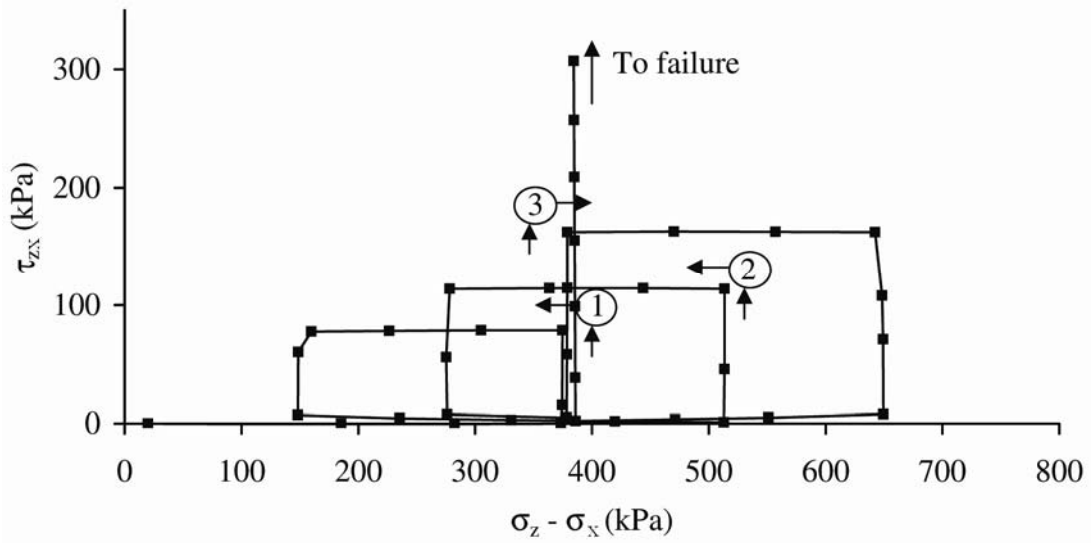

Figure 4.20: The stress path followed for test TS2 consist of three loops (two inside and one outside) and then shearing to failure.

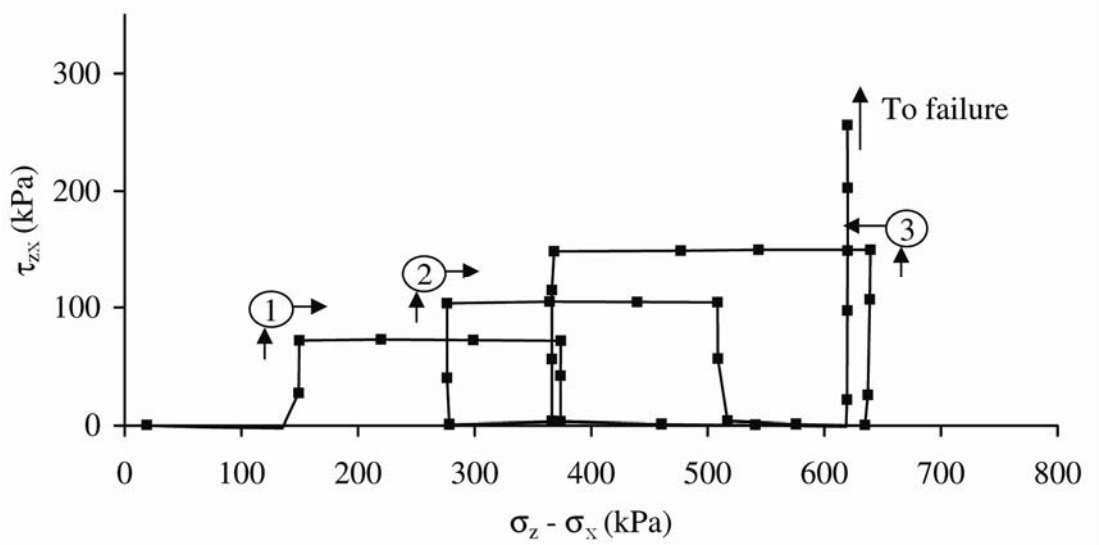

Figure 4.21: The stress path followed for test TS3 consist of three loops (two outside and one inside) and then shearing to failure.

obvious from the stress paths shown in Figure 4.20 and Figure 4.21, but shows up in the measured shear strains.

4.5 Results

The stresses and strains for the successful part of test TS1 and the two remaining tests (TS2 and TS3) can be found in Appendix D. A sketch of the failure mode for each of the specimens is also included.

4.5.1 Failure

The stresses recorded at failure can be found in Table 4.2. The tensile failure in test TS1 should only be taken as a minimum tensile strength as nothing was done to prevent progressive failure due to non uniform loading. Furthermore, the cement used for the first specimen (TS1) was from a different batch than the two remaining specimens. This may have resulted in a lower strength for the first specimen.

In all the tests, failure was abrupt and the specimens broke into multiple pieces. The mode of failure for test TS3 can be seen in Figure 4.22. The hatched areas were pulverized. Based on the failure mode recorded after the tests, there is no unambiguous shear band inclination. To get a better understanding of the failure mode, test TS3 was recorded by a web-camera and pictures taken 0.06 seconds apart at failure can be seen in Figure 4.23. It should be noted that the bottom three rows of squares were not recorded by the web-camera.

It is seen that an inclined shear band develops after which several horizontal and vertical failure bands follows. Based on the pictures in Figure 4.23, at least one shear

Table 4.2: Stresses at failure.

Test	Vertical stress, σ_z (kPa)	Shear stress, $\tau_{z\theta}$ (kPa)
TS1	- 44.2	0.0
TS1	88.6	160.1
TS2	364.0	441.7
TS3	600.8	562.2

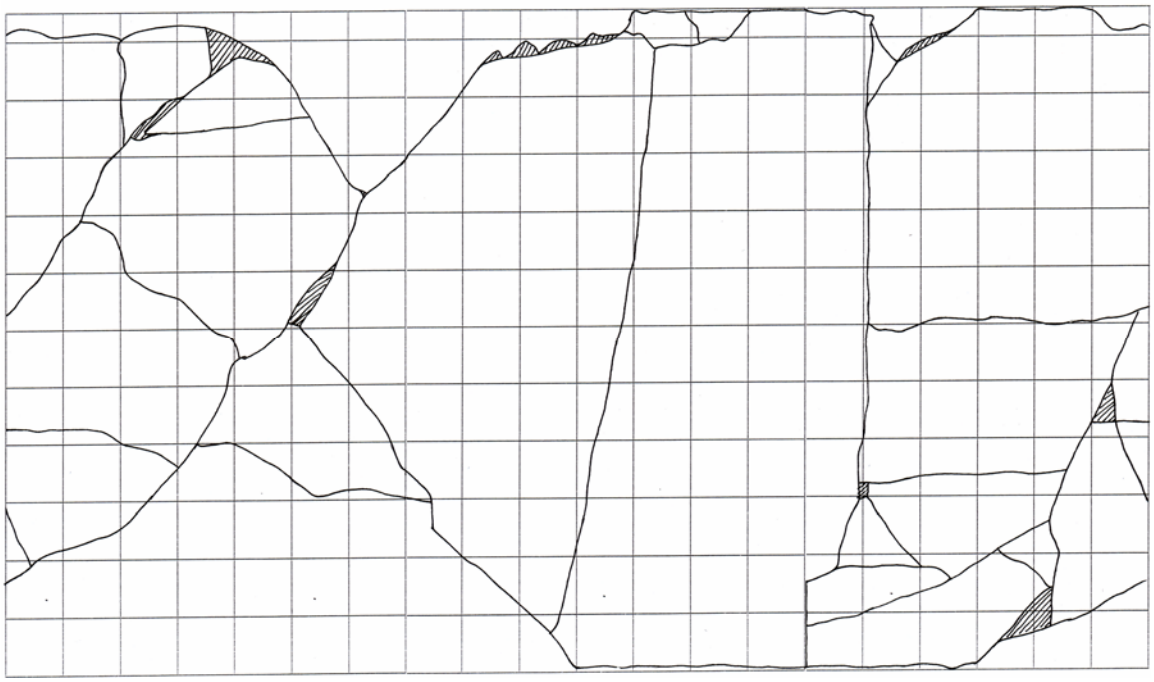

Figure 4.22: Failure mode for test TS3.

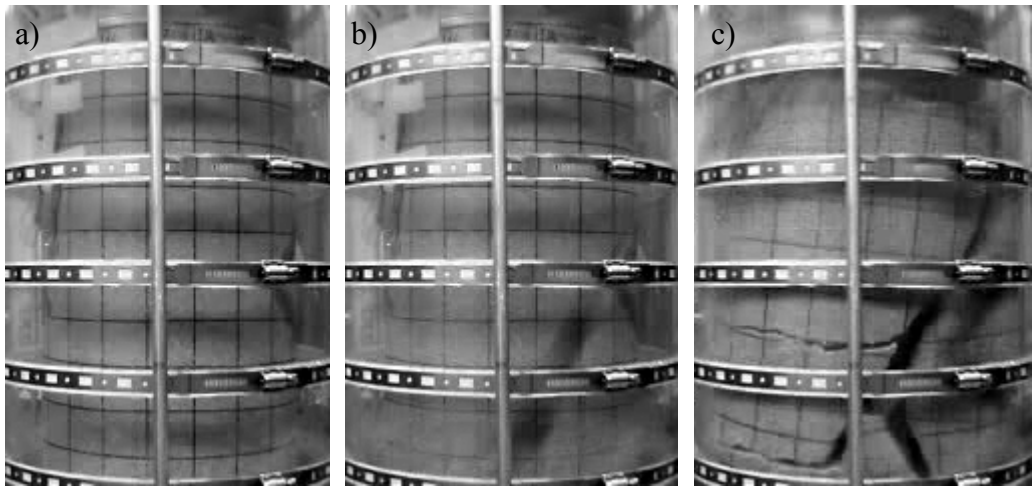

Figure 4.23: Series of subsequent pictures taken at failure of specimen TS3 with web-camera.

band (possibly two) have been recognized in test TS3. The horizontal failure lines could arise from tensile failure due to the sudden removal of the stresses at failure. Some of the horizontal bands were found to have prints after the rod used for compaction of the specimen, thus indicating reduced tensile strength along these lines.

Similarly, shear bands in tests TS1 and TS2 have been found and the inclinations with respect to vertical are recorded in Table 4.3. The inclination is found to decrease as the vertical stress at failure increases.

4.5.2 Elastic Behavior

The stress-strain curve for the initial loading and unloading-reloading at the beginning of test TS2 can be seen in Figure 4.24. As the vertical strains during the initial loading and the strains during unloading-reloading coincide, the material behaves reversible and elastic behavior is expected. The strains during the unloading-reloading cycle are linear and reversible. Note that this behavior, where the initial Young's modulus is almost identical the unloading-reloading modulus, is different from the behavior experienced in other sandstones (described in the beginning of this chapter).

The responses from the individual loops are shown in Figure 4.25 and Figure 4.26. The figures are showing the vertical strains, ε_z, versus the shear strain, γ_{zx}. This means, if the artificial sandstone behaves elastic, the response should be loops with 90^o angles and closed at the end. All loops show these characteristics, thus indicating elastic behavior. Both the inside loops and the outside loops are similar implying no yield surface is expanding during the tests.

Table 4.3: Shear band inclination.

Test	Inclination (^{o})
TS1	44.0
TS2	44.0 and 37.5
TS3	38.0 and 31.0

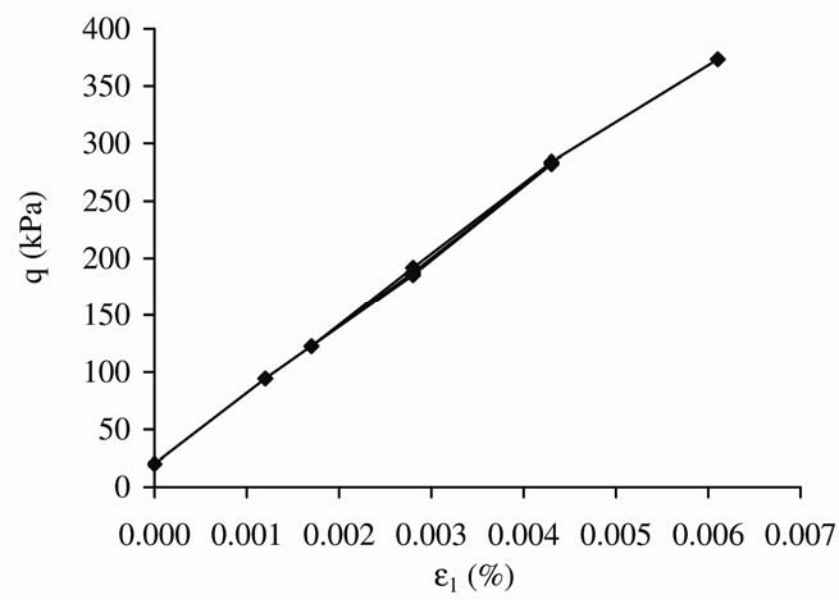

Figure 4.24: Stress strain curve for unloading-reloading in test TS2.

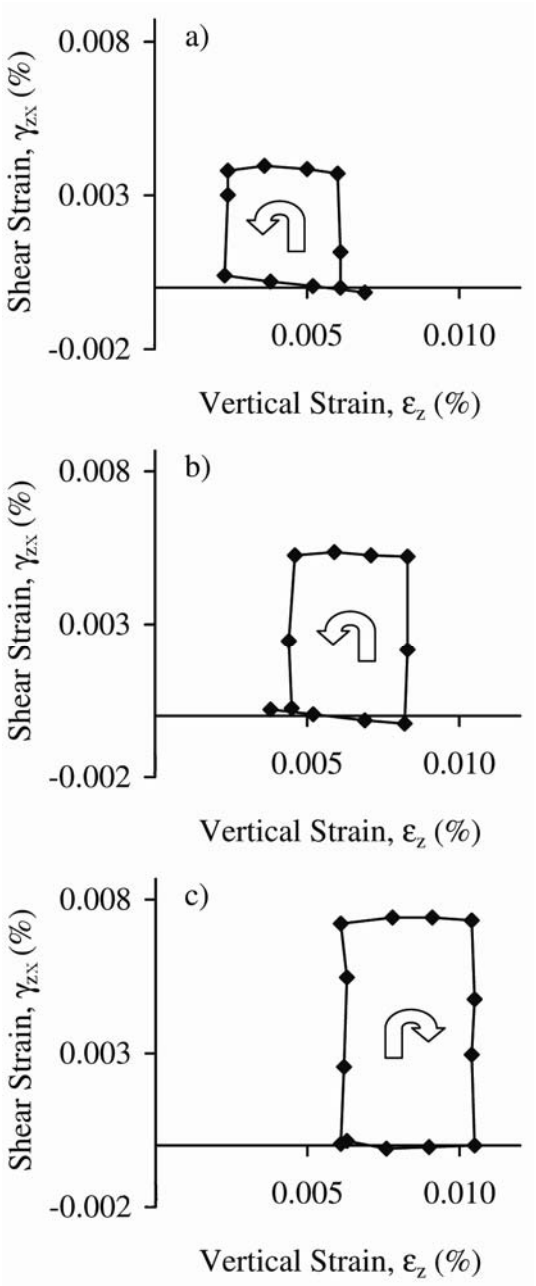

Figure 4.25: Strains recorded for test TS2. a) Inside loop. b) Inside loop. c) Outside loop.

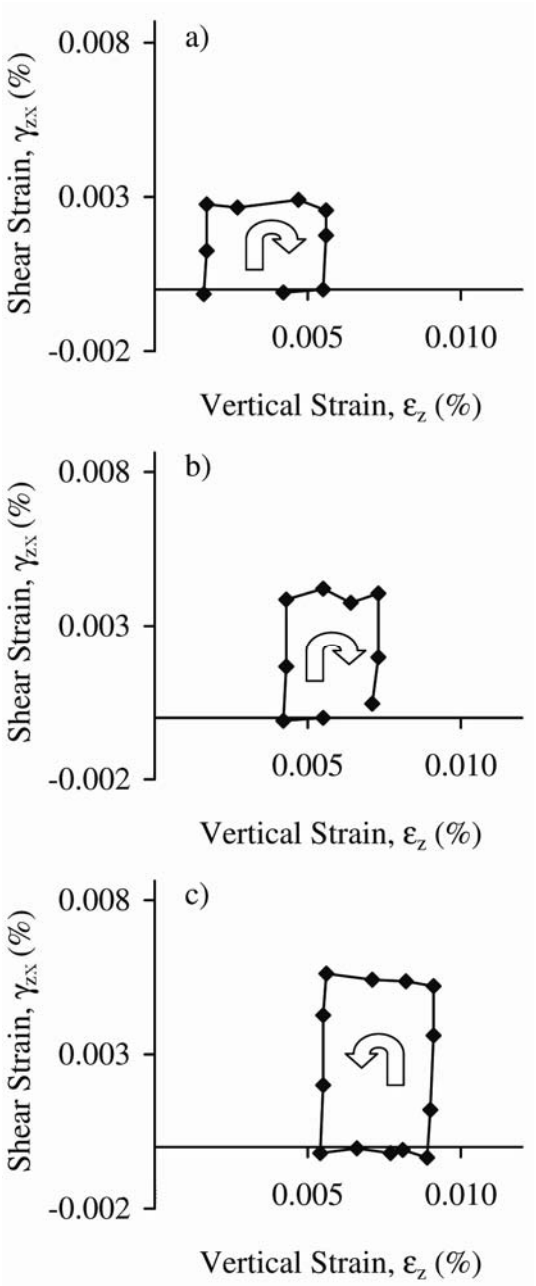

Figure 4.26: Strains recorded for test TS3. a) Outside loop. b) Outside loop. c) Inside loop.

Loop 1 and loop 2 in test TS2 (Figure 4.25 a) and b)) seem to have more vertical strain during loading than unloading. This is not due to plastic deformation, but is caused by the stresses at the end of the loops not being the same value as the stresses at the beginning of the loops. This can be confirmed by examining the stress path for the individual loops shown in Figure 4.27. Similarly, loops 1 and 2 in test TS3 are not closed. This is due to insufficient stress points, and not caused be plastic strains during vertical loading. The stress path for the individual loops in test TS3 can be seen in Figure 4.28.

In tests TS2, the shear strains decrease during the vertical reloading at the last leg of the first loop and at the first leg of the second loop as seen in Figure 4.25 a) and b). As the specimen is being reloaded, the behavior is believed to be a result of the shear stresses not being completely removed from the specimen, as discussed in section 4.2.7.

Although the stress paths were intended to be the same, the strains in test TS2 are slightly larger than in test TS3 indicating specimen TS2 to be softer than specimen TS3. How much softer depends on the exact stresses and this aspect is examined closer in section 4.3.3 where the elastic constants are calculated.

4.5.3 Elastic Constants

It has been found that the best and most consistent results are obtained by calculating the elastic constants over the entire straight-line increments in the stress paths, independent of how many measurements were made. Poisson's ratio is calculated for each increment using equation (4.8) and the results are plotted as a function of the mean normal stress for each increment in Figure 4.29. The diamond symbols represent test TS2 and the square

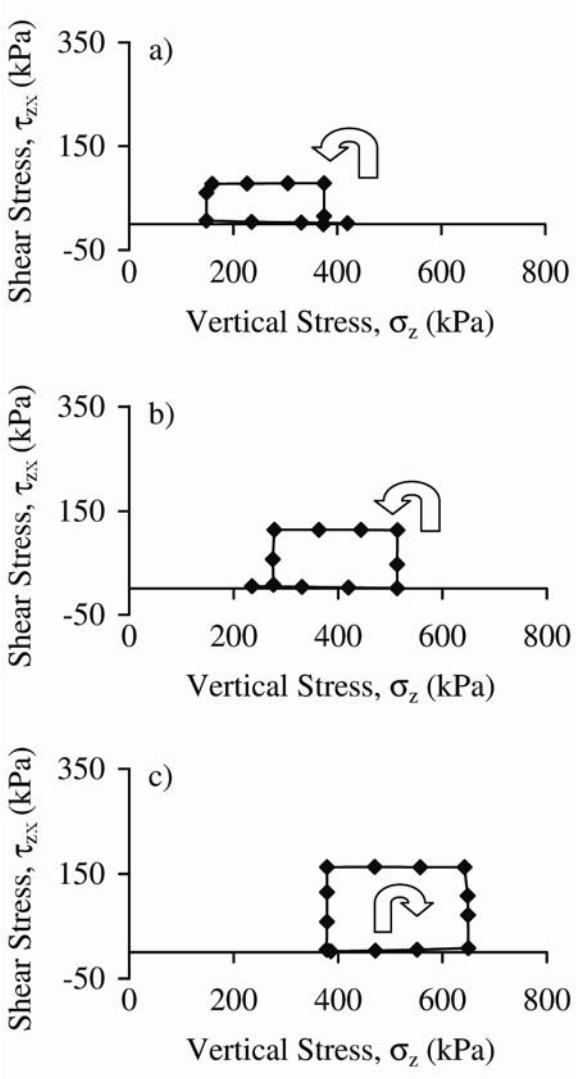

Figure 4.27: Stress path for test TS2. a) Inside loop. b) Inside loop. c) Outside loop.

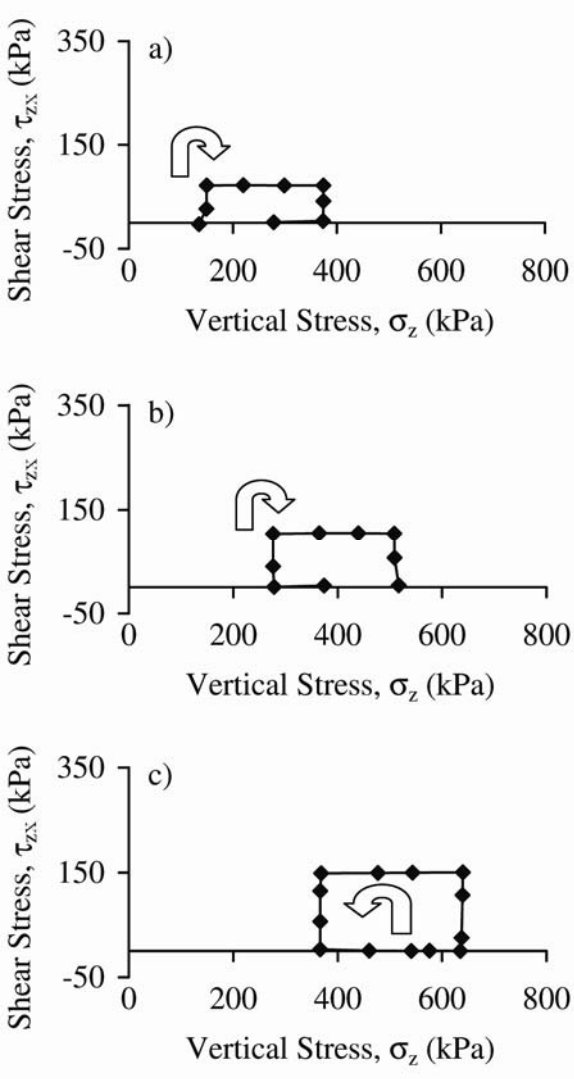

Figure 4.28: Stress path for test TS3. a) Outside loop. b) Outside loop. c) Inside loop.

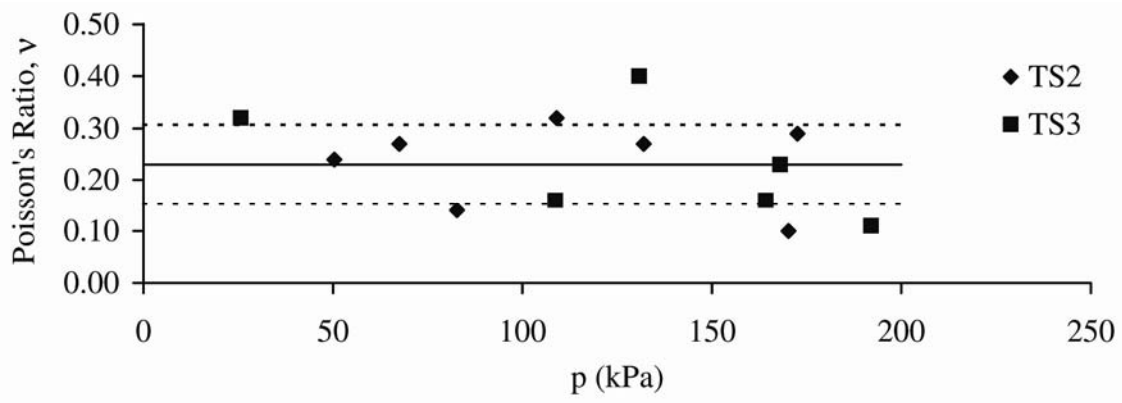

Figure 4.29: Poisson's ratio as a function of the mean stress, p.

symbols represent test TS3. There is some scatter for Poisson's ratio, but an average value of 0.23 ± 0.08 is obtained for both TS2 and TS3.

Young's modulus and the shear modulus are calculated for each increment using equation (4.7) and equation (4.9), respectively. The calculated moduli are plotted as a function of the mean stress, p corresponding to equation (4.11) and equation (4.12). The results, shown in Figure 4.30, reveal that both Young's modulus and the shear modulus increase as a function of the mean stress. Specimen TS2 has 15-20 % lower elastic and shear modulus than specimen TS3. The parameters K and n used in equation (4.11) and equation (4.12) are determined and the results are shown in Table 4.4. The parameter n, corresponding to the slope in Figure 4.30, has been forced to have the same value for Young's modulus and the shear modulus.

Similarly, the parameters M and λ from equation (4.13) and equation (4.14) have been determined for Young's modulus and the shear modulus (Figure 4.31 and Table 4.5). The parameter λ has been forced to have the same value for Young's modulus and the shear modulus.

In the calculation of the mean normal stress p, the first stress invariant I_1, and the second stress deviator invariant $J_2^{'}$, the effect of cementation is modeled by the parameter 'a'. The parameter 'a' is determined in Chapter 7 for artificial cross-anisotropic sandstone with equal amount of cement and with similar void ratio. The value determined in Chapter 7 of 'a' = 1.95 is used for this soil.

Both the simple variation (equation (4.11)), where the elastic moduli vary with p and the advanced equation suggested by Lade and Nelson (1987) fits the data. The values

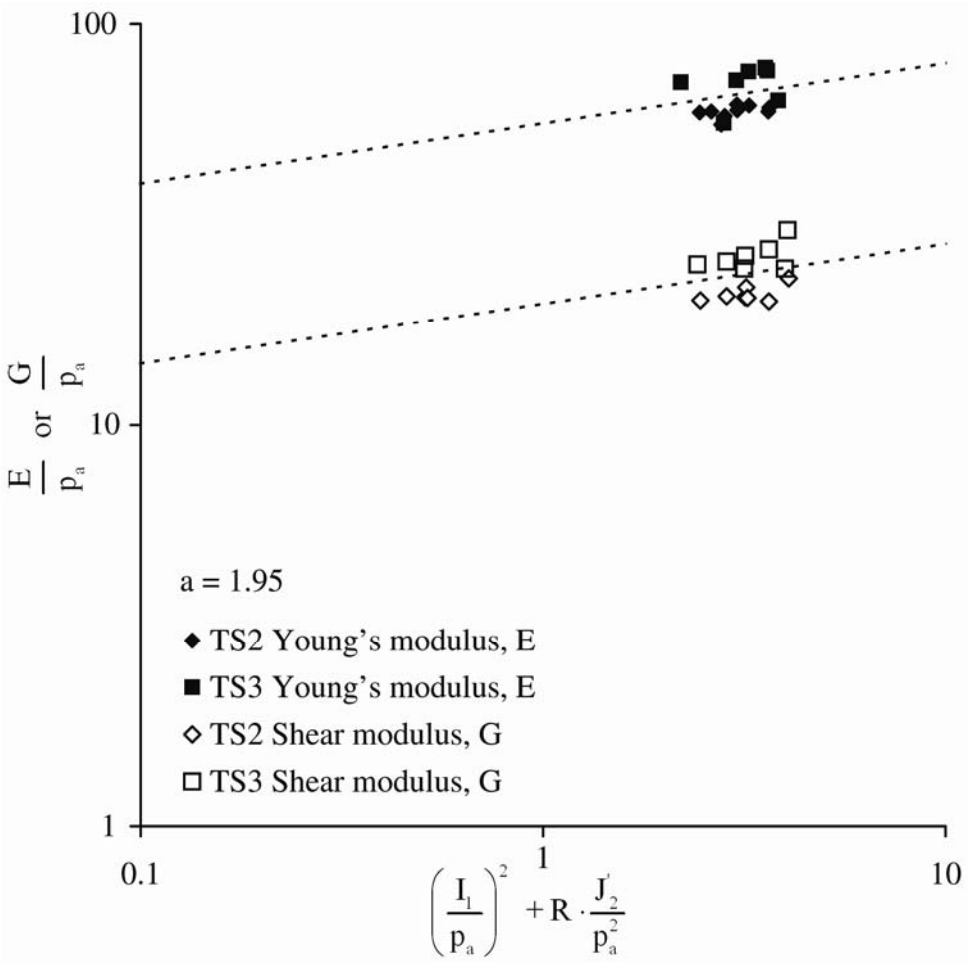

Figure 4.30: Young's modulus, E and shear modulus, G as a function of the mean stress, p.

Table 4.4: Parameters K and n determined for Young's modulus and shear modulus.

Modulus	K	n
E	56.6	0.15
G	20.1	0.15

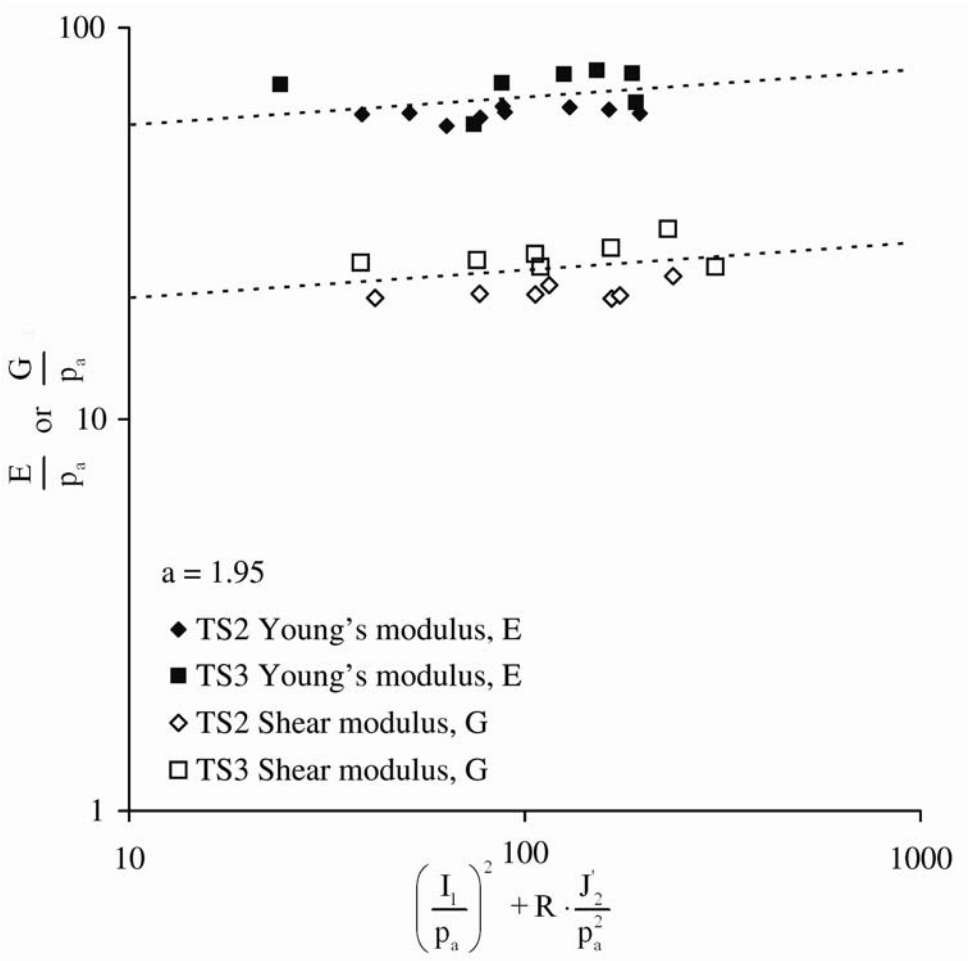

Figure 4.31: Young's modulus, E and shear modulus, G used for determination of parameters M and λ.

Table 4.5: Parameters M and λ determined for Young's modulus and shear modulus.

Modulus	M	λ
E	48.0	0.071
G	17.4	0.071

of the coefficient of determination, R^2 are generally low (< 0.5) due to the difference in the moduli between the two specimens. However, the simple variation gives slightly higher R^2-values, suggesting a better fit.

Using Young's modulus, E and the shear modulus, G, Poisson's ratio have been calculated using equation (4.10). As the parameters n and λ are the same for both Young's modulus and the shear modulus, Poisson's ratio does not vary with the stress state. Poisson's ratio from the simple variation and the advanced variation are 0.38 and 0.41, respectively. These values of Poisson's ratio are significantly higher than the average value of 0.23, determined directly from the measurements. An explanation could lie in the compaction during the production of the specimens. The compaction would result in anisotropic material, whereas equation (4.10) assumes the material to be isotropic.

4.6 Conclusion

By applying a combination of normal and shear stresses to a hollow cylinder torsion shear specimen, it has been shown that the artificially cemented sandstone behaves truly elastic inside the initial cementation yield surface. Furthermore, the isotropic elastic parameters have been determined for the artificially cemented sandstone.

5. Experiments on Artificial Cross-Anisotropic Sandstone

5.1 Material Tested

All experiments in this study were conducted on artificially cemented sandstone. The sandstone was produced from a mixture of Virginia Beach Sand and Type III Portland cement. The basic properties of Virginia Beach Sand are presented in Table 5.1. The sand is mostly made up of quartz with a small amount of feldspar and can be characterized as poorly graded. The sand was washed and sieved to ensure clean sand. Particles larger than 0.425 mm (Sieve no. 40) and smaller than 0.075 mm (Sieve no. 200) were discarded. The grain size distribution curve for the remaining Virginia Beach Sand is shown in Figure 5.1.

The minimum void ratio was determined by air pluviating 2000 g of sand through two no. 4 sieves into a 2000 ml graduated cylinder. By slow deposition of the sand from 40 cm height, the grains get knocked into a dense state and by measuring the volume the minimum void ratio can be calculated. The maximum void ratio was then determined by sealing the top of the cylinder and turning the cylinder upside down. This was repeated until a constant maximum volume was achieved.

Table 5.1: Properties of Virginia Beach Sand

Specific gravity, G_s	2.65
Min. void ratio, e_{min}	0.520
Max. void ratio, e_{max}	0.824
D_{10} (mm)	0.213
D_{30} (mm)	0.276
D_{50} (mm)	0.312
D_{60} (mm)	0.332
D_{100} (mm)	0.425
Coefficient of uniformity, C_u	1.56
Coefficient of curvature, C_c	1.08

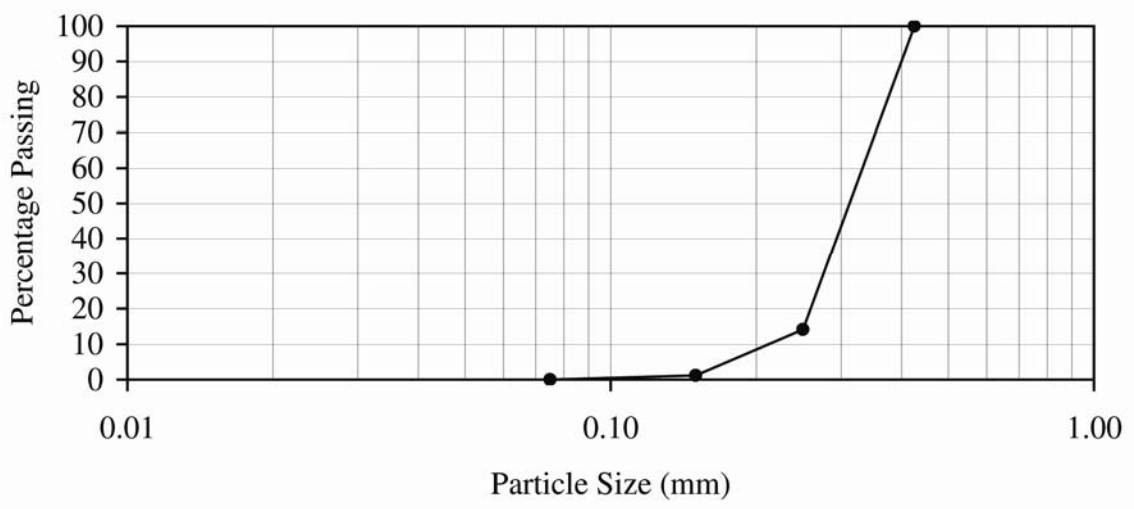

Figure 5.1: Grain size distribution curve for Virginia Beach Sand.

5.2 Specimen Fabrication

For this study, it was important that the initial yield surface created by cementation was located within the limiting capabilities of the equipment, requiring the sandstone to be relatively weak. However, the sandstone had to be strong enough to be cored without the specimens falling apart. Based on the stress-strain curves from Schnaid et al. (2001), and the strength determined by Lade and Overton (1989) a sandstone was produced with a relative density of 20 % (corresponding to a void ratio of 0.763) and with 6 % cement added to the sand. In addition to the amount of cement and the relative density, the water/cement-ratio influences the strength of cemented sand. A higher water/cement-ratio reduces the strength. To ensure the sandstone was strong enough to be cored, a series of 4 trial specimens with a diameter of 35.6 mm and a height of 100 mm were cast. They had water/cement-ratios at 0.5, 1.0, 1.5, and 2.0. After extruding the specimens from the compaction mold they were wrapped in a plastic bag and allowed to cure for two days before the cementation between the grains was examined. This was done to make sure the individual grains were cemented properly together, thereby allowing specimens to be cored. It was found, that both a water/cement-ratio of 1.0 and 1.5 produced the desired strength. However, the consistency of the sand/cement/water mixture with a water/cement-ratio of 1.5 was easier to work with during the deposition, and this ratio was therefore chosen.

When producing cross-anisotropic sandstone, the deposition and compaction method determines the orientation of the individual grains. According to Oda (1972)[b], the orientation of the long axis of the grains along with the direction of the normal to the

contact points are the dominant factors causing cross-anisotropic behavior. Furthermore, during triaxial deformation, the normal to the contact points align themselves parallel to the stress direction, and the long axes of the grains align themselves perpendicular to the stress direction, causing increased cross-anisotropic behavior.

Therefore, by applying a uniform load to each layer of the initial mix of sand, cement, and water, the sandstone becomes cross-anisotropic. This is illustrated in Figure 5.2. The sand/cement may be deposited in either wet or dry state. A dry deposition method would be to deposit the sand/cement in layers, compact each layer and then spray it with water, as done by Tien and Tsao (2000). The method chosen was to deposit the wet sand/cement in layers and then compact each layer by a uniform deformation.

To produce uniform specimens, the method of undercompaction (Ladd (1978)) was used. If each layer is compacted using the same amount of energy, then the compaction of each succeeding layer further densifies the soil below it. To prevent this, Ladd suggested undercompacting each layer. However, the right amount of undercompaction required to obtain a uniform specimen has to be determined beforehand. The amount of undercompaction for layer n, U_n, is calculated from the empirically determined equation (5.1):

$$U_n = U_{ni} - \frac{U_{ni}}{n_t - 1} \cdot (n - 1) \qquad (5.1)$$

where U_{ni} is the percent undercompaction for the first layer, n is the number of layer being considered, and n_t is the total number of layers.

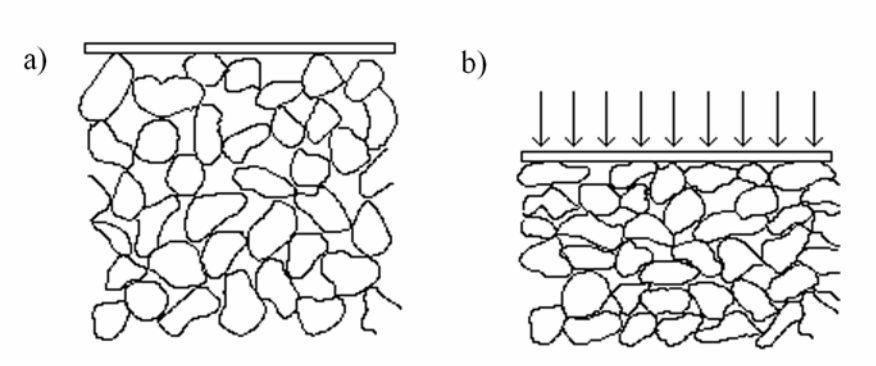

Figure 5.2: a) Before compaction the long axes of the grains are in random direction. b) After compaction the long axis of the grains are aligned primarily perpendicular to the stress direction.

The undercompaction for the first layer in equation (5.1) represents an increase in the void ratio. This is illustrated in Figure 5.3 where variation of the void ratio in the individual layers after compaction of each layer (dashed line) and after compaction of the entire specimen (massive line) is plotted. With no undercompaction (Figure 5.3 a)), the bottom layers of the specimen is too dense and the top layer to loose at the end of compaction. This is also the case in Figure 5.3 b), where to little undercompaction results in the bottom being to dense and the top to loose. However to a lesser extent than in Figure 5.3 a). With the right amount of undercompaction (Figure 5.3 c)), a uniform void ratio is achieved. Figure 5.3 d) represents a specimen exposed to too much undercompaction and as a result the bottom layer becomes too loose, and the top layer too dense. When determining the right amount of undercompaction, the variation of the void ration between the individual layers should be as small as possible, representing the right amount of undercompaction in Figure 5.3 c).

According to Ladd (1978) there are several methods of determining the right amount of undercompaction, e.g. find the maximum strength during cyclic loading, observe the behavior looking for necking or buckling during cyclic loading, find nonuniform vertical strains during unconsolidated undrained loading or measure the density/void ratio as a function of the specimen height.

The method found most suitable for this study was to determine the density/void ratio variation after compaction. Using a mold with a diameter of 35.6 mm and a height of 100 mm, the soil was compacted in 5 layers. The best method for determining the void ratio was obtained by compacting a layer, then putting a sheet of aluminum foil with a

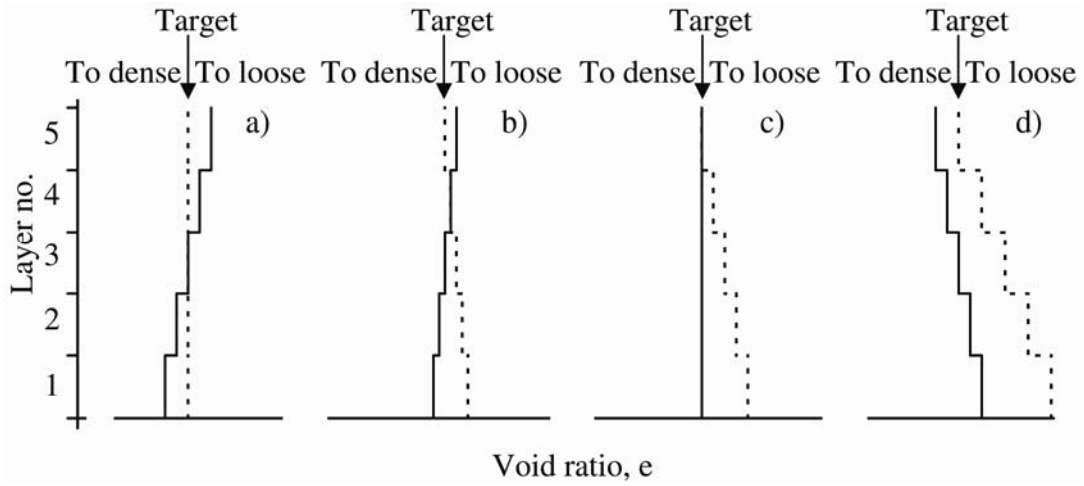

Figure 5.3: Void ratio after compaction of each layer (dashed line) and void ratio after compaction of the entire specimen (massive line). a) No undercompaction. b) To little undercompaction. c) Right amount of undercompaction. d) To much undercompaction.

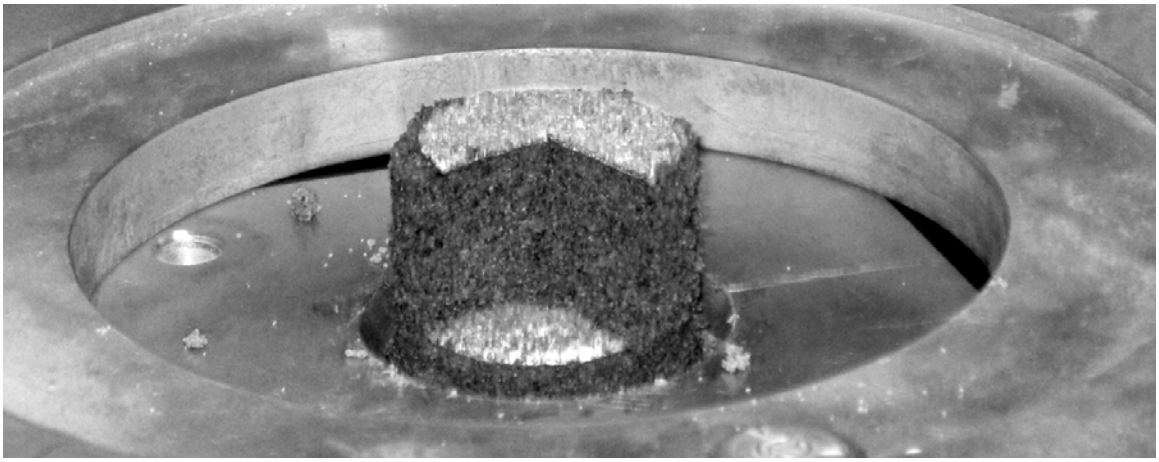

Figure 5.4: Extrusion of specimen and part cut to measure the height of the layer.

diameter of 34 mm into the mold, before compacting the next layer. The aluminum foil was flexible enough to allow the individual grains to move, and strong enough to separate the layers after compaction.

The specimens were extruded from the mold and a sector was cut out before they cured and the final thickness of each layer was measured. The average void ratio for all the layers and standard deviation for each amount of undercompaction is shown in Figure 5.5. The least variation was found with 6 % undercoampaction of the first layer, making it the optimum amount of undercompaction and resulting in uniform specimens.

Following this determination, two large blocks of artificial sandstone were cast in a specially fabricated aluminum mold with dimensions 10.0 cm x 10.3 cm x 30.7 cm. This mold was made so it could be disassembled with a minimum of disturbance to the block. A sketch of the mold can be seen in Figure 5.6. To prevent the sandstone from sticking to the mold, the sides were covered with cooking spray before the blocks were cast.

The two blocks of sandstone were made using the following procedure: First the sand and cement were mixed together and divided into five containers, one for each layer in the block. The appropriate amount of water was added to one container and the contents were thoroughly mixed before placing it in the mold. To ensure an even distribution of the soil, the mold was divided into three equally sized spaces, each receiving the same amount of soil. The surface was leveled and a plate with the same size as the mold was placed on the soil surface. A uniform load was then applied to compact it to the predetermined thickness. Before placing the next layer in the mold, the surface was

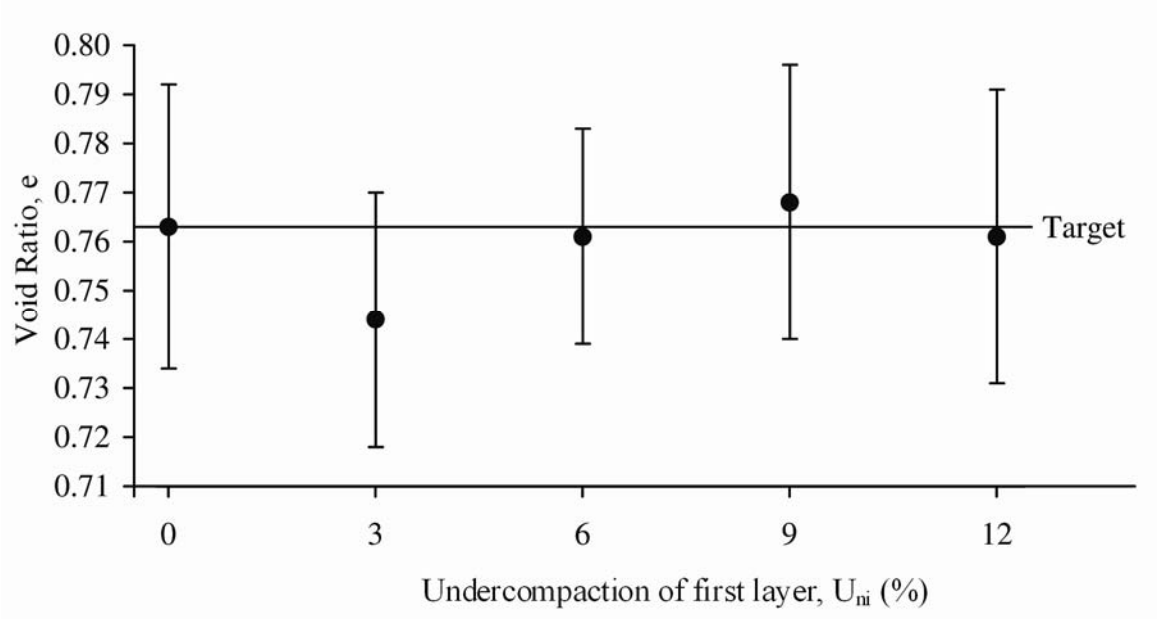

Figure 5.5: The mean value and standard deviation of void ratio as a function of the amount of undercompaction.

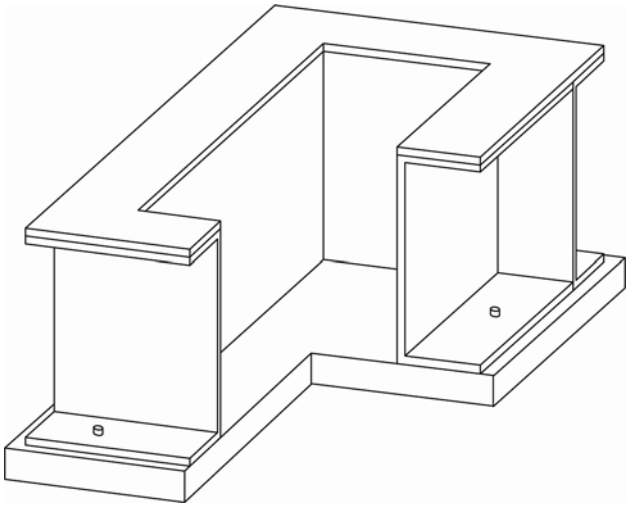

Figure 5.6: Sketch of mold used for fabrication of artificial anisotropic sandstone.

scarified to increase the contact between the soil layers. The whole process of making the sandstone block from the beginning when water was added to the first sand/cement-mixture till the final layer was in place took no more than 50 minutes. This is within the initial setting time for Type III cement which sets in 45-60 minutes.

After compacting the final layer, the vertical pressure was removed and the block was covered by a plastic bag and allowed to cure for 30 days. After 30 days the mold was disassembled and the sandstone block was removed and 8 horizontal and 8 vertical specimens were cored from each of the two blocks for a total of 32 specimens. Another 90 days went by before the triaxial testing started. The specimens were cored with a diameter of 36.5 mm and the ends were then trimmed to give the specimens a height of 97.6 mm. The average height to diameter ratio was 2.67 ± 0.02. The variation corresponds to a difference in height of approximately one average grain diameter. The mass of the specimens were determined and the void ratios were calculated, as seen in Figure 5.7.

The void ratios are found to be a little higher than the target of 0.763. This could be caused by the final height of the entire block being measured with the compaction load applied to the specimen. After the load was removed, the soil unloaded elastically. The averages of the void ratios of the vertical and horizontal specimens are close to each other, but with a variation in the horizontal specimens that is larger than that for the vertical specimens. The greater variation in the void ratio in the horizontal specimens indicates that the blocks were not completely uniform. A systematic variation in the void ratio depending on the location in the block was not found. This indicates that the under-

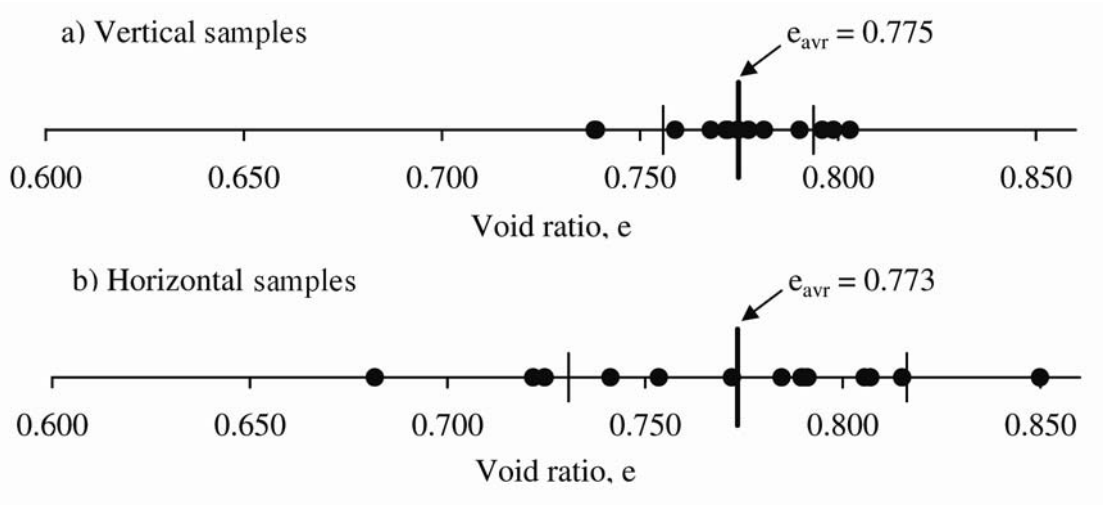

Figure 5.7: Void ratio for a) vertical specimens and b) horizontal specimens with indication of average values and standard deviations determined for all specimens from the two blocks.

compaction is not the source of the variation. Neither do the boundary conditions from the mold seem to cause the variation. Significant differences between the void ratios from block I and block II were not found. The possibility exists that local variations in void ratio could cause the variations depending on where the specimens were cored relative to the compaction layers. This scenario is illustrated in Figure 5.8. The difference between specimen A and specimen B is less than 5 mm. Unfortunately, the exact location where the specimens were cored are not known to the extent required for confirmation of this possibility.

5.3 Experimental Setup

5.3.1 Triaxial Compression Tests

The triaxial tests were carried out in a high pressure triaxial cell. A sketch of the cell can be seen in Figure 5.9. The specimen was placed between two filter stones to ensure drainage during the tests. Due to membrane puncture at higher confining pressures, a minimum of two rubber membranes with silicone grease in between separated the specimens from the cell water. The total number of membranes used, depended on the confining pressure in the test. At the highest confining pressures, four membranes were used. O-rings sealed the membranes at the cap and base. All specimens were saturated by the CO_2-method to enable measurement of volume changes during testing as described in section 5.4.2.

In tests at low confining pressures (0.5 MPa and below), the pressure was delivered from the house line of compressed air with a maximum pressure of 690 kPa. At

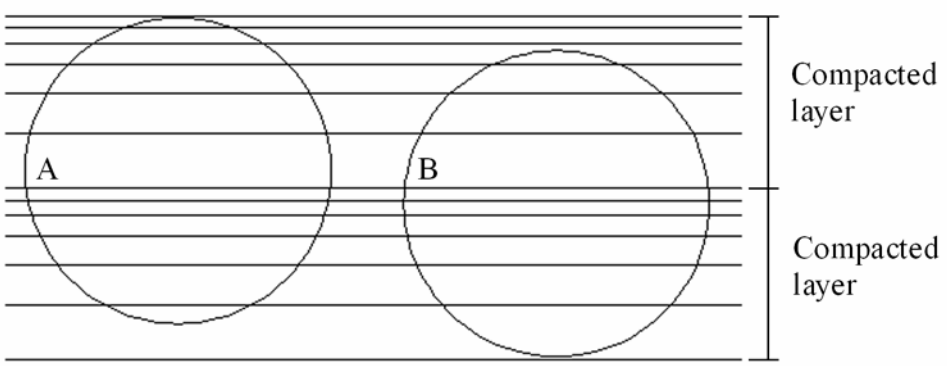

Figure 5.8: For void ratio variations within each compacted layer as indicated, specimen A would have a lower void ratio than specimen B.

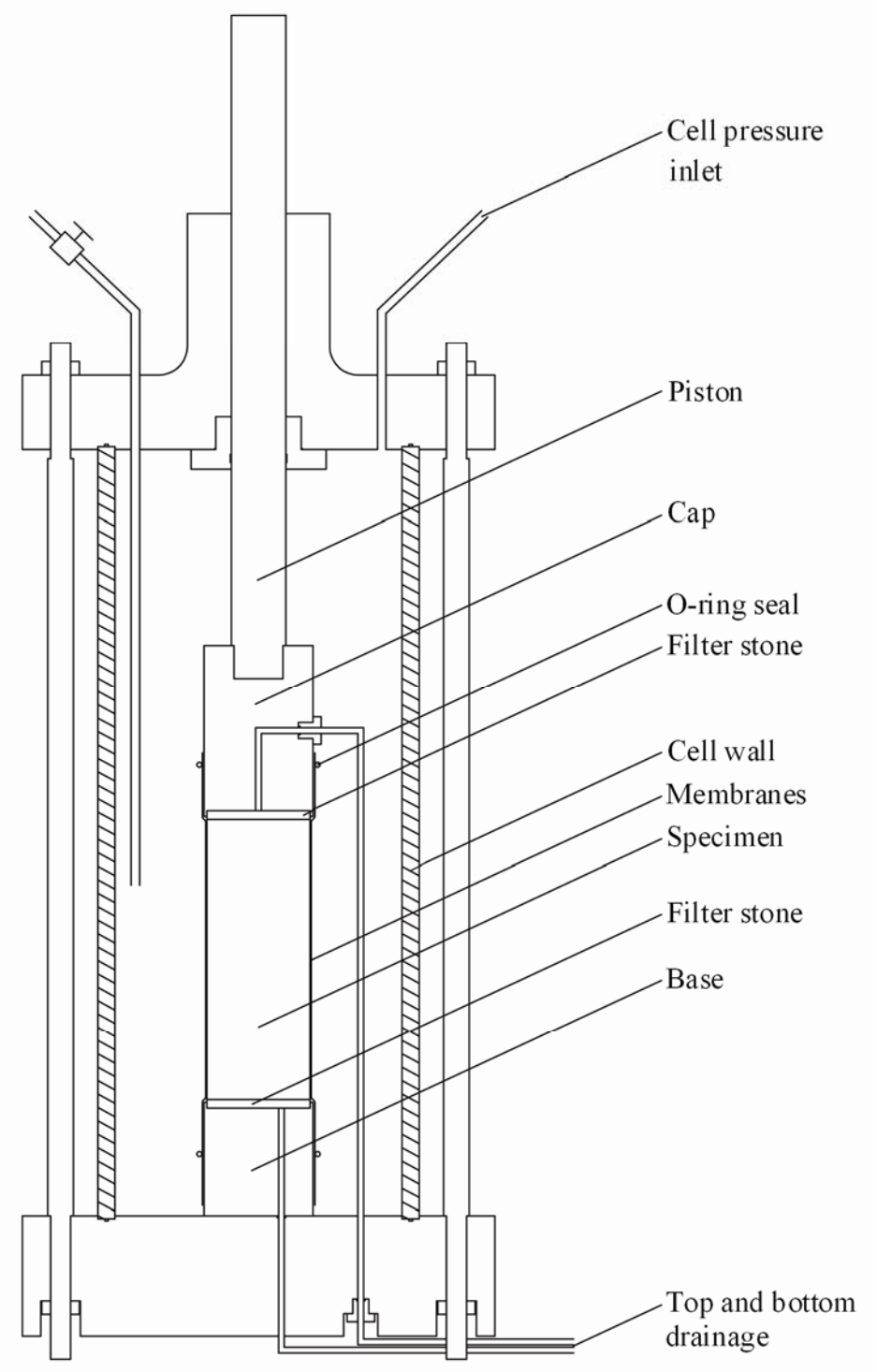

Figure 5.9: High pressure triaxial cell.

high confining pressures (above 0.5 MPa), the pressure was delivered from a tank of nitrogen able to produce a maximum pressure of 15.8 MPa. A deformation controlled loading machine with a maximum capacity of 100 kN delivered the vertical force. The vertical force was measured by a load cell with a capacity of 44.5 kN. An electronic dial gage measured the vertical deformation between the piston and the top of the cell. A burette type volume change device connected to the top and bottom drainage lines measured the volumetric change. During the tests, the confining pressure, the vertical load, and the back pressure were recorded along with the vertical deformation and volume change.

5.3.2 Isotropic Compression Tests

The isotropic compression tests were carried out in the same cell and with the same setup as the triaxial tests. However, the 19.05 mm (¾") diameter piston and the seal for this piston were exchanged with a 3.15 mm (⅛") diameter rod and a corresponding smaller seal in the cap plate of the triaxial cell. This was to achieve as close to isotropic compression as possible, i.e. without significant correction for piston uplift as for the larger piston. The much smaller piston uplift allowed for measurement of the vertical deformation of the specimen.

5.3.3 Brazilian Tests

In the Brazilian tests the cylindrical specimens were placed between two aluminum blocks as shown in Figure 5.10. The upper block was attached to a load cell and the lower

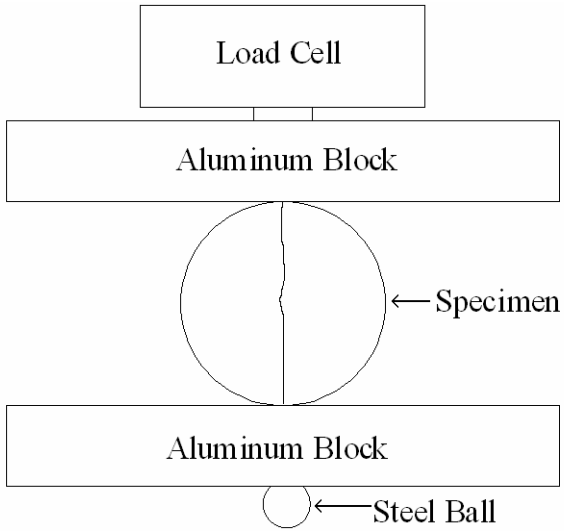

Figure 5.10: Experimental setup for Brazilian tests.

block was placed on a steel ball. This was done to ensure freedom for movement of the lower block in all directions. If the surfaces of the specimens were not perfect, the lower block could move, thereby allowing the lower block to apply a uniform line load and avoiding progressive failure. During the test the load was monitored. The maximum load and time to failure were recorded. Failure occurred by vertical splitting of the cylindrical specimens as indicated in Figure 5.10.

5.4 Details of Experimental Procedures

5.4.1 Test Temperature

All tests were carried out at temperatures between 24 ^{o}C and 27 ^{o}C.

5.4.2 Saturation

After the specimen was placed in the triaxial cell and the confining pressure was set to 50 kPa, the specimen was slowly flushed from the bottom with carbon dioxide for 20 minutes. As carbon dioxide is heavier than atmospheric air, carbon dioxide replaces the air in the specimen. Finally the specimen is flushed from the bottom with deaired water. One volume of deaired water can dissolve approximately one volume of carbon dioxide gas at room temperature. If pockets of carbon dioxide still exist in the specimen, the subsequent application of a back pressure of 200 kPa dissolves the carbon dioxide in the water. This results in a very high degree of saturation. After saturation the pore pressure coefficient, B, was measured to check that the saturation was successful. The stiffness of the material determines the maximum B-value corresponding to full saturation. A soft

material produces a high B-value close to 1.00, and the stiffer the material, the lower the B-value. All specimens were tested with B-values between 0.84 and 0.95 which was found to be satisfactory for cemented soil. However, all tests were completely drained tests and full saturation is not required for satisfactory volume change measurements.

When carbon dioxide dissolves in deaired water, some of the carbon dioxide reacts with the water to form the following equilibrium:

$$CO_2(aq) + H_2O(l) \rightleftarrows H_2CO_3(aq) \qquad (5.2)$$

in which (aq) stands for aqua, meaning both carbon dioxide (CO_2) and carbonic acid (H_2CO_3) are dissolved in water. The $H_2O(l)$ is water where the (l) indicate it being in the liquid state. The carbonic acid is a weak acid and can dissolve e.g. calcium carbonate or magnesium carbonate. These materials could be present from shell fragments in the beach sand. The carbonic acid can also dissolve Portland cement. In concrete this is known as carbonation. To avoid this reaction, the specimens were flushed with 2-3 pore volumes of deaired water, so the water in the specimen contained as little dissolved carbon dioxide as possible.

Before the Brazilian tests were performed, the specimens were placed in a tank with deaired water and vacuum were applied to the tank. After 15 minutes of vacuum, when no further air bubbled from the specimens, vacuum was removed and the specimens were moved from the water to the test setup. No more than 15 minutes occurred between a specimen was removed from the water to failure of that specimen. That time was kept as short as possible to keep the specimens from drying out.

5.4.3 Loading Rates

All the isotropic loading (both in the real isotropic tests and in the triaxial tests before shearing) was carried out under stress control with a rate of approximately 240 kPa/min. This was done by loading in steps of approximately 480 kPa every 2 minutes. The triaxial shearing, the K_0-loading, and the Brazilian tests were carried out under deformation control with a strain rate of 0.10 %/min. In the Brazilian tests the reference height was the diameter.

5.4 Testing Program

Of the 32 specimens cored from the two blocks, 22 were used for triaxial tests, 4 were used for isotropic compression tests, 4 were used for Brazilian tests and 2 were used for K_0-tests. The stress paths for the triaxial and isotropic tests are shown in Figure 5.11. The exact confining pressures for each test can be found in Appendix D along with the test results. After each of the four isotropic tests were finished, the specimens were still intact with partly broken cementation, so the specimens were used for a second test (2 Brazilian and 2 triaxial). The reason that the initial "isotropic" compression paths of the triaxial specimens are located below the hydrostatic axis is described in section 5.5.3.

5.5 Corrections

5.5.1 Correction for Membrane Penetration

In the isotropic and the K_0-tests where the confining pressure changes during the test, the measured volume change requires correction for membrane penetration. According to

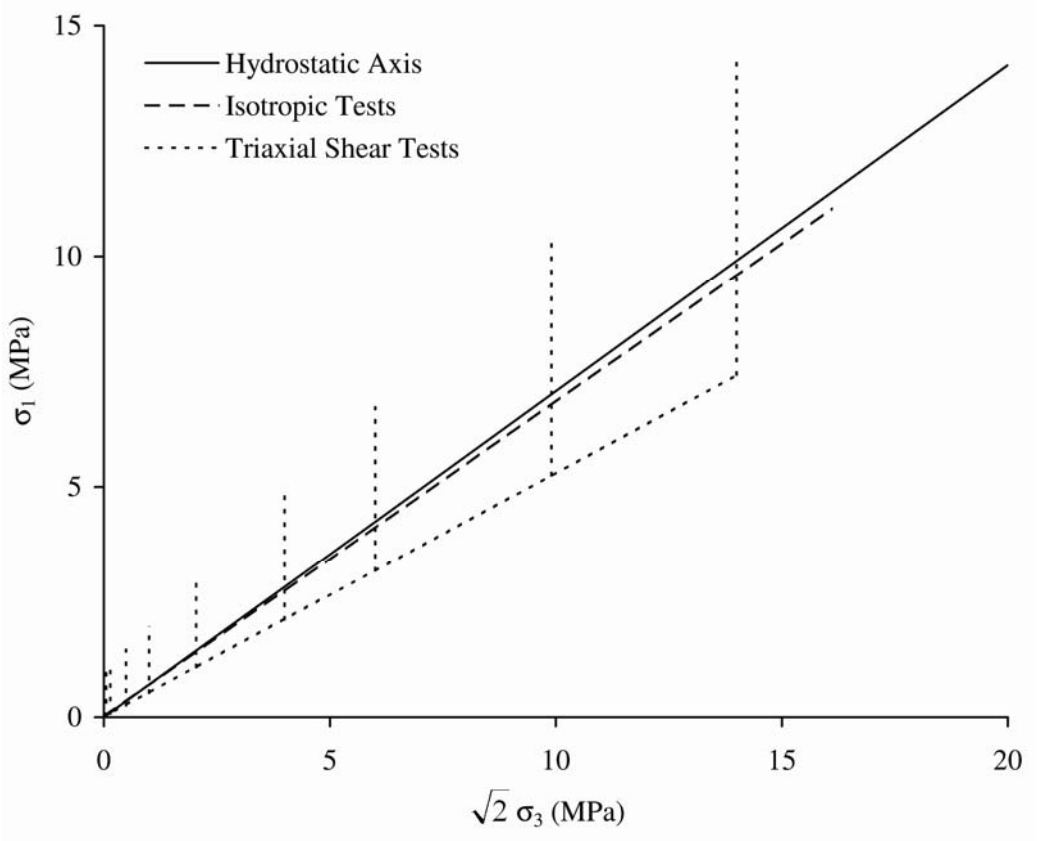

Figure 5.11: Stress paths for isotropic and triaxial shear tests.

Frydman et al. (1973), the volume change due to membrane penetration, ΔV_m, can be calculated as:

$$\Delta V_m = \Delta v_m \cdot A_m \tag{5.3}$$

where A_m is the area of the membrane and the membrane penetration per area, Δv_m, may be determined from:

$$\Delta v_m = S \cdot \log\left(\frac{p}{p_0}\right) \tag{5.4}$$

in which p is the confining pressure and p_0 is the confining pressure at the start of the test. The variable S can be determined as a function of the mean grain size, D_{50}:

$$S = 0.0124 + 0.0135 \cdot \log(D_{50}) \tag{5.5}$$

5.5.2 Area Correction

In all the triaxial tests the cross-sectional area is corrected as the tests progresses:

$$A = \frac{V_0 - \Delta V}{H_0 - \Delta H} \tag{5.6}$$

A is the cross-sectional area of the specimen, and V_0 and H_0 are the initial volume and initial height of the specimen, respectively. ΔV is the change in volume and ΔH is the vertical deformation. Equation (5.6) assumes that the specimens deform uniformly as right cylinders during the tests.

5.5.3 Piston Correction

During the isotropic part of the triaxial tests the vertical confining pressure was reduced due to piston uplift. The area of the piston takes up 25 % of the area of the cap, resulting

in a similar reduction in the vertical confining pressure. As a result of this, shearing starts below the hydrostatic axis, as seen in Figure 5.11. To be able to apply as close to isotropic compression as possible, a thin rod that only reduced the area by 3 % was used. This rod was used to gage the vertical compression of the specimen during isotropic compression.

5.5.4 Correction for Elastic Anisotropy in Brazilian Tests

In a cross-anisotropic material with specimens cored vertical and horizontal, there are three principal material orientations of the specimens. Figure 5.12 shows the three orientations where a) is from a vertically cored specimen, and b) and c) are from horizontally cored specimens.

Normally the material is assumed to be isotropic and the tensile stress at the disc center is calculated as:

$$\sigma_t = -\frac{P}{\pi \cdot R \cdot t} \tag{5.7}$$

Where σ_t is the tensile stress, P is the applied force, R is the radius of the specimen and t is the thickness of the specimen. The compressive stress at the disc center, σ_c is three times larger than the tensile stress:

$$\sigma_c = 3 \cdot \frac{P}{\pi \cdot R \cdot t} = -3 \cdot \sigma_t \tag{5.8}$$

Equation (5.7) and (5.8) were applied to the results from the vertical specimens (Figure 5.12 a)).

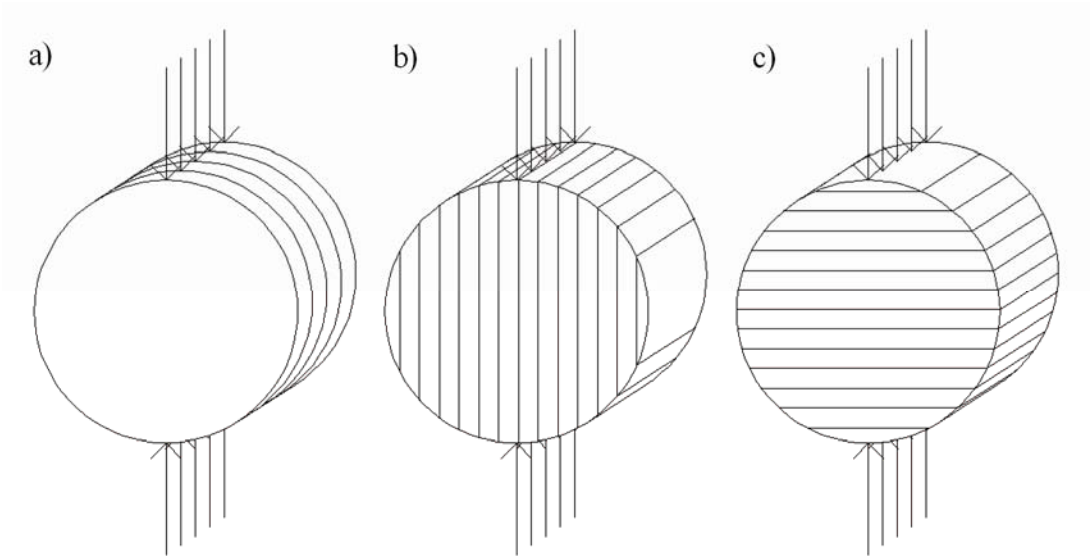

Figure 5.12: Possible specimen orientations for Brazilian tests on cross-anisotropic material.

Claesson and Bohloli (2002) developed an approximate equation for the principal stresses at the disc center of a cross-anisotropic material. The equations were derived from an analytical solution and were compared with results from tests on gneiss. The material is assumed to be linear elastic until failure, and the stress conditions at the disc center are based on the cross-anisotropic elastic parameters. The tensile stress, σ_t and the compressive stress, σ_c are found from equation (5.9) and equation (5.10). For isotropic elastic material equation (5.9) and equation (5.10) reduce to equation (5.7) and equation (5.8), respectively.

$$\sigma_t \cong -\frac{P}{\pi \cdot R \cdot t} \cdot \left[\left(\sqrt[4]{\frac{E_v}{E_h}} \right)^{\cos(2\cdot\theta)} - \frac{\cos(4\cdot\theta)}{4}(b - 1) \right] \tag{5.9}$$

$$\sigma_c \cong \frac{3 \cdot P}{\pi \cdot R \cdot t} \cdot \left[\left(\sqrt[4]{\frac{E_h}{E_v}} \right)^{\cos(2\cdot\theta)} + \frac{\cos(4\cdot\theta)}{4}(b - 1) \right] \tag{5.10}$$

As in equation (5.7), P, R, and t are defined as the applied force, the radius and the thickness of the specimen. E_v and E_h are the vertical and horizontal elastic moduli. θ is the angle between the bedding planes and the direction of the applied force. θ is defined to be zero when the applied force is perpendicular to the bedding planes. Therefore, in Figure 5.12: b), θ is equal to 90^o and in Figure 5.12: c), θ is equal to 0^o. The parameter b is defined as:

$$b = \frac{\sqrt{E_v \cdot E_h}}{2} \cdot \left(\frac{1}{G_{hv}} - \frac{2\nu_{hv}}{E_h} \right) \tag{5.11}$$

Again E_v and E_h are the vertical and horizontal elastic moduli, ν_{hv} is Poisson's ratio in the vertical direction when loading occur in the horizontal direction. G_{hv} is the shear modulus

in any vertical plane. This shear modulus cannot be found from triaxial tests, but according to Talesnick and Ringel (1999) a good approximation is:

$$G_{hv} = \frac{E_h \cdot E_v}{E_v \cdot (1 + 2 \cdot \nu_{vh}) + E_h} \cdot \frac{2 \cdot E_v - E_h}{E_v} \tag{5.12}$$

Where E_v and E_h are the vertical and horizontal elastic moduli and ν_{vh} is Poisson's ratio in the horizontal direction when loading occurs in the vertical direction.

5.5.5 Correction for Interface Compression

After completing the tests on the anisotropic sandstone, it was realized that a substantial amount of the measured deformation arose from interface compression at the ends of the specimens. Near the ends of the sample, the cementation either broke or the grains were crushed. Due to the weak cementation, the trimming of the ends could have compromised the strength of the cementation. The result is an increased amount of strain in the major principal direction and an increased volumetric contraction.

The deformation measured in the triaxial setup can be separated into four individual parts, as shown in Figure 5.13. The compression of the metal cap/base is considered negligible compared to the compression of the specimen and interfaces. The four parts contributing to the deformation are the interface between the cap/base and the filter stone, δ_a, the deformation of the filter stone, δ_b, the interface between the filter stone and the specimen, δ_c, and the deformation of the specimen δ_d.

The deformation of the specimen, δ_d is used in calculation of the strains, and can be calculated from:

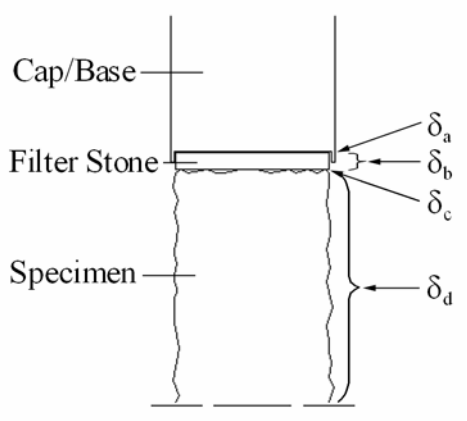

Figure 5.13: Deformation of individual parts in triaxial setup.

$$\delta_d = \delta_{measured} - \delta_{cor} \quad (5.13)$$

in which $\delta_{measured}$ is the measured deformation and δ_{cor} is a correction due to interface compression, which is defined in equation (5.14):

$$\delta_{cor} = \delta_a + \delta_b + \delta_c \quad (5.14)$$

in which δ_a is the deformation of the interface between the cap/base and the filter stone, δ_b is the deformation of the filter stone, and δ_c is the deformation of the interface between the filter stone and the specimen. The volumetric correction due to interface compression, ΔV_{cor} is considered a function of the correction factor, δ_{cor} :

$$\Delta V_{cor} = \delta_{cor} \cdot A \quad (5.15)$$

in which A is the area of the specimen.

To determine the individual quantities in the correction factor, three tests with different interfaces were performed. Two of the tests were performed on small specimens, cored from the remaining part of the two blocks. The interface compression was assumed to be independent of the anisotropy in the sample, and only one set of correction parameters are obtained. The three setups are depicted in Figure 5.14, where the first setup was similar to the triaxial tests. In the second test, the specimen was glued to the filter stones and in the third test only the filter stone was tested. All tests were performed unconfined, as the interface compression was considered a function of the major principal stress only.

The result from the first test (Figure 5.14 a)), can be seen in Figure 5.15 along with the function used to model the behavior. The relation between the measured defor-

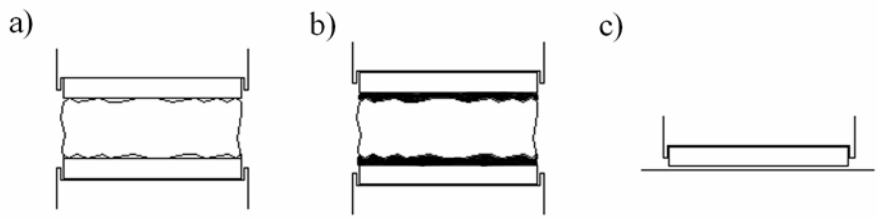

Figure 5.14: Tests performed to quantify amount of interface compression. a) Specimen with filter stones and cap/base. b) Specimen glued to filter stones. c) Filter stone between cap and metal surface.

mation and the major principal stress is given in equation (5.16). The relation used could fit the data better, but that would result in the correction exceeding the deformation measured in the triaxial tests at higher confining pressures.

$$\delta_{measured} \left(= \delta_a + \delta_b + \delta_c + \delta_d \right) = 0.010 \cdot \sigma_1^{0.45} \tag{5.16}$$

in which $\delta_{measured}$ is the deformation of specimen and interfaces and σ_1 is the major principal stress.

The result from the test with the specimen glued to the filter stones can be seen in Figure 5.16, and the result is modeled using a linear expression:

$$\delta_a + \delta_b + \delta_d = 0.0008 \cdot \sigma_1 \tag{5.17}$$

in which δ_a, δ_b, and δ_d are defined in Figure 5.13 and σ_1 is the major principal stress.

The results from the test in Figure 5.14 c) can be seen in Figure 5.17 and is modeled using the relation in equation (5.18) and equation (5.19).

$$\delta_a + 0.5 \cdot \delta_b = 0.013 \cdot \sin\left(\frac{\pi}{1200} \cdot \sigma_1 \right) \quad \text{for } \sigma_1 < 600 \text{ kPa} \tag{5.18}$$

$$\delta_a + 0.5 \cdot \delta_b = 0.013 \quad \text{for } \sigma_1 \geq 600 \text{ kPa} \tag{5.19}$$

in which δ_a is the deformation of the interface between the cap/base and the filter stone, δ_b is the deformation of the filter stone, and σ_1 is the major principal stress. The deformation is considered constant above 600 kPa. This indicates a high elastic modulus for the filter stone, and the deformation, δ_b can therefore be considered negligible.

Combining the relations in equation (5.16), (5.17), (5.18), and (5.19) results in the correction factor for stresses below 600 kPa in equation (5.20) and the correction factor

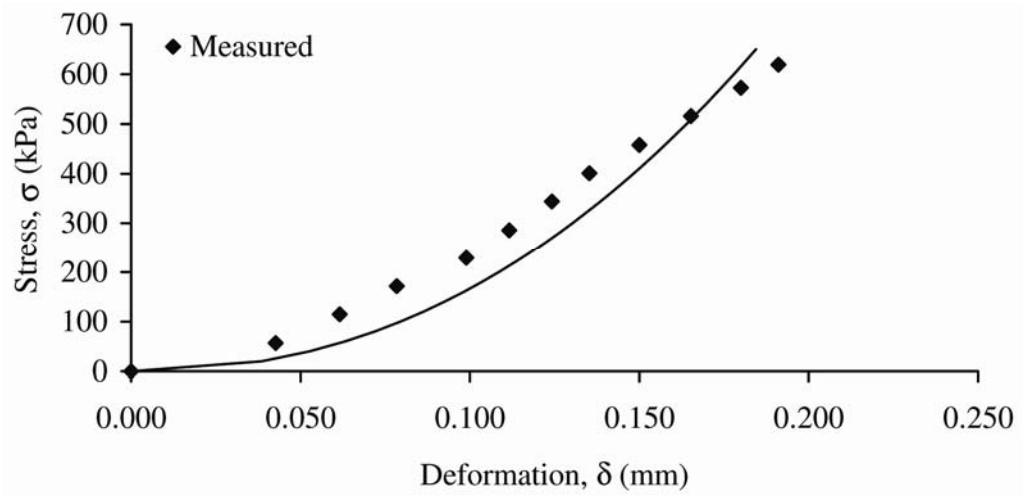

Figure 5.15: Results and modeled behavior for setup a) in Figure 5.14.

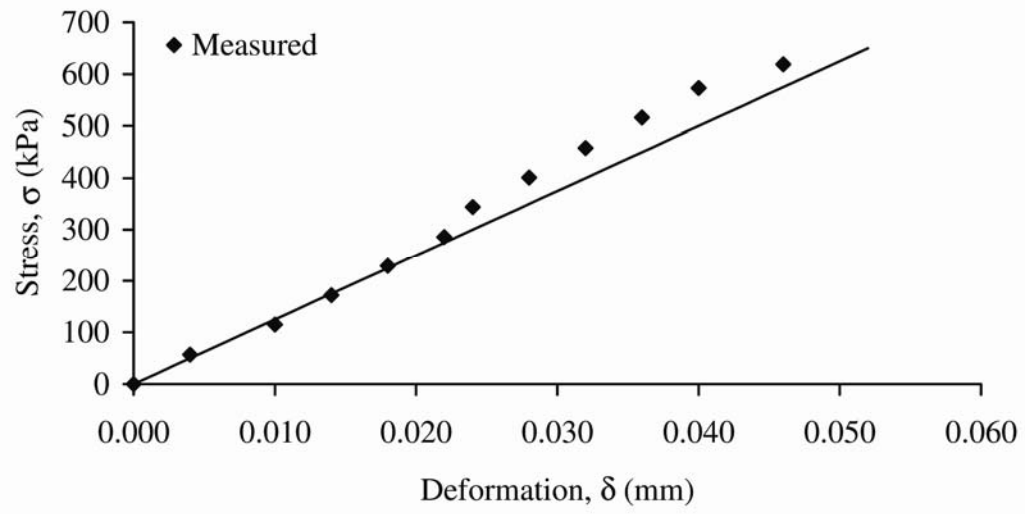

Figure 5.16: Results and modeled behavior for setup a) in Figure 5.14.

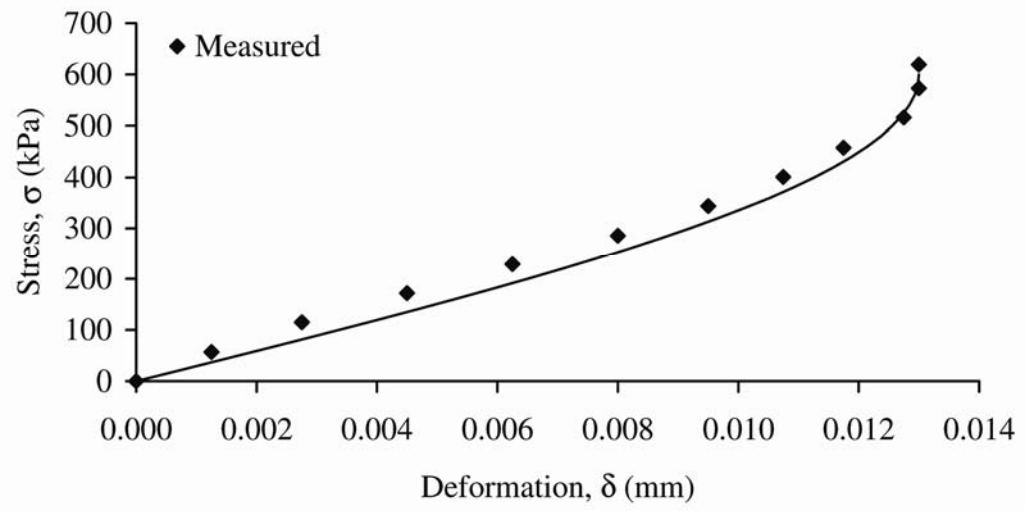

Figure 5.17: Results and modeled behavior for setup a) in Figure 5.14.

for stresses above 600 kPa in equation (5.21).

$$\delta_{cor} \left(= \delta_a + \delta_b + \delta_c\right) = 0.010 \cdot \sigma_1^{0.45} - 0.00008 \cdot \sigma_1 + 0.013 \cdot \sin\left(\frac{\pi}{1200} \cdot \sigma_1\right) \quad (5.20)$$

$$\delta_{cor} \left(= \delta_a + \delta_b + \delta_c\right) = 0.010 \cdot \sigma_1^{0.45} - 0.00008 \cdot \sigma_1 + 0.013 \quad (5.21)$$

in which σ_1 is the major principal stress. The correction in equation (5.21) has a maximum deformation of 0.164 mm at a major principal stress of 1550 kPa. Above that stress level, no further correction is performed. The maximum correction (0.164 mm) is the equivalent of half the average grain size. The correction is only performed during the virgin loading until failure, meaning this correction does not affect residual loading or unloading/reloading cycles during the test.

5.6 Discussion

5.6.1 Corrections Omitted

The stiffness of the membranes was found to be insignificant compared to the stiffness of the specimen, and no correction was performed. The mass of the cap and piston acts as an extra pressure on the specimen. However, the O-ring sealing the piston had a very tight fit, almost holding the cap and piston by itself. With uplift from the cell water, the extra pressure from the cap and piston was found to be negligible.

5.6.2 Difference in Stiffness and Strength between Triaxial and Torsion Shear Tests

The elastic modulus during virgin loading of the torsion shear tests was found to be higher than the elastic modulus of the triaxial tests. Furthermore, the torsion shear tests

had increased strength compared to the triaxial tests. Both triaxial and torsion shear specimens had comparable void ratios and cementation. This difference in stiffness and strength are the reason for the interface correction discussed in section 5.5.5. Other reasons for the difference could be size effects, pore fluids, boundary conditions, and method of measurement, all discussed in the following sections.

When testing materials with true cohesion, the size of the tested specimen affects the strength. According to Weibull (1951) a large specimen contains more flaws than a small specimen and the number of critical flaws is therefore greater. This causes the strength of a larger specimen to be lower than the strength of a smaller specimen with the same shape. The size effect also depends on the failure mode (Tsur-Lavie and Denekamp (1982)). For a single fracture plane the size effect is more pronounced than for failure distributed uniformly over the volume of material. E.g. the size effect in Brazilian tests is more pronounced than in triaxial tests. When comparing results from different types of tests the volume of the specimens should be of equal size. The size effect would result in the opposite behavior than the one observed in the triaxial and torsion shear specimens. Therefore, if size effect is present in the results, it can be considered negligible.

Triaxial tests on chalk performed by Risnes et al. (2004), show different strength and yield stress, depending on the pore fluids. This is attributed to the zeta-potential of the different fluids. When a particle with a negative surface charge is surrounded by liquid containing ions, the charge of the particle causes the concentration of positive ions to increase at the surface of the particle. It forms a solid positive charged layer called the Stern layer. This layer is only 1-2 molecules thick as the positively charged ions repel

each other. The concentration of positively charged ions decrease with distance from the particle as negatively charged ions start mixing until equilibrium is reached. See Figure 5.18 a). The zeta-potential is the difference in charge between the Stern layer and the diffuse layer. When measuring the zeta-potential, the charge in the Stern layer is assumed to vary linearly while the charge in the diffuse layer varies exponentially as shown in Figure 5.18 b). As a consequence, a dry specimen is stronger than a saturated specimen. Elmofty and Shokir (2003) found quartz to have zeta-potential, thereby indicating that the strength of sandstone is reduced by the pore fluids. This would result in a higher strength in the torsion shear tests as these were performed dry.

However, the effect of zeta-potential on the elastic modulus seems limited. To examine this further, an oddly shaped specimen was retrieved from the remaining parts of one of the blocks (The cross-sectional area was not constant). The specimen was exposed to unconfined loading in both dry and water saturated state. The vacuum procedure used for the Brazilian tests (section 5.4.2) was used for saturation. The results can be seen in Figure 5.19 where the stress-strain curves are plotted. The same specimen was tested in dry state first and then in saturated state. There is no significant difference between the results from the saturated and dry results to suggest that the pore fluid influences the elastic modulus of the artificial sandstone significantly, although the dry specimen is slightly stiffer than the saturated specimen.

The boundary conditions in the torsion shear tests differ from the triaxial tests due to end restrictions. In the torsion shear tests, the ends are glued to the cap and base rings, whereas the triaxial tests are performed with ends butting up to the filter stones with no

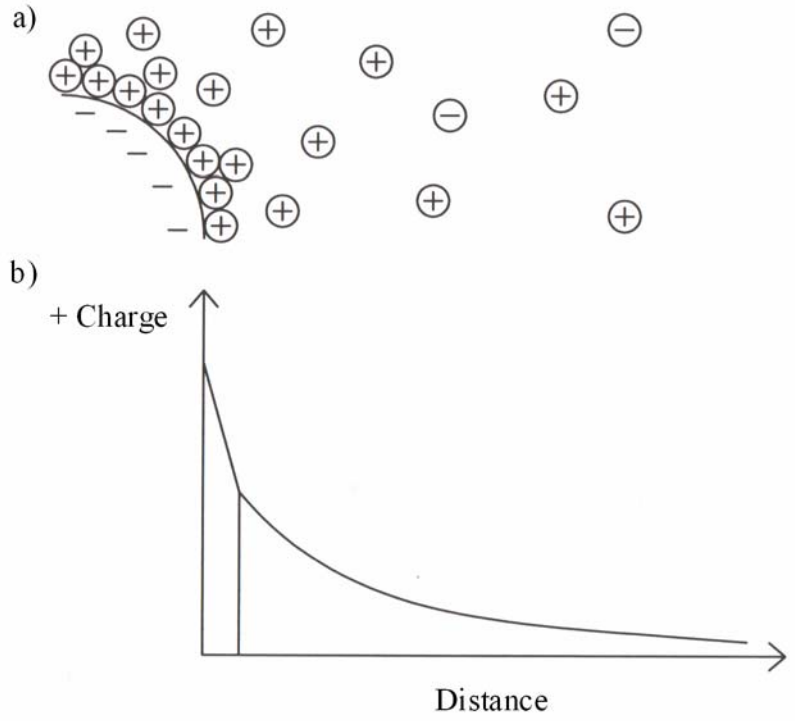

Figure 5.18: a) A negatively charged particle attracts positively charged ions b) The charge as a function of distance from the particle.

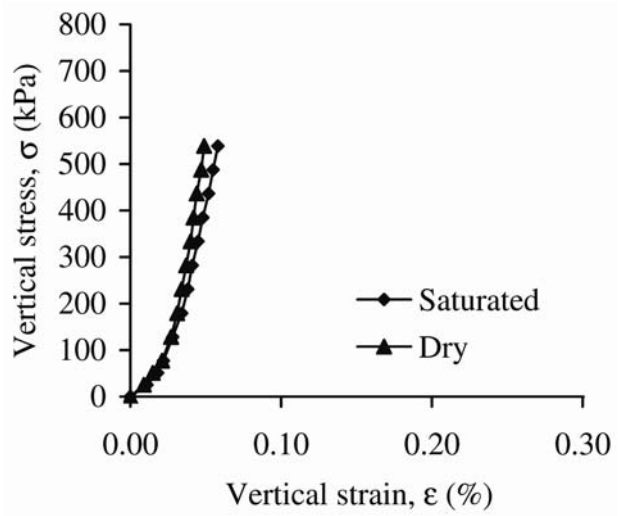

Figure 5.19: Deformation of artificial sandstone in dry and water saturated conditions.

glue at the ends. There is friction between the specimen and the filter stone in the triaxial tests, but compared to the torsion shear experiments the friction is low. According to Rowe and Barden (1964), frictionless ends in triaxial tests, reduce both the elastic modulus and the strength of the material.

In the triaxial tests, the major principal deformation is measured by a digital dial gage. In the torsion shear tests, the deformation is measured by strain gauges. Using the dial gage increases the deformation measured due to interface compression, resulting in apparent lower elastic modulus. The application of strain gages to porous material results in the glue penetrating the surface and influencing the properties of material locally. This increases the elastic modulus obtained.

None of the above discussed reasons are able to completely explain the difference in strength and stiffness between the triaxial tests and the torsion shear tests. Weather a combination of the above or something different is responsible for the difference remains unknown.

5.6.3 Gas Permeable Membranes

After all the triaxial tests were completed, it was discovered that the latex rubber membranes were permeable to nitrogen. The nitrogen used to produce the confining pressure dissolves in the cell water and migrates through the membranes. As the pressure in the specimen is lower, the nitrogen show up as air bubbles in the pore fluid, causing the measured volume change to be too contractive. Later tests on sand, in the same setup and with a similar specimen volume, showed the difference in volume change with and

without nitrogen penetration to be about 2.3 % of the volume of the specimen. This was for a 9 hour test and with fewer membranes. The rate of nitrogen penetration is believed to depend on the confining pressure, number of membranes, and how well the cell was filled with water. A higher confining pressure increases the amount of nitrogen dissolved in the cell water thereby increasing the rate of penetration, whereas an increase in the number of membranes will decrease the rate of penetration. If the bottom of the line feeding the confining pressure was filled with water, then the dissolved nitrogen would have a longer distance to diffuse before reaching the membranes. However, this issue is not considered to by important for the tests on cemented sand, and no correction for this potential error in volume change has been performed, because the test time is shorter, and a larger number of membranes were used.

5.6.4 Time Effects

At the end of isotropic compression and before triaxial loading was initiated, the specimens were allowed to creep between 6 and 10 minutes. This was done to make sure the membranes were not leaking, and to allow time to change the setup from the stress controlled isotropic compression to the deformation controlled loading. During creep, the yield surface moves out causing the specimen to be a little overconsolidated. The effect would show up in the first measurements during shearing as a reduction in the strains and consequent stiffer response, but this was found to be insignificant,

Another type of time effect (which did not affect the results) was observed in the Brazilian tests. After the maximum stress had been reached, the rupture was not always

visible in the specimen. Rather than wait for the crack to occur, the deformation rate was increased by a factor of approximately 30. This typically resulted in an increase in the stress, sometimes beyond the maximum reached in the test. This shows the effect of the deformation rate on the strength of the sandstone. Tests performed at a faster rate would consequently be stronger.

5.6.5 Reduction of Membrane Penetration

In the last test (V13) an attempt was made to try a procedure to reduce the membrane penetration, as shown in Figure 5.20 (Lo et al. 1989). This was done by smearing a thick layer of liquid rubber latex on the specimen. After the latex had dried the normal procedure with positioning of membranes and silicone grease was used.

In this test, the specimen was exposed to K_0-conditions, where the ratio between the vertical and the volumetric strains were kept constant by changing the confining pressure. The test was terminated at a confining pressure of 8.8 MPa.

After the test the membranes were removed and the specimen surface was examined. It was found that the rubber latex had been pushed into the specimen. At the high pressures employed in the test, the rubber latex behaved as a relatively soft substance and it filled the outer 1-2 mm of the specimen, as shown in Figure 5.21 b). This means, that instead of reducing the membrane effect, the rubber latex increased it. How much the rubber latex affected the volume change depends on the thickness of the initial layer, which in this test in unknown.

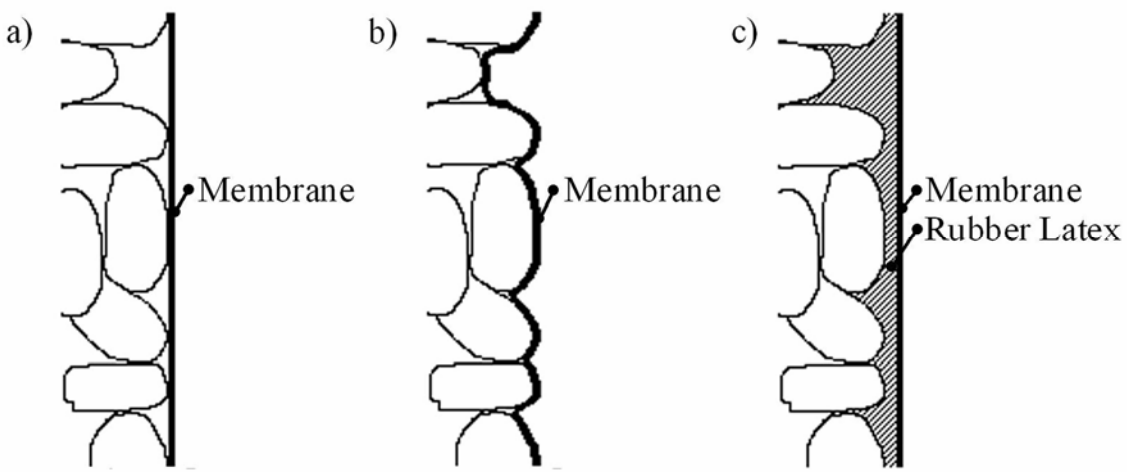

Figure 5.20: a) Membrane at the beginning of a test. b) At high pressures, the membrane is pressed into the voids between the grains. c) Rubber latex filling the outer voids, preventing membrane penetration.

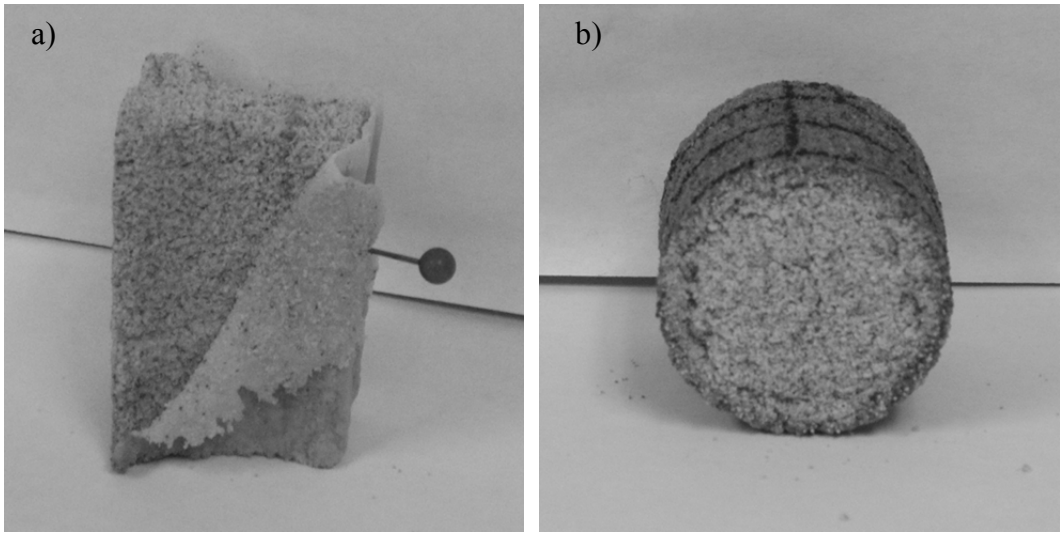

Figure 5.21: a) Rubber latex layer peeled off dummy specimen. b) After K_0-test at high confining pressures, the rubber membrane is pushed into the voids of the specimen.

The suggested procedure might be successful at low confining pressures where the latex is still rigid and therefore acts as a membrane. If the latex is only smeared on the specimens in a thin layer, just thick enough to fill the gaps, the procedure might also work. However, this method was not successful for the high pressure tests performed in this investigation.

6. Behavior of Cross-Anisotropic Sandstone

Based on the observed behavior of cemented sand four stages of cementation are suggested to describe the state of the sand cement matrix. No quantifications have been made except observations of the specimens at the end of each test. The four stages are illustrated in Figure 6.1. In stage I, there is full cementation between the grains. This is the initial state of the cemented sand, and it relates to the elastic behavior inside the cementation yield surface. Stage II is the behavior experienced between the cementation yield surface and the broken cementation yield surface. During stage II the tensile strength is reduced and eventually lost. Furthermore, the original structure of the sand cement matrix is mostly intact. In stage III, further bond breaking takes place and most of the original structure is lost. Individual grains move around while clusters of grains are still cemented together. During stage IV, only few clusters of grains remain cemented together. The structure at this stage is close to that of the uncemented sand where grain crushing and friction between the grains controls the behavior. Stage IV is observed in the specimens that reached the critical state line at failure. The locations of all four stages are shown in the pq-stress space in Figure 6.2.

6.1 Isotropic Compression

Four isotropic compression tests were performed on two vertical and two horizontal specimens, one vertical and one horizontal from each of the two blocks of the artificial cross-anisotropic sandstone. The tests were performed to confirm the reproducibility of

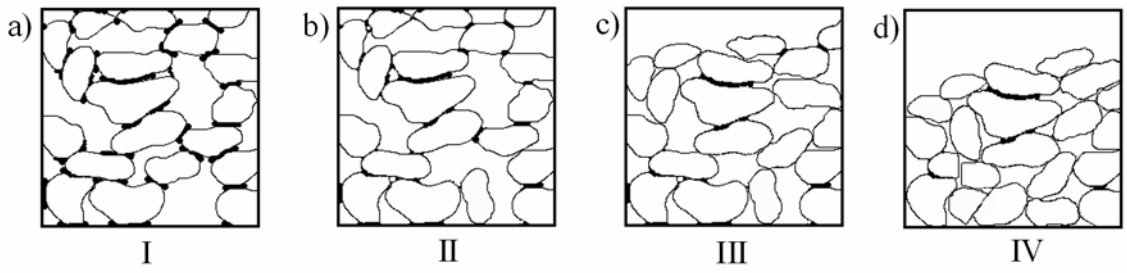

Figure 6.1: Four stages of decementation: a) Stage I; Full cementation. b) Stage II; loss of cohesion. c) Stage III; loss of original structure. d) Stage IV; Sand behavior.

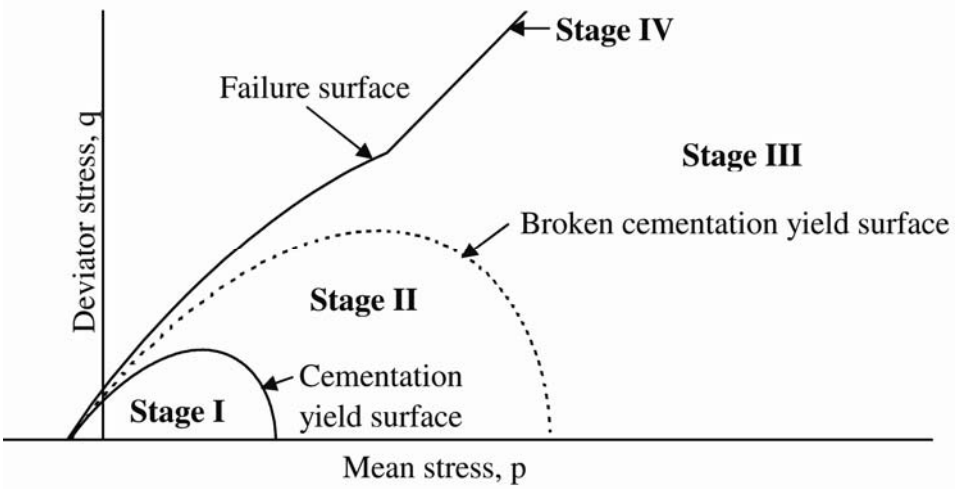

Figure 6.2: Location of the four stages of sand-cement matrix in the pq-stress space.

the artificial sandstone in the two blocks. The results of the tests can be seen in Figure 6.3 where the volumetric strain is plotted as a function of isotropic stress. The specimens from block I are plotted with the filled symbols and the specimens from block II are plotted with the open symbols. During isotropic compression, the volumetric response should be independent of the orientation of the specimen, meaning all tests should exhibit identical results. The stress-strain curves from three of the specimens (V4, H3, and H9) are similar, with a break in the curve at an isotropic stress of 4-6 MPa. The stress-strain curve from V9 does not have this break, but rather consists of a smooth curve. However, the void ratio of V9 is lower than those of the remaining specimens, which is a possible cause of the different results. The overall similarities are taken to indicate that the sandstone from the two blocks can be expected to behave similarly when the void ratios are comparable.

The results from the isotropic tests may also be used to indicate whether the corrections performed for membrane penetration are accurate. These corrections were explained in detail in chapter 5. The volumetric strain can be calculated as:

$$\varepsilon_{vol} = \varepsilon_v + 2 \cdot \varepsilon_h \qquad (6.1)$$

where ε_v is the major principal strain from the vertical specimens and ε_h is the major principal strain from the horizontal specimens. Due to the different behavior of specimen V9, the result from this test is omitted in the calculations. The average volumetric strain from V4, H3, and H9 is determined and the volumetric strain is calculated using equation (6.1). The results are compared in Figure 6.4. There is a good overall agreement between the two ways of obtaining the volumetric strain indicating the corrections are accurate.

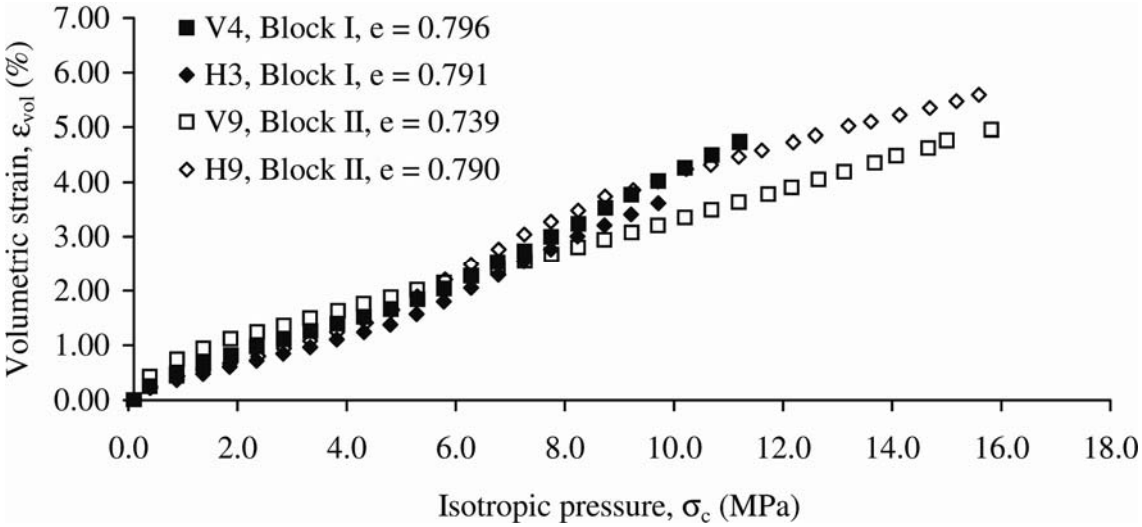

Figure 6.3: Volumetric strain as a function of confining pressure for isotropic tests on artificial cross-anisotropic sandstone.

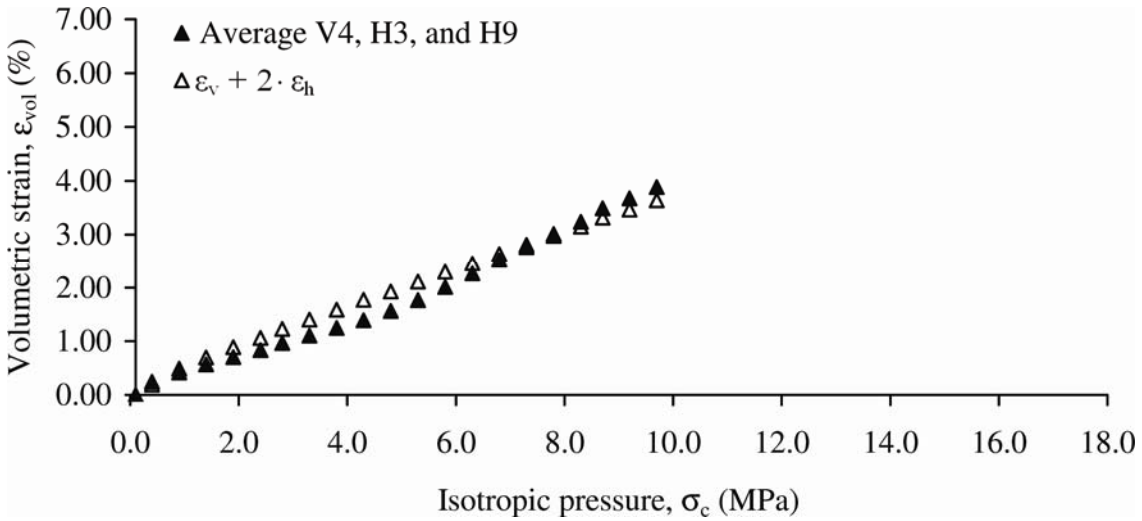

Figure 6.4: Comparison of volumetric strain obtained from volume change device and from major principal strain.

However, the calculated volumetric strain does not show the break in the curve that the average volumetric strain does.

6.1.1 Cementation Yield Surface from Isotropic Compression

The break on the stress-strain curve during the isotropic compression tests indicates the location of the initial yield surface due to cementation. When the stresses exceed this yield surface, the cementation starts breaking, and permanent damage (plastic work) takes place. From Figure 6.4 the cementation yield surface is determined to be at an isotropic stress of approximately 4-6 MPa. By plotting the void ratio as a function of the isotropic stress in a semi logarithmic coordinate system, a more precise determination of the cementation yield stress can be obtained. This is demonstrated in Figure 6.5, where the yield stress for test H3 is determined. The elastic part and the plastic part of the curve are each fitted with a straight line, and the yield stress is located where the two lines intersect. For test H3, the yield stress is determined to be 4.5 MPa.

This procedure has been used for the four isotropic compression tests and for the isotropic loading in the triaxial compression tests. The determined yield stress can be seen in Figure 6.6 as a function of the void ratio. The cementation yield surface is determined to intersect the hydrostatic axis at an average value of 4.3 MPa (σ_{cy}/p_a = 42.4).

As discussed in section 2.1.5, the cementation makes the transition from elastic to plastic more abrupt due to the initial cementation yield surface. This behavior can also be observed here. During the isotropic compression test shown in Figure 6.5, specimen H3

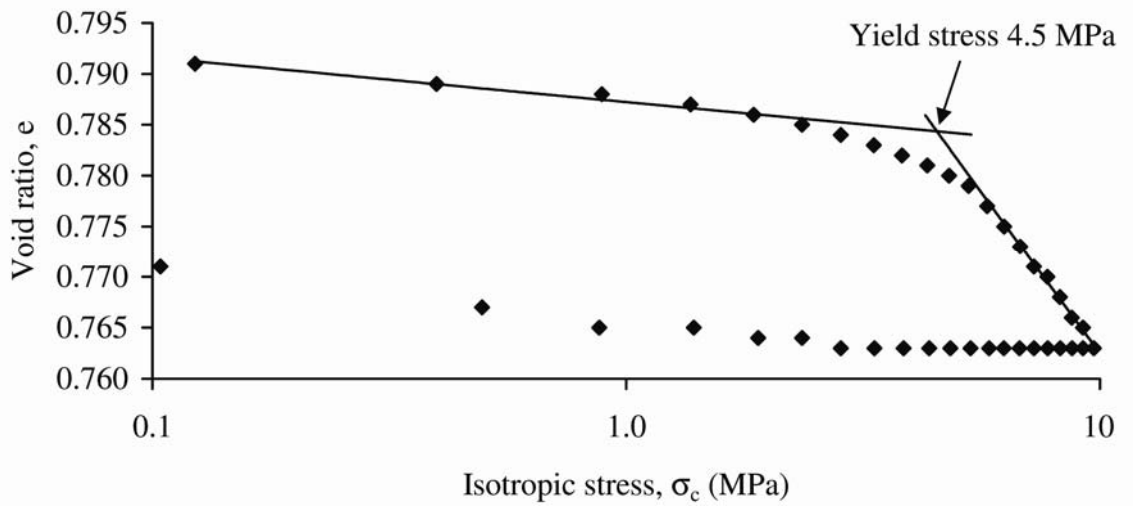

Figure 6.5: Determination of initial yield surface for specimen H3.

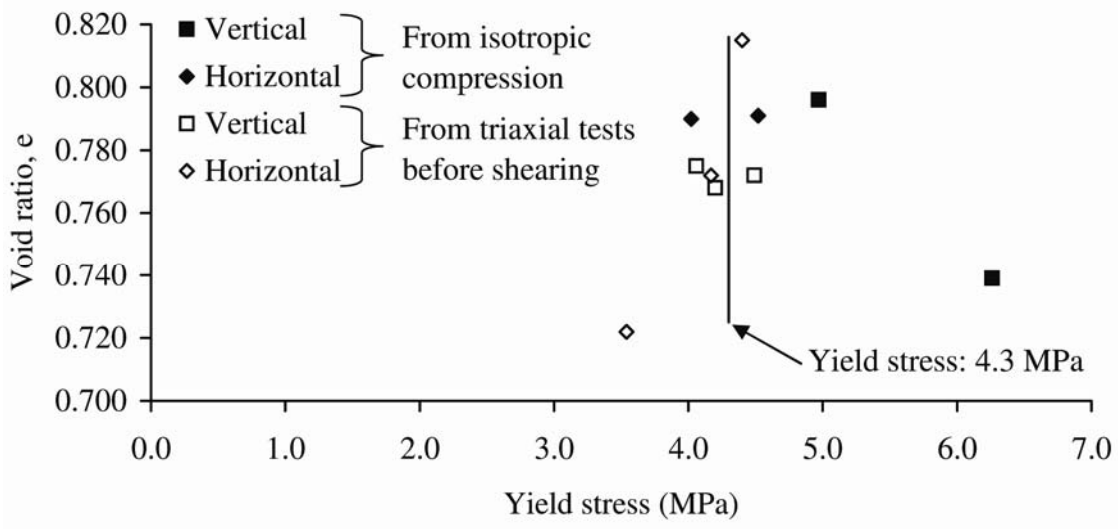

Figure 6.6: Isotropic yield stress as a function of initial porosity.

was loaded to 9.7 MPa. After unloading, the specimen was reloaded and the reduction in void ratio as a function of the isotropic stress can be seen in Figure 6.7 The transition from elastic to plastic is much smoother than during the first loading due to the gradual breaking of cementation. Using the procedure described in the previous section to determine the yield surface for the reloading is associated with more scatter. However, the new yield surface is determined to lie at 9.2 MPa which is 0.5 MPa lower than the initial loading would indicate. Breaking the cementation causes the cementation yield surface to become a regular yield surface, which can be determined upon reloading.

6.2 Triaxial Tests

6.2.1 Stress-Strain Relation

The stress-strain relations and the volume changes of the vertical and horizontal triaxial specimens are potted in Figure 6.8 and Figure 6.9, respectively. Unloading reloading cycles performed during the tests have been omitted in the plots. The horizontally cored specimens show more scatter than the vertically cored specimens. The scatter can arise from the greater variation of void ratio in the horizontally cored specimens determined in section 5.3.1.

The tests performed at confining pressures of 9.9 MPa and 14.0 MPa were terminated before failure. This was due to limits on the major principal strain, where approximately 25 % was the maximum.

At low confining pressures, the volumetric strain shows dilation, and as the confining pressure increases only contraction takes place. The transition from contraction

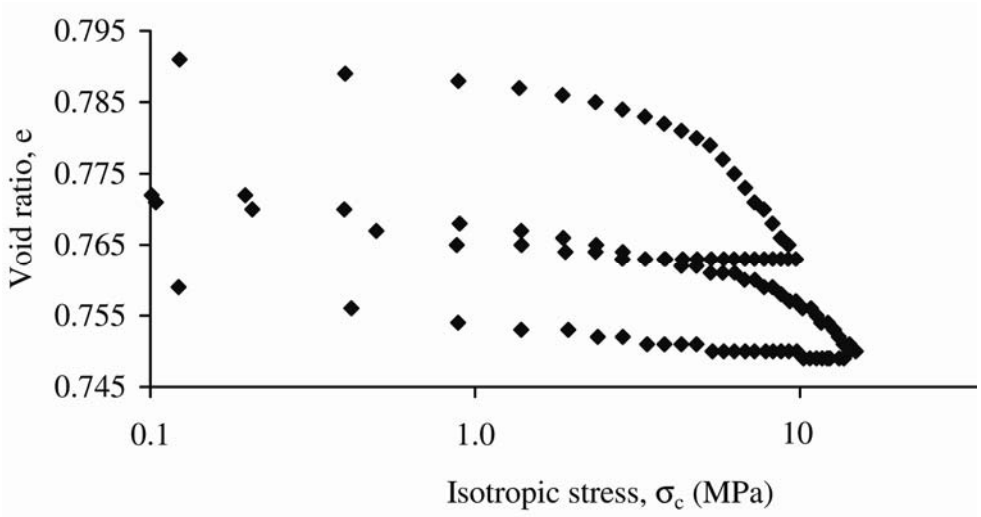

Figure 6.7: Initial isotropic loading and isotropic reloading of specimen H3.

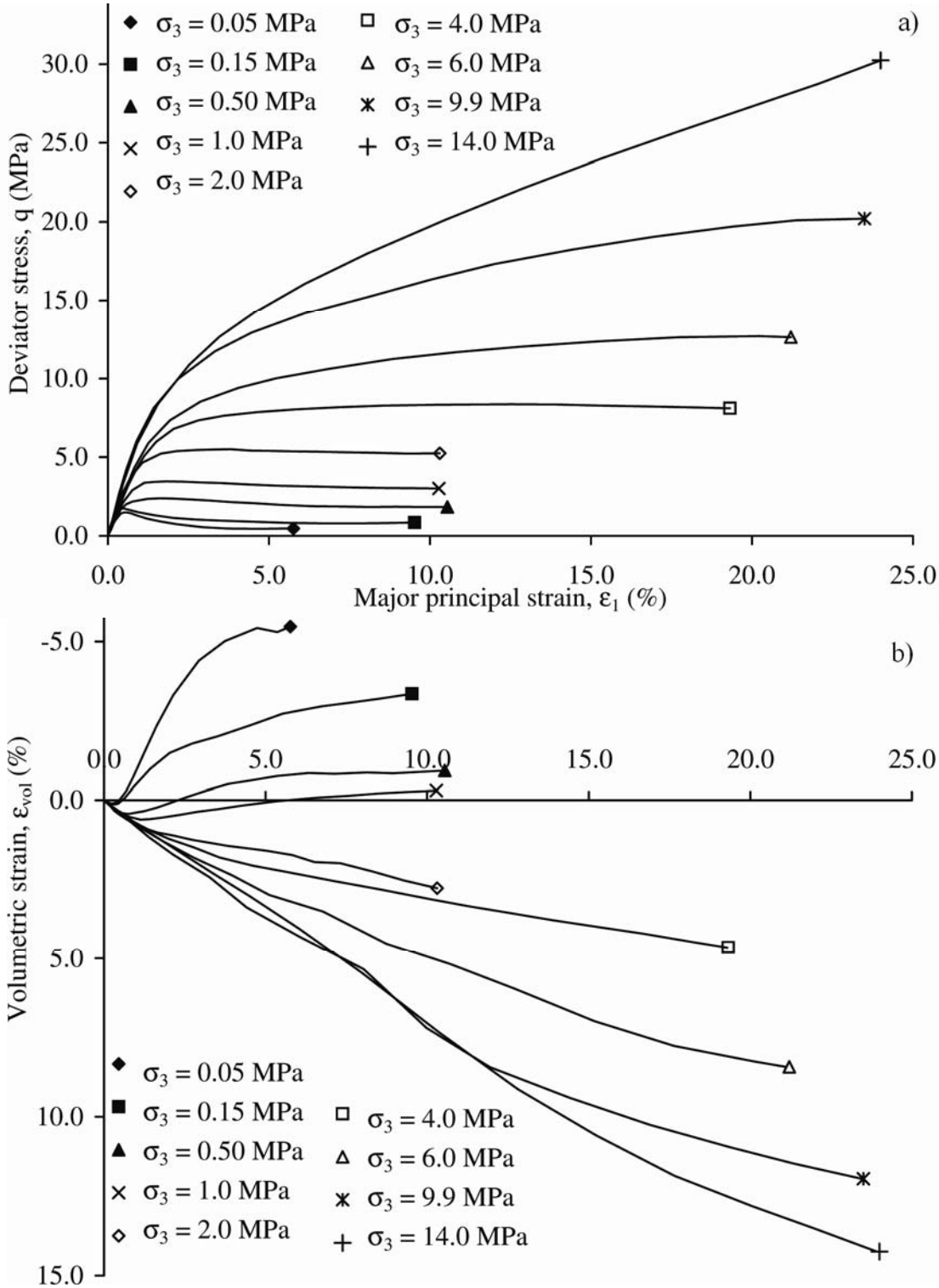

Figure 6.8: Behavior of vertically cored cross-anisotropic sandstone in triaxial compression. a) Stress-strain relations. b) Volume change relations.

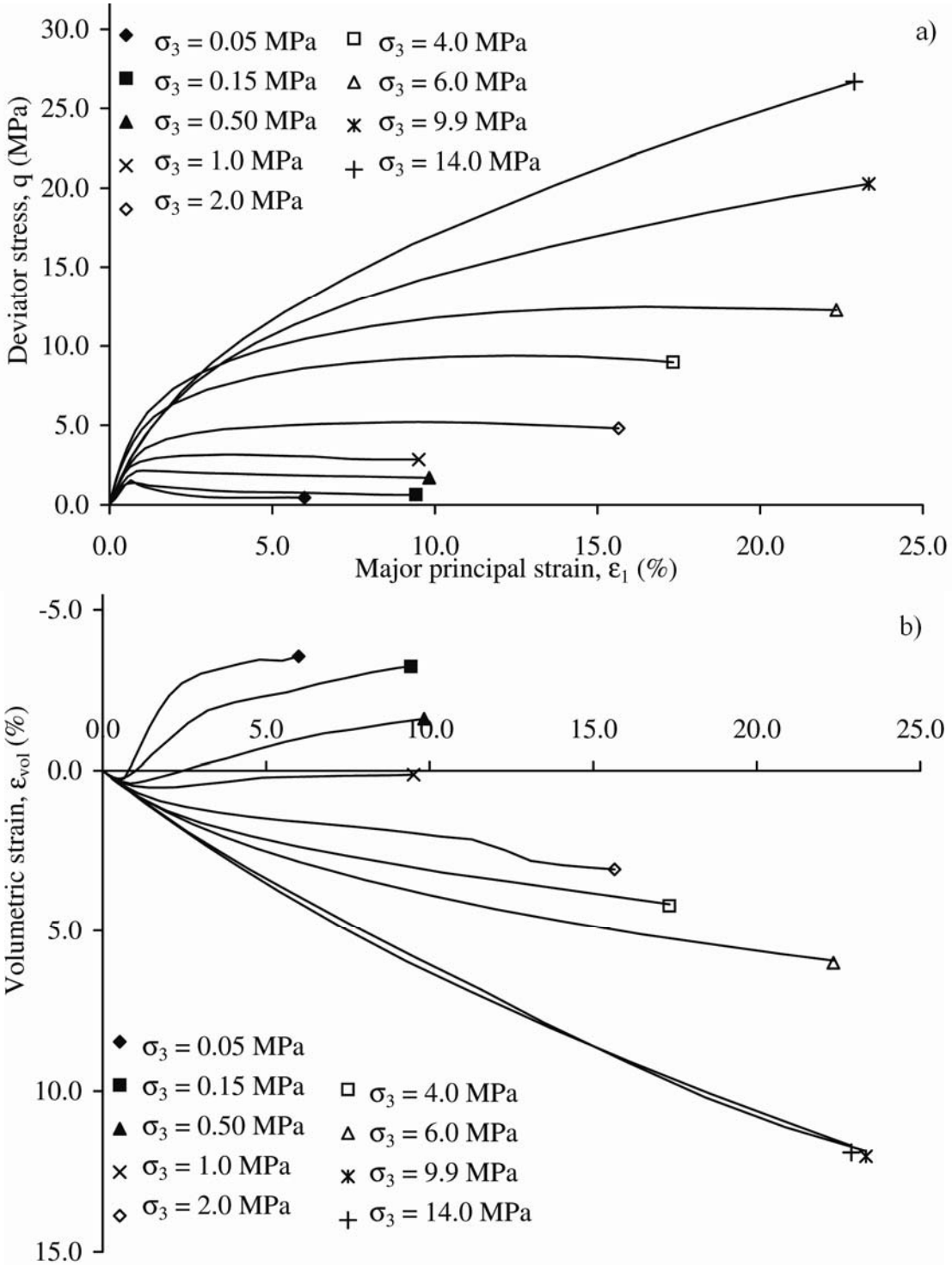

Figure 6.9: Behavior of horizontally cored cross-anisotropic sandstone in triaxial compression. a) Stress-strain relations. b) Volume change relations.

to dilation takes place before failure, indicating the cementation starts breaking prior to failure.

In vertical and horizontal direction, the two tests performed at confining pressures of 9.9 MPa and 14.0 MPa show almost identical volumetric responses. Similar behavior was observed at high pressure compression and extension tests on Cambria sand (Yamamuro and Lade 1996). The explanation for the behavior in the tests on the Cambria sand was related to the isotropic compression prior to shearing. During isotropic compression, the volume was reduced thereby causing less volume change during shearing. This can explain the volumetric behavior experienced here.

6.3 Failure

6.3.1 Failure Mode

The failure mode of the Brazilian tests was by splitting. All specimens failed by a fracture directly through the middle, from one force point to the other. No double fracture lines were observed.

The failure mode of the triaxial specimens can be divided into four categories (Figure 6.10). At low confining pressures (50 kPa and 150 kPa) the specimens failed by splitting as shown in Figure 6.10 a). The fracture line did not run directly down through the specimen, but started perpendicular to either the top or bottom face of the specimen and then diverted towards the vertical surface. In the tests with confining pressures from 500 kPa to 2.0 MPa, two kinds of failure modes were observed. Either a shear band developed (Figure 6.10 b)), or a part of the specimen plastically deformed (Figure 6.10

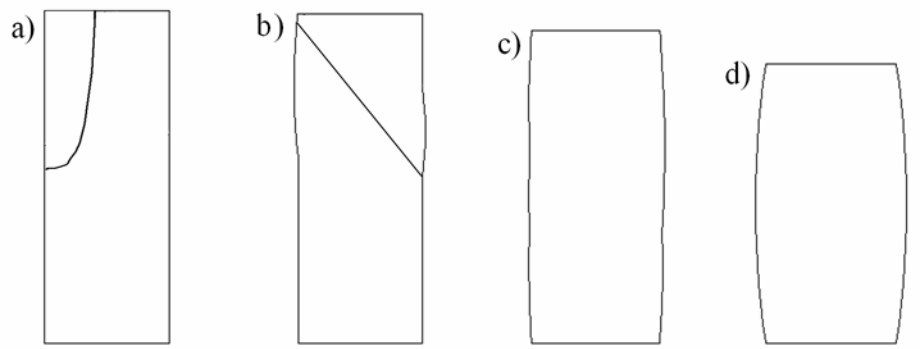

Figure 6.10: Failure mode for triaxial tests. a) Splitting of specimen. b) Shear band and partial plastic deformation of specimen. c) Partial plastic deformation of specimen. d) Full plastic deformation of specimen.

c)). One did not always exclude the other. In some tests both a shear band and partial plastic deformation were observed. At the highest confining pressures (4.0 MPa and above), the specimens failed by plastic deformation (Figure 6.10 d)) and after the tests the specimens also showed horizontal fracture bands. Pictures taken of the specimens, representing the different failure modes are shown in Figure 6.11.

Some of the horizontal bands experienced at high confining pressures were not visible before the inner membrane was removed from the specimen. The removal of the final membrane is believed to have amplified the visible damage and may have caused some of the fractures. Furthermore, the tests were performed until 20-25 % strain, and the membranes around the specimen were buckling due to the large strains. Horizontal splitting due to removal of vertical deviator stress while the cell pressure is still present will result in an extension stress condition because the piston uplift results in lower vertical stress than horizontal stress.

6.3.2 Tensile Strength

The tensile strength obtained from Brazilian testing is not directly comparable with the unconfined tensile strength. This can be realized from Figure 6.12 where the three possible orientations of the Brazilian disks are placed in the principal stress space. Also shown is the vertically and horizontally cored specimens tested in unconfined compression and extension. It can be seen that two orientations of the disks relate to the tensile strength of the horizontally cored triaxial specimens and one orientation relate to the vertically cored triaxial specimen. Unfortunately, the two orientations tested in this

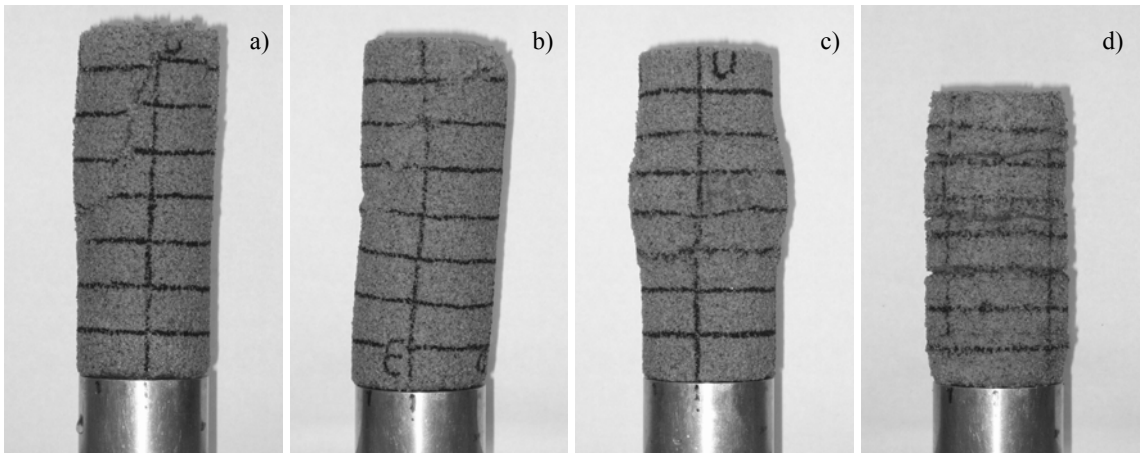

Figure 6.11: Failure mode for triaxial tests. a) Splitting of specimen at low confining pressure (50 kPa - 150 kPa). b) Shear band and partial plastic deformation (500 kPa - 2.0 MPa). c) Partial plastic deformation (1.0 MPa - 2.0 MPa). d) Plastic deformation of specimen at high confining pressures (4.0 MPa <), (Horizontal fractures lines possible developed during unloading).

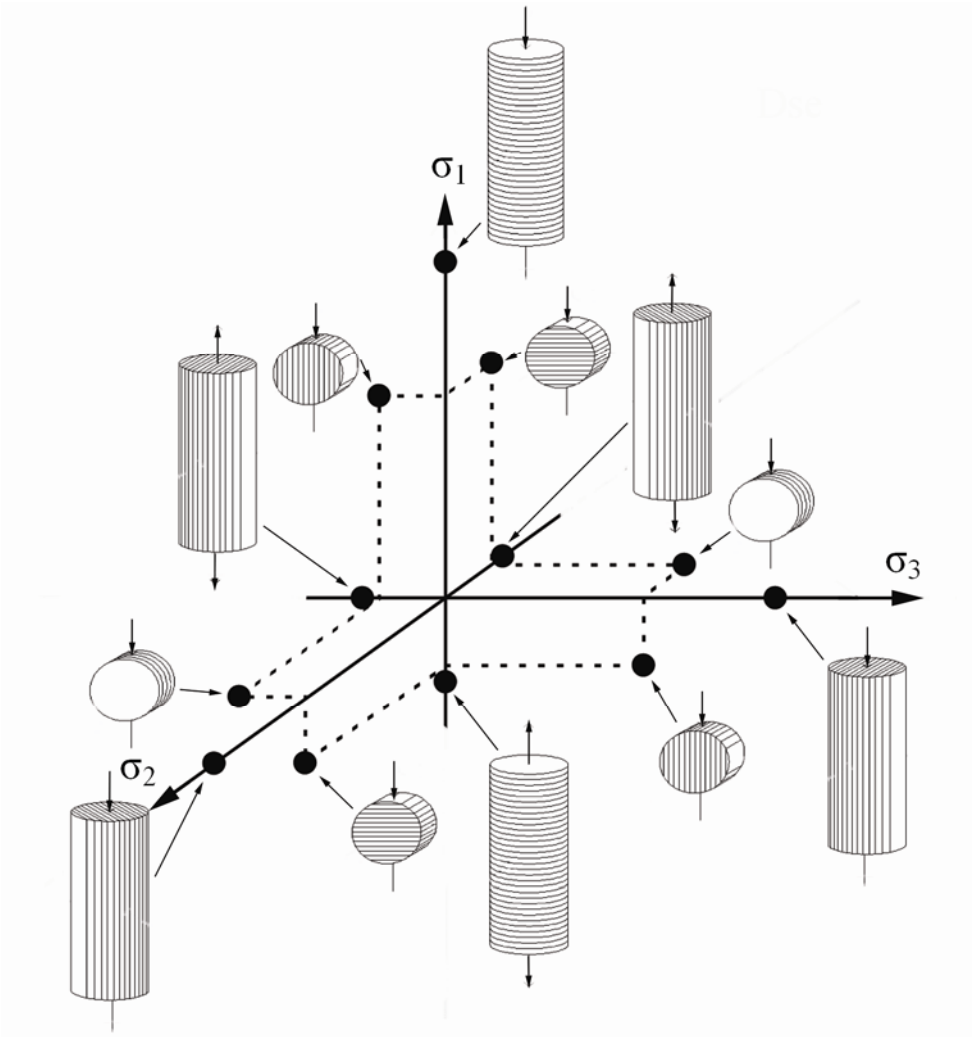

Figure 6.12: Location of Brazilian tests, unconfined compression tests, and unconfined extension tests in principal stress space.

study are the two orientations related to the horizontally cored triaxial specimens.

A total of 14 Brazilian tests were completed, and the results are presented in Figure 6.13 as a function of the void ratio. There seems to be a tendency towards a lower tensile strength as the void ratio increases. This tendency is more pronounced for the horizontally cored specimens than the vertically cored specimens. The average void ratio for all the specimens (triaxial and Brazilian) was 0.774. If this void ratio is used to determine the Brazilian tensile strength, a value of approximately 0.168 MPa is obtained. The difference in strength between the vertically cored specimens and the horizontally cored specimens lie within the scatter of the results, and no distinction in tensile strength between the two directions is made.

After the completion of the isotropic compression tests, the specimens were still intact. One vertically cored specimen and one horizontally cored specimen were each cut into three disks and the Brazilian tensile strength was determined. The purpose was to determine the reduction in tensile strength due to degradation of the cementation during isotropic loading. The results of the Brazilian tests on the isotropically loaded specimens are shown in Figure 6.14 as a function of the void ratio. Again, the void ratio of 0.774 is used as a reference point to determine the strength. A Brazilian strength of 0.014 MPa is obtained.

During isotropic loading, the specimens were loaded to 13.3 MPa ($\sigma_c/p_a = 131$) which resulted in a reduction of the Brazilian tensile strength of 92 %. This is illustrated in Figure 6.15 where the Brazilian tensile strength of the sandstone is plotted as a function of the isotropic stress. Note the scale of the vertical axis is hundred times smaller

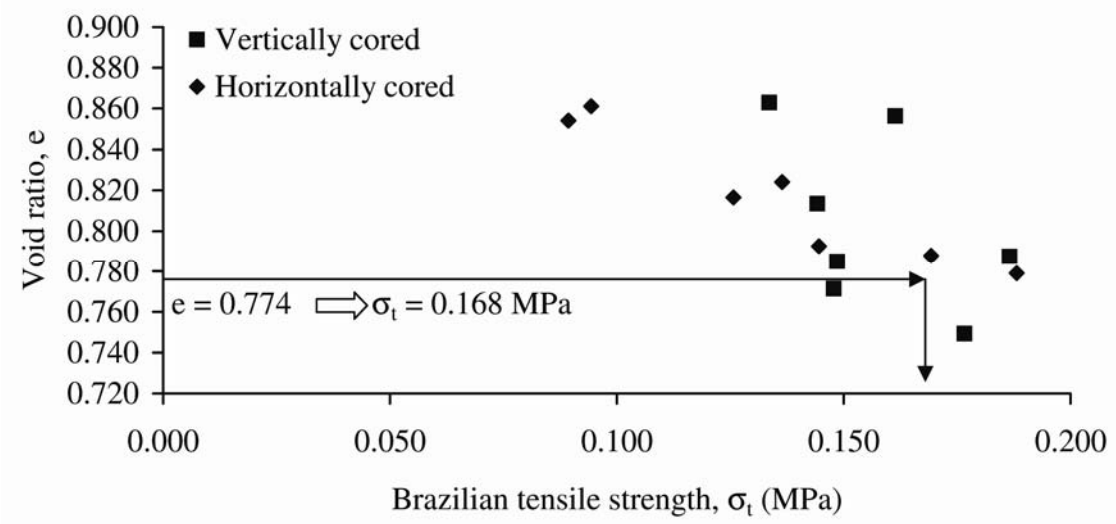

Figure 6.13: Variation of Brazilian tensile strength as a function of void ratio. The average void ratio of 0.774 corresponds to a Brazilian tensile strength of 0.168 MPa.

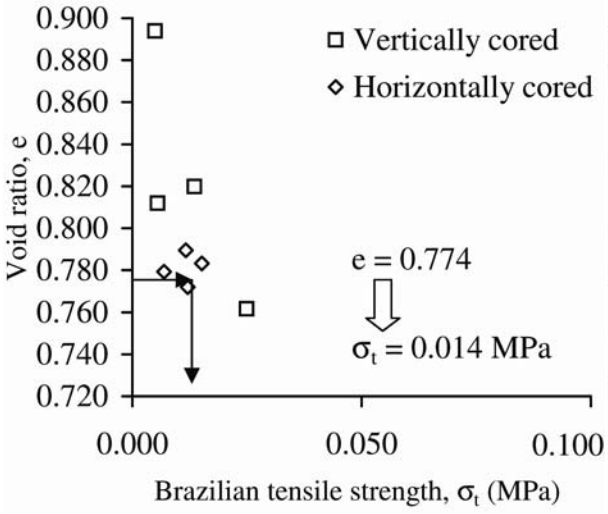

Figure 6.14: Variation of Brazilian tensile strength as a function of void ratio for specimens preloaded to isotropic stress of 13.3 MPa. The average void ratio of 0.774 corresponds to a Brazilian tensile strength of 0.014 MPa.

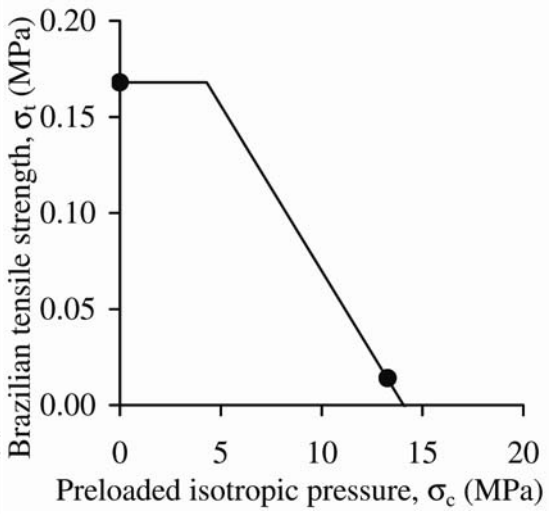

Figure 6.15: Tensile strength as a function of preloaded isotropic stress.

than the scale of the horizontal axis. The Brazilian tensile strengths after no preloading by isotropic stress are given in Figure 6.13. The isotropic tests indicated that the cementation yield surface intersected the hydrostatic axis at 4.3 MPa (σ_{cy}/p_a = 42.4). Isotropic stresses below 4.3 MPa would result in elastic behavior and no reduction in Brazilian tensile strength (Stage I in Figure 6.1). Above 4.3 MPa the cementation starts breaking down and at 13.3 MPa, a Brazilian tensile strength of 0.014 MPa is left (Stage II in Figure 6.1). The decay is here assumed to vary linear with the isotropic preloading stress. The isotropic stress at which the cementation is broken and stage III begins corresponds to 14.1 MPa (σ_c/p_a = 139.2).

6.3.3 Triaxial Failure

The failure points determined from the triaxial tests in vertically cored specimens and horizontally cored specimens are shown in Figure 6.16 and Figure 6.17, respectively. At low confining pressures, the failure surface is curved, and a detailed inspection reveals that the lower part of the curvature consists of a second curvature which is explored in detail in section 7.1.2. At high confining pressures the failure surface consists of a straight line indicating the critical state line is reached.

At low confining pressures, the failure surface from the vertically cored specimens is the strongest. At high confining pressures the failure surfaces in vertically cored specimens and horizontally cored specimens are almost identical indicating the cross-anisotropic behavior is reduced as the cementation breaks down.

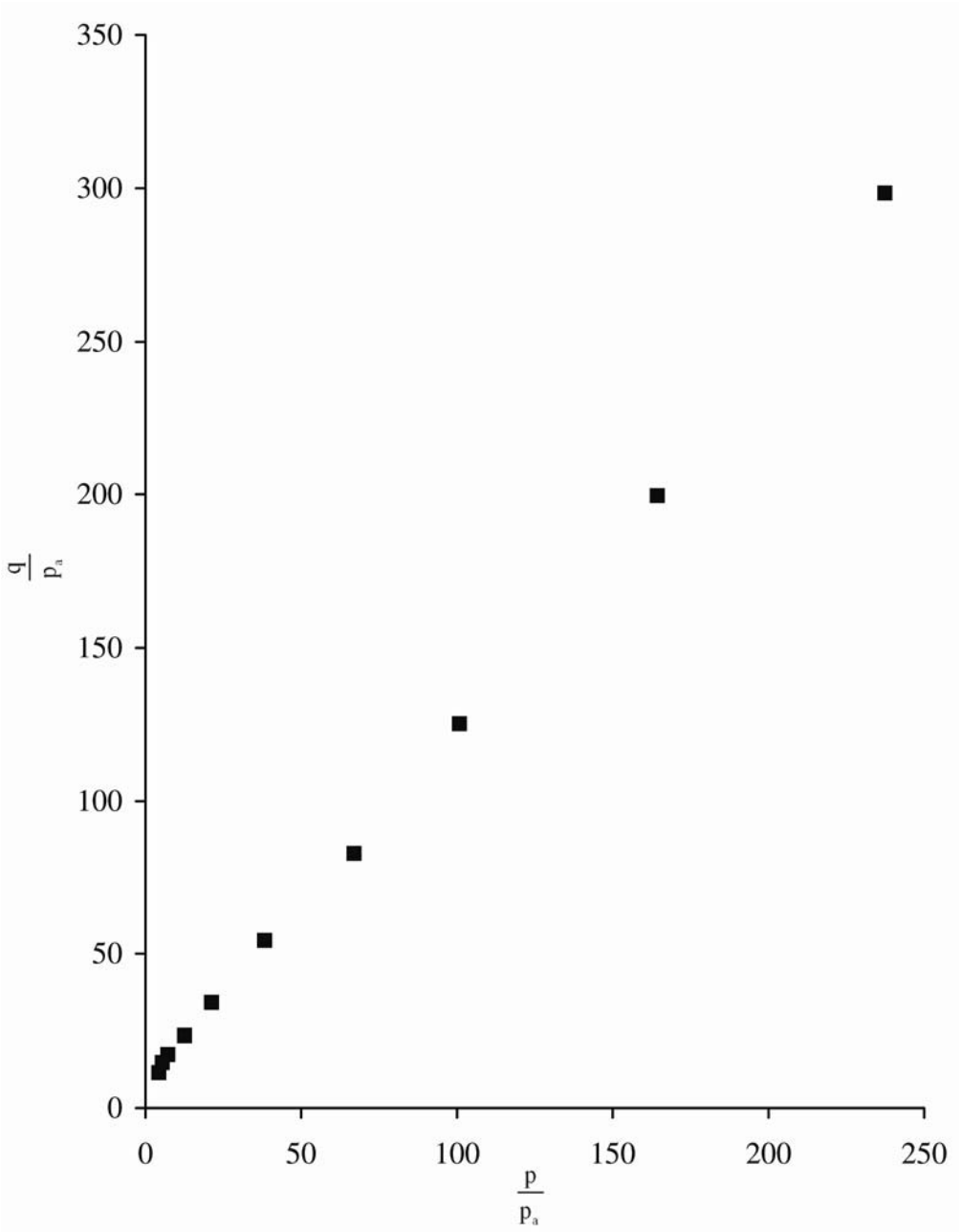

Figure 6.16: Failure points determined for vertically cored specimens.

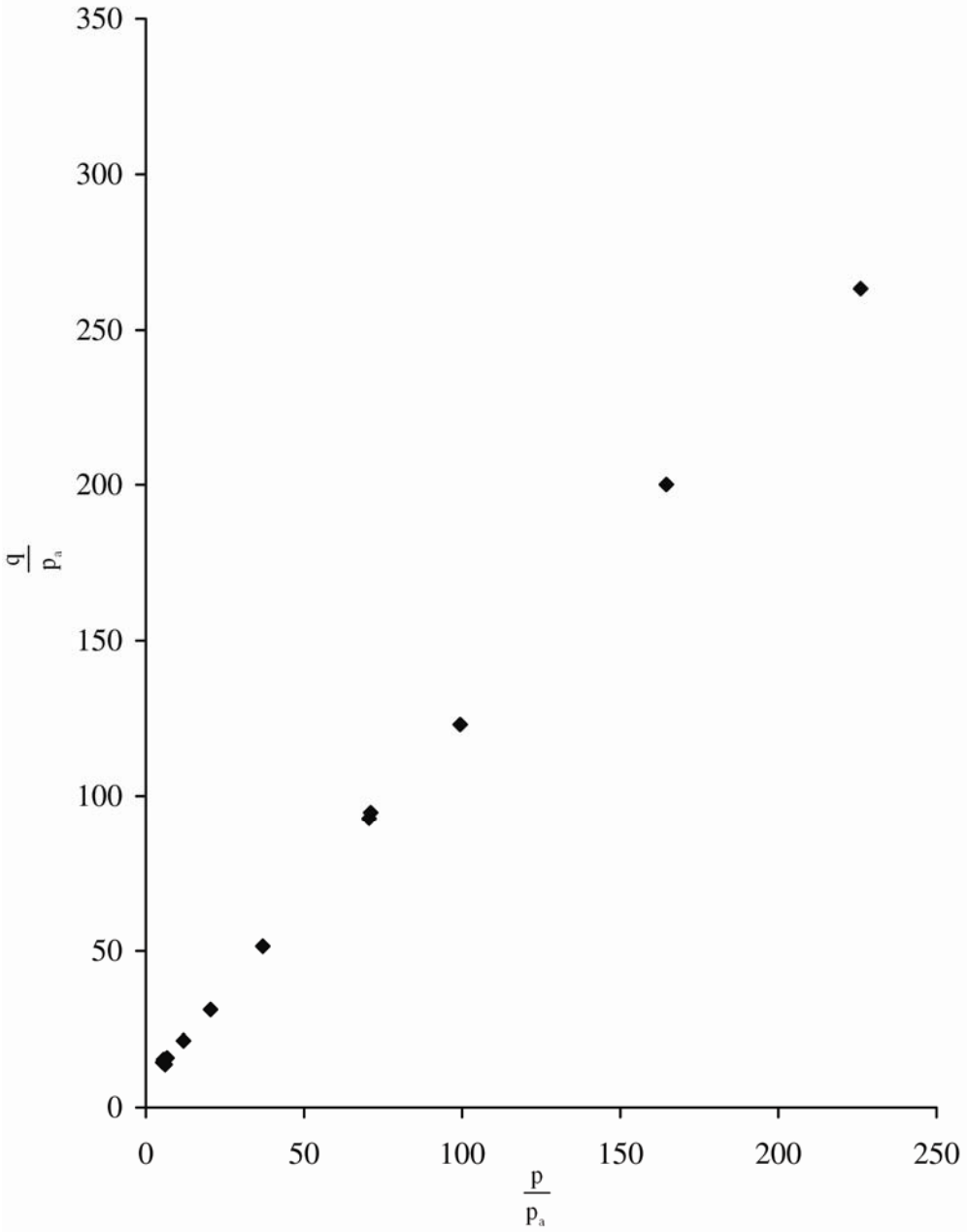

Figure 6.17: Failure points determined for horizontally cored specimens.

6.4 Elastic Behavior

The elastic behavior is determined several times during each test. Figure 6.18 shows the three areas where elastic parameters are determined from a typical stress-strain relation. The three areas are: a) Initial tangent; b) Small unloading-reloading cycle inside the cementation yield surface; c) Full unloading-reloading cycle at large strains, including the final unloading.

The elastic behavior determined from the initial tangent loading is softer than both the unloading-reloading cycles inside the cementation yield surface and the unloading-reloading at large strains. To be able to compare the elastic behavior before and after breaking of the cementation, Young's modulus determined from the unloading-reloading cycles is shown in Figure 6.19. There is considerable variation in the results in Figure 6.19, but the best fit lines indicate the cemented material to be the stiffest, until the cementation starts breaking. After the cementation is broken, the specimens are more affected by confining pressure. This can be seen by the steeper slope of the best fit. This behavior is in accordance with the behavior described in section 2.1.3. However due to the low degree of cementation in the artificial sandstone tested here, the difference between the fully cemented sandstone and that with broken cementation is small.

6.5 Cementation Yield Surface

The procedure described in section 2.1.2 to determine the initial yield stress from the stress strain relation was applied here. This is demonstrated in Figure 6.20 and Figure 6.21 where the yield stresses for a vertically cored specimen with a confining pressure of 0.48 MPa and a horizontally cored specimen with a confining pressure of 2.0 MPa are

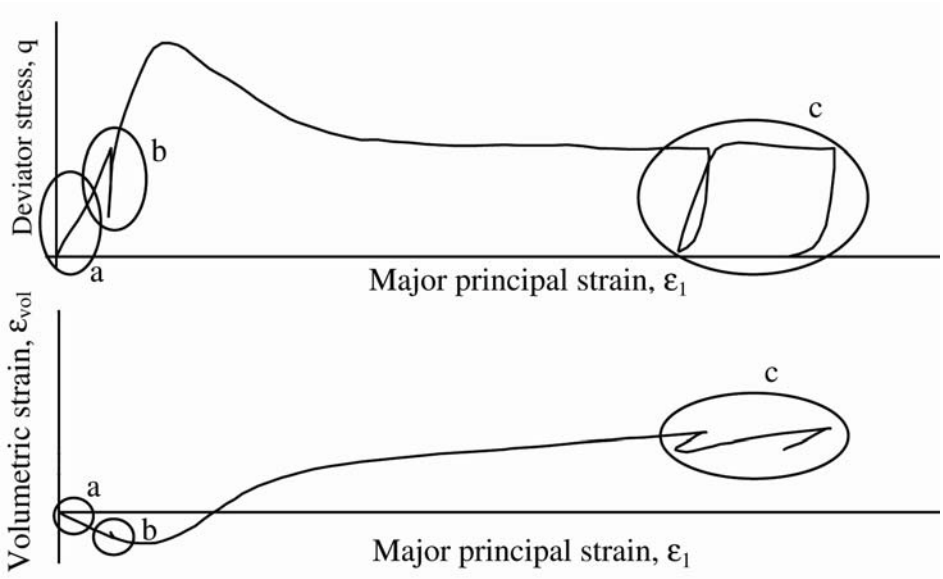

Figure 6.18: Stress-strain curve indicating where elastic parameters are determined

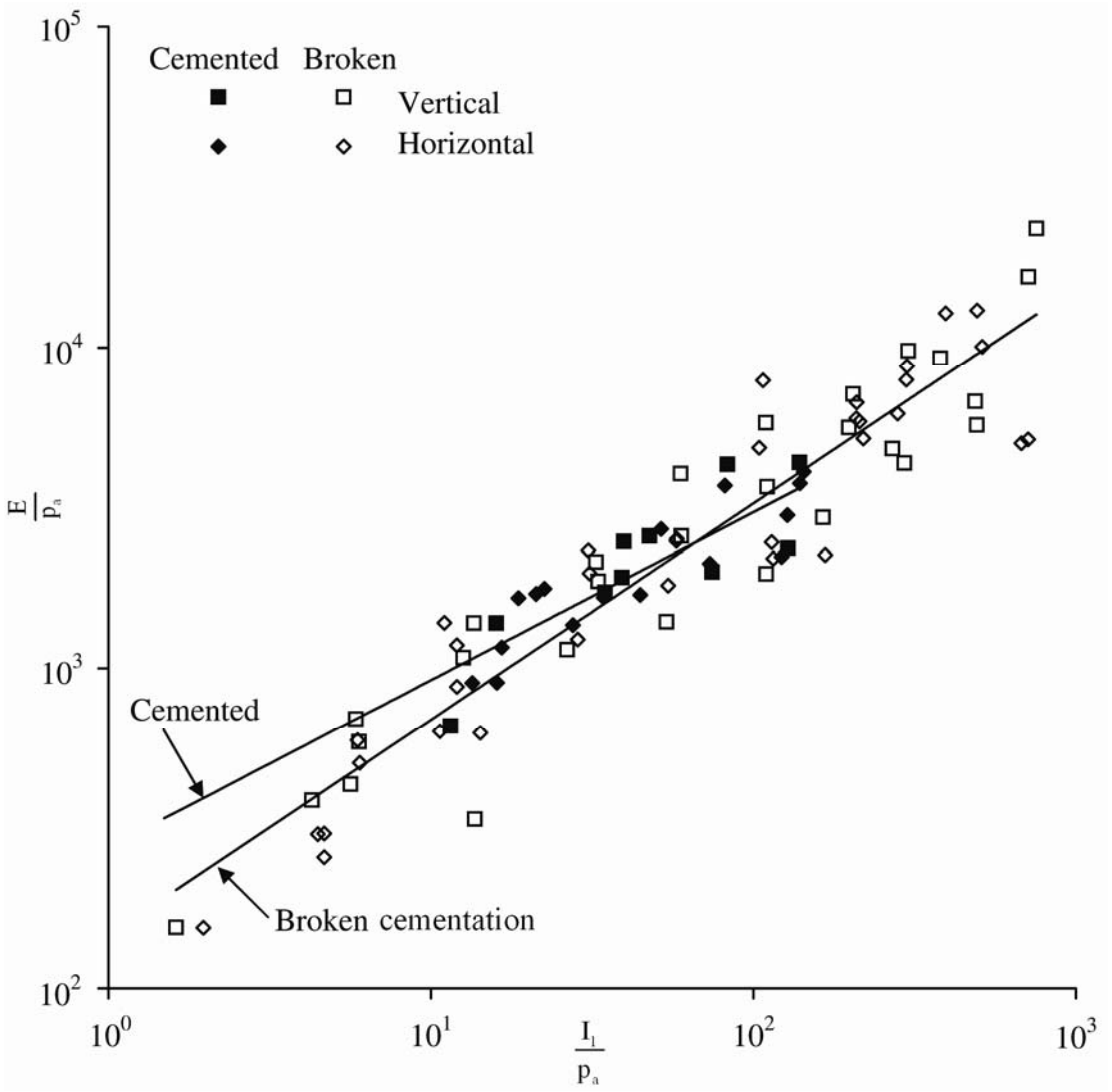

Figure 6.19: Young's modulus as a function of the first stress invariant, in cemented state and after breaking the cementation.

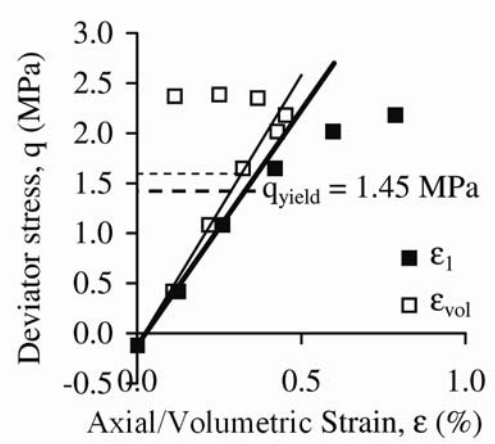

Figure 6.20: Determination of yield stress for triaxial test in vertical direction with confining pressure of 0.48 MPa.

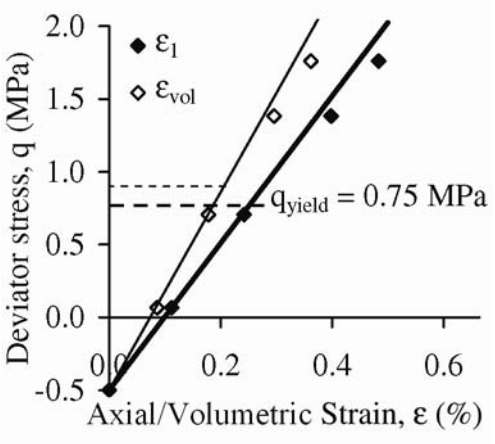

Figure 6.21: Determination of yield stress for triaxial test in horizontal direction with confining pressure of 2.0 MPa.

determined. In the vertical specimens, the major principal yield stress was determined to be 1.93 MPa (= 1.45 MPa + 0.48 MPa). In the horizontal specimens, the major principal yield stress was determined to be 2.75 MPa (= 0.75 MPa + 2.0 MPa). This procedure was used to determine the initial yield stress for all triaxial tests with confining pressures under 6.0 MPa. These initial yield points define the shape of the cementation yield surface.

In section 6.1.1 the hydrostatic yield stress was determined to be 4.3 MPa. The yield surfaces intersecting the hydrostatic axis at this confining pressure is shown in Figure 6.22 for vertically cored specimens and Figure 6.23 for horizontally cored specimens. Furthermore, the initial yield points determined from the triaxial tests is shown. The yield surface is much larger for the vertically cored specimens than for the horizontally cored specimens, indicating cross-anisotropy.

6.6 K_0-Loading

During K_0-loading of a vertically cored specimen the radial strains should be equal to zero. That condition was not entirely met in the K_0-test performed due to membrane penetration and end effects. The corrections for these conditions are described in Chapter 5. The corrections for these effects were performed after the test was concluded and as a result some radial strains were experienced. Under true K_0-conditions, the volumetric strains are equal to the axial strains, and the radial strains are equal to zero. This is shown in Figure 6.24 where the major principal strain and the volumetric strain are shown. The dotted line represents K_0-conditions, where the radial strains are equal to zero. At the beginning of the test, the loading deviates from the line, but after approximately 2-3 %

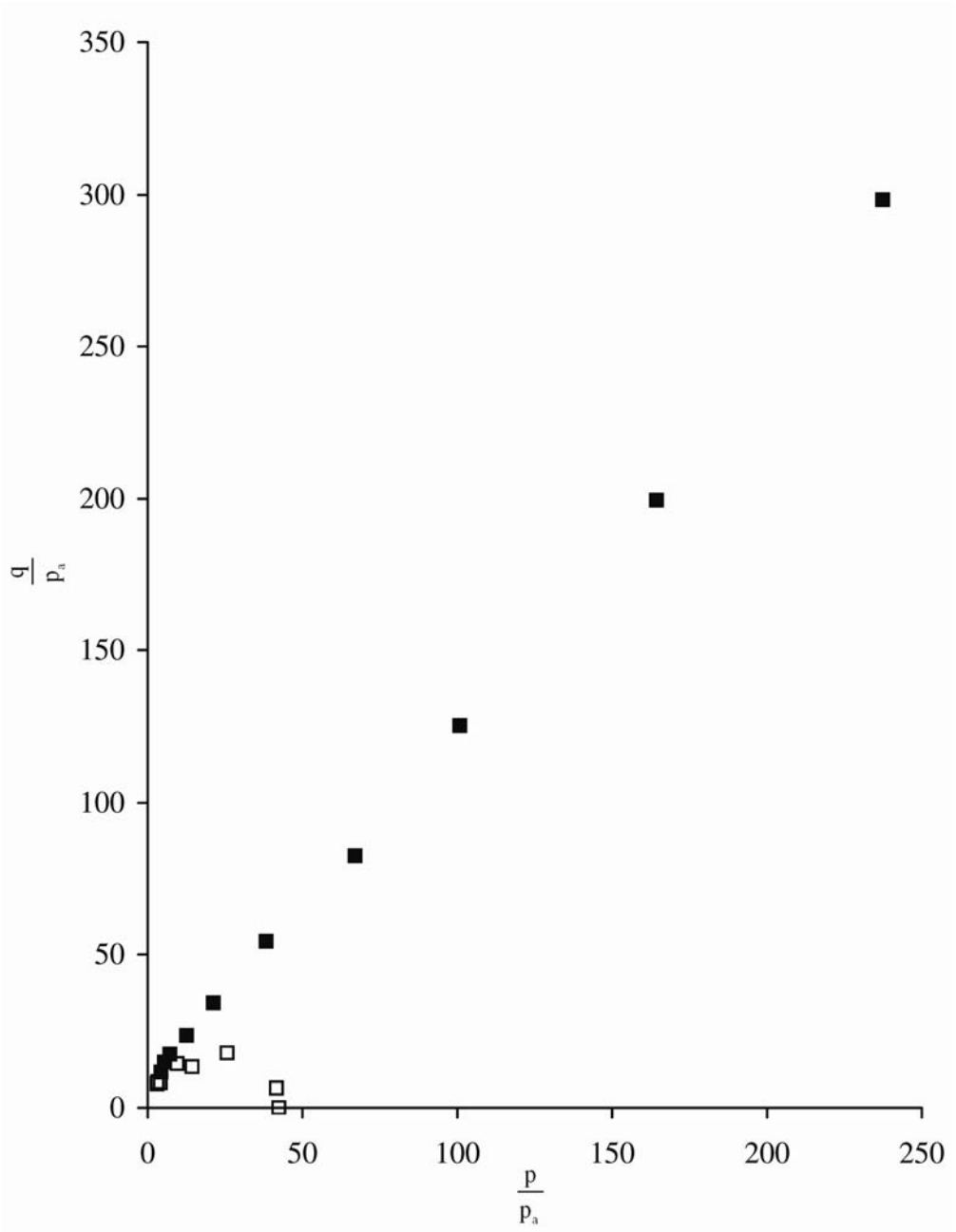

Figure 6.22: Determined failure points and yield points in vertical direction.

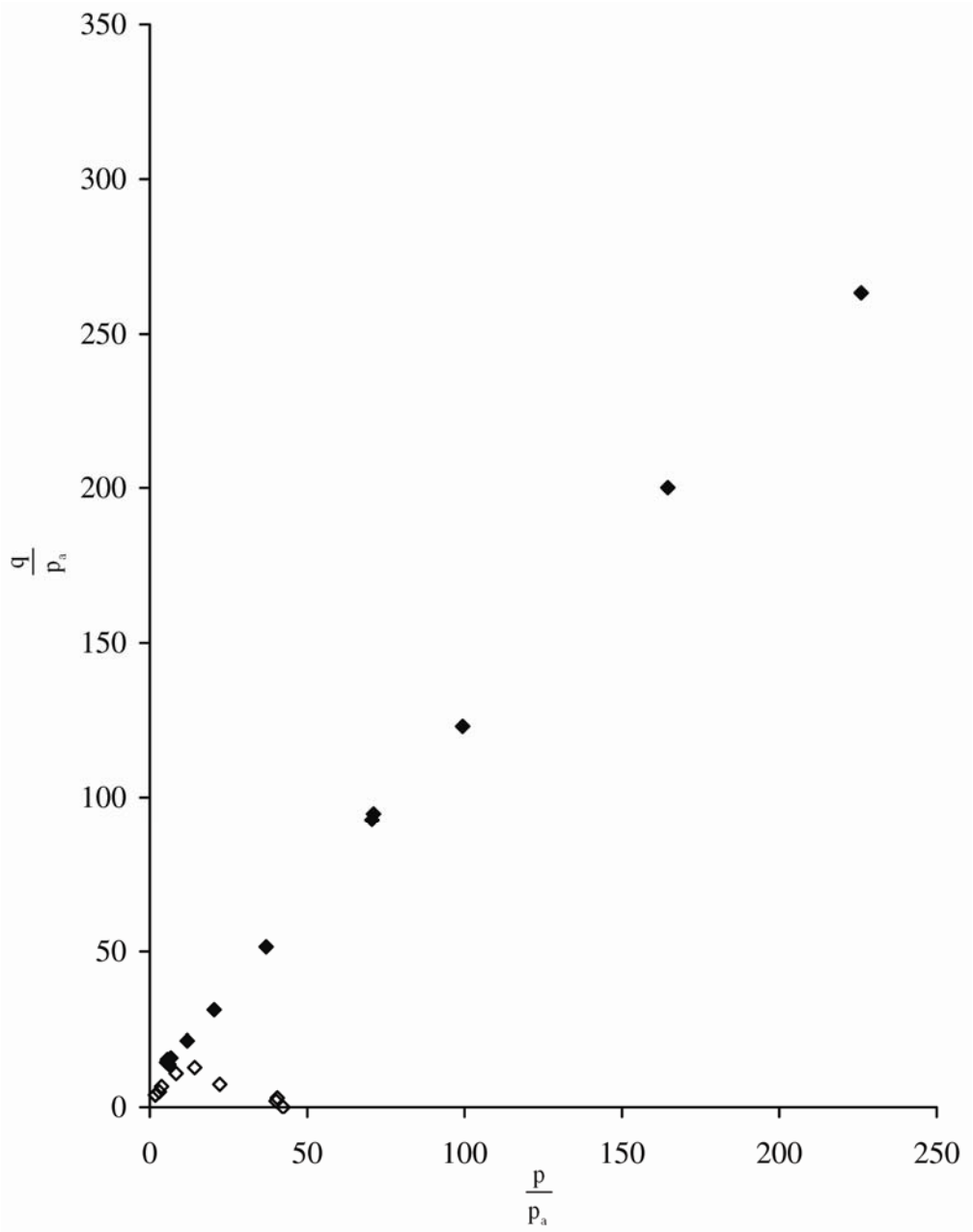

Figure 6.23: Determined failure points and yield points in horizontal direction.

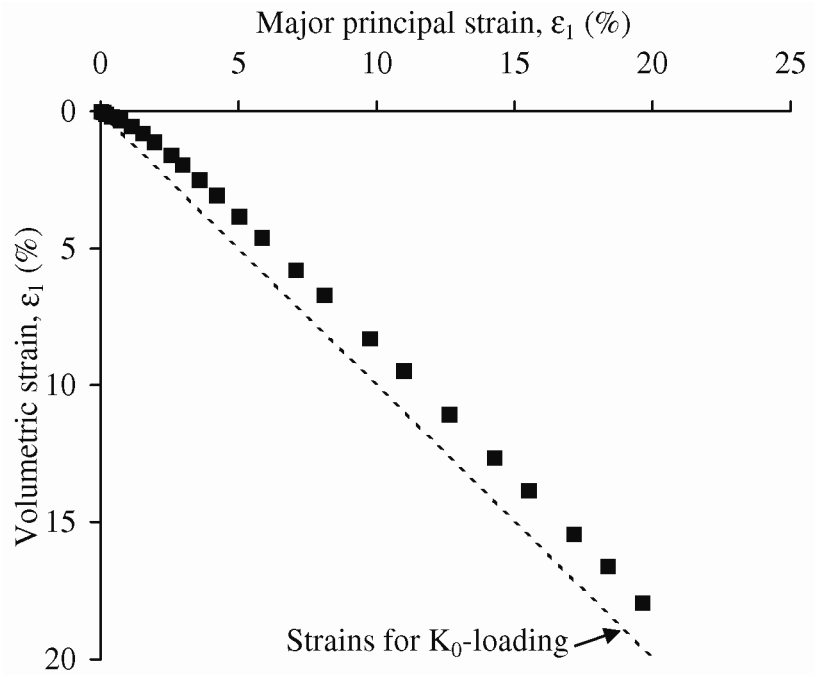

Figure 6.24: Major principal and volumetric strains during K_0-loading.

axial strain the test results become almost parallel to the K_0-condition. This means that the major part of the test is performed under K_0-conditions.

The stress path related to the strains in Figure 6.24 is shown in Figure 6.25 in the p-q stress space. The stress path starts inside the cementation yield surface, where a linear path is observed. This path continues until the broken cementation yield surface is reached. At the broken cementation yield surface, the stress path changes direction, and the stress path is between the broken cementation yield surface and the failure surface. This corresponds to the transition from stage II to stage III in Figure 6.1. Finally, the stress path changes direction and becomes parallel to the critical state line. It was not possible to identify the transition from stage III to stage IV in the K_0-loading.

The stress path followed during K_0-loading is closer to the failure surface than observed in the reviewed studies in Chapter 2. This is most likely due to the deviation from the K_0-condition as shown in Figure 6.24.

6.7 Triaxial Loading of Isotropically Preloaded Specimens

After completion of the isotropic compression tests, two specimens were kept in the cell and the setup was changed to triaxial loading. The triaxial tests were conducted at a confining pressure of 150 kPa for direct comparison with intact triaxial specimens. The goal was to observe the effect of preloading the specimens isotropically. During isotropic loading some of the cementation breaks. Both specimens were preloaded to a confining pressure of approximately 15.7 MPa, which is just beyond the broken cementation yield surface at 14.1 MPa. The preloading was carried into to stage III in Figure 6.2, where no tensile strength remains. It was speculated that the behavior would change towards lower

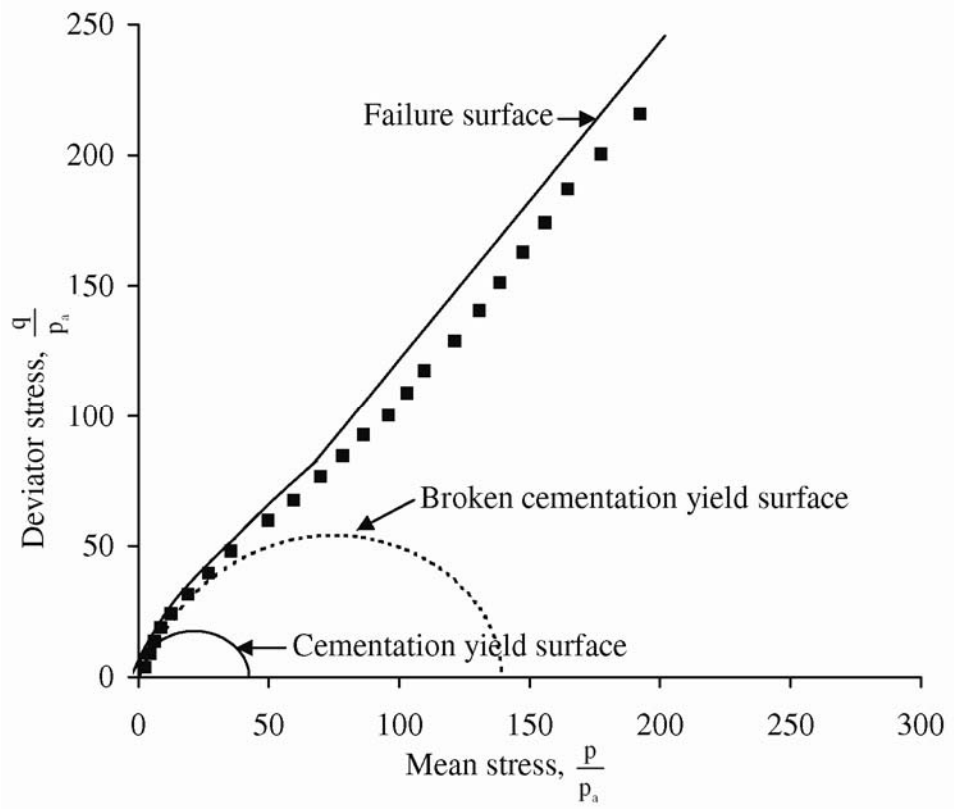

Figure 6.25: Stress path followed during K_0-loading.

strength and lower elastic modulus. The stress-strain and volume change behavior for the preloaded and intact vertically cored specimens are compared in Figure 6.26. The intact specimen is stronger and stiffer than the preloaded specimen. Furthermore, the volumetric strain shows increased contraction before dilation. The preloaded and intact horizontally cored specimens are compared in Figure 6.27. The preloaded volumetric and major principal strains are identical to those for the intact specimen. This indicates very little difference in behavior due to preloading. Furthermore, the preloaded specimen is stronger than the intact specimen. There is no obvious explanation for the difference in behavior for the two horizontal specimens and for the difference between the vertical and the horizontal specimens.

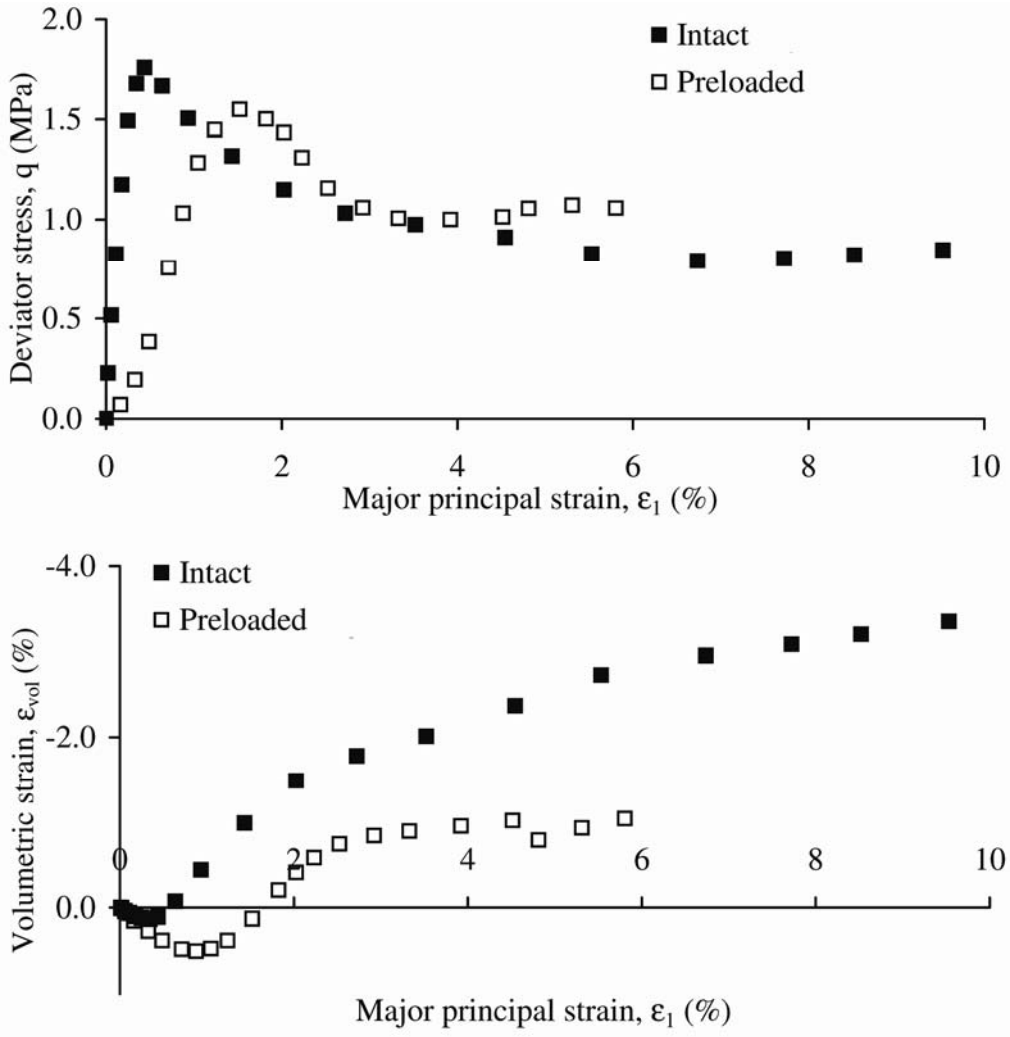

Figure 6.26: Comparison of intact and preloaded vertical specimens in triaxial compression. a) Stress-strain relation. b) Volume change.

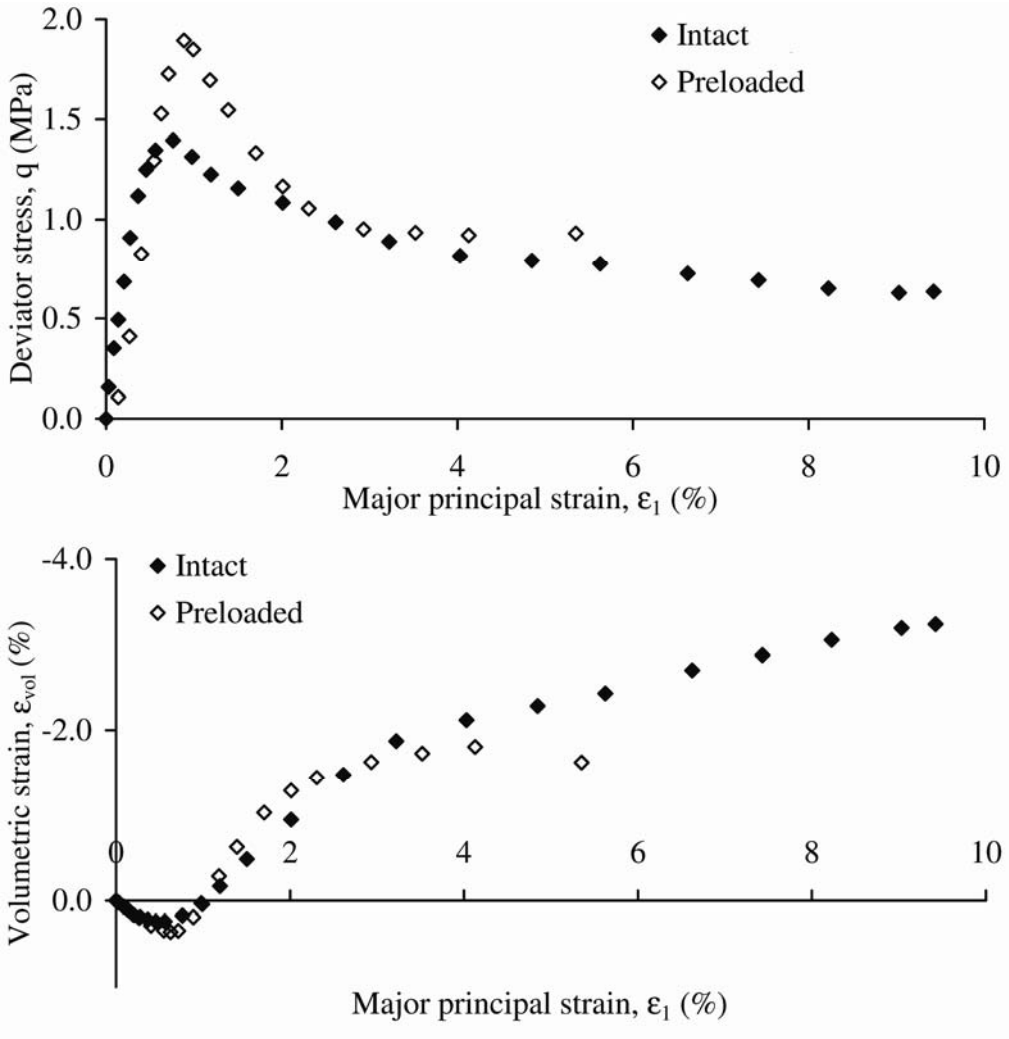

Figure 6.27: Comparison of intact and preloaded horizontal specimens in triaxial compression. a) Stress-strain relation. b) Volume change.

7. Parameter Determination for Cross-Anisotropic Extension to The Single Hardening Model

The cross-anisotropic version of The Single Hardening Model employed in Chapter 8 requires parameter determination of isotropic parameters on specimens cored in vertical and horizontal directions.

7.1 Failure Parameters

The failure criterion in The Single Hardening Model requires determination of three parameters. The opening angle is controlled by the parameter η_1 and the curvature of the failure surface is described by the parameter m. Furthermore, the parameter 'a' controls the translation of the stress space due to cohesion.

7.1.1 Parameter 'a'

The parameter 'a' is estimated from the Brazilian tensile strength determined in section 6.3.2. To simplify the predictions, one value of the parameter 'a' is assumed for both the vertical and the horizontal direction, despite the anisotropy of the material. As a result, the origin of the translated coordinate system remains on the hydrostatic axis.

As demonstrated in Figure 7.1 the tensile strength obtained from the Brazilian test is lower than the value of the parameter 'a'. First the tensile strength from the Brazilian

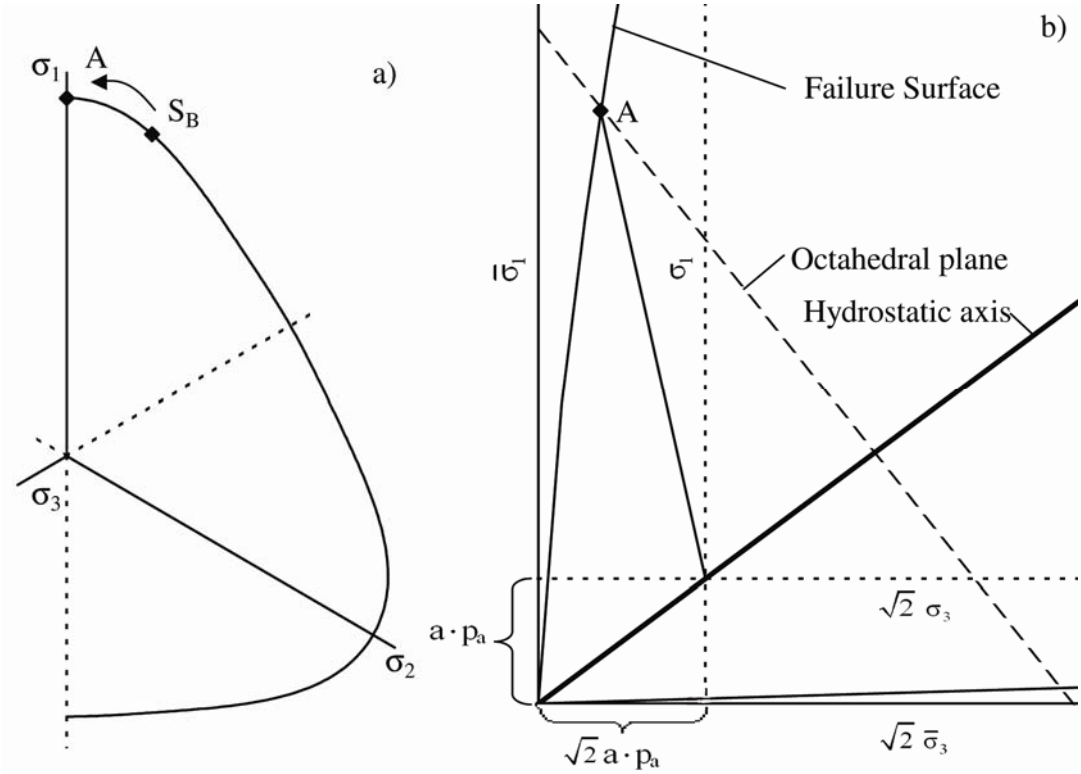

Figure 7.1: Comparison of Brazilian tensile strength with parameter ‘a’ in The Single Hardening Model. a) Octahedral plane. b) Triaxial plane.

test, S_B is projected along the failure surface to point A (Figure 7.1 a)). Point A is located on the triaxial plane in Figure 7.1 b), where a direct comparison with the parameter 'a' is possible.

In section 6.3.2 the Brazilian tensile strength was determined to be 0.168 MPa. This corresponds to $\sigma_t / p_a = 1.66$. Based on the minimum value of 'a' being 1.66 and the determination of the parameters η_1 and m is section 7.1.2, the value of the parameter 'a' at failure becomes 1.95.

7.1.2 Parameters η_1 and m

As discussed in section 6.3.3 the failure surface does not consist of one smooth surface. It can be divided into three separate sections, each corresponding to different stages of the sand cement matrix. These stages can also be recognized in the parameter determination process for the failure surface in The Single Hardening Model. The plots in Figure 7.2 and Figure 7.3 would normally be used to determine the parameters η_1 and m in vertical and horizontal direction. If all the failure points can be fitted to one line, the failure surface consists of one smooth curvature. Furthermore, if points form a horizontal line it corresponds to a straight line in the p-q stress space (or triaxial plane) indicating the critical state line is reached.

For both vertical and horizontal specimens, the failure points align into three separate sections each representing a stage of cementation from Figure 6.1. At low confining pressures (stage II) the large slope represent a failure surface with considerable curvature. Stage II represents the region between the initial cementation yield surface and

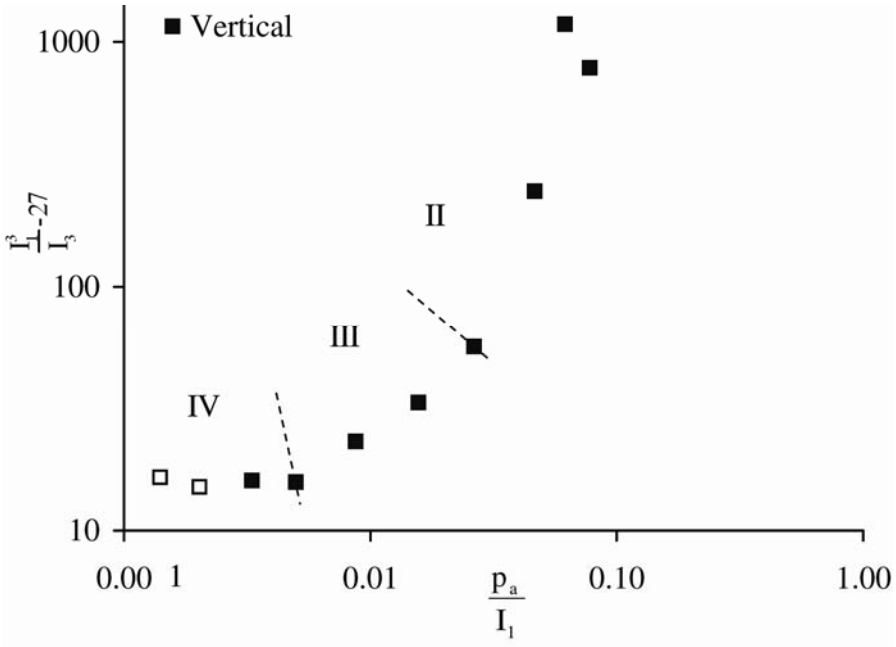

Figure 7.2: Failure points for vertically cored specimens.

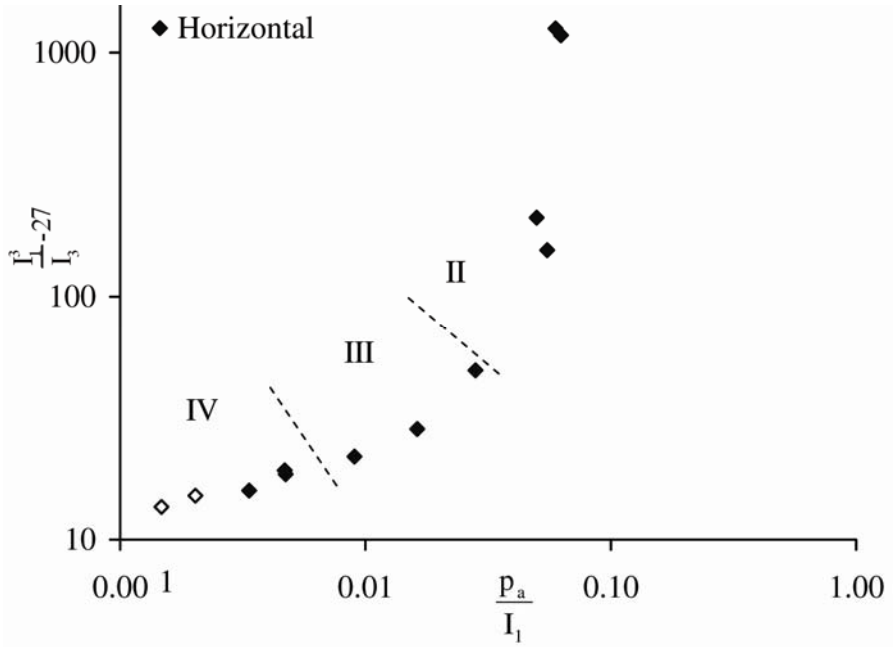

Figure 7.3: Failure points for horizontally cored specimens.

the broken cementation yield surface. As the confining pressure increases and the specimens fail in stage III, the curvature decreases. This is evident from the lower slope of the failure points in this stage. At high confining pressures the horizontal alignment of the failure points corresponds to the straight critical state line. There is more scatter in the failure points for the horizontal specimens than for the vertical specimens. Furthermore, the critical state line is reached at a lower confining pressure for the horizontal specimens than the vertical specimens.

The open symbols in Figure 7.2 and Figure 7.3 are the tests at confining pressures of 9.9 MPa and 14.0 MPa, where the tests did not reach failure. The points plotted are the maximum stress level reached near 25 % axial strain in the tests. A further increase in strength would move the points upwards and slightly to the left. For the tests on vertical specimens, this would result in a negative slope, meaning the critical state line curves outwards (or the critical state line is reached at confining pressures above the ones tested here.

The specimens failing in stage II had cementation remaining between the grains, and the parameter a = 1.95 is applied to these specimens. The parameter determination in the translated stress space is shown in Figure 7.4 and Figure 7.5. Note that a = 1.95 only apply to the specimens failing in stage II, including the Brazilian tests which is included in Figure 7.4 and Figure 7.5. In the cross-anisotropic extension to The Single Hardening Model presented in Chapter 8, the failure parameter m is assumed to have identical values in vertically and horizontally cored specimens. During the parameter determination for the artificial cross-anisotropic sandstone, the data is fitted for one value

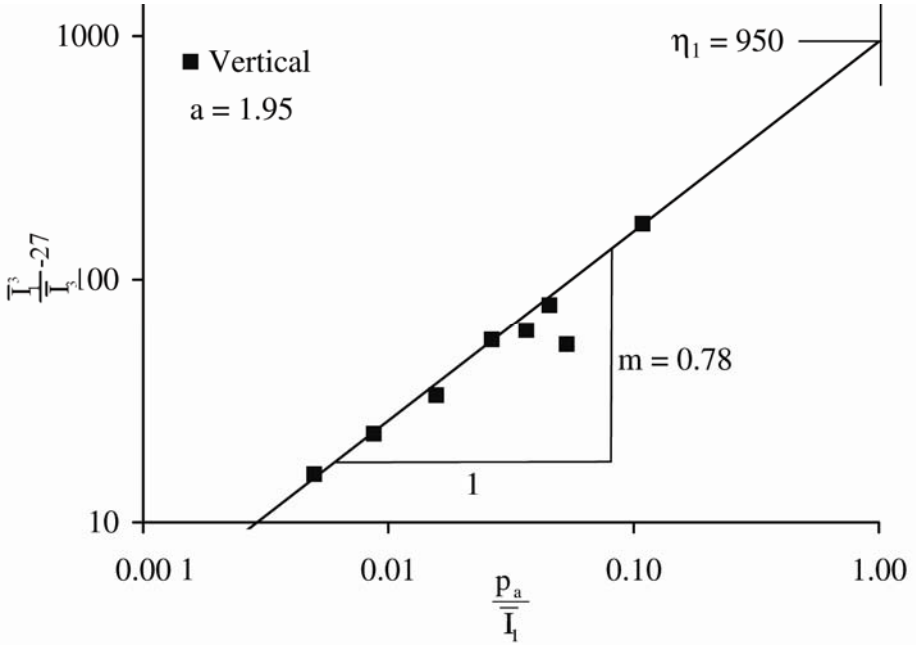

Figure 7.4: Determination of failure parameters in translated coordinate system for vertically cored specimens failing in stage II and stage III.

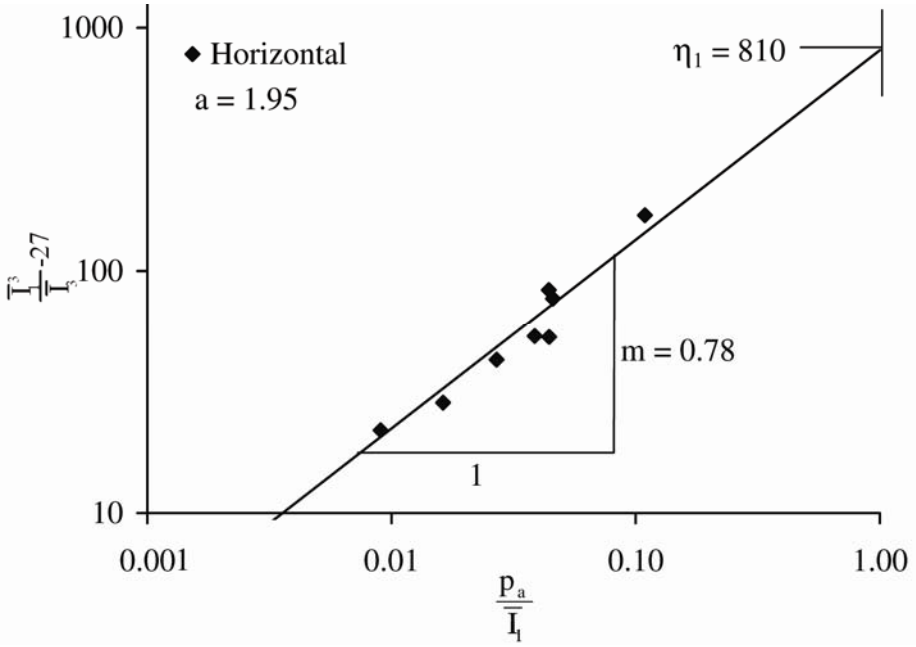

Figure 7.5: Determination of failure parameters in translated coordinate system for horizontally cored specimens failing in stage II and stage III.

of m in both vertically and horizontally cored specimens. The assumption of constant m is in accordance with the data. In vertical direction the failure parameters become m = 0.78 and η_1 = 950 and in horizontal direction m = 0.78 and η_1 = 810. Due to the parameter 'a' changing, the parameters determined for the failure surface, fits both stage II and stage III. This means m and η_1 are constant in stage II and stage III, only 'a' changes.

In stage IV where the critical state line is reached the failure surface can be characterized by one parameter, η_{CL}, where the parameter η_{CL} characterize a straight line without any curvature. For the vertically cored specimens, η_{CL} is 15.8 and for the horizontally cored specimens η_{CL} is 16.5. This corresponds to friction angles of 30.8^o and 31.3^o, respectively. The vertical and the horizontal values are almost identical indicating much of the initial cross-anisotropic fabric is lost during the crushing of the cementation.

The softening function developed in section 3.2.3 uses the parameter η_R to control the residual strength. In cohesionless soil, the critical state is reached at the residual strength. As a result, the parameter η_{CL} describing the critical stage line should correspond to the residual strength at low and intermediate confining pressures. However, this behavior is not observed here. The residual strength at low and intermediate confining pressures is determined from the stress plateau reached at large strains and does not describe a straight line. This curved residual strength surface can be described similar to the failure surface. This is shown in Figure 7.6 and Figure 7.7 where the residual strength parameters at low and intermediate confining pressures for the vertical and horizontal specimens are determined. However, to characterize the residual strength at

low and intermediate confining pressures in cemented sand it is necessary to introduce the parameter, m_R. The parameter m_R describes the curvature of the residual strength envelope. The parameters determined for the vertically cored specimens are $\eta_R = 415$ and $m_R = 0.64$. For the horizontally cored specimens, the residual strength parameters are $\eta_R = 30$ and $m_R = 0.64$. The horizontally cored specimens have lower values of η_R indicating more damage to the cementation during loading. The curved residual strength surface indicates the structure due to cementation is not completely degraded when the residual strength is reached. If completely degraded the residual strength should coincide with the critical state line determined at high confining pressures.

7.2 Elastic Parameters

The elastic parameters (ν and E) are determined several times during each test. Figure 6.17 shows the three areas where elastic parameters are determined on a typical stress-strain relation. The three areas are: a) Initial tangent; b) Small unloading-reloading cycle inside the cementation yield surface; c) Full unloading-reloading cycle at large strains, including the final unloading.

7.2.1 Poisson's Ratio

Poisson's ratio is determined from the volume change curves as described in section 3.1.1. The initial tangent Poisson's ratio is determined from the initial slope of the volume change curve for all the triaxial tests and the results can be seen in Figure 7.8 where Poisson's ratio is shown as a function of the first stress invariant. The first stress invariant is calculated in the translated coordinate system due to cementation. In the

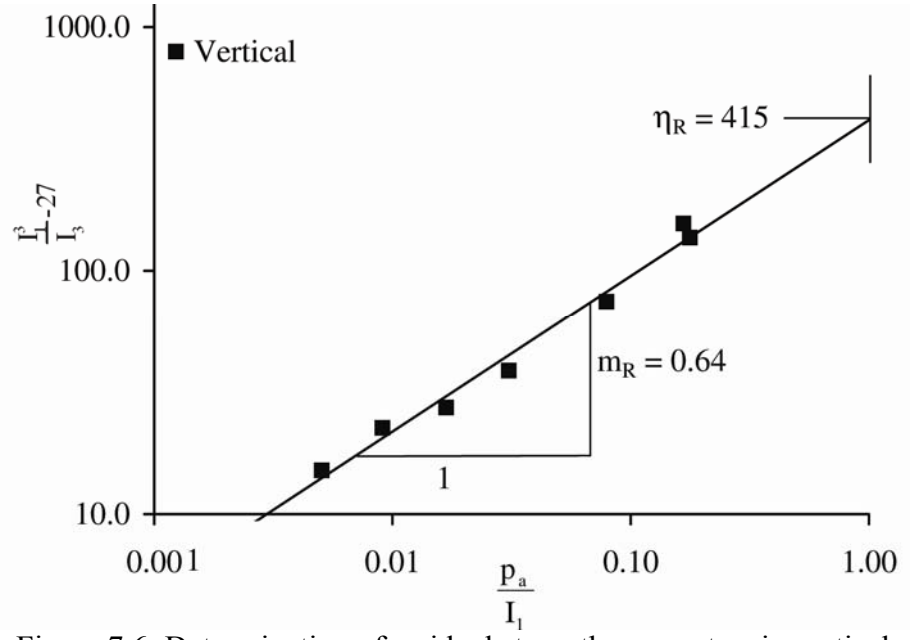

Figure 7.6: Determination of residual strength parameters in vertical direction.

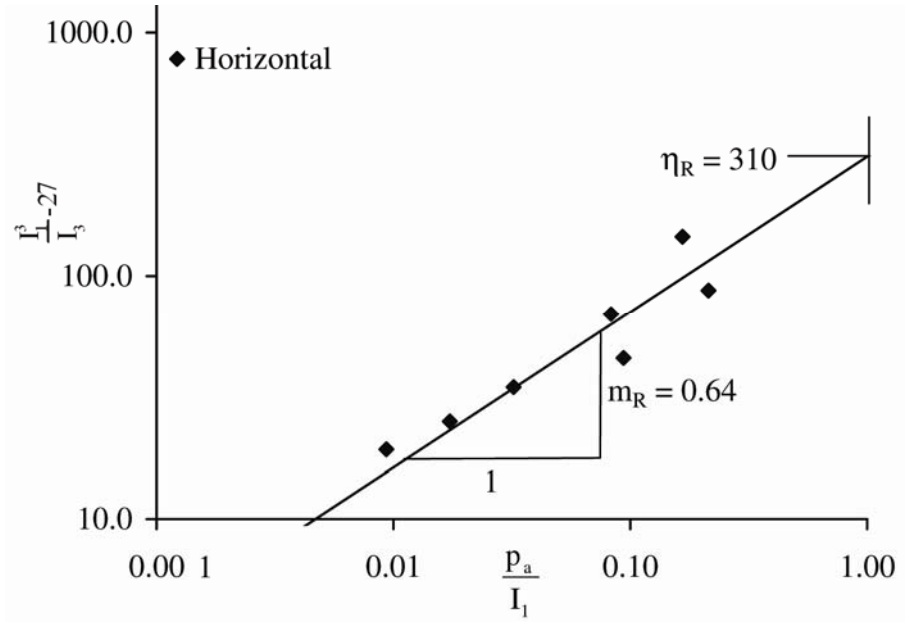

Figure 7.7: Determination of residual strength parameters in horizontal direction.

cemented region, the parameter 'a' is equal to 1.95 and then decreases as the stresses reach the broken cementation yield surface. There is no significant indication of variation in Poisson's ratio as the cementation starts breaking. The average value of Poisson's ratio is 0.11. If distinction is made between the vertically cored specimens and the horizontally cored specimens, the vertically cored specimens would have a Poisson's ratio of 0.10 and the horizontally cored specimens would have a Poisson's ratio of 0.12.

Note that Poisson's ratio determined from the horizontally cored specimens, ν_{hor} is an average value defined in equation (7.1):

$$\nu_{hor} = \frac{\nu_{hh} + \nu_{hv}}{2} \tag{7.1}$$

in which ν_{hh} is Poisson's ratio in the horizontal plane and ν_{hv} is Poisson's ratio of strain in vertical direction to applied strains in horizontal direction. The experimental setup where only the major principal strain and the volume change are measured makes it impossible to distinguish the two values of Poisson's ratio experienced on the horizontally cored specimens. This would require individually measured radial deformations in the two directions parallel and perpendicular to the bedding planes. Poisson's ratio from the vertically cored specimens, ν_{ver} is defined in equation (7.2):

$$\nu_{ver} = \nu_{vh} \tag{7.2}$$

in which ν_{vh} is Poisson's ratio of strain in horizontal direction to applied strains in vertical direction.

Poisson's ratio determined from small unloading/reloading cycles performed inside the cementation yield surface (confining pressure less than or equal to 4.0 MPa) is plotted as a function of the normalized first stress invariant in Figure 7.9. The average

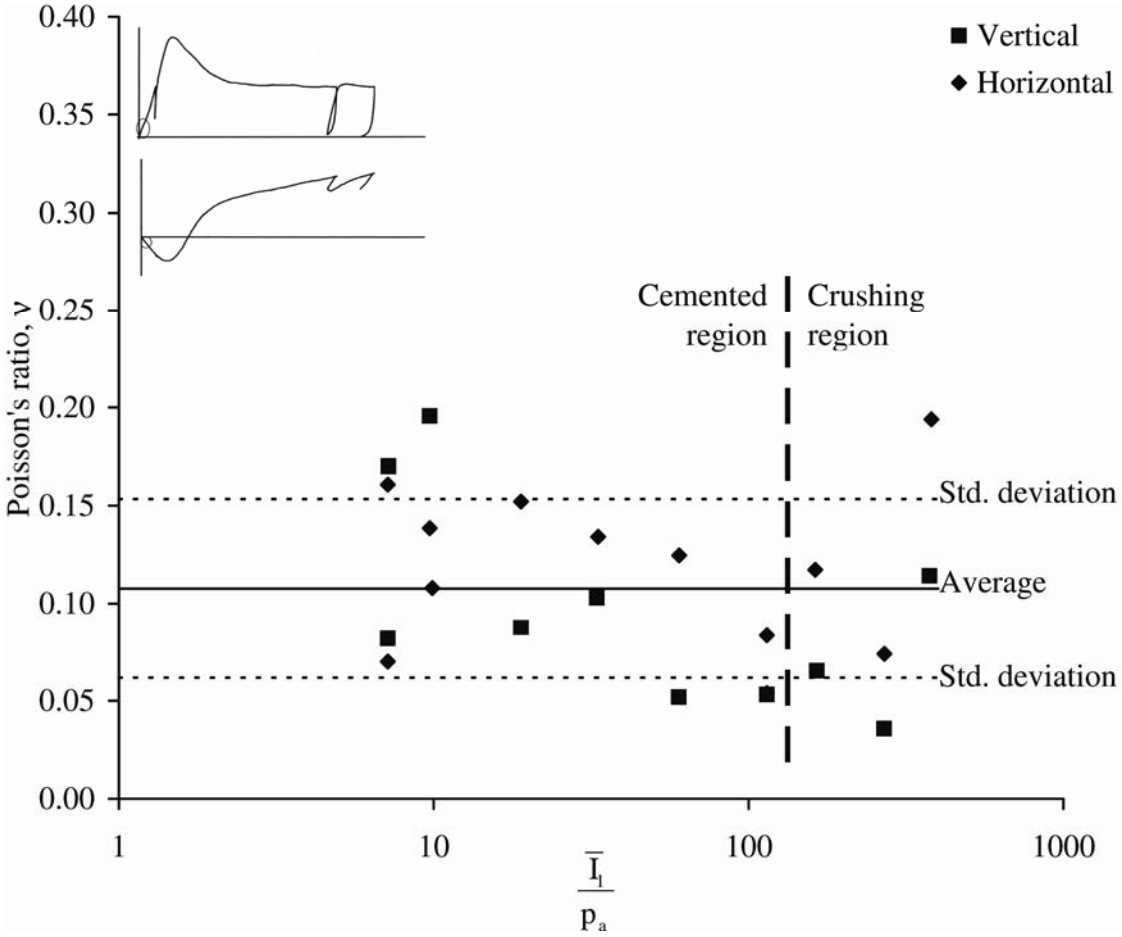

Figure 7.8: Initial tangent Poisson's ratio as a function of the first stress invariant.

value of Poisson's ratio is 0.16, and if the results from the vertically cored specimens are separated from the horizontally cored specimens, Poisson's ratio becomes 0.15 and 0.17 respectively.

The unloading-reloading cycles performed at large strains yield higher Poisson's ratio. The results are shown in Figure 7.10 where the average value of Poisson's ratio is 0.27. In this stage of the test, much of the cementation is broken and the sand cement matrix corresponds to stage III and stage IV in Figure 6.1. As the cementation is broken down, the individual grains can move more easily around and Poisson's ratio increases. If the vertically cored specimens are separated from the horizontally cored specimens, Poisson's ratio becomes 0.26 for the vertically cored specimens and 0.28 for the horizontally cored specimens.

In general, Poisson's ratio for vertical specimens is smaller than for horizontal specimens which suggests anisotropic behavior for the cemented sand. However, the difference is within the standard deviation.

It was not possible to determine Poisson's ratio during unloading because plastic strains occurred almost immediately upon unloading. The plastic strains might have affected Poisson's ratio during reloading as well. In some tests only one reading occurred before plastic strain started. This is illustrated in Figure 7.11 where the dots represent the measured strains and the curve represents the actual strains. Line a corresponds to the actual Poisson's ratio and line b shows the higher Poisson's ratio obtained by not measuring enough data points after stress reversal.

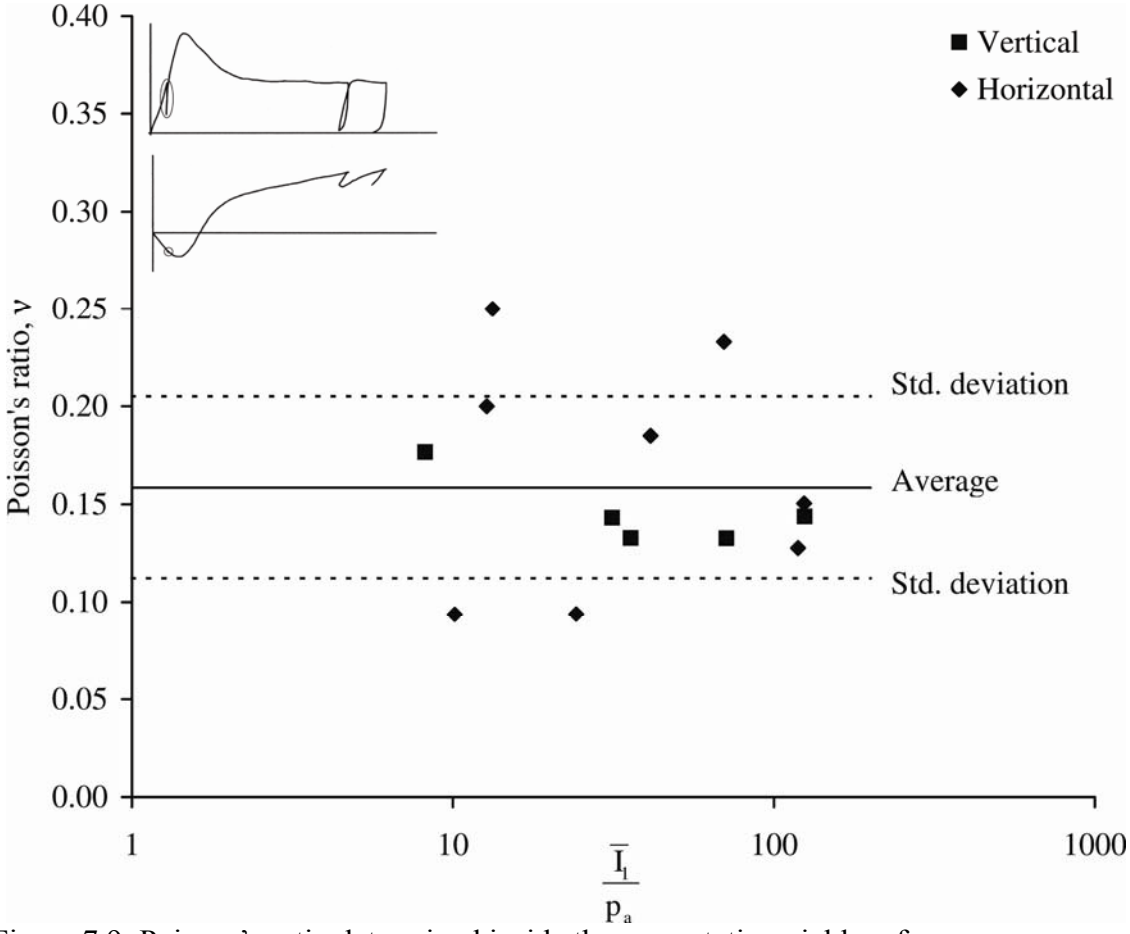

Figure 7.9: Poisson's ratio determined inside the cementation yield surface.

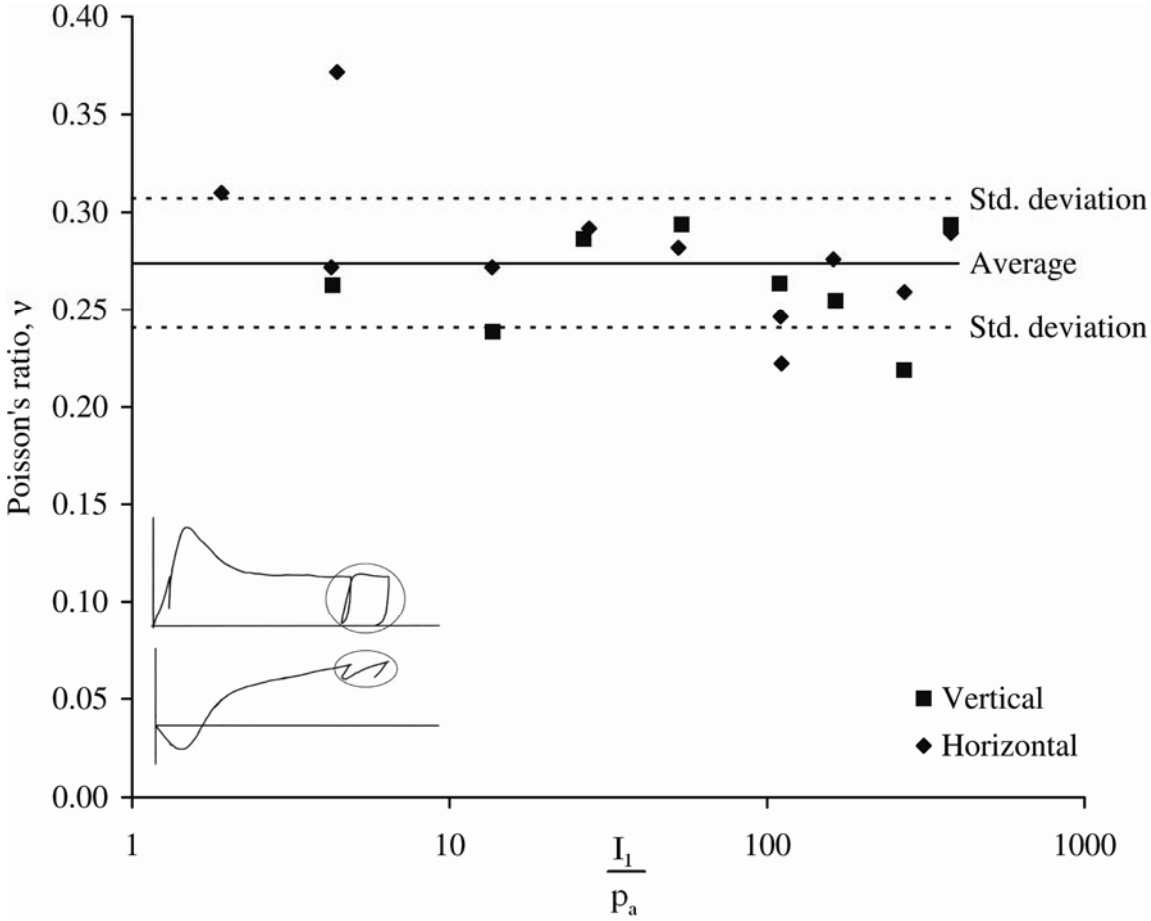

Figure 7.10: Poisson's ratio determined during the final unloading-reloading cycle as a function of the normalized first stress invariant.

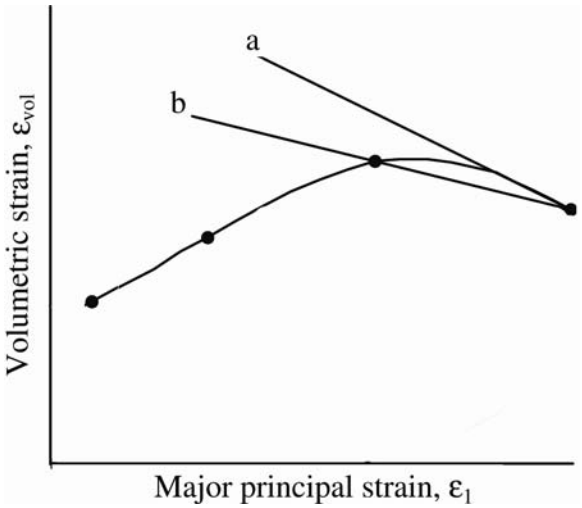

Figure 7.11: Plastic deformation occurring as part of the initial response due to unloading causing too high Poisson's ratio.

7.2.3 Young's Modulus

Young's modulus is determined right after unloading and right after reloading. The results showed higher modulus during unloading than during reloading. This could arise from creep and is illustrated in Figure 7.12. After unloading from point a in Figure 7.12 the specimen creeps in the axial direction giving rise to positive strains. As a result, point b in Figure 7.12 includes more axial strain than pure elastic unloading would suggest. Young's modulus between point a and point b would therefore be too high. As the specimen is further unloaded, the creep becomes insignificant, and Young's modulus calculated between point b and point c yields more realistic results. During some tests, the creep was so pronounced that point b corresponded to more strain than point a, making Young's modulus negative. The unloading moduli were therefore rarely employed in the modeling of the elastic modulus.

The initial tangent Young's moduli are plotted and the parameters M and λ in the elastic model in The Single Hardening Model are determined in Figure 7.13. The parameter M becomes 930 and the parameter λ becomes 0.22. If the parameters are determined separately for the vertically cored specimens and the horizontally cored specimens, M becomes 1630 and 890, respectively. Similarly λ becomes 0.17 and 0.23.

Young's moduli determined during the unloading-reloading cycle performed inside the cementation yield surface is shown in Figure 7.14, where the isotropic elastic parameters become $\lambda = 0.28$ and $M = 2265$. For cross-anisotropic parameters, $\lambda = 0.28$ and $M = 2530$ in vertically cored specimens and $\lambda = 0.25$ and $M = 2950$ for horizontally cored specimens.

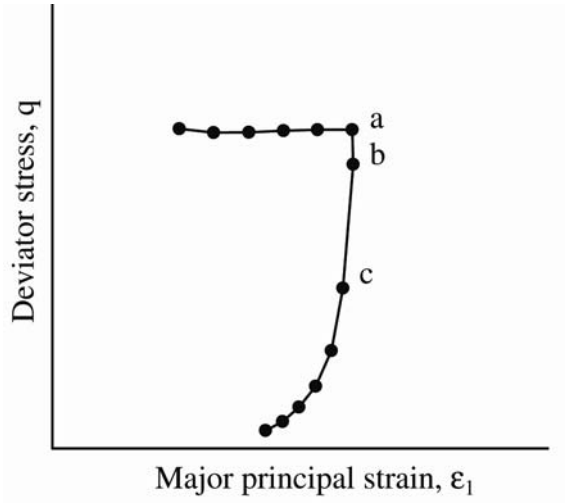

Figure 7.12: Creep causing the elastic modulus to increase.

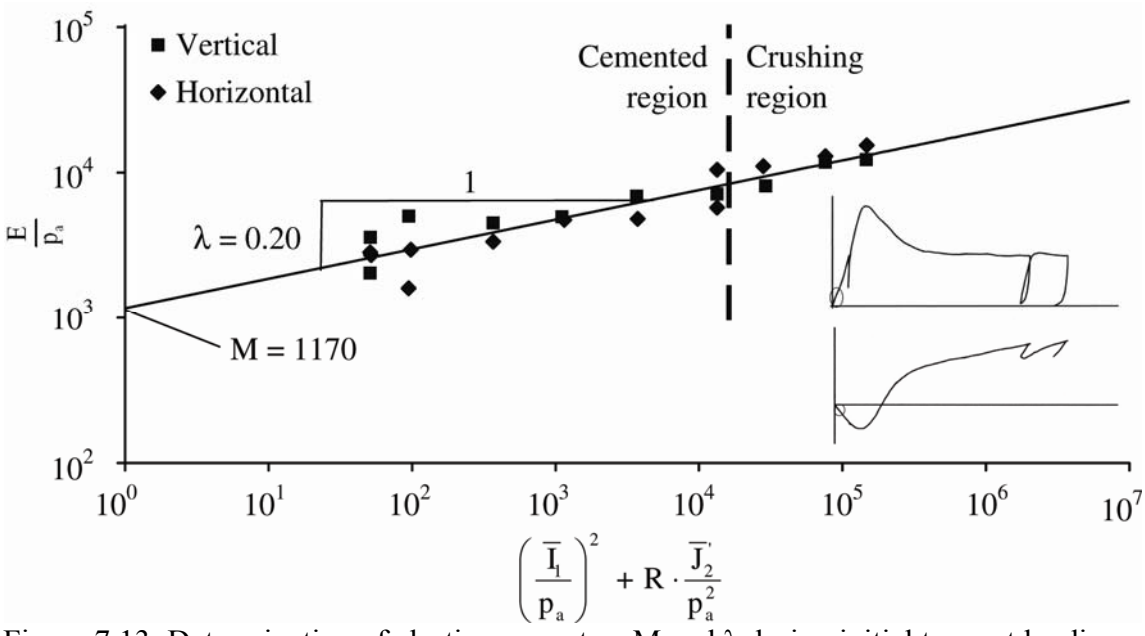

Figure 7.13: Determination of elastic parameters M and λ during initial tangent loading.

The elastic parameters for the final unloading-reloading cycle are determined in Figure 7.15. Assuming the material is isotropic, the parameter M becomes 1055 and the parameter λ becomes 0.35. If cross-anisotropy is implied, M becomes 1055 in vertical direction and 1070 in horizontal direction. The parameter λ does not change and remains 0.35 in both directions. At this stage, most of the elastic cross-anisotropic behavior is lost and the sand cement matrix corresponds to stage III and stage IV in Figure 6.1.

The isotropic elastic parameters are summarized in Table 7.1 and the cross-anisotropic elastic parameters are summarized in Table 7.2.

7.3 Work Hardening Parameters

The plastic work produced during isotropic compression has been calculated to determine the parameters C and p in The Single Hardening Model. The plastic work is calculated using equation (3.23), reintroduced here in equation (7.3):

$$W_p = \int \left\{ \sigma_c \cdot d\varepsilon_{vol}^p \right\} \tag{7.3}$$

where σ_c is the confining pressure during isotropic compression and $d\varepsilon_{vol}^p$ is the incremental volumetric plastic strain. The plastic strains are calculated by subtracting the elastic strains from the measured strains. The elastic strains are calculated using the isotropic initial tangent elastic parameters determined in section 7.2.

The plastic work determined from the isotropic compression tests is shown in Figure 7.16 as a function of the first stress invariant, I_1. The results from test V9 deviates from the remaining isotropic compression tests, due to difference in void ratio. In cohesionless materials the relation between the plastic work, W_p and the first stress invariant, I_1 usually yields a straight line in a double logarithmic coordinate system (a

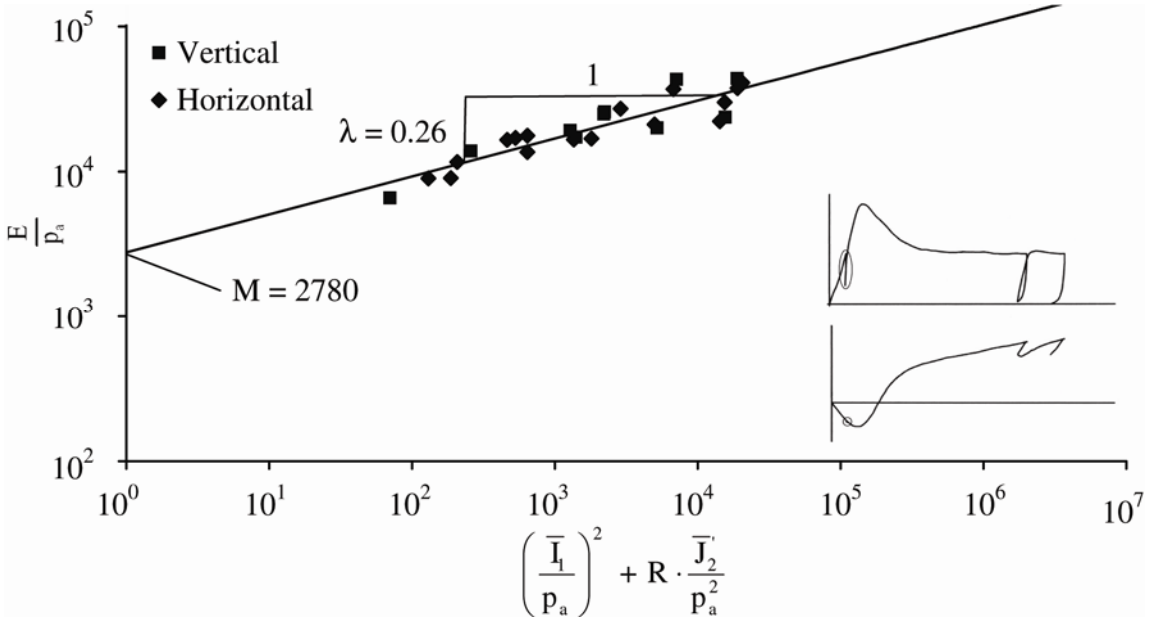

Figure 7.14: Determination of elastic parameters M and λ during unloading-reloading inside the cementation yield surface.

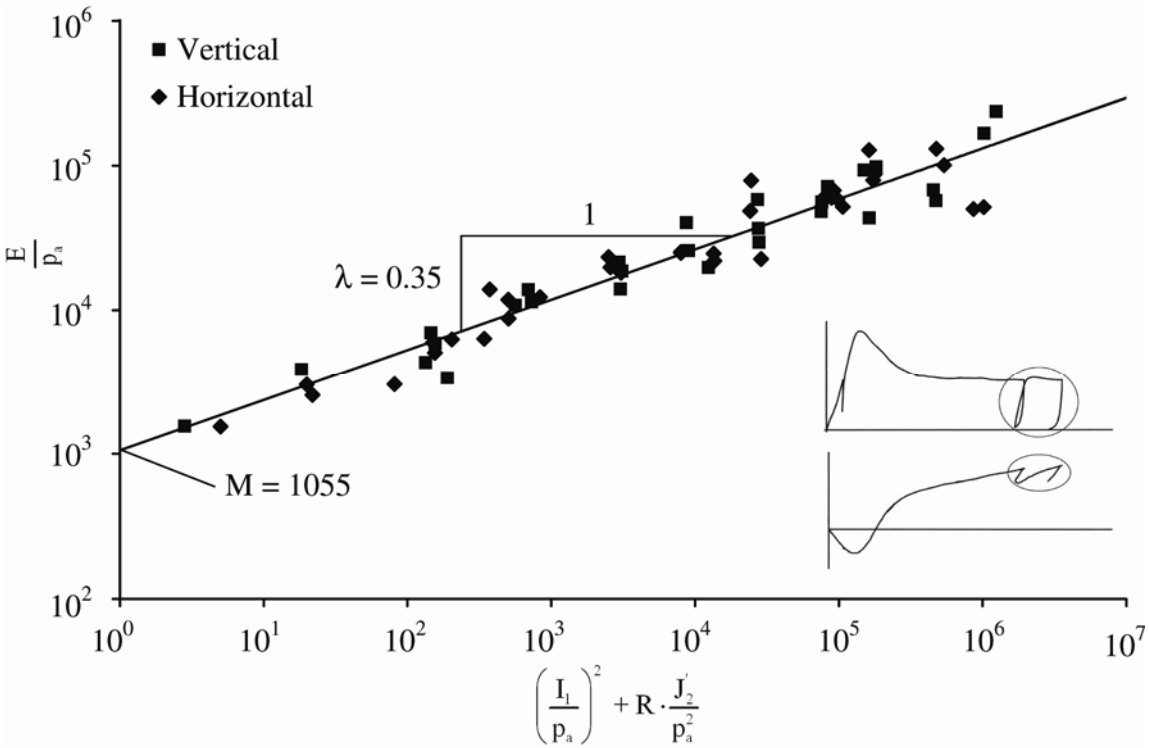

Figure 7.15: Determination of elastic parameters M and λ during the final unloading-reloading cycle.

Table 7.1: Isotropic elastic parameters

	Initial tangent	Cemented	Final unloading/reloading
Poisson's ratio, ν	0.11	0.16	0.27
M	1170	2780	1055
λ	0.20	0.26	0.35

Table 7.2: Cross-anisotropic elastic parameters

	Initial tangent		Cemented		Final unloading/reloading	
	Vertical	Horizontal	Vertical	Horizontal	Vertical	Horizontal
Poisson's ratio, ν	0.10	0.12	0.15	0.17	0.26	0.28
M	1630	890	2530	2950	1055	1070
λ	0.17	0.23	0.28	0.25	0.35	0.35

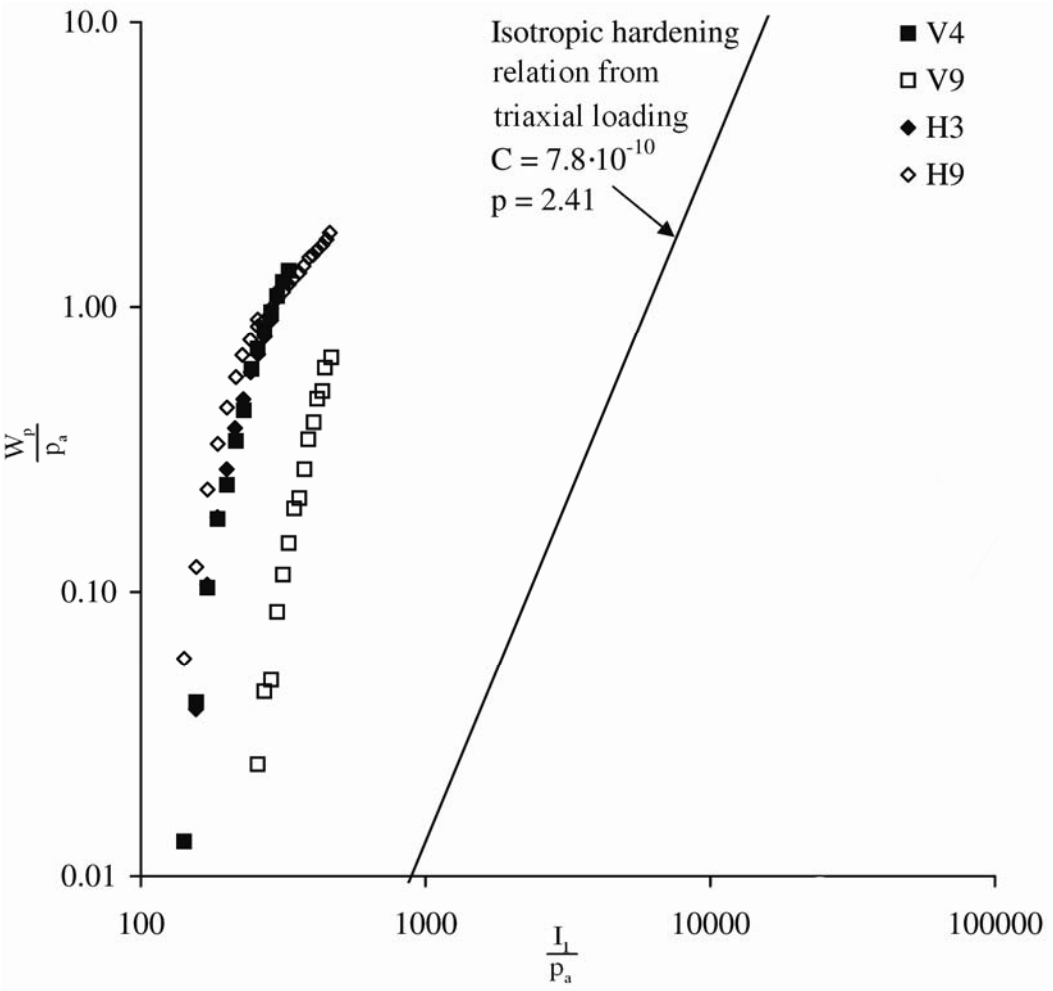

Figure 7.16: Plastic work during isotropic compression.

deviation being loose silty sand, as discussed in section 3.2.1). As shown in Figure 7.16, the relation between the plastic work and the first stress invariant does not follow a straight line for the artificially cemented sand.

Instead, the procedure described in chapter 3, where the plastic work during triaxial compression is used to determine the isotropic work parameters have been applied. The result is shown in Figure 7.16 as the straight line with the parameters of C = $7.8 \cdot 10^{-10}$ and p = 2.14. The optimum work parameters determined from the triaxial compression tests does not describe the work determined from isotropic compression.

7.4 Plastic Potential Parameters

Determination of the plastic potential parameters and the yield parameters requires loading with plastic work. As the behavior inside the cementation yield surface is considered elastic, tests performed with stress paths primarily inside the cementation yield surface have not been used for determination of parameters for The Single Hardening Model. Furthermore, the parts of the stress-strain relation inside the cementation yield surface have been omitted from the parameter determination. The tests found most suitable for the yield surface and plastic potential parameters were performed at confining pressures of 1.0, 2.0, and 4.0 MPa.

Applying the new plastic potential function presented in section 3.2.2 requires determination of the parameters μ and b. The parameter μ is determined in Figure 7.17 and Figure 7.18 for the vertically and horizontally cored specimens, respectively. Note that the parameter on the y-axis is the ξ'_y from the new plastic potential function:

$$\xi_y' = \xi_y - \psi_{2,0} \tag{7.4}$$

in which ξ_y is defined in equation (3.19) and $\psi_{2,0}$ is defined in equation (3.38).

The variation in the plastic potential parameters was too small to distinguish the vertically cored specimens from the horizontally cored specimens. As a result, the plastic potential parameter μ are the same in vertically cored and horizontally cored specimens.

The determination of the parameter b is shown in Figure 7.19 and Figure 7.20 for the vertically and horizontally cored specimens, respectively. The parameter b becomes 0.0007 for the vertically cored and the horizontally cored specimens.

7.5 Yield Parameters

The parameter h is determined for three tests in vertical direction and two tests in horizontal direction. The average value of the parameter h from equation 3.33 was 0.31 in vertical direction and 0.15 in horizontal direction.

Once the parameter h is known, the relation between the sub-parameter q and the stress level S can be plotted to determine the parameter α. This is done in Figure 7.21 and Figure 7.22 for vertical and horizontal direction, respectively. The tests in Figure 7.21 and Figure 7.22 started their stress paths inside the cementation yield surface which is why data is absent at low stress levels. The hyperbolic expression used to describe the relation between q and S does not fit the data at low stress levels. To simplify the parameters both data sets have been fitted with a straight line representing the value of α being 1.00.

The shape of the yield surface in The Single Hardening Model is defined by contours of constant plastic work. In section 6.1.1 the hydrostatic yield stress was

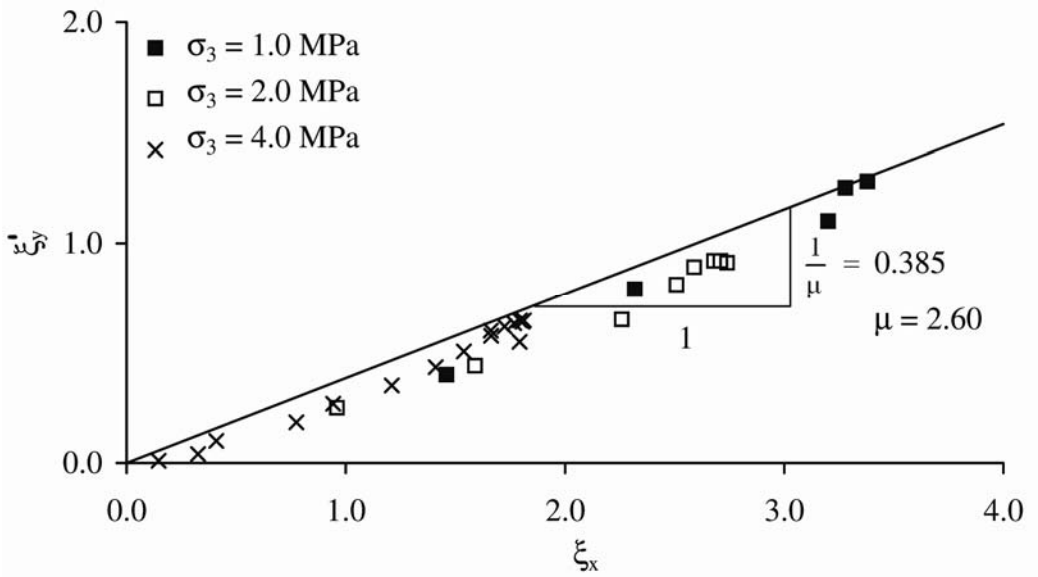

Figure 7.17: Determination of plastic potential parameter μ for vertically cored specimens

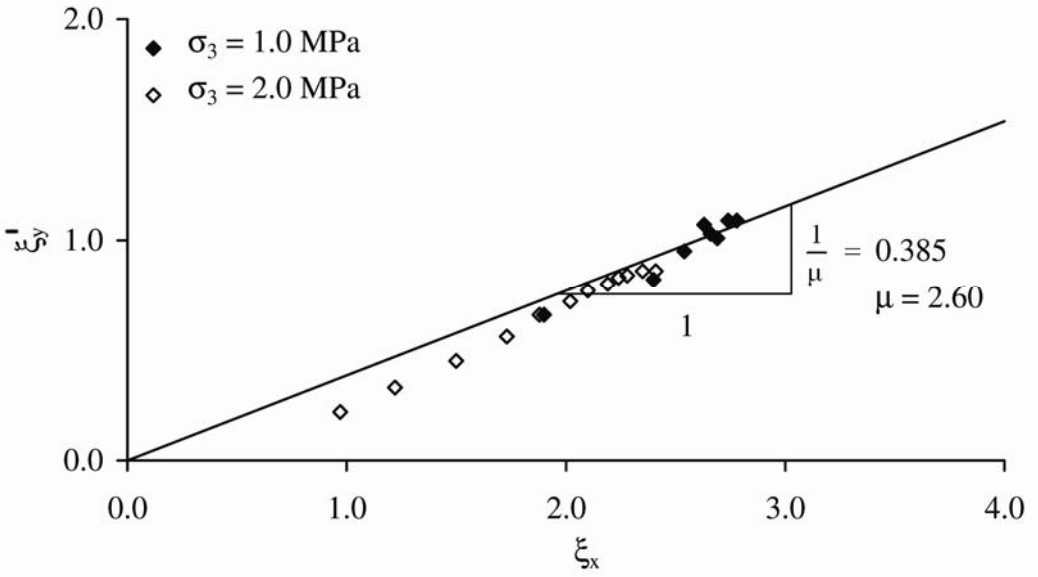

Figure 7.18: Determination of plastic potential parameter μ for horizontally cored specimens

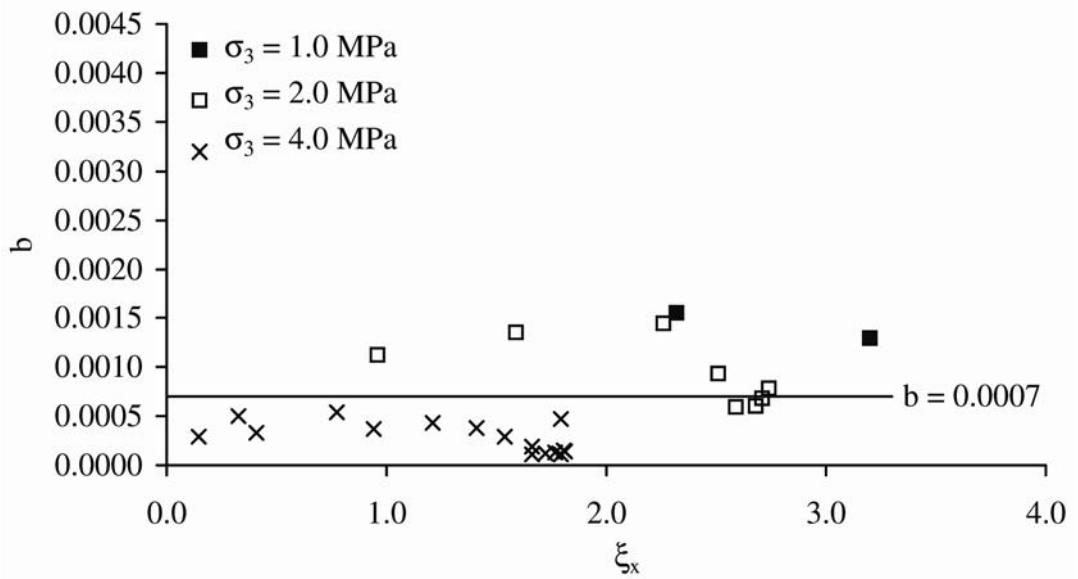

Figure 7.19: Determination of plastic potential parameter b for vertically cored specimens.

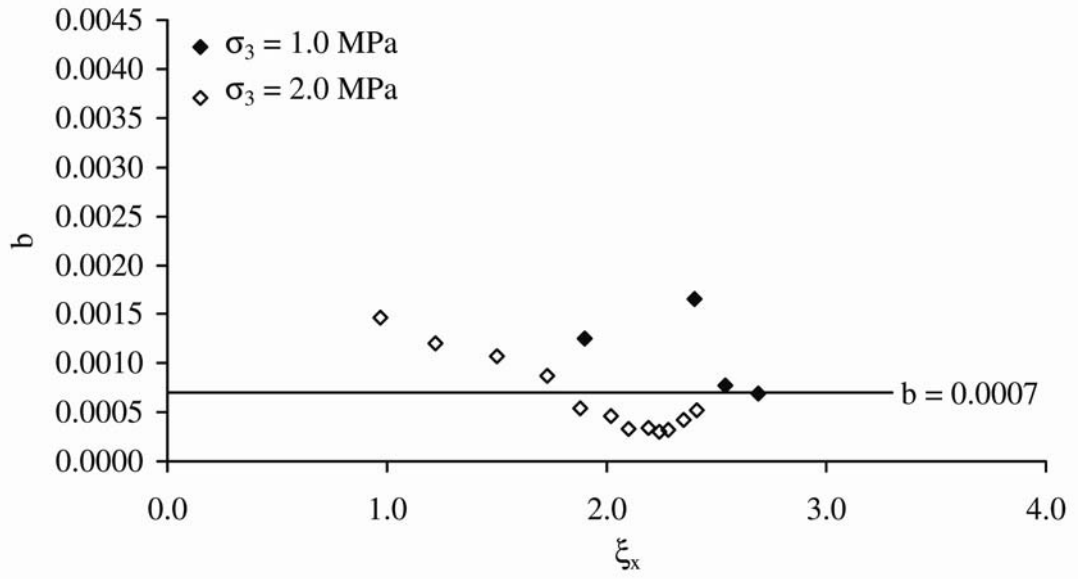

Figure 7.20: Determination of plastic potential parameter b for horizontally cored specimens.

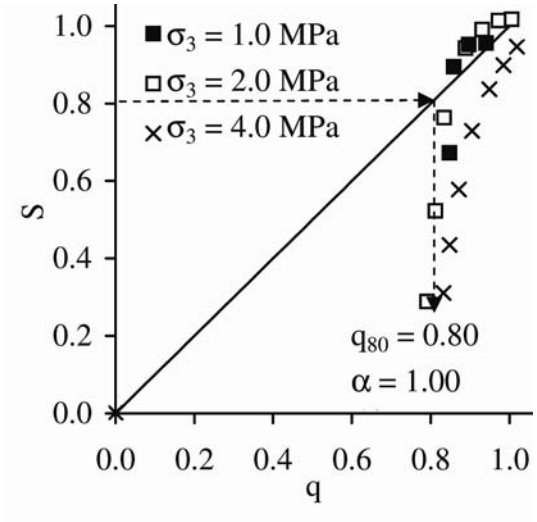

Figure 7.21: Determination of yield parameter α for vertical specimens.

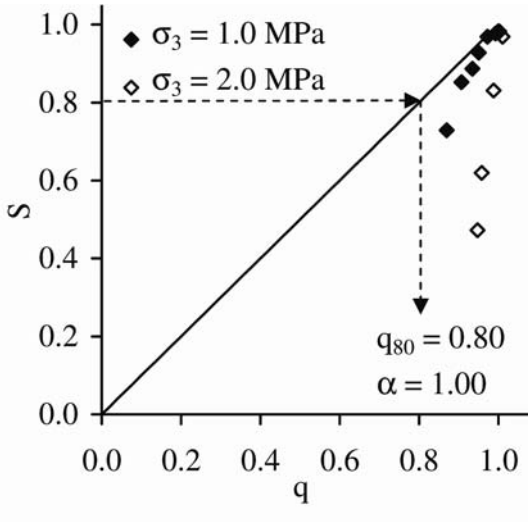

Figure 7.22: Determination of yield parameter α for horizontal specimens.

determined to be 4.3 MPa. Using the yield surface parameters determined in the previous section, the vertical and horizontal initial cementation yield surface can be determined. This is shown in Figure 7.23 for vertically cored specimens and Figure 7.24 for horizontally cored specimens. Furthermore, the initial yield points determined in section 6.5 from the triaxial tests are shown. The translated stress space is employed meaning the yield surface intersects with the origin. There is overall good agreement between the yield stresses determined from the triaxial tests and the shape of the yield surface from the yield parameters in The Single Hardening Model. This is the case in vertically cored specimens and horizontally cored specimens. This agreement indicates that the shape of the cementation yield surface is consistent with the yield surface described by the contours of constant plastic work. As a consequence, one set of parameters can describe the shape of the cementation yield surface as well as control the work when the yield surface expands.

The parameters to control the size of the initial cementation yield surface and the broken cementation yield surface are the intersection with the hydrostatic axis. The parameter describing the cementation yield surface, H_C becomes 42.4, and the parameter describing the broken cementation yield surface, H_B becomes 139.2. Figure 7.25 shows the location of H_C and H_B.

7.6 Summary of Parameters Determined

The parameters determined for vertical and horizontal specimens for The Single Hardening Model are summarized in Table 7.3. These parameters correspond to the behavior in stage II and stage III in Figure 6.1 and Figure 6.2.

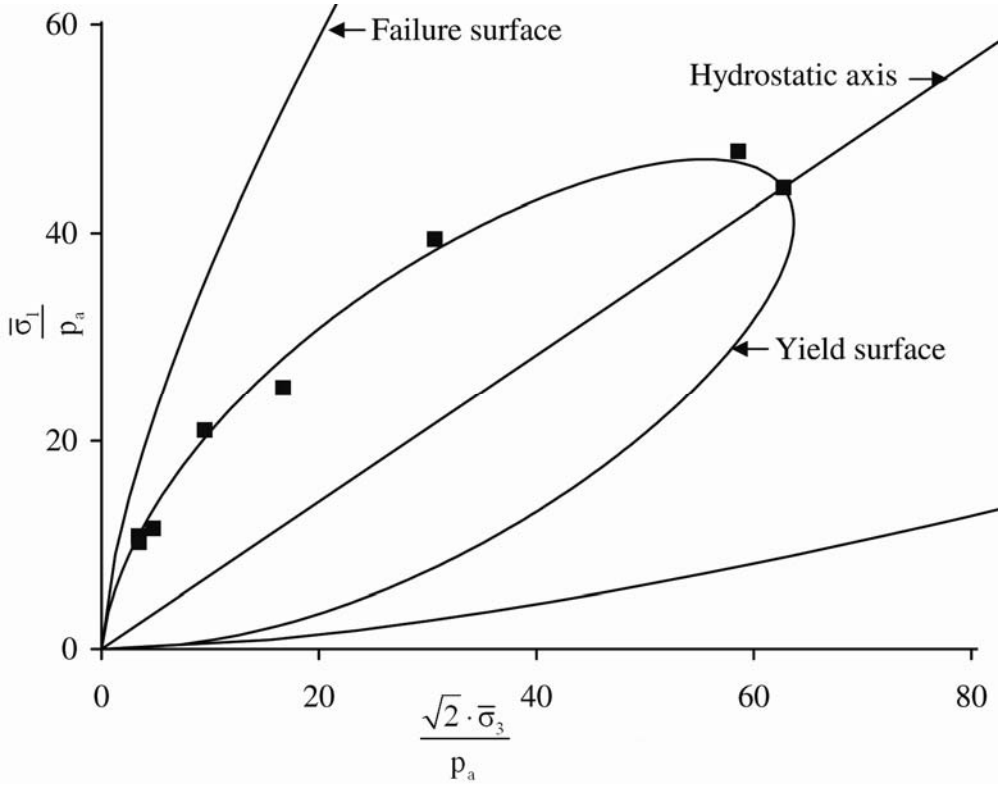

Figure 7.23: Failure surface and yield surface along with determined initial yield stresses in vertical direction.

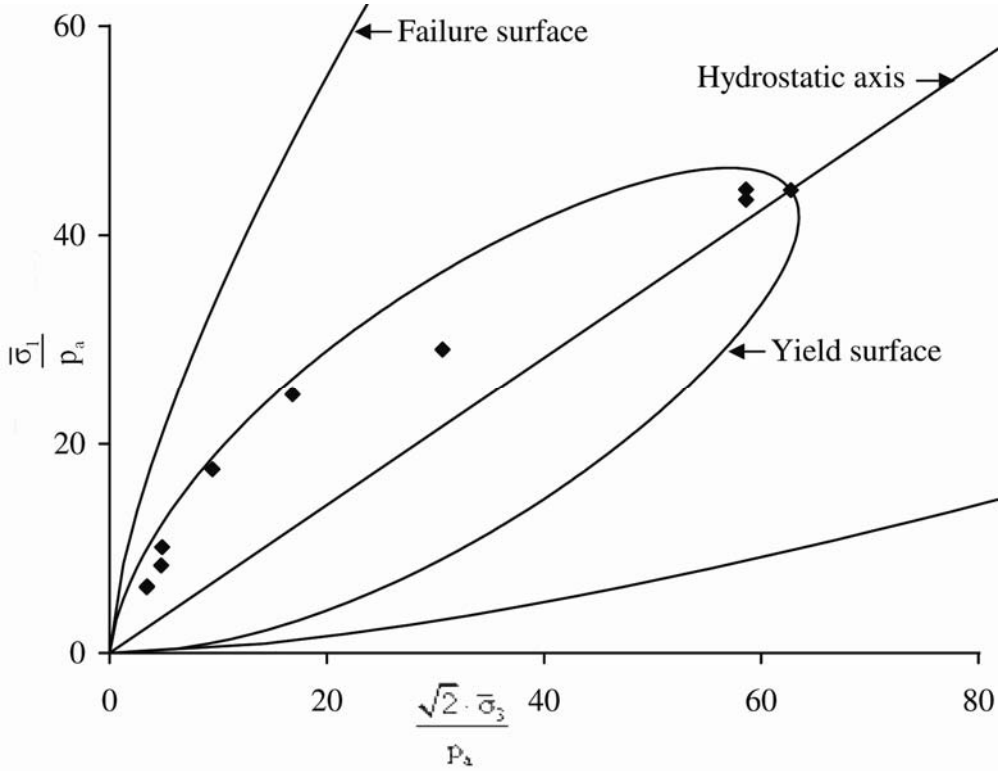

Figure 7.24: Failure surface and yield surface along with determined initial yield stresses in horizontal direction.

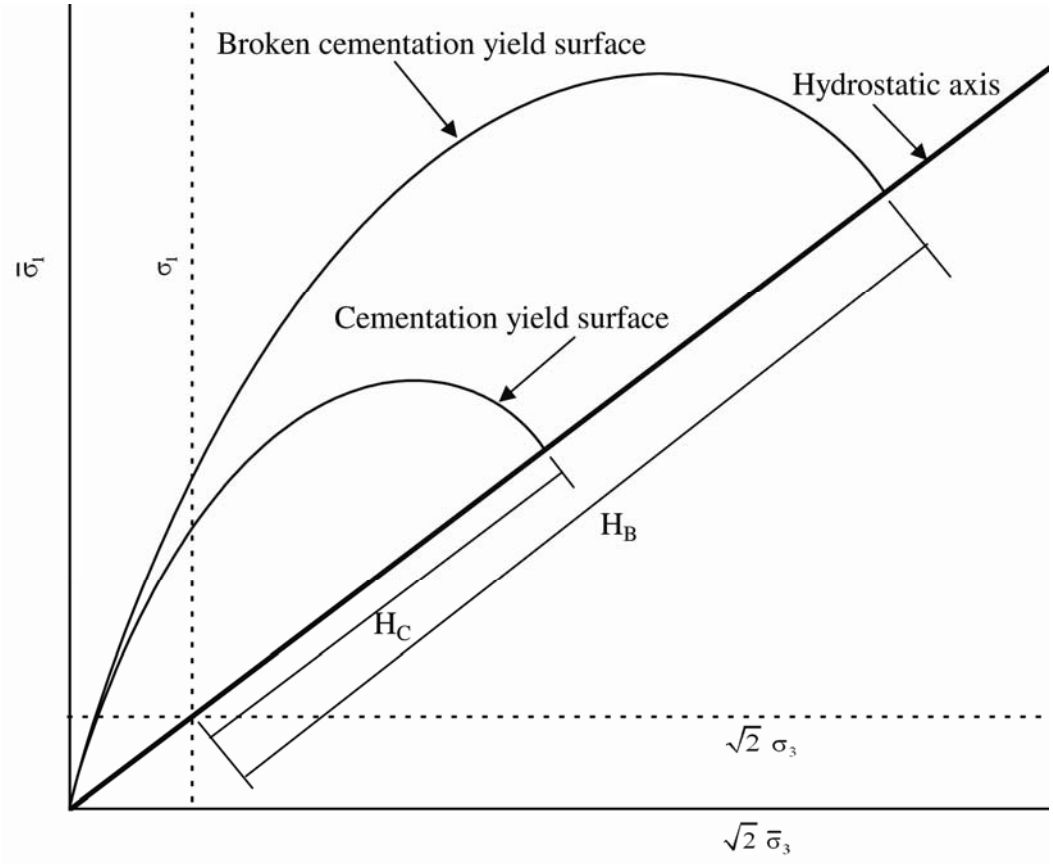

Figure 7.25: Definition of parameters H_C and H_B.

Table 7.3: Parameters determined for The Single Hardening Model.

Parameter	Vertical	Horizontal	Vertical	Horizontal
Stage	II	II	III	III
Elastic, initial				
ν	0.11	0.11	0.11	0.11
M	1170	1170	1170	1170
λ	0.20	0.20	0.20	0.20
Elastic, unloading-reloading				
ν	0.16	0.16	0.27	0.27
M	2780	2780	1055	1055
λ	0.26	0.26	0.35	0.35
Translation of coordinate system				
a	1.95	1.95	0	0
Failure				
η_1	950	810	950	810
m	0.78	0.78	0.78	0.78
Residual strength				
η_R	415	210	415	210
m_R	0.64	0.48	0.64	0.48
Hardening				
C	$7.8 \cdot 10^{-10}$	$7.8 \cdot 10^{-10}$	$7.8 \cdot 10^{-10}$	$7.8 \cdot 10^{-10}$
p	2.41	2.41	2.41	2.41
Yield function				
h	0.31	0.27	0.31	0.27
α	1.00	1.00	1.00	1.00
Plastic potential function				
μ	2.64	2.64	2.64	2.64
b	0.0007	0.0007	0.0007	0.0007
Initial yield surface				
H_C	42.4	42.4	42.4	42.4
H_B	139.2	139.2	139.2	139.2

8. Modeling the Behavior of Artificial Cross-Anisotropic Sandstone

The modeling of the behavior of artificial cross-anisotropic sandstone takes place in two steps. First, the vertical and horizontal directions are treated as two individual soils, and the focus on the modeling is on capturing the transition from brittle to ductile behavior. Later, the two results from the two directions are combined into one soil with cross-anisotropic behavior. This is done with the cross-anisotropic extension to The Single Hardening Model.

8.1 Cementation and Degradation of Cementation

The cementation is modeled using translation of the stress space along the hydrostatic axis. As the cohesion gets reduced during loading, the stress space moves back towards the location of the uncemented soil. This concept was used by Nova et al. (2003) to model the degradation of the soil structure. In this study it is applied to the yield surface, the plastic potential surface, the failure surface, and the surface of constant elastic modulus.

The stresses in the translated stress space are used as input when calculating the strains. As the cohesion gets reduced the parameter ‘a’ decreases towards zero. This is illustrated in Figure 8.1, where two stress paths during triaxial loading are shown in the triaxial plane of the translated coordinate system.

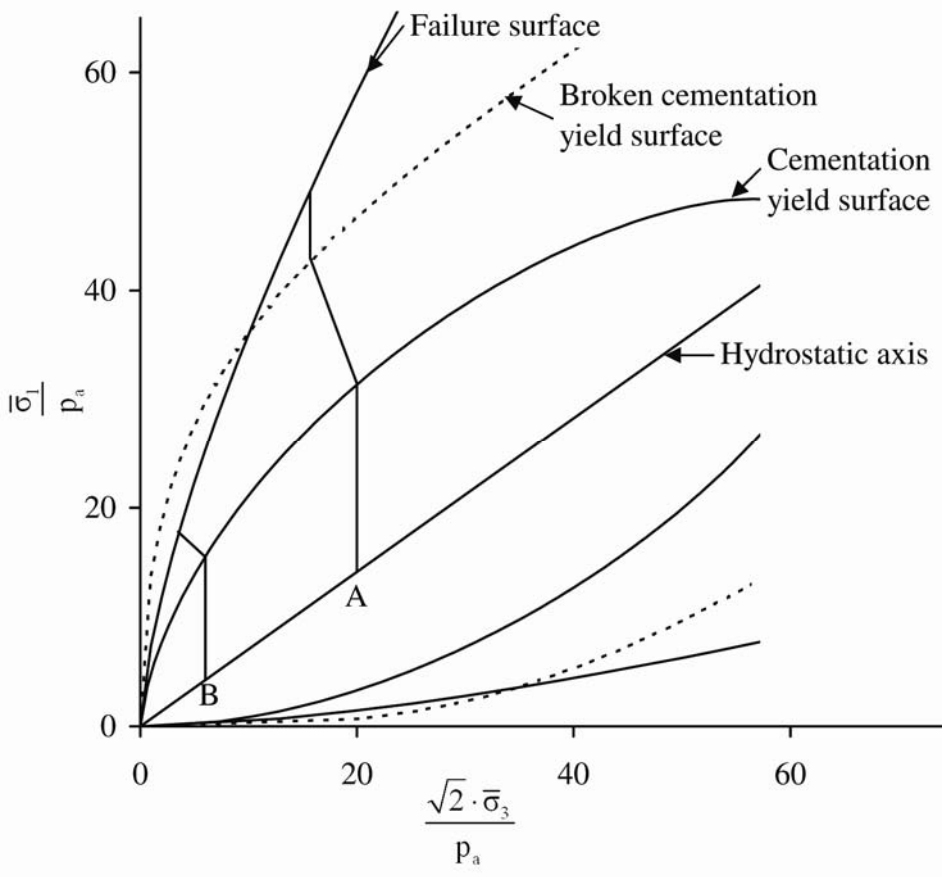

Figure 8.1: The stress paths followed during triaxial loading in the translated coordinate system.

In Figure 8.1, stress path A represents intermediate confining pressures, where the cohesion gets reduced to zero before failure. Inside the cementation yield surface, the behavior is elastic, and the parameter ‘a’ remains constant. Between the initial cementation yield surface and the broken cementation yield surface the cohesion is reduced to zero, which is equivalent to changing the direction of the stress path. After the cementation is broken, the stress path change direction again and become similar to a triaxial test with a lower confining pressure.

Stress path B in Figure 8.1, represents triaxial tests at low confining pressures, and starts with elastic loading inside the cementation yield surface where the parameter ‘a’ is constant. Between the initial cementation yield surface and the broken cementation yield surface the cohesion gets reduced until failure. However, for stress path B, the failure surface is inside the broken cementation yield surface and as a result, there is cohesion left at failure.

8.1.1 Cementation Yield Surface

The shape of the initial cementation yield surface in The Single Hardening Model can be captured using the yield surface parameters determined for the yield surface of constant plastic work.

8.1.2 Elastic Behavior

As described in Chapter 4, the behavior inside the cementation yield surface can be characterized as purely elastic. However, in the triaxial tests, the initial tangent modulus

and the unloading-reloading modulus were different. The unloading-reloading cycles indicated much stiffer material than the initial tangent modulus. To be able to successfully predict the stress-strain behavior inside the cementation yield surface using only elastic strains, the elastic parameters determined from the initial loading are used.

The elastic parameters change as the bonds in the cementation starts breaking. After failure, much of the cementation is broken, and the elastic properties have changed. However, the elastic strains after failure are significantly smaller than the plastic strains and the difference in the predictions by changing the elastic parameters are insignificant. Therefore, only the initial set of elastic parameters is applied in the predictions.

Finally, as discussed in section 7.2 during the parameter determination for the elastic parameters, the difference between the elastic parameters in the vertically and horizontally cored specimens are very small. As a result, the isotropic elastic model associated with The Single Hardening Model can successfully predict the elastic behavior.

8.2 Cross-Anisotropy

The cross-anisotropic formulation of The Single Hardening Model employs a microstructural tensor to describe the anisotropy. No measurement of cross-anisotropic microstructural features such as distribution of voids, fissures, grain contacts or cementation is required. The failure surface, the yield surface and the plastic potential surface are all formulated in terms of the stress state and a microstructural tensor derived from the observed behavior in vertically and horizontally cored specimens. This means that the tensor is a measure of the microstructural cross-anisotropy derived from the

macroscopic behavior. The formulation used here, follows the work of Pietruszczak and Mroz (2000).

To formulate the cross-anisotropic microstructural tensor, a vector defining the loading direction with respect to the microstructural bedding planes is introduced. The generalized loading vector L_i is shown in equation (8.1):

$$L_i = L_x \cdot e_i^{(x)} + L_y \cdot e_i^{(y)} + L_z \cdot e_i^{(z)} = (L_x, L_y, L_z) \tag{8.1}$$

where L_x, L_y, and L_z are defined in equation (8.2), (8.3), and (8.4) as the magnitudes of resultant of stresses acting on a small cube with sides aligned with the direction of the microstructural anisotropy. The unit vectors $e_i^{(x)}$, $e_i^{(y)}$, $e_i^{(z)}$ are defined by the coordinate axes. This is illustrated in Figure 8.2, where the coordinate system and the stresses acting on a small cube are shown. The magnitudes of the resultant of the stresses are:

$$L_x = \sqrt{\sigma_{xx}^2 + \tau_{xy}^2 + \tau_{xz}^2} \tag{8.2}$$

$$L_y = \sqrt{\tau_{xy}^2 + \sigma_{yy}^2 + \tau_{yz}^2} \tag{8.3}$$

$$L_z = \sqrt{\tau_{zx}^2 + \tau_{zy}^2 + \sigma_{zz}^2} \tag{8.4}$$

in which the direction of the normal and shear stresses (σ_{xx}, σ_{yy}, σ_{zz}, τ_{xy}, τ_{yz}, τ_{zx}) are defined in Figure 8.2 where the first suffix refers to the direction of the normal to the plane on which the stress act, and the second suffix refers to the direction of the stress component itself. The loading direction is defined by a unit vector relative to the material axis:

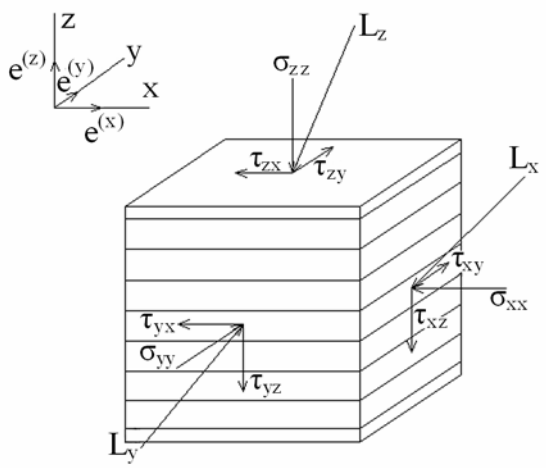

Figure 8.2: Loading direction relative to microstructural bedding planes in the soil.

$$\left(\ell_x,\ \ell_y,\ \ell_z\right) = \frac{(L_x, L_y, L_z)}{\sqrt{L_x^2 + L_y^2 + L_z^2}} \tag{8.5}$$

where L_x, L_y, and L_z are defined in equation (8.2), (8.3), and (8.4), respectively.

Following the formulation of the anisotropic failure surface suggested by Pietruszczak and Mroz (2000), the general anisotropic version of an isotropic function in The Single Hardening Model is shown in equation (8.6).

$$f = f_0 \cdot \left[1 + \Omega_{ij} \cdot \ell_i \cdot \ell_j\right] \tag{8.6}$$

where f is a function of stresses describing either the failure surface or the yield surface. The value of the function f changes with the loading direction relative to the microstructural anisotropy (ℓ_i and ℓ_j), and f_0 is the average value of the function f over a sphere. The variation from the sphere is described by Ω_{ij}.

According to Pietruszczak and Mroz (2000), equation (8.6) can be expressed as:

$$f = f_0 \cdot \left[1 + \Omega_1 \cdot \ell_x^2 + \Omega_2 \cdot \ell_y^2 + \Omega_3 \cdot \ell_z^2\right] \tag{8.7}$$

where Ω_1, Ω_2, and Ω_3 refers to the variation in the directions of ℓ_x, ℓ_y, and ℓ_z, defined in equation (8.5). Due to symmetry, the cross-anisotropic formulation of equation (8.7) reduce to equation (8.8). According to Pietruszczak and Mroz (2000), the cross-anisotropy yields the following conditions: $\Omega_1 = \Omega_2$, $\Omega_1 + \Omega_2 + \Omega_3 = 0$, and $\ell_x^2 + \ell_y^2 + \ell_z^2 = 1$, resulting in equation (8.8).

$$f = f_0 \cdot \left[1 + \Omega_1 \cdot \left(1 - 3 \cdot \ell_z^2\right)\right] \tag{8.8}$$

8.2.1 Cross-Anisotropic Failure Surface

To model the failure in cross-anisotropic sandstone, the procedure outlined by Lade (2007, 2008) is followed. The isotropic failure criterion in The Single Hardening Model is presented in equation (8.9) and rearranged in equation (8.10) where the parameters η_1 and m are on the right hand side in the equation.

$$f_n = \left(\frac{I_1^3}{I_3} - 27\right)\left(\frac{I_1}{p_a}\right)^m = \eta_1 \tag{8.9}$$

in which I_1 and I_3 are the first and third stress invariant, η_1 and m are non-dimensional parameters, and p_a is atmospheric pressure in the same units as the stresses used in the calculations of I_1 and I_3. Rearranging equation (8.9) yields:

$$f_n = \left(\frac{I_1^3}{I_3} - 27\right) = \eta_1 \cdot \left(\frac{p_a}{I_1}\right)^m \tag{8.10}$$

The value of the right hand side of equation (8.10) differs depending on the loading direction due to the difference in the parameters η_1 in vertical and horizontal direction. The parameter m is considered independent of the loading direction, which in section 7.1 was found to be a reasonable assumption. Combining the right hand side of equation (8.10) with the cross-anisotropic extension in equation (8.8) yields:

$$f = \eta_1 \cdot \left(\frac{p_a}{I_1}\right)^m = f_{0F}\left[1 + \Omega_{1F} \cdot \left(1 - 3 \cdot \ell_z^2\right)\right] \tag{8.11}$$

The sub-parameter f_{0F} is the average value of the left hand side over a sphere, and Ω_{1F} describes the variation from the sphere depending on the loading direction ℓ_z. If Ω_{1F} becomes equal to zero, the material behaves isotropically. The suffix F in f_{0F} and Ω_{1F}

indicates the sub-parameters are related to the failure criterion, since similar sub-parameters are derived for the yield criterion. The input required to determine the cross-anisotropic failure surface is a vertical and a horizontal set of failure parameters (η_{1v}, η_{1h}, and m). The cross-anisotropic failure criterion combines the failure surface in vertical direction with the failure surface in horizontal direction into one smooth failure surface. This is illustrated in Figure 8.3 where the cross-anisotropic failure surface is shown in the octahedral plane along with failure surfaces representing vertical and horizontal directions. The cross-anisotropic failure surface is symmetrical around the z-axis. In the z-direction and the y-direction, the cross-anisotropic failure surface is equal to the failure surfaces in vertical and horizontal direction, respectively. The transition from vertical to horizontal takes place in sector I at b-values greater than 0.5 and in most of sector II. The definition of b is show in equation (8.13). In sector III, the cross-anisotropic failure surface is almost identical to the failure surface in horizontal direction. However, the cross-anisotropic failure surface is slightly within the horizontal failure surface.

The parameter determination of the sub-parameters f_{oF} and Ω_{1F} are incorporated into the prediction program. This is done because the degree of anisotropy changes with I_1 and needs to be determined for each loading step.

According to Lade (2007, 2008), the loading direction ℓ_z can be expressed as a function of the major principal stress ratio R and the b-value, defined in equation (8.12) and (8.13), respectively.

$$R = \frac{\sigma_1}{\sigma_3} \tag{8.12}$$

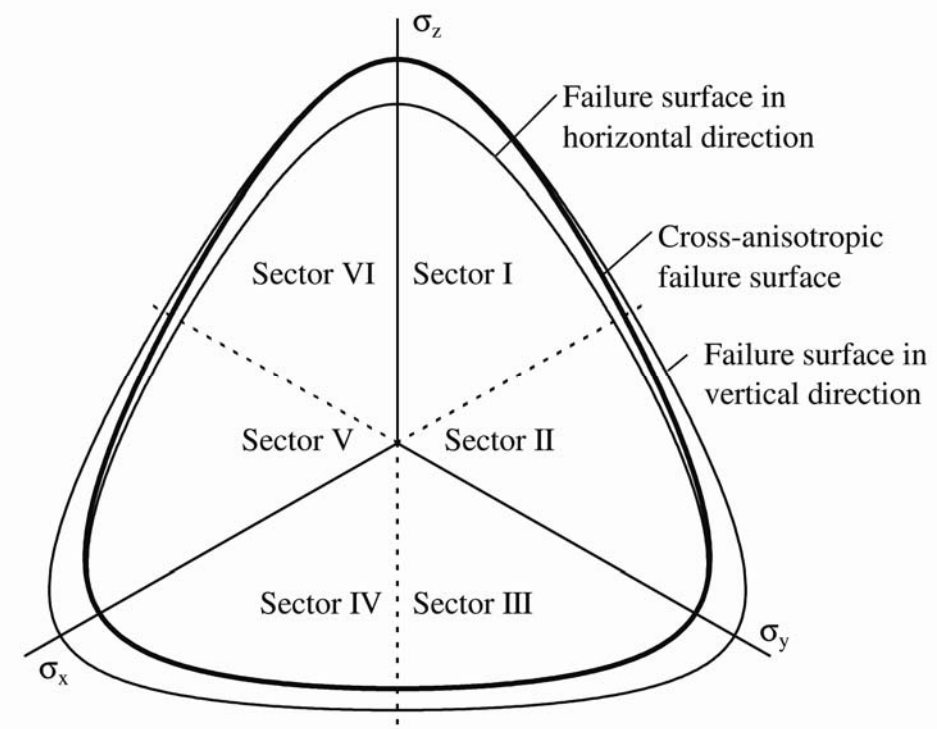

Figure 8.3: The shape of the cross-anisotropic failure surface varies between the vertical and horizontal failure surfaces in the octahedral plane.

$$b = \frac{\sigma_2 - \sigma_3}{\sigma_1 - \sigma_3} \tag{8.13}$$

in which the σ_1, σ_2, and σ_3 is the major, intermediate and minor principal stresses. The loading direction for triaxial compression in sector I (vertically cored specimens, b = 0) ℓ_{zv} is expressed in equation (8.14) and the loading direction for triaxial compression in sector II and sector III (horizontally cored specimens, b = 0) ℓ_{zh} is expressed in equation (8.15).

$$\ell_{zv}^2 = \frac{R^2}{R^2 + 2} \tag{8.14}$$

$$\ell_{zh}^2 = \frac{1}{R^2 + 2} \tag{8.15}$$

In which R is the major principal stress ratio defined in equation (8.12). Furthermore, the left hand side of the failure criterion in equation (8.10) can also be expressed in terms of the major principal stress ratio R. This is shown in equation (8.16):

$$f_n = \frac{(R+2)^3}{R} - 27 = \eta_1 \cdot \left(\frac{p_a}{I_1}\right)^m \tag{8.16}$$

Solving equation (8.16) with respect to R yields the major principal stress ratio. This is done using the values of the parameters η_1 and m for vertical and horizontal specimens. Once the major principal stress ratio R is determined, the loading directions corresponding to vertical and horizontal directions can be calculated from equation (8.14) and (8.15). Finally, the parameter Ω_{1F} can be calculated using equation (8.17):

$$\Omega_{1F} = \frac{f_{nv} - f_{nh}}{f_{nh} \cdot \left(1 - 3 \cdot \ell_{zv}^2\right) - f_{nv} \cdot \left(1 - 3 \cdot \ell_{zh}^2\right)} \tag{8.17}$$

in which f_{nv} and f_{nh} are the left hand side of equation (8.16) for the vertical and horizontal direction, respectively. Once the parameter Ω_{1F} is determined, the parameter f_{0F} can be determined from equation (8.18):

$$f_{0F} = \frac{f_{nv}}{1+\Omega_{1F}\cdot\left(1-3\cdot\ell_{zv}^2\right)} \tag{8.18}$$

8.2.2 Cross-Anisotropic Yield Surface

The isotropic formulation of the yield function is shown in equation (8.19):

$$f_p' = \left[\psi_1\cdot\frac{I_1^3}{I_3} - \frac{I_1^2}{I_2}\right]\left[\frac{I_1}{p_a}\right]^h\cdot e^q \tag{8.19}$$

in which I_1, I_2, and I_3 are the first, second and third stress invariants. The parameter ψ_1 is a function of the parameter m, which is determined to be independent of the loading direction. The parameter h varies with loading direction, and two values are known, h_v and h_h corresponding to the vertical and horizontal directions. The parameter q is a function of the stress level, S and is defined in equation (8.23). With the two values of h, the cross-anisotropic formulation of the yield function becomes:

$$f_p^{'} = \left[\psi_1\cdot\frac{I_1^3}{I_3} - \frac{I_1^2}{I_2}\right]\left[\frac{I_1}{p_a}\right]^{h_0\cdot\left[1+\Omega_{1Y}\cdot\left(1-3\cdot\ell_z^2\right)\right]}\cdot e^q \tag{8.20}$$

in which h_0 is the average value of the parameter h, and the parameter Ω_{1Y} describes the variation of h_0 depending on the loading direction ℓ_z. The vertical and horizontal values of the parameter h are determined at failure. The loading direction ℓ_z at failure is known

from the determination of the cross-anisotropic failure parameters, resulting in determination of the yield parameter Ω_{1Y} from equation (8.21):

$$\Omega_{1Y} = \frac{h_v - h_h}{h_h\left(1-3\cdot\ell_{zv}^2\right) - h_v\left(1-3\cdot\ell_{zh}^2\right)} \tag{8.21}$$

Once the parameter Ω_{1Y} is known, the parameter h_0 can be calculated as:

$$h_0 = \frac{h_v}{1+\Omega_{1Y}\cdot\left(1-3\cdot\ell_{zv}^2\right)} \tag{8.22}$$

Due to q being a function of the stress level, S the shape of the yield function in The Single Hardening Model, depends on the shape of the failure surface. This means the cross-anisotropic yield surface is a function of the cross-anisotropic failure surface. The variation of q with S is shown in equation (8.23).

$$q = \frac{\alpha\cdot S}{1 - \left(1 - \alpha\right)\cdot S} \tag{8.23}$$

where α is a parameter (determined to be equal in horizontal and vertical direction in section 7.4) and S is the stress level determined from the cross-anisotropic version of the failure surface:

$$S = \frac{f_{n0}}{\eta_0\cdot\left[1+\Omega_{1F'}\cdot\left(1-3\cdot\ell_z^2\right)\right]} = \frac{\left[\frac{I_1^3}{I_3} - 27\right]}{\eta_0\cdot\left[1+\Omega_{1F}\cdot\left(1-3\cdot\ell_z^2\right)\right]} \tag{8.24}$$

in which I_1 and I_3 are the first and third stress invariants, ℓ_z is the loading direction, η_0 and Ω_{1F} are cross-anisotropic failure parameters, all described in section 8.2.1.

8.2.3 Cross-Anisotropic Hardening

During hardening, the value of f_p varies on a yield surface, depending on the loading direction. For a constant amount of plastic work the value of f_p'' can be expresses as in equation (8.20):

$$f_p'' = \left[\psi_1 \cdot 27 + 3\right]\left[\frac{W_p}{C \cdot p_a}\right]^{\frac{h_0}{p}\cdot\left[1+\Omega_{1Y}\cdot\left(1-3\cdot\ell_z^2\right)\right]} \tag{8.25}$$

in which ψ_1 is a function of the parameter m, W_p is the plastic work, and C and p are parameters in the isotropic hardening function. The cross-anisotropic parameters are h_0 and Ω_{1Y}, where h_0 is the average value of the parameter h, and the parameter Ω_{1Y} describes the variation of h_0 depending on the loading direction ℓ_z.

The work hardening relation is shown in Figure 8.4 for the cross-anisotropic version of The Single Hardening Model. The work hardening relation for vertically and horizontally cored specimens is shown. Depending on the loading direction, the value of f_p'' varies for constant amount of plastic work. This is illustrated for $W_p/p_a = 2.0$. The cross-anisotropic version of work hardening relation corresponds to the value of $h = h_0$.

8.3 Predictions

The cross-anisotropic version of The Single Hardening Model presented here, is described and implemented into a program capable of predicting strains in drained true triaxial tests and torsion shear tests. The tests performed on artificial cross-anisotropic sandstone can only be used for back prediction, as the tests were performed in the vertical and horizontal triaxial plane. True triaxial tests were not performed on the cross-

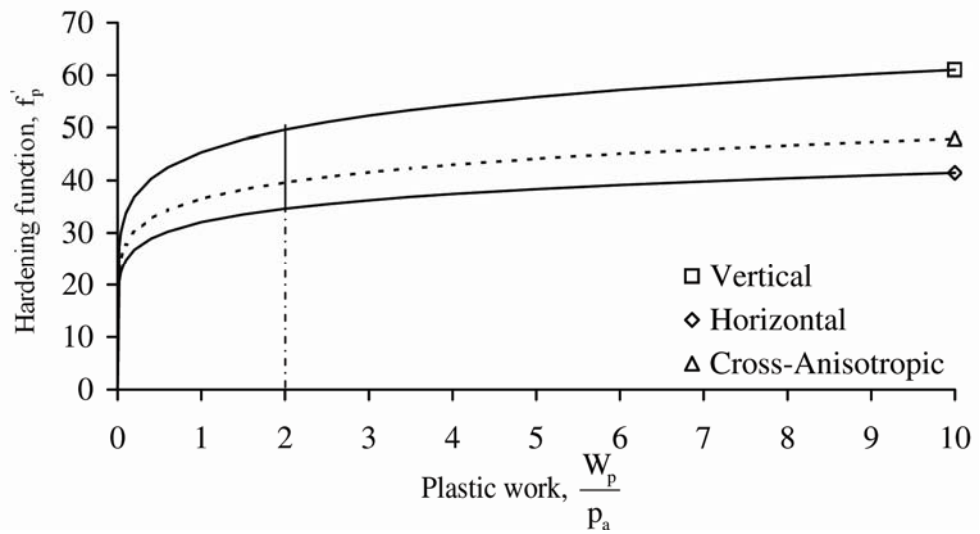

Figure 8.4: Work hardening relation for cross-anisotropic version of The Single Hardening Model.

anisotropic cemented sand, so exercising the model outside the vertically and horizontally cored specimens is not possible.

The results of the predictions are shown in Figure 8.5 for the vertically cored specimens and in Figure 8.6 for the horizontally cored specimens. At low confining pressures, the behavior predicted by The Single Hardening Model shows too much major principal strain near failure. This is to be expected, as the failure mechanism was splitting, and Single Hardening Model assumes smooth peak failure.

Generally, The Single Hardening Model captures the stress-strain behavior and volume change up to approximately $\sigma_3/p_a = 20$. This is the range where the parameters are determined and the model predicts the behavior with good accuracy. As the confining pressure increases, the state of the soil changes and The Single Hardening Model can not predict the observed behavior with accuracy. A new set of parameters would be required to predict the behavior at high confining pressures, where most of the cementation is broken.

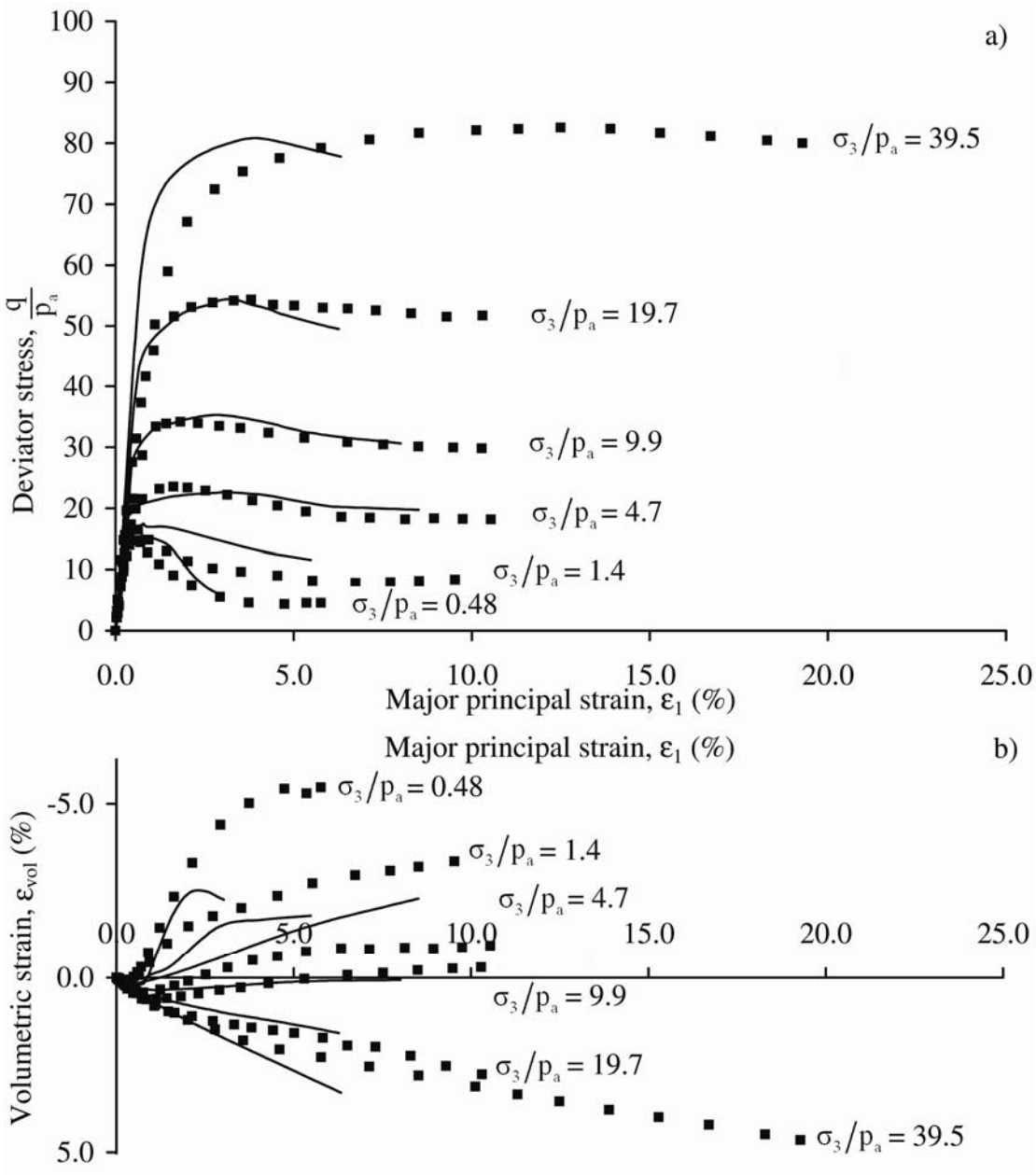

Figure 8.5: Observed and predicted behavior of specimens cored in vertical direction. a) Stress-stain relation. b) Volume change relation.

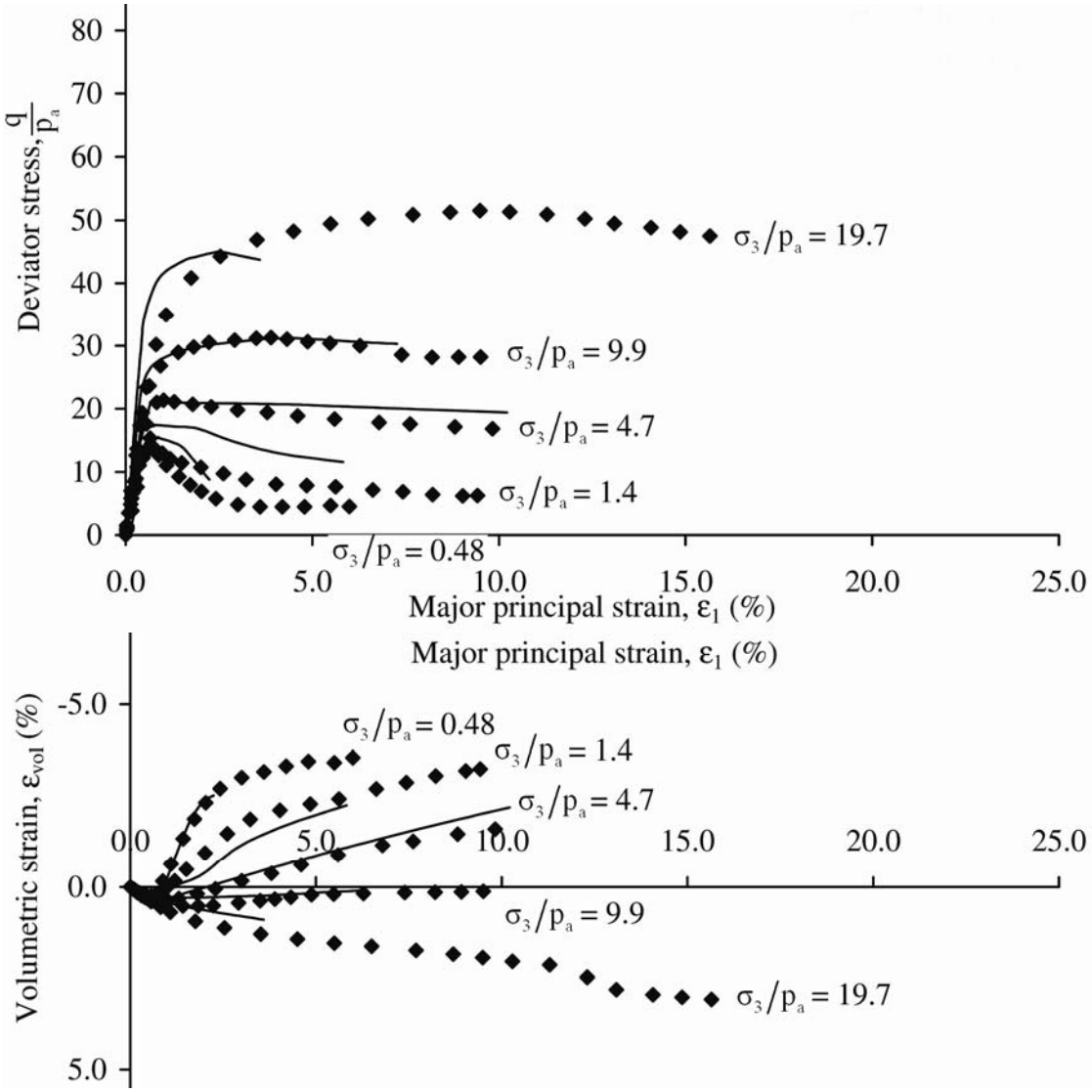

Figure 8.6: Observed and predicted behavior of specimens cored in horizontal direction. a) Stress-stain relation. b) Volume change relation.

9. Summary and Conclusions

This investigation has highlighted features caused by cementation and cross-anisotropy in the behavior of sandstone. Furthermore the behavior of the cross-anisotropic sandstone was successfully modeled using an initial cementation yield surface and a cross-anisotropic extension to The Single Hardening Model.

9.1 Review of The Single Hardening Model

The review of The Single Hardening Model resulted in a new plastic potential function, improving the predictions of the volumetric strains at high confining pressures. In the new plastic potential function, the parameter ψ_2 is replaced by the constant $\psi_{2,0}$ and by a function of the first stress invariant and a new parameter b.

The problems rising from ambiguous yield function parameters previously determined for loose silty sand has been resolved using a new parameter determination procedure for the work hardening parameters. The problem arises when the work produced during the isotropic compression test only represents a fraction of the work produced during the triaxial compression test. Using the new procedure, yield parameters obtained for loose silty sand are unambiguous and back predicting the behavior during triaxial compression shows good agreement between the predictions and the test results.

A new softening function developed to ensure a smooth transition from hardening to softening is presented. The new softening function takes over from the hardening relation prior to failure and controls the work until the residual strength is reached. In

cohesionless soil the residual strength corresponds to the critical state line, which is described by a surface similar to the failure surface. However, only one new parameter, η_R is needed to describe the residual strength surface. All other parameters in the new softening function can be determined as functions of known parameters.

Finally, the enhanced version of The Single Hardening Model was used to predict torsion shear tests performed on Santa Monica Beach Sand. There was an overall agreement between the predictions and the experiments. Stress paths with different combinations of triaxial loading and shearing all yielded good agreement between the predictions and the measured strains.

9.2 Experiments on Sandstone

Hollow cylinder torsion shear tests performed on artificially cemented sand revealed truly elastic behavior inside the cementation yield surface. By applying a combination of normal and shear stresses the elastic nature of the material was unveiled by the strains. The response to an increase or decrease in normal stresses was purely normal strains and the response to an increase or decrease in shear stresses was purely shear strains, indicating truly elastic behavior. Furthermore, the isotropic elastic parameters representing the material were determined.

The isotropic compression tests on artificial cross-anisotropic sandstone revealed the location of the cementation yield surface on the hydrostatic axis. The shape of the cementation yield surface was determined from the triaxial compression tests.

After completion of the isotropic tests, the specimens were used to determine the degree of bond breaking taking place during isotropic compression. The tests showed a

significant drop in Brazilian tensile strength after preloading the specimens isotropically, whereas the results from the triaxial tests were ambiguous.

The failure surface was determined from triaxial compression tests and consisted of three distinctive sections. At low confining pressures, where the cementation yield surface was close to the failure surface, the strength of the sandstone increased in a way similar to an overconsolidated soil. However, the cementation yield surface did not become the failure surface, as plastic deformation was observed prior to failure. At intermediate confining pressures, the failure surface was found to curve towards the critical state line, which was reached at high confining pressures. However, due to the large reduction in void ratio taking place during the loading prior to failure, a tendency towards a critical state line with increasing friction angle was observed.

The residual strength envelope at low and intermediate confining pressures was curved, and did therefore not correspond to the critical state line determined at high confining pressures. This is most likely due to segments of the specimens still consisting of grains cemented together and acting as larger particles.

At low confining pressures, where splitting was observed as the failure mechanism, the horizontally cored specimens were the strongest. At intermediate confining pressures, the vertically cored specimens were the strongest, and at the critical state line, the cross-anisotropy had almost vanquished, since much of the original structure was destroyed prior to failure.

The elastic behavior followed the same trends as found in previously published results on cemented soils. With cementation intact, the sandstone behaved much stiffer

than after the cementation was broken. Furthermore, as the cementation breaks down, the material becomes more influenced by the confining pressure. The anisotropy index in the cemented state revealed a stiffer material in vertical direction than in horizontal direction. Finally, the elastic anisotropy was found to decrease as the bonds in the cementation was breaking down.

9.3 Modeling the Behavior of Cross-Anisotropic Sandstone

To capture the behavior due to cementation the stress space was translated back along the hydrostatic axis and an initial cementation yield surface was defined. Inside the initial cementation yield surface the behavior of the sandstone was modeled as elastic. The breaking of the bonds in the cementation was captured by translating the stress space back towards the position of the uncemented sand. The rate of the translation was controlled by a second yield surface relating to the stress conditions where the cohesion was reduced to zero.

The parameter determination for The Single Hardening Model revealed that the elastic behavior in vertical and horizontal direction could be successfully modeled with one set of isotropic parameters. Though elastic cross-anisotropy was observed, the elastic strains were significantly smaller than the plastic strains and the precision gained by using the cross-anisotropic parameters was insignificant. Similar observations were made for the plastic potential parameters, where the vertically and horizontally cored specimens yielded almost identical results.

It was found that the cross-anisotropic behavior in the artificially cemented sandstone could be captured by The Single Hardening Model, if the failure criterion and

the yield function were modified by a microstructural tensor. By defining the loading direction with respect to the cross-anisotropic planes, it became possible to capture the different behavior in the different loading directions.

Appendix A: Condition of Irreversibility and Parameter Determination for Plastic Potential Function

Condition of Irreversibility

The condition of irreversibility and the parameter determination are demonstrated on the logarithmic version of the plastic potential function:

$$g_p = \left[\Psi_1 \cdot \frac{I_1^3}{I_3} - \frac{I_1^2}{I_2} + \psi_{2,0} + b \cdot \ln\left(\frac{I_1}{p_a} + 1\right)\right]\left[\frac{I_1}{p_a}\right]^{\mu} \tag{A.1}$$

By differentiating with respect to σ_{xx}:

$$\begin{aligned}\frac{\partial g_p}{\partial \sigma_{xx}} = & \left[\psi_1 \cdot \frac{I_1^3}{I_3} - \frac{I_1^2}{I_2} + \psi_{2,0} + b \cdot \ln\left(\frac{I_1}{p_a} + 1\right)\right] \cdot \mu \cdot \left[\frac{I_1}{p_a}\right]^{\mu-1} \cdot \frac{1}{p_a} \\ & + \left[\psi_1 \cdot \frac{3 \cdot I_1^2 \cdot I_3 - I_1^3 \cdot \left(\sigma_{yy} \cdot \sigma_{zz} - \tau_{yz} \cdot \tau_{zy}\right)}{I_3^2}\right. \\ & \left. - \frac{2 \cdot I_1 \cdot I_2 + I_1^2 \cdot \left(\sigma_{yy} + \sigma_{zz}\right)}{I_2^2} + \frac{b}{I_1 + p_a}\right] \cdot \left[\frac{I_1}{p_a}\right]^{\mu}\end{aligned} \tag{A.2}$$

Rearranging:

$$\begin{aligned}\frac{\partial g_p}{\partial \sigma_{xx}} = & \left[\frac{I_1}{p_a}\right]^{\mu} \cdot \left[\mu \cdot \psi_1 \cdot \frac{I_1^2}{I_3} - \mu \cdot \frac{I_1}{I_2} + \mu \cdot \psi_{2,0} \cdot \frac{1}{I_1} + \mu \cdot \frac{b}{I_1} \ln\left(\frac{I_1}{p_a} + 1\right)\right. \\ & + 3 \cdot \Psi_1 \cdot \frac{I_1^2}{I_3} - \psi_1 \cdot \frac{I_1^3}{I_3^2} \cdot \left(\sigma_{yy} \cdot \sigma_{zz} - \tau_{yz} \cdot \tau_{zy}\right) - 2 \cdot \frac{I_1}{I_2} - \frac{I_1^2}{I_2^2} \cdot \left(\sigma_{yy} + \sigma_{zz}\right) \\ & \left. + \frac{b}{p_a + I_1}\right]\end{aligned} \tag{A.3}$$

Rearranging again:

$$\frac{\partial g_p}{\partial \sigma_{xx}} = \left[\frac{I_1}{p_a}\right]^{\mu} \cdot \left[\psi_1 \cdot (\mu + 3) \cdot \frac{I_1^2}{I_3} - (\mu + 2) \cdot \frac{I_1}{I_2} + \mu \cdot \left(\psi_{2,0} + b \cdot \ln\left(\frac{I_1}{p_a} + 1\right)\right) \cdot \frac{1}{I_1} + \frac{b}{I_1 + p_a} - \frac{I_1^2}{I_2^2} \cdot (\sigma_{yy} + \sigma_{zz}) - \psi_1 \cdot \frac{I_1^3}{I_3^2} \cdot (\sigma_{yy} \cdot \sigma_{zz} - \tau_{yz} \cdot \tau_{zy})\right] \quad (A.4)$$

Rearranging again:

$$\frac{\partial g_p}{\partial \sigma_{xx}} = \left[\frac{I_1}{p_a}\right]^{\mu} \cdot \left[G - \frac{I_1^2}{I_2^2} \cdot (\sigma_{yy} + \sigma_{zz}) - \psi_1 \cdot \frac{I_1^3}{I_3^2} \cdot (\sigma_{yy} \cdot \sigma_{zz} - \tau_{yz}^2)\right] \quad (A.5)$$

where

$$G = \psi_1 \cdot (\mu + 3) \cdot \frac{I_1^2}{I_3} - (\mu + 2) \cdot \frac{I_1}{I_2} + \mu \cdot \left(\psi_{2,0} + b \cdot \ln\left(\frac{I_1}{p_a} + 1\right)\right) \cdot \frac{1}{I_1} + \frac{b}{I_1 + p_a} \quad (A.6)$$

In a similar way the differentiation with respect to σ_{yy} and σ_{zz} gives:

$$\frac{\partial g_p}{\partial \sigma_{yy}} = \left[\frac{I_1}{p_a}\right]^{\mu} \cdot \left[G - \frac{I_1^2}{I_2^2} \cdot (\sigma_{zz} + \sigma_{xx}) - \psi_1 \cdot \frac{I_1^3}{I_3^2} \cdot (\sigma_{zz} \cdot \sigma_{xx} - \tau_{zx}^2)\right] \quad (A.7)$$

$$\frac{\partial g_p}{\partial \sigma_{zz}} = \left[\frac{I_1}{p_a}\right]^{\mu} \cdot \left[G - \frac{I_1^2}{I_2^2} \cdot (\sigma_{xx} + \sigma_{yy}) - \psi_1 \cdot \frac{I_1^3}{I_3^2} \cdot (\sigma_{xx} \cdot \sigma_{yy} - \tau_{xy}^2)\right] \quad (A.8)$$

By differentiating the plastic potential function with respect to τ_{yz}, τ_{zx} and τ_{xy}:

$$\frac{\partial g_p}{\partial \tau_{yz}} = \left[\frac{I_1}{p_a}\right]^{\mu} \cdot \left[\frac{I_1^2}{I_2^2} \cdot \tau_{yz} - \psi_1 \cdot \frac{I_1^3}{I_3^2} \cdot (\tau_{xy} \cdot \tau_{zx} - \sigma_{xx} \cdot \tau_{yz})\right] \quad (A.9)$$

$$\frac{\partial g_p}{\partial \tau_{zx}} = \left[\frac{I_1}{p_a}\right]^{\mu} \cdot \left[\frac{I_1^2}{I_2^2} \cdot \tau_{zx} - \psi_1 \cdot \frac{I_1^3}{I_3^2} \cdot (\tau_{xy} \cdot \tau_{yz} - \sigma_{yy} \cdot \tau_{zx})\right] \quad (A.10)$$

$$\frac{\partial g_p}{\partial \tau_{xy}} = \left[\frac{I_1}{p_a}\right]^{\mu} \cdot \left[\frac{I_1^2}{I_2^2} \cdot \tau_{xy} - \psi_1 \cdot \frac{I_1^3}{I_3^2} \cdot \left(\tau_{yz} \cdot \tau_{zx} - \sigma_{zz} \cdot \tau_{xy}\right)\right] \tag{A.11}$$

The flow rule:

$$d\varepsilon_{ij}^p = d\lambda_p \cdot \frac{\partial g_p}{\partial \sigma_{ij}} \tag{A.12}$$

When applying the flow rule, the engineering shear strains are used, resulting in:

$$\begin{Bmatrix} d\varepsilon_{xx}^p \\ d\varepsilon_{yy}^p \\ d\varepsilon_{zz}^p \\ d\gamma_{yz}^p \\ d\gamma_{zx}^p \\ d\gamma_{xy}^p \end{Bmatrix} = d\lambda_p \cdot \left[\frac{I_1}{p_a}\right]^{\mu} \cdot \begin{Bmatrix} G - \frac{I_1^2}{I_2^2} \cdot \left(\sigma_{yy} + \sigma_{zz}\right) - \psi_1 \cdot \frac{I_1^3}{I_3^2} \cdot \left(\sigma_{yy} \cdot \sigma_{zz} - \tau_{yz}^2\right) \\ G - \frac{I_1^2}{I_2^2} \cdot \left(\sigma_{zz} + \sigma_{xx}\right) - \psi_1 \cdot \frac{I_1^3}{I_3^2} \cdot \left(\sigma_{zz} \cdot \sigma_{xx} - \tau_{zx}^2\right) \\ G - \frac{I_1^2}{I_2^2} \cdot \left(\sigma_{xx} + \sigma_{yy}\right) - \psi_1 \cdot \frac{I_1^3}{I_3^2} \cdot \left(\sigma_{xx} \cdot \sigma_{yy} - \tau_{xy}^2\right) \\ 2 \cdot \frac{I_1^2}{I_2^2} \cdot \tau_{yz} - 2 \cdot \psi_1 \cdot \frac{I_1^3}{I_3^2} \cdot \left(\tau_{xy} \cdot \tau_{zx} - \sigma_{xx} \cdot \tau_{yz}\right) \\ 2 \cdot \frac{I_1^2}{I_2^2} \cdot \tau_{zx} - 2 \cdot \psi_1 \cdot \frac{I_1^3}{I_3^2} \cdot \left(\tau_{yz} \cdot \tau_{xy} - \sigma_{yy} \cdot \tau_{zx}\right) \\ 2 \cdot \frac{I_1^2}{I_2^2} \cdot \tau_{xy} - 2 \cdot \psi_1 \cdot \frac{I_1^3}{I_3^2} \cdot \left(\tau_{zx} \cdot \tau_{yz} - \sigma_{zz} \cdot \tau_{xy}\right) \end{Bmatrix} \tag{A.13}$$

The condition of irreversibility requires:

$$dW_p = \sigma_{ij} \cdot d\varepsilon_{ij}^p \geq 0 \tag{A.14}$$

Combining equation (A.14) with equation (A.12) gives:

$$dW_p = \sigma_{ij} \cdot d\lambda_p \cdot \frac{\partial g_p}{\partial \sigma_{ij}} \geq 0 \tag{A.15}$$

As $d\lambda_p$ is greater than zero, the condition of irreversibility reduces to:

$$\sigma_{ij} \cdot \frac{\partial g_p}{\partial \sigma_{ij}} \geq 0 \tag{A.16}$$

Where the left hand side becomes:

$$\begin{aligned}
\sigma_{ij}\cdot\frac{\partial g_p}{\partial \sigma_{ij}} \;=\; & \left[\frac{I_1}{p_a}\right]^{\mu}\cdot\left[G - \frac{I_1^2}{I_2^2}\cdot\left(\sigma_{yy}+\sigma_{zz}\right) - \psi_1\cdot\frac{I_1^3}{I_3^2}\cdot\left(\sigma_{yy}\cdot\sigma_{zz} - \tau_{yz}^2\right)\right]\cdot\sigma_{xx} \\
& + \left[\frac{I_1}{p_a}\right]^{\mu}\cdot\left[G - \frac{I_1^2}{I_2^2}\cdot\left(\sigma_{zz}+\sigma_{xx}\right) - \psi_1\cdot\frac{I_1^3}{I_3^2}\cdot\left(\sigma_{zz}\cdot\sigma_{xx} - \tau_{zx}^2\right)\right]\cdot\sigma_{yy} \\
& + \left[\frac{I_1}{p_a}\right]^{\mu}\cdot\left[G - \frac{I_1^2}{I_2^2}\cdot\left(\sigma_{xx}+\sigma_{yy}\right) - \psi_1\cdot\frac{I_1^3}{I_3^2}\cdot\left(\sigma_{xx}\cdot\sigma_{yy} - \tau_{xy}^2\right)\right]\cdot\sigma_{zz} \\
& + \left[\frac{I_1}{p_a}\right]^{\mu}\cdot\left[2\cdot\frac{I_1^2}{I_2^2}\cdot\tau_{yz} - 2\cdot\psi_1\cdot\frac{I_1^3}{I_3^2}\cdot\left(\tau_{xy}\cdot\tau_{zx} - \sigma_{xx}\cdot\tau_{yz}\right)\right]\cdot\tau_{yz} \\
& + \left[\frac{I_1}{p_a}\right]^{\mu}\cdot\left[2\cdot\frac{I_1^2}{I_2^2}\cdot\tau_{zx} - 2\cdot\psi_1\cdot\frac{I_1^3}{I_3^2}\cdot\left(\tau_{yz}\cdot\tau_{xy} - \sigma_{yy}\cdot\tau_{zx}\right)\right]\cdot\tau_{zx} \\
& + \left[\frac{I_1}{p_a}\right]^{\mu}\cdot\left[2\cdot\frac{I_1^2}{I_2^2}\cdot\tau_{xy} - 2\cdot\psi_1\cdot\frac{I_1^3}{I_3^2}\cdot\left(\tau_{zx}\cdot\tau_{yz} - \sigma_{zz}\cdot\tau_{xy}\right)\right]\cdot\tau_{xy}
\end{aligned} \tag{A.17}$$

Rearranging:

$$\begin{aligned}
\sigma_{ij}\cdot\frac{\partial g_p}{\partial \sigma_{ij}} \;=\; & \left[\frac{I_1}{p_a}\right]^{\mu}\cdot\left[G\cdot I_1 - \left(\sigma_{xx}\cdot\sigma_{yy}+\sigma_{zz}\cdot\sigma_{xx}+\sigma_{yy}\cdot\sigma_{zz}+\sigma_{xx}\cdot\sigma_{yy}\right.\right. \\
& \left. + \sigma_{zz}\cdot\sigma_{xx}+\sigma_{yy}\cdot\sigma_{zz} - 2\cdot\tau_{yz}^2 - 2\cdot\tau_{zx}^2 - 2\cdot\tau_{xy}^2\right)\cdot\frac{I_1^2}{I_2^2} \\
& - \psi_1\cdot\left(\sigma_{xx}\cdot\sigma_{yy}\cdot\sigma_{zz} - \sigma_{xx}\cdot\tau_{yz}^2 + \sigma_{xx}\cdot\sigma_{yy}\cdot\sigma_{zz} - \sigma_{yy}\cdot\tau_{zx}^2\right. \\
& \left.\left. + \sigma_{xx}\cdot\sigma_{yy}\cdot\sigma_{zz} - \sigma_{zz}\cdot\tau_{xy}^2 + 2\cdot\tau_{xy}\cdot\tau_{yz}\cdot\tau_{zx} - \sigma_{xx}\cdot\tau_{yz}^2\right.\right. \\
& \left.\left. + 2\cdot\tau_{xy}\cdot\tau_{yz}\cdot\tau_{zx} - \sigma_{yy}\cdot\tau_{zx}^2 + 2\cdot\tau_{xy}\cdot\tau_{yz}\cdot\tau_{zx} - \sigma_{zz}\cdot\tau_{xy}^2\right)\cdot\frac{I_1^3}{I_3^2}\right]
\end{aligned} \tag{A.18}$$

Further reduction yields:

$$\sigma_{ij}\cdot\frac{\partial g_p}{\partial \sigma_{ij}} \;=\; \left[\frac{I_1}{p_a}\right]^{\mu}\cdot\left[G\cdot I_1 + 2\cdot I_2\cdot\frac{I_1^2}{I_2^2} - \psi_1\cdot 3\cdot I_3\cdot\frac{I_1^3}{I_3^2}\right] \tag{A.19}$$

Inserting G from equation (A.6):

$$\sigma_{ij} \cdot \frac{\partial g_p}{\partial \sigma_{ij}} = \left[\frac{I_1}{p_a}\right]^{\mu} \cdot \left[\psi_1 \cdot (\mu + 3) \cdot \frac{I_1^3}{I_3} - (\mu + 2) \cdot \frac{I_1^2}{I_2} + \mu \cdot \left(\psi_{2,0} + b \cdot \ln\left(\frac{I_1}{p_a} + 1\right)\right) + \frac{b \cdot I_1}{I_1 + p_a} + 2 \cdot \frac{I_1^2}{I_2} - \psi_1 \cdot 3 \cdot \frac{I_1^3}{I_3}\right] \quad \text{(A.20)}$$

Rearranging:

$$\sigma_{ij} \cdot \frac{\partial g_p}{\partial \sigma_{ij}} = \mu \cdot g_p + \frac{b}{I_1 + p_a}\left(\frac{I_1}{p_a}\right)^{\mu+1} \quad \text{(A.21)}$$

The condition of reversibility becomes:

$$\mu \cdot g_p + \frac{b}{I_1 + p_a}\left(\frac{I_1}{p_a}\right)^{\mu+1} \geq 0 \quad \text{(A.22)}$$

resulting in

$$\mu > 0 \quad \text{(A.23)}$$

and

$$b > o \quad \text{(A.24)}$$

and

$$g_p > 0 \quad \text{(A.25)}$$

It further follows:

$$\psi_{2,0} \geq -(27 \cdot \psi_1 + 3) \quad \text{(A.26)}$$

By applying the same calculations as above to the linear version (equation (A.27)) and the cubic root version (equation (A.28)) of the plastic potential functions the following results are achieved.

$$g_p = \left[\Psi_1 \cdot \frac{I_1^3}{I_3} - \frac{I_1^2}{I_2} + \psi_{2,0} + b \cdot \frac{I_1}{p_a} \right] \left[\frac{I_1}{p_a} \right]^{\mu} \tag{A.27}$$

$$g_p = \left[\Psi_1 \cdot \frac{I_1^3}{I_3} - \frac{I_1^2}{I_2} + \psi_{2,0} + b \cdot \left(\frac{I_1}{p_a} \right)^{\frac{1}{3}} \right] \left[\frac{I_1}{p_a} \right]^{\mu} \tag{A.28}$$

Equation (A.6) is changed to

$$G = \psi_1 \cdot (\mu + 3) \cdot \frac{I_1^2}{I_3} - (\mu + 2) \cdot \frac{I_1}{I_2} + \psi_{2,0} \cdot \mu \cdot \frac{1}{I_1} + (\mu + 1) \cdot \frac{b}{p_a} \tag{A.29}$$

for the linear version and

$$G = \psi_1 \cdot (\mu + 3) \cdot \frac{I_1^2}{I_3} - (\mu + 2) \cdot \frac{I_1}{I_2} + \mu \cdot \left(\psi_{2,0} + b \cdot \left(\frac{I_1}{p_a} \right)^{\frac{1}{3}} \right) \cdot \frac{1}{I_1} + \frac{b}{3 (I_1)^{\frac{2}{3}} \cdot (p_a)^{\frac{1}{3}}} \tag{A.30}$$

for the cubic root version. The condition of irreversibility yields:

$$\mu \cdot g_p + b \left(\frac{I_1}{p_a} \right)^{\mu+1} \geq 0 \tag{A.31}$$

for the linear version and

$$\mu \cdot g_p + \frac{b}{3 (I_1)^{\frac{2}{3}} \cdot (p_a)^{\frac{1}{3}}} \left(\frac{I_1}{p_a} \right)^{\mu+1} \geq 0 \tag{A.32}$$

for the cubic root version.

Parameter Determination

The parameter determination from triaxial testing gives the following stress conditions:

$$\tau_{xy} = \tau_{yz} = \tau_{zx} = 0 \tag{A.33}$$

$$\sigma_{xx} = \sigma_{yy} = \sigma_3 \tag{A.34}$$

$$\sigma_{zz} = \sigma_1 \tag{A.35}$$

The incremental plastic strain ratio:

$$\nu_p = -\frac{d\varepsilon_3^p}{d\varepsilon_1^p} \tag{A.36}$$

Inserting the plastic strains from equation (A.13) under the stress conditions in equation (A.33), equation (A.34), and equation (A.35), yields:

$$\nu_p = -\frac{G - \frac{I_1^2}{I_2^2}\cdot(\sigma_3 + \sigma_1) - \psi_1 \cdot \frac{I_1^3}{I_3^2}\cdot\sigma_3\cdot\sigma_1}{G - \frac{I_1^2}{I_2^2}\cdot(\sigma_3 + \sigma_3) - \psi_1 \cdot \frac{I_1^3}{I_3^2}\cdot\sigma_3\cdot\sigma_3} \tag{A.37}$$

Inserting G from equation (A.6) and rearranging:

$$\begin{aligned}
&\psi_1\cdot(\mu+3)\cdot\frac{I_1^2}{I_3}\cdot\nu_p - (\mu+2)\cdot\frac{I_1}{I_2}\cdot\nu_p + \mu\cdot\left(\psi_{2,0} + b\cdot\ln\left(\frac{I_1}{p_a}+1\right)\right)\cdot\frac{1}{I_1}\cdot\nu_p \\
&+\frac{b}{I_1+p_a}\cdot\nu_p - \frac{I_1^2}{I_2^2}\cdot(\sigma_3+\sigma_3)\cdot\nu_p - \psi_1\cdot\frac{I_1^3}{I_3^2}\cdot\sigma_3\cdot\sigma_3\cdot\nu_p + \psi_1\cdot(\mu+3)\cdot\frac{I_1^2}{I_3} \\
&-(\mu+2)\cdot\frac{I_1}{I_2} + \mu\cdot\left(\psi_{2,0} + b\cdot\ln\left(\frac{I_1}{p_a}+1\right)\right)\cdot\frac{1}{I_1} + \frac{b}{I_1+p_a} - \frac{I_1^2}{I_2^2}\cdot(\sigma_3+\sigma_1) \\
&-\psi_1\cdot\frac{I_1^3}{I_3^2}\cdot\sigma_3\cdot\sigma_1 = 0
\end{aligned} \tag{A.38}$$

Rearranging:

$$\psi_1 \cdot \mu \cdot \frac{I_1^2}{I_3} \cdot \nu_p + \psi_1 \cdot 3 \cdot \frac{I_1^2}{I_3} \cdot \nu_p - \mu \cdot \frac{I_1}{I_2} \cdot \nu_p - 2 \cdot \frac{I_1}{I_2} \cdot \nu_p + \mu \cdot \psi_{2,0} \cdot \frac{1}{I_1} \cdot \nu_p$$
$$+ \mu \cdot b \cdot \ln\left(\frac{I_1}{p_a} + 1\right) \cdot \frac{1}{I_1} \cdot \nu_p + \frac{b}{I_1 + p_a} \cdot \nu_p - \frac{I_1^2}{I_2^2} \cdot 2 \cdot \sigma_3 \cdot \nu_p - \psi_1 \cdot \frac{I_1^3}{I_3^2} \cdot \sigma_3^2 \cdot \nu_p$$
$$+ \psi_1 \cdot \mu \cdot \frac{I_1^2}{I_3} + \psi_1 \cdot 3 \cdot \frac{I_1^2}{I_3} - \mu \cdot \frac{I_1}{I_2} - 2 \cdot \frac{I_1}{I_2} + \mu \cdot \psi_{2,0} \cdot \frac{1}{I_1} \qquad \text{(A.39)}$$
$$+ \mu \cdot b \cdot \ln\left(\frac{I_1}{p_a} + 1\right) \cdot \frac{1}{I_1} + \frac{b}{I_1 + p_a} - \frac{I_1^2}{I_2^2} \cdot (\sigma_3 + \sigma_1) - \psi_1 \cdot \frac{I_1^3}{I_3^2} \cdot \sigma_3 \cdot \sigma_1 = 0$$

Rearranging:

$$\mu \cdot (1 + \nu_p) \cdot \left[\psi_1 \cdot \frac{I_1^2}{I_3} - \frac{I_1}{I_2} + \psi_{2,0} \cdot \frac{1}{I_1} + b \cdot \ln\left(\frac{I_1}{p_a} + 1\right) \cdot \frac{1}{I_1}\right]$$
$$+ (1 + \nu_p) \cdot \left[\psi_1 \cdot 3 \cdot \frac{I_1^2}{I_3} - 2 \cdot \frac{I_1}{I_2} + \frac{b}{I_1 + p_a}\right] \qquad \text{(A.40)}$$
$$= \frac{I_1^2}{I_2^2} \cdot (2 \cdot \sigma_3 \cdot \nu_p + \sigma_3 + \sigma_1) + \psi_1 \cdot \frac{I_1^3}{I_3^2} (\sigma_3^2 \cdot \nu_p + \sigma_3 \cdot \sigma_1)$$

By multiplying by I_1, equation (A.40) can be reduced to:

$$\psi_1 \cdot \frac{I_1^2}{I_3} - \frac{I_1}{I_2} + \psi_{2,0} \cdot \frac{1}{I_1} + b \cdot \ln\left(\frac{I_1}{p_a} + 1\right) \cdot \frac{1}{I_1} =$$
$$\left[\frac{I_1^2}{I_2^2} \cdot (2 \cdot \sigma_3 \cdot \nu_p + \sigma_3 + \sigma_1) + \psi_1 \cdot \frac{I_1^3}{I_3^2} (\sigma_3^2 \cdot \nu_p + \sigma_3 \cdot \sigma_1)\right] \cdot \frac{1}{\mu \cdot (1 + \nu_p)} \qquad \text{(A.41)}$$
$$- \frac{1}{\mu} \cdot \left[3 \cdot \psi_1 \cdot \frac{I_1^2}{I_3} - 2 \cdot \frac{I_1}{I_2} + \frac{b}{I_1 + p_a}\right]$$

By defining the sub-parameters ξ_x and ξ_y, equation (A.41) becomes:

$$\xi_y = \frac{1}{\mu} \cdot \xi_x - b\left[\ln\left(\frac{I_1}{p_a} + 1\right) + \frac{1}{\mu \cdot (I_1 + p_a)}\right] \qquad \text{(A.42)}$$

in which

$$\xi_y = \psi_1 \frac{I_1^3}{I_3} - \frac{I_1^2}{I_2} + \psi_{2,0} \qquad \text{(A.43)}$$

and

$$\xi_x = \frac{1}{1+\nu^p}\left[\frac{I_1^3}{I_2^2}\left(\sigma_1+\sigma_3+2\nu^p\sigma_3\right)+\psi_1\frac{I_1^4}{I_3^2}\left(\sigma_1\sigma_3+\nu^p\sigma_3^2\right)\right]-3\psi_1\frac{I_1^3}{I_3}+2\frac{I_1^2}{I_2} \tag{A.44}$$

The parameter b can then be calculated as:

$$b = \frac{\frac{1}{\mu}\cdot\xi_x-\xi_y}{\ln\left(\frac{I_1}{p_a}+1\right)+\frac{1}{\mu\cdot\left(I_1+p_a\right)}} \tag{A.45}$$

By applying the same calculations as above to the linear version (equation (A.27)) and the cubic root version (equation (A.28)) of the plastic potential functions the following results are achieved. For the parameter determination, the relation between ξ_y and ξ_x becomes:

$$\xi_y = \frac{1}{\mu}\cdot\xi_x-b\cdot\frac{I_1}{p_a}\cdot\left(1+\frac{1}{\mu}\right) \tag{A.46}$$

for the linear version and

$$\xi_y = \frac{1}{\mu}\cdot\xi_x-b\left[\ln\left(\frac{I_1}{p_a}+1\right)+\frac{1}{\mu\cdot3\left(I_1\right)^{\frac{2}{3}}\cdot\left(p_a\right)^{\frac{1}{3}}}\right] \tag{A.47}$$

for the cubic root version.

Appendix B: Determination of Parameters for the Softening Function

The suggested softening function:

$$f''_{ps} = A_S \cdot W_p^{B_S} \cdot \exp\left[C_S \cdot \left(W_p - W_{p,95} \right)^{D_S} \right] + E_S \tag{B.1}$$

Differentiating equation (B.1) with respect to W_p yields:

$$\frac{df''_{ps}}{dW_p} = \left[C_S \cdot D_S \cdot \left(W_p - W_{p,95} \right)^{D_S - 1} \cdot W_p^{B_S} + B_S \cdot W_p^{B_S - 1} \right] \cdot A_S \cdot \exp\left[C_S \cdot \left(W_p - W_{p,95} \right)^{D_S} \right] \tag{B.2}$$

The five boundary conditions for the softening function described in section 3.2.3 are:

$$f''_{ps} \rightarrow f''_{p,r} \text{ for } W_p \rightarrow \infty \tag{B.3}$$

$$f''_{ph}(W_{p,95}) = f''_{ps}(W_{p,95}) \tag{B.4}$$

$$\frac{df''_{ph}(W_{p,95})}{dW_p} = \frac{df''_{ps}(W_{p,95})}{dW_p} \tag{B.5}$$

$$\frac{df''_{ps}(W_{p,peak})}{dW_p} = 0 \tag{B.6}$$

$$f''_{ps}(W_{p,peak}) = f''_{ph,f} \tag{B.7}$$

Applying the first boundary condition described in equation (B.3), gives:

$$f''_{ps} = A_S \cdot \infty^{B_S} \cdot \exp\left[C_S \cdot \left(\infty - W_{p,95} \right)^{D_S} \right] + E_S \tag{B.8}$$

for $C_S < 0$ the first term goes towards zero, resulting in:

$$f''_{ps} \rightarrow E_S \quad \text{for} \quad W_p \rightarrow \infty \tag{B.9}$$

It further follows that:

$$E_S = f''_{p,r} \tag{B.10}$$

For equation (B.10) to be true, the constant C must be negative. Under which conditions C in negative is discussed at the end of this appendix.

Applying the second boundary condition, in equation (B.4):

$$f''_{ph}(W_{p,95}) = f''_{ps}(W_{p,95}) \tag{B.11}$$

Inserting equation (B.1):

$$f''_{ph,95} = A_S \cdot W_{p,95}^{B_S} \cdot \exp\left[C_S \cdot \left(W_{p,95} - W_{p,95} \right)^{D_S} \right] + E_S \tag{B.12}$$

Reducing:

$$f''_{ph,95} = A_S \cdot W_{p,95}^{B_S} + E_S \tag{B.13}$$

Rearranging:

$$A_S = \frac{f''_{ph,95} - E_S}{W_{p,95}^{B_S}} \tag{B.14}$$

The third boundary condition, in equation (B.5):

$$\frac{df''_{ph}(W_{p,95})}{dW_p} = \frac{df''_{ps}(W_{p,95})}{dW_p} \tag{B.15}$$

Inserting equation (B.2):

$$\begin{aligned} \frac{df''_{ph,95}}{dW_p} = & \left[C_S \cdot D_S \cdot \left(W_{p,95} - W_{p,95} \right)^{D_S - 1} \cdot W_{p,95}^{B_S} + B_S \cdot W_{p,95}^{B_S - 1} \right] \cdot A_S \\ & \cdot \exp\left[C_S \cdot \left(W_{p,95} - W_{p,95} \right)^{D_S} \right] \end{aligned} \tag{B.16}$$

Reducing:

$$\frac{df''_{ph,95}}{dW_p} = A_S \cdot B_S \cdot W_{p,95}^{B_S-1} \tag{B.17}$$

Inserting equation (B.14) in equation (B.17) gives:

$$\frac{df''_{ph,95}}{dW_p} = \frac{f''_{ph,95} - E_S}{W_{p,95}^{B_S}} \cdot B_S \cdot W_{p,95}^{B_S-1} \tag{B.18}$$

Reducing:

$$\frac{df''_{ph,95}}{dW_p} = \frac{f''_{ph,95} - E_S}{W_{p,95}} \cdot B_S \tag{B.19}$$

Rearranging:

$$B_S = \frac{\frac{df''_{ph,95}}{dW_p} \cdot W_{p,95}}{f''_{ph,95} - E_S} \tag{B.20}$$

Applying the fourth boundary condition, defined in equation (B.6), gives:

$$\frac{df''_{ps}(W_{p,peak})}{dW_p} = 0 \tag{B.21}$$

Inserting equation (B.2):

$$\begin{aligned} 0 = {} & \left[C_S \cdot D_S \cdot \left(W_{p,peak} - W_{p,95} \right)^{D_S-1} \cdot W_{p,peak}^{B_S} + B_S \cdot W_{p,peak}^{B_S-1} \right] \cdot A_S \\ & \cdot \exp\left[C_S \cdot \left(W_{p,peak} - W_{p,95} \right)^{D_S} \right] \end{aligned} \tag{B.22}$$

Rearranging:

$$0 = C_S \cdot D_S \cdot \left(W_{p,peak} - W_{p,95} \right)^{D_S-1} \cdot W_{p,peak}^{B_S} + B_S \cdot W_{p,peak}^{B_S-1} \tag{B.23}$$

Reducing:

$$0 = C_S \cdot D_S \cdot \left(W_{p,peak} - W_{p,95}\right)^{D_S-1} \cdot W_{p,peak} + B_S \tag{B.24}$$

Rearranging:

$$C_S = \frac{-B_S}{D_S \cdot \left(W_{p,peak} - W_{p,95}\right)^{D_S-1} \cdot W_{p,peak}} \tag{B.25}$$

Applying the fifth boundary condition, defined in equation (B.7), gives:

$$f''_{ps}(W_{p,peak}) = f''_{ph,f} \tag{B.26}$$

Inserting equation (B.1):

$$f''_{ph,f} = A_S \cdot W_{p,peak}^{B_S} \cdot \exp\left[C_S \cdot \left(W_{p,peak} - W_{p,95}\right)^{D_S}\right] + E_S \tag{B.27}$$

Inserting equation (B.25) in equation (B.27), gives:

$$f''_{ph,f} = A_S \cdot W_{p,peak}^{B_S} \cdot \exp\left[\frac{-B_S \cdot \left(W_{p,peak} - W_{p,95}\right)^{D_S}}{D_S \cdot \left(W_{p,peak} - W_{p,95}\right)^{D_S-1} \cdot W_{p,peak}}\right] + E_S \tag{B.28}$$

Reducing:

$$f''_{ph,f} = A_S \cdot W_{p,peak}^{B_S} \cdot \exp\left[\frac{B_S \cdot \left(W_{p,95} - W_{p,peak}\right)}{W_{p,peak}} \cdot \frac{1}{D_S}\right] + E_S \tag{B.29}$$

Rearranging:

$$\frac{f''_{ph,f} - E_S}{A_S \cdot W_{p,peak}^{B_S}} = \exp\left[\frac{B_S \cdot \left(W_{p,95} - W_{p,peak}\right)}{W_{p,peak}} \cdot \frac{1}{D_S}\right] \tag{B.30}$$

Rearranging:

$$D_S = \frac{B_S \cdot \left(W_{p,95} - W_{p,peak}\right)}{\ln\left[\frac{f''_{ph,f} - E_S}{A_S \cdot W_{p,peak}^{B_S}}\right] \cdot W_{p,peak}} \tag{B.31}$$

In summary, the five constants, E_S, B_S, A_S, D_S, and C_S are defined in equation (B.32), (B.33), (B.34), (B.35), and (B.36), respectively.

$$E_S = f''_{p,r} \tag{B.32}$$

$$B_S = \frac{\frac{df''_{ph,95}}{dW_p} \cdot W_{p,95}}{f''_{ph,95} - E_S} \tag{B.33}$$

$$A_S = \frac{f''_{ph,95} - E_S}{W_{p,95}^{B_S}} \tag{B.34}$$

$$D_S = \frac{B_S \cdot \left(W_{p,95} - W_{p,peak}\right)}{\ln\left[\frac{f''_{ph,f} - E_S}{A_S \cdot W_{p,peak}^{B_S}}\right] \cdot W_{p,peak}} \tag{B.35}$$

$$C_S = \frac{-B_S}{D_S \cdot \left(W_{p,peak} - W_{p,95}\right)^{D_S - 1} \cdot W_{p,peak}} \tag{B.36}$$

By definition, the plastic work produced at peak is higher than the plastic work produced at cut-off. The value of the hardening function at failure is also higher than the value at cut-off.

The definition of A_S in equation (B.34) and the definition of E_S in equation (B.32) are substituted into the natural logarithm in equation (B.35). For D_S to be positive, the natural logarithm used in equation (B.35) has to have an input smaller than one:

$$0 < \frac{f''_{ph,f} - f''_{p,r}}{\frac{f''_{ph,95} - f''_{p,r}}{W_{p,95}^{B_S}} \cdot W_{p,peak}^{B_S}} < 1 \tag{B.37}$$

Rearranging:

$$0 < \frac{f''_{ph,f} - f''_{p,r}}{f''_{ph,95} - f''_{p,r}} \cdot \left(\frac{W_{p,95}}{W_{p,peak}} \right)^{B_S} < 1 \qquad \text{(B.38)}$$

As the residual value, $f''_{p,r}$ goes towards the cut-off value, $f''_{ph,95}$ the first term and B_S goes toward infinity:

$$\text{For } f''_{p,r} \rightarrow f''_{ph,95}, \quad \frac{f''_{ph,f} - f''_{p,r}}{f''_{ph,95} - f''_{p,r}} \rightarrow \infty \qquad \text{(B.39)}$$

$$\text{For } f''_{p,r} \rightarrow f''_{ph,95}, \quad B_S \rightarrow \infty \qquad \text{(B.40)}$$

Since the fraction in the second term of equation (B.38) is less than one, the input for the natural logarithm is also less than one. This means D_S is positive as long as the residual value, $f''_{p,r}$ is less than the cut-off value, $f''_{ph,95}$.

Combining equation (B.20) and equation (B.10) with equation (B.25) yields:

$$C_S = \frac{-\dfrac{\dfrac{df''_{ph,95}}{dW_p} \cdot W_{p95}}{f''_{ph,95} - f''_{p,r}}}{D_S \cdot \left(W_{p,peak} - W_{p,95} \right)^{D_S - 1} \cdot W_{p,peak}} \qquad \text{(B.41)}$$

Rearranging:

$$C_S = -\frac{\dfrac{df''_{ph,95}}{dW_p} \cdot W_{p95}}{\left(f''_{ph,95} - f''_{p,r} \right) \cdot D_S \cdot \left(W_{p,peak} - W_{p,95} \right)^{D_S - 1} \cdot W_{p,peak}} \qquad \text{(B.42)}$$

Again, as long as the residual value is lower than the cut-off value, C_S is negative, as required by equation (B.10).

Appendix C: Predictions Using New Plastic Potential Function and New Softening Function

Two new plastic potential functions have been compared with the original function. First the linear version is compared with the original version, and then the logarithmic version is compared with the original version. Finally the cubic root version is compared with the original version. These comparisons are done for F1-Sand, L1-Sand, L2-Sand, and L8-Sand.

Predictions with the new softening function are compared with the original softening function using the linear version of the plastic potential. Again, the predictions are performed on F1-Sand, L1-Sand, L2-Sand, and L8-Sand.

F1-Sand

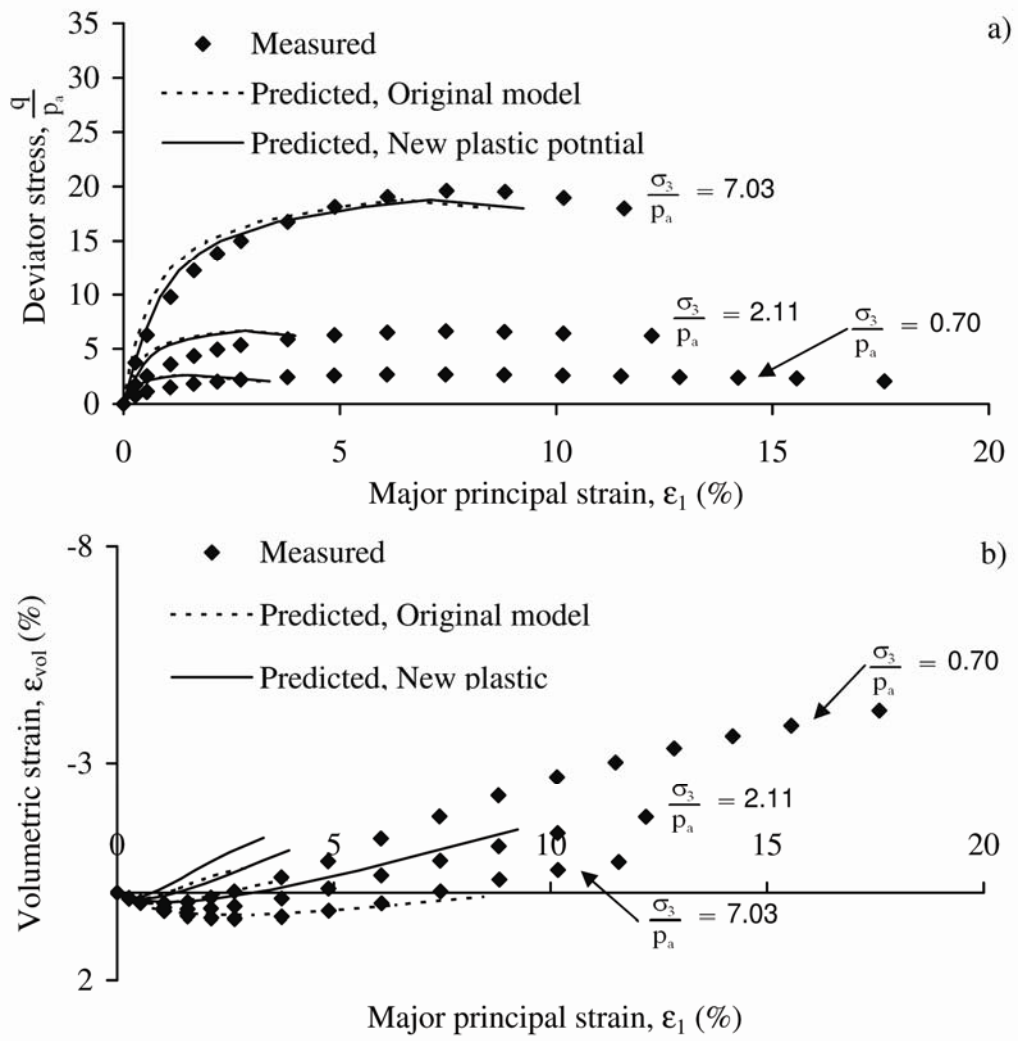

Comparison of original and linear plastic potential function for F1-Sand at low confining pressures. a) Stress-strain. b) Volume change.

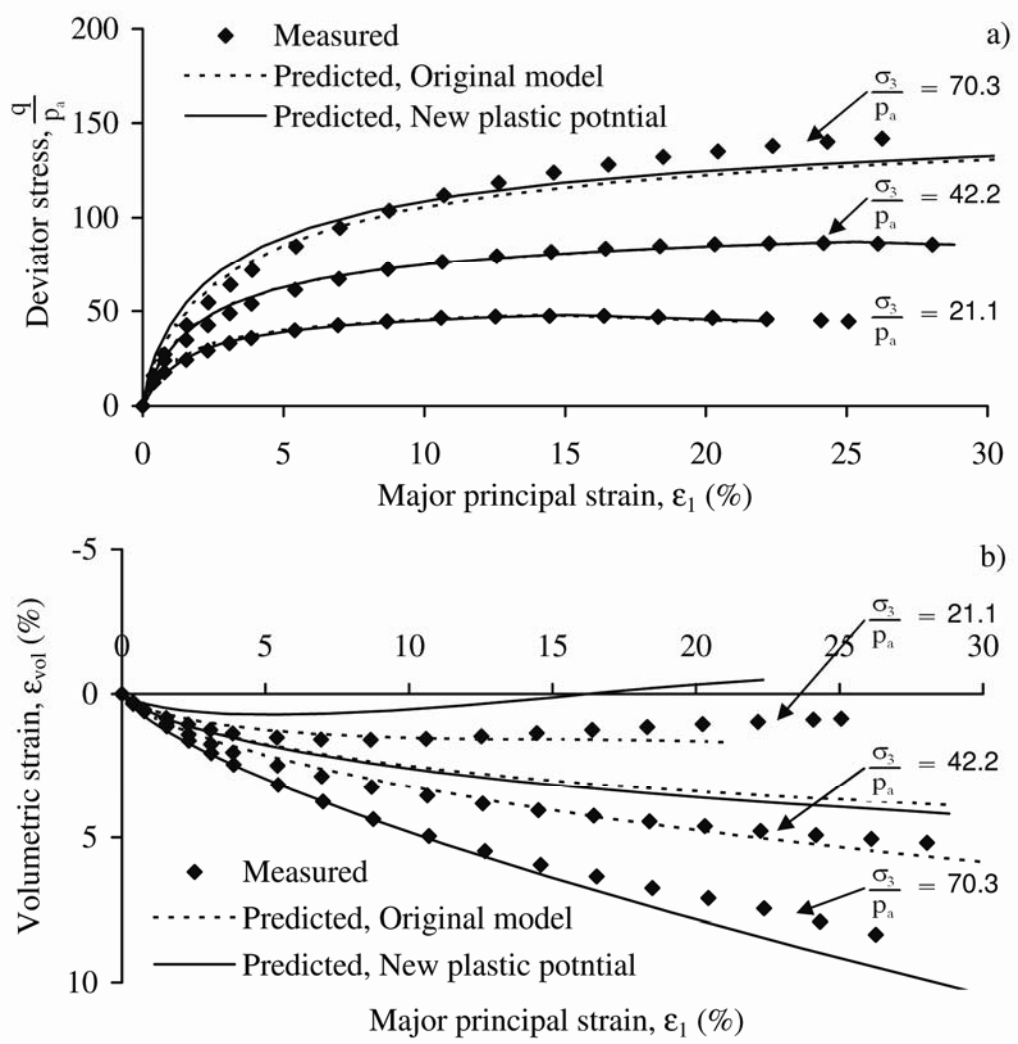

Comparison of original and linear plastic potential function for F1-Sand at high confining pressures. a) Stress-strain. b) Volume change.

L1-Sand

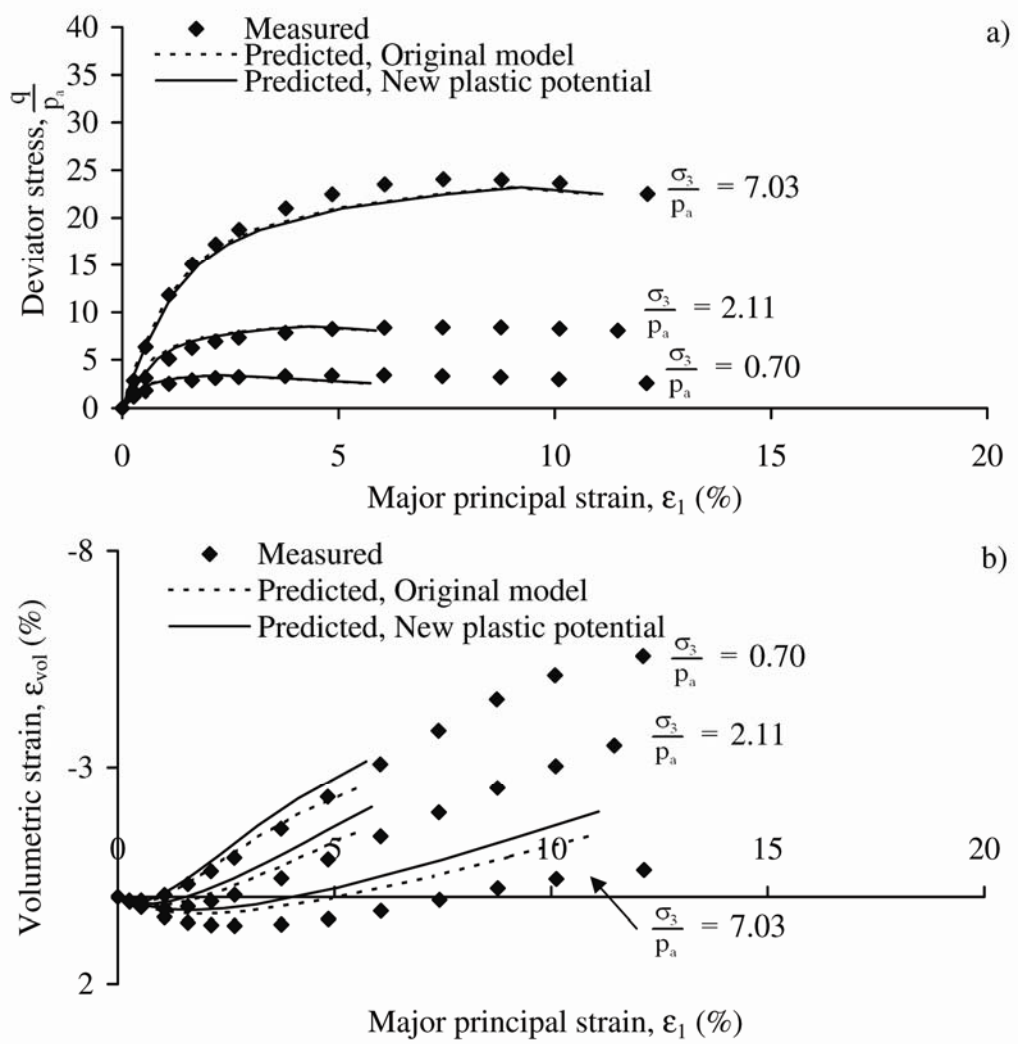

Comparison of original and linear plastic potential function for L1-Sand at low confining pressures. a) Stress-strain. b) Volume change.

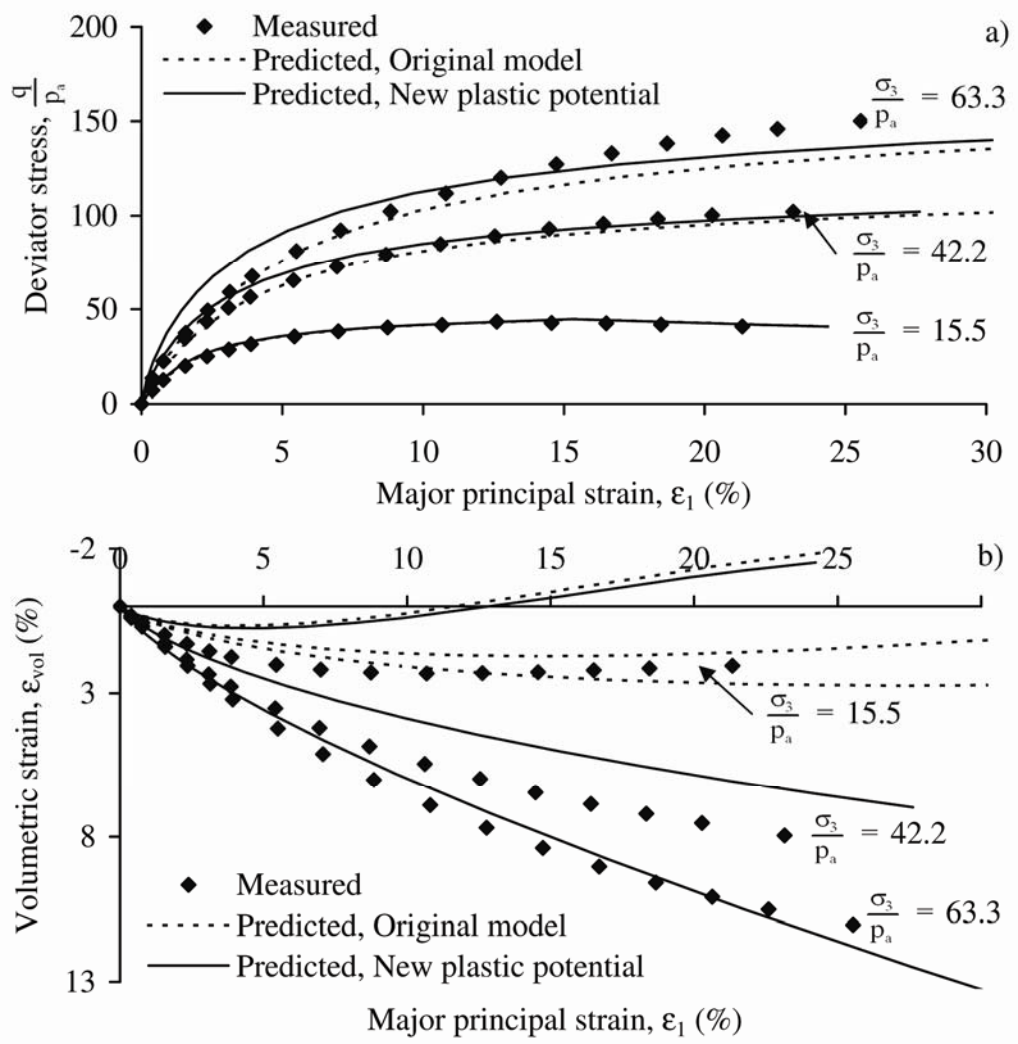

Comparison of original and linear plastic potential function for L1-Sand at high confining pressures. a) Stress-strain. b) Volume change.

L2-Sand

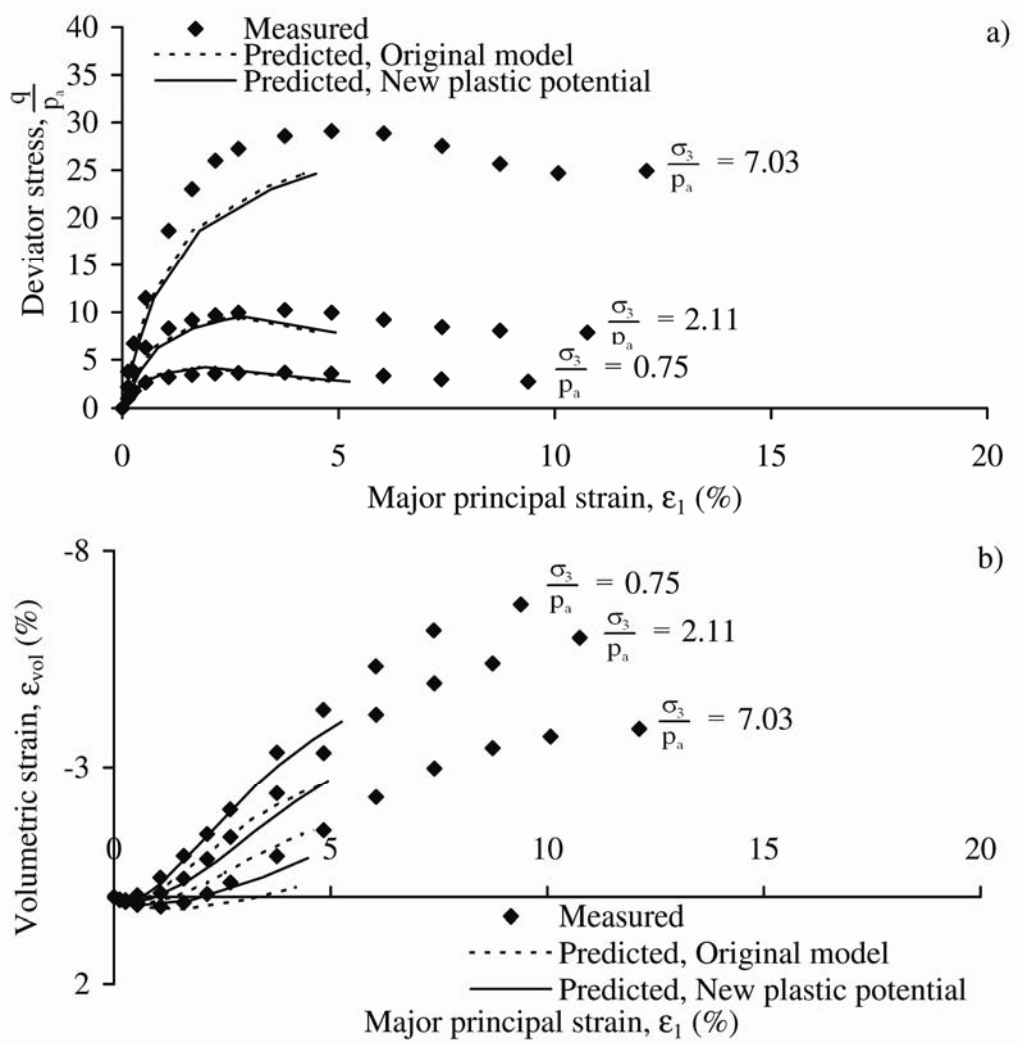

Comparison of original and linear plastic potential function for L2-Sand at low confining pressures. a) Stress-strain. b) Volume change.

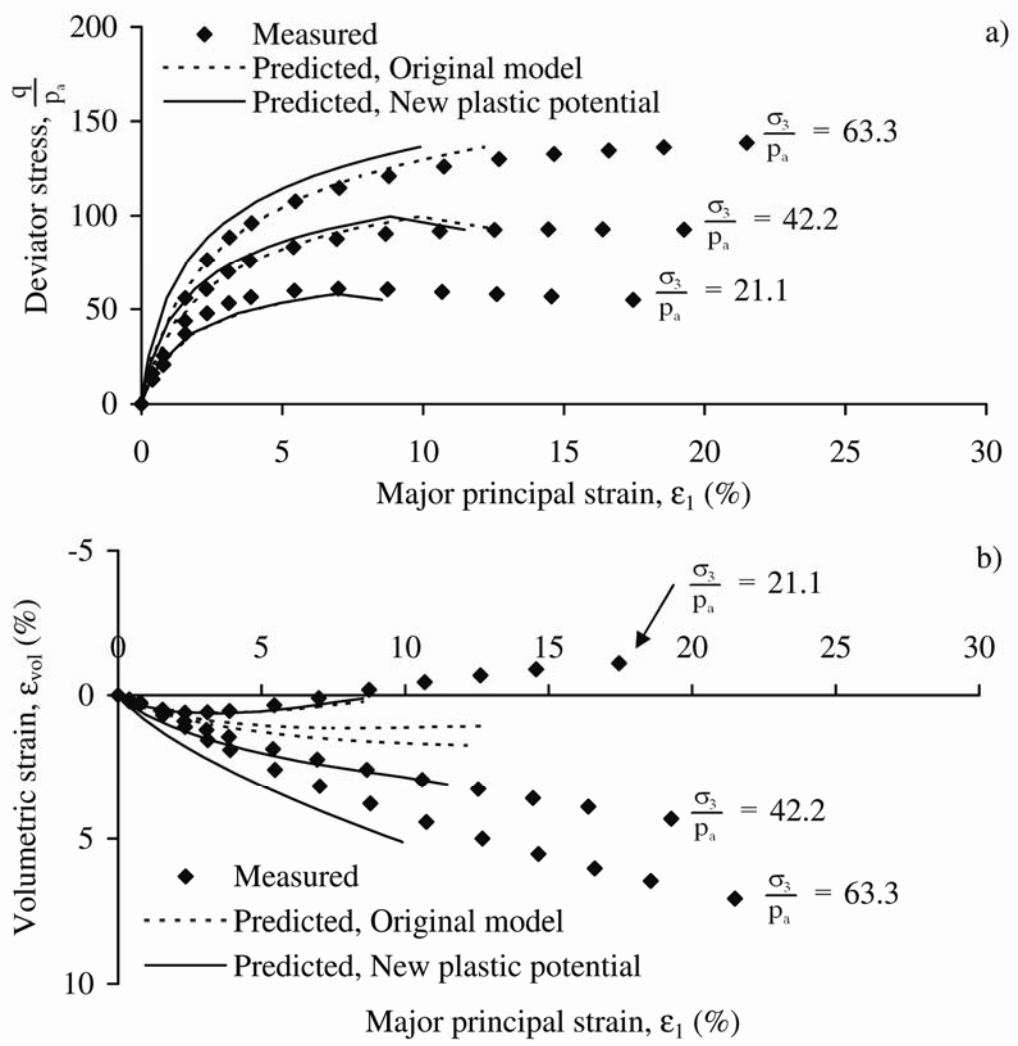

Comparison of original and linear plastic potential function for L2-Sand at high confining pressures. a) Stress-strain. b) Volume change.

L8-Sand

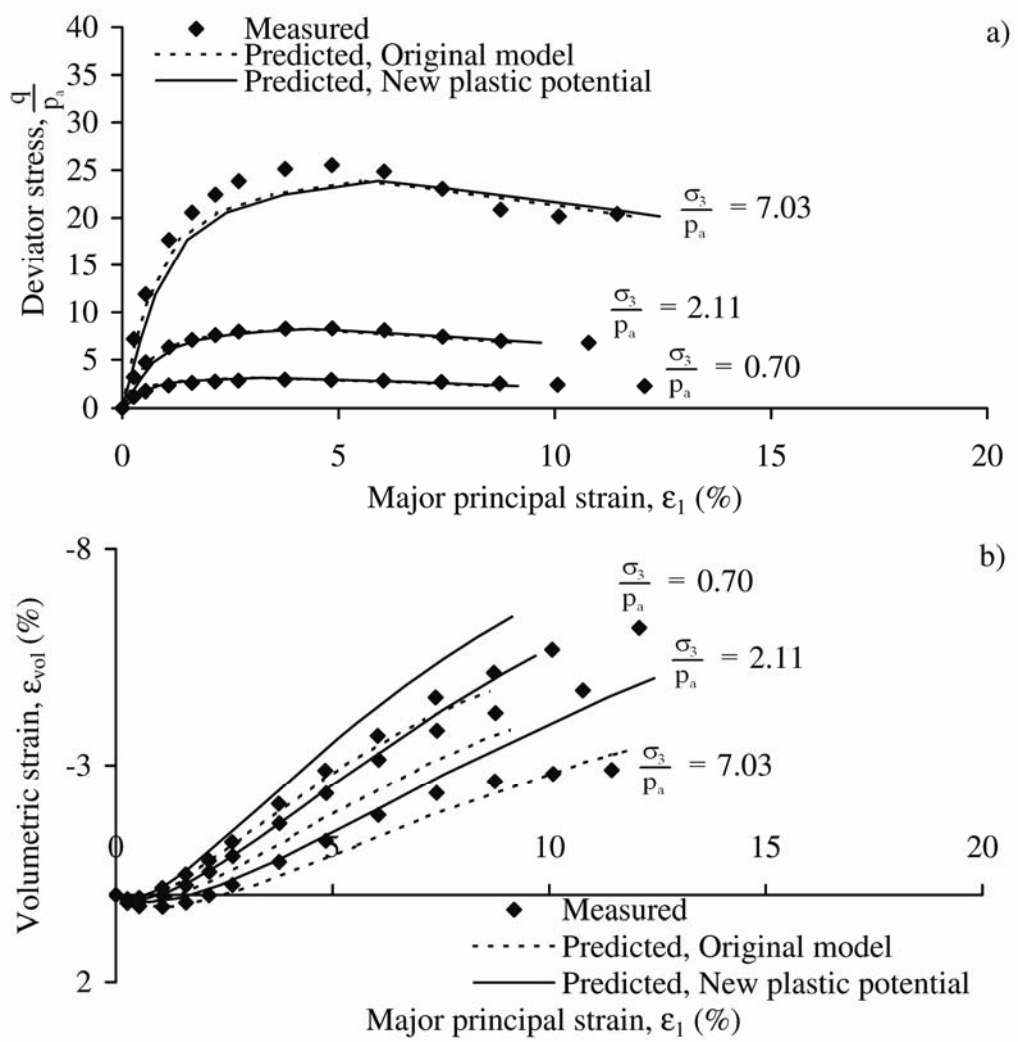

Comparison of original and linear plastic potential function for L8-Sand at low confining pressures. a) Stress-strain. b) Volume change.

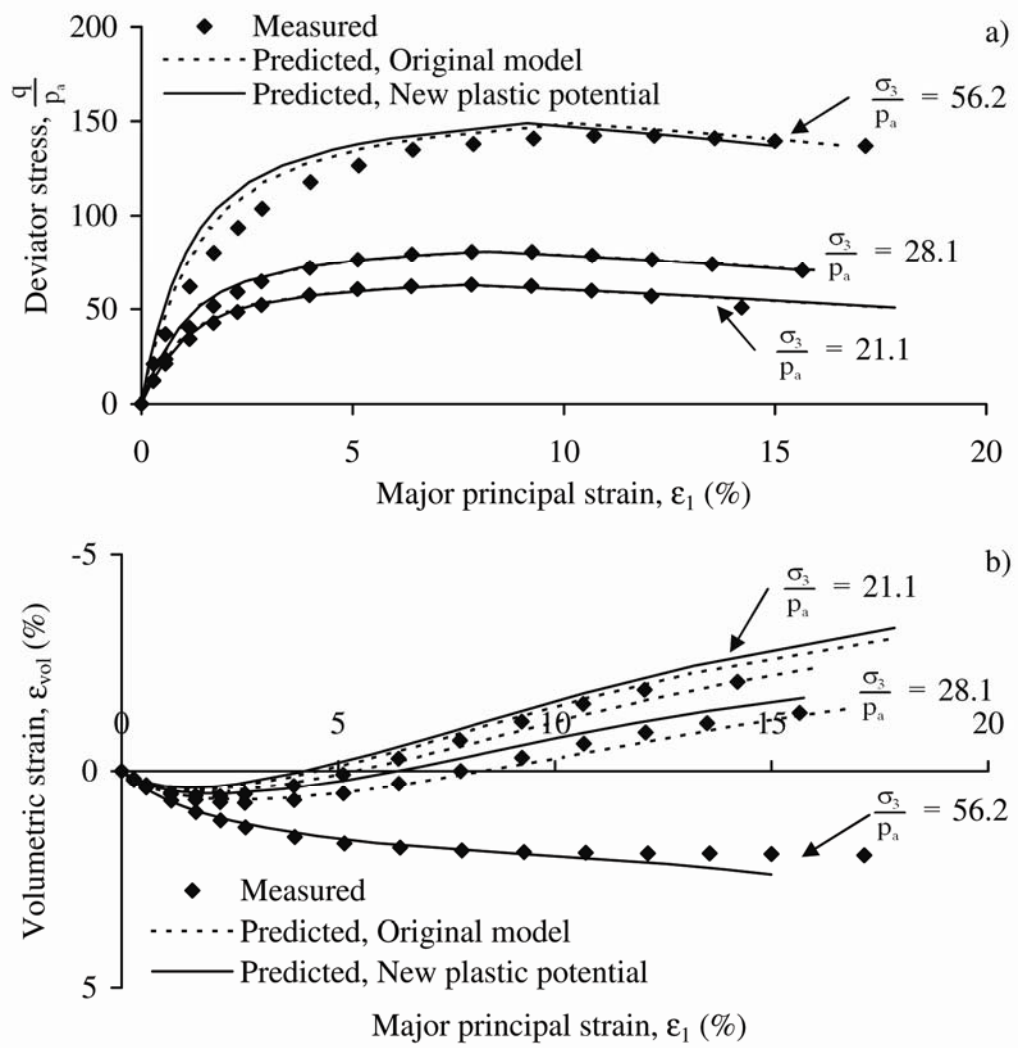

Comparison of original and linear plastic potential function for L8-Sand at high confining pressures. a) Stress-strain. b) Volume change.

F1-Sand

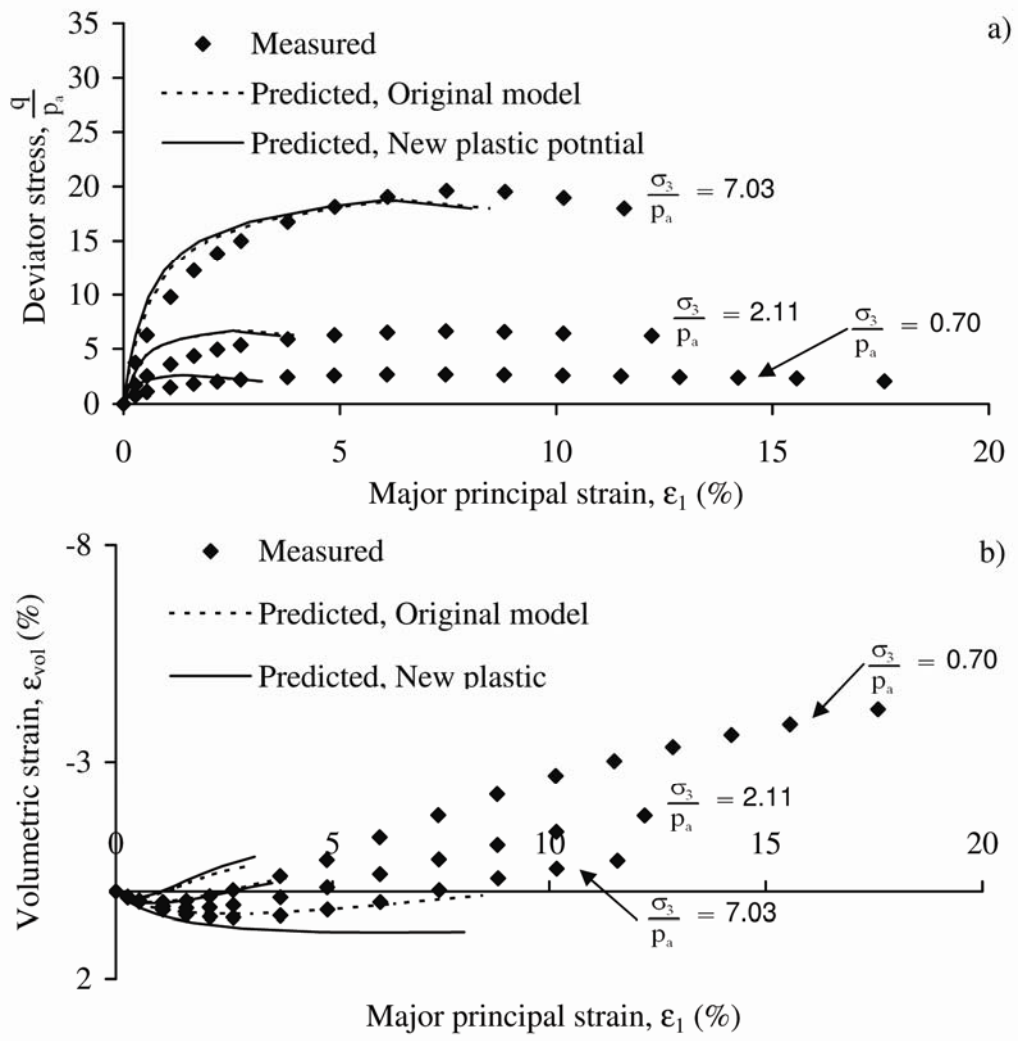

Comparison of original and logarithmic plastic potential function for F1-Sand at low confining pressures. a) Stress-strain. b) Volume change.

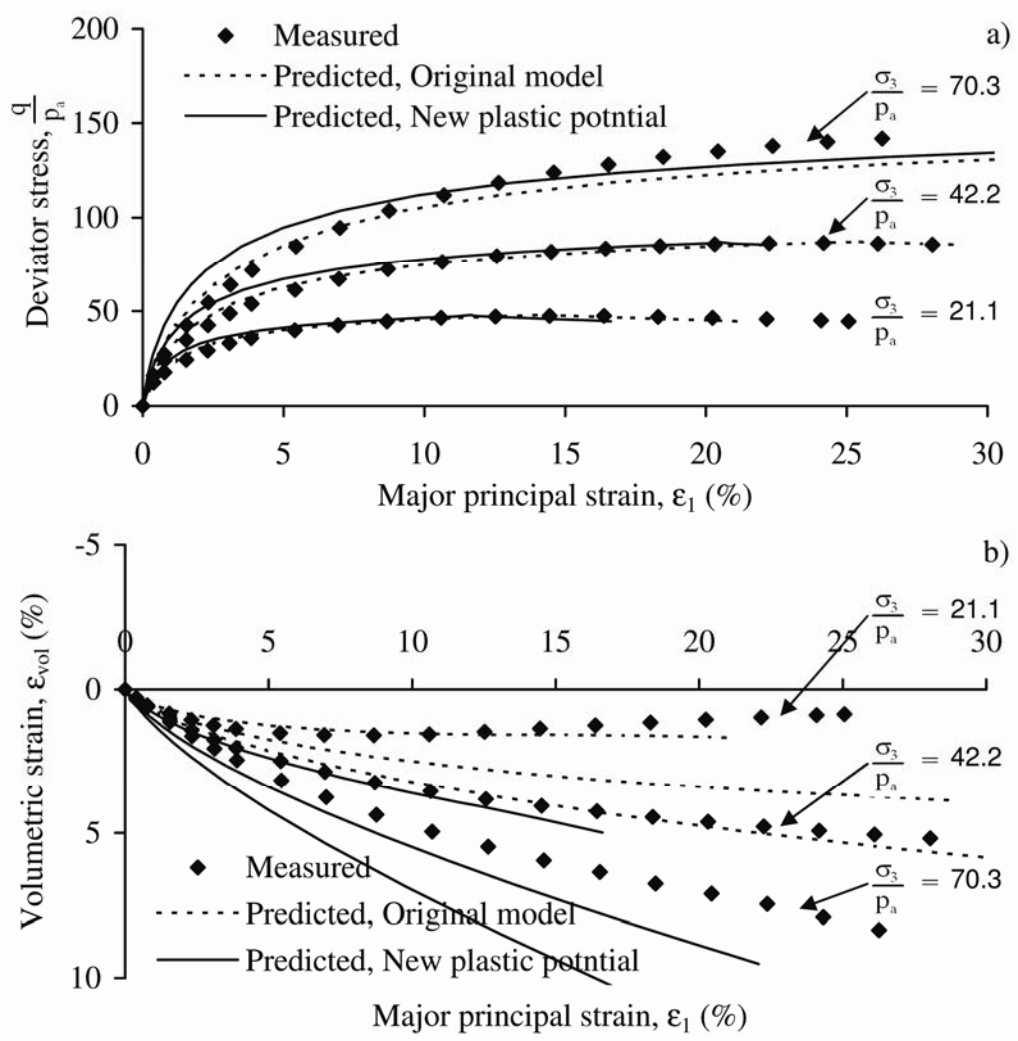

Comparison of original and logarithmic plastic potential function for F1-Sand at high confining pressures. a) Stress-strain. b) Volume change.

L1-Sand

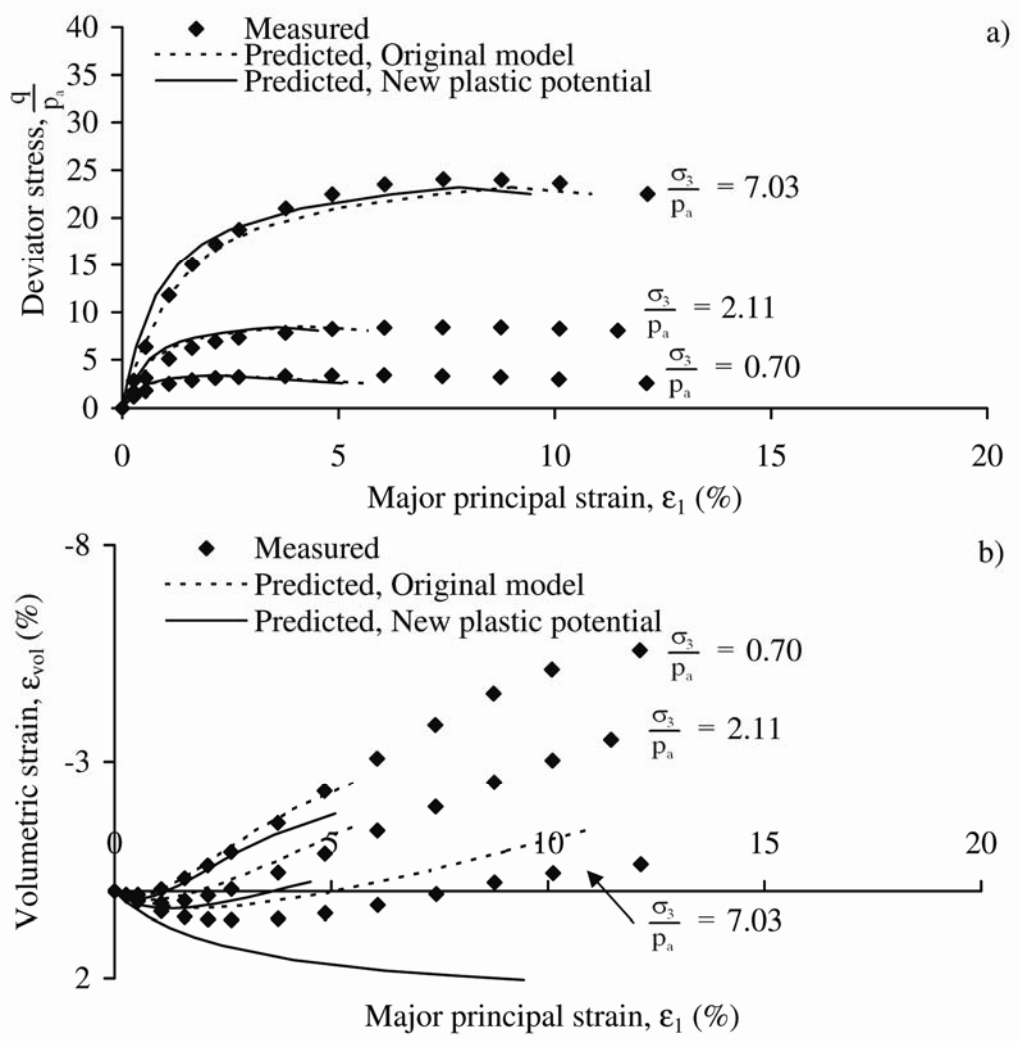

Comparison of original and logarithmic plastic potential function for L1-Sand at low confining pressures. a) Stress-strain. b) Volume change.

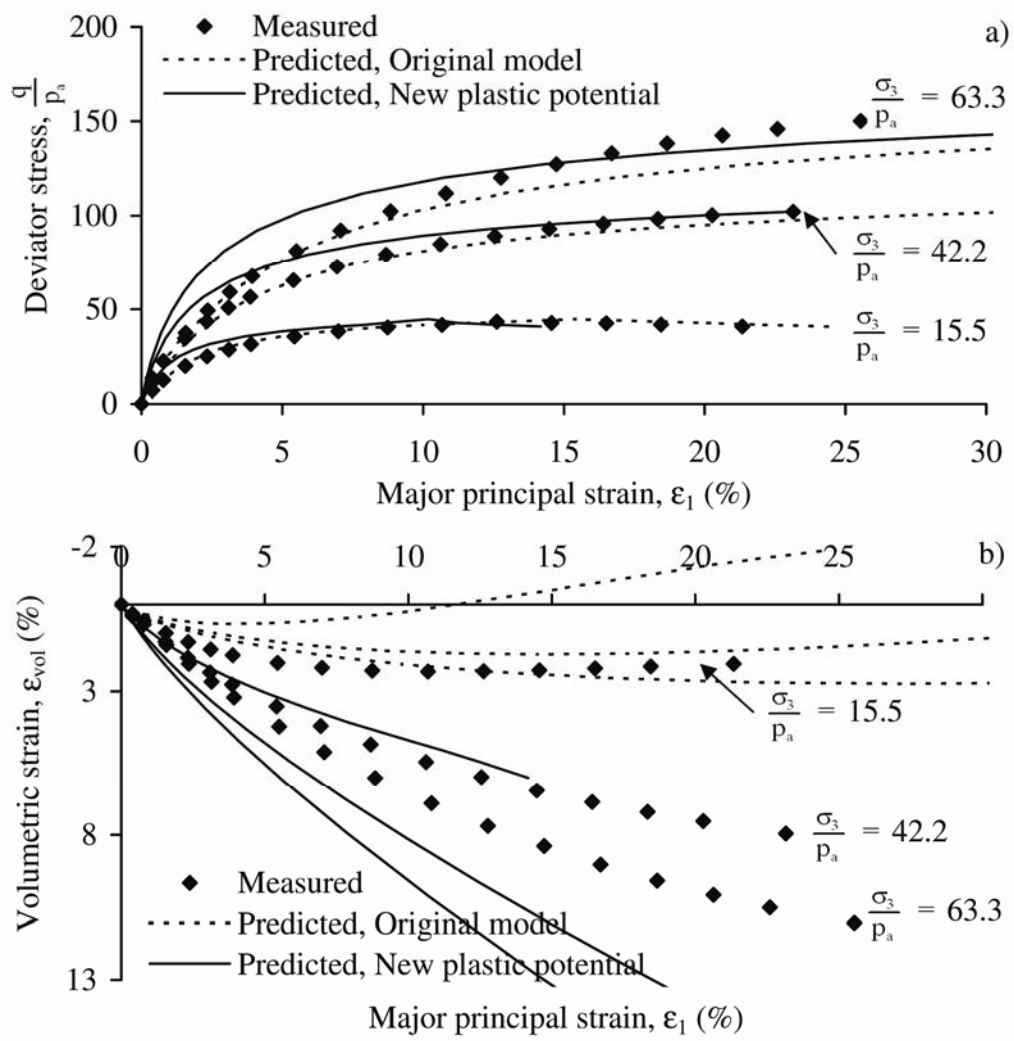

Comparison of original and logarithmic plastic potential function for L1-Sand at high confining pressures. a) Stress-strain. b) Volume change.

L2-Sand

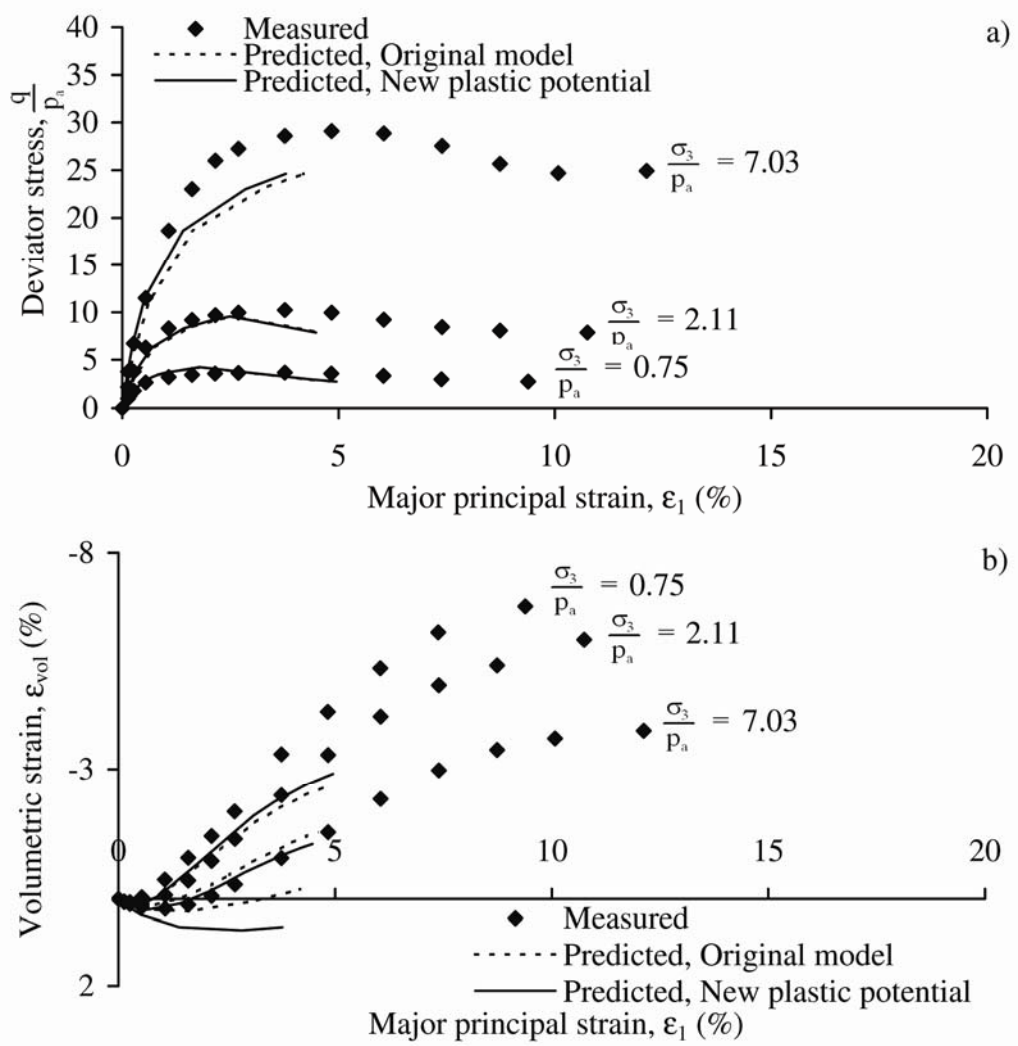

Comparison of original and logarithmic plastic potential function for L2-Sand at low confining pressures. a) Stress-strain. b) Volume change.

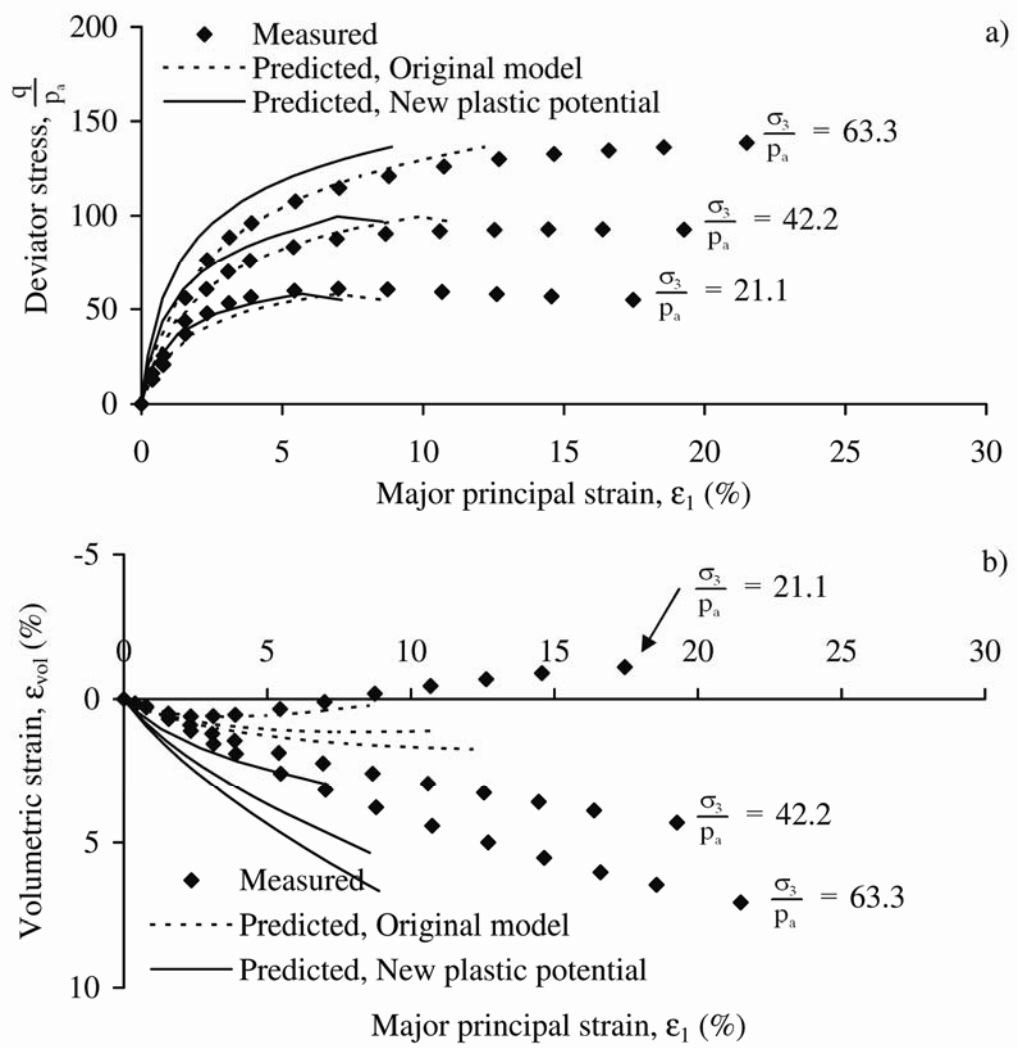

Comparison of original and logarithmic plastic potential function for L2-Sand at high confining pressures. a) Stress-strain. b) Volume change.

L8-Sand

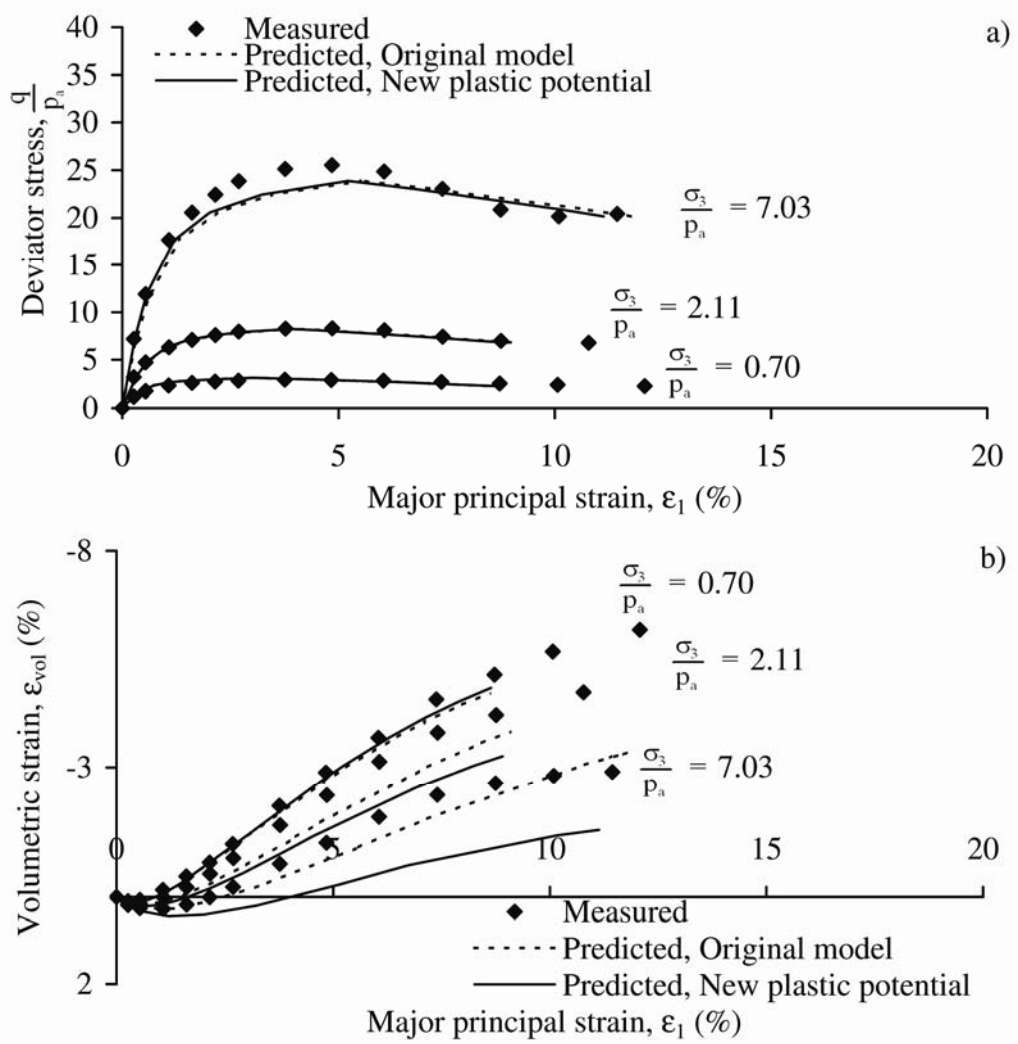

Comparison of original and logarithmic plastic potential function for L8-Sand at low confining pressures. a) Stress-strain. b) Volume change.

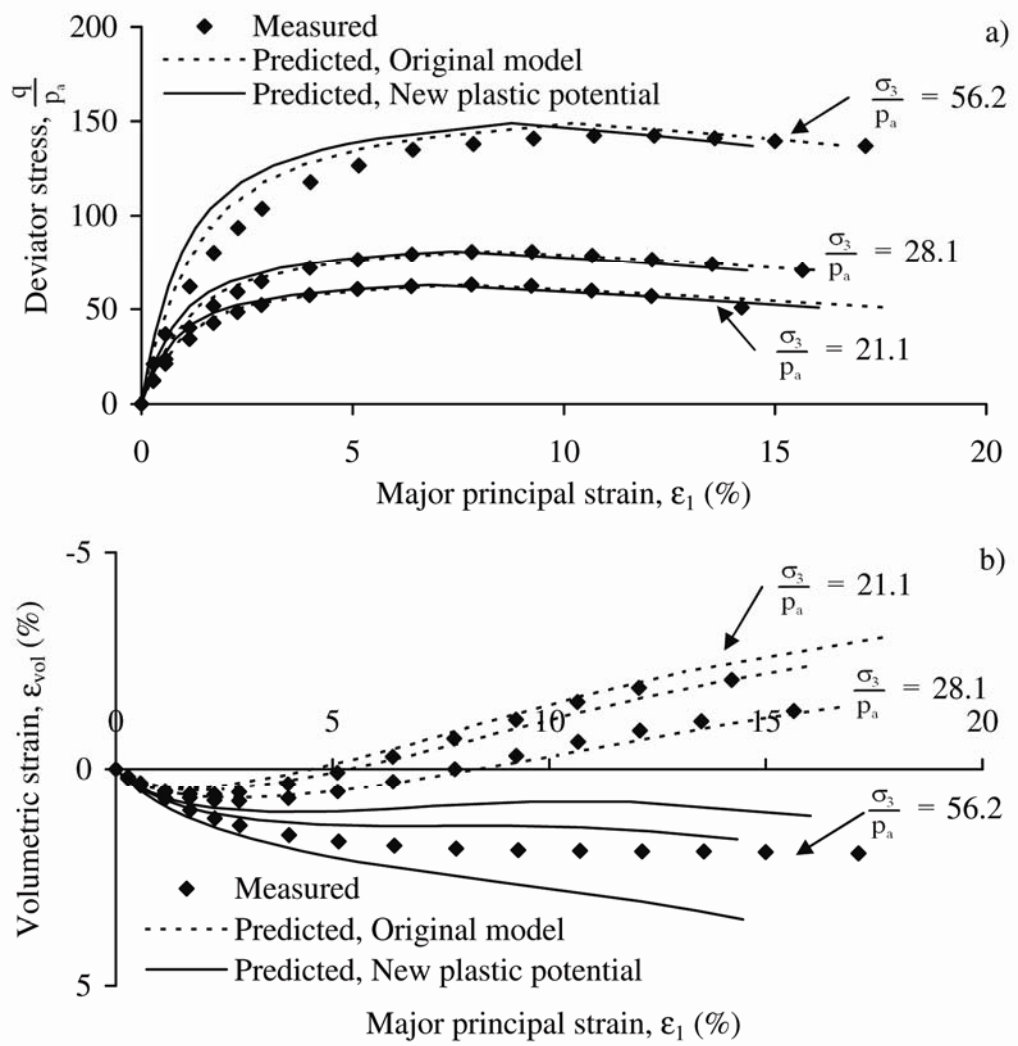

Comparison of original and logarithmic plastic potential function for L8-Sand at high confining pressures. a) Stress-strain. b) Volume change.

F1-Sand

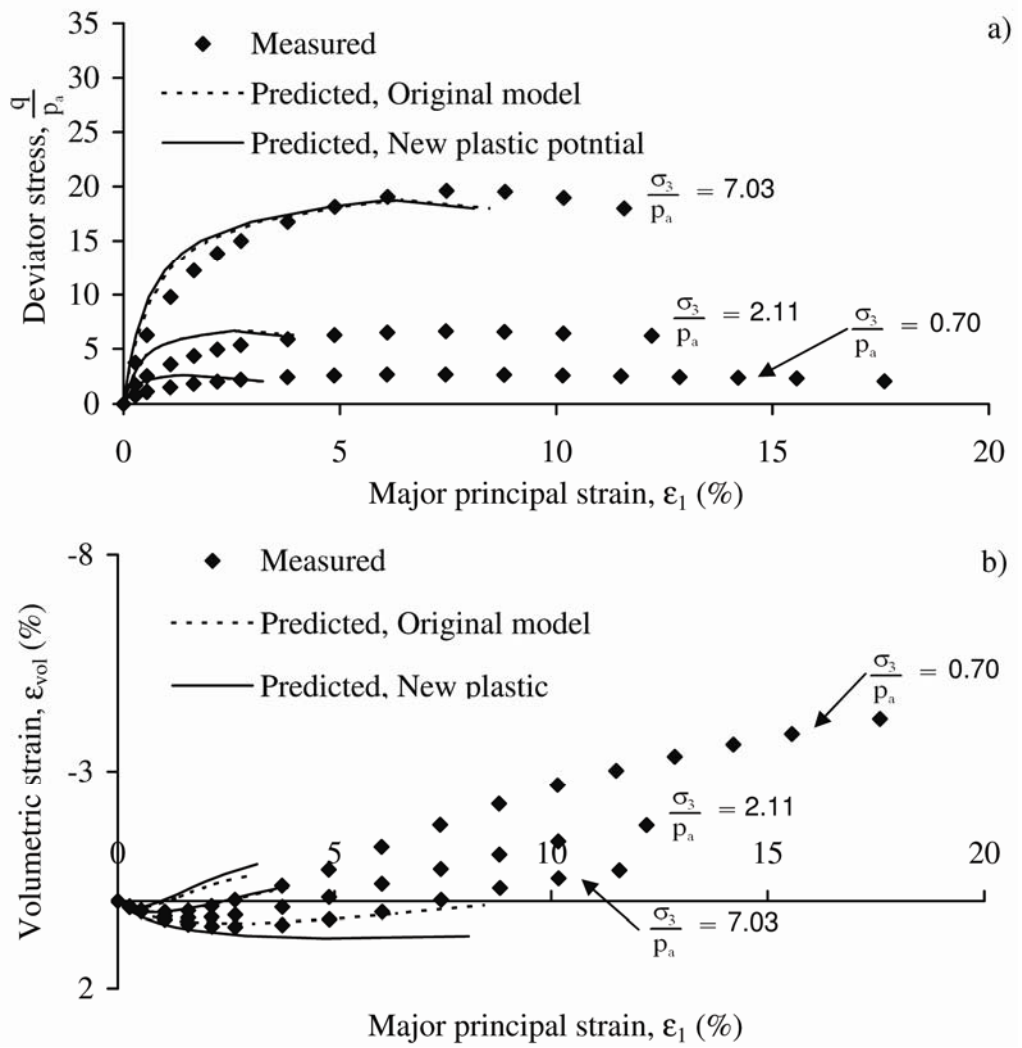

Comparison of original and cubic root plastic potential function for F1-Sand at low confining pressures. a) Stress-strain. b) Volume change.

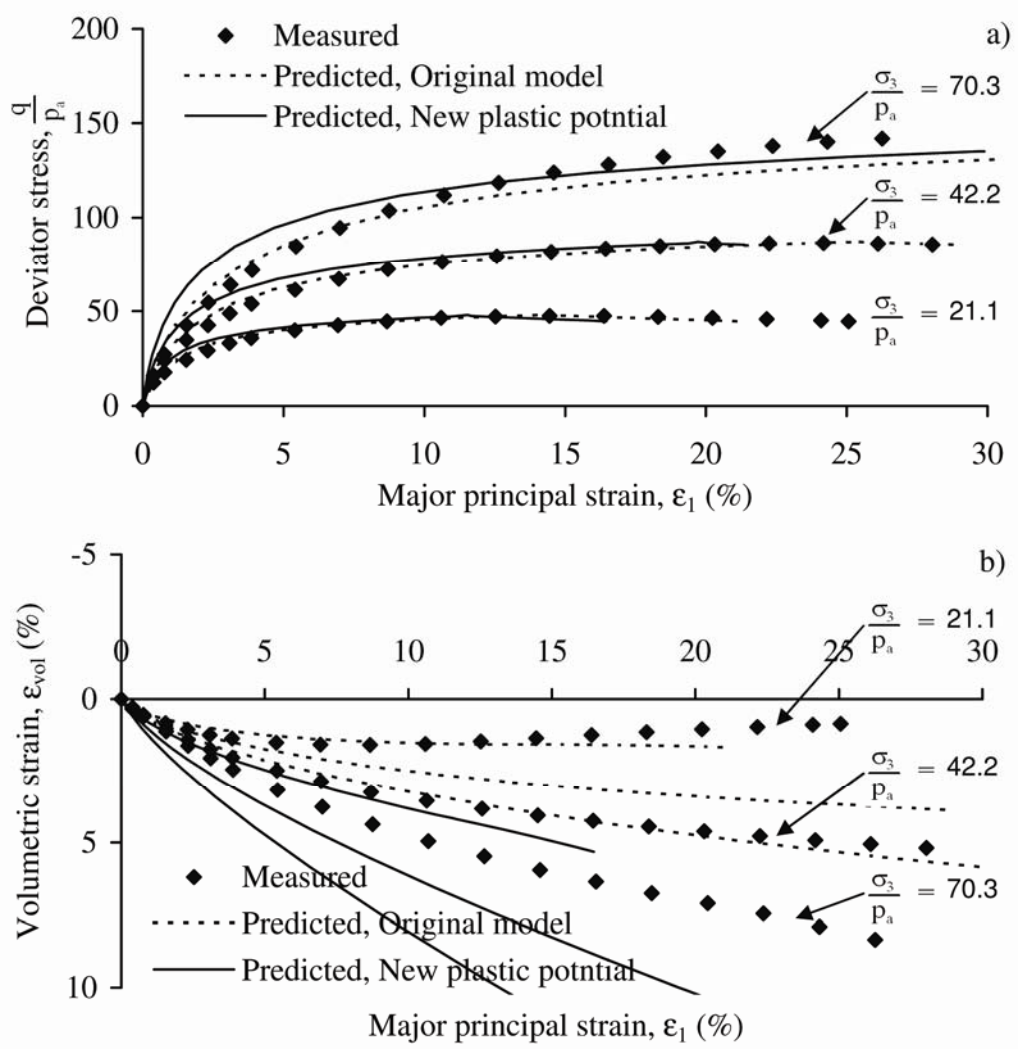

Comparison of original and cubic root plastic potential function for F1-Sand at high confining pressures. a) Stress-strain. b) Volume change.

L1-Sand

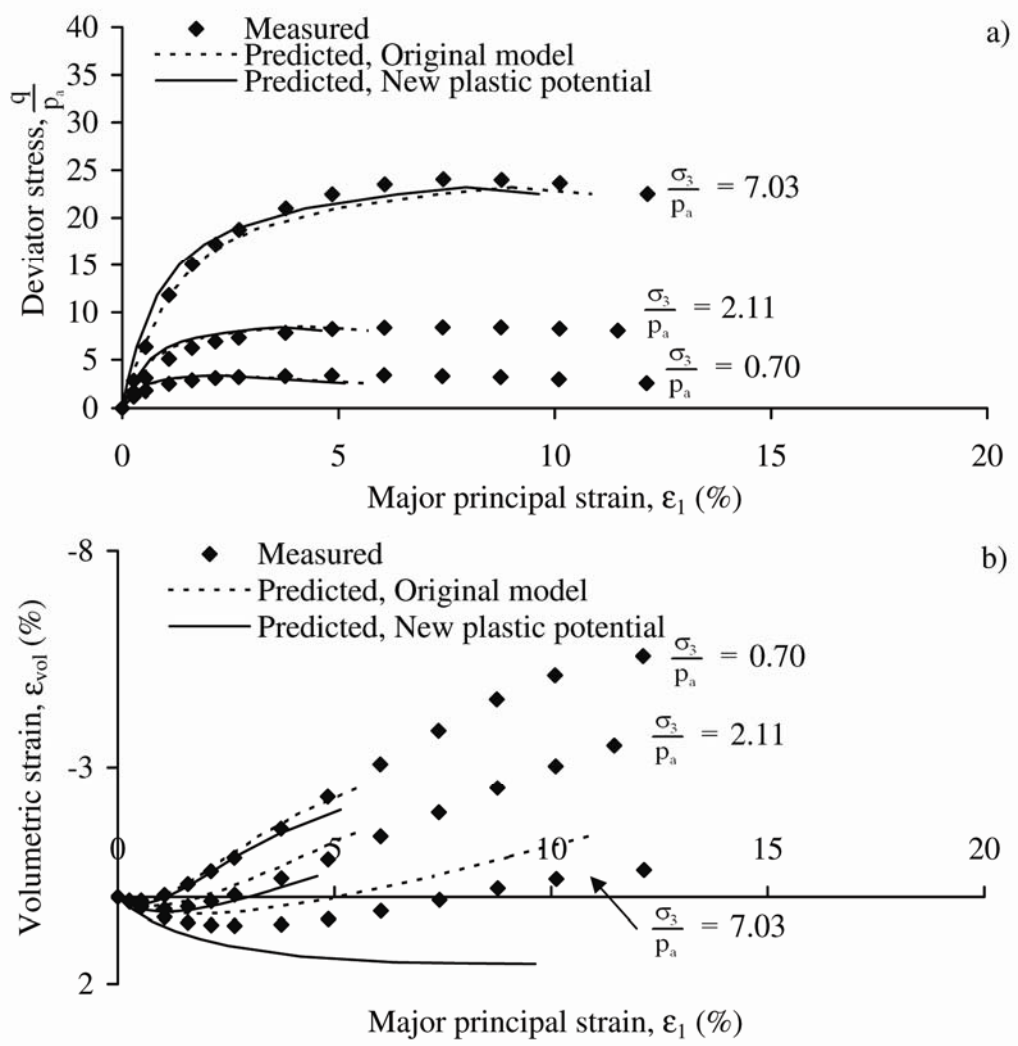

Comparison of original and cubic root plastic potential function for L1-Sand at low confining pressures. a) Stress-strain. b) Volume change.

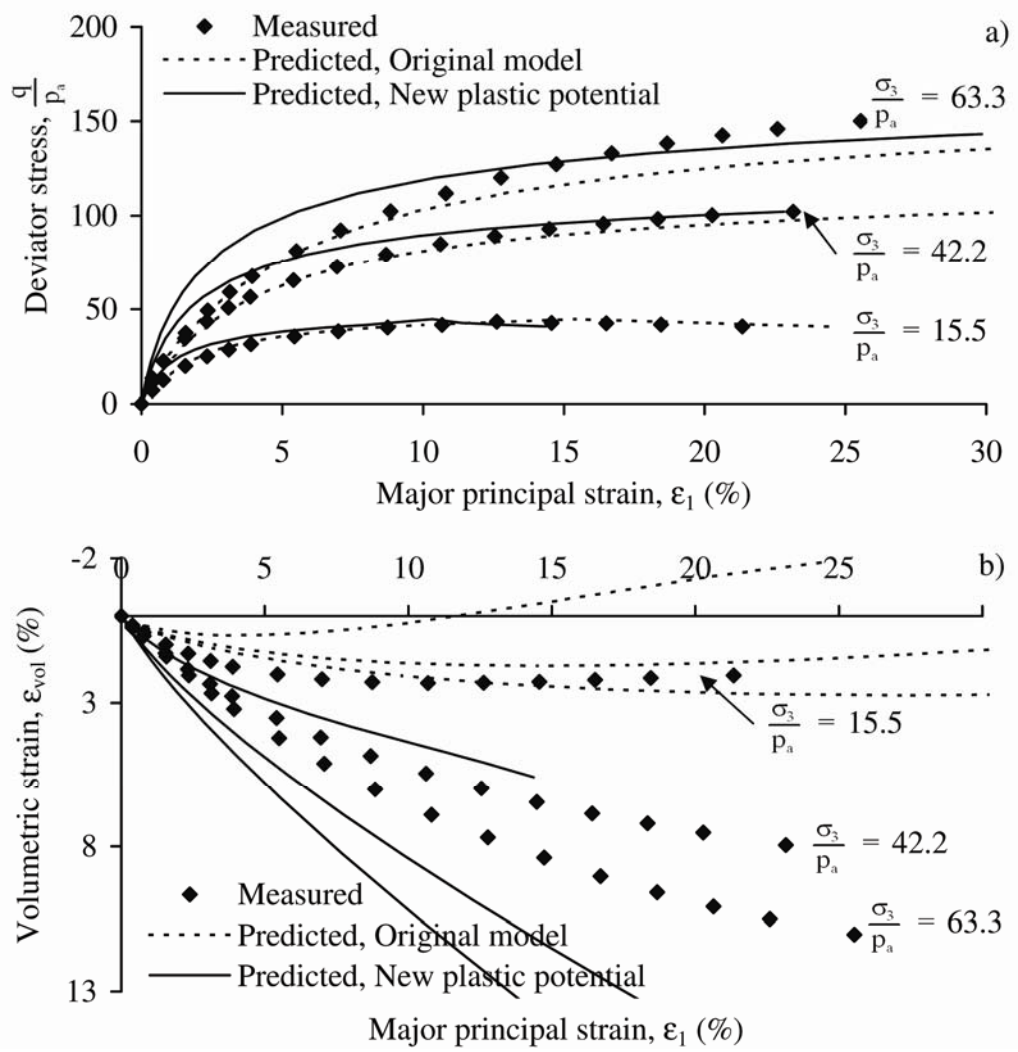

Comparison of original and cubic root plastic potential function for L1-Sand at high confining pressures. a) Stress-strain. b) Volume change.

L2-Sand

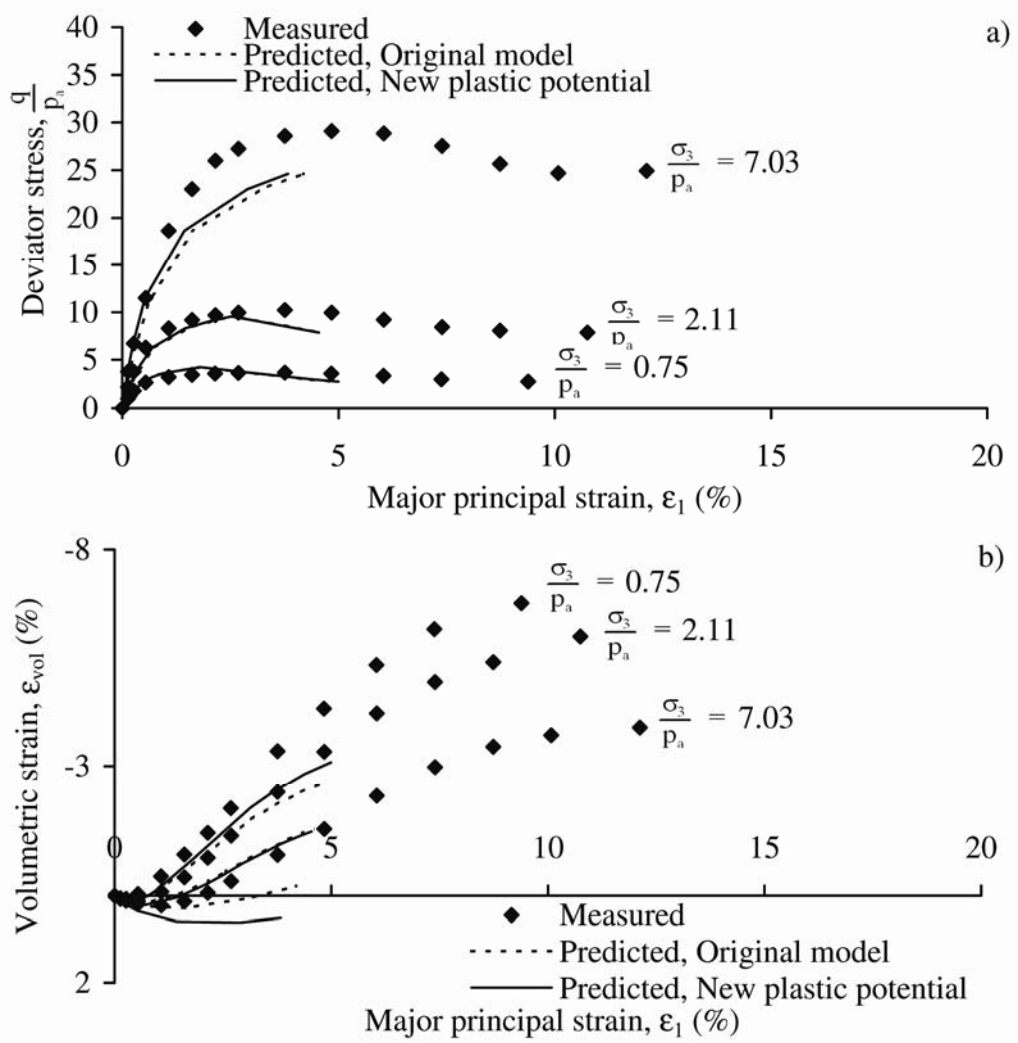

Comparison of original and cubic root plastic potential function for L2-Sand at low confining pressures. a) Stress-strain. b) Volume change.

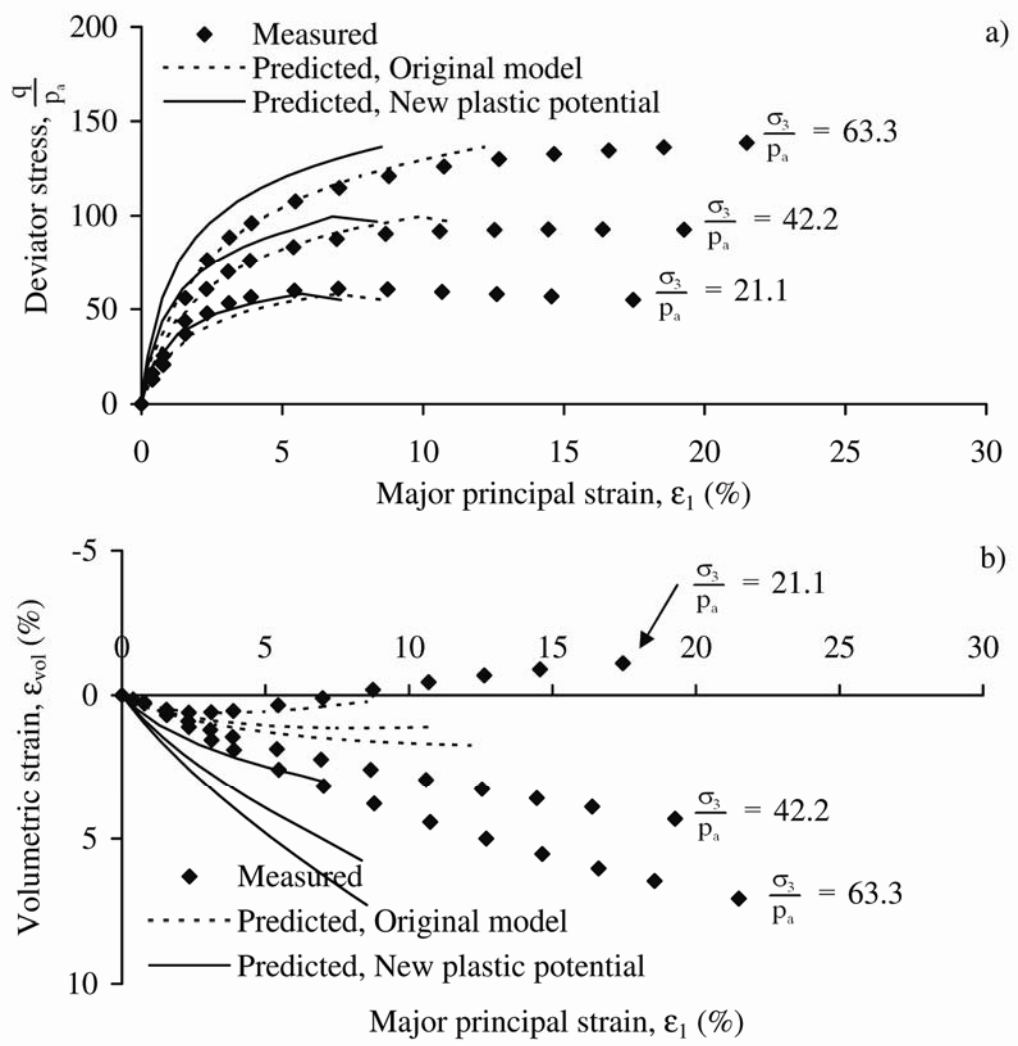

Comparison of original and cubic root plastic potential function for L2-Sand at high confining pressures. a) Stress-strain. b) Volume change.

L8-Sand

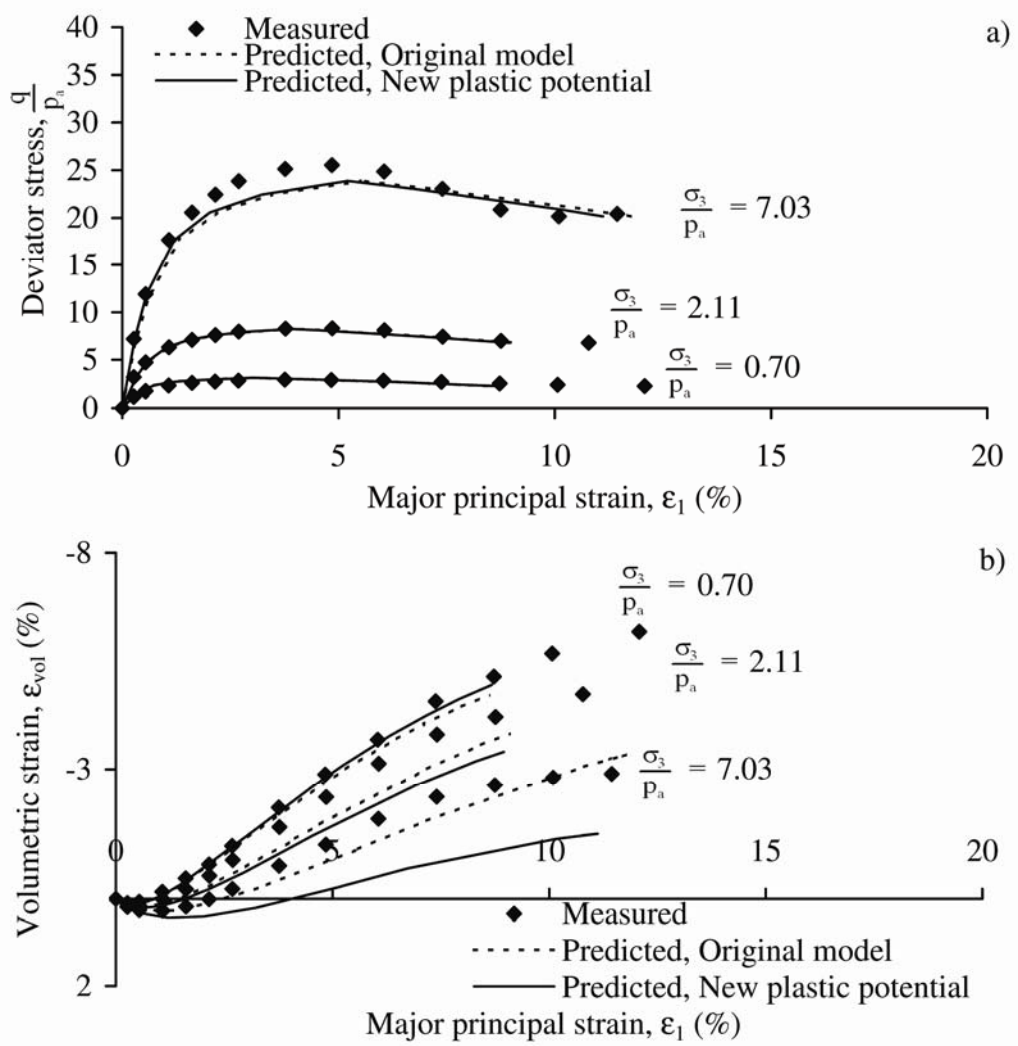

Comparison of original and cubic root plastic potential function for L8-Sand at low confining pressures. a) Stress-strain. b) Volume change.

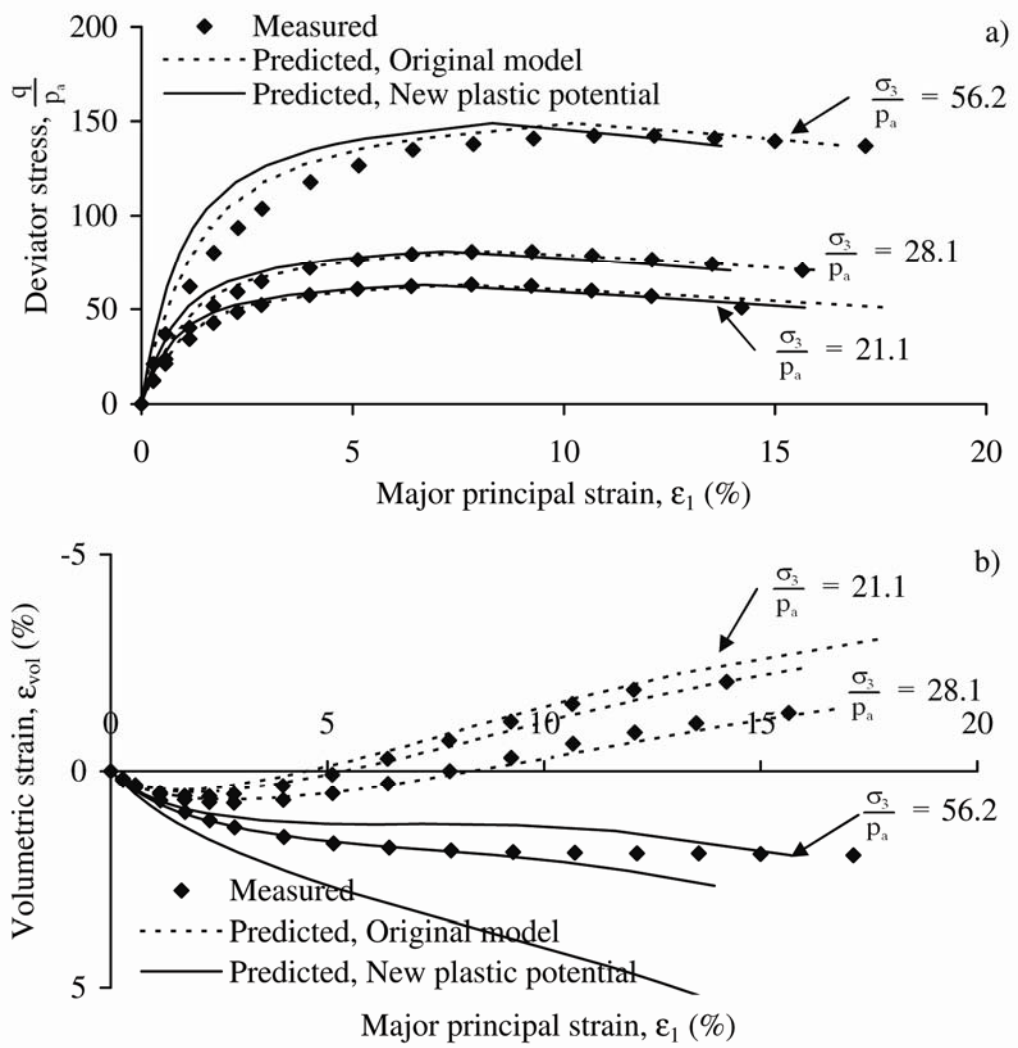

Comparison of original and cubic root plastic potential function for L8-Sand at high confining pressures. a) Stress-strain. b) Volume change.

F1-Sand

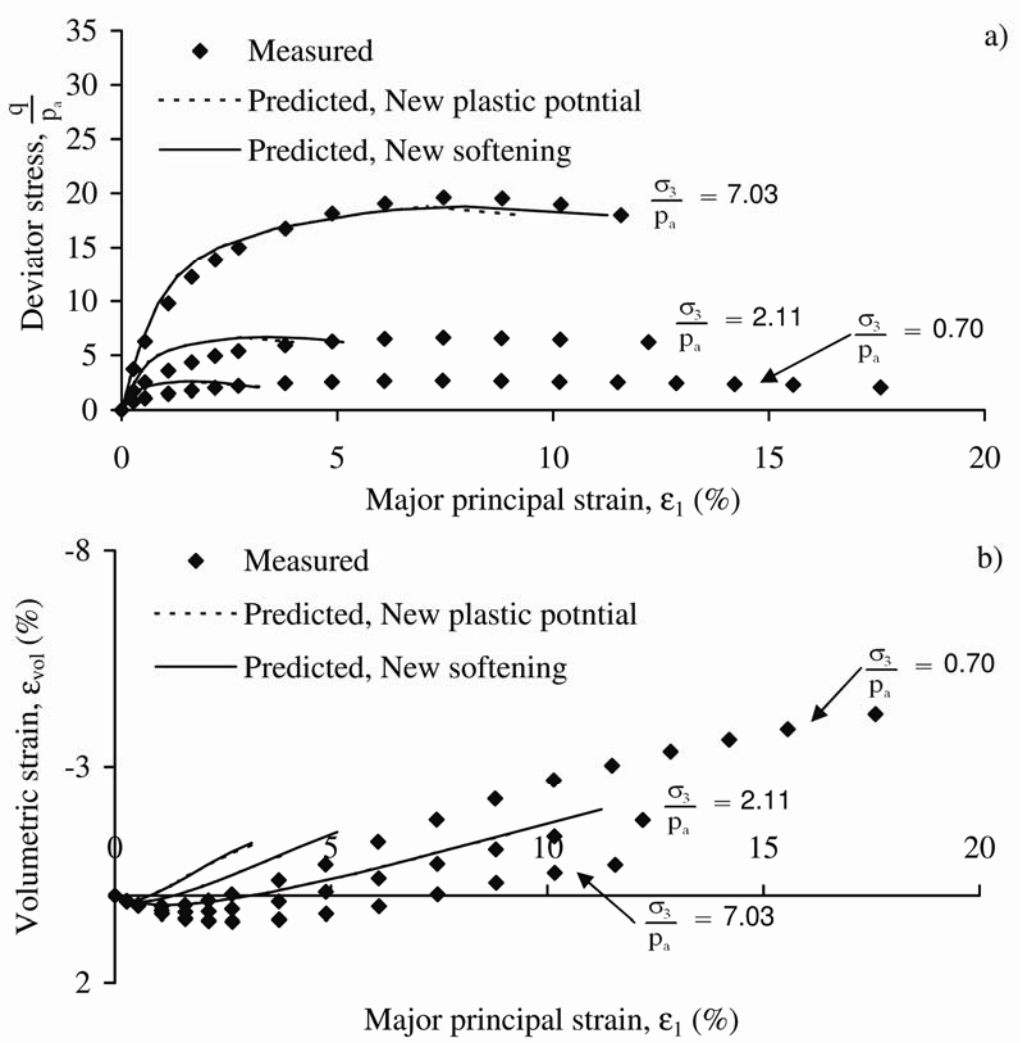

Comparison of original and new softening function for F1-Sand at low confining pressures. With linear version of plastic potential function. a) Stress-strain. b) Volume change.

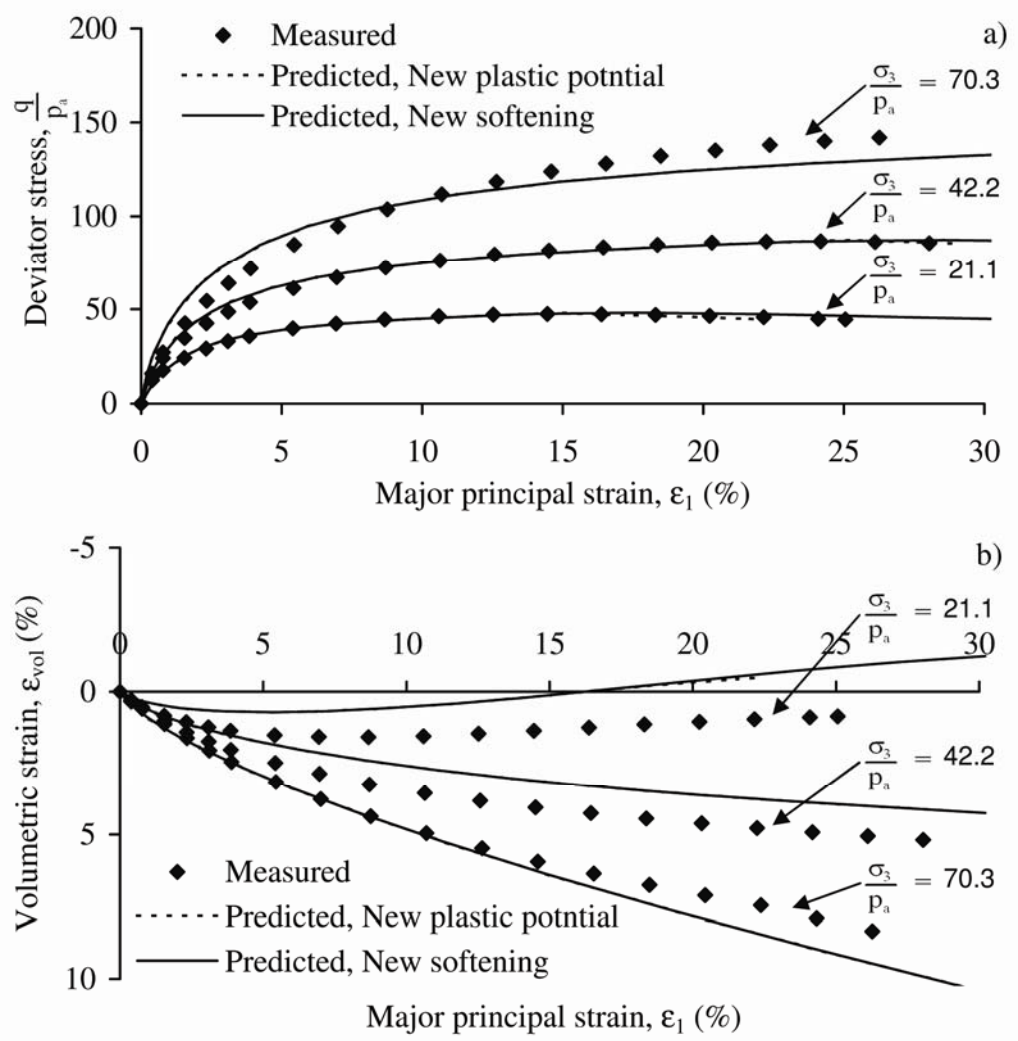

Comparison of original and new softening function for F1-Sand at high confining pressures. With linear version of plastic potential function. a) Stress-strain. b) Volume change.

L1-Sand

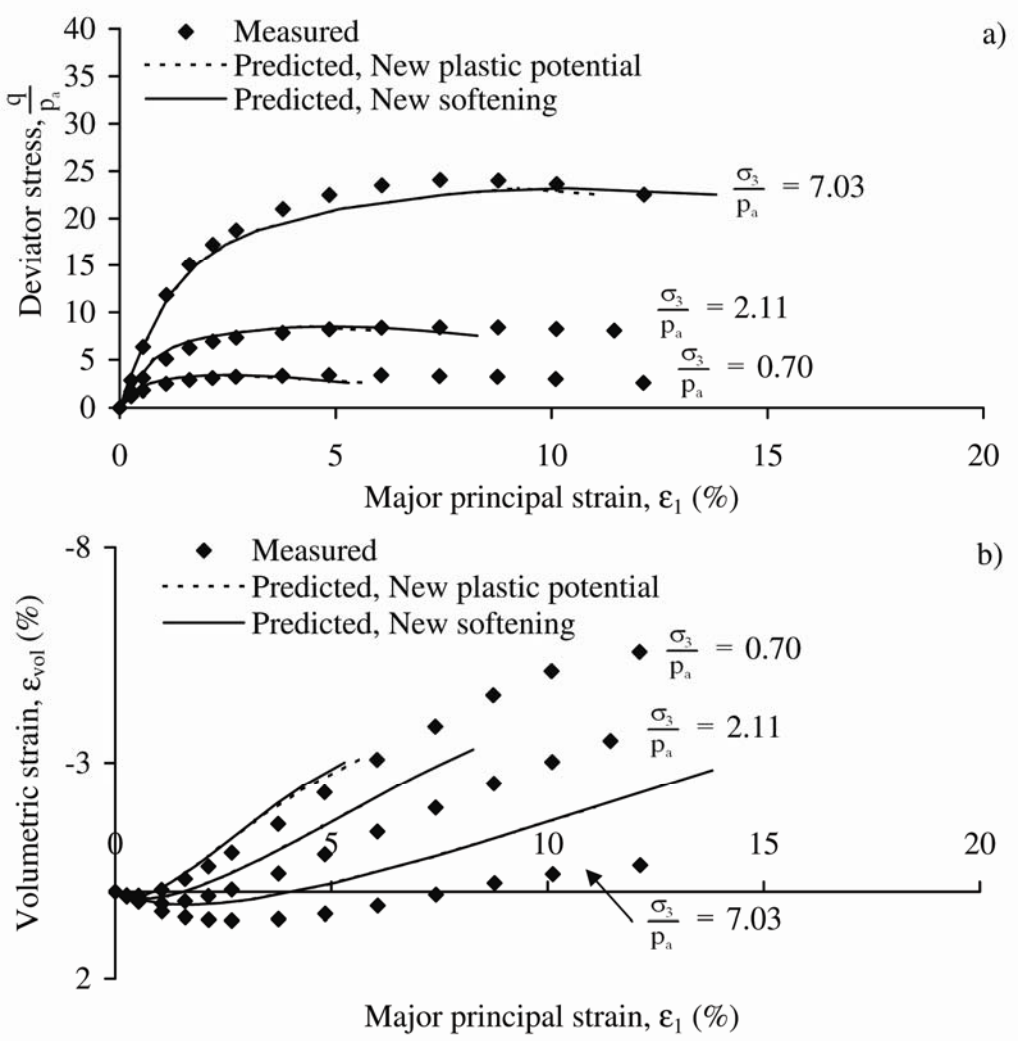

Comparison of original and new softening function for L1-Sand at low confining pressures. With linear version of plastic potential function. a) Stress-strain. b) Volume change.

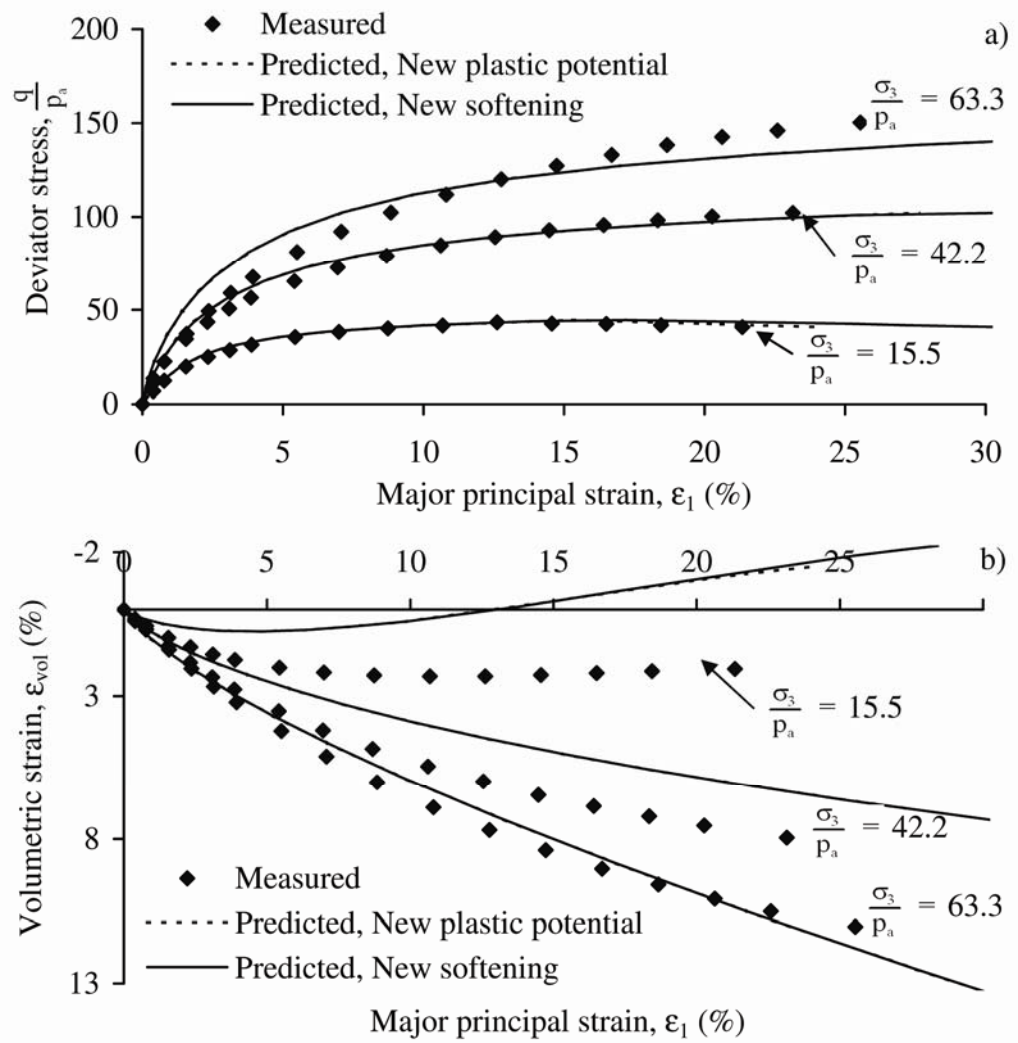

Comparison of original and new softening function for L1-Sand at high confining pressures. With linear version of plastic potential function. a) Stress-strain. b) Volume change.

L2-Sand

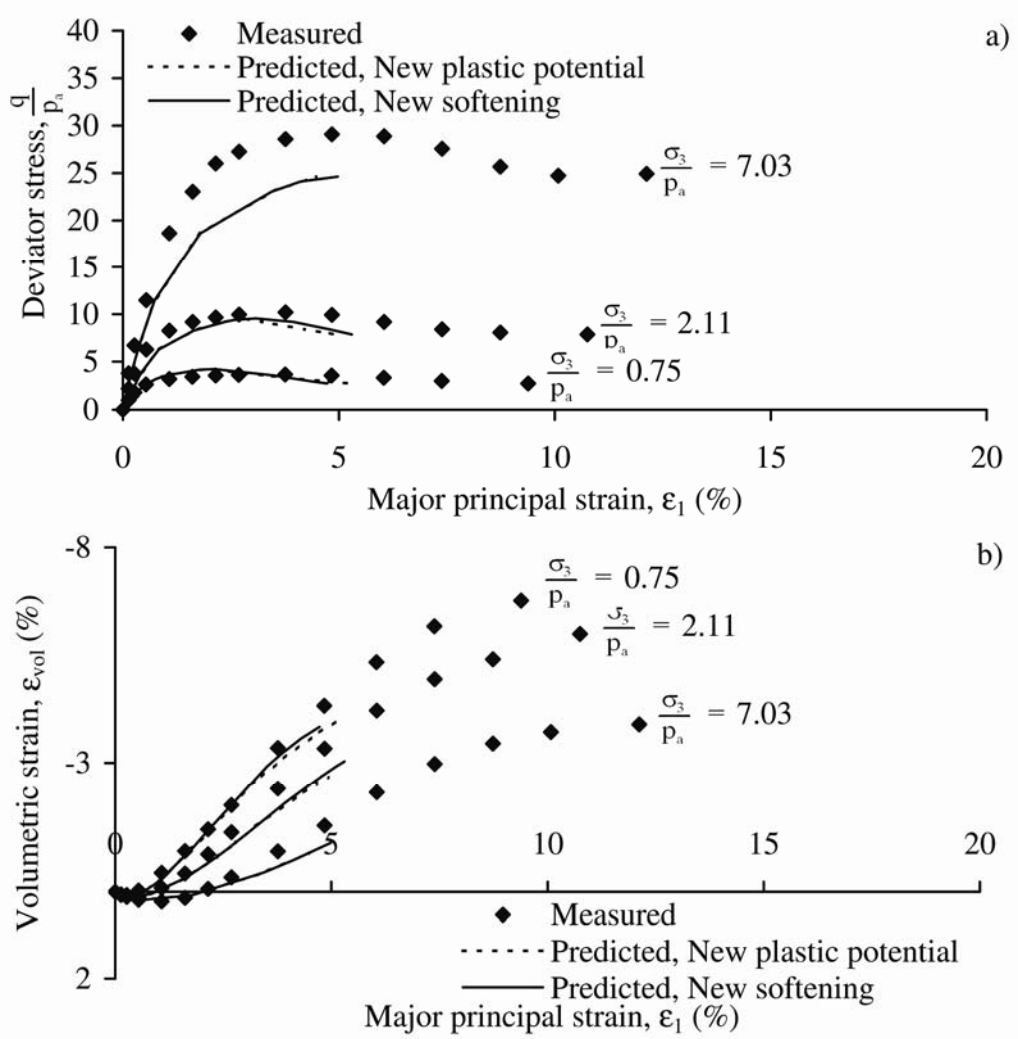

Comparison of original and new softening function for L2-Sand at low confining pressures. With linear version of plastic potential function. a) Stress-strain. b) Volume change.

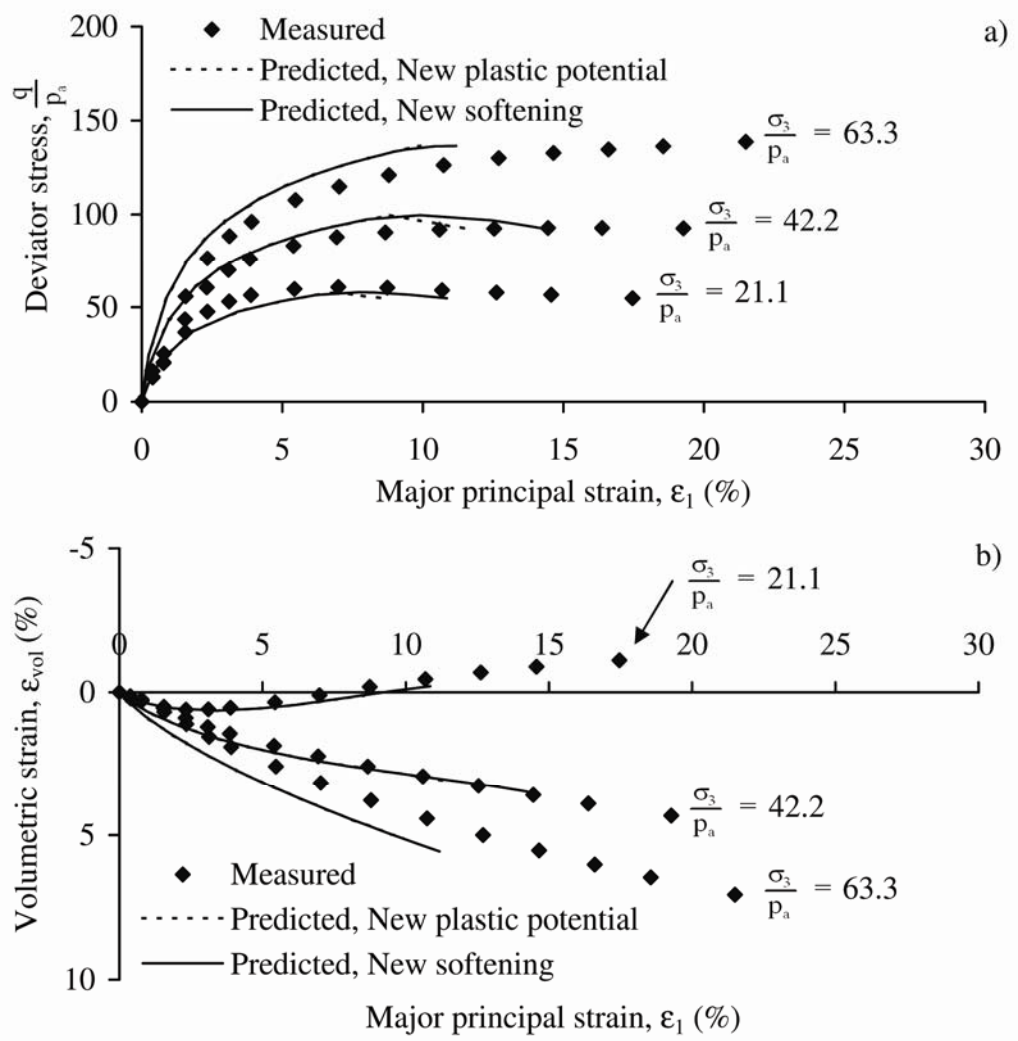

Comparison of original and new softening function for L2-Sand at high confining pressures. With linear version of plastic potential function. a) Stress-strain. b) Volume change.

L8-Sand

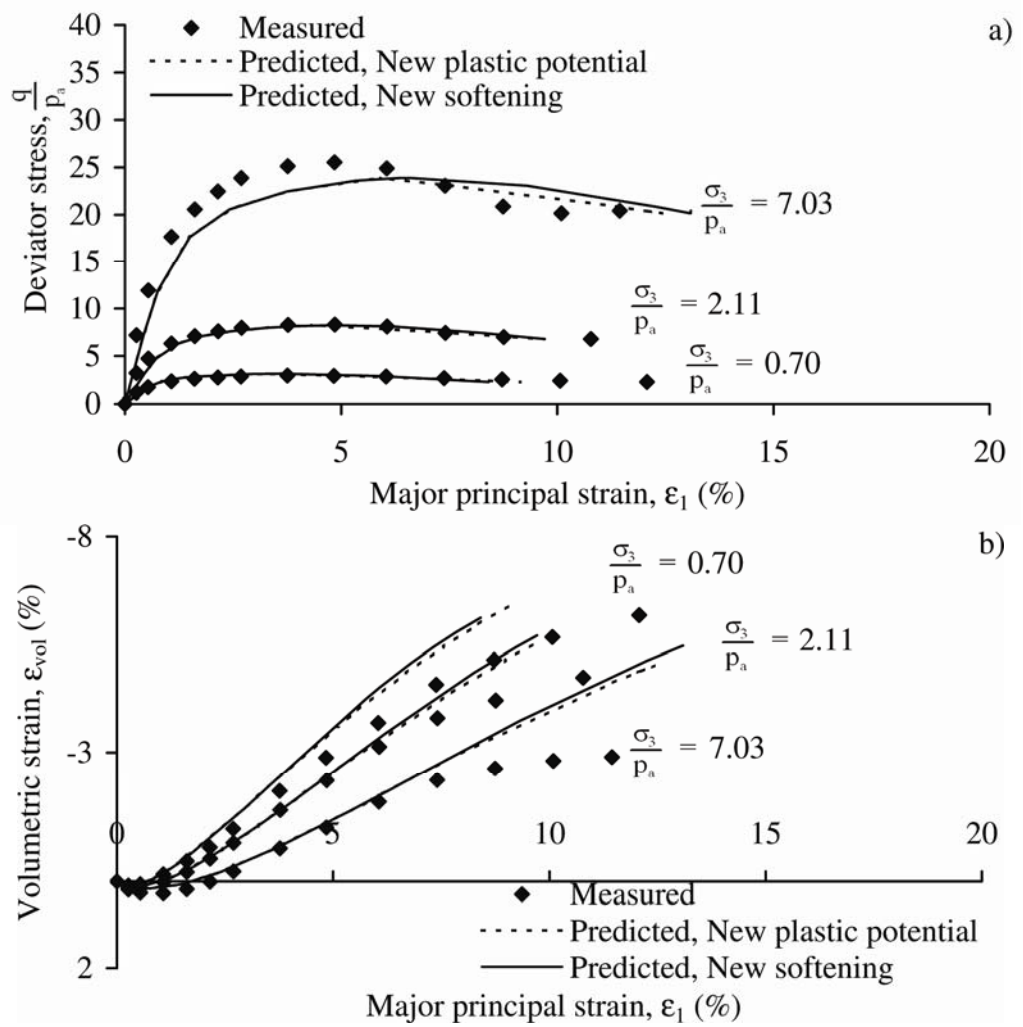

Comparison of original and new softening function for L8-Sand at low confining pressures. With linear version of plastic potential function. a) Stress-strain. b) Volume change.

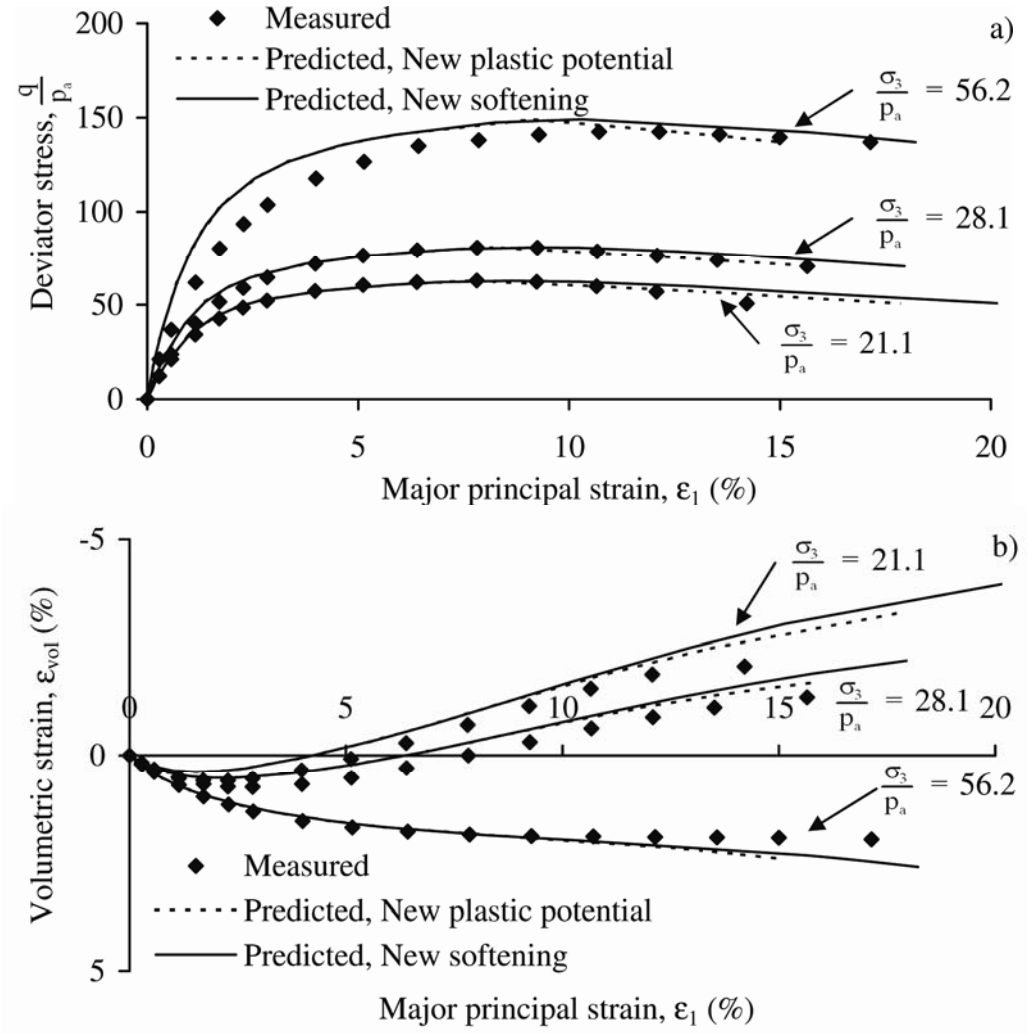

Comparison of original and new softening function for L8-Sand at high confining pressures. With linear version of plastic potential function. a) Stress-strain. b) Volume change.

Appendix D: Test Data

Data from triaxial, isotropic, K_0, Brazilian, and torsion shear tests.

Triaxial tests

Vertical tests		Horizontal tests	
V3	σ_3 = 0.05 MPa	H2	σ_3 = 0.05 MPa
V10	σ_3 = 0.05 MPa	H10	σ_3 = 0.05 MPa
V5	σ_3 = 0.14 MPa	H4	σ_3 = 0.14 MPa
V1	σ_3 = 0.48 MPa	H5	σ_3 = 0.15 MPa
V6	σ_3 = 1.0 MPa	H1	σ_3 = 0.48 MPa
V7	σ_3 = 2.0 MPa	H8	σ_3 = 1.0 MPa
V8	σ_3 = 4.0 MPa	H7	σ_3 = 2.0 MPa
V14	σ_3 = 6.0 MPa	H6	σ_3 = 4.0 MPa
V15	σ_3 = 9.9 MPa	H13	σ_3 = 4.0 MPa
V16	σ_3 = 14.0 MPa	H16	σ_3 = 5.9 MPa
V9*	σ_3 = 0.15 MPa	H14	σ_3 = 9.9 MPa
		H15	σ_3 = 14.0 MPa
		H9*	σ_3 = 0.15 MPa

Isotropic tests

Vertical tests		Horizontal tests	
V4*	(Brazilian)	H3*	(Brazilian)
V9*	(Triaxial)	H9*	(Triaxial)

K_0-tests

Vertical tests
V11
V13**

Brazilian tests

Vertical tests	Horizontal tests
V2	H11
V12	H12
V4*	H3*

Torsion shear tests

TS1
TS2
TS3

*The cementation was not broken after the isotropic tests, so the specimens were used for a second test.

**No volume change correction on this test, due to the extra layer of rubber latex.

Specimen	**V3**		Porosity	43.7	%
Cored from block	I		Void ratio	0.777	
Orientation	Vertical				
Initial height	9.760	cm	Back pressure	98	kPa
Initial diameter	3.676	cm	Saturation index, B	0.91	
Initial mass	156.2	g			

	Time sec.	σ_3' MPa	σ_1' MPa	ε_1 %	ε_{vol} %
Triaxial loading	0	0.048	0.036	0.000	0.000
	240	0.048	0.202	0.325	0.239
	300	0.048	0.317	0.393	0.279
	360	0.048	0.474	0.457	0.307
	420	0.048	0.593	0.509	0.324
Unloading	480	0.048	0.383	0.494	0.318
	540	0.048	0.143	0.426	0.279
Reloading	600	0.048	0.195	0.485	0.311
	660	0.048	0.536	0.536	0.344
Triaxial loading	720	0.048	0.766	0.600	0.355
	780	0.048	0.920	0.682	0.357
	840	0.048	1.027	0.781	0.341
	900	0.048	1.142	0.869	0.300
	960	0.048	1.210	0.964	0.202
	1080	0.048	1.082	1.176	-0.123
	1320	0.049	0.874	1.594	-0.791
	1620	0.048	0.716	2.106	-1.493
	2220	0.049	0.599	2.729	-2.103
	2580	0.049	0.516	3.335	-2.603
	3000	0.049	0.461	4.054	-2.986
	3600	0.049	0.441	5.021	-3.284
	4200	0.050	0.441	6.033	-3.511
	4920	0.049	0.459	6.887	-3.583
	5280	0.049	0.473	7.474	-3.693
Unloading	5340	0.050	0.258	7.425	-3.648
	5400	0.049	0.166	7.331	-3.492
	5520	0.049	0.118	7.126	-3.239
	5640	0.049	0.093	6.931	-3.057
	5700	0.049	0.088	6.826	-2.986

Specimen	**V10**		Porosity	42.5	%
Cored from block	II		Void ratio	0.739	
Orientation	Vertical				
Initial height	9.766	cm	Back pressure	98	kPa
Initial diameter	3.644	cm	Saturation index, B	0.92	
Initial mass	157.0	g			

	Time sec.	σ_3' MPa	σ_1' MPa	ε_1 %	ε_{vol} %
Triaxial loading	0	0.049	0.037	0.000	0.000
	120	0.049	0.262	0.048	0.009
	180	0.049	0.528	0.089	0.025
	240	0.049	0.785	0.155	0.078
	300	0.049	1.033	0.231	0.098
	360	0.049	1.282	0.320	0.087
	420	0.049	1.462	0.399	0.060
	480	0.049	1.538	0.493	-0.026
	540	0.049	1.542	0.594	-0.158
	600	0.050	1.509	0.699	-0.310
	720	0.050	1.345	0.903	-0.725
	900	0.050	1.147	1.225	-1.445
	1140	0.050	0.967	1.630	-2.336
	1440	0.050	0.800	2.141	-3.312
	1920	0.050	0.612	2.940	-4.401
	2400	0.050	0.520	3.742	-5.015
	3000	0.050	0.494	4.740	-5.431
Unloading	3120	0.050	0.240	4.704	-5.378
	3180	0.049	0.116	4.618	-5.207
	3360	0.049	0.067	4.421	-4.797
Reloading	3420	0.049	0.183	4.495	-4.797
	3540	0.049	0.365	4.683	-4.910
Triaxial loading	3660	0.049	0.482	4.868	-5.042
	3960	0.049	0.511	5.366	-5.306
	4200	0.049	0.510	5.766	-5.477
Unloading	4260	0.049	0.218	5.717	-5.444
	4380	0.049	0.105	5.630	-5.279
	4500	0.049	0.057	5.424	-4.962
	4680	0.049	0.037	5.156	-4.665

Specimen	**V5**		Porosity	43.9	%
Cored from block	I		Void ratio	0.781	
Orientation	Vertical				
Initial height	9.785	cm	Back pressure	98	kPa
Initial diameter	3.678	cm	Saturation index, B	0.94	
Initial mass	156.4	g			

	Time sec.	σ_3' MPa	σ_1' MPa	ε_1 %	ε_{vol} %
Triaxial loading	0	0.142	0.107	0.000	0.000
	60	0.142	0.368	0.027	0.001
	120	0.142	0.659	0.061	0.036
	180	0.142	0.967	0.116	0.058
	240	0.142	1.316	0.183	0.098
	306	0.142	1.634	0.253	0.116
	360	0.142	1.820	0.349	0.129
	420	0.142	1.900	0.442	0.103
	540	0.142	1.809	0.643	-0.071
	720	0.142	1.646	0.937	-0.440
	1020	0.142	1.458	1.437	-0.989
	1380	0.142	1.290	2.031	-1.487
	2040	0.143	1.175	2.727	-1.778
	2520	0.143	1.117	3.528	-2.011
	3120	0.143	1.052	4.549	-2.367
	3720	0.143	0.969	5.536	-2.729
	4680	0.144	0.934	6.741	-2.955
	5520	0.144	0.946	7.727	-3.084
	6000	0.144	0.963	8.526	-3.201
	6600	0.144	0.989	9.534	-3.350
Unloading	6660	0.144	0.803	9.532	-3.343
	6720	0.144	0.563	9.495	-3.337
	6780	0.144	0.341	9.438	-3.278
	6900	0.144	0.187	9.261	-3.039
	7080	0.144	0.153	9.063	-2.813
Reloading	7140	0.144	0.361	9.132	-2.781
	7260	0.144	0.523	9.302	-2.793
	7380	0.144	0.750	9.460	-2.845
	7500	0.144	0.959	9.638	-2.923
	7680	0.144	1.052	9.938	-3.033
Triaxial loading	8160	0.144	1.079	10.728	-3.285
	8640	0.144	1.090	11.519	-3.492
Unloading	8760	0.144	0.642	11.487	-3.472
	8820	0.144	0.365	11.433	-3.427

8940	0.144	0.196	11.261	-3.201
9120	0.144	0.132	10.987	-2.929
9240	0.144	0.111	10.812	-2.800

Specimen	**V1**		Porosity	43.6	%
Cored from block	I		Void ratio	0.772	
Orientation	Vertical				
Initial height	9.792	cm	Back pressure	98	kPa
Initial diameter	3.670	cm	Saturation index, B	0.92	
Initial mass	156.7	g			

	Time sec.	σ_3' MPa	σ_1' MPa	ε_1 %	ε_{vol} %
Triaxial loading	0	0.481	0.361	0.000	0.000
	120	0.482	0.898	0.126	0.110
	240	0.481	1.561	0.260	0.219
	360	0.482	2.128	0.420	0.323
Unloading	450	0.482	1.625	0.408	0.329
	570	0.482	1.008	0.368	0.336
Reloading	660	0.482	1.825	0.431	0.381
Triaxial loading	780	0.482	2.496	0.597	0.427
	900	0.482	2.661	0.787	0.453
	1200	0.482	2.832	1.264	0.368
	1440	0.482	2.865	1.660	0.251
	1680	0.482	2.850	2.053	0.115
	1980	0.482	2.802	2.551	-0.067
	2340	0.483	2.729	3.165	-0.274
	2760	0.483	2.636	3.871	-0.489
	3480	0.483	2.553	4.573	-0.599
	3960	0.483	2.453	5.378	-0.735
	4560	0.483	2.364	6.369	-0.826
	5280	0.483	2.348	7.169	-0.800
	5880	0.483	2.325	8.159	-0.846
	6600	0.483	2.339	8.971	-0.820
	7080	0.483	2.326	9.780	-0.865
	7560	0.483	2.321	10.570	-0.904
Unloading	7680	0.483	1.736	10.543	-0.878
	7740	0.483	1.166	10.483	-0.839
	7800	0.483	0.862	10.410	-0.774
	7920	0.483	0.596	10.249	-0.599
	8220	0.483	0.411	9.878	-0.242
Reloading	8340	0.483	0.842	10.002	-0.177
	8460	0.483	1.227	10.169	-0.151
	8640	0.483	1.777	10.418	-0.196
	8820	0.483	2.228	10.684	-0.274
Triaxial loading	9120	0.483	2.414	11.166	-0.391
	9600	0.483	2.412	11.952	-0.534

	10200	0.483	2.374	12.946	-0.677
Unloading	10320	0.483	1.807	12.916	-0.644
	10380	0.483	1.236	12.860	-0.612
	10440	0.483	0.906	12.789	-0.540
	10560	0.483	0.618	12.635	-0.372
	10740	0.483	0.446	12.365	-0.125
	10920	0.483	0.369	12.143	0.063

Specimen	**V6**		Porosity	44.5	%
Cored from block	I		Void ratio	0.803	
Orientation	Vertical				
Initial height	9.779	cm	Back pressure	98	kPa
Initial diameter	3.679	cm	Saturation index, B	0.90	
Initial mass	154.5	g			

	Time sec.	σ_3' MPa	σ_1' MPa	ε_1 %	ε_{vol} %
Triaxial loading	0	1.000	0.750	0.000	0.000
	120	1.000	1.295	0.122	0.098
	240	1.000	1.889	0.240	0.182
Unloading	330	1.000	1.027	0.207	0.182
Reloading	360	1.000	1.086	0.208	0.182
	390	1.000	1.416	0.227	0.188
Triaxial loading	480	0.981	2.263	0.308	0.247
	660	1.030	3.214	0.550	0.428
	840	1.020	3.926	0.813	0.558
	1080	1.020	4.404	1.187	0.649
	1260	0.990	4.423	1.483	0.630
	1500	1.000	4.462	1.879	0.584
	1800	1.000	4.439	2.373	0.506
	2160	1.000	4.392	2.967	0.402
	2760	1.000	4.357	3.560	0.325
	3240	1.000	4.279	4.350	0.208
	3840	1.000	4.195	5.361	0.078
	4560	0.99	4.116	6.571	-0.039
	5400	0.99	4.074	7.573	-0.097
	6000	1.000	4.048	8.555	-0.169
	6840	0.991	4.026	9.537	-0.227
	7320	1.000	4.020	10.335	-0.260
Unloading	7440	1.000	3.203	10.299	-0.253
	7500	1.000	2.389	10.244	-0.247
	7620	1.000	1.520	10.110	-0.149
	7800	1.000	1.021	9.873	0.052
	8040	0.971	0.737	9.560	0.260
Reloading	8160	0.971	1.061	9.588	0.299
	8280	0.981	1.653	9.702	0.338
	8460	0.981	2.492	9.934	0.344
	8700	0.981	3.504	10.27	0.273
	8880	0.981	3.942	10.552	0.208
Triaxial loading	9360	0.981	4.109	11.353	0.058
	9960	0.981	4.090	12.336	-0.052

Unloading	10080	0.981	3.253	12.304	-0.045
	10140	0.981	2.460	12.25	-0.026
	10260	0.981	1.566	12.118	0.039
	10440	0.981	1.046	11.878	0.234
	10740	0.971	0.724	11.487	0.487

Specimen	**V7**		Porosity	44.1	%
Cored from block	I		Void ratio	0.790	
Orientation	Vertical				
Initial height	9.766	cm	Back pressure	98	kPa
Initial diameter	3.681	cm	Saturation index, B	0.91	
Initial mass	155.6	g			

	Time sec.	σ_3' MPa	σ_1' MPa	ε_1 %	ε_{vol} %
Triaxial loading	0	2.001	1.500	0.000	0.000
	120	2.001	2.227	0.098	0.110
	300	2.001	3.500	0.295	0.285
Unloading	360	2.001	2.840	0.281	0.304
	480	2.001	2.627	0.275	0.324
Reloading	540	2.001	3.334	0.31	0.349
Triaxial loading	600	2.001	3.984	0.38	0.401
	720	2.001	4.793	0.539	0.518
	900	2.001	5.780	0.788	0.686
	1140	2.010	6.672	1.140	0.887
	1500	2.010	7.236	1.713	1.087
	1800	2.020	7.402	2.200	1.184
	2160	2.020	7.475	2.793	1.314
	2520	2.040	7.533	3.388	1.424
	2820	2.040	7.544	3.876	1.508
	3180	2.000	7.421	4.486	1.586
	3540	2.000	7.405	5.082	1.663
	4020	2.000	7.371	5.891	1.799
	4680	2.000	7.355	6.586	2.019
	5160	2.000	7.325	7.377	2.052
	5760	1.991	7.267	8.365	2.311
	6600	1.991	7.216	9.365	2.608
	7200	1.971	7.216	10.373	2.848
Unloading	7260	2.020	6.325	10.349	2.880
	7320	2.015	5.276	10.290	2.926
	7440	2.005	3.767	10.165	3.016
	7620	1.991	2.545	9.932	3.249
	7860	1.971	1.836	9.609	3.540
	8100	1.971	1.501	9.306	3.773
Reloading	8160	1.971	1.869	9.332	3.825
	8280	1.971	2.668	9.440	3.877
	8460	1.971	3.970	9.655	3.935
	8700	1.961	5.464	9.973	3.942
	8940	1.951	6.667	10.325	3.877

Triaxial loading	9240	1.951	7.247	10.796	3.780
	9840	1.961	7.260	11.786	3.670
	10440	1.961	7.147	12.778	3.605
Unloading	10500	1.961	6.263	12.763	3.605
	10560	1.971	5.254	12.710	3.625
	10620	1.971	4.406	12.652	3.644
	10740	1.971	3.233	12.517	3.715
	10920	1.971	2.310	12.285	3.884
	11160	1.951	1.736	11.956	4.078
	11400	1.942	1.460	11.663	4.233

Specimen	**V8**		Porosity	44.4	%
Cored from block	I		Void ratio	0.799	
Orientation	Vertical				
Initial height	9.734	cm	Back pressure	96	kPa
Initial diameter	3.677	cm	Saturation index, B	0.92	
Initial mass	154.0	g			

	Time sec.	σ_3' MPa	σ_1' MPa	ε_1 %	ε_{vol} %
Isotropic loading	240	0.109	0.082	0.000	0.000
	360	0.491	0.368	0.095	0.503
	480	0.982	0.736	0.219	0.874
	600	1.472	1.104	0.309	1.141
	720	1.962	1.472	0.375	1.354
	840	2.472	1.854	0.421	1.547
	960	2.992	2.244	0.484	1.770
	1080	3.512	2.634	0.529	1.975
	1200	4.002	3.002	0.576	2.181
Triaxial loading	0	4.002	3.002	0.000	0.000
	60	4.002	3.552	0.054	0.059
	180	4.002	4.335	0.181	0.163
	300	4.002	5.143	0.325	0.280
Unloading	480	4.002	4.046	0.300	0.293
Reloading	600	4.002	5.585	0.406	0.358
Triaxial loading	660	4.002	6.012	0.487	0.410
	840	4.002	7.185	0.726	0.572
	1020	4.003	8.220	0.980	0.748
	1200	4.003	9.095	1.240	0.898
	1440	4.003	9.975	1.601	1.093
	1800	4.003	10.803	2.149	1.340
	2280	4.003	11.343	2.920	1.606
	2760	4.003	11.636	3.709	1.925
	3360	4.003	11.860	4.739	2.179
	4080	3.993	12.020	5.913	2.406
	4920	3.983	12.150	7.267	2.667
	5760	3.993	12.270	8.656	2.927
	6720	3.983	12.306	10.261	3.245
	7448	3.983	12.325	11.448	3.467
	8160	3.993	12.361	12.63	3.668
	9000	3.973	12.321	14.029	3.902
	9840	3.974	12.251	15.428	4.117
	10680	3.973	12.194	16.841	4.338
	11640	3.973	12.128	18.429	4.611

	12240	3.973	12.080	19.423	4.774
Unloading	12360	3.973	9.260	19.343	4.806
	12540	3.973	6.322	19.150	4.891
	12720	3.973	4.774	18.946	5.040
	12960	3.973	3.708	18.622	5.288
	13200	3.973	3.169	18.318	5.496
Reloading	13320	3.973	4.095	18.38	5.561
	13440	3.973	5.326	18.504	5.632
	13620	4.003	7.267	18.716	5.717
	13800	4.003	8.972	18.945	5.749
	13980	4.003	10.516	19.181	5.769
	14220	4.003	11.973	19.538	5.769
	14640	4.003	12.647	20.204	5.795
Unloading	14700	4.003	11.269	20.185	5.808
	14760	3.990	9.803	20.134	5.808
	14880	3.965	7.452	20.013	5.840
	15060	3.927	5.208	19.817	5.925
	15300	3.877	3.688	19.504	6.101
	15660	3.729	2.797	19.133	6.224
Isotropic unloading	15660	3.729	2.797	19.133	6.224
	15780	3.337	2.502	19.098	6.227
	15900	2.944	2.208	19.067	6.228
	16020	2.483	1.863	19.031	6.214
	16140	1.973	1.480	18.987	6.184
	16260	1.492	1.119	18.930	6.127
	16380	0.992	0.744	18.857	6.039
	16500	0.492	0.369	18.722	5.859

Specimen	**V14**		Porosity	43.7	%
Cored from block	II		Void ratio	0.775	
Orientation	Vertical				
Initial height	9.761	cm	Back pressure	99	kPa
Initial diameter	3.627	cm	Saturation index, B	0.93	
Initial mass	152.3	g			

	Time	σ_3'	σ_1'	ε_1	ε_{vol}
	sec.	MPa	MPa	%	%
Isotropic loading	240	0.108	0.081	0.000	0.000
	360	0.598	0.448	-0.001	0.271
	480	1.088	0.816	0.040	0.397
	600	1.578	1.184	0.086	0.530
	720	2.059	1.545	0.128	0.696
	840	2.550	1.912	0.166	0.853
	960	3.060	2.295	0.206	1.011
	1080	3.550	2.662	0.244	1.171
	1200	4.039	3.030	0.284	1.357
	1320	4.530	3.397	0.324	1.599
	1440	5.020	3.765	0.328	1.898
	1560	5.020	3.765	0.331	2.058
	1680	5.520	4.140	0.381	2.346
	1800	6.010	4.508	0.417	2.690
Triaxial loading	0	6.011	4.508	0.000	0.000
	120	6.011	5.651	0.114	0.107
	300	6.011	7.172	0.317	0.280
	480	6.011	8.618	0.550	0.467
	726	6.001	10.339	0.894	0.733
	1020	6.001	11.900	1.331	1.040
	1440	6.001	13.342	1.999	1.440
	2040	6.001	14.532	2.958	1.966
	2760	6.001	15.408	4.130	2.519
	3480	6.001	16.010	5.295	3.139
	4500	6.001	16.609	6.952	3.666
	5700	5.991	17.236	8.922	4.692
	6900	5.991	17.667	10.884	5.345
	8100	5.991	18.006	12.867	6.118
	9600	5.982	18.350	15.348	7.145
	11100	5.982	18.614	17.820	7.925
	12600	5.991	18.679	20.297	8.418
	13200	6.001	18.632	21.283	8.591
Unloading	13320	6.001	15.162	21.216	8.618
	13500	6.001	10.924	21.044	8.665

	13740	5.981	7.529	20.767	8.758
	14040	5.981	5.489	20.388	9.018
	14280	5.981	4.714	20.109	9.171
Reloading	14400	5.981	5.728	20.143	9.218
	14585	5.981	8.313	20.321	9.298
	14760	5.981	10.776	20.531	9.358
	15004	5.981	14.004	20.828	9.404
	15240	5.991	16.683	21.136	9.424
	15540	6.001	18.704	21.575	9.444
	15960	6.001	19.410	22.237	9.484
	16500	6.011	19.425	23.135	9.584
	17400	6.050	19.315	24.626	9.764
Unloading	17520	6.050	15.688	24.568	9.784
	17640	6.050	12.582	24.461	9.804
	17820	6.030	9.209	24.279	9.871
	18060	5.991	6.560	23.988	10.018
	18300	5.981	5.227	23.680	10.164
	18600	5.981	4.488	23.380	10.317
Isotropic unloading	18600	5.981	4.486	23.380	10.317
	18720	5.510	4.133	23.337	10.346
	18840	5.030	3.772	23.306	10.337
	18960	4.520	3.390	23.295	10.345
	19080	4.020	3.015	23.239	10.330
	19200	3.539	2.654	23.203	10.324
	19320	3.039	2.279	23.165	10.311
	19440	2.509	1.882	23.118	10.282
	19560	2.058	1.544	23.071	10.249
	19680	1.588	1.191	23.013	10.211
	19800	1.088	0.816	22.926	10.139
	19920	0.588	0.441	22.780	10.017
	20040	0.117	0.088	22.231	9.427

Specimen	**V15**		Porosity	43.4	%
Cored from block	II		Void ratio	0.768	
Orientation	Vertical				
Initial height	9.771	cm	Back pressure	97	kPa
Initial diameter	3.635	cm	Saturation index, B	0.94	
Initial mass	153.7	g			

	Time	σ_3'	σ_1'	ε_1	ε_{vol}
	sec.	MPa	MPa	%	%
Isotropic loading	240	0.109	0.082	0.000	0.000
	360	0.599	0.449	0.040	0.232
	480	1.089	0.817	0.098	0.370
	600	1.570	1.177	0.155	0.503
	720	2.080	1.560	0.209	0.665
	840	2.570	1.927	0.250	0.814
	960	3.051	2.288	0.286	1.001
	1088	3.531	2.649	0.322	1.200
	1200	4.032	3.024	0.359	1.410
	1320	4.512	3.384	0.394	1.579
	1440	5.022	3.766	0.430	1.730
	1560	5.512	4.134	0.465	1.944
	1680	5.993	4.494	0.494	2.147
	1800	6.483	4.862	0.526	2.358
	1920	6.963	5.223	0.554	2.578
	2040	7.473	5.605	0.580	2.844
	2160	7.944	5.958	0.606	3.060
	2280	8.464	6.348	0.631	3.289
	2400	8.935	6.701	0.654	3.487
	2520	9.415	7.061	0.674	3.678
	2640	9.915	7.436	0.696	3.870
Triaxial loading	3240	9.905	7.429	0.000	0.000
	3420	9.905	8.764	0.088	0.093
	3600	9.905	10.664	0.275	0.259
	3780	9.905	12.461	0.495	0.438
	3960	9.895	14.084	0.728	0.637
	4200	9.886	15.936	1.058	0.902
	4560	9.886	18.012	1.585	1.346
	5040	9.886	19.869	2.346	1.903
	5760	9.886	21.609	3.485	2.626
	6480	9.886	22.807	4.623	3.581
	7500	9.886	24.028	6.259	4.503
	8700	9.876	25.099	8.24	5.544
	9900	9.876	26.202	10.187	7.401

	11100	9.867	27.178	12.154	8.635
	12600	9.906	28.166	14.618	9.597
	14100	9.905	28.955	17.095	10.452
	15600	9.905	29.607	19.571	11.149
	16800	9.925	30.033	21.543	11.666
	18000	9.915	30.130	23.661	12.150
Unloading	18120	9.915	25.720	23.509	12.183
	18300	9.905	20.101	23.363	12.223
	18540	9.905	14.506	23.128	12.316
	18840	9.856	10.353	22.786	12.495
	19080	9.856	8.492	22.474	12.654
	19260	9.847	7.687	22.292	12.747
Reloading	19380	9.847	9.152	22.322	12.800
	19560	9.915	12.604	22.488	12.886
	19800	9.915	17.077	22.741	12.972
	20040	9.905	21.461	23.012	13.032
	20280	9.905	25.609	23.292	13.079
	20640	9.915	29.864	23.767	13.145
	21120	9.915	31.518	24.523	13.258
	21600	9.925	31.752	25.303	13.384
	22200	9.925	31.642	26.293	13.543
Unloading	22320	9.935	27.065	26.248	13.569
	22500	9.935	21.055	26.106	13.616
	22740	9.916	15.321	25.895	13.695
	22980	9.906	11.495	25.634	13.828
	23280	9.866	8.681	25.276	13.994
	23820	9.827	7.372	24.948	14.180
Isotropic unloading	23820	9.827	7.370	24.948	14.180
	23940	9.415	7.061	24.928	14.191
	24060	8.837	6.627	24.904	14.208
	24180	8.395	6.296	24.884	14.215
	24300	7.964	5.973	24.865	14.222
	24420	7.493	5.620	24.843	14.225
	24540	6.964	5.223	24.817	14.225
	24660	6.454	4.840	24.790	14.219
	24780	5.983	4.487	24.765	14.219
	24900	5.473	4.105	24.736	14.216
	25020	5.002	3.752	24.708	14.213
	25140	4.522	3.391	24.676	14.207
	25260	4.022	3.016	24.640	14.199
	25380	3.512	2.634	24.600	14.188
	25500	3.041	2.281	24.564	14.173
	25620	2.561	1.920	24.517	14.153
	25740	2.070	1.552	24.460	14.123

25860	1.580	1.185	24.379	14.083
25980	1.099	0.825	24.254	14.013
26100	0.589	0.442	24.024	14.617
26220	0.109	0.081	23.316	13.980

Specimen	**V16**		Porosity	43.6	%
Cored from block	II		Void ratio	0.772	
Orientation	Vertical				
Initial height	9.775	cm	Back pressure	99	kPa
Initial diameter	3.628	cm	Saturation index, B	0.91	
Initial mass	152.8	g			

	Time sec.	σ_3' MPa	σ_1' MPa	ε_1 %	ε_{vol} %
Isotropic loading	240	0.117	0.113	0.000	0.000
	360	0.686	0.665	0.030	0.186
	480	1.185	1.150	0.079	0.285
	600	1.685	1.635	0.128	0.388
	720	2.166	2.101	0.171	0.481
	840	2.656	2.577	0.213	0.600
	960	3.156	3.062	0.257	0.694
	1080	3.637	3.528	0.296	0.796
	1200	4.127	4.003	0.334	0.915
	1320	4.618	4.480	0.371	1.038
	1440	5.138	4.984	0.407	1.210
	1560	5.589	5.421	0.437	1.380
	1680	6.079	5.897	0.470	1.611
	1800	6.579	6.382	0.503	1.843
	1920	7.070	6.858	0.532	2.077
	2040	7.579	7.352	0.563	2.338
	2160	8.040	7.799	0.590	2.568
	2280	8.531	8.275	0.617	2.832
	2400	9.031	8.760	0.644	3.070
	2520	9.511	9.226	0.668	3.296
	2640	10.001	9.701	0.692	3.489
	2760	10.492	10.177	0.713	3.662
	2880	10.992	10.663	0.739	3.843
	3000	11.483	11.138	0.762	4.005
	3120	11.973	11.614	0.783	4.160
	3240	12.463	12.089	0.805	4.309
	3360	13.052	12.660	0.830	4.470
	3480	13.434	13.031	0.845	4.589
	3600	14.003	13.583	0.873	4.751
Triaxial loading	0	13.827	10.370	0.000	0.000
	180	13.983	12.807	0.158	0.120
	360	14.111	14.983	0.376	0.286
	600	14.062	17.391	0.692	0.513
	900	14.032	19.892	1.123	0.832

	1320	14.032	22.418	1.767	1.285
	1920	14.023	24.896	2.738	1.918
	2520	14.022	26.677	3.679	2.537
	3240	14.013	28.294	4.819	3.256
	4200	14.013	30.078	6.336	4.281
	5400	14.003	32.000	8.271	5.686
	6900	14.003	34.131	10.679	7.577
	8400	13.993	36.119	13.113	9.362
	9900	13.993	38.004	15.534	10.813
	11400	13.974	39.714	17.949	12.085
	12900	13.974	41.388	20.369	13.050
	14100	13.974	42.746	22.301	13.750
	15300	13.973	44.209	24.211	14.469
Unloading	15420	13.954	38.893	24.161	14.522
	15600	13.954	31.496	24.024	14.589
	15780	13.935	25.563	23.869	14.655
	16020	13.935	19.486	23.634	14.802
	16260	13.935	15.173	23.372	14.968
	16500	13.944	12.379	23.091	15.155
	16800	13.944	10.567	22.797	15.368
Reloading	16920	13.944	11.763	22.802	15.428
	17040	13.944	14.760	22.864	15.501
	17220	13.944	19.082	23.025	15.587
	17460	13.944	24.884	23.271	15.681
	17700	13.944	30.461	23.527	15.747
	17940	13.944	35.836	23.798	15.807
	18240	13.944	41.653	24.166	15.874
	18600	13.944	45.564	24.665	15.967
	18960	13.944	47.069	25.208	16.073
	19440	13.944	47.915	25.963	16.247
	20040	13.944	48.509	26.920	16.466
Unloading	20160	13.944	43.022	26.875	16.506
	20340	13.944	34.728	26.761	16.540
	20580	13.944	26.399	26.565	16.606
	20820	13.934	19.982	26.339	16.706
	21060	13.934	15.444	26.081	16.819
	21360	13.934	11.864	25.740	16.959
	21660	13.925	10.406	25.520	17.085
Isotropic unloading	21840	13.925	10.444	25.520	17.085
	21960	13.435	10.076	25.479	17.095
	22080	12.905	9.679	25.459	17.112
	22200	12.454	9.341	25.442	17.129
	22320	11.954	8.965	25.421	17.140
	22440	11.454	8.590	25.396	17.151

22560	10.973	8.230	25.378	17.162
22680	10.473	7.855	25.348	17.175
22800	9.924	7.443	25.329	17.183
22920	9.512	7.134	25.304	17.194
23040	9.032	6.774	25.278	17.201
23160	8.600	6.450	25.260	17.201
23280	8.061	6.046	25.235	17.205
23400	7.560	5.670	24.986	17.202
23520	7.080	5.310	25.165	17.213
23640	6.639	4.979	25.129	17.203
23760	6.139	4.604	25.088	17.211
23880	5.590	4.192	25.058	17.209
24000	5.119	3.839	24.996	17.199
24120	4.628	3.471	24.952	17.340
24240	4.138	3.103	24.905	17.323
24360	3.667	2.750	24.807	17.288
24480	3.049	2.287	24.709	17.245
24600	2.667	2.000	24.583	17.187
24720	2.206	1.654	24.439	17.118
24840	1.666	1.250	24.176	16.960
24960	1.137	0.853	23.899	16.789
25080	0.647	0.485	23.599	16.593
25200	0.098	0.073	22.580	15.706

Specimen	**V9**		Porosity	42.5	%
Cored from block	II		Void ratio	0.739	
Orientation	Vertical				
Initial height	9.749	cm	Back pressure	201	kPa
Initial diameter	3.638	cm	Saturation index, B	0.84	
Initial mass	156.2	g			

	Time	σ_3'	σ_1'	ε_1	ε_{vol}
	sec.	MPa	MPa	%	%
Triaxial loading	120	0.143	0.140	0.000	0.000
	240	0.143	0.213	0.170	0.156
	360	0.143	0.336	0.336	0.276
	480	0.143	0.526	0.495	0.383
	660	0.143	0.899	0.718	0.485
	780	0.143	1.175	0.883	0.506
	900	0.143	1.426	1.053	0.478
	1020	0.143	1.592	1.246	0.385
	1200	0.143	1.692	1.531	0.133
	1380	0.143	1.645	1.830	-0.199
	1500	0.143	1.577	2.033	-0.405
	1620	0.143	1.451	2.239	-0.577
	1800	0.143	1.300	2.532	-0.736
	2040	0.143	1.202	2.930	-0.834
	2280	0.143	1.149	3.337	-0.887
	2640	0.143	1.143	3.928	-0.946
	3000	0.143	1.155	4.524	-1.013
Unloading	3120	0.143	0.782	4.494	-1.013
	3180	0.143	0.502	4.419	-0.986
	3300	0.143	0.288	4.275	-0.854
	3480	0.143	0.164	4.003	-0.615
Reloading	3600	0.143	0.303	4.044	-0.569
	3720	0.143	0.559	4.206	-0.535
	3840	0.143	0.798	4.370	-0.588
Triaxial loading	3960	0.143	1.054	4.535	-0.661
	4140	0.143	1.198	4.820	-0.781
	4440	0.143	1.214	5.317	-0.927
	4740	0.143	1.200	5.811	-1.033
	4800	0.143	1.080	5.814	-1.046
Unloading	4860	0.143	0.811	5.771	-1.046
	4920	0.143	0.514	5.697	-1.006
	5040	0.143	0.303	5.558	-0.913
	5160	0.143	0.203	5.370	-0.761

Specimen	**H2**		Porosity	42.6	%
Cored from block	I		Void ratio	0.741	
Orientation	Horizontal				
Initial height	9.762	cm	Back pressure	98	kPa
Initial diameter	3.675	cm	Saturation index, B	0.91	
Initial mass	159.4	g			

	Time sec.	σ_3' MPa	σ_1' MPa	ε_1 %	ε_{vol} %
Triaxial loading	0	0.048	0.036	0.000	0.000
	60	0.048	0.127	0.073	0.044
	120	0.048	0.261	0.129	0.088
	180	0.048	0.400	0.185	0.141
	240	0.048	0.547	0.243	0.168
	300	0.048	0.687	0.303	0.206
	360	0.048	0.871	0.360	0.225
Unloading	420	0.048	0.853	0.371	0.225
	480	0.048	0.502	0.338	0.205
	540	0.048	0.337	0.334	0.205
Reloading	600	0.048	0.629	0.366	0.231
	660	0.048	1.110	0.431	0.245
Triaxial loading	720	0.048	1.355	0.511	0.249
	780	0.048	1.520	0.599	0.210
	900	0.048	1.342	0.816	-0.160
	1080	0.048	1.053	1.151	-0.900
	1260	0.048	0.838	1.467	-1.595
	1440	0.049	0.681	1.782	-2.069
	1680	0.049	0.575	2.193	-2.471
	2280	0.049	0.517	2.815	-2.835
	2760	0.049	0.489	3.616	-3.166
	3600	0.049	0.471	4.600	-3.529
	4200	0.049	0.413	5.614	-4.088
	4800	0.049	0.377	6.611	-4.477
	5880	0.049	0.386	7.819	-4.704
	6600	0.050	0.374	8.995	-4.906
Unloading	6720	0.049	0.211	8.942	-4.795
	6780	0.049	0.136	8.855	-4.620
	6900	0.049	0.065	8.677	-4.328

Specimen	**H10**		Porosity	40.5	%
Cored from block	II		Void ratio	0.682	
Orientation	Horizontal				
Initial height	9.770	cm	Back pressure	98	kPa
Initial diameter	3.623	cm	Saturation index, B	0.94	
Initial mass	160.5	g			

	Time sec.	σ_3' MPa	σ_1' MPa	ε_1 %	ε_{vol} %
Triaxial loading	0	0.049	0.036	0.000	0.000
	60	0.049	0.178	0.035	0.027
	180	0.049	0.437	0.171	0.145
	300	0.049	0.821	0.308	0.243
	420	0.049	1.286	0.465	0.301
	540	0.049	1.605	0.658	0.246
	660	0.049	1.325	0.882	-0.161
	780	0.049	1.164	1.098	-0.629
	965	0.050	0.987	1.431	-1.337
	1140	0.050	0.854	1.728	-1.878
	1320	0.050	0.750	2.031	-2.325
	1560	0.050	0.636	2.421	-2.712
	1920	0.050	0.538	3.004	-3.006
	2280	0.050	0.504	3.603	-3.167
	2640	0.050	0.504	4.202	-3.314
	3000	0.050	0.502	4.796	-3.447
Unloading	3120	0.050	0.267	4.757	-3.434
	3180	0.050	0.146	4.669	-3.320
	3300	0.050	0.094	4.568	-3.120
Reloading	3360	0.050	0.205	4.639	-3.093
	3420	0.050	0.333	4.721	-3.113
	3480	0.050	0.461	4.808	-3.153
	3660	0.050	0.531	5.094	-3.287
	3900	0.050	0.524	5.494	-3.414
	4200	0.051	0.508	5.995	-3.554
Unloading	4320	0.051	0.253	5.945	-3.547
	4440	0.051	0.087	5.763	-3.334
	4620	0.051	0.040	5.505	-3.060

Specimen	**H4**		Porosity	43.0	%
Cored from block	I		Void ratio	0.754	
Orientation	Horizontal				
Initial height	9.723	cm	Back pressure	98	kPa
Initial diameter	3.662	cm	Saturation index, B	0.86	
Initial mass	156.5	g			

	Time sec.	σ_3' MPa	σ_1' MPa	ε_1 %	ε_{vol} %
Triaxial loading	0	0.142	0.107	0.000	0.000
	120	0.142	0.308	0.145	0.105
	306	0.142	0.577	0.385	0.283
	480	0.142	0.937	0.614	0.426
Unloading	540	0.142	0.643	0.613	0.426
	660	0.142	0.414	0.584	0.406
Reloading	720	0.142	0.826	0.629	0.433
	780	0.142	1.064	0.709	0.469
Triaxial loading	900	0.142	1.365	0.879	0.525
	960	0.142	1.508	0.974	0.531
	1020	0.142	1.629	1.065	0.531
	1140	0.142	1.748	1.253	0.478
	1260	0.142	1.733	1.458	0.353
	1440	0.142	1.597	1.764	0.058
	1680	0.142	1.444	2.162	-0.343
	1920	0.142	1.274	2.560	-0.671
	2400	0.142	1.141	2.972	-0.868
	2760	0.142	1.027	3.590	-1.052
	3240	0.142	0.982	4.393	-1.19
	3720	0.142	0.957	5.192	-1.295
	4440	0.142	0.961	6.001	-1.387
	5040	0.142	0.935	7.000	-1.525
	5760	0.142	0.935	8.194	-1.676
Unloading	5880	0.142	0.528	8.160	-1.669
	5940	0.142	0.341	8.092	-1.617
	6000	0.142	0.230	8.015	-1.538
	6120	0.142	0.146	7.823	-1.374
Reloading	6240	0.142	0.290	7.870	-1.308
	6300	0.142	0.448	7.957	-1.288
	6420	0.142	0.699	8.116	-1.341
	6542	0.142	0.928	8.291	-1.400
	6720	0.142	0.982	8.585	-1.499
	6960	0.142	0.960	8.991	-1.604
	7440	0.142	0.937	9.793	-1.755

Unloading	7560	0.142	0.547	9.749	-1.748
	7620	0.142	0.347	9.689	-1.702
	7740	0.142	0.177	9.521	-1.551
	7980	0.142	0.107	9.203	-1.341

Specimen	**H5**		Porosity	45.9	%
Cored from block	I		Void ratio	0.850	
Orientation	Horizontal				
Initial height	9.714	cm	Back pressure	91	kPa
Initial diameter	3.662	cm	Saturation index, B	0.93	
Initial mass	148.2	g			

	Time sec.	σ_3' MPa	σ_1' MPa	ε_1 %	ε_{vol} %
Triaxial loading	0	0.149	0.112	0.000	0.000
	60	0.149	0.306	0.035	0.028
	120	0.149	0.501	0.093	0.073
	180	0.149	0.643	0.144	0.110
	240	0.149	0.834	0.210	0.168
	306	0.149	1.056	0.282	0.195
Unloading	360	0.149	0.725	0.273	0.189
	480	0.149	0.457	0.252	0.175
Reloading	540	0.149	0.926	0.292	0.195
	600	0.149	1.267	0.371	0.225
Triaxial loading	660	0.149	1.399	0.464	0.244
	720	0.149	1.494	0.568	0.244
	840	0.149	1.545	0.768	0.178
	960	0.149	1.463	0.986	0.033
	1080	0.149	1.374	1.200	-0.164
	1260	0.149	1.306	1.511	-0.480
	1800	0.149	1.234	2.019	-0.940
	2160	0.149	1.135	2.621	-1.472
	2520	0.149	1.038	3.230	-1.867
	3000	0.149	0.966	4.037	-2.117
	3485	0.149	0.942	4.855	-2.281
	4200	0.149	0.925	5.631	-2.425
	4800	0.149	0.875	6.629	-2.695
	5520	0.149	0.842	7.437	-2.872
	6000	0.149	0.800	8.234	-3.050
	6480	0.149	0.778	9.037	-3.188
	6720	0.149	0.784	9.428	-3.234
Unloading	6960	0.149	0.711	9.631	-3.254
	7080	0.149	0.318	9.508	-3.116
	7260	0.149	0.169	9.229	-2.734
Reloading	7380	0.149	0.160	9.121	-2.596
	7500	0.149	0.423	9.290	-2.583
	7687	0.149	0.672	9.556	-2.702
	7860	0.149	0.794	9.837	-2.826

	8100	0.149	0.820	10.239	-2.951
	8460	0.149	0.817	10.822	-3.103
Unloading	8580	0.149	0.817	11.024	-3.155
	8700	0.149	0.578	11.007	-3.142
	8880	0.149	0.249	10.818	-2.899
	9180	0.149	0.126	10.343	-2.419

Specimen	**H1**		Porosity	44.7	%
Cored from block	I		Void ratio	0.807	
Orientation	Horizontal				
Initial height	9.760	cm	Back pressure	98	kPa
Initial diameter	3.660	cm	Saturation index, B	0.93	
Initial mass	152.3	g			

	Time sec.	σ_3' MPa	σ_1' MPa	ε_1 %	ε_{vol} %
Triaxial loading	0	0.482	0.362	0.000	0.000
	60	0.482	0.587	0.078	0.053
	120	0.482	0.842	0.136	0.088
	180	0.482	1.072	0.200	0.141
	240	0.482	1.342	0.274	0.183
	300	0.482	1.576	0.347	0.222
Unloading	360	0.482	1.088	0.318	0.215
	390	0.482	0.891	0.317	0.215
Reloading	450	0.482	1.005	0.332	0.228
	540	0.482	1.832	0.427	0.281
Triaxial loading	660	0.482	2.264	0.599	0.359
	840	0.482	2.609	0.874	0.425
	960	0.482	2.645	1.055	0.412
	1140	0.482	2.618	1.344	0.346
	1440	0.482	2.578	1.841	0.215
	1740	0.482	2.541	2.331	0.078
	2160	0.482	2.489	3.040	-0.145
	2880	0.482	2.450	3.839	-0.348
	3360	0.482	2.396	4.645	-0.590
	3960	0.482	2.344	5.640	-0.865
	4680	0.482	2.289	6.829	-1.127
	5400	0.482	2.265	7.662	-1.238
	6120	0.482	2.217	8.858	-1.435
	6960	0.482	2.189	9.867	-1.572
	7500	0.482	2.175	10.661	-1.644
Unloading	7560	0.482	1.574	10.631	-1.625
	7620	0.482	1.092	10.571	-1.559
	7740	0.482	0.681	10.414	-1.376
	8040	0.482	0.406	9.979	-0.911
Reloading	8160	0.482	0.674	10.021	-0.839
	8280	0.482	1.125	10.160	-0.813
	8460	0.482	1.624	10.415	-0.885
	8640	0.482	2.019	10.681	-1.009
Triaxial loading	8820	0.482	2.170	10.972	-1.120

	9120	0.482	2.197	11.462	-1.258
	9600	0.482	2.174	12.250	-1.435
	10200	0.482	2.145	13.251	-1.592
Unloading	10320	0.482	1.508	13.224	-1.553
	10380	0.482	1.055	13.162	-1.494
	10500	0.482	0.672	13.006	-1.304
	10680	0.482	0.476	12.751	-1.029
	10920	0.482	0.365	12.408	-0.734

Specimen	**H8**		Porosity	44.0	%
Cored from block	I		Void ratio	0.785	
Orientation	Horizontal				
Initial height	9.732	cm	Back pressure	98	kPa
Initial diameter	3.671	cm	Saturation index, B	0.93	
Initial mass	154.7	g			

	Time sec.	σ_3' MPa	σ_1' MPa	ε_1 %	ε_{vol} %
Triaxial loading	0	1.010	0.758	0.000	0.000
	60	1.010	1.093	0.088	0.069
	180	1.010	1.600	0.205	0.150
	300	1.010	2.290	0.344	0.248
Unloading	360	1.010	2.067	0.345	0.255
	480	1.010	1.560	0.322	0.255
Reloading	540	1.010	2.143	0.356	0.268
Triaxial loading	660	1.010	2.973	0.511	0.366
	780	1.010	3.406	0.694	0.444
	975	1.020	3.738	0.999	0.529
	1260	1.010	3.941	1.480	0.575
	1500	1.029	4.050	1.891	0.581
	1742	1.029	4.121	2.298	0.568
	2160	1.010	4.140	2.984	0.490
	2520	1.020	4.180	3.567	0.431
	2760	1.020	4.188	3.956	0.385
	3000	1.030	4.173	4.386	0.333
	3360	1.030	4.134	4.945	0.268
	3960	1.059	4.139	5.541	0.255
	4440	1.069	4.106	6.347	0.235
	5100	1.000	3.892	7.460	0.209
	5820	1.000	3.855	8.277	0.196
	6240	1.000	3.859	8.984	0.190
	6600	1.000	3.857	9.574	0.177
Unloading	6720	1.000	3.165	9.547	0.190
	6780	1.000	2.397	9.493	0.196
	6900	1.000	1.509	9.354	0.268
	7080	0.991	1.002	9.125	0.438
	7320	0.991	0.818	8.867	0.588
Reloading	7380	0.991	1.122	8.906	0.607
	7500	0.991	1.741	9.027	0.653
	7680	0.991	2.612	9.257	0.653
	7800	0.991	3.187	9.427	0.614
	7927	0.991	3.665	9.609	0.581

	8160	0.991	3.920	9.983	0.496
Triaxial loading	8520	0.991	3.883	10.572	0.438
	9000	0.991	3.861	11.377	0.392
Unloading	9120	0.991	3.128	11.348	0.405
	9180	0.991	2.383	11.289	0.412
	9300	0.990	1.517	11.142	0.477
	9480	0.990	1.018	10.900	0.627
	9780	0.981	0.738	10.542	0.790

Specimen	**H7**		Porosity	44.6	%
Cored from block	I		Void ratio	0.806	
Orientation	Horizontal				
Initial height	9.759	cm	Back pressure	97	kPa
Initial diameter	3.649	cm	Saturation index, B	0.92	
Initial mass	151.5	g			

	Time sec.	σ_3' MPa	σ_1' MPa	ε_1 %	ε_{vol} %
Triaxial loading	0	2.002	1.501	0.000	0.000
	120	2.002	2.068	0.112	0.086
	240	2.002	2.709	0.242	0.178
	360	1.982	3.364	0.398	0.296
Unloading	420	1.982	2.986	0.395	0.310
	540	1.982	2.516	0.377	0.310
Reloading	600	2.012	3.223	0.410	0.323
	660	2.012	3.771	0.483	0.362
Triaxial loading	780	2.012	4.381	0.651	0.481
	960	2.012	5.073	0.916	0.639
	1140	2.012	5.554	1.180	0.771
	1560	2.012	6.153	1.851	1.021
	2040	2.011	6.500	2.634	1.205
	2640	2.021	6.777	3.612	1.377
	3240	2.002	6.893	4.599	1.508
	3840	2.002	7.012	5.591	1.620
	4440	2.002	7.095	6.592	1.713
	5160	2.002	7.157	7.792	1.818
	5760	2.002	7.201	8.791	1.923
	6240	2.002	7.226	9.587	2.022
	6720	2.002	7.205	10.385	2.121
	7320	2.002	7.162	11.389	2.213
	7920	2.002	7.091	12.398	2.549
	8400	1.972	6.989	13.187	2.885
	9240	2.002	6.954	14.169	3.023
	9720	2.002	6.882	14.954	3.089
	10200	2.012	6.827	15.749	3.155
Unloading	10320	2.021	5.868	15.737	3.188
	10440	2.021	4.086	15.626	3.359
	10620	1.943	2.596	15.422	4.485
	10860	1.943	1.870	15.112	4.848
	11160	1.924	1.484	14.700	5.105
Reloading	11280	1.914	1.796	14.717	5.157
	11400	1.914	2.605	14.825	5.210

	11580	1.884	3.744	15.040	5.276
	11820	1.884	5.101	15.357	5.276
	12120	1.884	6.415	15.782	5.197
	12360	1.884	6.802	16.170	5.138
	12720	1.904	6.853	16.769	5.091
	13200	1.904	6.758	17.579	5.072
Unloading	13260	1.933	5.970	17.563	5.078
	13380	1.933	4.725	17.506	5.118
	13440	1.933	4.105	17.457	5.131
	13560	1.904	2.961	17.322	5.230
	13740	1.904	2.108	17.087	5.388
	13980	1.894	1.651	16.787	5.572
	14220	1.884	1.420	16.531	5.724

Specimen	**H6**		Porosity	44.1	%
Cored from block	I		Void ratio	0.790	
Orientation	Horizontal				
Initial height	9.729	cm	Back pressure	97	kPa
Initial diameter	3.669	cm	Saturation index, B	0.91	
Initial mass	154.0	g			

	Time sec.	σ_3' MPa	σ_1' MPa	ε_1 %	ε_{vol} %
Isotropic loading	240	0.099	0.000	0.000	0.000
	360	0.501	0.154	0.146	0.577
	480	0.982	0.074	0.251	0.911
	600	1.501	0.376	0.322	1.128
	720	2.041	0.736	0.382	1.319
	840	2.531	1.126	0.429	1.491
	960	3.041	1.531	0.472	1.698
	1080	3.511	1.898	0.512	1.921
	1200	4.002	2.281	0.551	2.135
Triaxial loading	0	4.002	3.001	0.000	0.000
	60	4.002	3.643	0.081	0.105
	180	4.002	4.389	0.209	0.268
	300	4.002	5.175	0.360	0.445
Unloading	360	4.002	4.260	0.336	0.484
	420	4.002	3.453	0.304	0.491
Reloading	480	4.002	3.994	0.328	0.517
	540	4.002	4.928	0.371	0.550
	600	4.002	5.574	0.450	0.608
Triaxial loading	720	4.002	6.268	0.606	0.746
	900	4.002	7.177	0.866	0.968
	1140	4.002	8.132	1.220	1.295
	1440	4.002	9.007	1.682	1.681
	1800	4.002	9.722	2.254	2.054
	2280	4.002	10.401	3.018	2.473
	3000	4.002	11.101	4.205	3.055
	3900	4.002	11.726	5.693	3.762
	4800	4.002	12.191	7.149	4.507
	5700	4.002	12.587	8.607	5.207
	6600	4.002	12.834	10.099	5.901
	7500	4.002	13.042	11.572	6.463
	8400	4.002	13.236	13.051	6.993
	9300	4.002	13.382	14.544	7.438
	10260	4.002	13.525	15.757	7.909
	11100	4.002	13.561	17.143	8.374

	11700	4.002	13.592	18.129	8.714
Unloading	11760	4.002	12.167	18.123	8.746
	11820	4.002	10.739	18.081	8.779
	11940	4.002	8.150	17.973	8.851
	12120	4.002	5.664	17.780	9.015
	12360	3.993	4.056	17.481	9.289
	12600	3.993	3.263	17.171	9.545
Reloading	12660	3.993	3.729	17.192	9.590
	12720	3.993	4.366	17.241	9.630
	12840	3.993	5.899	17.358	9.695
	13020	3.993	8.193	17.560	9.780
	13208	4.002	10.313	17.774	9.819
	13440	4.002	12.671	18.080	9.852
	13683	4.002	13.854	18.446	9.904
	14100	4.002	14.244	19.121	10.022
	14700	4.002	14.189	20.135	10.225
Unloading	14760	4.002	12.787	20.122	10.245
	14820	4.002	11.141	20.077	10.277
	14940	4.002	8.465	19.963	10.343
	15120	4.002	5.820	19.778	10.480
	15360	3.992	4.047	19.473	10.722
	15720	3.993	2.997	19.055	11.056
Isotropic unloading	15720	3.993	2.994	19.055	11.056
	15840	3.502	2.627	19.012	11.090
	15960	3.022	2.266	18.983	11.116
	16080	2.502	1.876	18.952	11.101
	16200	1.992	1.494	18.914	11.089
	16320	1.482	1.111	18.864	11.056
	16440	0.992	0.744	18.806	10.991
	16560	0.492	0.369	18.709	10.837
	16680	0.109	0.082	18.411	10.252

Specimen	**H13**		Porosity	42.0	%
Cored from block	II		Void ratio	0.725	
Orientation	Horizontal				
Initial height	9.765	cm	Back pressure	97	kPa
Initial diameter	3.646	cm	Saturation index, B	0.94	
Initial mass	158.4	g			

	Time sec.	σ_3' MPa	σ_1' MPa	ε_1 %	ε_{vol} %
Isotropic loading	240	0.108	0.081	0.000	0.000
	360	0.510	0.383	0.043	0.563
	480	1.030	0.773	0.113	0.741
	600	1.501	1.126	0.141	0.909
	720	1.982	1.486	0.172	1.036
	840	2.541	1.906	0.208	1.155
	960	3.022	2.266	0.239	1.215
	1080	3.512	2.634	0.269	1.274
	1200	4.002	3.002	0.301	1.351
Triaxial loading	1500	4.002	3.001	0.000	0.000
	1620	4.002	3.763	0.068	0.040
	1740	4.002	4.610	0.188	0.132
	1860	4.002	5.592	0.330	0.238
Unloading	1980	4.002	3.976	0.291	0.251
Reloading	2100	4.002	5.376	0.348	0.277
Triaxial loading	2160	4.002	6.126	0.415	0.343
	2280	4.002	6.938	0.581	0.469
	2460	4.002	7.955	0.833	0.647
	2640	3.992	8.737	1.105	0.832
	2880	3.992	9.515	1.471	1.030
	3240	3.992	10.313	2.044	1.320
	3900	3.982	11.241	3.116	1.709
	4800	3.992	12.047	4.603	2.112
	5700	3.992	12.575	6.069	2.442
	6600	4.012	12.935	7.539	2.726
	7500	4.012	13.176	9.041	2.996
	8400	4.021	13.344	10.530	3.260
	9600	4.021	13.411	12.509	3.531
	10800	4.032	13.372	14.517	3.828
	12000	4.032	13.155	16.490	4.112
	12600	4.041	13.018	17.444	4.244
Unloading	12720	4.041	10.142	17.375	4.263
	12900	4.051	6.804	17.208	4.356
	13140	4.022	4.591	16.928	4.580

	13380	4.022	3.635	16.611	4.791
	13560	3.992	3.189	16.387	4.937
	13620	3.992	3.539	16.401	4.976
Reloading	13740	3.982	4.681	16.519	5.036
	13920	3.982	6.837	16.719	5.115
	14100	3.973	9.131	16.974	5.167
	14340	3.963	11.101	17.248	5.167
	14640	3.963	12.835	17.673	5.148
	15000	3.972	13.224	18.232	5.148
Unloading	15120	3.972	10.314	18.165	5.167
	15300	3.973	6.861	17.990	5.240
	15540	3.953	4.435	17.702	5.392
	15780	3.953	3.432	17.407	5.537
	16020	3.933	2.942	17.164	5.662
Isotropic unloading	16080	3.943	2.957	17.164	5.662
	16200	3.433	2.575	17.123	5.666
	16320	2.962	2.222	17.090	5.672
	16440	2.501	1.876	17.048	5.651
	16560	1.942	1.457	16.990	5.613
	16680	1.501	1.126	16.935	5.576
	16800	0.982	0.736	16.852	5.491
	16920	0.491	0.368	16.729	5.358
	17040	0.138	0.104	16.433	4.909

Specimen	**H16**		Porosity	41.9	%
Cored from block	II		Void ratio	0.722	
Orientation	Horizontal				
Initial height	9.770	cm	Back pressure	98	kPa
Initial diameter	3.631	cm	Saturation index, B	0.92	
Initial mass	157.5	g			

	Time sec.	σ_3' MPa	σ_1' MPa	ε_1 %	ε_{vol} %
Isotropic loading	240	0.117	0.088	0.000	0.000
	360	0.490	0.367	0.040	0.165
	480	1.000	0.750	0.103	0.280
	600	1.490	1.117	0.149	0.370
	720	1.961	1.471	0.188	0.473
	840	2.461	1.846	0.226	0.572
	960	2.942	2.206	0.258	0.651
	1080	3.442	2.581	0.293	0.749
	1200	3.942	2.957	0.329	0.839
	1320	4.432	3.324	0.363	0.927
	1440	4.913	3.685	0.398	1.033
	1560	5.396	4.047	0.434	1.140
	1680	5.933	4.449	0.469	1.255
Triaxial loading	2520	5.933	4.449	0.000	0.000
	2700	5.923	5.354	0.064	0.053
	2820	5.923	6.440	0.189	0.146
	2940	5.923	7.560	0.342	0.266
	3060	5.913	8.559	0.504	0.399
	3180	5.913	9.454	0.675	0.525
	3360	5.913	10.591	0.933	0.711
	3600	5.913	11.742	1.308	0.957
	4080	5.913	13.208	2.095	1.389
	4560	5.913	14.134	2.865	1.761
	5160	5.903	14.986	3.833	2.166
	5790	5.903	15.694	4.858	2.538
	6600	5.903	16.372	6.176	2.964
	7800	5.903	17.144	8.177	3.515
	9000	5.903	17.695	10.131	3.987
	10200	5.903	18.033	12.140	4.426
	11400	5.903	18.252	14.120	4.798
	12900	5.913	18.383	16.601	5.223
	14400	5.923	18.301	19.033	5.582
	15600	5.962	18.295	20.893	5.841
	16500	5.982	18.232	22.481	6.054

Unloading	16620	5.982	14.964	22.403	6.074
	16800	5.972	10.715	22.221	6.127
	16980	5.972	7.960	22.016	6.220
	17220	5.942	5.903	21.708	6.413
	17580	5.903	4.590	21.286	6.645
Reloading	17700	5.884	5.571	21.329	6.692
	17880	5.884	8.025	21.507	6.765
	18060	5.884	10.526	21.711	6.818
	18240	5.884	12.936	21.944	6.845
	18420	5.884	15.135	22.182	6.851
	18600	5.893	16.917	22.439	6.851
	18840	5.893	18.285	22.808	6.845
	19320	5.913	18.805	23.580	6.851
	20100	5.952	18.696	24.850	6.924
	21000	5.952	18.447	26.341	7.051
Unloading	21120	5.972	15.013	26.269	7.077
	21300	5.972	10.749	26.099	7.124
	21480	5.962	7.983	25.899	7.223
	21720	5.942	5.914	25.598	7.396
	21960	5.883	4.844	25.308	7.556
	22200	5.883	4.414	25.094	7.675
Isotropic unloading	22200	5.883	4.413	25.094	7.675
	22320	5.393	4.045	25.057	7.692
	22440	4.893	3.670	25.030	7.685
	22560	4.403	3.302	25.002	7.686
	22680	3.922	2.942	24.975	7.684
	22800	3.432	2.574	24.945	7.666
	22920	2.942	2.206	24.913	7.681
	23040	2.441	1.831	24.876	7.637
	23160	1.961	1.470	24.833	7.616
	23280	1.480	1.110	24.782	7.598
	23400	1.000	0.750	24.707	7.543
	23520	0.500	0.375	24.542	7.415
	23640	0.176	0.132	24.139	7.035

Specimen	**H14**		Porosity	43.6	%
Cored from block	II		Void ratio	0.772	
Orientation	Horizontal				
Initial height	9.753	cm	Back pressure	98	kPa
Initial diameter	3.625	cm	Saturation index, B	0.92	
Initial mass	152.2	g			

	Time sec.	σ_3' MPa	σ_1' MPa	ε_1 %	ε_{vol} %
Isotropic loading	240	0.108	0.081	0.000	0.000
	360	0.588	0.441	0.048	0.254
	480	1.078	0.809	0.097	0.392
	600	1.569	1.177	0.137	0.497
	720	2.059	1.544	0.173	0.602
	840	2.550	1.912	0.213	0.732
	960	3.050	2.288	0.253	0.858
	1088	3.540	2.655	0.291	0.986
	1200	4.031	3.023	0.331	1.138
	1320	4.521	3.391	0.369	1.281
	1440	5.001	3.751	0.406	1.455
	1560	5.501	4.126	0.465	1.675
	1680	5.982	4.486	0.483	1.908
	1800	6.482	4.861	0.522	2.174
	1920	6.982	5.237	0.561	2.462
	2040	7.453	5.590	0.595	2.672
	2160	7.943	5.957	0.634	2.889
	2280	8.434	6.325	0.670	3.114
	2400	8.924	6.693	0.704	3.319
	2520	9.414	7.061	0.741	3.492
	2640	9.905	7.429	0.778	3.679
Triaxial loading	3240	9.905	7.429	0.000	0.000
	3420	9.905	8.505	0.080	0.080
	3600	9.905	10.007	0.288	0.247
	3780	9.905	11.267	0.548	0.435
	4020	9.885	12.729	0.896	0.709
	4320	9.885	14.225	1.360	1.063
	4680	9.904	15.694	1.927	1.477
	5280	9.905	17.535	2.865	2.132
	5880	9.915	18.961	3.821	2.741
	6480	9.915	20.108	4.774	3.322
	7200	9.915	21.260	5.951	3.984
	8400	9.915	22.831	7.909	5.074
	9600	9.905	24.114	9.851	6.083

	10800	9.914	25.184	11.829	7.073
	12000	9.905	26.204	13.788	8.122
	13500	9.905	27.326	16.261	9.312
	15000	9.905	28.394	18.711	10.442
	16500	9.905	29.348	21.161	11.364
	18000	9.915	30.187	23.616	12.106
Unloading	18120	9.915	25.774	23.545	12.140
	18300	9.924	20.203	23.383	12.173
	18480	9.924	15.840	23.199	12.227
	18660	9.914	12.602	23.01	12.307
	18900	9.905	9.748	22.687	12.441
	19260	9.895	7.643	22.292	12.621
Reloading	19380	9.895	8.887	22.321	12.641
	19500	9.895	10.962	22.431	12.701
	19680	9.895	14.192	22.629	12.761
	19920	9.905	18.836	22.902	12.828
	20160	9.905	23.298	23.184	12.875
	20400	9.905	27.162	23.49	12.902
	20760	9.905	30.368	24.004	12.975
	21240	9.925	31.514	24.773	13.116
	22140	9.934	32.069	26.248	13.430
Unloading	22260	9.934	27.604	26.177	13.457
	22440	9.944	21.709	26.013	13.497
	22623	9.934	16.905	25.834	13.550
	22800	9.934	13.455	25.651	13.624
	23040	9.905	10.215	25.371	13.751
	23280	9.885	8.273	25.085	13.871
	23760	9.846	7.387	24.839	14.005
Isotropic unloading	23760	9.846	7.385	24.839	14.005
	23880	9.493	7.120	24.821	14.008
	24000	8.895	6.671	24.796	14.012
	24120	8.434	6.325	24.777	14.019
	24240	7.944	5.958	24.753	14.022
	24360	7.453	5.590	24.730	14.026
	24480	6.973	5.230	24.706	14.030
	24600	6.522	4.891	24.683	14.015
	24720	6.031	4.523	24.655	14.009
	24840	5.472	4.104	24.624	14.008
	24960	5.002	3.751	24.592	13.985
	25080	4.551	3.413	24.562	13.977
	25200	4.031	3.023	24.524	13.969
	25320	3.521	2.640	24.481	13.952
	25440	3.040	2.280	24.438	13.931
	25560	2.560	1.920	24.388	13.910

25680	2.060	1.545	24.323	13.875
25800	1.569	1.177	24.240	13.834
25920	1.079	0.809	24.123	13.767
26040	0.589	0.442	23.915	13.648
26160	0.147	0.110	23.123	12.922

Specimen	**H15**		Porosity	44.9	%
Cored from block	II		Void ratio	0.815	
Orientation	Horizontal				
Initial height	9.763	cm	Back pressure	98	kPa
Initial diameter	3.623	cm	Saturation index, B	0.93	
Initial mass	148.6	g			

	Time sec.	σ_3' MPa	σ_1' MPa	ε_1 %	ε_{vol} %
Isotropic loading	240	0.147	0.110	0.000	0.000
	360	0.686	0.515	0.083	0.317
	480	1.196	0.897	0.162	0.492
	600	1.677	1.257	0.228	0.629
	720	2.177	1.632	0.291	0.765
	840	2.667	2.000	0.342	0.898
	960	3.148	2.361	0.389	1.020
	1080	3.638	2.729	0.432	1.142
	1200	4.129	3.096	0.476	1.275
	1320	4.609	3.457	0.518	1.420
	1440	5.109	3.832	0.563	1.606
	1560	5.590	4.192	0.603	1.823
	1680	6.080	4.560	0.645	2.068
	1800	6.580	4.935	0.688	2.314
	1920	7.080	5.310	0.728	2.535
	2040	7.551	5.663	0.766	2.732
	2160	8.041	6.031	0.806	2.909
	2280	8.551	6.413	0.850	3.133
	2400	9.022	6.766	0.887	3.326
	2520	9.531	7.148	0.926	3.485
	2640	10.002	7.502	0.962	3.639
	2760	10.503	7.877	1.000	3.793
	2880	10.983	8.237	1.036	3.942
	3000	11.483	8.612	1.073	4.084
	3120	11.983	8.987	1.110	4.219
	3240	12.533	9.399	1.150	4.375
	3360	13.023	9.767	1.185	4.505
	3480	13.503	10.128	1.220	4.649
	3600	14.053	10.539	1.262	4.812
Triaxial loading	4200	14.033	10.525	0.000	0.000
	4440	14.033	11.926	0.108	0.087
	4680	14.013	14.057	0.407	0.301
	4920	13.945	15.667	0.749	0.575
	5160	13.994	17.132	1.110	0.849

	5520	14.072	18.888	1.663	1.283
	6120	14.004	21.126	2.609	1.965
	6720	13.906	22.863	3.556	2.627
	7320	14.004	24.463	4.523	3.262
	8100	14.102	26.264	5.784	4.058
	9300	14.003	28.389	7.724	5.201
	10500	14.003	30.449	9.695	6.264
	11700	13.935	32.037	11.631	7.193
	13200	14.004	34.177	14.077	8.323
	14700	13.974	36.055	16.521	9.379
	16200	14.004	37.834	18.955	10.368
	17700	14.004	39.463	21.380	11.284
	18900	14.003	40.696	23.294	11.999
Unloading	19020	14.003	36.333	23.204	12.039
	19200	13.974	29.829	23.027	12.080
	19440	13.964	22.869	22.783	12.153
	19680	13.974	17.698	22.513	12.247
	19980	13.945	13.309	22.135	12.400
	20340	13.935	10.618	21.748	12.561
Reloading	20520	13.935	13.429	21.822	12.634
	20760	13.925	18.612	22.078	12.735
	21000	13.935	23.798	22.349	12.828
	21300	13.945	30.351	22.700	12.922
	21600	13.964	36.213	23.070	13.009
	21900	13.984	40.209	23.495	13.102
	22320	13.974	42.334	24.165	13.276
	23100	13.974	43.427	25.424	13.597
	23760	13.974	44.050	26.491	13.871
Unloading	23880	13.974	39.281	26.394	13.911
	24060	13.964	32.422	26.228	13.945
	24240	13.935	26.682	26.046	13.978
	24480	13.935	20.576	25.788	14.072
	24780	13.925	15.201	25.451	14.199
	25020	13.925	12.378	25.158	14.312
	25560	13.925	10.448	24.802	14.493
Isotropic unloading	25560	13.925	10.444	24.802	14.493
	25680	13.444	10.083	24.779	14.509
	25800	13.003	9.752	24.760	14.518
	25920	12.464	9.348	24.739	14.536
	26040	12.042	9.032	24.721	14.545
	26160	11.542	8.656	24.701	14.556
	26280	10.885	8.164	24.674	14.572
	26400	10.473	7.855	24.654	14.576
	26520	10.022	7.516	24.635	14.587

26640	9.532	7.149	24.611	14.601
26760	9.061	6.796	24.590	14.608
26880	8.541	6.406	24.562	14.597
27000	8.041	6.031	24.534	14.606
27120	7.551	5.663	24.507	14.616
27240	7.070	5.302	24.478	14.607
27360	6.580	4.935	24.447	14.613
27480	6.080	4.560	24.414	14.607
27600	5.599	4.199	24.378	14.609
27720	5.109	3.832	24.339	14.587
27840	4.628	3.471	24.295	14.587
27960	4.119	3.089	24.244	14.558
28080	3.618	2.714	24.187	14.532
28200	3.138	2.353	24.124	14.517
28320	2.667	2.000	24.044	14.480
28440	2.167	1.625	23.925	14.422
28560	1.657	1.243	23.763	14.326
28680	1.186	0.890	23.514	14.229
28800	0.696	0.522	23.344	14.070
28920	0.137	0.103	22.556	13.548

Specimen	**H9**		Porosity	44.1	%
Cored from block	II		Void ratio	0.790	
Orientation	Horizontal				
Initial height	9.749	cm	Back pressure	245	kPa
Initial diameter	3.625	cm	Saturation index, B	0.82	
Initial mass	150.6	g			

	Time sec.	σ_3' MPa	σ_1' MPa	ε_1 %	ε_{vol} %
Triaxial loading	360	0.143	0.130	0.000	0.000
	480	0.143	0.251	0.154	0.116
	600	0.143	0.554	0.283	0.211
	720	0.143	0.969	0.419	0.301
	840	0.143	1.438	0.566	0.355
	900	0.143	1.672	0.643	0.375
	960	0.143	1.870	0.730	0.361
	1080	0.143	2.037	0.905	0.201
	1140	0.143	1.992	1.009	0.054
	1260	0.143	1.839	1.198	-0.274
	1380	0.143	1.689	1.407	-0.615
	1560	0.143	1.476	1.720	-1.016
	1740	0.143	1.309	2.030	-1.276
	1920	0.143	1.198	2.325	-1.429
	2280	0.143	1.094	2.950	-1.615
	2640	0.143	1.076	3.538	-1.715
	3000	0.143	1.064	4.144	-1.795
Unloading	3120	0.143	0.705	4.108	-1.781
	3180	0.143	0.477	4.029	-1.728
	3300	0.143	0.293	3.865	-1.548
	3420	0.143	0.209	3.673	-1.380
	3600	0.143	0.165	3.480	-1.220
Reloading	3780	0.143	0.508	3.720	-1.133
	3960	0.143	0.842	3.983	-1.213
Triaxial loading	4140	0.143	1.073	4.265	-1.347
	4320	0.143	1.104	4.563	-1.454
	4560	0.143	1.096	4.964	-1.541
	4800	0.143	1.073	5.367	-1.608
Unloading	4860	0.143	0.766	5.357	-1.608
	4980	0.143	0.474	5.257	-1.581
	5100	0.143	0.289	5.082	-1.461
	5220	0.143	0.206	4.901	-1.334

Specimen	**V4**		Porosity	44.3	%
Cored from block	I		Void ratio	0.796	
Orientation	Vertical				
Initial height	9.787	cm	Back pressure	93	kPa
Initial diameter	3.680	cm	Saturation index, B	0.94	
Initial mass	155.3	g			

	Time sec.	σ_3' MPa	σ_1' MPa	ε_1 %	ε_{vol} %
Isotropic loading	240	0.103	0.100	0.000	0.000
	360	0.396	0.385	0.040	0.254
	480	0.887	0.861	0.132	0.446
	600	0.887	0.861	0.135	0.472
	720	1.378	1.336	0.212	0.658
	840	1.878	1.821	0.286	0.822
	960	2.358	2.288	0.350	0.981
	1080	2.849	2.763	0.406	1.112
	1200	3.338	3.238	0.464	1.258
	1320	3.829	3.714	0.518	1.396
	1440	4.320	4.190	0.572	1.520
	1560	4.810	4.666	0.625	1.659
	1680	5.300	5.141	0.680	1.841
	1800	5.790	5.617	0.733	2.037
	1920	6.281	6.092	0.786	2.274
	2040	6.771	6.568	0.839	2.526
	2160	7.262	7.044	0.889	2.733
	2280	7.752	7.520	0.940	2.994
	2400	8.253	8.005	0.989	3.236
	2520	8.743	8.480	1.040	3.531
	2640	9.223	8.947	1.087	3.769
	2760	9.713	9.422	1.132	4.020
	2880	10.204	9.898	1.182	4.265
	3000	10.694	10.373	1.227	4.499
	3120	11.204	10.868	1.271	4.732
	3240	11.675	11.325	1.316	4.941
Isotropic unloading	3360	11.214	10.878	1.320	5.080
	3480	10.743	10.421	1.315	5.118
	3600	9.988	9.689	1.300	5.169
	3750	8.929	8.661	1.278	5.205
	3870	8.252	8.005	1.263	5.239
	3990	7.752	7.520	1.249	5.268
	4110	7.262	7.044	1.235	5.298
	4230	6.781	6.578	1.221	5.316

4350	6.330	6.140	1.205	5.328
4470	5.820	5.645	1.187	5.337
4590	5.340	5.179	1.169	5.340
4710	4.840	4.694	1.148	5.340
4830	4.330	4.200	1.126	5.337
4950	3.849	3.734	1.102	5.323
5070	3.359	3.258	1.077	5.307
5190	2.878	2.792	1.047	5.277
5310	2.359	2.288	1.012	5.245
5430	1.898	1.841	0.973	5.186
5550	1.398	1.356	0.926	5.112
5670	0.986	0.956	0.882	5.145
5790	0.839	0.814	0.860	4.959
5910	0.496	0.481	0.816	4.779
6030	0.202	0.196	0.774	4.459

Specimen	**V9**		Porosity	42.5	%
Cored from block	II		Void ratio	0.739	
Orientation	Vertical				
Initial height	9.749	cm	Back pressure	86	kPa
Initial diameter	3.638	cm	Saturation index, B	0.94	
Initial mass	156.2	g			

	Time sec.	σ_3' MPa	σ_1' MPa	ε_1 %	ε_{vol} %
Isotropic loading	240	0.098	0.095	0.000	0.000
	360	0.393	0.382	0.070	0.429
	480	0.892	0.866	0.164	0.746
	600	1.373	1.332	0.245	0.941
	720	1.873	1.817	0.317	1.117
	840	2.363	2.292	0.378	1.241
	960	2.853	2.768	0.437	1.363
	1080	3.334	3.234	0.491	1.494
	1200	3.844	3.729	0.549	1.629
	1320	4.315	4.185	0.600	1.757
	1440	4.815	4.671	0.653	1.874
	1560	5.296	5.137	0.703	2.014
	1680	5.786	5.612	0.754	2.143
	1800	6.286	6.097	0.797	2.267
	1920	6.776	6.573	0.850	2.413
	2040	7.267	7.049	0.896	2.547
	2160	7.757	7.524	0.943	2.675
	2280	8.247	8.000	0.986	2.805
	2400	8.728	8.466	1.033	2.943
	2520	9.228	8.951	1.077	3.080
	2640	9.708	9.417	1.119	3.206
	2760	10.199	9.893	1.161	3.352
	2880	10.689	10.368	1.204	3.492
	3000	11.189	10.853	1.247	3.633
	3120	11.729	11.377	1.287	3.779
	3240	12.160	11.795	1.322	3.902
	3360	12.651	12.271	1.362	4.051
	3480	13.121	12.728	1.401	4.194
	3600	13.680	13.270	1.447	4.355
	3720	14.072	13.650	1.484	4.487
	3840	14.661	14.221	1.528	4.628
	3960	15.004	14.554	1.561	4.762
	4080	15.818	15.344	1.618	4.953

Specimen	**H3**		Porosity	44.2	%
Cored from block	I		Void ratio	0.791	
Orientation	Horizontal				
Initial height	9.755	cm	Back pressure	102	kPa
Initial diameter	3.671	cm	Saturation index, B	0.95	
Initial mass	154.5	g			

	Time sec.	σ_3' MPa	σ_1' MPa	ε_1 %	ε_{vol} %
Isotropic loading	240	0.123	0.119	0.000	0.000
	360	0.398	0.386	0.031	0.216
	480	0.888	0.861	0.104	0.373
	600	1.368	1.327	0.165	0.478
	720	1.859	1.803	0.231	0.605
	840	2.350	2.279	0.289	0.719
	960	2.840	2.755	0.347	0.845
	1080	3.330	3.230	0.404	0.966
	1200	3.821	3.706	0.469	1.105
	1320	4.321	4.191	0.532	1.242
	1440	4.801	4.657	0.591	1.384
	1560	5.282	5.123	0.656	1.567
	1680	5.782	5.608	0.719	1.804
	1800	6.282	6.093	0.785	2.049
	1920	6.782	6.579	0.846	2.289
	2040	7.253	7.035	0.905	2.538
	2160	7.743	7.511	0.967	2.768
	2280	8.233	7.986	1.028	3.006
	2400	8.724	8.462	1.087	3.206
	2520	9.214	8.938	1.149	3.412
	2640	9.714	9.423	1.207	3.620
Isotropic unloading	2760	9.204	8.928	1.212	3.673
	2880	8.734	8.472	1.212	3.700
	3000	8.243	7.996	1.206	3.715
	3120	7.753	7.521	1.198	3.718
	3240	7.253	7.035	1.190	3.723
	3360	6.763	6.560	1.180	3.728
	3480	6.272	6.084	1.169	3.729
	3600	5.831	5.656	1.158	3.728
	3720	5.331	5.171	1.145	3.719
	3840	4.831	4.686	1.130	3.706
	3960	4.360	4.229	1.116	3.701
	4080	3.850	3.735	1.096	3.681
	4200	3.340	3.240	1.076	3.654

	4320	2.840	2.755	1.052	3.631
	4440	2.350	2.279	1.025	3.590
	4560	1.898	1.841	0.997	3.542
	4680	1.388	1.347	0.954	3.462
	4800	0.878	0.852	0.903	3.342
	4920	0.496	0.481	0.852	3.180
	5040	0.104	0.101	0.765	2.654
Isotropic loading	11640	0.101	0.098	0.739	2.426
	11760	0.395	0.384	0.779	2.673
	11880	0.896	0.869	0.849	2.946
	12000	1.386	1.344	0.900	3.130
	12120	1.867	1.811	0.942	3.293
	12240	2.357	2.287	0.980	3.446
	12360	2.848	2.762	1.011	3.540
	12480	3.338	3.238	1.039	3.615
	12600	3.828	3.713	1.065	3.696
	12720	4.319	4.189	1.090	3.775
	12840	4.809	4.665	1.114	3.812
	12960	5.309	5.150	1.137	3.883
	13080	5.789	5.616	1.159	3.939
	13200	6.289	6.101	1.183	4.001
	13320	6.760	6.557	1.204	4.060
	13440	7.260	7.043	1.228	4.126
	13560	7.751	7.518	1.253	4.194
	13680	8.232	7.985	1.279	4.262
	13800	8.751	8.489	1.309	4.351
	13920	9.301	9.022	1.339	4.432
	14040	9.712	9.421	1.368	4.505
	14160	10.202	9.896	1.399	4.577
	14280	10.801	10.477	1.440	4.673
	10800	11.262	10.924	1.475	4.792
	14520	11.634	11.285	1.509	4.874
	14640	12.183	11.818	1.546	4.960
	14760	12.742	12.360	1.595	5.065
	14880	13.164	12.769	1.635	5.161
	15000	13.635	13.226	1.680	5.262
	15120	14.204	13.778	1.730	5.369
	15240	14.861	14.415	1.788	5.487
Isotropic unloading	15360	14.204	13.778	1.792	5.525
	15480	13.655	13.245	1.793	5.542
	15600	13.213	12.817	1.789	5.544
	15720	12.350	11.980	1.776	5.549
	15840	12.144	11.780	1.775	5.547
	15960	11.703	11.352	1.769	5.550

16080	11.233	10.896	1.761	5.548
16200	10.732	10.410	1.750	5.547
16320	10.252	9.944	1.742	5.539
16440	9.781	9.488	1.732	5.532
16560	9.251	8.974	1.721	5.527
16680	8.761	8.498	1.708	5.522
16800	8.271	8.023	1.695	5.505
16920	7.839	7.604	1.682	5.493
17040	7.251	7.033	1.666	5.481
17160	6.790	6.586	1.651	5.459
17280	6.280	6.092	1.635	5.447
17400	5.829	5.654	1.617	5.428
17520	5.378	5.216	1.599	5.403
17640	4.809	4.665	1.576	5.381
17760	4.319	4.189	1.554	5.344
17880	3.829	3.714	1.531	5.317
18000	3.387	3.285	1.505	5.284
18120	2.847	2.762	1.474	5.232
18240	2.387	2.315	1.446	5.181
18360	1.935	1.877	1.408	5.113
18480	1.386	1.345	1.357	5.006
18600	0.886	0.859	1.307	4.859
18720	0.416	0.403	1.260	4.603
18840	0.122	0.118	1.235	4.284

Specimen	**H9**		Porosity	44.1	%
Cored from block	II		Void ratio	0.790	
Orientation	Horizontal				
Initial height	9.749	cm	Back pressure	99	kPa
Initial diameter	3.625	cm	Saturation index, B	0.91	
Initial mass	150.6	g			

	Time sec.	σ_3' MPa	σ_1' MPa	ε_1 %	ε_{vol} %
Isotropic loading	240	0.097	0.094	0.000	0.000
	360	0.401	0.389	0.027	0.254
	480	0.901	0.874	0.080	0.438
	600	1.372	1.331	0.126	0.565
	720	1.862	1.806	0.175	0.677
	840	2.382	2.311	0.227	0.805
	960	2.853	2.768	0.280	0.944
	1080	3.334	3.234	0.336	1.083
	1200	3.824	3.709	0.395	1.240
	1320	4.354	4.223	0.459	1.412
	1440	4.834	4.689	0.514	1.645
	1560	5.295	5.136	0.574	1.895
	1680	5.805	5.631	0.640	2.205
	1800	6.285	6.097	0.696	2.484
	1920	6.785	6.582	0.758	2.765
	2040	7.256	7.038	0.815	3.041
	2160	7.746	7.514	0.873	3.277
	2280	8.247	8.000	0.931	3.481
	2400	8.747	8.485	0.992	3.686
	2520	8.738	8.475	1.007	3.740
	2640	9.257	8.980	1.045	3.858
	2760	9.708	9.417	1.100	4.013
	2880	10.238	9.931	1.162	4.186
	3000	10.228	9.921	1.177	4.246
	3120	10.679	10.359	1.207	4.321
	3240	11.189	10.853	1.265	4.469
	3360	11.611	11.262	1.312	4.587
	3480	12.189	11.824	1.381	4.734
	3600	12.591	12.214	1.426	4.852
	3840	13.199	12.803	1.494	5.027
	3960	13.611	13.203	1.530	5.099
	4080	14.141	13.716	1.587	5.222
	4200	14.690	14.249	1.652	5.353
	4320	15.180	14.725	1.709	5.478

	4440	15.592	15.124	1.761	5.591
Isotropic unloading	5040	15.592	15.124	1.809	5.738
	5160	15.092	14.639	1.807	5.747
	5280	14.611	14.173	1.801	5.755
	5400	14.072	13.650	1.792	5.759
	5520	13.572	13.165	1.785	5.762
	5640	13.170	12.775	1.778	5.763
	5760	12.650	12.271	1.769	5.754
	5880	12.160	11.795	1.760	5.751
	6000	11.689	11.339	1.750	5.755
	6120	11.189	10.853	1.740	5.746
	6240	10.699	10.378	1.730	5.745
	6360	10.198	9.892	1.718	5.731
	6480	9.708	9.417	1.706	5.731
	6600	9.228	8.951	1.694	5.717
	6720	8.728	8.466	1.681	5.706
	6840	8.247	8.000	1.668	5.701
	6960	7.776	7.543	1.656	5.690
	7080	7.286	7.067	1.639	5.674
	7200	6.786	6.582	1.623	5.666
	7320	6.276	6.088	1.605	5.647
	7465	5.786	5.612	1.586	5.628
	7560	5.325	5.165	1.569	5.604
	7680	4.815	4.670	1.545	5.577
	7800	4.315	4.185	1.523	5.546
	7920	3.824	3.710	1.497	5.518
	8040	3.334	3.234	1.470	5.481
	8160	2.844	2.758	1.441	5.444
	8280	2.334	2.264	1.403	5.389
	8400	1.863	1.807	1.367	5.343
	8520	1.383	1.341	1.318	5.262
	8640	0.902	0.875	1.257	5.148
	8760	0.392	0.381	1.161	4.903
	8880	0.108	0.105	1.065	4.519

Specimen	**V11**		Porosity	43.1	%
Cored from block	II		Void ratio	0.759	
Orientation	Vertical				
Initial height	9.731	cm	Back pressure	Variable, above 80 kPa	
Initial diameter	3.633	cm	Saturation index, B	0.88	
Initial mass	153.7	g			

	Time sec.	σ_3' MPa	σ_1' MPa	ε_1 %	ε_{vol} %
K_0-loading	0	0.113	0.085	0.000	0.000
	84	0.114	0.502	0.033	0.029
	120	0.142	1.067	0.113	0.048
	267	0.158	1.551	0.212	0.114
	405	0.229	2.157	0.417	0.216
	607	0.449	2.897	0.726	0.336
	882	0.868	4.066	1.137	0.561
	1146	1.385	5.396	1.548	0.823
	1410	1.967	6.841	1.959	1.129
	1794	3.019	9.083	2.575	1.615
	2045	3.744	10.597	2.987	1.958
	2431	4.488	12.259	3.603	2.509
	2809	5.075	13.646	4.220	3.076
	3313	5.616	15.008	5.042	3.849
	3820	6.324	16.480	5.864	4.617
	4566	6.757	17.798	7.097	5.800
	5185	7.135	19.045	8.125	6.711
	6186	7.934	20.993	9.769	8.309
	6933	8.500	22.745	11.002	9.504
	7931	8.938	24.258	12.646	11.090
	8933	9.433	25.940	14.291	12.676
	9683	9.915	27.559	15.524	13.862
	10680	10.356	29.308	17.168	15.450
	11430	11.205	31.520	18.401	16.622
	12189	12.198	34.058	19.645	17.953

Specimen	**V13**		Porosity	43.7	%
Cored from block	II		Void ratio	0.777	
Orientation	Vertical				
Initial height	9.787	cm	Back pressure	Variable, above 100 kPa	
Initial diameter	3.644	cm	Saturation index, B	0.79	
Initial mass	153.9	g			

	Time sec.	σ_3' MPa	σ_1' MPa	ε_1 %	ε_{vol} %
K_0-loading	0	0.122	0.092	0.000	0.000
	164	0.207	0.603	0.131	0.137
	390	0.370	1.466	0.417	0.420
	609	0.502	2.239	0.724	0.730
	802	0.681	2.887	1.030	1.039
	1078	0.823	3.457	1.439	1.448
	1340	0.995	3.962	1.848	1.856
	1659	1.203	4.579	2.359	2.370
	2043	1.506	5.329	2.972	2.989
	2539	1.932	6.365	3.789	3.819
	2923	2.282	7.283	4.402	4.438
	3171	2.750	8.224	4.811	4.847
	3426	3.059	9.007	5.220	5.255
	3681	3.454	9.806	5.628	5.663
	3938	4.216	11.136	6.037	6.072
	4194	4.648	12.134	6.446	6.493
	4447	5.201	13.130	6.854	6.902
	4700	5.723	14.202	7.263	7.310
	4953	6.407	15.402	7.672	7.718
	5199	7.084	16.633	8.081	8.127
	5444	7.806	17.844	8.489	8.535
	5697	8.317	18.892	8.898	8.943
	5946	8.845	19.627	9.307	9.365

Specimen	**V2a**		Porosity	42.8	%
Cored from block	I		Void ratio	0.749	
Orientation	Vertical				
Initial height	4.127	cm	Loading direction:		
Initial diameter	3.668	cm			
Initial mass	66.8	g			
Failure:	420	N			
Time to failure:	10:30	min			

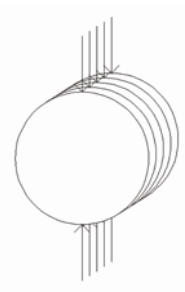

Specimen	**V2b**		Porosity	44.1	%
Cored from block	I		Void ratio	0.787	
Orientation	Vertical				
Initial height	2.933	cm	Loading direction:		
Initial diameter	3.673	cm			
Initial mass	46.6	g			
Failure:	316	N			
Time to failure:	6:00	min			

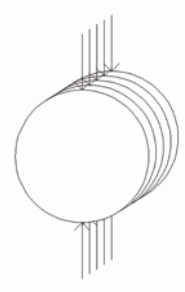

Specimen	**V2c**		Porosity	46.3	%
Cored from block	I		Void ratio	0.863	
Orientation	Vertical				
Initial height	2.810	cm	Loading direction:		
Initial diameter	3.680	cm			
Initial mass	43.0	g			
Failure:	217	N			
Time to failure:	10:00	min			

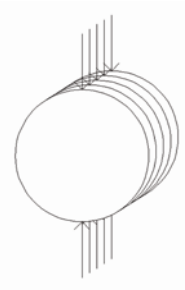

Specimen	**V12a**		Porosity	46.1	%
Cored from block	II		Void ratio	0.856	
Orientation	Vertical				
Initial height	2.410	cm	Loading direction:		
Initial diameter	3.635	cm			
Initial mass	36.1	g			
Failure:	222	N			
Time to failure:	10:40	min			

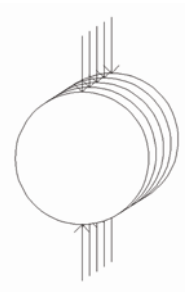

Specimen	**V12b**		Porosity	44.9	%
Cored from block	II		Void ratio	0.813	
Orientation	Vertical				
Initial height	2.331	cm	Loading direction:		
Initial diameter	3.642	cm			
Initial mass	35.9	g			
Failure:	192	N			
Time to failure:	11:50	min			

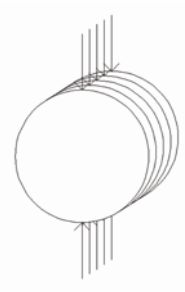

Specimen	**V12c**		Porosity	43.5	%
Cored from block	II		Void ratio	0.771	
Orientation	Vertical				
Initial height	2.242	cm	Loading direction:		
Initial diameter	3.635	cm			
Initial mass	35.2	g			
Failure:	189	N			
Time to failure:	7:50	min			

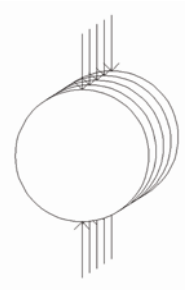

Specimen	**V12d**		Porosity	44.0	%
Cored from block	II		Void ratio	0.785	
Orientation	Vertical				
Initial height	2.496	cm	Loading direction:		
Initial diameter	3.645	cm			
Initial mass	39.1	g			
Failure:	212	N			
Time to failure:	11:05	min			

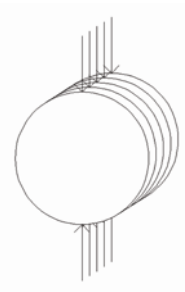

Specimen	**V4a**		Porosity	47.2	%
Cored from block	I		Void ratio	0.894	
Orientation	Vertical				
Initial height	1.933	cm	Loading direction:		
Initial diameter	3.680	cm			
Initial mass	29.1	g			
Failure:	5.5	N			
Time to failure:	5:30	min			

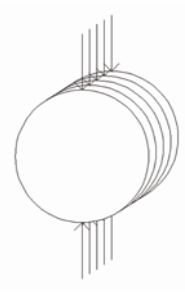

Specimen	**V4b**		Porosity	44.8	%
Cored from block	I		Void ratio	0.812	
Orientation	Vertical				
Initial height	2.021	cm	Loading direction:		
Initial diameter	3.680	cm			
Initial mass	31.8	g			
Failure:	6.5	N			
Time to failure:	2:10	min			

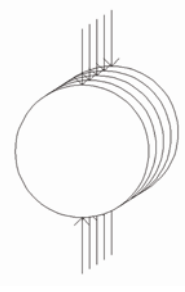

Specimen	**V4c**		Porosity	43.2	%
Cored from block	I		Void ratio	0.762	
Orientation	Vertical				
Initial height	4.004	cm	Loading direction:		
Initial diameter	3.680	cm			
Initial mass	64.8	g			
Failure:	57.8	N			
Time to failure:	6:10	min			

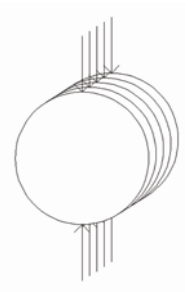

Specimen	**V4d**		Porosity	45.0	%
Cored from block	I		Void ratio	0.820	
Orientation	Vertical				
Initial height	1.679	cm	Loading direction:		
Initial diameter	3.680	cm			
Initial mass	26.3	g			
Failure:	13.2	N			
Time to failure:	3:17	min			

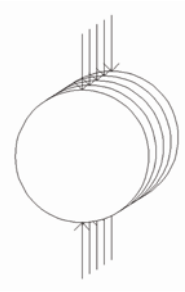

Specimen	**H11a**		Porosity	43.8	%
Cored from block	II		Void ratio	0.779	
Orientation	Horizontal				
Initial height	3.293	cm	Loading direction:		
Initial diameter	3.632	cm			
Initial mass	51.4	g			
Failure:	356	N			
Time to failure:	10:30	min			

Specimen	**H11b**		Porosity	44.2	%
Cored from block	II		Void ratio	0.793	
Orientation	Horizontal				
Initial height	3.312	cm	Loading direction:		
Initial diameter	3.632	cm			
Initial mass	51.3	g			
Failure:	275	N			
Time to failure:	7:30	min			

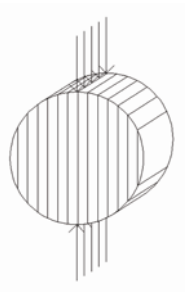

Specimen	**H11c**		Porosity	44.1	%
Cored from block	II		Void ratio	0.788	
Orientation	Horizontal				
Initial height	3.358	cm	Loading direction:		
Initial diameter	3.647	cm			
Initial mass	52.6	g			
Failure:	328	N			
Time to failure:	10:00	min			

Specimen	**H12a**		Porosity	45.2	%
Cored from block	II		Void ratio	0.824	
Orientation	Horizontal				
Initial height	2.568	cm	Loading direction:		
Initial diameter	3.637	cm			
Initial mass	39.2	g			
Failure:	202	N			
Time to failure:	9:00	min			

Specimen	**H12b**		Porosity	46.1	%
Cored from block	II		Void ratio	0.854	
Orientation	Horizontal				
Initial height	2.330	cm	Loading direction:		
Initial diameter	3.632	cm			
Initial mass	34.9	g			
Failure:	120	N			
Time to failure:	8:40	min			

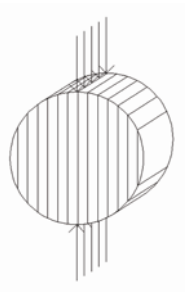

Specimen	**H12c**		Porosity	46.3	%
Cored from block	II		Void ratio	0.861	
Orientation	Horizontal				
Initial height	2.366	cm	Loading direction:		
Initial diameter	3.642	cm			
Initial mass	35.5	g			
Failure:	129	N			
Time to failure:	8:00	min			

Specimen	**H12d**		Porosity	45.0	%
Cored from block	II		Void ratio	0.817	
Orientation	Horizontal				
Initial height	2.535	cm	Loading direction:		
Initial diameter	3.635	cm			
Initial mass	38.8	g			
Failure:	183	N			
Time to failure:	9:40	min			

Specimen	**H3a**		Porosity	44.1	%
Cored from block	I		Void ratio	0.790	
Orientation	Horizontal				
Initial height	2.222	cm	Loading direction:		
Initial diameter	3.670	cm			
Initial mass	35.2	g			
Failure:	15.2	N			
Time to failure:	3:40	min			

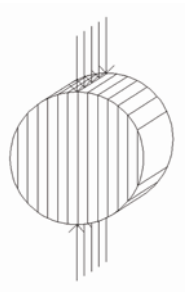

Specimen	**H3b**		Porosity	43.9	%
Cored from block	I		Void ratio	0.783	
Orientation	Horizontal				
Initial height	2.289	cm	Loading direction:		
Initial diameter	3.670	cm			
Initial mass	36.4	g			
Failure:	20.4	N			
Time to failure:	3:10	min			

Specimen	**H3c**		Porosity	43.8	%
Cored from block	I		Void ratio	0.779	
Orientation	Horizontal				
Initial height	2.202	cm	Loading direction:		
Initial diameter	3.670	cm			
Initial mass	35.1	g			
Failure:	9.0	N			
Time to failure:	1:30	min			

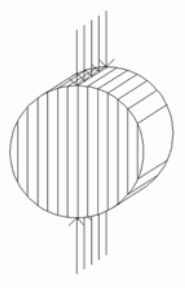

Specimen	**H3d**		Porosity	43.6	%
Cored from block	I		Void ratio	0.772	
Orientation	Horizontal				
Initial height	2.350	cm	Loading direction:		
Initial diameter	3.670	cm			
Initial mass	37.6	g			
Failure:	16.7	N			
Time to failure:	6:40	min			

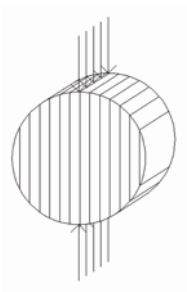

Specimen	**TS1**		Porosity	42.4	%
Orientation	N/A		Void ratio	0.736	
Initial height	39.84	cm			
Initial inside diameter	18.0	cm			
Initial outside diameter	22.0	cm			
Initial mass	7727.8	g			

Time	$\sigma_z' - \sigma_\theta'$	$\tau_{z\theta}$	ε_z	ε_θ	$\gamma_{z\theta}$
sec.	kPa	kPa	%	%	%
0	20.0	0.0	0.0000	N/A	0.0000
180	23.7	0.0	0.0000	N/A	-0.0002
360	85.0	0.1	0.0006	N/A	0.0000
540	106.1	21.0	0.0003	N/A	0.0009
720	108.0	86.7	-0.0002	N/A	0.0034
900	108.6	137.9	-0.0008	N/A	0.0054
1080	108.6	160.1			

Shear band/fracture lines after failure for specimen TS1:

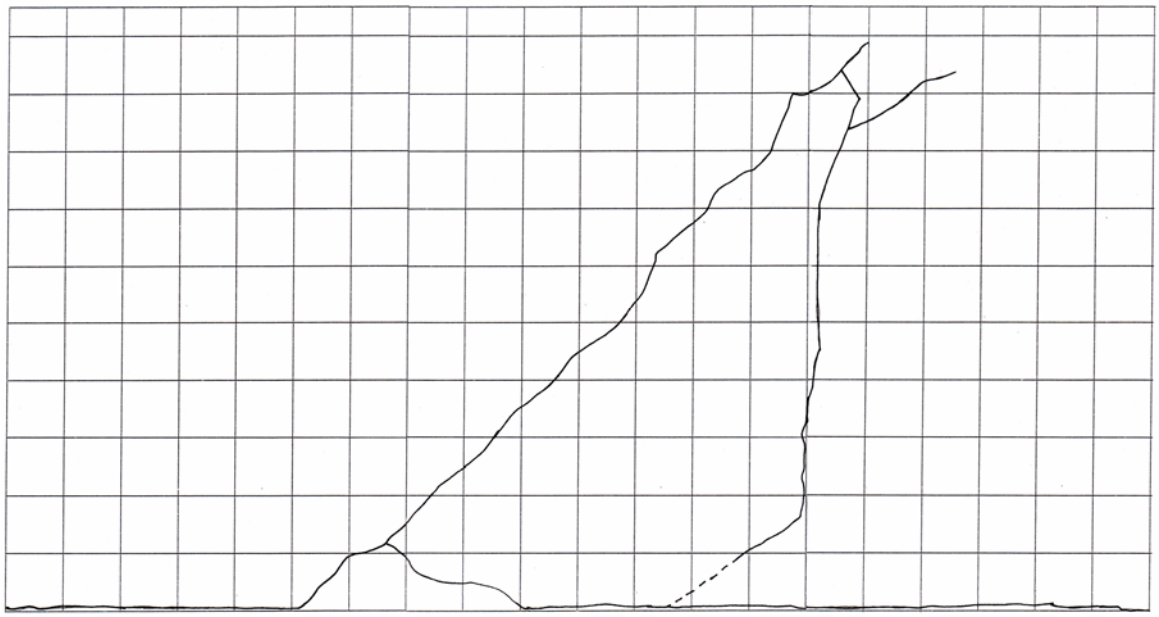

Specimen	**TS2**		Porosity	43.6	%
Orientation	N/A		Void ratio	0.774	
Initial height	39.61	cm			
Initial inside diameter	18.0	cm			
Initial outside diameter	22.0	cm			
Initial mass	7520.1	g			

Time	$\sigma_z' - \sigma_\theta'$	$\tau_{z\theta}$	ε_z	ε_θ	$\gamma_{z\theta}$
sec.	kPa	kPa	%	%	%
0	20.0	0.0	0.0000	0.0000	0.0000
180	94.5	-0.2	0.0012	-0.0003	0.0002
360	185.4	-0.1	0.0028	-0.0008	-0.0002
540	282.4	0.0	0.0043	-0.0010	-0.0002
720	187.7	-0.2	0.0028	-0.0007	-0.0001
900	122.6	-0.2	0.0017	-0.0003	-0.0001
1080	191.8	-0.2	0.0028	-0.0005	0.0001
1260	284.1	-0.2	0.0043	-0.0006	-0.0001
1440	373.4	0.1	0.0061	-0.0009	0.0000
1620	374.6	15.5	0.0061	-0.0006	0.0012
1800	374.9	78.7	0.0060	-0.0006	0.0037
1980	305.1	78.6	0.0050	-0.0005	0.0039
2160	226.6	78.2	0.0036	-0.0006	0.0040
2340	159.8	77.7	0.0024	-0.0010	0.0038
2520	148.6	60.3	0.0024	-0.0007	0.0030
2700	148.4	7.0	0.0023	0.0000	0.0004
2880	235.4	4.4	0.0038	0.0002	0.0002
3060	331.0	3.1	0.0052	0.0003	0.0001
3240	419.7	2.0	0.0069	0.0003	-0.0002
3420	513.1	1.0	0.0082	0.0001	-0.0003
3600	513.5	45.9	0.0083	0.0001	0.0022
3780	513.6	113.8	0.0083	-0.0001	0.0052
3960	443.8	114.4	0.0071	0.0001	0.0053
4140	363.7	114.4	0.0059	0.0005	0.0054
4320	278.3	114.1	0.0046	0.0009	0.0053
4500	275.2	55.8	0.0044	0.0010	0.0025
4680	276.0	7.6	0.0045	0.0012	0.0003
4860	378.3	4.8	0.0061	0.0007	0.0001
5040	378.7	58.4	0.0062	0.0010	0.0026
5220	378.9	114.8	0.0063	0.0004	0.0055
5400	378.8	162.6	0.0061	0.0000	0.0072
5580	470.3	163.1	0.0078	0.0002	0.0074
5760	557.2	162.8	0.0091	-0.0005	0.0074
5940	642.4	162.6	0.0104	-0.0004	0.0073

6120	648.5	108.2	0.0105	-0.0006	0.0048
6300	649.3	71.2	0.0104	-0.0005	0.0030
6480	649.5	8.0	0.0105	-0.0004	0.0000
6660	551.1	4.9	0.0090	0.0000	-0.0001
6840	471.3	3.5	0.0076	0.0005	-0.0001
7020	386.0	2.1	0.0063	0.0008	0.0002
7200	385.8	38.6	0.0064	0.0008	0.0019
7380	385.5	99.1	0.0062	0.0007	0.0044
7560	385.2	155.5	0.0061	0.0011	0.0070
7740	384.8	209.1	0.0060	0.0005	0.0093
7920	384.6	257.2	0.0056	0.0004	0.0113
8100	384.4	307.0	0.0056	0.0001	0.0134
8280	384.2	347.0	0.0056	-0.0001	0.0149
8460	384.2	388.0	0.0055	-0.0004	0.0170
8640	384.0	441.7	0.0058	-0.0009	0.0190

Shear band/fracture lines after failure for specimen TS2:

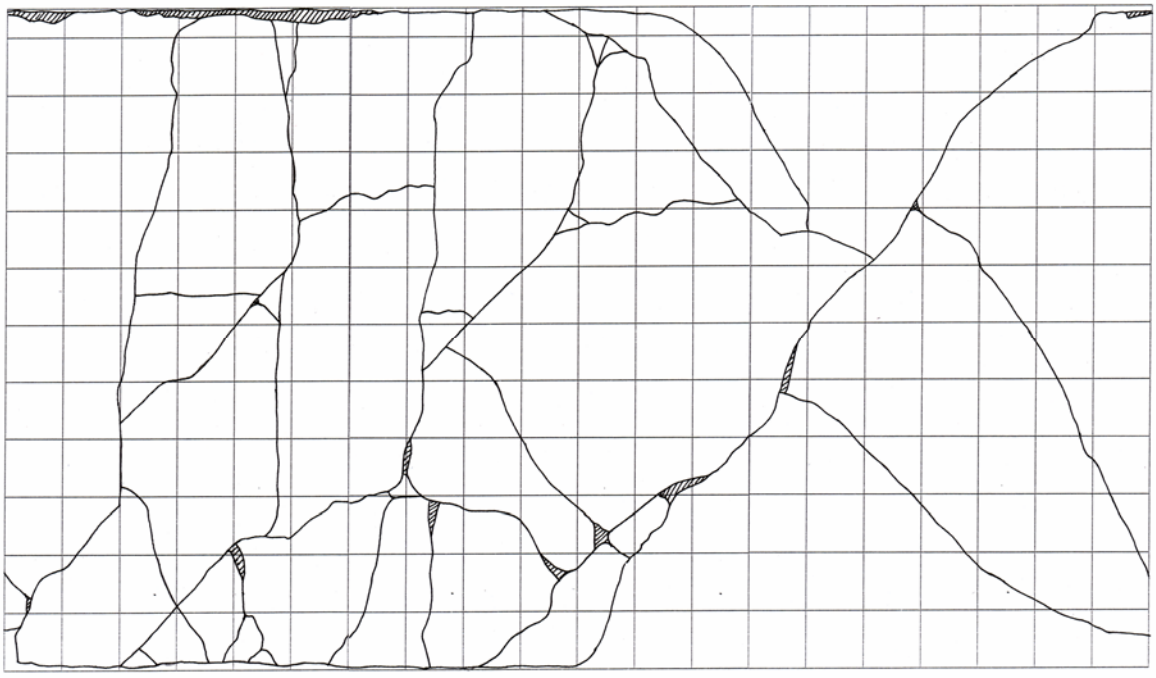

Specimen	**TS3**		Porosity	42.4	%
Orientation	N/A		Void ratio	0.736	
Initial height	39.99	cm			
Initial inside diameter	18.0	cm			
Initial outside diameter	22.0	cm			
Initial mass	7758.1	g			

Time	$\sigma_z' - \sigma_\theta'$	$\tau_{z\theta}$	ε_z	ε_θ	$\gamma_{z\theta}$
sec.	kPa	kPa	%	%	%
0	18.9	0.0	0.0000	0.0000	0.0000
180	70.7	-1.3	0.0008	-0.0003	0.0002
360	135.1	-2.3	0.0016	-0.0005	-0.0002
540	149.2	27.2	0.0017	-0.0006	-0.0002
720	149.7	72.1	0.0017	-0.0007	-0.0001
900	219.7	72.7	0.0027	-0.0009	-0.0001
1080	298.9	72.2	0.0047	0.0000	0.0001
1260	373.9	71.8	0.0056	-0.0003	-0.0001
1440	373.8	41.9	0.0056	-0.0003	0.0000
1620	373.8	3.3	0.0055	-0.0003	0.0012
1800	278.3	0.9	0.0042	-0.0001	0.0037
1980	276.5	40.2	0.0043	0.0002	0.0039
2160	276.5	103.7	0.0043	0.0004	0.0040
2340	364.5	104.9	0.0055	-0.0004	0.0038
2520	439.4	104.8	0.0064	-0.0006	0.0030
2700	508.3	104.4	0.0073	-0.0008	0.0004
2880	508.7	56.5	0.0073	-0.0008	0.0002
3060	517.0	3.9	0.0071	-0.0008	0.0001
3240	575.7	1.1	0.0081	-0.0007	-0.0002
3420	634.8	0.1	0.0089	-0.0010	-0.0003
3600	637.3	25.5	0.0090	-0.0013	0.0022
3780	638.9	107.1	0.0091	-0.0013	0.0052
3960	639.5	150.2	0.0091	-0.0014	0.0053
4140	543.5	149.9	0.0082	-0.0011	0.0054
4320	476.8	149.2	0.0071	-0.0011	0.0053
4500	368.2	148.8	0.0056	-0.0006	0.0025
4680	366.4	114.8	0.0055	-0.0010	0.0003
4860	366.4	56.3	0.0055	-0.0009	0.0001
5040	366.4	3.4	0.0054	-0.0010	0.0026
5220	460.4	1.0	0.0066	-0.0009	0.0055
5400	540.9	0.2	0.0077	-0.0014	0.0072
5580	618.7	-0.9	0.0086	-0.0015	0.0074

5760	619.5	21.5	0.0089	-0.0015	0.0074
5940	619.8	97.4	0.0089	-0.0017	0.0073
6120	620.0	149.3	0.0089	-0.0015	0.0048
6300	619.9	202.7	0.0089	-0.0017	0.0030
6480	619.8	256.1	0.0005	-0.0020	0.0000
6660	619.9	312.9	0.0005	-0.0020	-0.0001
6840	619.8	363.8	0.0005	-0.0021	-0.0001
7020	619.7	419.8	0.0005	-0.0022	0.0002
7200	619.7	475.2	0.0005	-0.0025	0.0019
7380	619.7	520.9	0.0005	-0.0026	0.0044
7560	619.7	562.2	Failure	Failure	Failure

Shear band/fracture lines after failure for specimen TS3:

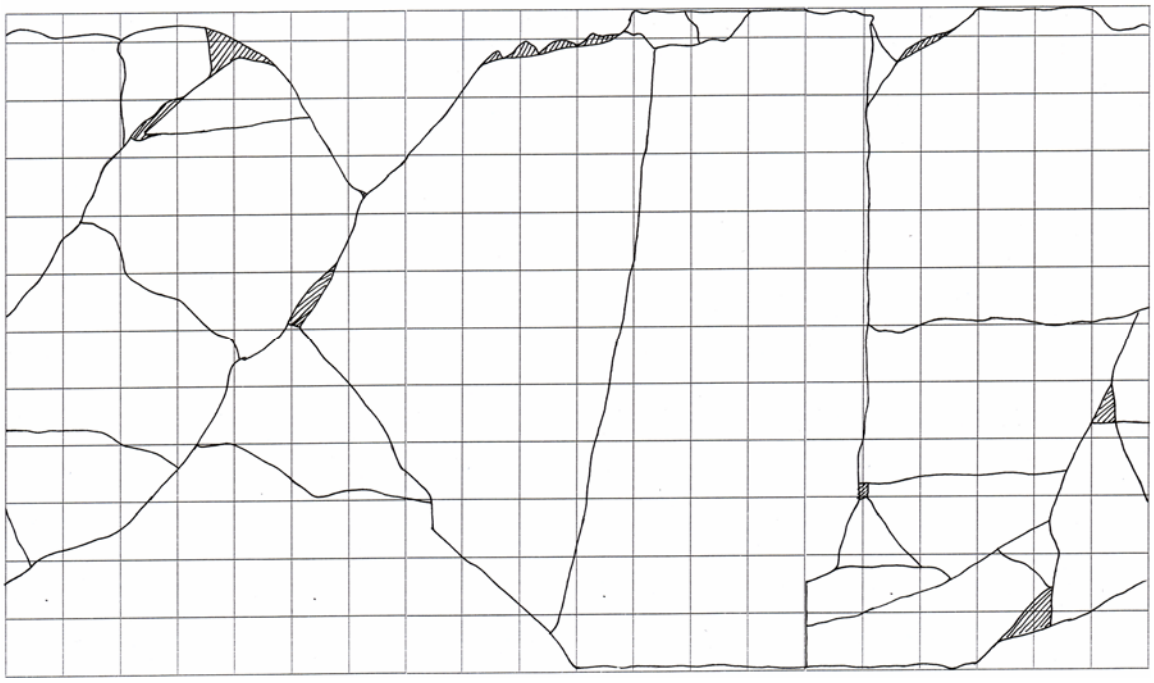

Appendix E: Test Data

Data from triaxial loading on F1-Sand, L1-Sand, L2-Sand, and L8-Sand. Properties of sands are shown in Table E.1.

Table E.1: Properties F1-Sand, L1-Sand, L2-Sand, and L8-Sand.

Sand	F1-Sand	L1-Sand	L2-Sand	L8-Sand
Specific gravity, G_s	2.68	2.65	2.66	2.72
Min. void ratio, e_{min}	0.701	0.679	0.540	0.511
Max. void ratio, e_{max}	1.018	0.989	0.851	0.724
D_{10} (mm)	0.15	0.16	0.37	0.095
D_{60} (mm)	0.22	0.28	0.58	0.28
Coefficient of uniformity, C_u	1.47	1.75	1.57	2.95

Sand:	F1-Sand
Test no.:	1
Void ratio:	0.644
Relative density:	118.0 %

σ_3'	σ_1'	ε_1	ε_{vol}
-	-	%	%
0.703	0.703	0.000	0.000
0.703	1.479	0.271	0.140
0.703	1.780	0.541	0.204
0.703	2.178	1.083	0.245
0.703	2.487	1.624	0.212
0.703	2.707	2.165	0.111
0.703	2.889	2.706	-0.033
0.703	3.126	3.789	-0.357
0.703	3.257	4.871	-0.723
0.703	3.341	6.089	-1.248
0.703	3.349	7.442	-1.762
0.703	3.339	8.796	-2.250
0.703	3.254	10.149	-2.686
0.703	3.214	11.502	-3.024
0.703	3.129	12.855	-3.350
0.703	3.046	14.208	-3.629
0.703	2.992	15.562	-3.870
0.703	2.750	17.591	-4.218

Sand:	F1-Sand
Test no.:	2
Void ratio:	0.637
Relative density:	120.2 %

σ_3'	σ_1'	ε_1	ε_{vol}
-	-	%	%
2.109	2.109	0.000	0.000
2.109	3.803	0.271	0.138
2.109	4.608	0.542	0.228
2.109	5.700	1.084	0.337
2.109	6.468	1.626	0.375
2.109	7.052	2.168	0.361
2.109	7.483	2.710	0.306
2.109	8.015	3.794	0.133
2.109	8.385	4.878	-0.094
2.109	8.611	6.098	-0.400
2.109	8.735	7.453	-0.739
2.109	8.672	8.808	-1.072
2.109	8.541	10.163	-1.373
2.109	8.324	12.209	-1.750

Sand:	F1-Sand
Test no.:	3
Void ratio:	0.591
Relative density:	134.7 %

σ_3'	σ_1'	ε_1	ε_{vol}
-	-	%	%
7.030	7.030	0.000	0.000
7.030	10.767	0.271	0.116
7.030	13.297	0.543	0.236
7.030	16.808	1.085	0.417
7.030	19.258	1.628	0.528
7.030	20.857	2.171	0.576
7.030	22.012	2.714	0.588
7.030	23.786	3.799	0.546
7.030	25.183	4.885	0.411
7.030	26.083	6.106	0.244
7.030	26.658	7.463	-0.030
7.030	26.577	8.820	-0.301
7.030	25.997	10.176	-0.525
7.030	25.025	11.574	-0.712

Sand:	F1-Sand
Test no.:	4
Void ratio:	0.615
Relative density:	127.1 %

σ_3'	σ_1'	ε_1	ε_{vol}
-	-	%	%
21.092	21.092	0.000	0.000
21.092	33.199	0.385	0.319
21.092	38.570	0.771	0.544
21.092	45.200	1.541	0.835
21.092	50.122	2.312	1.061
21.092	53.989	3.083	1.245
21.092	56.829	3.854	1.367
21.092	60.865	5.395	1.517
21.092	63.515	6.936	1.580
21.092	65.674	8.671	1.586
21.092	67.424	10.597	1.552
21.092	68.177	12.524	1.467
21.092	68.507	14.451	1.361
21.092	68.437	16.378	1.250
21.092	68.071	18.304	1.145
21.092	67.509	20.231	1.048
21.092	66.883	22.158	0.966
21.092	66.074	24.085	0.892
21.092	65.695	25.062	0.863

Sand:	F1-Sand
Test no.:	5
Void ratio:	0.624
Relative density:	124.3 %

σ_3'	σ_1'	ε_1	ε_{vol}
-	-	%	%
42.184	42.184	0.000	0.000
42.184	57.968	0.387	0.353
42.184	66.018	0.774	0.592
42.184	76.775	1.547	1.026
42.184	84.678	2.321	1.417
42.184	90.893	3.095	1.744
42.184	96.011	3.868	2.034
42.184	103.513	5.416	2.487
42.184	109.250	6.963	2.865
42.184	114.565	8.704	3.243
42.184	118.432	10.638	3.548
42.184	121.575	12.573	3.817
42.184	123.867	14.507	4.050
42.184	125.568	16.441	4.245
42.184	126.911	18.375	4.437
42.184	128.036	20.309	4.610
42.184	128.542	22.244	4.769
42.184	128.718	24.178	4.916
42.184	128.394	26.112	5.052
42.184	127.790	28.046	5.183

Sand:	F1-Sand
Test no.:	6
Void ratio:	0.629
Relative density:	122.7 %

σ_3'	σ_1'	ε_1	ε_{vol}
-	-	%	%
70.307	70.307	0.000	0.000
70.307	86.007	0.389	0.289
70.307	97.305	0.778	0.598
70.307	112.843	1.556	1.125
70.307	124.781	2.335	1.620
70.307	134.378	3.113	2.057
70.307	142.259	3.891	2.456
70.307	155.013	5.447	3.163
70.307	164.849	7.004	3.755
70.307	173.947	8.755	4.365
70.307	182.074	10.700	4.947
70.307	188.676	12.646	5.471
70.307	194.146	14.591	5.947
70.307	198.456	16.537	6.352
70.307	202.449	18.482	6.751
70.307	205.332	20.428	7.098
70.307	208.306	22.374	7.445
70.307	210.443	24.319	7.908
70.307	212.236	26.265	8.351

Sand:	L1-Sand
Test no.:	1
Void ratio:	0.620
Relative density:	119.0 %

σ_3'	σ_1'	ε_1	ε_{vol}
-	-	%	%
0.703	0.703	0.000	0.000
0.703	1.926	0.269	0.082
0.703	2.484	0.538	0.087
0.703	3.177	1.077	-0.042
0.703	3.573	1.615	-0.296
0.703	3.785	2.153	-0.587
0.703	3.905	2.692	-0.903
0.703	4.006	3.769	-1.575
0.703	4.080	4.845	-2.311
0.703	4.098	6.057	-3.072
0.703	3.989	7.402	-3.847
0.703	3.903	8.748	-4.578
0.703	3.677	10.094	-5.132
0.703	3.274	12.127	-5.577

Sand:	L1-Sand
Test no.:	2
Void ratio:	0.607
Relative density:	123.2 %

σ_3'	σ_1'	ε_1	ε_{vol}
-	-	%	%
2.109	2.109	0.000	0.000
2.109	3.774	0.270	0.115
2.109	5.194	0.539	0.205
2.109	7.220	1.078	0.275
2.109	8.379	1.617	0.220
2.109	9.026	2.156	0.099
2.109	9.444	2.695	-0.051
2.109	9.964	3.774	-0.423
2.109	10.338	4.852	-0.865
2.109	10.492	6.065	-1.393
2.109	10.535	7.412	-1.951
2.109	10.517	8.760	-2.517
2.109	10.369	10.108	-3.026
2.109	10.199	11.456	-3.513
2.109	9.990	12.803	-3.936
2.109	9.652	14.829	-4.456

Sand:	L1-Sand
Test no.:	3
Void ratio:	0.610
Relative density:	122.3 %

σ_3'	σ_1'	ε_1	ε_{vol}
-	-	%	%
7.031	7.031	0.000	0.000
7.031	9.857	0.270	0.095
7.031	13.401	0.540	0.234
7.031	18.855	1.080	0.458
7.031	22.113	1.619	0.584
7.031	24.227	2.159	0.644
7.031	25.764	2.699	0.663
7.031	28.013	3.779	0.628
7.031	29.516	4.858	0.505
7.031	30.544	6.073	0.319
7.031	31.089	7.422	0.068
7.031	31.032	8.772	-0.196
7.031	30.670	10.121	-0.409
7.031	29.552	12.146	-0.615

Sand:	L1-Sand
Test no.:	4
Void ratio:	0.614
Relative density:	121.0 %

σ_3'	σ_1'	ε_1	ε_{vol}
-	-	%	%
15.468	15.468	0.000	0.000
15.468	22.379	0.388	0.314
15.468	27.793	0.777	0.565
15.468	35.316	1.553	0.979
15.468	40.420	2.330	1.299
15.468	44.076	3.107	1.554
15.468	46.902	3.883	1.745
15.468	50.952	5.437	2.015
15.468	53.652	6.990	2.178
15.468	55.677	8.738	2.279
15.468	57.111	10.680	2.316
15.468	58.812	12.621	2.310
15.468	58.158	14.563	2.269
15.468	57.955	16.505	2.203
15.468	57.350	18.447	2.138
15.468	56.218	21.340	2.053

Sand:	L1-Sand
Test no.:	5
Void ratio:	0.613
Relative density:	121.3 %

σ_3'	σ_1'	ε_1	ε_{vol}
-	-	%	%
42.184	42.184	0.000	0.000
42.184	55.669	0.386	0.391
42.184	64.563	0.772	0.693
42.184	76.606	1.544	1.279
42.184	85.704	2.317	1.834
42.184	92.953	3.089	2.344
42.184	98.697	3.861	2.766
42.184	107.654	5.405	3.529
42.184	114.931	6.950	4.197
42.184	121.307	8.687	4.846
42.184	126.939	10.618	5.457
42.184	131.305	12.548	5.980
42.184	135.074	14.479	6.453
42.184	137.865	16.409	6.850
42.184	140.389	18.340	7.203
42.184	142.421	20.270	7.524
42.184	144.319	23.147	7.953

Sand:	L1-Sand
Test no.:	6
Void ratio:	0.618
Relative density:	119.7

σ_3'	σ_1'	ε_1	ε_{vol}
-	-	%	%
63.276	63.276	0.000	0.000
63.276	74.912	0.393	0.332
63.276	85.774	0.786	0.689
63.276	100.588	1.572	1.392
63.276	112.631	2.358	2.048
63.276	122.362	3.143	2.673
63.276	130.862	3.929	3.212
63.276	144.410	5.501	4.220
63.276	155.378	7.073	5.111
63.276	165.629	8.841	6.015
63.276	175.092	10.806	6.893
63.276	183.395	12.770	7.686
63.276	190.539	14.735	8.388
63.276	196.395	16.699	9.032
63.276	201.563	18.664	9.578
63.276	205.844	20.629	10.066
63.276	209.290	22.593	10.502
63.276	213.536	25.544	11.035

Sand:	L2-Sand
Test no.:	1
Void ratio:	0.577
Relative density:	88.1 %

σ_3'	σ_1'	ε_1	ε_{vol}
-	-	%	%
0.753	0.753	0.000	0.000
0.753	1.773	0.134	0.061
0.753	2.518	0.268	0.074
0.753	3.371	0.537	-0.031
0.753	3.946	1.074	-0.438
0.753	4.179	1.611	-0.945
0.753	4.304	2.148	-1.444
0.753	4.379	2.685	-2.013
0.753	4.410	3.758	-3.349
0.753	4.311	4.832	-4.333
0.753	4.073	6.040	-5.339
0.753	3.728	7.383	-6.169
0.753	3.463	9.387	-6.765

Sand:	L2-Sand
Test no.:	2
Void ratio:	0.586
Relative density:	85.2 %

σ_3'	σ_1'	ε_1	ε_{vol}
-	-	%	%
2.109	2.109	0.000	0.000
2.109	4.272	0.134	0.077
2.109	5.868	0.269	0.115
2.109	8.394	0.538	0.120
2.109	10.407	1.075	-0.088
2.109	11.298	1.613	-0.422
2.109	11.792	2.151	-0.867
2.109	12.073	2.688	-1.382
2.109	12.326	3.763	-2.395
2.109	12.056	4.839	-3.331
2.109	11.312	6.048	-4.222
2.109	10.539	7.392	-4.943
2.109	10.190	8.737	-5.404
2.109	9.988	10.753	-5.995

Sand:	L2-Sand
Test no.:	3
Void ratio:	0.583
Relative density:	86.2 %

σ_3'	σ_1'	ε_1	ε_{vol}
-	-	%	%
7.031	7.031	0.000	0.000
7.031	10.814	0.134	0.077
7.031	13.773	0.269	0.123
7.031	18.540	0.538	0.185
7.031	25.669	1.075	0.224
7.031	30.057	1.613	0.139
7.031	33.031	2.151	-0.062
7.031	34.268	2.688	-0.332
7.031	35.618	3.763	-0.934
7.031	36.124	4.839	-1.536
7.031	35.899	6.048	-2.307
7.031	34.591	7.392	-2.979
7.031	32.686	8.737	-3.450
7.031	31.737	10.081	-3.720
7.031	31.962	12.124	-3.897

Sand:	L2-Sand
Test no.:	4
Void ratio:	0.583
Relative density:	86.2 %

σ_3'	σ_1'	ε_1	ε_{vol}
-	-	%	%
21.092	21.092	0.000	0.000
21.092	34.007	0.388	0.218
21.092	41.425	0.777	0.293
21.092	57.898	1.553	0.504
21.092	68.767	2.330	0.601
21.092	74.286	3.107	0.595
21.092	77.549	3.883	0.542
21.092	80.937	5.437	0.352
21.092	81.844	6.990	0.102
21.092	81.549	8.738	-0.181
21.092	80.192	10.680	-0.451
21.092	78.990	12.621	-0.689
21.092	77.802	14.563	-0.890
21.092	75.931	17.456	-1.110

Sand:	L2-Sand
Test no.:	5
Void ratio:	0.603
Relative density:	79.7 %

σ_3'	σ_1'	ε_1	ε_{vol}
-	-	%	%
42.184	42.184	0.000	0.000
42.184	54.790	0.385	0.143
42.184	62.910	0.771	0.248
42.184	85.795	1.541	0.552
42.184	102.775	2.312	0.899
42.184	112.125	3.083	1.203
42.184	118.116	3.854	1.446
42.184	125.427	5.395	1.867
42.184	129.948	6.936	2.232
42.184	132.528	8.671	2.585
42.184	133.991	10.597	2.940
42.184	134.610	12.542	3.268
42.184	134.933	14.451	3.587
42.184	134.968	16.378	3.891
42.184	134.729	19.268	4.313

Sand:	L2-Sand
Test no.:	6
Void ratio:	0.581
Relative density:	86.8 %

σ_3'	σ_1'	ε_1	ε_{vol}
-	-	%	%
63.277	63.277	0.000	0.000
63.277	79.314	0.391	0.177
63.277	88.588	0.781	0.278
63.277	119.150	1.563	0.688
63.277	139.553	2.334	1.104
63.277	151.660	3.125	1.552
63.277	159.323	3.906	1.906
63.277	170.804	5.469	2.587
63.277	177.969	7.031	3.168
63.277	184.184	8.789	3.780
63.277	189.415	10.742	4.417
63.277	193.310	12.695	4.991
63.277	196.038	14.648	5.534
63.277	197.894	16.602	6.026
63.277	199.567	18.555	6.462
63.277	201.929	21.492	7.067

Sand:	L8-Sand
Test no.:	1
Void ratio:	0.530
Relative density:	91.1 %

σ_3'	σ_1'	ε_1	ε_{vol}
-	-	%	%
0.703	0.703	0.000	0.000
0.703	1.874	0.268	0.097
0.703	2.437	0.537	0.066
0.703	3.023	1.074	-0.159
0.703	3.290	1.611	-0.468
0.703	3.426	2.148	-0.786
0.703	3.535	2.685	-1.219
0.703	3.638	3.758	-2.102
0.703	3.608	4.832	-2.879
0.703	3.544	6.040	-3.691
0.703	3.379	7.383	-4.574
0.703	3.241	8.725	-5.144
0.703	3.108	10.067	-5.674
0.703	2.967	12.077	-6.177

Sand:	L8-Sand
Test no.:	2
Void ratio:	0.537
Relative density:	87.9 %

σ_3'	σ_1'	ε_1	ε_{vol}
-	-	%	%
2.109	2.109	0.000	0.000
2.109	5.321	0.270	0.146
2.109	6.847	0.539	0.155
2.109	8.440	1.078	0.013
2.109	9.210	1.617	-0.217
2.109	9.716	2.156	-0.526
2.109	10.082	2.695	-0.889
2.109	10.398	3.774	-1.654
2.109	10.419	4.852	-2.348
2.109	10.215	6.065	-3.135
2.109	9.555	7.412	-3.803
2.109	9.119	8.760	-4.214
2.109	8.894	10.782	-4.736

Sand:	L8-Sand
Test no.:	3
Void ratio:	0.541
Relative density:	85.9 %

σ_3'	σ_1'	ε_1	ε_{vol}
-	-	%	%
7.031	7.031	0.000	0.000
7.031	14.237	0.269	0.186
7.031	18.955	0.538	0.265
7.031	24.685	1.077	0.274
7.031	27.575	1.615	0.177
7.031	29.473	2.153	0.009
7.031	30.893	2.692	-0.230
7.031	32.159	3.769	-0.761
7.031	32.574	4.845	-1.248
7.031	31.906	6.057	-1.849
7.031	30.085	7.402	-2.354
7.031	27.898	8.748	-2.628
7.031	27.195	10.094	-2.805
7.031	27.462	11.447	-2.893

Sand:	L8-Sand
Test no.:	4
Void ratio:	0.532
Relative density:	90.0 %

σ_3'	σ_1'	ε_1	ε_{vol}
-	-	%	%
21.092	21.092	0.000	0.000
21.092	33.044	0.284	0.211
21.092	42.121	0.568	0.344
21.092	55.212	1.136	0.513
21.092	63.818	1.705	0.586
21.092	69.590	2.273	0.591
21.092	73.274	2.841	0.541
21.092	78.540	3.977	0.348
21.092	81.739	5.114	0.082
21.092	83.314	6.392	-0.289
21.092	84.129	7.812	-0.710
21.092	83.440	9.233	-1.150
21.092	80.972	10.653	-1.553
21.092	78.055	12.074	-1.878
21.092	71.847	14.212	-2.066

Sand:	L8-Sand
Test no.:	5
Void ratio:	0.537
Relative density:	87.9 %

σ_3'	σ_1'	ε_1	ε_{vol}
-	-	%	%
28.123	28.123	0.000	0.000
28.123	40.279	0.284	0.174
28.123	51.627	0.569	0.326
28.123	68.296	1.138	0.546
28.123	79.721	1.707	0.675
28.123	87.300	2.276	0.734
28.123	92.911	2.845	0.744
28.123	100.124	3.983	0.679
28.123	104.561	5.121	0.528
28.123	107.493	6.401	0.298
28.123	108.906	7.824	0.000
28.123	108.842	9.246	-0.312
28.123	106.874	10.669	-0.633
28.123	104.596	12.091	-0.895
28.123	102.248	13.514	-1.111
28.123	98.894	15.651	-1.349

Sand:	L8-Sand
Test no.:	6
Void ratio:	0.528
Relative density:	92.0 %

σ_3'	σ_1'	ε_1	ε_{vol}
-	-	%	%
56.246	56.246	0.000	0.000
56.246	77.190	0.286	0.213
56.246	92.939	0.571	0.394
56.246	118.313	1.143	0.696
56.246	136.459	1.714	0.965
56.246	149.747	2.286	1.155
56.246	159.970	2.857	1.313
56.246	173.989	4.000	1.540
56.246	182.820	5.143	1.684
56.246	191.123	6.429	1.782
56.246	194.195	7.857	1.847
56.246	197.190	9.286	1.884
56.246	198.681	10.714	1.898
56.246	198.604	12.143	1.912
56.246	197.268	13.571	1.916
56.246	195.742	15.000	1.927
56.246	193.274	17.143	1.963

Bibliography

Abelev, A.V. (2001), “Cross-anisotropic behavior of granular material under three-dimensional loading conditions”, Dissertation, The John Hopkins University, Baltimore

Abelev, A.V., Gutta, S.K., Lade, P.V. and Yamamuro, J.A. (2007), “Modeling cross anisotropy in granular materials”, *Journal of Engineering Mechanics*, 130 (8), 919-932

Abelev, A.V. and Lade, P.V. (2003), ”Effects of cross anisotropy on three-dimensional behavior of sand. I: stress-strain behavior and shear banding” *Journal of Engineering Mechanics*, 129 (2), 160-166

Airey, D.W. (1993), “Triaxial testing of naturally cemented carbonate soil”, *Journal of Geotechnical Engineering*, 119 (9), 1379-1398

Al-Ajmi, A.M. and Zimmerman, R.W. (2005), “Relation between the Mogi and the Coulomb failure criteria”, *International Journal of Rock Mechanics and Mining Sciences*, 42 (3), 431-439

Al-Harthi, A.A. (1998), “Effect of planar structures on the anisotropy of Ranyah sandstone, Saudi Arabia”, *Engineering Geology*, 50 (1-2), 49-57

Attewell, P.B. and Sandford, M.R. (1974), “Intrinsic shear strength of a brittle, anisotropic rock - I Experimental and mechanical interpretation”, *International Journal of Rock Mechanics and Mining Sciences & Geomechanics Abstracts*, 11 (11), 423-430

Baig, S., Picornell, M. and Nazarian, S. (1997), “Low strain moduli of cemented sand”, *Journal of Geotechnical and Geoenvironmental Engineering*, 123 (6), 540-545

Baud, P., Klein, E. and Wong, T.-f. (2004), “Compaction localization in porous sandstones: spatial evolution of damage and acoustic emission activity”, *Journal of Structural Geology*, 26, 603-624

Benson, P.M., Meredith, P.G., Platzman, E.S. and White, R.E. (2005), “Pore fabric shape anisotropy in porous sandstone and its relation to elastic wave velocity and permeability anisotropy under hydrostatic pressure”, *International Journal of Rock Mechanics and Mining Sciences*, 42 (7-8), 890-899

Bernabé, Y., Fryer, D.T. and Shively R. M. (1994), “Experimental observations of the elastic and inelastic behaviour of porous sandstones”, *Geophysical Journal International*, 117 (2), 403-418

Bésuelle, P. Desrues, J. and Raynaud, S. (2000), “Experimental characterization of the localization phenomenon inside a Vosges sandstone in a triaxial cell”, *International Journal of Rock Mechanics and Mining Sciences*, 37 (8), 1223-1237

Boonyachut, S. (1977), “Experimental study of the behavior of cohesionless soil during stress reversals”, Ph.D. dissertation, University of California, Los Angeles

Claesson, J. and Bohloli, B. (2002), “Brazilian test: Stress field and tensile strength of anisotropic rocks using an analytical solution”, *International Journal of Rock Mechanics and Mining Sciences*, 39 (8), 991-1004

Clough, G.W., Sitar, N. and Bachus, R.C. (1981), “Cemented sand under static loading”, *Journal of the Geotechnical Engineering Division*, 107 GT6, 799-817

Consoli, N.C., Foppa, D., Festugato. L. and Heineck, K.S. (2007), “Key parameters for strength control of artificially cemented soils”, *Journal of Geotechnical and Geoenvironmental Engineering*, 133 (2), 197-205

Coop, M.R. and Atkinson, J.H. (1993), “The mechanics of cemented carbonate sands”, *Géotechnique*, 43 (1), 53-67

Crawford, B.R., Smart, B.G.D., Main, I.G. and Liakopoulou-Morris, F. (1995), “Strength characteristics and shear acoustic anisotropy of rock core subjected to true triaxial compression”, *International Journal of Rock Mechanics and Mining Sciences & Geomechanics Abstracts*, 32 (3), 189-200

Cuccovillo, T. and Coop, M.R. (1999), “On the mechanics of structured sands” *Géotechnique*, 49 (6), 741-760

Cuss, R.J., Rutter, E.H. and Holloway R.F. (2003), “The application of critical state soil mechanics to the mechanical behaviour of porous sandstones”, *International Journal of Rock Mechanics & Mining Sciences*, 40, 847–862

Dafalias, Y.F., Papadimitriou, A.G. and Li, X.S. (2004), “Sand plasticity model accounting for inherent fabric anisotropy”, *Journal of Engineering Mechanics*, 130 (11), 1319-1333

David, C., Menéndez, B. and Bernabé, Y. (1998), “The mechanical behaviour of synthetic sandstone with varying brittle cement content”, *International Journal of Rock Mechanics and Mining Sciences*, 35 (6), 759-779

Desai, C.S., Jagannath, S.V. and Kundu, T. (1995), “Mechanical and ultrasonic anisotropic response of soil”, *Journal of Engineering Mechanics*, 121 (6), 744-752

Donath, F.A. (1964), “Strength variation and deformational behavior in anisotropic rock”, State of stress in the Earth’s crust, W.R. Judd, ed., American Elsevier Publishing Co., New York, N.Y., 281-297

Duveau, G. and Shao, J.F. (1998), “A modified single plane of weakness theory for the failure of highly stratified rocks”, *International Journal of Rock Mechanics and Mining Sciences*, 35 (6), 807-813

El Bied, A., Sulem, J. and Martineau, F (2002), “Microstructure of shear zones in Fontainebleau sandstone”, Technical Note, *International Journal of Rock Mechanics & Mining Sciences*, 39 (7), 917–932

Elmofty, S.E. and Shokir, E.M.El-M. (2003), “Effect of surface active agents on electrokinetic and wettability changes of reservoir rocks”, *Emirates Journal for Engineering Research*, 8 (1), 35-40

Fernandez, A.L. and Santamarina, J.C. (2001), “Effect of cementation on the small-strain parameters of sand”, *Canadian Geotechnical Journal*, 38 (1), 191-199

Frydman, S., Zeitlen, J.G. and Alpan, I. (1973), “The membrane effect in triaxial testing of granular soils”, *Journal of testing and evaluation*, 1 (1), 37-41

Gatelier, N., Pellet, F. and Loret, B. (2002), “Mechanical damage of an anisotropic porous rock in cyclic triaxial tests”, *International Journal of Rock Mechanics and Mining Sciences*, 39 (3), 335-354

Gautam, R. and Wong, R.C.K. (2006), “Transversely isotropic stiffness parameters and their measurement in Colorado shale”, *Canadian Geotechnical Journal*, 43 (12) 1290-1305

Geiger, E. (1979), Experimental study of the behavior of cohesionless soil during large stress reversals and reorientation of principal stresses" M.S. dissertation, University of California, Los Angeles

Hicher, P.-Y. and Chang, C.S. (2006), "Anisotropic nonlinear elastic model for particulate materials", *Journal of Geotechnical and Geoenvironmental Engineering*, 132 (8), 1052-1061

Hoek, E. (1964), "Fracture of anisotropic rock", *Journal of the South African Institute of Mining and Metallurgy*, 64 (10), 501-518

Holt, R.M., Brignoli, M. and Kenter, C.J. (2000), "Core quality: quantification of coring-induced rock alteration", *International Journal of Rock Mechanics and Mining Sciences*, 37, 889-907

Huang, J.T. and Airey, D.W. (1998), "Properties of artificially cemented carbonate sand", *Journal of Geotechnical and Geoenvironmental Engineering*, 124 (6), 492-499

Jardine, R.J. (1992), "Some observations on the kinematic nature of soil stiffness" *Soils and Foundations*, 32 (2), 111-124

Katsman, R and Aharonov, E. (2006), "A study of compaction bands originating from cracks, notches, and compacted defects", *Journal of Structural Geology*, 28 (3), 508–518

Kim, M.K. and Lade, P.V. (1984), "Modeling rock strength in three dimensions", *International Journal of Rock Mechanics and Mining Sciences and Geomechanical Abstracts*, 21 (1), 21-33

Kim, M.K. and Lade, P.V. (1988), “Single hardening constitutive model for frictional materials I. Plastic Potential Function” *Computers and Geotechnics*, 5, 307-324

Kirkgard, M.M. and Lade, P.V. (1991), “Anisotropy of normally consolidated San Francisco bay mud”, *Geotechnical Testing Journal*, 14 (3), 231-246

Klein, E., Baud P., Reuschlé, T. and Wang, T.-f. (2001), “Mechanical behaviour and failure mode of Bentheim Sandstone under triaxial compression”, *Physics and Chemistry of the Earth (A)*, 26 (1-2), 21-25

Kranz, R.L. (1983), “Microcracks in rocks: A review”, *Tectonophysics*, 100 (1-3), 448-480

Ladd, R.S. (1978), “Preparing test specimens using undercompaction”, *Geotechnical Testing Journal*, 1 (1), 16-23

Lade, P.V. (1977), “Elasto-plastic stress-strain theory for cohesionless soil with curved yield surfaces”, *International Journal of Solids and Structures*, 13 (11), 1019–1035

Lade, P.V. (1981), “Torsion shear apparatus for soil testing”, *Laboratory Shear Strength of Soil*, ASTM STP 740, R.N. Young and F.C. Townsend, Eds., American Society for Testing and Materials, 145-163

Lade, P.V. (1982), “Three-parameter failure criterion for concrete”, *Journal of the Engineering Mechanics Division*, 108 (5), 850-863

Lade, P.V. (1992), “Modification of Single Hardening Model and Determination of parameters of L-8, F-1, L-1, and L-2 Soils”, Report to: Measurement Analysis Corporation 23850 Madison Street, Torrance, California 90505

Lade, P.V. (2005), “Single hardening model for soils: Parameter determination and typical values”, in *Soil Constitutive Models: Evaluation, Selection, and Calibration*, Edited by: J.A. Yamamuro, V.N. Kaliakin, ASCE, Geotechnical Special Publication, 128, 290-309

Lade, P.V. (2007), “Modeling failure in cross-anisotropic frictional materials”, *International Journal of Solids and Structures*, 44 (16), 5146-5162

Lade, P.V. (2008), “Failure criterion for cross-anisotropic soils”, *Journal of Geotechnical and Geoenvironmental Engineering*, 134 (1), 117-124

Lade, P.V. and Inel, S. (1997), “Rotational kinematic hardening model for sand. Part I concept of rotating yield and plastic potential surfaces”, *Computers and Geotechnics*, 21 (3), 183-216

Lade, P.V. and Kim, M.K. (1988)[a], “Single hardening constitutive model for frictional materials II. Yield criterion and plastic work contours”, *Computers and Geotechnics*, 6, 13-29

Lade, P.V. and Kim, M.K. (1988)[b], ”Single hardening constitutive model for frictional materials III. Comparisons with experimental data”, *Computers and Geotechnics*, 6, 31-47

Lade, P.V. and Nelson, R.B. (1987), ”Modelling the elastic behaviour of granular materials”, *International Journal for Numerical and Analytical Methods in Geomechanics*, 11, 521-542

Lade, P.V. and Overton, D.D. (1989), ”Cementation effects in frictional materials”, *Journal of Geotechnical Engineering*, 115 (10), 1373-1387

Lade, P.V. and Yamamuro, J.A. (1997), “Effects of nonplastic fines on static liquefaction of sands”, *Canadian Geotechnical Journal*, 34 (6), 918-928

Lagioia, R. and Nova, R. (1995), “An experimental and theoretical study of the behaviour of a calcarenite in triaxial compression”, *Géotechnique*, 45 (4), 633-648

Lee, D.-H., Jueng, C.H., Chen, J.-W., Lin, H.-M. and Shieh, W.-H. (1999), “Stress paths and mechanical behavior of a sandstone in hollow cylinder tests”, *International Journal of Rock Mechanics and Mining Sciences*, 36 (7), 857-870

Lee, D.-H., Jueng, C.H., Chen, J.-W., Lin, H.-M. and Yeh, S.-H. (2002), “Mechanical behavior of Tien-Liao mudstone in hollow cylinder tests” *Canadian Geotechnical Journal*, 39 (3), 744–756

Leroueil, S. and Vaughan, P.R. (1990), “The general and congruent effect of structure in natural soils and weak rock”, *Géotechnique*, 40 (3), 467-488

Li, L. and Aubertin, M. (2002), “A crack-induced stress approach to describe the tensile strength of transversely isotropic rocks”, *Canadian Geotechnical Journal*, 39, 1-13

Li, X.S. and Dafalias, Y.F. (2002), “Constitutive modeling of inherently anisotropic sand behavior”, *Journal of Geotechnical and Geoenvironmental Engineering*, 128 (10), 868-880

Li, X.S. and Dafalias, Y.F. (2004), “A constitutive framework for anisotropic sand including non-proportional loading”, *Géotechnique*, 54 (1), 41-55

Liao, J.J., Yang, M.-T. and Hsieh, H.-Y. (1997), “Direct tensile behavior of a transversely isotropic rock” *International Journal of Rock Mechanics and Mining Sciences and Geomechanical Abstracts*, 34 (5), 837-849

Lo, S.-C.R., Chu, J. and Lee, I.K. (1989), "A technique for reducing membrane penetration and bedding errors", *Geotechnical Testing Journal*, 12 (4), 311-316

Lockner, D.A. and Beeler, N.M. (2003), "Stress-induced anisotropic poroelasticity response in sandstone", Electronic Proceeding, 16th ASCE Engineering Mechanics Conference, University of Washington, Seattle, WA, July 16-18, 2003

Louis, L., David, C., Metz, V., Robion, P., Menéndez, B. and Kissel C. (2005), "Microstructural control on the anisotropy of elastic and transport properties in undeformed sandstones", *International Journal of Rock Mechanics & Mining Sciences*, 42 (7-8), 911-923

McLamore, R. and Gray, K.E. (1967), "The mechanical behavior of anisotropic sedimentary rocks", *Journal of Engineering for Industry*, Transactions of the ASCE, 89, Series B, (1), 62-73

Measurement Group (1992), "Student manual for strain gage technology", A brief introduction and guide to - Selection, - Instalation, - Instrumentation, *Measurement Group, Inc.*, Bulletin 309D

Muhunthan, B., Chambau, J.L. and Masad, E. (1996), "Fabric effects on the yield behaviour of soils", *Soils and Foundations*, 36 (3), 85-97

Muhunthan, B. and Chambau, J.L. (1997), "Void fabric tensor and ultimate state surface of soils", *Journal of Geotechnical and Geoenvironmental Engineering*, 123 (2), 173-181

Nasseri, M.H.B., Rao, K.S. and Ramamurthy, T. (2003), "Anisotropic strength and deformational behaviour of Himalayan schiests", *International Journal of Rock Mechanics & Mining Sciences*, 40 (1), 3-23

Nova, R., Castellanza, R. and Tamagnini, C. (2003), "A constitutive model for bonded geomaterials subject to mechanical and/or chemical degradation", *International Journal for Numerical and Analytical Methods in Geomechanics*, 27, 705-732

Oda, M. (1972)[a], "Initial fabrics and their relations to mechanical properties of granular material", *Soils and Foundations*, 12 (1), 17-36

Oda, M. (1972)[b], "The mechanism of fabric changes during compressional deformation of sand", *Soils and Foundations*, 12 (2), 1-18

Oda, M. (1972)[c], "Deformation of sand in triaxial compression tests", *Soils and Foundations*, 12 (4), 45-63

Oda, M. and Nakayama, H. (1989), "Yield function for soil with anisotropic fabric", *Journal of Engineering Mechanics*, 115 (1), 89-104

Olsson, W.A. (1999), "Theoretical and experimental investigation of compaction bands in porous rock", *Journal of Geophysical Research*, 104 (B4), 7219-7228

Ord, A., Vardoulakis, I. and Kajewski, R. (1991), "Shear band formation in Gosford Sandstone", *International Journal of Rock Mechanics and Mining Sciences & Geomechanics Abstracts*, 28 (5), 397-409

Papamichos, E. (2004), "Plasticity model for stress-release induced damage", *International Journal of Geomechanics*, 4 (1), 13-18

Pestman, B.J. and Van Munster, J.G. (1996), "An acoustic emission study of damage development and stress-memory effects in sandstone", *International Journal of Rock Mechanics and Mining Sciences & Geomechanics Abstracts*, 33 (6), 585-593

Pietruszczak, S. and Mroz, Z. (2000), "Formulation of anisotropic failure criteria incorporating a microstructure tensor", *Computers and Geotechnics*, 26 (2), 105-112

Pietruszczak, S. and Mroz, Z. (2001), "On failure criteria for anisotropic cohesive-frictional materials", *International Journal for Numerical and Analytical Methods in Geomechanics*, 25 (5), 509-524

Pietruszczak, S., Lydzba, D. and Shao, J.F. (2002), "Modelling of inherent anisotropy in sedimentary rocks", *International Journal of Solids and Structures*, 39 (3), 637-648

Pomeroy, C.D., Hobbs, D.W. and Mahmoud A. (1970), "The effect of weakness-plane orientation on the fracture of Barnsley Hards by triaxial compression", *International Journal of Rock Mechanics and Mining Sciences & Geomechanics Abstracts*, 8 (3), 227-238

Ramez, M.R.H. (1966), "Fractures and the strength of a sandstone under triaxial compression", *International Journal of Rock Mechanics and Mining Sciences & Geomechanics Abstracts*, 4 (3), 257-368

Reddy, K.R. and Saxena, S.K. (1993), "Effects of cementation on stress-strain and strength characteristics of sand", *Soils and Foundations*, 33 (4), 121-134

Risnes, R., Hole, M. and Kwabiah, N.K. (2004), "Chalk-fluid interactions with glycol and brines", *Tectonophysics*, 370, 213-226

Rotta, G.V., Consoli, N.C., Prietto, P.D.M. and Graham, J. (2003), "Isotropic yielding in an artificially cemented soil cured under stress", *Géotechnique*, 53 (5), 493-501

Rowe, P.W. and Barden, L. (1964), "Importance of free ends in triaxial testing", *Journal of the Soil Mechanics and Foundations Division, ASCE*, 90 (SM1), 1-27

Sargand, S.M. and Hazen, G.A. (1987), "Deformation behaviour of shales", *International Journal of Rock Mechanics and Mining Sciences & Geomechanics Abstracts*, 24 (6), 365-370

Saroglou H. and Tsiambaos, G. (2008), "A modified Hoek-Brown failure criterion for anisotropic intact rock", *International Journal of Rock Mechanics and Mining Sciences*, 45 (2), 223-234

Schnaid, F., Prietto, P.D.M. and Consoli, N.C. (2001), "Characterization of cemented sand in triaxial compression", *Journal of Geotechnical and Geoenvironmental Engineering*, 127 (10), 857-868

Scott Jr., T.E. and Abousleiman, Y. (2005), "Acoustic measurements of the anisotropy of dynamic elastic poromechanics moduli under three stress/strain pathways" *Journal of Engineering Mechanics*, 131 (9), 937-946

Sharma, S.S. and Fahey, M. (2003), "Degradation of stiffness of cemented calcareous soil in cyclic triaxial tests", *Journal of Geotechnical and Geoenvironmental Engineering*, 129 (7), 619-629

Sharma, S.S. and Fahey, M. (2004), "Deformation characteristic of two cemented calcareous soils", *Canadian Geotechnical Journal* 41 (6), 1139-1151

Sulem, J. and Ouffroukh, H. (2006), “Shear banding in drained and undrained triaxial tests on a saturated sandstone: Porosity and permeability evolution”, *International Journal of Rock Mechanics and Mining Sciences*, 43 (2), 292-310

Takahashi, M. and Koide, H. (1989), “Effect of the intermediate principal stress on strength and deformation behavior of sedimentary rocks at the depth shallower than 2000 m” *Rock at great depth*, Editors: Maury V. and Fourmaintraux D., Rotterdam: Balkema; 19–26

Talesnick, M.L., Katz, A. and Ringel, M. (2000), “An investigation of the elastic stress-strain behavior of a banded sandstone and a sandstone-like material”, *Geotechnical Testing Journal*, 23 (3), 257-273

Talesnick, M.L. and Ringel, M. (1999), “Completing the hollow cylinder methodology for testing of transversely isotropic rocks: torsion testing”, *International Journal of Rock Mechanics and Mining Sciences*, 36 (5), 627-639

Tien, Y.M., Kuo, M.C. and Juang, C.H. (2006), “An experimental investigation of the failure mechanism of simulated transversely isotropic rocks”, *International Journal of Rock Mechanics and Mining Sciences*, 43 (8), 1163-1181

Tien, Y.M. and Tsao, P.F. (2000), “Preparation and mechanical properties of artificial transversely isotropic rock”, *International Journal of Rock Mechanics and Mining Sciences*, 37, 1001-1012

Tsur-Lavie, Y. and Denekamp, S.A. (1982), “Comparison of size effect for different types of strength tests”, *Rock Mechanics* 15, 243-254

Vatsala, A., Nova, R. and Murthy, B.R.S. (2001), "Elastoplastic model for cemented soils", *Journal of geotechnical and geoenvironmental engineering*, 127 (8), 679-687

Voyiadjis, G.Z. and Kattan, P.I. (2007), "Evolution of fabric tensors in damage mechanics of solids with micro-cracks: Part I – Theory and fundamental concepts", *Mechanics Research Communications*, 34 (2), 145-154

Weibull, W. (1951), "A statistical distribution function of wide applicability", *Journal of Applied Mechanics* 18, 293-297

Whittles, D.N., Yasar, E., Reddish, D.J. and Lloid, P.W. (2002), "Anisotropic strength and stiffness properties of some UK Coal Measure siltstones", *Quarterly Journal of Engineering Geology and Hydrogeology*, 35 (2), 155-166

Wong, R.K.S. and Arthur, J.R.F. (1985), "Induced and inherent anisotropy in sand", *Géotechnique*, 35 (4), 471-481

Wong, T.-f., David, C. and Zhu, W. (1997), "The transition from brittle faulting to cataclastic flow in porous sandstones: Mechanical deformation", *Journal of Geophysical Research*, 102 (B2), 3009-3025

Wu, X.Y., Baud, P. and Wong T.-f. (2000), "Micromechanics of compressive failure and spatial evolution of anisotropic damage in Darley Dale sandstone", *International Journal of Rock Mechanics and Mining Sciences*, 37 (1-2), 143-160

Yamamuro, J.A. and Lade, P.V. (1996), "Drained sand behavior in axisymmetric tests at high pressures", *Journal of Geotechnical Engineering*, 122 (2), 109-119

Yamamuro, J.A. and Lade, P.V. (1997), "Static liquefaction of very loose sands", *Canadian Geotechnical Journal*, 34 (6), 905-917

Yamamuro, J.A. and Lade, P.V. (1999), “Experiments and modeling of silty sands susceptible to static liquefaction”, *Mechanics of Cohesive-frictional Materials*, 4 (6), 545-564

Yu, S. and Dakoulas P. (1993), “General stress-dependent elastic moduli for cross-anisotropic soils”, Journal of Geotechnical Engineering, 119 (10), 1568-1586

Yun, T.S. and Santamarina, J.C. (2005), “Decementation, softening, and collapse: Changes in small-strain shear stiffness in K_0 loading”, *Journal of Geotechnical and Geoenvironmental Engineering*, 131 (3), 350-358